TERRESTRIAL IMPACTS OF THE HOLOCENE ASIAN MONSOON

EDITED BY: Anoop Ambili, Praveen K. Mishra, Stefan Lauterbach,
Joyanto Routh and Nicolas Waldmann
PUBLISHED IN: Frontiers in Earth Science

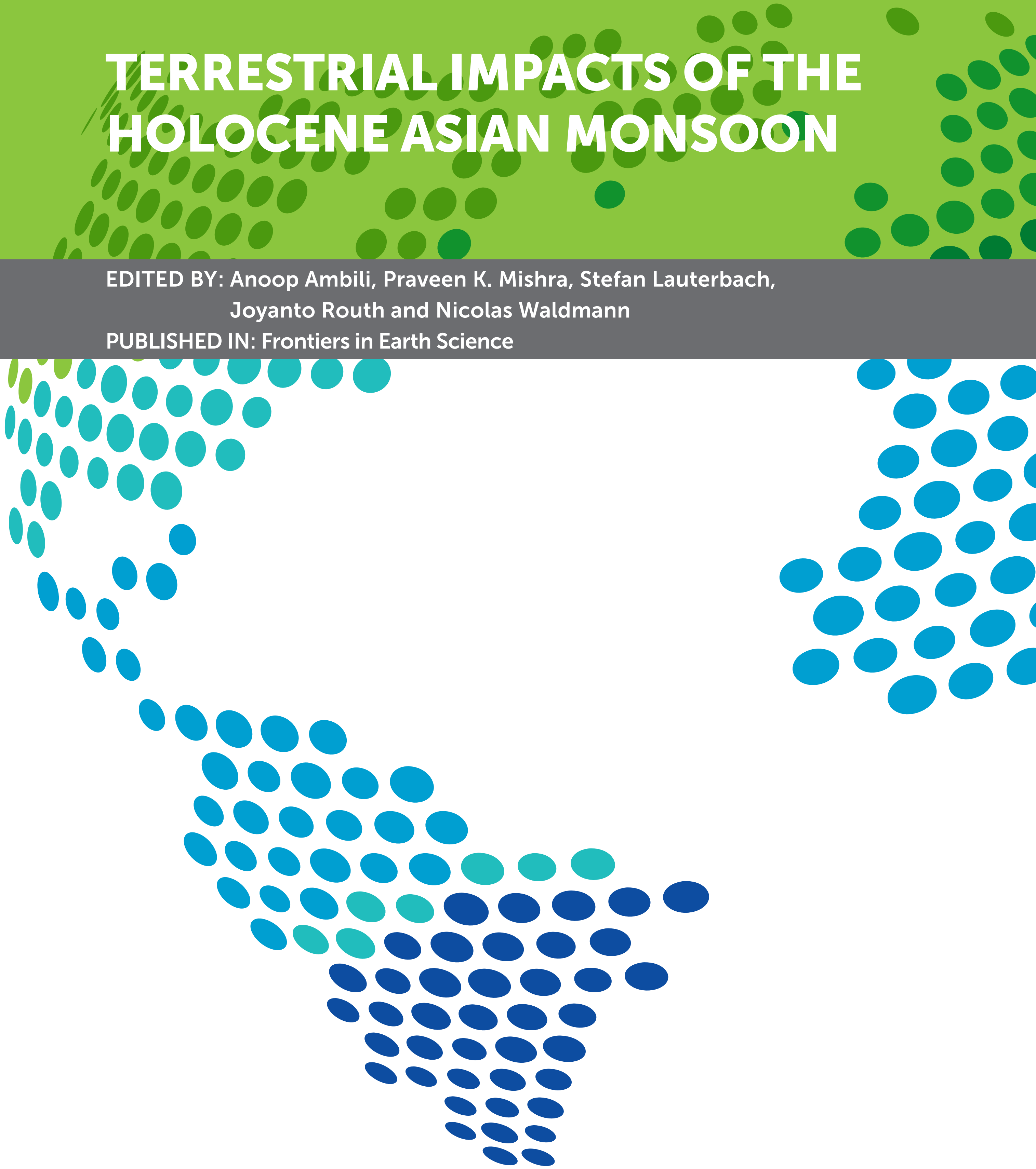

frontiers Research Topics

ISSN 1664-8714
ISBN 978-2-88976-981-0
DOI 10.3389/978-2-88976-981-0

About Frontiers

Frontiers is more than just an open-access publisher of scholarly articles: it is a pioneering approach to the world of academia, radically improving the way scholarly research is managed. The grand vision of Frontiers is a world where all people have an equal opportunity to seek, share and generate knowledge. Frontiers provides immediate and permanent online open access to all its publications, but this alone is not enough to realize our grand goals.

Frontiers Journal Series

The Frontiers Journal Series is a multi-tier and interdisciplinary set of open-access, online journals, promising a paradigm shift from the current review, selection and dissemination processes in academic publishing. All Frontiers journals are driven by researchers for researchers; therefore, they constitute a service to the scholarly community. At the same time, the Frontiers Journal Series operates on a revolutionary invention, the tiered publishing system, initially addressing specific communities of scholars, and gradually climbing up to broader public understanding, thus serving the interests of the lay society, too.

Dedication to Quality

Each Frontiers article is a landmark of the highest quality, thanks to genuinely collaborative interactions between authors and review editors, who include some of the world's best academicians. Research must be certified by peers before entering a stream of knowledge that may eventually reach the public - and shape society; therefore, Frontiers only applies the most rigorous and unbiased reviews.
Frontiers revolutionizes research publishing by freely delivering the most outstanding research, evaluated with no bias from both the academic and social point of view. By applying the most advanced information technologies, Frontiers is catapulting scholarly publishing into a new generation.

What are Frontiers Research Topics?

Frontiers Research Topics are very popular trademarks of the Frontiers Journals Series: they are collections of at least ten articles, all centered on a particular subject. With their unique mix of varied contributions from Original Research to Review Articles, Frontiers Research Topics unify the most influential researchers, the latest key findings and historical advances in a hot research area! Find out more on how to host your own Frontiers Research Topic or contribute to one as an author by contacting the Frontiers Editorial Office: frontiersin.org/about/contact

TERRESTRIAL IMPACTS OF THE HOLOCENE ASIAN MONSOON

Topic Editors:
Anoop Ambili, Indian Institute of Science Education and Research Mohali, India
Praveen K. Mishra, Indian Institute of Science Education and Research Mohali, India
Stefan Lauterbach, University of Kiel, Germany
Joyanto Routh, Linköping University, Sweden
Nicolas Waldmann, University of Haifa, Israel

Citation: Ambili, A., Mishra, P. K., Lauterbach, S., Routh, J., Waldmann, N., eds. (2022). Terrestrial Impacts of the Holocene Asian Monsoon. Lausanne: Frontiers Media SA. doi: 10.3389/978-2-88976-981-0

Table of Contents

frontiers in Earth Science

ORIGINAL RESEARCH
published: 15 April 2021
doi: 10.3389/feart.2021.634354

Multi-Proxy Records of Late Holocene Flood Events From the Lower Reaches of the Narmada River, Western India

Prabhin Sukumaran[1], Dhananjay A. Sant[2]*, K. Krishnan[3], Govindan Rangarajan[4], Nathani Basavaiah[5] and Jean-Luc Schwenninger[6]

[1] Department of Civil Engineering, Chandubhai S. Patel Institute of Technology, Charotar University of Science and Technology, Changa, India, [2] Department of Geology, Faculty of Science, The Maharaja Sayajirao University of Baroda, Vadodara, India, [3] Department of Archaeology and Ancient History, Faculty of Arts, The Maharaja Sayajirao University of Baroda, Vadodara, India, [4] Department of Mathematics, Indian Institute of Science, Bengaluru, India, [5] Indian Institute of Geomagnetism, Mumbai, India, [6] Research Laboratory for Archaeology and the History of Art, School of Archaeology, University of Oxford, Oxford, United Kingdom

Edited by:
Joyanto Routh,
Linköping University, Sweden

Reviewed by:
Manoj Jaiswal,
Indian Institute of Science Education and Research Kolkata, India
Lisa Ely,
Central Washington University, United States

***Correspondence:**
Dhananjay A. Sant
sant.dhananjay-geology@msubaroda.ac.in

Specialty section:
This article was submitted to Quaternary Science, Geomorphology and Paleoenvironment, a section of the journal Frontiers in Earth Science

Received: 27 November 2020
Accepted: 22 March 2021
Published: 15 April 2021

Citation:
Sukumaran P, Sant DA, Krishnan K, Rangarajan G, Basavaiah N and Schwenninger J-L (2021) Multi-Proxy Records of Late Holocene Flood Events From the Lower Reaches of the Narmada River, Western India. Front. Earth Sci. 9:634354. doi: 10.3389/feart.2021.634354

Analyses of a fluvial sedimentary sequence from the lower reaches of the Narmada River establish a record of rhythmic cycles of sediment facies that represent floods during the late Holocene. The south-west Indian monsoon strongly influences the study area, and heavy rainfall or cyclones which originate from either the Bay of Bengal or the Arabian Sea, also affect the region. Optically stimulated luminescence dating places the 8 m thick sediment sequence in the climate transition phase which ranges from the Medieval Warm Period to the Little Ice Age. Multi-proxy analyses including high-resolution granulometry, magnetic susceptibility, ferromagnetic mineral concentration, facies major oxide geochemistry, and micro-fossil records (from two sedimentary units) are used to study these late Holocene flood events. The latter are characterised by multiple sediment facies, depositional events, changes in channel morphology, and distinctive flood signatures. Integration of these records enables to identify two distinct aggradations viz. phase I and phase II, as well as a relative change in channel morphology. The study describes 11 flooding events and their imprints over multi-proxy records. Historic documents and instrumental records from the town of Bharuch referring to floods, movement of channel sand, channel shallowing, and the dysfunction of the ancient port of Bharuch further validate the inferences drawn from the sedimentary sequence. The study exemplifies the need to use high resolution and multi-proxy studies to interpret paleoflood records and climate signatures in order to build archives of monsoonal rivers.

Keywords: Little Ice Age, southwest Indian monsoon, flood events, magnetic susceptibility, ferromagnetic mineral concentration, geochemistry

---

Abbreviations: LIA, Little Ice Age; MWP, Medieval Warm Period; SwIM, Southwest Indian Monsoon; LrNR, Lower reaches of Narmada River; OSL, Optically Stimulated Luminescence; MS, Magnetic susceptibility; FMC, Ferrimagnetic Mineral Concentration; CIA, Chemical Index of Alteration; AP I, Aggradation Phase I and AP II, Aggradation Phase II; MSD, Monsoonal Storm Deposits.

INTRODUCTION

Globally, river terrace sequences are widely recognised as sources for understanding Quaternary paleo-environments over the continent (Gao et al., 2016; Kolb et al., 2016; Stanford et al., 2016; Sun et al., 2016; Vázquez et al., 2016). In India, several studies have revealed that the sedimentary sequences along monsoonal rivers are not different, and preserve Quaternary flood events (**Table 1**). The Narmada River is one of the most significant, westerly flowing rivers that emerges from the Maikala Range (1,057 m a.s.l) of the Amarkantak Plateau in Central India (**Figure 1**). It flows into the Gulf of Cambay in the Arabian Sea about 50 km west of the town of Bharuch. The Narmada River's flood-prone character is substantiated by the consistent presence of a low-pressure track along the Narmada River valley during the monsoonal months (June–September). During these months, the low-pressure track steers the moisture-laden clouds (tropical storms) toward the northwest and north after gathering over the Bay of Bengal and the Arabian Sea, respectively, which regulate the distribution of rainfall, and thereby the floods over the Indian subcontinent. The river terrace sediments from the lower Narmada River valley may be considered a reliable proxy for monsoonal floods, assuming they can be systematically decoded.

The drainage basin of the lower reaches of the Narmada River (LrNR) exposes five distinct lithological terrains, namely, Proterozoic crystalline rocks (Lunavada Group, Champaner Group, and Godhra granite), Cretaceous infra-trappeans (Bagh Group and Lameta Formation), Deccan Trap, Tertiary sediments and Quaternary valley-fill deposits (**Figure 1-III**). The Orsang River forms the major tributary of the Narmada River on the northern bank. It covers a broad catchment over crystalline rocks exposed in the north-western Narmada Basin. The silica sand that fills the present-day channel is brought into the Narmada channel through the Orsang River. The Narmada River and the Karjan River (a major southern bank tributary of the Narmada River), both emerge from the Deccan Trap terrain and remain a significant sediment source other than silica sand.

Geomorphologically, the LrNR draws attention to three prominent landforms, namely, relic alluvial fans, paleo-banks, and neo-banks (**Figure 1-IV**). Each of these landforms is characterised by distinctive litho-units (Bedi and Vaidyanadhan, 1982; Sant and Karanth, 1993; Sridhar and Chamyal, 2010; Sukumaran et al., 2012a,b; Sridhar et al., 2015). The minimum age of these landforms is estimated from the chronology of the sedimentary sequence with alluvial fans dating to the early late Pleistocene (∼90 ka: Chamyal et al., 2002; Joshi et al., 2013), paleo-bank deposits dating to the middle-late Pleistocene (∼24.5–74 ka; Chamyal et al., 2002; Raj, 2008) and neo-bank sedimentary units dating to the late Holocene (Raj and Yadava, 2009; Sridhar et al., 2015).

The present study examines neo-bank sequences that preserve historic flood imprints and help to understand changes in the southwest Indian monsoon (SwIM) dynamics. A high-resolution, multi-proxy fluvial record from the site of Uchediya (21°43′ 2.22″ N, 73° 6′ 26.22″ E) located 10 m a.s.l in the core portion of "the neo-bank" is the focus of this study. This landform has laterally aggraded for about 45 km (from the village of Rajpardi in the east to the village of Hansot in the west) within the southern Narmada paleo-bank (**Figure 1-IV**). The high-resolution granulometric data and micropaleontological findings for the Uchediya site have been discussed previously (Sukumaran et al., 2012a,b). In the present study, we further integrate available findings on granulometric and micropaleontological data with three new dates obtained by optically stimulated luminescence (OSL) as well as high-resolution magnetic susceptibility (MS), ferromagnetic mineral concentration (FMC) and facies representative major oxide geochemistry (FMoG). Our findings lead us to propose an aggradation model with the sequence of change in the channel morphology corresponding to late Holocene climate and flood events.

METHODS AND RESULTS

Chronology of the Uchediya Sequence

Samples for optically stimulated luminescence (OSL) dating (Aitken, 1998) were collected in steel tubes at regular 50 cm intervals along the exposed section whilst taking good care to avoid accidental exposure to sunlight (**Figure 2**). Following detailed sedimentological studies, three samples (X3543, X3544, and X3545) taken from 50, 200, and 800 cm below the modern surface were selected for analysis to bracket the landform's primary aggradation time frame. Sample preparation and measurements were conducted at the luminescence dating laboratory of the Research Laboratory for Archaeology and the History of Art, University of Oxford. Sample preparation took place under low-intensity safe-lighting provided by filtered sodium lamps (emitting at 588 nm). Standard laboratory preparation techniques were applied to yield sand-sized (180–255 μm) grains of quartz for optical dating. These included wet sieving, HCl (10%) treatment to remove carbonates, 30% H_2O_2 treatment to remove organic matter and HF (68%) etching to remove the outer (∼10 mic) rind of quartz grains affected by alpha irradiation and to dissolve feldspathic minerals. Heavy minerals were removed by density gradient separation using a liquid solution of sodium polytungstate (delta = 2.65 gcm $^{-3}$) followed by renewed rinsing in HCl (10%) to eliminate potential fluorite contaminants with a final cleaning in demineralised water. Dried quartz grains were then mounted onto aluminium discs as small (diam. = 2 mm) multigrain (n = 50–100 grains) aliquots using a silicon oil adhesive (Viscasil 60,000).

OSL measurements were conducted using an automated Risø TL/OSL-DA-15 luminescence reader (Bøtter-Jensen, 1997) and are based on a conventional single-aliquot regeneration (SAR) measurement protocol (Murray and Wintle, 2000). Repeat palaeodose measurements were made for each sample (n = 18 or 28), and optical stimulation was provided by blue light-emitting diodes (42 Nichia 470Δ20 nm; 36 mW cm^{-2}). Given the young age of the sediment, the natural and regenerative doses were preheated at a relatively low temperature of 200°C for 10 s and the fixed test doses (which are used to correct for any sensitivity changes) were preheated at a reduced temperature of 180°C for 10 s, before optical stimulation. In order to minimise the contribution of residual feldspathic components

TABLE 1 | Various flood sequence sites studied along monsoonal rivers across the Indian subcontinent.

Sr No	Site	River	Landform	Max age	Min age	No. of flood events	References
1.	Sakarghat	Central Narmada	Terrace within George	1923 ± 86*BP*	690 ± 45*BP*	26	Kale et al., 1997b
2.	Bhuka	Luni	Terrace within George	990 ± 130*BP*	540 ± 80*BP*	21	Kale and Baker, 2006
3.	Guttigarh,	Tapi Upland	Terrace within George	240 ± 50*BP*	156 ± 52*BP*	4–5	Kale et al., 2003
4.	Teska	Tapi Upland	Terrace within George	225 ± 40*BP*	Post-1950	6–9	Kale et al., 2003
5.	Khapa	Tapi Upland	Terrace within George	380 ± 45*BP*	Younger	13	Kale et al., 2003
6.	Chahin Nala	Central Narmada	Terrace within George	Older	1720 ± 185*BP*	4	Ely et al., 1996
7.	Chahin Nala	Central Narmada	Terrace within George	1720 ± 185*BP*	650 ± 70*BP*	5	Ely et al., 1996
8.	Dhamnacha	Lower Narmada	Terrace	1350 ± 80*BP*	360 ± 65*BP*	–	Sridhar et al., 2016
9.	Ranipura	Lower Narmada	Terrace	2230 ± 90*BP*	1010 ± 80*BP*	–	Sridhar et al., 2015
10.	Srisailam	Krishna	Terrace within George	1690 ± 50*BP*	1025 ± 55*BP*	58	Kale and Baker, 2006
11.	Kodepudi	Godavari River	Terrace within George	2108 ± 58*BP*	780 ± 60*BP*	∼24	Kale and Baker, 2006
12.	Racherla	Penner	Abandoned channel, Paleoflood and Pond deposits	2860 ± 310*BP*(*OSL*)	90 ± 15*BP*(*OSL*)	–	Thomas et al., 2007
13.	Punasa	Central Narmada	Terrace within George	1450 ± 80*BP*	445 ± 60*BP*	–	Baker, 1995
14.	Siddapur	Kaveri Upland	Terrace	7900 ± 700(*OSL*)	1700 ± 200(*OSL*)	∼6	Kale et al., 2010
15.	Timbi lake	Dhadhar	Lake deposits	4220 ± 30*BP*	250 ± 30*BP*	–	Sridhar et al., 2020
16.	Uchediya	Lower Narmada	Regional Terrace	565 ± 60*Years*	195 ± 25*Years*	2-AP I 11-AP II	Present study

to the quartz signal, each OSL measurement was proceeded by an infrared bleach at 50°C for 25 s before blue-light stimulation (Banerjee et al., 2001). The ultraviolet OSL emission of quartz at ∼370 nm was detected using an Electron Tubes Ltd 9235QA photomultiplier tube fitted with a blue-green sensitive bialkali photocathode and 7.5 mm of Hoya U-340 glass filter. Laboratory doses used for constructing dose-response curves were given using the ^{90}Sr/^{90}Y beta source housed within the reader. This source was calibrated against a gamma irradiated quartz standard supplied by Risø (Hansen et al., 2015).

The recorded OSL data were analysed with the "*Analyst*" software developed by Duller (2015), and a weighted mean equivalent dose (De) was calculated using the "*Luminescence*" package developed by Kreutzer et al. (2012) for the statistical programming language "*R*." The concentrations of radioactive elements (potassium, rubidium, thorium, and uranium) were determined by elemental analysis using ICP-MS/AES and converted to dose rates and luminescence age estimates using the conversion factors of Guérin et al. (2011) and the "*DRAC*" software developed by Durcan et al. (2015). The contribution of cosmic radiation to the total dose rate was calculated as a function of latitude, altitude and burial depth based on data by Prescott and Hutton (1994) and assuming an average overburden density of 1.9 gcm^{-3}. The sediment's recorded moisture content was found to be very low, with the upper sample containing only 3% water and the deeper samples X3544 and X3545, both providing even lower values around 1%. These measurements are not considered to be reliable, and the sediment almost certainly lost its pore water during the long 2 year storage period before the samples were sent for analysis. Therefore, the dose rate calculations are based on a more realistic estimated mean water content of 6% for sample X3543, 8% for X3544 and 10% for the basal sample X3545. A relatively large error of ± 5% was attached to each value to further compensate for this uncertainty, including likely seasonal variations in the sediment's uptake of water.

The paleodose (De) was determined by integrating the counts from the first second of the OSL decay curve, using the final 5 s as background noise. Dose response curves were fitted using a double saturating exponential function and are based on the weighted mean value derived from individual multigrain OSL measurements. A systematic laboratory reproducibility uncertainty of four per cent was added to each De measurement error to account for uncertainties in the calibration of the beta source. The majority of aliquots displayed high sensitivity, and the decay curves typically show a fast decreasing OSL signal. Measurements also showed a well-defined 110°C TL peak which is characteristic of quartz. Few aliquots revealed a noticeable response to infrared light stimulation, thereby confirming that good sample preparation had been achieved and/or relative sparseness of feldspathic components. Repeat measurements of the luminescence signal resulting from the first regeneration dose (recycling test) indicate that the adopted SAR procedure provides adequate correction for sensitivity changes with the mean value being close to unity (1.03). The same is also valid for recuperation which is generally below 3% as monitored by the OSL response after a regeneration dose of zero. A dose recovery test using the same preheat and measurement procedures as outlined above, was also performed on two aliquots from each sample (total $n = 6$). For this, mineral grains were first bleached in daylight for 3 h before they were given a small laboratory dose equivalent to 0.67Gy. The recovered mean dose for all six aliquots was 0.68 Gy (within 3%), thus confirming the suitability of the adopted measurement procedures. OSL age estimates are shown in **Table 2** alongside the radioactivity data and are based on a weighted mean. Kernel density plots

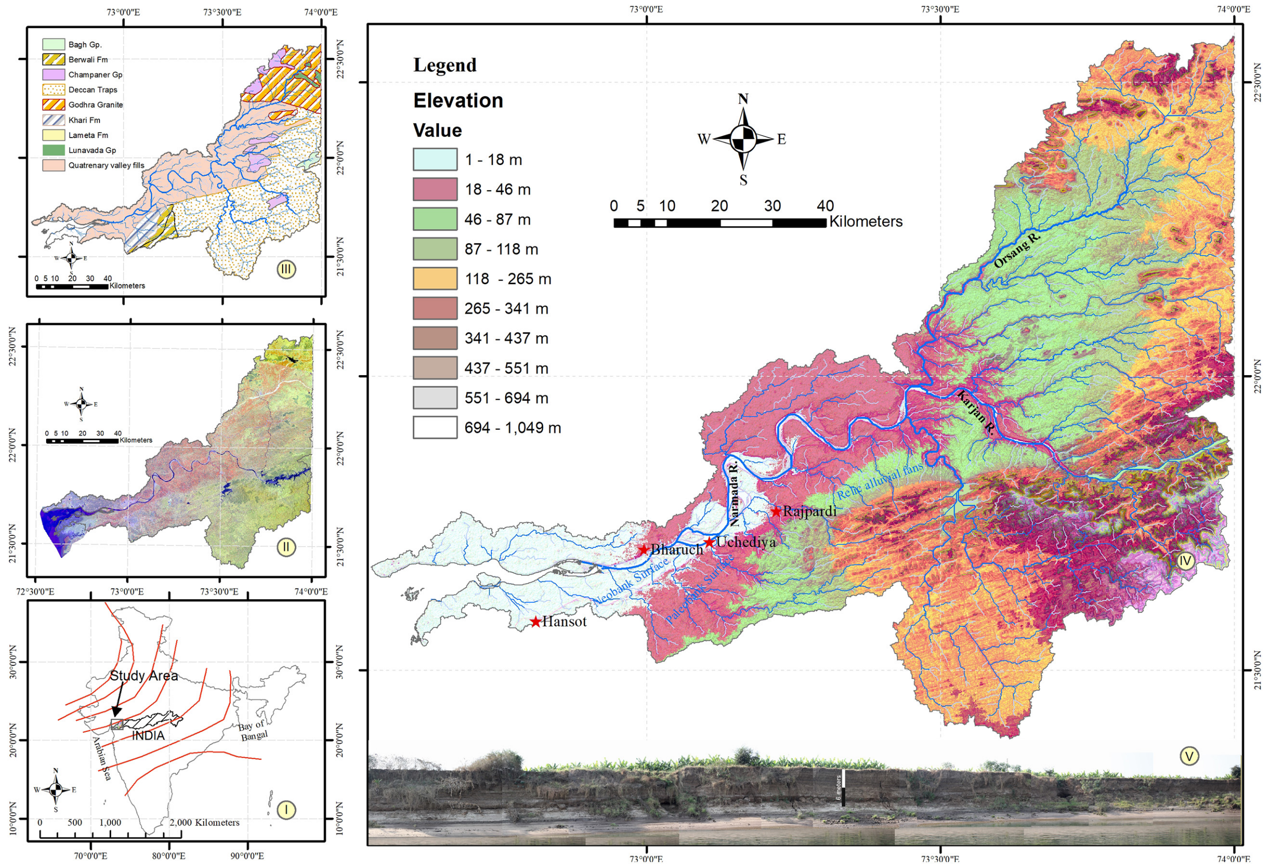

FIGURE 1 | (I) Index map of the study area showing normal withdrawal track (source: Indian Meteorological Department) of SW Indian monsoon **(II)** Landsat 8, false colour compost map of the study area with band composites Band 5 (NIR), Band 6 (SWIR-1) and Band 2 (Blue). **(III)** Geological map of the study area modified after the Geological Survey of India Geological map (https://bhukosh.gsi.gov.in/Bhukosh/MapViewer.aspx). **(IV)** Geomorphological map of the study area. Locations of important places mentioned in the text are marked. The neobank surface is bounded within the elevation of 1–18 m and the paleo-bank surface is bound between 18 and 46 m. Above 46 m the topography is produced by relict fanglomerates and upland rocks. **(V)** A regional view of the neobank sequence.

featuring the distribution of individual De values for each sample are presented in **Figure 3**, along with additional statistical information. Despite their fluvial nature, neither of the three samples was considered to suffer from partial bleaching and provided acceptable overdispersion levels ranging from 16 to 45%. Four high outlier values were identified among the 28 aliquots measured for sample X3545, and these were removed from the calculation of the weighted mean paleodose.

Sample X3543 collected from a depth of 50 cm provided an age of 195 ± 25 years, sample X3544 from a depth of 200 cm provided an age of 625 ± 45 years, and sample X3545 from a depth of 800 cm (base of the sequence) provided an age of 565 ± 60 years. Sample X3544 was collected from the interface of two sub-facies in the sediment sequence. This age estimate could be an overestimation of the actual age because the sample was collected from the boundary of coarser and finer sediment sub-facies. In the absence of *in situ* radioactivity measurements with a calibrated gamma-ray spectrometer, it is impossible to correctly assess the external gamma dose contribution to the total dose received by this sample. However, to evaluate the assumption further, we also considered a 50% contribution to the external gamma dose rate from the overlying fine sediment facies (X3543) for the age calculation of X3544. The resultant revised age estimate would be 550 ± 50 years, and this result would be in better agreement with the date of 565 ± 60 years obtained for the underlying basal sample X3545.

The OSL dating results strongly suggest that the bulk of the sediment at the base of the section (from 200 to 800 cm) was deposited within a relatively short period of time. In contrast, the overlaying 200 cm comprising finer facies took around 500 years. A relative maximum age determined using ^{14}C dating on a sequence from the same landform upstream of the Uchediya range dates from 1010 ± 60 to 2230 ± 90 years BP (Sridhar et al., 2015). With the above understanding, the sediment sequence is bracketed between 565 ± 60 years before 2020, i.e., 1395–1515 AD at a depth of 800 cm to 195 ± 25 years before 2020, i.e., 1800–1850 AD at a depth of 50 cm.

High-Resolution Granulometric Records

Sediment samples were collected from a cut open trench of the present-day river bank (**Figure 2**). All 401 samples were collected

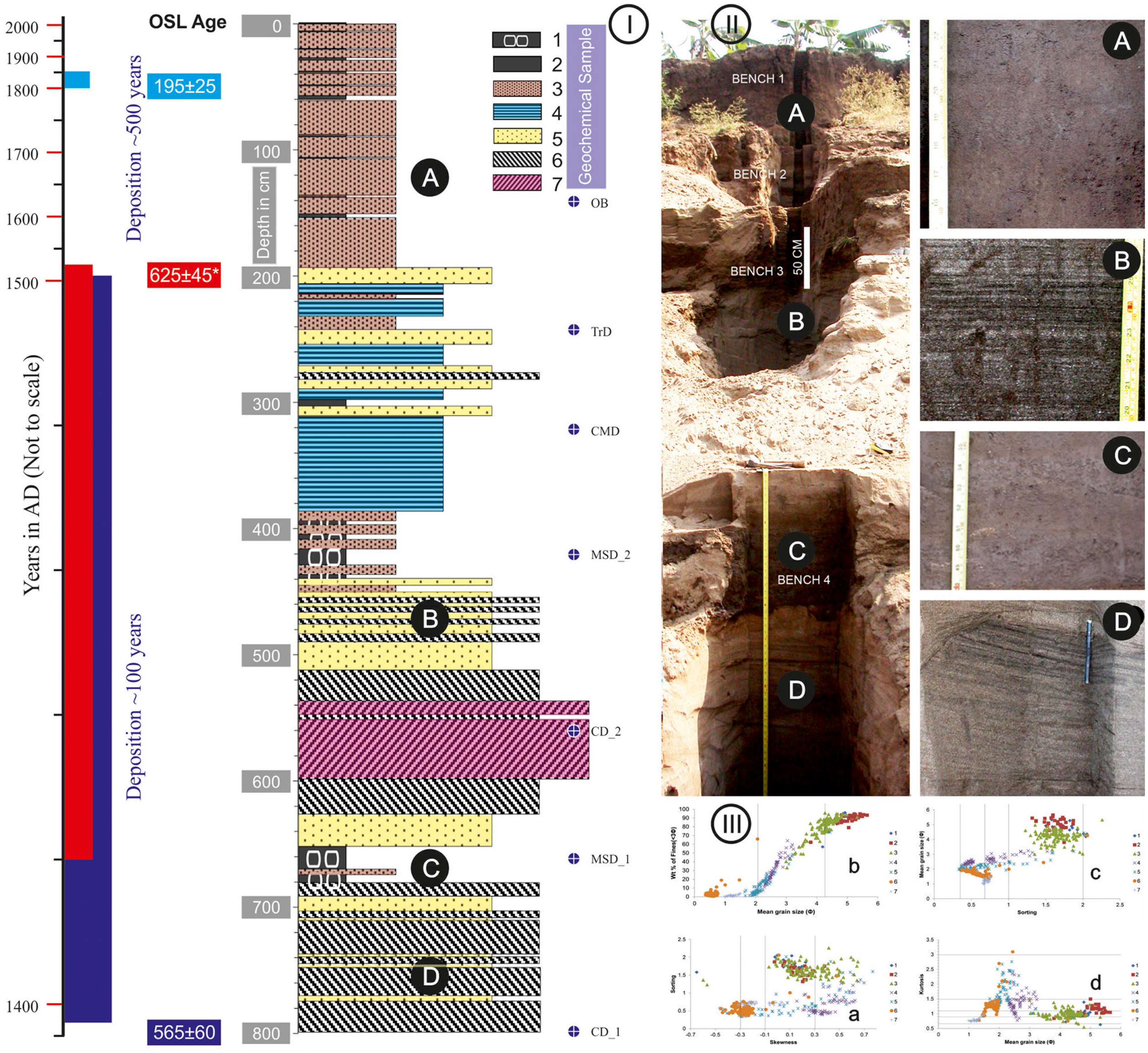

* Refer text for the justifications of over-estimation

FIGURE 2 | Details of Uchediya sequence modified after Sukumaran et al. (2012b) summarising different characteristics of the Uchediya sequence **(I)** Change in sediment facies along depth profile (1, $Fm_{SILT+VFS}$ (T); 2, $Fm_{SILT+VFS}$ (O); 3, $Fm_{SILT+VFS+FS}$; 4, Sl_{FS+VFS}; 5, Sm_{FS+MS}; 6, $St_{MS+FS+CS}$; 7, St_{MS+CS}). CD-Channel deposit; MSD-monsoonal storms deposits; CMD-Channel margin deposits; TrD-Transition deposit; OB-Overbank deposits. **(II)** Filed photograph of a cut-open trench of the Uchediya sequence. **(A–D)** are photographs of different sub-facies. **(III)** Bivariate plots of different granulometric parameters.

TABLE 2 | Summary of OSL dating and radioactivity data.

Lab. code	Field code	Depth (cm)	Water (%)	K (%)	Th (ppm)	U (ppm)	External (Gy/ka)	Cosmic (Gy/ka)	Total dose rate (Gy/ka)	Number aliquots	De (Gy)	OSL age[b] (years)
X3543	DUCH1	50	6±5	1.00	10.3	1.9	0.955±0.06	0.19±0.02	2.18±0.12	18	0.43±0.05	195±25
X3544	DUCH4	200	8±5	1.27	5.9	1.1	0.722±0.04	0.15±0.05	*1.89±0.12*	28	1.18±0.04	*625±45*
X3545	DUCH16	800	10±5	1.26	2.8	0.7	0.526±0.04	0.08±0.01	1.50±0.11	28	0.85±0.06	565±60

[a] *Measurements were made on dried, homogenised and powdered material by ICP-MS/AES with an assigned systematic uncertainty of ± 10%. Dry beta and gamma dose rates were calculated from these activities and were adjusted for the estimated field water content.*

[b] *The age datum refers to AD 2020 and the luminescence dates are based on a weighted mean palaeodose.*

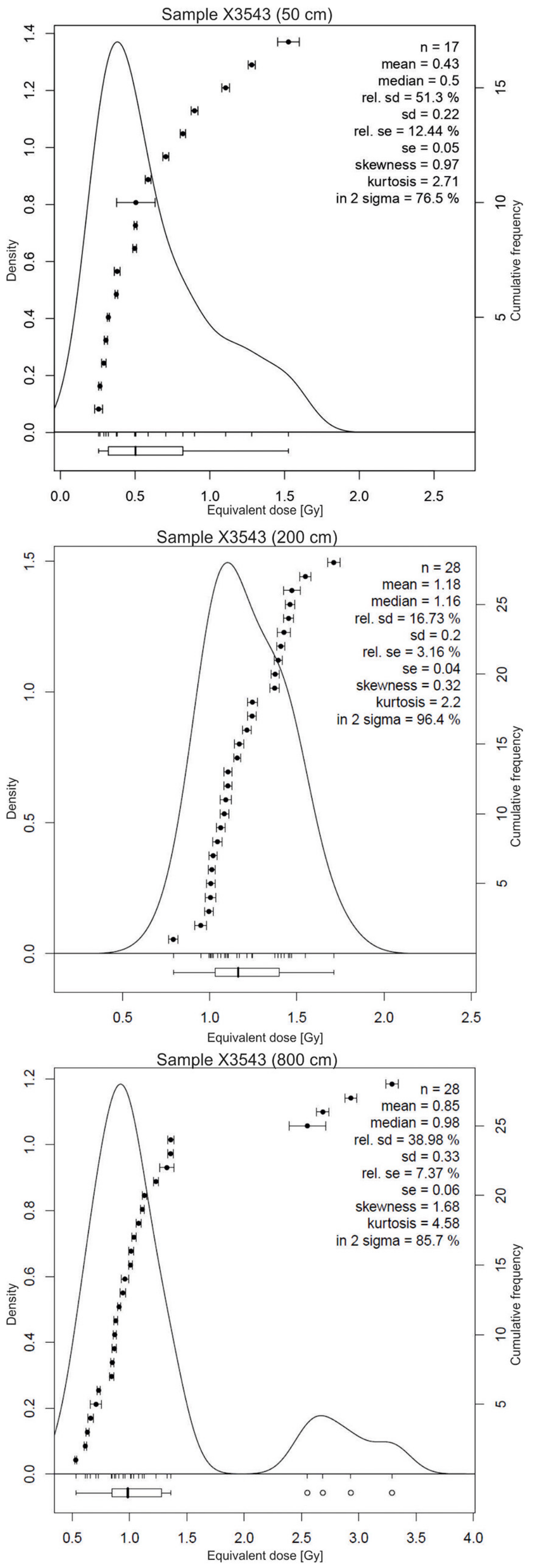

FIGURE 3 | Kernel density plots featuring the distribution of individual paleodose values and associated statistical summary for each sample.

TABLE 3 | Summary of sub-facies notations, code and their description.

Sr No	Sediment facies name	Sub-facies code	Sediment facies description
1.	Fm$_{SILT+VFS(T)}$	1	Massive muddy sub-facies with silt and very fine sand with the presence of foraminifera.
2.	Fm$_{SILT+VFS(O)}$	2	Massive muddy sub-facies, with silt and very fine sand without foraminifera.
3.	Fm$_{SILT+VFS+FS}$	3	Massive muddy sub-facies with silt, very fine sand and fine sand.
4.	Sl$_{FS+VFS}$	4	Laminated sandy facies with fine sand and very fine sand
5.	Sm$_{FS+MS}$	5	Massive sandy facies with fine sand and medium sand
6.	St$_{MS+FS+CS}$	6	Trough cross-bedded sandy facies with medium sand, fine sand and coarse sand
7.	St$_{MS\ +CS}$	7	Trough cross-bedded sandy facies with medium sand, fine sand and coarse sand

at 2 cm intervals from 8 m thick sedimentary deposits. High-resolution granulometric data were generated using the sieve and pipette method, and their sedimentological relevance was discussed earlier by Sukumaran et al. (2012b). In the present study, we attempt to integrate granulometric data with other proxies, such as MS and FMC, to determine the tracer capturing the flooding phases.

The description of facies and sub-facies of the Uchediya sediment sequence was decoded using high-resolution granulometric data by applying the cluster analysis method to 14 grain size fractions from 401 samples (Sukumaran et al., 2012b). Each cluster was quantitatively determined, compared, evaluated, and supplemented with field base details to derive the sediment sub-facies. The terminology of the sediment sub-facies was adopted based on the abundance of grain size and primary sedimentary structures in line with lithofacies classification after Miall (1978, 1985) and Martinius (2000). The Uchediya sequence is broadly represented by two facies, viz. sandy facies and muddy facies. The muddy facies are classified into three sub-facies, namely, 1 [Fm$_{SILT+VFS}$ (T)], 2 [Fm $_{SILT+VFS}$ (O)] and 3 (Fm$_{SILT+VFS+FS}$). The sandy facies are further classified into four sub-facies, viz. 4 (Sl $_{FS+VFS}$), 5 (Sm $_{FS+MS}$), 6 (St $_{MS+FS+CS}$), and 7 (St $_{MS\ +CS}$) (**Table 3** and **Figure 2**).

The sediment facies deduced from high-resolution granulometric data revealed that the Uchediya sediment sequence was aggraded in two distinct phases, namely, aggradation phase I (AP-I) and aggradation phase II (AP-II) (**Figure 4**). AP-I represents a 608 cm thick sandy facies deposited between 194 and 802 cm. The chronological bracket of the sequence suggests that the sequence aggraded in a relatively short period of time. Three distinct sediment sub-facies characterise AP-I. The sub-facies suggest that enough energy conditions were available to mobilise sand viz. channel deposits (couplets of sub-facies 6 and 5 as well as sub-facies 7 and 6) followed by channel margin deposits (sub-facies 4) and transitional deposits (intercalation of sub-facies 2-3-4-5-6; **Figure 2-I**).

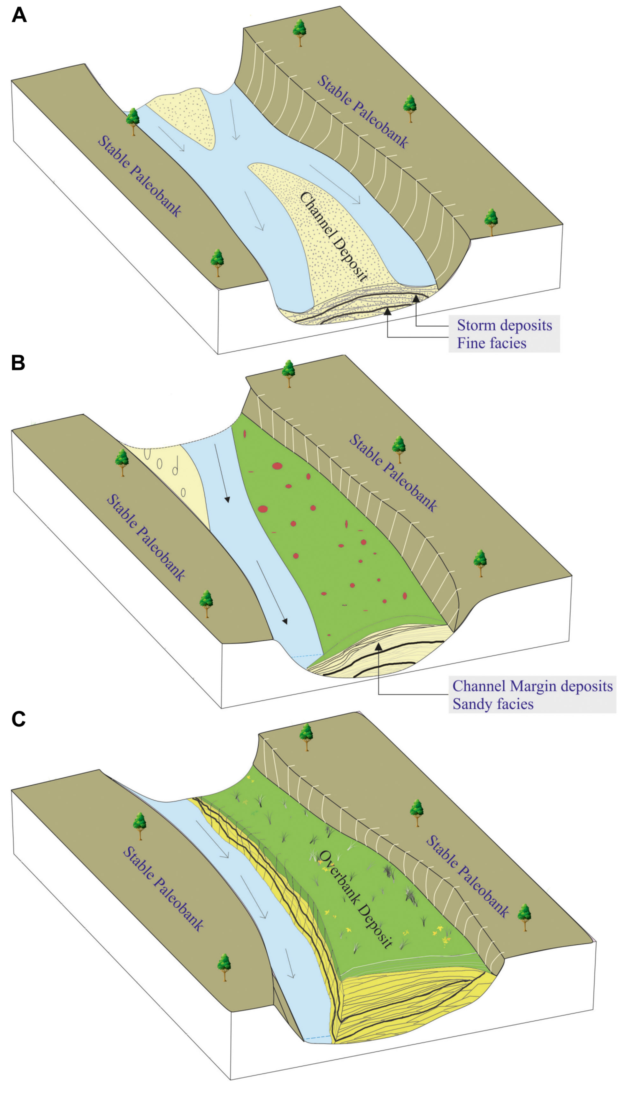

FIGURE 4 | A simplified depositional model of Neo-bank development. **(A)** Initiation and aggradation of bar within the channel due to large scale sand movement. **(B)** Stabilisation and merging of the bar with paleobank, sandwiching layers of fine-grained sediments deposited by monsoonal storm deposits, and finally giving way for development of overbank deposits. **(C)** Migration and fixing of the new channel, dominated by bank erosion and down cutting.

Sub-facies 1 are recorded at two depths measured to be from 684 to 638 cm (within two channel facies) and 450–376 cm (within the channel facies to channel margin facies) (**Figure 2-I**). These planktonic microforms bearing unsorted sediments are interpreted as two direct manifestations of monsoonal storms which exerted an influence approximately 56 km inland from the river mouth (Sukumaran et al., 2012a). The evidence of catastrophic storms and channel modifications (change of facies from channel to channel margin and to transition facies) during a brief period of time indicates a changing climate phase in the fluvial archive.

The later phase of sediment aggradation (AP-II) is represented by a 194 cm thick muddy facies (depth from 194 cm to the top of the sequence). The AP II sequence showed distinct disconformity with the underlying AP 1 sequence. The muddy facies are characterised by the intercalation of sub-facies 3 and sub-facies 2, representing overbank deposits (**Figure 2-I**).

Ferromagnetic Mineral Concentration

Highly magnetic (ferromagnetic) minerals, such as magnetite, are readily separated by the use of a magnet. The ferromagnetic minerals in the present context are the opaque minerals which are naturally magnetic. Primarily such minerals have a very high specific gravity (~5) compared to the rest of the non-magnetic or paramagnetic minerals in the bulk sediments. Because of their heaviness, they usually travel with light minerals such as quartz averaging 0.5–1.0 phi larger than their size, and they stand as a proxy for hydraulic factors (Folk, 1974). The enrichment or depletion of FMC within the sediment facies is anticipated under two possible conditions: *(i)* the FMCs are mobilised and redistributed in accordance with the energy condition and represented part of the sediment facies; *(ii)* the enrichment of FMC is due to lag, while finer sediments were washed from bulk sediments before the next package of sediment deposited. In either case, FMC remains a part of a sediment facies and represents the fluvial system's energy condition.

FMC is separated from the bulk sediment using a sheath-covered hand-magnet (Rosenblum et al., 2000; Collinson, 2013). A 10 gm of bulk sample was scanned using the hand-magnet and the latter was passed near over such that it did not touch the sample. Several iterations were undertaken to ensure complete extraction. To confirm the effectiveness of the separation, 20 samples were tested with the washing method. The left-out fractions of non-magnetic minerals were transferred to a high-speed stirrer and 50 ml of demineralised water were added and stirred for 10 min. This solution was then stirred for 15 min using a sheath-covered magnetic stirrer. The fraction of FMC attracted to the stirrer was then collected and weighed after drying in a hot air oven. In all the cases, the additional minerals separated from the left-out portion were less than 1.8% of the amount of FMC separated using a hand-magnet. The results of this test confirm the applicability of the adopted method and the obtained results. A total of 205 samples were analysed in this way for the Uchediya sequence. The resolution for the selection of samples for analysis was based on sedimentological inputs. Muddy facies (194 cm from the top of the section) were analysed at 2 cm intervals, whereas sandy facies (196–802 cm) were analysed at 10 cm intervals. The FMC plot against depth differentiates the distribution pattern, capturing three distinct depositional environments: bar sequence, transition sequence, and overbank sequence, suggesting a close relationship of FMC with sediment facies (**Figure 5**).

Magnetic Susceptibility

As a rapid analytical procedure with a reproducible result, this method has attracted the attention of climate researchers who have used MS as an environmental proxy for the last few decades (Thompson and Morton, 1979; Thompson et al., 1980;

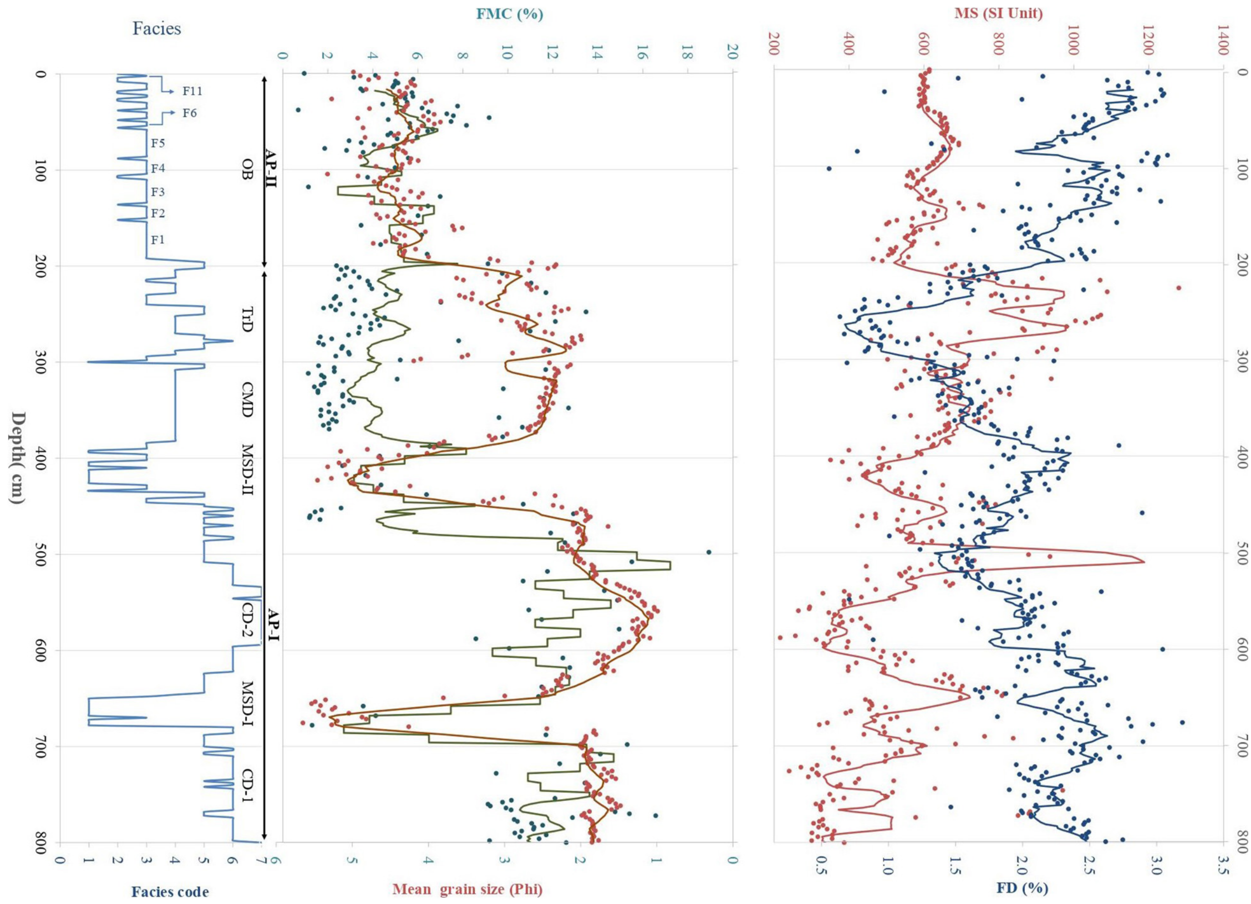

FIGURE 5 | Multi-proxy records of the Uchediya section showing depth-wise variation in sediment sub-facies, ferromagnetic mineral concentration (FMC%), mean grain size (Phi), magnetic susceptibility (χ_{lf}) and frequency-dependent susceptibility (χFD%). The plots distinguish the Aggradation phase I and Aggradation phase II. Aggradation phase I further deciphers Channel Deposit (CD, couplets of 6 and 5 sub-facies and couplets of 6 and 7 sub-facies), Channel Margin Deposits (CMD, sub-facies 4), and Transition Deposit (TrD intercalation of 2, 3, 4, 5, and 6 sub-facies) from 802 to 194 cm. The two phases of monsoonal storms deposits (MSD, sub-facies 1) are conspicuous from 684 to 638 cm (MSD-I) and 450–376 cm (MSD-II) depth. Aggradation phase II highlights overbank deposits (OB, intercalation of 2 and 3 sub-facies) from 194 to 0 cm. F1–F11 indicate inferred flood events.

Heller and Tung-Sheng, 1986; Kukla et al., 1988; Begét et al., 1990; An et al., 1991; Heller et al., 1991; Grimley et al., 1998; Basavaiah and Khadkikar, 2004; Deotare et al., 2004; Rajshekhar et al., 2004; Pant et al., 2005; Pattan et al., 2008; Juyal et al., 2009; Liu et al., 2010). These studies mainly focused on the climate signatures from aeolian sections, paleosols, lacustrine deposits and mudflats, whereas those of fluvial sediments are rarely studied. However, recent investigations have demonstrated that MS can be effectively used as a proxy for high-resolution cross facies correlation in general fluvial systems (Püspöki et al., 2020).

Low field MS was measured on all 401 samples every 2 cm using a multi-functional automated MFK-1 Kapabridge with a sensitivity of 2×10^{-6} (SI units). The measurements were done at 976 and 3,904 Hz with a field strength of 133 A/m. The results of the analysis are exhibited in terms of MS and frequency-dependent mineral MS (χFD%). The frequency effect is usually expressed as a percentage of the MS's difference at lower and high frequencies to the value taken with the lower frequency. MS usually reflects the concentrations of magnetic minerals independent of differences in grain size, while χFD% is sensitive to the presence of superparamagnetic (SP) particles, which usually are < 100 nm (<0.1μm) in diameter (Dearing et al., 1996; Basavaiah, 2011). Overall, χFD% values vary from 0.135 to 4.67% for all studied samples. The MS and χFD% plots along the depth profile differentiate sandy and muddy facies (**Figure 5**). MS represents the contributions from both fine pedogenic particles and coarse detrital sediment input, whereas χFD% represents the enhancement in the ultrafine magnetic particles during soil formation (Oldfield and Yu, 1994; Basavaiah, 2011).

Together, MS and χFD% variations, which are anti-correlated, determined the sediment source's signature (**Figure 5**). The sediment sources determine the mineralogy while transport conditions and depositional environments control concentration and grain-size distribution of magnetic minerals. The values of χFD% of 2.0% indicate virtually no SP grains, between 2.0 and 10.0% they indicate an admixture of SP and coarser non-SP grains, between 10.0 and 14.0% they indicate all SP grains (Dearing et al., 1996; Basavaiah, 2011; Basavaiah et al., 2015, 2019). Relatively high χFD% values of between 2 and 5% indicate a higher proportion of soil component in a relatively weathered sediment, which is generally characterised by a slower deposition rate. However, low χFD% values < 2% with a higher sedimentation rate indicate freshly derived rock-debris-derived sediment. The MS curve (**Figure 5**) shows marked fluctuations indicating a fluctuating concentration of ferrimagnetic minerals in the sediment input. Generally, higher (or lower) MS values are associated with unaltered (or altered) sediment types during periods of increased (or decreased) sedimentation rates (also evident in anti-correlated χFD% values). Rock magnetic properties help us characterise the type of source responsible for sedimentation (Basavaiah and Khadkikar, 2004; Basavaiah et al., 2010; Basavaiah, 2011; Basavaiah et al., 2019).

Facies Representative Major Oxide Geochemistry (FMoG)

To assess the possibility of a change in sediment provenance, major element geochemistry was determined from seven distinct sedimentary depositional environments. Each depositional environment was identified and described in terms of sub-facies level well before selecting the samples for analysis (Sukumaran et al., 2012b). The major oxide geochemistry of seven representative samples along the depth profile was studied using ICP AES with a microwave-digested sample, a facility made available by the Department of Earth Sciences at the Indian Institute of Technology in Powai, Mumbai. Major elements such as Al, Fe, Ti, K, Mg, Mn, Na, P, Ca, and Si were quantified and represented as a corresponding oxide weight percentage.

Geochemical records of major elements, namely, Al, Fe, Ti, K, Mg, Mn, Na, P, Ca, and Si, were calculated to their respective oxides. The abundance of oxides representing various depositional environments is tabulated in their percentages (**Table 4**). The correlation matrix of the ten major oxides (**Table 5**) showed that SiO_2 (ranging from 62.543 to 84.764%) had a strong negative correlation (−0.9889 to −0.8199 significance) with the other 8 oxides (Al_2O_3, Fe_2O_3, TiO_2, CaO, Na_2O, MgO, MnO, and P_2O_5). However, SiO_2 showed a moderate positive correlation with K_2O (0.558). The correlation matrix further suggested that the oxides, namely Al_2O_3, Fe_2O_3, TiO_2, CaO, Na_2O, MgO, MnO, and P_2O_5 had mutual strong positive (0.9937–0.66559) correlation, except for K_2O, which showed moderate to low negative correlation (−0.6236 to −0.0815) with all other oxides. The present analysis cannot ascertain the K_2O anomaly, and would require a more detailed study at a higher resolution. In other ways, the data indicates a uniformity of sediment source throughout the entire sequence and the variations in composition are only considered to represent selective reworking of hydrodynamic conditions.

DISCUSSION: INTEGRATION OF PROXY RECORDS

Here, we discuss the interrelationship of the proxies as outlined in the above paragraphs for the 8 m thick sequence at Uchediya. The sediment sequence represents a 45 km long neo-bank on the river Narmada's southern bank in the lower reaches. The interrelationship between proxies enhances the sediment source history, mode of transport and hydrodynamic factors of the SwIM River. We discuss a few scatter plots within the FMoG that provide an overall understanding of sediment uniformity and their source area weathering. The scatter plots between MS, FMC, and granulometric parameters point toward the river system's hydrodynamic conditions during variations in climate in the Holocene. The MS and FMC are mutually dependent variables, where MS is the measure of magnetisable mineral percentage in standard volume, and FMC is the percentage of magnetic minerals in weight percentage. The plot between MS and FMC shows relative density differences between magnetic and non-magnetic minerals, whereas the envelope of sediment sub-facies tends to capture the environment of deposition of these sediments and their hydrodynamics.

TABLE 4 | Major elemental geochemistry and CIA of samples.

Sample no		UCH 60	UCH 120	UCH 160	UCH 210	UCH 280	UCH 330	UCH 400
Depth (cm)		120	240	320	420	560	660	800
Facies		3	3	4	1	7	1	7
Depositional Environment		OB	TrD	CMD	MSD-2	CD	MSD-1	CD
	SiO_2	62.95	64.15	73.47	62.54	84.76	60.55	82.56
	Al_2O_3	12.87	10.06	8.25	12.65	5.29	13.28	6.17
	Fe_2O_3	11.20	11.07	7.25	10.48	3.20	11.15	3.74
	CaO	5.20	6.74	4.48	6.90	2.95	7.72	3.06
	MgO	2.65	2.83	2.04	2.48	0.99	2.64	1.09
Element (Wt %)	TiO_2	2.09	2.25	1.38	1.99	0.54	1.91	0.55
	Na_2O	1.33	1.26	1.25	1.27	0.84	1.21	1.03
	K_2O	1.29	1.29	1.65	1.33	1.29	1.11	1.60
	MnO	0.17	0.14	0.09	0.11	0.05	0.15	0.11
	P_2O_5	0.13	0.13	0.11	0.13	0.06	0.14	0.08
	LOI	0.11	0.08	0.04	0.13	0.03	0.15	0.03
	CIA	62.20	52.0	52.80	57.12	51.00	56.95	52.01

TABLE 5 | Correlation coefficients of major elemental concentrations.

	SiO_2	$Al2O_3$	CaO	Fe_2O_3	K_2O	MgO	MnO	Na_2O	P_2O_5	TiO_2	LOI
SiO_2	1.00										
Al_2 O_3	–0.97	1.00									
CaO	–0.94	0.88	1.00								
Fe_2O_3	–0.99	0.94	0.91	1.00							
K_2O	0.56	-0.58	–0.62	–0.54	1.00						
MgO	–0.97	0.89	0.90	0.99	–0.48	1.00					
MnO	–0.82	0.82	0.67	0.84	–0.42	0.80	1.00				
Na_2O	–0.86	0.81	0.70	0.88	–0.08	0.89	0.78	1.00			
P_2O_5	–0.99	0.94	0.90	0.99	–0.47	0.99	0.86	0.91	1.00		
TiO_2	–0.97	0.89	0.88	0.99	–0.49	0.99	0.79	0.88	0.98	1.00	
LOI	–0.91	0.96	0.89	0.87	–0.72	0.80	0.75	0.64	0.86	0.79	1.00

The Uchediya sequence's age bracket falls from 1395 to 1850 AD and coincides with the globally accepted transition phase of the Medieval Warm Period (MWP) to the Little Ice Age (LIA). The LIA is inconsistently defined between a broad time frame of 14th century (AD 1300–1400) and 19th century (AD 1850 and 1900) whereas, the MWP falls ~1000–1300 AD (Crowley, 2000; Crowley and Lowery, 2000; Mann, 2002; Jones and Mann, 2004). Mostly, the onset of LIA is taken as 1440 AD and ends as late as 1920 AD. The period within the LIA from 1570 to 1750 AD is considered to be the peak phase. Two of the most intense grand solar minima, the Spörer (~AD 1390–1540) and the Maunder minima (~ AD 1645–1715) fall within the broader range of LIA (Eddy, 1976; Owens et al., 2017). From the chronology and aggradation model deciphered from the sedimentological analysis, the entire sequence correlates well with the Holocene climate phases. The lower sequence AP-I (CD, CMD, and TrD) preserves the signatures of the waning phase of the MWP, whereas the AP-II (OB) decode the signatures of fluvial responses during the LIA. Considering the LIA phase is said to be globally significant for its socio-cultural and economic impact, and both are associated with manmade and natural calamities (Lamb, 2002; Baker, 2006; Adger et al., 2012), we attempt to establish the interrelationship between various fluvial proxies and understanding sediment transport, distribution, sediment facies and flood events from the Uchediya sequence. Studies from the Paria River basin and the southern Colorado Plateau in the United States have shown that valley-fill alluvium during LIA is a mappable stratigraphic unit within the larger alluvial valley (Hereford, 2002). By contrast, such reports from major SwIM Rivers are sparse.

FMoG reveals the relative variation of sediment geochemistry across the section. The percentage of SiO_2 has been plotted against other oxides viz. Al_2O_3, TiO_2, Fe_2O_3, Na_2O, CaO, MgO, MnO, and P_2O_5 (**Figure 6**). Also, immobile and mobile oxides were plotted against each other viz. Al_2O_3 vs. Fe_2O_3, Al_2O_3 vs. TiO_2, Fe_2O_3 vs. TiO_2, Na_2O vs. K_2O, K_2O vs. P_2O_5, and CaO vs. Na_2O (**Figure 6**). The scatter plots of various oxides against SiO_2 show an inverse relationship. With the decrease in SiO_2, the percentage of other oxides also increases, whereas K_2O behaves differently. The various oxides are highest in the facies representing OB, TrD and two storm units (MSD-I and MSD-II). Whereas in the case of CMD and CD, they have a higher percentage of SiO_2 than other oxides. Fe_2O_3 and TiO_2 plotted against Al_2O_3 and TiO_2 vs. Fe_2O_3 show that they increase together and are directly proportional to each other. A distinct position of channel marginal deposits in all the bivariate plots indicates a selective reworking.

Estimating each sample's degree of chemical weathering was obtained by calculating the chemical index of alteration (CIA) (Nesbitt and Young, 1982). Different researchers have extensively used these parameters to understand chemical maturity and provenance weathering (Singh and Rajamani, 2001; Lee et al., 2005; Das and Krishnaswami, 2007; Tripathi et al., 2007; Manikyamba et al., 2008; Oh et al., 2008; Roy et al., 2008; Singh, 2009; Singh, 2010). The CIA values of fresh rocks and minerals are consistently near 50 whereas samples with values below 60 are considered to display low chemical weathering; between 60 and 80, they indicate moderate chemical weathering and values over 80 are seen as exhibiting extreme chemical weathering (Fedo et al., 1995; **Table 4**). The sample (UCH 60) taken from the overbank deposit, indicates moderate chemical weathering (62.20) and further supports the reworking of sediments from older deposits. Simultaneously, lower CIA values recorded from channel deposits, channel margin deposits, and transitional deposits indicate that the sediments are freshly derived from parent rock and reflect a significant fluvial influx.

The plot between MS vs. mean grain size demonstrates two distinct trends clustered by fine and sandy facies (**Figure 7-I**). A positive trend of increase in MS with an increase in mean size is observed in the fine facies that includes sub-facies 1, 2, and 3. In the sand facies, a negative trend is observed in the cluster of sandy facies, which includes sub-facies 4, 5, 6, and 7. The plot of FMC's vs. mean grain size (**Figure 7-II**) demonstrates a uniform trend of MS variation. In both, the fine facies (1, 2, and 3) and the sandy facies (4, 5, 6, and 7), there is a slight increase in FMC with an

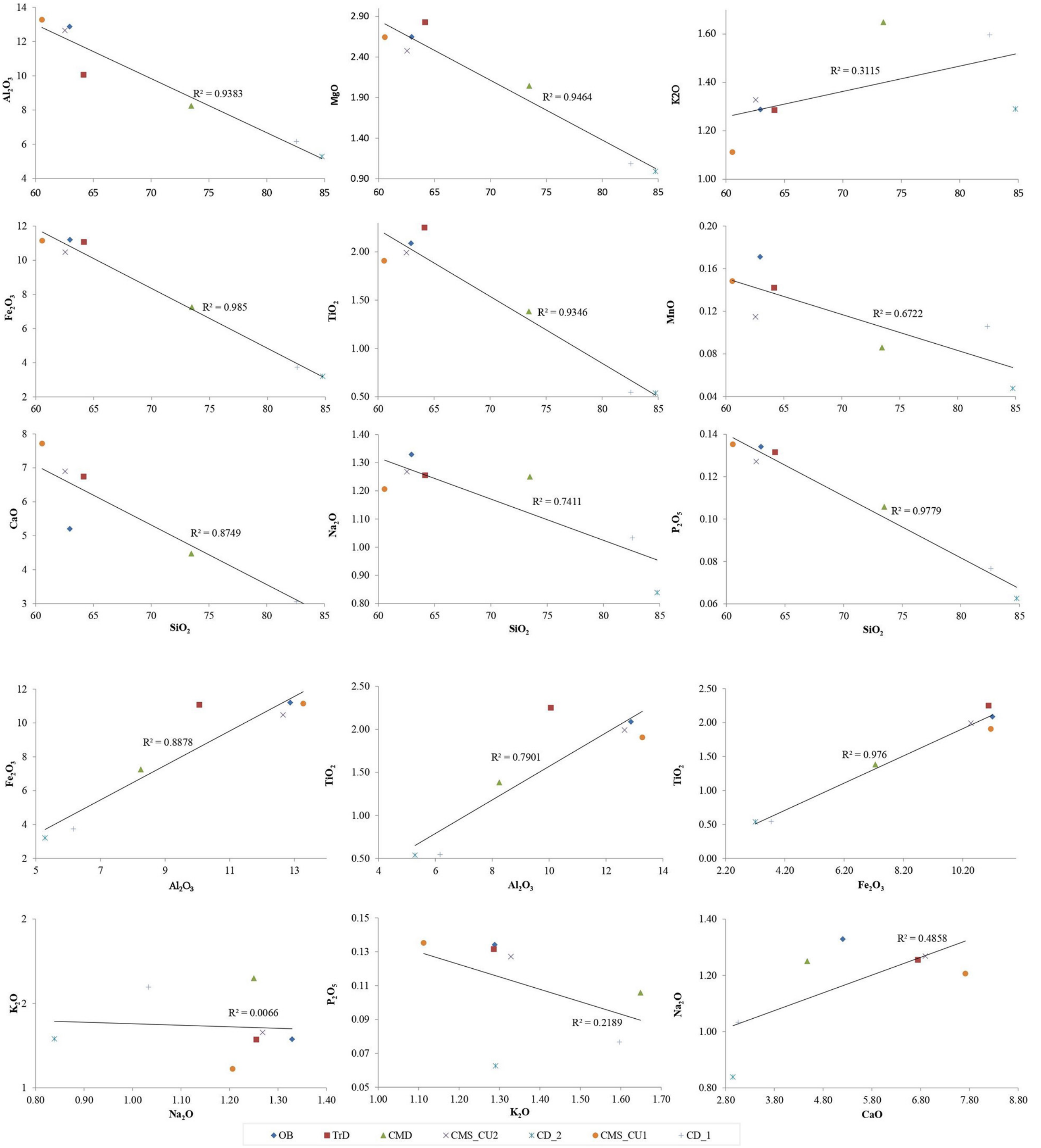

FIGURE 6 | Variation diagram of major oxides weight percentage against SiO_2 and other oxides.

increase in mean grain size. We consider that the ferromagnetic minerals that travel along with quartz grains would have a relative size variation (an average of 0.5–1.0 phi larger quartz compared to ferromagnetic minerals) due to the heaviness of ferromagnetic minerals (Folk, 1974). Together, MS and FMC may offer the potential to distinguish between alluvium delivered directly from the slopes and material produced by changes in channel morphology. The plot of the ratio of FMC and MS against mean grain size shows a clustering of the sub-facies and a clear trend of variation of the magnetic parameter with mean grain size (**Figure 7-III**). Thus, the relation between FMC and MS appears to establish a sub-facies level interrelationship in recent sediments deposited in a fluvial environment.

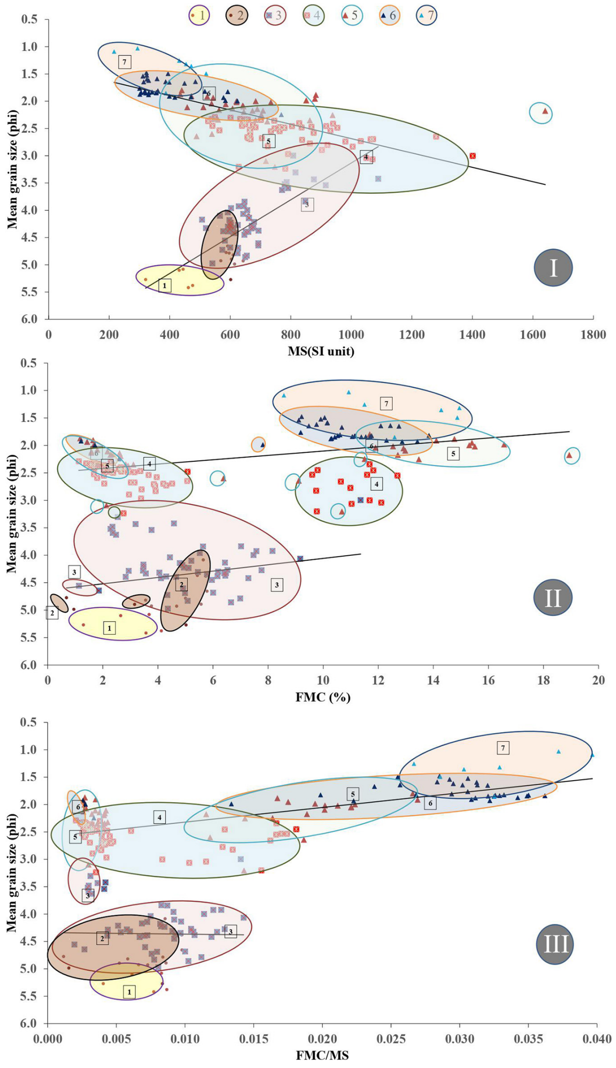

FIGURE 7 | Cross plots FMC, MS, and Facies. **(I)** MS vs. Mean grain size showing two distinct trends in fine facies and sandy facies. **(II)** FMC vs. Mean grain size showing two similar trends in fine facies and sandy facies. **(III)** FMC/MS vs. Mean grain size showing two similar trends in fine facies and sandy facies. Coloured circles envelopes similar sediment sub-facies.

The FMC vs. MS scatter-plot demonstrates two clusters roughly demarcated by 8% FMC (**Figure 8**). The cluster of data with more than 8% FMC results from sandy facies, viz. sub-facies 4, 5, 6, and 7. The sub-facies 6, having a higher weight percentage of FMC (8.57–14.94%) but a low MS (216–669 $\times 10^{-6} m^3 kg^{-1}$) may be interpreted as a primary event of sand deposition. Such a situation is possible when the bulk of the sediment contains an abundance of low-density minerals. Sub-facies 7 which is encountered at a depth ranging from 5.34 m to 5.94, is a channel deposit and further supports rapid aggradation and preservation of the sub-facies without any evidence of reworking by the river channel. The other three sandy sub-facies 4, 5, and 6, feature clusterings in excess of 8% FMC as well as minor clustering < 8% FMC. This is likely to be indicative of reworking of channel sand and the three sub-facies are considered to represent channel deposits, channel marginal deposits or transitional deposits.

A second cluster in the FMC vs. MS plot, having less than 8% of FMC and variable MS percentages, includes fine sub-facies, viz. 1, 2, 3, and sandy sub facies viz. 4, 5, and 6. These sandy facies consist of the channel deposit, channel marginal deposits and transitional deposits resulting from the reworking of older deposits. The fine sub-facies, 1 is primarily the result of a tidal influx; the other two fine facies, namely sub facies 2 and 3, are the only sub-facies with distinct depositional characteristics. A specific overlapping and a matching trend of sub-facies 2 and 3 may be interpreted as a characteristic signature of a flood event which was responsible for the deposition of these couplets. Sub-facies 2 and 3 is a primary constituent of the overbank depositional environment, which has preserved at least 11 such couplets that can be interpreted as representing individual flood events (**Figure 5**). The variation of these couplets' thickness may also hint toward the floods' relative energy conditions (Kochel and Baker, 1988). A fundamental reason to consider the flood deposit thickness as a proxy to evaluate the flood energy is the assumption that most other geographic factors remained the same; only the duration of a flood can increase the deposit's thickness. The high-resolution sedimentary record suggests at least five (out of 11) discrete flood events (as the thickness of sediment couplet is between 14 and 40 cm indicating a prolonged submersion of elevated land; F1–F5, **Figure 5**), which had relatively higher energy in comparison with the six flood events (thickness of sediment couplet is between 2 and 8 cm; F6–F11, **Figure 5**). These multiple flood events led to the aggradation of an overbank.

The signatures of climate and flood deciphered from the high-resolution multi-proxy records from the Uchediya sequence help us to compare them with available records of historical flood descriptions from the town of Bharuch which is located on the northern bank of the Narmada River (**Table 6**; Forbes, 1813; Gazetteer, 1961, 1877). One of the factors that may have led to the construction of a fort wall along the Narmada bank in 1094–1143 AD might be related to a past attempt at preventing erosion caused by high energy flow along the northern bank during this period. Rebuilding and strengthening the fort wall during 1526–1536 AD may also testify to the continuation of high energy conditions within the Narmada channel. Until then, the river sustained the passage of large vessels right up to the fort wall. However, a large inflow of sand during 1673–1681 AD led to a shallowing of the channel where vessels with skilled navigators could only reach up to the city walls. Large magnitude flood events were recorded in 1781, 1825, 1835, 1836, 1837, 1860, 1864, 1868, 1870–1877, and 1897 AD, where geomorphic changes such as channel shallowing (1825 AD), the southerly shift of the thalweg line (1860 AD) and erosion of the southern bank (1870–1877 AD) have been documented. Historical evidence such as the rebuilding of the fort wall during the years 1526–1536 AD, the large inflow of sand recorded between 1673 and 1681 AD as well as a shallowing of the river

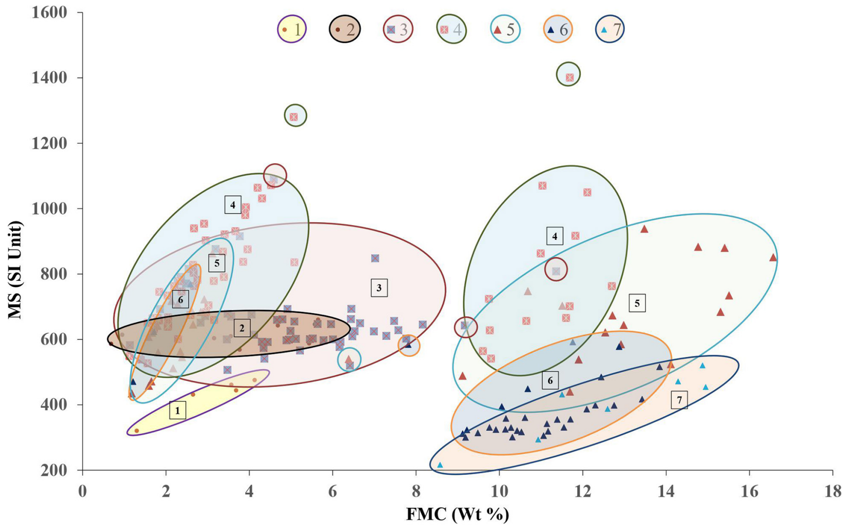

FIGURE 8 | The Cross plot of MS vs. FMC shows two groups of clusters roughly demarcated by 8% FMC. < 8% cluster includes sub-facies 1–6 and > 8% cluster includes sub-facies 4–7. The fine sub-facies, 1 is distinct and belongs to tidal influx; the other two fine sub facies 2 and 3 are a primary constituent of the overbank deposits. The overlapping/matching trend of sub-facies 2 and 3, therefore, considered capturing facies-couplets representing flood events.

TABLE 6 | Historical records documented for Bharuch town with respect to changes in the Narmada River.

Period	Description
1094–1143	The archaeological structure, Fort Wall built on the right bank of Narmada to prevent the city from erosion was built by Sidh Raj Jaisinhji of Anhilwara during 1094–1143 (Bombay presidency gazetteer 1877–1905, p. 551).
1526–1536	Bahadur Shah strengthened and rebuilt the Fort wall. This is also noted that the large ships were reaching up to the city wall during the period (Bombay presidency gazetteer 1877–1905, p. 55).
1673–1681	*-Two hundred years ago when Fryer (1673–1681) crossed the river at Broach, he found the stream broad, swift and deep, but adds that, on account of the sand forced down to the rain skilful pilots are required, by whose direction good lusty vessels are brought up to the city walls* (Bombay presidency gazetteer 1877–1905).
1781	A storm passed over the district of Bharuch, of which Mr. Forbes has left an account in the Oriental memories- Forbes Oriental Memoirs, vol-III, 53. *"Two years before I left India, some weeks before the setting into the south-west monsoon (May), we had the most deadly storm ever remembered in Gujarat. It ravage by sea and land were terrible, the damage at Broch was very great, and the loss of life considerable".*
1822	*Large flood (*Kale et al., 1997a*).*
1825	*-Bishop Herber (1825) visited Broch, he noticed that the Narmada was very shallow and that then no vessel larger than moderately sized lighters could come beyond the bar.* (Bombay presidency gazetteer 1877–1905).
1835	Cold environment (Gazetteer, 1961, p. 303).
1836	Heavy rain (Gazetteer, 1961, p. 303).
1837	*-Great flood-1937, when the water of Narbada and Tapi are said to be have joined. No damage would seem to have been caused either to the district or the city of Broch it has not done much damage to the Broach city* (Gazetteer, 1877, page 410).
1838	Failure of Rain (Gazetteer, 1961, p. 303).
1840	Failure of Rain (Gazetteer, 1961, p. 303).
1860	Nineteenth century story of Narmada was much devastating. *-At the time when the original bridge was built the heavy current of the stream lays on the right bank. Since then the main channel of the river has so entirely shifted toward the left bank* (Bombay Presidency Gazetteer of the year 1877-1905 is about the built of Golden bridge; from page 419 and 420).
1864	*- A flood rising within 21 feet rail level carried away six spans in the deep water channel* (Bombay Presidency Gazetteer of year 1877–1905 is about the built of Golden bridge; from page 419 and 420).
1868	*-August flood rising to 18 feet of rail level carried away four spans* (Bombay Presidency Gazetteer of the year 1877–1905 is about the built of Golden bridge; from page 419 and 420).
1870–1877	*-During 7 years the southern bank was gradually washed away, and driven back upward of 1000 feet.* (Bombay Presidency Gazetteer of the year 1877–1905 is about the built of Golden bridge; from page 419 and 420).
1878	*Large flood* (Kale et al., 1997a).
1891	*Large flood* (Kale et al., 1997a).
1894	*Large flood* (Kale et al., 1997a).
1897	*-The water rising suddenly to the unprecedented height of 35 feet above high water mark or within 13'6" of rail level, washed away twenty-six spans or upwards of 1600 feet of the southern portion of the bridge.* (Bombay Presidency Gazetteer of the year 1877–1905 is about the built of Golden bridge; from page 419 and 420).

channel lend additional support to the inferences made from the multi-proxy fluvial record.

CONCLUSION

- A multi-proxy high-resolution record proposed a stage-wise aggradation history of the neo-bank sedimentary sequence. Rapid aggradation of channel sediments and tidal surges occurred during the initiation of channel modifications and are capped by an overlying 2 m thick overbank deposit.
- A fresh deposit of sandy sediment, frequent channel modifications and high energy conditions close to the 565 ± 60 years before 2020 was broadly interpreted as the signature for the MWP waning phase and the onset of the LIA in a SwIM river in western India.
- A couplet of sub-facies 2 ($Fm_{SILT+VFS}$ (O) and 3 ($Fm_{SILT+VFS+FS}$) of overbank deposits were inferred as a signature of past flood events.
- Multi-proxy records enabled to identify signatures of at least 11 distinct flood events within the overbank sediment sequence during a time frame of 500 years.
- MS is a potential proxy to distinguish between sediment delivered directly from the slopes and reworked sediment deposited due to changes in channel morphology. Higher MS and lower χFD% in coarser unaltered sediments reflect high stream energies and episodes of accelerated delivery of ferrimagnetic minerals of primary origin.
- FMC and MS were effectively utilised as proxies capturing the hydrodynamic conditions of the fluvial system. More such studies from varied depositional environments might help to derive an empirical relationship between FMC, MS, and other granulometric parameters that effectively correlate to past climatic and associated hydrodynamic conditions.
- The study is a step forward toward building a high resolution, multi-proxy sediment archive of monsoonal rivers.

DATA AVAILABILITY STATEMENT

The raw data supporting the conclusions of this article will be made available by the authors, without undue reservation.

AUTHOR CONTRIBUTIONS

PS worked for his Ph.D. thesis taking this as study area. DS guided PS throughout his research and contributed in all aspects of the research. KK and GR were co-investigators on the project and participated in the collection of samples, the analysis of data, and the interpretation of results. NB contributed toward magnetic study and interpretation of the results. J-LS carried out the luminescence dating. All authors contributed to the article and approved the submitted version.

FUNDING

The present work was carried out with project grant from Department of Science and Technology, India under Shallow Sub-surface Science Program, Narmada Window (SR/S4/ES-21/NARMADA WINDOW/P 6). GR was also supported by the J. C. Bose National Fellowship and UGC Center for Advanced Studies.

ACKNOWLEDGMENTS

We thank the Department of Earth Sciences, Indian Institute of Technology, Powai, Mumbai, for extending the ICP AES, facility. We thank Professor Mark Maslin, Department of Geography, University College London, and Prof. Robert J. Wasson, Emeritus Professor at the Australian National University for reviewing and suggesting modifications to the manuscript and figures. PS is thankful to Dr. Hiteshri Shastri for sharing the hydro-climatology laboratory facility for the geospatial analysis. A critical review and suggestions by two reviewers have substantially improved the manuscript in many aspects.

REFERENCES

Adger, W. N., Kelly, P. M., and Ninh, N. H. (2012). *Living with Environmental Change: Social Vulnerability, Adaptation and Resilience in Vietnam*. London: Routledge.

Aitken, M. J. (1998). *An Introduction to Optical Dating*. Oxford: Oxford University Press.

An, Z., Kukla, S., Porter, S. C., and Xiao, J. L. (1991). Magnetic susceptibility evidence of monsoon variation on the Loess Plateau of Central China during the last 13 000 years. *Quat. Res.* 36, 29–36. doi: 10.1016/0033-5894(91)90015-w

Baker, V. (1995). Global paleohydrological change. *Quaestiones Geogr.* 4, 27–35.

Baker, V. R. (2006). Palaeoflood hydrology in a global context. *Catena* 66, 161–168. doi: 10.1016/j.catena.2005.11.016

Banerjee, D., Murray, A. S., Bøtter-Jensen, L., and Lang, A. (2001). Equivalent dose estimation using a single aliquot of polymineral fine grains. *Radiat. Meas.* 33, 73–94. doi: 10.1016/s1350-4487(00)00101-3

Basavaiah, N. (2011). *Geomagnetism: Solid Earth and Upper Atmosphere Perspectives*. Dordrecht: Springer.

Basavaiah, N., Appel, E., Lakshmi, B. V., Deenadayalan, K., Satyanarayana, K. V. V., Misra, S., et al. (2010). Revised magnetostratigraphy and nature of the fluvio-lacustrine sedimentation of the Kashmir basin, India, during Pliocene-Pleistocene. *J. Geophys. Res.* 115: B08105.

Basavaiah, N., Babu, J. M., Gawali, P., Kumar, K. C. V. N., Demudu, G., Prizomwala, S. P., et al. (2015). Late quaternary environmental and sea level changes from Kolleru Lake, SE India: inferences from mineral magnetic, geochemical and textural analyses. *Quat. Int.* 371, 197–208. doi: 10.1016/j.quaint.2014.12.018

Basavaiah, N., Babu, J. M., Prizomwala, S., Achyuthan, H., Siva, V., and Boral, P. (2019). Proxy mineral magnetic and elemental analyses for 2004 tsunami impact deposit along the Muttukadu backwater, East Coast of India: scope of the palaeotsunami studies. *Quat. Int.* 507, 224–232. doi: 10.1016/j.quaint.2018.10.038

Basavaiah, N., and Khadkikar, A. S. (2004). Environmental magnetism and it s application towards palaeomonsoon reconstruction. *J. Indian Geophys. Union* 8, 1–14.

Bedi, N., and Vaidyanadhan, R. (1982). Effect of neotectonics on the morphology of the Narmada river in Gujarat, Western India *Z.Geomorph.N.F*, 87–102.

Begét, J. E., Stone, D. B., and Hawkins, D. B. (1990). Paleoclimatic forcing of magnetic susceptibility variations in Alaskan loess during the late Quaternary. *Geology* 18, 40–43. doi: 10.1130/0091-7613(1990)018<0040:pfomsv>2.3.co;2

Bøtter-Jensen, L. (1997). Luminescence techniques: instrumentation and methods. *Radiat. Meas.* 27, 749–768. doi: 10.1016/s1350-4487(97)00206-0

Chamyal, L. S., Maurya, D. M., Bhandari, S., and Raj, R. (2002). Late quaternary geomorphic evolution of the lower Narmada valley, Western India: implications for neotectonic activity along the Narmada-Son Fault. *Geomorphology* 46, 177–202. doi: 10.1016/s0169-555x(02)00073-9

Collinson, D. (2013). *Methods in Rock Magnetism and Palaeomagnetism: Techniques and Instrumentation*. Berlin: Springer Science & Business Media.

Crowley, T. J. (2000). Causes of climate change over the past 1000 years. *Science* 289, 270–277. doi: 10.1126/science.289.5477.270

Crowley, T. J., and Lowery, T. S. (2000). How warm was the medieval warm period? *AMBIO J. Hum. Environ.* 29, 51–54. doi: 10.1579/0044-7447-29.1.51

Das, A., and Krishnaswami, S. (2007). Elemental geochemistry of river sediments from the Deccan Traps, India: implications to sources of elements and their mobility during basalt–water interaction. *Chem. Geol.* 242, 232–254. doi: 10.1016/j.chemgeo.2007.03.023

Dearing, J. A., Dann, R., Hay, K., Lees, J., Loveland, P., Maher, B. A., et al. (1996). Frequency-dependent susceptibility measurements of environmental materials. *Geophys. J. Int.* 124, 228–240. doi: 10.1111/j.1365-246x.1996.tb06366.x

Deotare, B., Kajale, M., Rajaguru, S., and Basavaiah, N. (2004). Late quaternary geomorphology, palynology and magnetic susceptibility of playas in western margin of the Indian Thar Desert. *Indian Geophys. Union* 8, 15–25.

Duller, G. (2015). The Analyst software package for luminescence data: overview and recent improvements. *Anc. TL* 33, 35–42.

Durcan, J. A., King, G. E., and Duller, G. A. (2015). DRAC: dose rate and age calculator for trapped charge dating. *Quat. Geochronol.* 28, 54–61. doi: 10.1016/j.quageo.2015.03.012

Eddy, J. A. (1976). The maunder minimum. *Science* 192, 1189–1202.

Ely, L. L., Enzel, Y., Baker, V. R., Kale, V. S., and Mishra, S. (1996). Changes in the magnitude and frequency of late holocene monsoon floods on the Narmada River, central India. *Geol. Soc. Am. Bull.* 108, 1134–1148. doi: 10.1130/0016-7606(1996)108<1134:citmaf>2.3.co;2

Fedo, C. M., Wayne Nesbitt, H., and Young, G. M. (1995). Unraveling the effects of potassium metasomatism in sedimentary rocks and paleosols, with implications for paleoweathering conditions and provenance. *Geology* 23, 921–924. doi: 10.1130/0091-7613(1995)023<0921:uteopm>2.3.co;2

Folk, R. L. (1974). *Petrology of Sedimentary Rocks*. Austin, TX: Hemphil Publishing Company.

Forbes, J. (1813). *Oriental Memoirs*. White, Cochrane, and Co: London.

Gao, H., Li, Z., Pan, B., Liu, F., and Liu, X. (2016). Fluvial responses to late quaternary climate change in the Shiyang River drainage system, western China. *Geomorphology* 258, 82–94. doi: 10.1016/j.geomorph.2016.01.018

Gazetteer, B. P. (1877). *Bombay Presidency Gazetteer*. Broch dist.

Gazetteer, B. P. (1961). *Bombay Presidency Gazetteer 1877–1905*. Government Central Press, Bombay.

Grimley, D. A., Follmer, L. R., and Mckay, E. D. (1998). Magnetic susceptibility and mineral zonations controlled by provenance in loess along the Illinois and Central Mississippi River Valleys. *Quat. Res.* 49, 24–36. doi: 10.1006/qres.1997.1947

Guérin, G., Mercier, N., and Adamiec, G. (2011). Dose-rate conversion factors: update. *Anc. TL* 29, 5–8.

Hansen, V., Murray, A., Buylaert, J.-P., Yeo, E.-Y., and Thomsen, K. (2015). A new irradiated quartz for beta source calibration. *Radiat. Meas.* 81, 123–127. doi: 10.1016/j.radmeas.2015.02.017

Heller, F., Liu, X., Liu, T., and Xu, T. (1991). Magnetic susceptibility of loess in China. *Earth Planet. Sci. Lett.* 103, 301–310. doi: 10.1016/0012-821x(91)90168-h

Heller, F., and Tung-Sheng, L. (1986). Palaeoclimatic and sedimentary history from magnetic susceptibility of loess in China. *Geophys. Res. Lett.* 13, 1169–1172. doi: 10.1029/gl013i011p01169

Hereford, R. (2002). Valley-fill alluviation during the Little Ice Age (ca. A.D. 1400–1880), Paria River basin and southern Colorado Plateau, United States. *GSA Bull.* 114, 1550–1563. doi: 10.1130/0016-7606(2002)114<1550:vfadtl>2.0.co;2

Jones, P. D., and Mann, M. E. (2004). Climate over past millennia. *Rev. Geophys.* 42:RG2002.

Joshi, P. N., Maurya, D. M., and Chamyal, L. S. (2013). Tectonic and climatic controls on late Quaternary bajada sedimentation along Narmada-Son Fault (NSF), Gujarat, Western India. *Int. J. Sediment Res.* 28, 66–76. doi: 10.1016/s1001-6279(13)60019-0

Juyal, N., Pant, R. K., Basavaiah, N., Bhushan, R., Jain, M., Saini, N. K., et al. (2009). Reconstruction of last glacial to early Holocene monsoon variability from relict lake sediments of the Higher Central Himalaya, Uttrakhand, India. *J. Asian Earth Sci.* 34, 437–449. doi: 10.1016/j.jseaes.2008.07.007

Kale, V., Achyuthan, H., Jaiswal, M., and Sengupta, S. (2010). Palaeoflood records from upper Kaveri River, southern India: evidence for discrete floods during Holocene. *Geochronometria* 37, 49–55. doi: 10.2478/v10003-010-0026-0

Kale, V. S., and Baker, V. R. (2006). An extraordinary period of low-magnitude floods coinciding with the Little Ice Age: palaeoflood evidence from Central and Western India. *J. Geol. Soc. India* 68, 477–483.

Kale, V. S., Hire, P., and Baker, V. R. (1997a). Flood hydrology and geomorphology of monsoon-dominated rivers: the Indian Peninsula. *Water Int.* 22, 259–265. doi: 10.1080/02508069708686717

Kale, V. S., Mishra, S., and Baker, V. (1997b). A 2000-year palaeoflood record from Sakarghat on Narmada, Central India. *J. Geol. Soc. India* 50, 283–288.

Kale, V. S., Mishra, S., and Baker, V. R. (2003). Sedimentary records of palaeofloods in the bedrock gorges of the Tapi and Narmada rivers, central India. *Curr. Sci.* 84, 1072–1079.

Kochel, R. C., and Baker, V. R. (1988). "Palaeoflood analysis using slackwater deposits," in *Flood Geomorphology*, eds V. R. Baker, R. C. Kochel, and P. C. Patton (New York, NY: John Wiley), 357–376.

Kolb, T., Fuchs, M., and Zöller, L. (2016). Deciphering fluvial landscape evolution by luminescence dating of river terrace formation: a case study from Northern Bavaria, Germany. *Z. Geomorphol.* 60, 29–48. doi: 10.1127/zfg_suppl/2015/s-00193

Kreutzer, S., Schmidt, C., Fuchs, M. C., Dietze, M., Fischer, M., and Fuchs, M. (2012). Introducing an R package for luminescence dating analysis. *Anc. TL* 30, 1–8. doi: 10.1007/978-94-007-6326-5_121-2

Kukla, G., Heller, F., Ming, L. X., Chun, X. T., Sheng, L. T., and Sheng, A. Z. (1988). Pleistocene climates in China dated by magnetic susceptibility. *Geology* 16, 811–814. doi: 10.1130/0091-7613(1988)016<0811:pcicdb>2.3.co;2

Lamb, H. H. (2002). *Climate, History and the Modern World*. Abingdon: Taylor & Francis.

Lee, J. I., Park, B. K., Jwa, Y. J., Yoon, H. I., Yoo, K. C., and Kim, Y. (2005). Geochemical characteristics and the provenance of sediments in the Bransfield Strait, West Antarctica. *Mar. Geol.* 219, 81–98. doi: 10.1016/j.margeo.2005.06.002

Liu, J., Chen, Z., Chen, M., Yan, W., Xiang, R., and Tang, X. (2010). Magnetic susceptibility variations and provenance of surface sediments in the South China Sea. *Sediment. Geol.* 230, 77–85. doi: 10.1016/j.sedgeo.2010.07.001

Manikyamba, C., Kerrich, R., González–Lvarez, I., Mathur, R., and Khanna, T. C. (2008). Geochemistry of Paleoproterozoic black shales from the Intracontinental Cuddapah basin, India: implications for provenance, tectonic setting, and weathering intensity. *Precambrian Res.* 162, 424–440. doi: 10.1016/j.precamres.2007.10.003

Mann, M. E. (2002). "Little ice age," *Encyclopedia of Global Environmental Change*, Vol. 1, eds M. C. MacCracken, and J. S. Perry (Chichester: Wiley), 504–509.

Martinius, A. W. (2000). Labyrinthine facies architecture of the Tortola Fluvial system and controls on deposition (late Oligocene-Early Miocene, Loranca Basin, Spain). *J. Sediment. Res.* 70, 850–867. doi: 10.1306/2dc4093d-0e47-11d7-8643000102c1865d

Miall, A. D. (1978). Lithofacies types and vertical profile models in braided river deposits: a summary. *Fluvial Sedimentol.* 5, 597–604.

Miall, A. D. (1985). Architectural-element analysis: a new method of facies analysis applied to fluvial deposits. *Earth Sci. Rev.* 22, 261–308. doi: 10.1016/0012-8252(85)90001-7

Murray, A. S., and Wintle, A. G. (2000). Luminescence dating of quartz using an improved single-aliquot regenerative-dose protocol. *Radiat. Meas.* 32, 57–73. doi: 10.1016/s1350-4487(99)00253-x

Nesbitt, H. W., and Young, G. M. (1982). Early Proterozoic climates and plate motions inferred from major element chemistry of lutites. *Nature* 299, 715–717. doi: 10.1038/299715a0

Oh, K.-C., Kim, J.-Y., Yang, D.-Y., Lee, J.-Y., and Hong, S.-S. (2008). An assessment of the sand resources in old riverbeds and flood plain deposits within a branch of the Geum River, South Korea. *Quat. Int.* 176-177, 156–171. doi: 10.1016/j.quaint.2007.06.003

Oldfield, F., and Yu, L. (1994). The influence of particle size variations on the magnetic properties of sediments from the north-eastern Irish Sea. *Sedimentology* 41, 1093–1108. doi: 10.1111/j.1365-3091.1994.tb01443.x

Owens, M. J., Lockwood, M., Hawkins, E., Usoskin, I., Jones, G. S., Barnard, L., et al. (2017). The Maunder minimum and the Little Ice Age: an update from recent reconstructions and climate simulations. *J. Space Weather Space Clim.* 7:A33.

Pant, R. K., Basavaiah, N., Juyal, N., Saini, N. K., Yadava, M. G., Appel, E., et al. (2005). A 20−ka climate record from Central Himalayan loess deposits. *J. Quat. Sci.* 20, 485–492. doi: 10.1002/jqs.938

Pattan, J. N., Parthiban, G., Banakar, V. K., Tomer, A., and Kulkarni, M. (2008). Relationship between chemical composition and magnetic susceptibility in sediment cores from Central Indian Ocean Basin. *J. Earth Syst. Sci.* 117, 113–119. doi: 10.1007/s12040-008-0002-5

Prescott, J. R., and Hutton, J. T. (1994). Cosmic ray contributions to dose rates for luminescence and ESR dating: large depths and long-term time variations. *Radiat. Meas.* 23, 497–500. doi: 10.1016/1350-4487(94)90086-8

Püspöki, Z., Fogarassy-Pummer, T., Thamó-Bozsó, E., Berényi, B., Cserkész-Nagy, Á, Szappanos, B., et al. (2020). High-resolution stratigraphy of a Quaternary fluvial deposit based on magnetic susceptibility variations (Jászság Basin, Hungary). *Boreas* 49, 181–199. doi: 10.1111/bor.12412

Raj, R. (2008). Occurrence of volcanic ash in the Quaternary alluvial deposits, lower Narmada basin, western India. *J. Earth Syst. Sci.* 117, 41–48. doi: 10.1007/s12040-008-0011-4

Raj, R., and Yadava, M. G. (2009). Late Holocene uplift in the lower Narmada basin, western India. *Curr. Sci.* 96, 985–988.

Rajshekhar, C., Gawali, P., Mudgal, T., Reddy, P., and Basavaiah, N. (1991). Micropaleontology and mineral magnetic evidences of the Holocene mudflats of Navlakhi, Gulf of Kachchh. *J. Ind. Geophys. Union* 8, 71–77.

Rajshekhar, C., Gawali, P. B., Mudgal, T. R., Reddy, P. P., and Basavaiah, N. (2004). Micropaleontology and mineral magnetic evidences of the Holocene mudflats of Navlakhi, Gulf of Kuchchh. *J. Ind. Geophys. Union* 8, 71–77.

Rosenblum, S., Leo, G. W., and Srivastava, S. P. (2000). *Methods and Preliminary Results of Heavy-Mineral Studies in Liberia*. Denver, CO: US Department of the Interior, US Geological Survey.

Roy, P. D., Caballero, M., Lozano, R., and Smykatz-Kloss, W. (2008). Geochemistry of late quaternary sediments from Tecocomulco lake, central Mexico: implication to chemical weathering and provenance. *Chem. Erde Geochem.* 68, 383–393. doi: 10.1016/j.chemer.2008.04.001

Sant, D. A., and Karanth, R. V. (1993). Drainage evolution of the lower Narmada valley, western India. *Geomorphology* 8, 221–244.

Singh, P. (2009). Major, trace and REE geochemistry of the Ganga River sediments: influence of provenance and sedimentary processes. *Chem. Geol.* 266, 251–264.

Singh, P. (2010). Geochemistry and provenance of stream sediments of the Ganga River and its major tributaries in the Himalayan region, India. *Chem. Geol.* 269, 220–236. doi: 10.1016/j.chemgeo.2009.09.020

Singh, P., and Rajamani, V. (2001). Geochemistry of the floodplain sediments of the Kaveri River, Southern India. *J. Sediment. Res.* 71, 50–60. doi: 10.1306/042800710050

Sridhar, A., Bhushan, R., Balaji, D., Band, S., and Chamyal, L. S. (2016). Geochemical and Sr–Nd isotopic variations in palaeoflood deposits at mainstem–tributary junction, western India: implications on late Holocene flood events. *Catena* 139, 32–43. doi: 10.1016/j.catena.2015.12.004

Sridhar, A., and Chamyal, L. S. (2010). Sediment records as archives of the Late Pleistocene-Holocene hydrological change in the alluvial Narmada River basin, western India. *Proc. Geol. Assoc.* 121, 195–202. doi: 10.1016/j.pgeola.2010.01.001

Sridhar, A., Laskar, A., Prasad, V., Sharma, A., Tripathi, J. K., Balaji, D., et al. (2015). Late Holocene flooding history of a tropical river in western India in response to southwest monsoon fluctuations: a multi proxy study from lower Narmada valley. *Quat. Int.* 371, 181–190.

Sridhar, A., Thakur, B., Basavaiah, N., Seth, P., Tiwari, P., and Chamyal, L. (2020). Lacustrine record of high magnitude flood events and climate variability during mid to late Holocene in the semiarid alluvial plains, western India. *Palaeogeogr. Palaeoclimatol. Palaeoecol.* 542:109581.

Stanford, S. D., Witte, R. W., Braun, D. D., and Ridge, J. C. (2016). Quaternary fluvial history of the Delaware River, New Jersey and Pennsylvania, USA: the effects of glaciation, glacioisostasy, and eustasy on a proglacial river system. *Geomorphology* 264, 12–28.

Sukumaran, P., Rajshekhar, C., Sant, D. A., and Krishnan, K. (2012a). Late holocene storm records from lower reaches of Narmada Valley, western India. *J. Geol. Soc. India* 80, 403–408.

Sukumaran, P., Sant, D. A., Krishnan, K., and Rangarajan, G. (2012b). High resolution facies record on late holocene flood plain sediments from lower reaches of Narmada Valley, Western India. *J. Geol. Soc. India* 79, 41–52.

Sun, X., Li, Y., Feng, X., Lu, C., Lu, H., Yi, S., et al. (2016). Pedostratigraphy of aeolian deposition near the Yunxian Man site on the Hanjiang River terraces, Yunxian Basin, central China. *Quat. Int.* 400, 187–194.

Thomas, P. J., Juyal, N., Kale, V. S., and Singhvi, A. K. (2007). Luminescence chronology of late Holocene extreme hydrological events in the upper Penner River basin, South India. *J. Quat. Sci.* 22, 747–753.

Thompson, R., and Morton, D. (1979). Magnetic susceptibility and particle size distribution in recent sediments of the Loch Lomond drainage basin, Scotland. *J. Sediment. Petrol.* 49, 0801–0812.

Thompson, R., Stober, J., Turner, G., Oldfield, F., Bloemendal, J., Dearing, J., et al. (1980). Environmental applications of magnetic measurements. *Science* 207, 481–486.

Tripathi, J. K., Ghazanfari, P., Rajamani, V., and Tandon, S. K. (2007). Geochemistry of sediments of the Ganges alluvial plains: evidence of large-scale sediment recycling. *Quat. Int.* 159, 119–130.

Vázquez, G., Solís, B., Solleiro-Rebolledo, E., and Goguitchaichvili, A. (2016). Mineral magnetic properties of an alluvial paleosol sequence in the Maya Lowlands: late Pleistocene–Holocene paleoclimatic implications. *Quat. Int.* 418, 10–21.

Conflict of Interest: The authors declare that the research was conducted in the absence of any commercial or financial relationships that could be construed as a potential conflict of interest.

frontiers
in Earth Science

ORIGINAL RESEARCH
published: 13 May 2021
doi: 10.3389/feart.2021.666846

The Probable Critical Role of Early Holocene Monsoon Activity in Siting the Origins of Rice Agriculture in China

John Dodson[1,2]*, Hsiao-chun Hung[3], Chenzi Li[1], Jianyong Li[4], Fengyan Lu[1] and Hong Yan[1]

[1] State Key Laboratory of Loess and Quaternary Geology, Institute of Earth Environment, Chinese Academy of Sciences, Xi'an, China, [2] School of Earth, Atmospheric and Life Sciences, University of Wollongong, Wollongong, NSW, Australia, [3] Department of Archaeology and Natural History, Australian National University, Canberra, ACT, Australia, [4] Shaanxi Key Laboratory of Earth Surface and Environmental Carring Capacity, College of Urban and Environmental Sciences, Northwest University, Xi'an, China

Edited by:
Anoop Ambili,
Indian Institute of Science Education and Research Mohali, India

Reviewed by:
Xinxin Zuo,
Fujian Normal University, China
Qianli Sun,
East China Normal University, China

****Correspondence:***
John Dodson
john@ieecas.cn

Specialty section:
This article was submitted to Quaternary Science, Geomorphology and Paleoenvironment, a section of the journal Frontiers in Earth Science

Received: *11 February 2021*
Accepted: *22 March 2021*
Published: *13 May 2021*

Citation:
Dodson J, Hung H-c, Li C, Li J, Lu F and Yan H (2021) The Probable Critical Role of Early Holocene Monsoon Activity in Siting the Origins of Rice Agriculture in China. Front. Earth Sci. 9:666846. doi: 10.3389/feart.2021.666846

The long process of rice domestication likely started 10,000–8,000 years ago in China, and the pre-existing hunter-gatherer communities gradually adopted more sedentary lifestyles with the dependence of rice agricultural economies. The archeological evidence builds a strong case for the first domestication of rice to *Oryza sativa* centered in the Middle-Lower Yangtze Valley during the early Holocene. The genetic evidence identifies the main ancestor of *O. sativa* was *O. rufipogon,* however, this now occurs naturally south of the Yangtze where its distribution is limited by summer temperatures and mean annual temperature. The mismatch between occurrence of ancestors and presumed sites of early cultivation leads to a number of hypotheses. These include that first domestication actually took place further south, such as in the Pearl River valley but archeological evidence is currently lacking for this. Or domestication took place, when *O. rufipogon* had a more extensive natural range in the past. Early to mid-Holocene palaeoclimate reconstructions show that the East Asian Summer Monsoon was more active in the early Holocene and estimates show that the temperature requirements for *O. rufipogon* were met for a substantial area of northeast China at the time. This would mean that earliest known domestication sites and presumed ancestor distribution coincided for several millennia. Thus early records of rice farming in Henan and Shandong were easily accommodated by early to mid Holocene climates.

Keywords: early rice agriculture, role of Holocene monsoon activity, wild rice climate controls, Yangtze and NE China Holocene climates, role of summer and annual temperatures

INTRODUCTION

Cereal crops became an important part of human activity in the early Holocene, in several places. These were millets and rice in China, and wheat and barley in the Fertile Crescent of western Eurasia. Several hypotheses have been developed around the timing of this, and a common theme that the Holocene was a time of more reliable and stable climate than that of the late Pleistocene and human populations had begun to increase. New methods of providing food were essential to continue this as hunting and gathering was dependent on the success of finding food as the seasons came and went, and thus usually required a nomadic lifestyle to chase the spoils. The new methods involved herding animals and farming crops. As a result of stable food supply, the population increased substantially with the development of agriculture. Crop production required land management and some form of land ownership. People then developed a more sedentary lifestyle, and once food production became more reliable and surpluses were established, settlements, division of labor, time for innovation and cultural differentiation followed.

Rice is one of the world's most important crops. It is widely believed that rice agriculture first developed in the Middle to Lower Yangtze valley region of China since archaeobotanical data for a wider consideration of areas is scarce. The success of growing rice comes from its high grain yields, in the right environmental setting, and today two or sometimes three crops per year can be grown, and that the grain keeps well in storage. Several species of the rice genus *Oryza* occur naturally in China. The supposed trajectory of rice agriculture developed from a period where the grains were gathered from wild species, at some point plants were deliberately planted beyond their normal range, which of course worked where conditions were within their ecological tolerance. Then followed a gradual domestication process, which Gross and Zhao (2014) and Stevens and Fuller (2017) postulated took 1–2,000 years or more. Domestication was accompanied by improved tools for cultivation, and resulted in plants which could grow in additional ecological settings, some of which were created by humans. Overall grain productivity was gradually enhanced. In the course of this the domesticated form had become an annual species. The latter trait helped because ripening narrowed the time period required for harvesting the grain, and storage was also convenient. Crop enhancement processes for rice continue to the present day.

The early sites where rice was apparently cultivated seem to be focused on the Middle to Lower Yangtze valley and sites nearby. These include sites in Hunan (e.g., Anping, 1998; Hunan Provincial Institution of Archaeology and Cultural Relics [HPIACR]., 2006; Gross and Zhao, 2014; Guo and Guo, 2014), Zhejiang (e.g., Fuller et al., 2007, 2009, 2011; Zuo et al., 2017; Qiu et al., 2019), southwest Henan (e.g., Zhang and Hung, 2013; Deng et al., 2015), Jiangsu (e.g., Zhang et al., 2014; Qiu et al., 2018), and near the Jiangsu-Shanghai border (Atahan et al., 2008). The problem with interpretation of the early dates is that sites are often not always associated with the tools of cultivation or clear evidence of sedentary societies associated with the crops. Often the evidence for early pre-domestication cultivation is associated with considerable amounts of wild foods and animals or fish which suggest a hunting and gathering life-style was supplemented with some cropping. The turning point of clear domestication is best documented for the Hemudu cultural sites around 4000 BC (Fuller et al., 2009).

The apparent site of origin of rice agriculture is outside the natural range of its supposed ancestors. Here we review the archeological record of growing rice in the Neolithic period, and consider whether the main ancestor of domesticated rice had a wider distribution in the past. For this we estimate the parameters which define the natural occurrence of *Oryza rufipogon* and consider early Holocene climates of eastern China as a possible reason for a much wider distribution in the past. The latter could account for several other early sites known for rice farming.

THE GENUS *ORYZA*

Oryza is a genus of about 24 species, with four occurring naturally or naturalized in China. *O. latifolia* was probably brought to China from Central or South America (Wu et al., 2006). The widely cultivated form is *O. sativa*, and the subspecies *indica* and *japonica* varieties of it; it is an annual aquatic plant. This is the main domesticated species (and subspecies). *Oryza glaberrima* is the other cultivated species, it is also an annual, it is grown in Hainan and Yunnan, and is much less widely grown than *O. sativa.* Several species of *Oryza* occur in Bangladesh, Cambodia, India, Indonesia, Malaysia, Myanmar, New Guinea, Sri Lanka, Philippines, Thailand, Vietnam and northern Australia. According to the Flora of China the three main native species of *Oryza* are perennials and grow in flooded environments in lowland settings. Many are weeds in cultivated rice fields. The natural occurrence of the native species are generally in Guangdong, Guanxi, Hunan, Jiangxi, Yunnan and the islands of Hainan and Taiwan. *O. rufipogon* is the most common wild form in China, and intermediates with *O. sativa* occur. *O. meyeriana* is regarded as the genetically most primitive form of the genus. *O. glaberrima* occurs in Hainan and Yunnan. **Figure 1** shows the natural distribution of *Oryza rufipogon* in China and elsewhere.

O. rufipogon is regarded as the immediate ancestor of *O. sativa* and its most widely spread cultivars (*O. sativa* var *japonica* and *O. sativa* var *indica*). Huang et al. (2012) analyzed 446 genome sequences of a diverse array of domesticated varieties and *O. rufipogon* from within a cross-section of its natural range. They concluded that first development of cultivated rice likely occurred in the middle reaches of the Pearl River valley in Guangxi. Wei et al. (2012) also suggested that domestication may have been centered on southern China, perhaps 10,000 years ago, with *O. sativa* ssp. *indica*, arising from lower latitude forms, and *O. sativa* ssp. *japonica* from higher latitude forms of *Oryza rufipogon* in line with their different tolerance ranges and attributes. Kovach et al. (2007) and Gross and Zhao (2014) observe there is a case that can be built on genetics for multiple sites and times of domestication. There is currently insufficient archeological evidence to test these hypotheses and consider a southern origin for domestication of rice. Perhaps abundant food resources in southern China made cropping an unnecessary activity in the early Holocene.

Huang and Schaal (2012) used a climate envelope approach to investigate the possible past distribution of *O. rufipogon* in an attempt to account for the richness of the genetic groups within the species. A predicted Last Glacial Maximum range was raised as a possible explanation for the derivation of the range of traits observed amongst the richness of the present genetic diversity seen for the species. Using the present range of the species they found that annual precipitation, mean temperature of diurnal

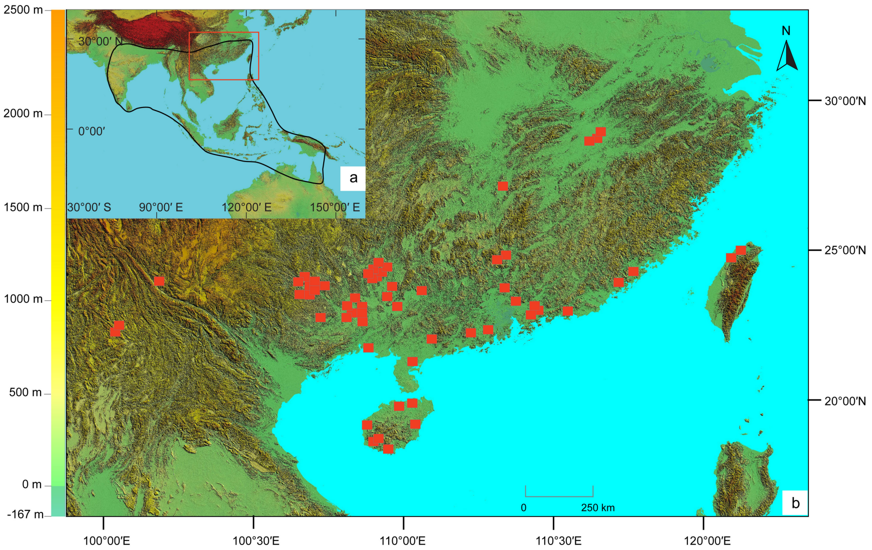

FIGURE 1 | Natural distribution of *Oryza rufipogon*. Inset shows full natural distribution. On the mainland the distribution is in Yunnan, Guangxi, Guangdong, Hunan, Jiangxi, and offshore on the islands of Hainan and Taiwan. The natural populations in Jiangxi and Taiwan are extinct due to habitat destruction. Based on Flora of China, *Oryza*, in volume 22, Huang and Schaal (2012) and Zhou et al. (2010).

range in the warmest quarter and minimum temperatures of the coldest months gave the main explanations for the observed modern range. There is no definitive fossil evidence for Last Glacial Maximum range of *O. rufipogon* outside the current known range, but it probably does not preserve well as fossils.

Early domestication beyond the natural limit of *O. rufipogon* has been used to suggest that the native species was possibly transported northward for possible cultivation purposes or that a Holocene climatic optimum may have been essential for the establishment of a more northerly distribution of rice farming, including the Yangtze Valley (Fan et al., 1999; Fuller, 2011). But the latter has not been tested against the tolerance limits of *O. rufipogon.*

Zhou et al. (2013) examined the geographic variation of a number of traits across the climatic range of *O. rufipogon* in China. The traits differed in northern and southern populations. The main climate controls were mean annual temperature, mean temperature of the warmest quarter and mean temperature of the wettest quarter. They also carried out some transplantation experiments in Hubei and Hainan to test the viability of several groups. The northern populations were better able to survive the Winter in Hubei. We examine this in more detail below.

THE ARCHEOLOGICAL RECORD

The number of sites with early rice in the Chinese archeological record is vast. Only a general summary can be presented here. A summary of many of the main arguments are given in Fuller (2011) and Gross and Zhao (2014). The archeological records center mainly on the middle to lower Yangtze River in Zheijiang, Hunan, Jiangsu and southwest Henan, dated to as early as 8700-8000 BP. Most of these are based on distinctive phytoliths (e.g., Wu et al., 2014; Ma et al., 2016; Qiu et al., 2018), individually dated seeds or seeds in a stratigraphic context (e.g., see Deng et al., 2015; Yang et al., 2018), and cereal pollen of presumed rice origin (e.g., Dodson et al., 2006).

Beyond the core areas of the Middle to Lower Yangtze, a similar date (about 8,700–8,300 BP) has been reported for a primitive form of rice from Jiahu, located in the east on the Huai River in Henan province, south of Zhengzhou (Zhang and Tang, 1996; Zhang and Wang, 1998; Zhang and Hung, 2013). Crawford et al. (2016) report what is probably domesticated rice from Yuezhuang in Shandong at about 8,000–7,700 cal BP, and d'Alpoim Guedes et al. (2015) regard these as within the tolerance range of *O. sativa*. Rice dated to similar age, ca. 8000 BP, was reported from another site (Xihe) in Shandong, although its identification was uncertain as possible wild, cultivated, or domesticated (Jin et al., 2014). It is unclear how far along the pathway to domestication these samples were. There is evidence that rice was grown in the Guangzhong basin of Shaanxi, on the Loess Plateau, and in Henan in the mid-Holocene (e.g., Li et al., 2009; Rosen et al., 2017). In fact, mid to late Holocene dates are widespread, including from Shandong (Jin et al., 2016) to Hainan provinces (Wu et al., 2016; see below). Zhang and Hung (2010) and Yang et al. (2018) summarized the published evidence and they present a case for routes taking rice agriculture southward from the Yangtze area. This included a route to the southeast through Fujian and to Taiwan, and a route to the southwest that led to Mainland southeast Asia.

The earliest record of rice farming in Guangdong is particularly interesting. As it stands rice was introduced into the Pearl River Delta, Guangdong, around 4,000 BP (Yang et al., 2018) or 4,500–3,700 BP (Xia et al., 2019), and diffused elsewhere from there. Thus, there is no hard evidence to suggest domestication took place there and in any case the dates are significantly later than the Yangtze records. The early date for domesticated rice in Hainan, 5,600 cal BP (Wu et al., 2016), does not fit with the larger picture. So far the earliest known domesticated rice in coastal southern China is no earlier than 5,000 cal BP. This may need further clarification. Apparently rice agriculture contracted southward after the mid-Holocene Optimum, and retreated from more marginal areas in the north and west. The pathways to Fujian and Guangdong were likely along river valleys and radiocarbon dates based on phytoliths in sediment sequences and archeological sites show an orderly transfer of rice farming to these areas between 5 and 4 kyr BP. Even though rice appears to be present, often the number of recovered grains is small and it can be difficult to prove that rice was actually intensively grown in them as sometimes no accompanying sedentary living sites or agricultural tools are reported in association.

The low numbers of rice grains in the early sites and the note that they are usually accompanied by many wild species of plants and animals, suggests a mix of hunting and gathering was accompanied by some cropping. In other words, there appears to be no hard boundary between hunting and gathering and agriculture.

What is clear from the available records is that the earliest known sites are outside the natural range of native *Oryza* species.

CLIMATE CONTROLS ON THE NATURAL DISTRIBUTION OF *ORYZA RUFIPOGON*

Zhou et al. (2013) found that mean annual temperature and mean temperature of the warmest quarter were important controls on the natural distribution of *O. rufipogon,* and that more northerly natural populations were able to better withstand winters, for example, when transplanted to Hubei. To examine this in more detail we collected the mean monthly temperature data for 20 sites across Guangxi, Jiangxi, Hunan and Fujian where *O. rufipogon* occurs. These were averages across a 30 years period from 1981 to 2010 (China Meteorological Data Service Centre [CMDSC]., 2020), which is presumed to be a fitting period for a perennial species. We selected sites around 100 m asl as modern distributions are rarely much below this. The data for the sites is shown in **Table 1**.

In general, a comparison of the means from the climate data across the 20 sites show that monthly temperatures are in decline after summer and by September at all stations, and while mean temperatures for the warmest quarter are generally around 26–27°C the mean annual temperatures show differences between provinces, with Guangxi (the most southerly and warmest) to more inland provinces (Hunan, the coolest). But none of the differences appear to be pronounced. Mean annual temperatures around 17–21°C predominate, with the lower values due to lower temperatures in winter months, which are likely important for a perennial species. To examine the likelihood of expanded *O. rufipogon* distribution further north than today would require mean summer temperatures above about 26°C and mean annual temperatures above 17°C. The modern climate of Changsha (Hunan), Zhengzhou (Henan) and Shanghai shows they have mean summer temperatures of 29, 27, and 27°C, respectively, and they all have mean annual temperatures well below 17°C. While favorable specialized niches for *O. rufipogon* may exist around the Yangtze and beyond, generally speaking, the modern distribution as published in the Flora of China does not identify these.

TABLE 1 | Mean temperatures (°C) averaged from 1981 to 2010 from selected sites in Guangxi, Jiangxi, Hunan and Fujian.

Site	Elevation (m asl)	June	July	August	September	Mean for warmest quarter	Mean annual
Guangxi							
Liucheng	108	27.1	28.4	28.5	26.4	27.6	20.3
Pingle	106	27.2	28.8	28.6	26.4	27.8	20.3
Tiandong	111	27.8	28.4	28.3	26.4	27.7	22.2
Shanglin	115	27.1	27.9	28	26.2	27.3	21
Xiangzhou	91	27.4	28.7	28.4	26.5	27.8	20.8
Jiangxi							
Xiushui	147	24.9	28.1	27.3	23.6	26	16.8
Yifeng	92	25.5	28.5	27.9	24.3	26.6	17.4
Fenyi	94	25.9	29.1	28.2	24.6	27	17.9
Wanan	102	26.5	29.3	28.4	24.8	27.3	18.5
Nankang	127	26.8	29.2	28.5	25.4	27.5	19.3
Hunan							
Ningxiang	75	25.5	28.9	28	23.5	26.5	17.1
Pingjiang	106	25.2	28.4	27.6	23.6	26.2	17
Anren	102	26.4	29.6	28.4	24.5	27.2	18
Yongxing	124	26.2	28.9	27.8	24.2	26.8	17.9
Shuangfeng	100	25.6	28.9	28	23.8	26.6	17.2
Fujian							
Shaxian	121	26.1	28.6	28.1	25.6	27.1	19.6
Youxi	137	25.7	28	27.4	24.9	26.5	19.2
Fuzhou	84	26.1	29.2	28.8	26.1	27.6	20.1
Anxi	68	26.7	28.9	28.5	26.6	27.6	21.2
Yongtai	86	26.1	28.7	28	25.5	27.1	19.9

The early to mid Holocene climates of northeastern China.

A case for a more northerly distribution of *O. rufipogon*, and overlapping early rice farming sites would require a warmer and possibly wetter climate north of the Yangtze compared to today. This would imply a more active East Asian Summer Monsoon.

There are now many data sets that have been used to reconstruct early to mid-Holocene temperatures in northern China. Zhou et al. (2010) and Li et al. (2011) examined lipids in peat in Jilin and pollen from Jingbo lake in Heilongjiang and identified warmer climates than today from about 10.5 kyr to about 6 kyr BP. They invoked a stronger East Asian Summer Monsoon to account for this. The Sihailongwan Maar in NE China (Jilin) has annually laminated sediments and high-resolution pollen analysis has been used to reconstruct temperatures for the past 15,000 years (Stebich et al., 2015). Zheng et al. (2018) measured organic compounds in peats from northeast China and estimated that temperatures were ∼5–7°C warmer than today, and that soil moisture increased from the early to late Holocene. Zhang et al. (2018) used two stalagmite records to infer that monsoon intensity was greater in the early

Holocene in north China. The current mean July temperatures are about 20–21°C, however, these are estimated to be above 26°C between 8,500 and 4,200 cal yr BP. Branched membrane lipids from soil bacteria in the Mangshan loess, near Zhengzhou in central China, have been used to model July temperatures. These were, with tolerable errors, over 26°C between 8,700 and 4,200 cal yr BP (Peterse et al., 2011). Zhang Z.Q. et al. (2020) argued that an expansion of trees in Heilongjiang suggested it was warmer there from about 8–4.6 kyr BP. Overall, the start and end dates of the warmest and wettest periods do not match precisely, but it is clear that the early to mid-Holocene of northeastern China was warmer than today, while the various records show some disagreement about whether the climate was necessarily wetter than today. Moisture definitely increased in the later Holocene but this may have been due to reduced evapotranspiration when temperatures were lower. Goldsmith et al. (2017), Zhang Z.Q. et al. (2020), and Zhang R. et al. (2020), suggest that a stronger East Asian Summer Monsoon in northeast China was due to orbital configurations and a reduction in northern ice sheet cover.

The climate around the earliest archeological sites in the Yangtze valley during the Holocene may have been critical for the domestication of rice. Yi et al. (2003a,b) found that there was a wet and warm climate in the Lower Yangtze Valley from about 10,300–9,000 cal yr BP, it cooled a little after that until about 7,600 cal yr BP then warmed again. Li et al. (2018) estimated that climates were warmer and wetter between 10,000 and 7,000 cal yr BP also in the lower Yangtze region, and there were strong oscillations after 7,000 cal yr BP. Fu et al. (2018) also found that summer rainfall was about 30% higher than modern between about 10,000 and 6,000 cal yr BP. While the modeled temperature estimates are for July, the warmest month, they can probably be extrapolated across summers. Reconstructions for the Lower Yangtze also easily exceed the requirements based on modern day *O. rufipogon* distribution (Li et al., 2018), and indeed precipitation was perhaps 30% higher than present.

In summary, early Holocene climates show warmer and wetter conditions compared to today, and these brought a much wider area within the tolerance limits and therefore distribution of *O. rufipogon*. The driving force behind this was a more active East Asian Summer Monsoon, which was controlled by orbital forcing and a reducing northern ice sheet.

DISCUSSION

The importance of rice as a crop is widely recognized due to its characteristics, productivity and storage capabilities. Once domestication was well- advanced it was spread widely in China and elsewhere.

As the record stands the most compelling evidence that agricultural systems with rice as their center were first established in the Middle to Lower Yangtze valley region (**Figure 2**). The main domesticated form of rice in China is *Oryza sativa,* an annual, and its subspecies. It is well-established that the key ancestor was *O. rufipogon*, a perennial species. The path to domestication probably took place over many centuries. The genetic diversity of native species of *Oryza* is probably centered on the Pearl River Valley in southern China, and the modern natural occurrence of native species is south of the sites where early cultivated rice appears in archeological records.

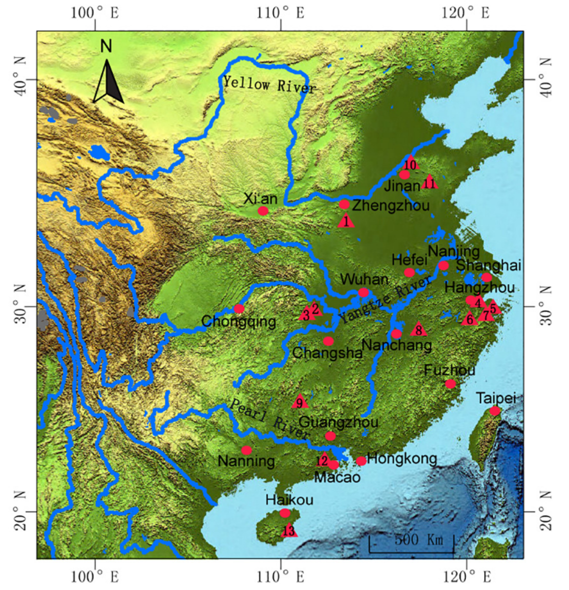

FIGURE 2 | Map showing important sites related to this study. (1) Jiahu, (2) Bashidang, (3) Pengtoushan, (4) Kuahuqiao, (5) Hemudu, (6) Shangshan, (7) Xiaohuangshan, (8) Dingnan Jiangxi, (9) Xianrendong/Daotonghuan, (10) Yuezhuang, (11) Xihe, (12) Pearl River delta.

The mismatch in distribution of *O. sativa* in the early archeological record and modern natural distribution of *O. rufipogon* requires some explanation, and this may shed light on how, where and when domestication took place. The most parsimonious explanations are that domestication took place further south where *O. rufipogon* occurs, but an archeological record for this is missing, or that *O. rufipogon* had a wider distribution in the past into the area where we do see early domesticated rice. It seems unlikely that wild *O. rufipogon* plants were transplanted to the north where we currently see that domesticated forms developed.

Many plant and animal species were first domesticated in the Pearl River Valley (Dodson and Dong, 2016) but rice is missing from that list. If *O. rufipogon* had a more northerly occurrence in the past it may have overlapped with the first farming sites for rice. *O. rufipogon* can occur outside its natural range and occurs as a weed in *O. sativa* paddy fields. This is likely due to habitats and microclimates created by humans to grow rice crops. Climate tolerance limits for *O. rufipogon*, based on its natural occurrence are warm summers with temperatures above about 26°C, and mean annual temperatures above 17°C. Today these conditions are generally south on the Yangtze, and in the provinces including Fujian, Hunan and Guangdong.

Some have argued that domestication of rice took place just very close to the natural limit of *Oryza rufipogon* in the Yangtze valley (e.g., Fuller, 2011). If this was the case the species may have been under stress and therefore malleable to change to the domesticated form. However, as a perennial grass it probably had wide dispersible capacity, and may have been able to colonize areas within its environmental envelope quite quickly.

Warmer and perhaps wetter climate occurred much further north that today in the early Holocene. And where temperatures can be quantified they easily exceed the minimal requirements for *O. rufipogon*. These conditions were driven by a more intense East Asian Summer Monsoon, and this is recorded in a wide variety of records. The most likely cause of this was the orbital forcing which enabled monsoon activity to expand into the region as far as northeast China. It appears that once the northern ice sheets decayed sufficiently the Westerlies became more intense and the northeast cooled and became drier, and warmth loving species retreated southward. While there is no clear evidence of *O. rufipogon* in northeast China during the early Holocene it is clear that conditions were suitable for its occurrence and with sufficient overlap in time in sites where rice was fully domesticated and probably beyond.

A wider occurrence of *O. rufipogon* into northeast China provides support for the early evidence of domesticated rice in Shandong and elsewhere in the northeast.

CONCLUSION

There is a mismatch between the current distribution of native *Oryza* species and the earliest known sites of domestication into *Oryza sativa*. This may indicate that *Oryza rufipogon*, in particular, had a much wider distribution in the past, and overlapped with the earliest sites of domestication, or that the latter first occurred in the Pearl River basin. There is no compelling evidence to support a Pearl River basin origin. The bulk of evidence for first rice farming is centered around the Yangtze valley or nearby. However there are a small number of intriguing cases that point to early domesticated rice north of the Yangtze. Additional research to identify early *O.rufipogon* occurring much further north, and overlapping the early archeological sites is needed to test this.

As things stand the simplest explanation for the development of rice agriculture in the Lower Yangtze Valley possibly took place from native *O. rufipogon* growing nearby when the climate of the early to mid-Holocene had extended that species range much further north compared to today. This would require a more active East Asian Summer Monsoon compared to today and there is abundant evidence to support this from northeast China, perhaps as far north as Shandong or even further north into Jilin as the climate envelopes are suitable according to quantitative climate estimates. This makes the apparent outliers of early rice in Shandong and elsewhere well within the bounds of possibility.

DATA AVAILABILITY STATEMENT

The raw data supporting the conclusions of this article will be made available by the authors, without undue reservation.

AUTHOR CONTRIBUTIONS

JD conceived the main idea. HH fleshed out the archeological side. FL, JL, CL, and HY helped with the analyses and writing. All authors contributed to the article and approved the submitted version.

FUNDING

This work was supported by the Strategic Priority Research Program of the Chinese Academy of Sciences XDB40000000 and the National Natural Science Foundation of China 2077413.

REFERENCES

Anping, P. (1998). Notes on new advancements and revelations in the agricultural archaeology of early rice domestication in the Dongting Lake region. *Antiquity* 72, 878–885. doi: 10.1017/s0003598x00087512

Atahan, P., Itzstein-Davey, F., Taylor, D., Dodson, J., Qin, J., Zheng, H., et al. (2008). Holocene-aged sedimentary records of environmental changes and early agriculture in the lower Yangtze, China. *Quat. Sci. Rev.* 27, 556–570. doi: 10.1016/j.quascirev.2007.11.003

China Meteorological Data Service Centre [CMDSC]. (2020). *China Meteorological Data Service Centre*. Available online at: https://data.cma.cn/ (accessed July, 2020).

Crawford, G. W., Chen, X. X., Luan, F., and Wang, J. (2016). People and plant interaction at the Houli Culture Yuezhuang site in Shandong province, China. *Holocene* 26, 1594–1604. doi: 10.1177/0959683616650269

d'Alpoim Guedes, J., Guiyun, J., and Bocinsky, R. K. (2015). The impact of climate on the spread of rice to north-east China: a new look at the data from Shandong Province. *PLoS One* 10:e0130430. doi: 10.1371/journal.pone.0130430

Deng, Z., Qing, L., Gao, Y., Weisskopf Alison, R., Zhang, C., and Fuller, Q. D. (2015). From early domesticated rice rice in the Middle Yangtze basin to millet, rice and wheat agriculture: archaeobotanical macro-remains from Balgang, Nanyang basin, Central China, 6700 -500 BC. *PLoS One* 10:e0239865. doi: 10.1371/journal.pone.0139885

Dodson, J. R., and Dong, G. H. (2016). What do we know about domestication in eastern Asia? *Quat. Int.* 426, 2–9. doi: 10.1016/j.quaint.2016.04.005

Dodson, J. R., Hickson, S., Khoo, R., Li, X.-Q., Toia, J., and Zhou, W. J. (2006). Vegetation and environmental history for the past 14 000 yr BP from Dingnan, Jiangxi Province, South China. *J. Integr. Plant Biol.* 48, 1018–1027. doi: 10.1111/j.1744-7909.2006.00274.x

Fan, S. G., Zhang, Z. J., Liu, L., Liu, H. X., and Liang, C. Y. (1999). "Species and geographical distribution of wild rice and their biological characteristic in China," in *Proceedings of the Third National Symposium on the Conservation and Sustainable Use of Biological Diversity*, (Beijing: China Forestry Publishing House)

Fu, F., Ma, C., Zhu, C., Lu, H. Y., Zhang, X. J., Huang, K. Y., et al. (2018). Variability of East Asian summer monsoon precipitation during the Holocene and possible forcing mechanisms. *Clim. Dyn.* 52, 969–989. doi: 10.1007/s00383-018-4175-6

Fuller, D. Q. (2011). Pathways to Asian civilizations: tracing the origins and spread of rice and rice cultures. *Rice* 4, 78–92.

Fuller, D. Q., Qin, L., and Harvey, E. (2007). "Evidence for a late onset of agriculture in the Lower Yangtze region and challenges for an archaeobotany of rice," in

Human Migrations in Continental East Asia and Taiwan: genetic, Linguistic and Archaeological Evidence, eds A. Sanchez-Mazas, R. Blench, M. D. Ross, M. Lin, and I. Pejros (London: Taylor and Francis).

Fuller, D. Q., Qin, L., Zhao, Z. J., Zheng, Y. F., Hosoya, L. A., Chen, X. G., et al. (2011). "Study on the botanic remains from the Tianluoshan site, in Center for the Study of Chinese Archaeology," in *Integrated Studies on the Cultural Remains from Tianluoshan*, ed. Peking University and Zhenjiang Province Institute of Archaeology and Cultural Heritage (Beijing: Wenwu Press), 470–496.

Fuller, D. Q., Qin, L., Zheng, Y. F., Zhao, Z. J., Chen, X. G., Hosoya, L. A., et al. (2009). The domestication process and domestication rate in rice, spikelet bases from the Lower Yangtze. *Science* 323, 1607–1610. doi: 10.1126/science.1166605

Goldsmith, Y., Broecker, W. S., Xu, H., Pratigya, J., de Menocal, P. B., and Porat, N. (2017). Northward extent of East Asian monsoon covaries with intensity on orbital and millennial timescales. *Proc. Nat. Acad. Sci.* 114, 1817–1821. doi: 10.1073/pnas.1616708114

Gross, B. L., and Zhao, Z. (2014). Archaeological and genetic insights into the origins of domesticated rice. *Proc. Nat. Acad. Sci.* 111, 6190–6197. doi: 10.1073/pnas.1308942110

Guo, J. Y., and Guo, L. X. (2014). The origins and formation of rice cultivation: spatio-temporal parameters. *Agric. Hist. China* 2014:05.

Huang, P., and Schaal, B. A. (2012). Association between the geographic distribution during the last Glacial maximum of Asian wild rice, *Oryza rufipogon* (Poaceae), and its current genetic variation. 2012. *Amer. J. Bot.* 99, 1866–1874. doi: 10.3732/ajb.1200348

Huang, X., Kurata, N., Wei, X., Wang, Z. X., Wang, A., Zhao, Y., et al. (2012). A map of rice genome variation reveals the origin of cultivated rice. *Nature* 490, 497–501.

Hunan Provincial Institution of Archaeology and Cultural Relics [HPIACR]. (2006). *Pengtoushan and Bashidang*. Beijing: Science Press.

Jin, G. Y., Wagner, M., Tarasov, P. E., Wang, F., and Liu, Y. C. (2016). Archaeobotanical records of Middle and Late Neolithic agriculture from Shandong Province, east China, and a major change in regional subsistence during the Dawenkou Culture. *Holocene* 26, 1605–1610. doi: 10.1177/0959683616641746

Jin, G. Y., Wu, W. W., Zhang, K. S., Wang, Z. B., and Wu, X. H. (2014). 8000 year-old rice remains from the north edge of the Shandong Highlands, east China. *J. Archaeol. Sci.* 51, 34–42. doi: 10.1016/j.jas.2013.01.007

Kovach, M. J., Sweeney, M. T., and McCounch, S. R. (2007). New insights into the history of rice domestication. *Trends Gene.* 23, 578–587. doi: 10.1016/j.tig.2007.08.012

Li, C., Wu, Y., and Hou, X. (2011). Holocene vegetation and climate in Northeast China revealed from Jingbo Lake sediment. *Quat. Int.* 229, 67–73. doi: 10.1016/j.quaint.2009.12.015

Li, J. Y., Dodson, J. R., Yan, H., Wang, W. M., Innes, J. B., Zong, Y. Q., et al. (2018). Quantitative Holocene climatic reconstructions for the lower Yangtze region of China. *Clim. Dyn.* 50, 1101–1113. doi: 10.1007/s00382-017-3664-3

Li, X. Q., Shang, X., Dodson, J. R., and Zhou, X. Y. (2009). Holocene agriculture in the Guanzhong basin in northwest China indicated by pollen and charcoal evidence. *Holocene* 19, 1213–1220. doi: 10.1177/0959683609345083

Ma, Y., Yang, X., Huan, W., and Zhuang, Y. (2016). Rice bulliform phytolith reveal the process of rice domestication in the Neolithic Lower Yangtze River region. *Quat. Int.* 426, 126–132. doi: 10.1016/j.quaint.2016.02.030

Peterse, F., Prins, M. A., Beets, C., Troelstra, S. R., Zheng, H., Gu, Z., et al. (2011). Decoupled warming and monsoon precipitation in East Asia over the last deglaciation. *Earth Planet. Sci. Lett.* 301, 256–264. doi: 10.1016/j.epsl.2010.11.010

Qiu, Z. W., Zhuang, L. N., and Lin, L. G. (2018). Phytolith evidence for rice domestication of the Hanjing Site in Sihong, Jiangsu Province and the related issues. *Southeast Cult.* 2018, 71–80.

Qiu, Z., Leping, J., Changsui, W., David, V. H., and Yan, W. (2019). New evidence for rice cultivation from the early Neolithic Hehuashan site. *Archaeol. Anthropol. Sci.* 11, 1259–1272. doi: 10.1007/s12520-018-0602-1

Rosen, A., Macphail, R., Li, L., Chen, X. C., and Weisskopf, A. (2017). Rising social complexity, agricultural intensification and the earliest rice paddies in the Loess Plateau of northern China. *Quat. Int.* 437, 50–59. doi: 10.1016/j.quaint.2015.10.013

Stebich, M., Rehfeld, K., Schlütz, F., Taraov, P. E., Liu, J., and Mingram, J. (2015). Holocene vegetation and climate dynamics of NE China based on the pollen record from Sihailongwan Maar Lake. *Quat. Sci. Rev.* 124, 275–289. doi: 10.1016/j.quascirev.2015.07.021

Stevens, C. J., and Fuller, D. Q. (2017). "The spread of agriculture in eastern Asia," in *Language Dynamics and Change*, ed. J. Good (Brill Publications).

Wei, X., Wang, R. S., Cao, L., Yuan, N., Huang, J., Qiao, W., et al. (2012). Origin of Oryza sativa in China inferred by nucleotide polymorphisms of organelle DNA. *PLoS One* 7:e49546. doi: 10.1371/journal.pone.0049546

Wu, Y., Jiang, L., Zheng, Y., Wang, C., and Zhao, Z. (2014). Morphological trend analysis of rice phytoliths during the early Neolithic in the Lower Yangtze. *J. Archaeol. Sci.* 49, 326–331. doi: 10.1016/j.jas.2014.06.001

Wu, Y., Mao, L., Wang, C., Zhang, J., and Zhao, Z. (2016). Phytolith evidence suggests early domesticated rice since 5600 cal BP on Hainan Island of South China. *Quat. Int.* 426, 120–125. doi: 10.1016/j.quaint.2016.01.008

Wu, Z. Y., Raven, P. H., and Hong, D. Y. (2006). *Flora of China, Volume 22: Poaceae*. Beijing: Science Press. Available online at: http://flora.huh.harvard.edu/china (accessed July, 2020).

Xia, X. M., Zhang, P., and Wu, Y. (2019). The analysis of rice remains from the Chaling Site in the Pearl River Delta, Guangdong Province. *Quat. Sci.* 39, 24–36.

Yang, X., Chen, Q., Ma, Y., Li, Z., Hung, H.-C., Zhang, Q., et al. (2018). New radiocarbon and archaeobotanical evidence reveal the timing and route of southward dispersal of rice farming in South China. *Sci. Bull.* 63, 1495–1501. doi: 10.1016/j.scib.2018.10.011

Yi, S., Saito, Y., Oshima, H., Zhou, Y., and Wei, H. (2003a). Holocene environmental history inferred from pollen assemblages in the Huanghe (Yellow River) delta, China: climatic change and human impact. *Quat. Sci. Rev.* 22, 609–628. doi: 10.1016/s0277-3791(02)00086-0

Yi, S., Saito, Y., Zhao, Q., and Wang, P. (2003b). Vegetation and climatic changes in the Changjiang (Yangtze River) Delta, China, during the past 13,000 years inferred from pollen records. *Quat. Sci. Rev.* 22, 1501–1519. doi: 10.1016/s0277-3791(03)00080-5

Zhang, C., and Hung, H. C. (2010). The emergence of agriculture in southern China. *Antiquity* 84, 11–25. doi: 10.1017/s0003598x00099737

Zhang, C., and Hung, H. C. (2013). Jiahu 1: earliest farmers beyond the Yangtze River. *Antiquity* 87, 46–63. doi: 10.1017/s0003598x00048614

Zhang, J. H., and Wang, W. K. (1998). Notes on the recent discovery of ancient cultivated rice at Jiahu, Henan Province: a new theory concerning the origin of *Oryza japonica* in China. *Antiquity* 72, 897–901. doi: 10.1017/s0003598x00087536

Zhang, J., Weiya, L., Chenglong, Y., Zhijie, C., Yuzhang, Y., Luo, W., et al. (2014). Plant resource utilization at Shunshanji site in Jiangsu province based on plant remains analysis. *East Asia Archaeol.* 11, 365–373.

Zhang, M., and Tang, L. (1996). The primitive rice agriculture in the east of the Yangzte River and Huai River. *Agricult. Archaeol.* 1996, 106–121.

Zhang, N., Yang, Y., Cheng, H., Zhao, J. Y., Yang, X. L., Liang, S., et al. (2018). Timing and duration of the East Asian summer monsoon maximum during the Holocene based on stalagmite data from North China. *Holocene* 28, 1631–1641. doi: 10.1177/0959683618782606

Zhang, R., Jiang, D. B., and Cheng, Z. G. (2020). Holocene precipitation changes in NE China from CCSM3 transient climate simulations. *Holocene* 31:095968362096148. doi: 10.1177/0959683620961485

Zhang, Z. Q., Bianchette, T. A., Meng, C., Xu, Q., and Jiang, M. (2020). Holocene vegetation-hydrology-climate interactions of wetlands on the Heixiaji Island, China. *Sci. Total Environ.* 743:140777. doi: 10.1016/j.scitotenv.2020.140777

Zheng, Y. H., Pancost, R. D., Naafs, B. D. A., Li, Q. Y., Liu, Z., and Yang, H. (2018). Transition from a warm and dry to a cold and wet climate in NE China across the Holocene. *Earth Planet. Sci. Lett.* 493, 36–46. doi: 10.1016/j.epsl.2018.04.019

Zhou, W., Wang, Z. X., Davy, A. J., and Liu, G. H. (2013). Geographic variation and local adaptation in *Oryza rufipogon* across its climatic range in China. *J. Ecol.* 101, 1498–1508. doi: 10.1111/1365-2745.12143

Zhou, W. J., Zheng, Y. H., Meyers, P. A., Jull, A. J., and Xie, S. C. (2010). Postglacial climate-change record in biomarker lipid compositions of the hani peat sequence, Northeastern China. *Earth Planet. Sci. Lett.* 294, 37–46. doi: 10.1016/j.epsl.2010.02.035

Zuo, X., Lu, H., Jiang, L., Zhang, J., Yang, X., Huan, X., et al. (2017). Dating rice remains through phytolith radiocarbon reveals domestication at the beginning of the Holocene. *Proc. Nat. Acad. Sci.* 114, 6486–6491. doi: 10.1073/pnas.1704304114

Conflict of Interest: The authors declare that the research was conducted in the absence of any commercial or financial relationships that could be construed as a potential conflict of interest.

frontiers
in Earth Science

ORIGINAL RESEARCH
published: 14 May 2021
doi: 10.3389/feart.2021.631310

The Importance of the Orbital Parameters for the Indian Summer Monsoon During the Mid-Holocene, as Deciphered From Atmospheric Model Experiments

Charan Teja Tejavath[1], Karumuri Ashok[1]* and Supriyo Chakraborty[2]*

[1] Centre for Earth, Ocean and Atmospheric Sciences, University of Hyderabad, Hyderabad, India, [2] Indian Institute of Tropical Meteorology, Ministry of Earth Sciences (MoES), Pune, India

Proxy and model-based studies suggest multi-scale temporal variability in the Indian summer monsoon (ISM). In this study, using the CESM1 atmospheric general circulation model, we carried out multiple ensemble AGCM simulations for the Mid-Holocene (MH; ≈ 6 kyr BP), Medieval Warm Period (MWP; ≈ 1 kyr BP), Little Ice Age (LIA; ≈ 0.35 kyr BP), and Historical (HS; ≈ CE 2000) periods. We used the PMIP3/CMIP5 boundary conditions for this purpose. Our simulations indicate that the ISM during the MH was stronger compared to HS and the rainfall higher, in agreement with several proxy studies. The experiments also suggest that the ISM rainfall (ISMR) was higher during MWP relative to the LIA in agreement with our earlier results from the PMIP3 models. A relatively northward migration of the ITCZ over the Indian region and strengthening of the neighboring subtropical high over the northwestern Pacific, both associated with stronger insolation associated with the obliquity and precision during the MH, seem to be important reason Indian summer monsoon during the MH.

Keywords: Indian summer monsoon, Mid-Holocene, orbital forcings, Medieval Warm Period, Little Ice Age, ENSO

Edited by:
Anoop Ambili,
Indian Institute of Science Education and Research Mohali, India

Reviewed by:
Dhrubajyoti Samanta,
Nanyang Technological University, Singapore
A. P. Dimri,
Jawaharlal Nehru University, India

****Correspondence:***
Charan Teja Tejavath
charan0239@gmail.com
Karumuri Ashok
ashokkarumuri@uohyd.ac.in

Specialty section:
This article was submitted to Quaternary Science, Geomorphology and Paleoenvironment, a section of the journal Frontiers in Earth Science

Received: *19 November 2020*
Accepted: *15 April 2021*
Published: *14 May 2021*

Citation:
Tejavath CT, Ashok K and Chakraborty S (2021) The Importance of the Orbital Parameters for the Indian Summer Monsoon During the Mid-Holocene, as Deciphered From Atmospheric Model Experiments. Front. Earth Sci. 9:631310. doi: 10.3389/feart.2021.631310

INTRODUCTION

The Indian monsoon system is a complex phenomenon. Its seasonal evolution and variability on multiple time scales involve individual and coupled land, ocean, and atmospheric processes, in addition to the annual progression of the Earth's revolution around the Sun. From June to September, the country receives roughly 75% of the annual rainfall (**Supplementary Figure 1**). The seasonally phase-locked rainfall and associated circulation are referred to as the southwest monsoon or Indian summer monsoon (ISM). Any changes in the average seasonal rainfall patterns have a profound effect on agriculture, and therefore the livelihood of 1.5 billion people in South Asia (Gadgil and Rupa Kumar, 2006). The Indian summer monsoon rainfall (ISMR) is weakening over several regions (e.g., Krishnan et al., 2020), with a simultaneous increase in the extreme events in the recent ∼150 years (Boyaj et al., 2020, and the references therein). Observation-based studies in the last 50–100 years suggest that, on interannual time scales, tropical oceanic phenomena such as the ENSO dominantly influence the ISM variability (see Webster et al., 1998, and the recent reviews by Ashok et al., 2019; Mohanty et al., 2020, and the references therein). However, Proxy studies indicate that ISMR also varied on the decadal, centennial, and millennial to multi-millennial time scales, in addition to intra-annual, and interannual scales (e.g., Ramesh et al., 2010; Chakraborty et al., 2012).

The relevance of internal climate variabilities, such as ENSO or multi-decadal variations in the tropical pacific circulation, is shown to be important even in the last millennium, through analysis of PMIP3 outputs (e.g., Tejavath et al., 2020).

On the other hand, external forcings are suggested to play major roles in manifesting various past climate periods. For example, changes in the strength of monsoon over the glacial-interglacial transition are suggested to be due to changes in orbital parameters (Kutzbach and Otto-Bliesner, 1982; Kutzbach and Guetter, 1986). Earth's precession cycle of 23 kyr plays a dominant role in modulating the tropical precipitation by changing the seasonal and meridional distribution of incoming solar radiation (Kutzbach, 1981; Pokras and Mix, 1987). Speleothem reconstructions suggest that changing precession leads to antisymmetric precipitation patterns in the southern and northern hemispheres (Wang et al., 2007). Several proxy and modeling studies show that the strength of the monsoon has changed in proportion with changes in insolation on orbital scales (Kutzbach, 1981; Tuenter et al., 2005; Wang et al., 2007; Kutzbach et al., 2008; Weber and Tuenter, 2011; Shi, 2016; Kathayat et al., 2017).

The distinct external forcings have been said to have manifested the MH climate in India. A study by Gupta et al. (2005) shows that slight changes in solar radiation have brought changes in the tropical monsoon systems during the Holocene. Studies also show that Earth's climate is sensitive to small changes in solar radiation on the centennial to the millennial time scale during the Holocene (Rind and Overpeck, 1993; Shindell et al., 2001; Hu et al., 2003). Signatures of changes in insolation are reflected in the changes of the northern hemisphere monsoon systems (Staubwasser et al., 2003). Past climate records based on proxy reconstructions from India and neighborhood surroundings of the Indian region (see the review by Dixit and Tandon, 2016; Banerji et al., 2020; Tejavath et al., 2020 for the details and references) report centennial to millennial-scale changes in the ISMR during the Holocene ($\simeq$ 12 kyr BP to present). These studies, in general, show that from the early Holocene period (9 kyr BP) to late Holocene (3 kyr BP), the ISMR shows a long-term decreasing trend. A single model study by Kumar et al. (2019) and a multi-model study by Tejavath et al. (2020) using PMIP3 (Paleoclimate Modelling Intercomparison Project 3) show that during the mid-Holocene (MH; $\simeq$ 6 kyr BP), the ISM was stronger relative to the present day. An analysis of the PMIP3 simulations by Tejavath et al. (2020) suggests that a robust large-scale convergence over the Indian region at 850 hPa may have been the reason for strong ISM during the MH. A study by Cobb et al. (2013) purports a highly variable ENSO during the Holocene period. However, several other proxy reconstruction studies (e.g., Gill et al., 2016, 2017) suggest that there was reduced ENSO activity during the MH period, and dominated by La Niña type SSTs over the tropical eastern pacific. There is another argument that the ENSO activity during the MH was indeed relatively subdued (An and Choi, 2014; Chen et al., 2019), and that such suppression is due to the enhanced Asian monsoon activity (Chen et al., 2019; Crétat et al., 2020). An ocean-atmospheric coupled model study by Crétat et al. (2020) shows orbitally driven trends during the MH to the current day (i.e., 0 kyr BP). The study also claims an increased influence of ENSO on ISMR and Indian Ocean Dipole (IOD) during the MH.

Studies based on paleo reconstruction data identify two significant periods in the last millennium (LM). These two periods, commonly known as Medieval Climate Anomaly (MWP; CE 950–1350) (e.g., Lamb, 1965)—a relatively warmer period, followed by a relatively more cooling period referred to as the Little Ice Age (LIA, CE 1500–1850) (e.g., Grove, 1988). Studies based on proxy and modeling show wetter and stronger ISM during MWP, and drier and weaker ISM during LIA relative to the LM mean (see Dixit and Tandon, 2016; Tejavath et al., 2019 for further references).

Various mechanisms have been proposed for ISM variability during the Holocene period, in addition to the changes in the orbital parameters (e.g., precession). For example, during the early Holocene climatic period, the mean latitudinal position of the Intertropical convergence zone (ITCZ) shifted northwards, resulting in an increase in the ISMR in response to the changes in the solar insolation (Fleitmann et al., 2007). Early climate model sensitivity experiments show that the timing of Northern Hemisphere (NH) summer monsoon strength has, or should have the near-zero phase relative to maxima of NH precession-driven radiation (Clemens and Prell, 2007). A proxy reconstruction study by Dixit et al. (2014a,b) shows that solar insolation played a significant role in strengthening the ISM during the early Holocene period. A study by Polanski et al. (2012) based on proxy and modeling shows that solar insolation changes strongly influenced the MH climate. Several other modeling studies suggest enhancing the northern hemisphere monsoon systems due to changes in insolation (Braconnot et al., 2007a,b; Bosmans et al., 2012; Marzin et al., 2013; Zheng et al., 2008). A recent modeling study suggests that a decrease in Saharan vegetation may have resulted in droughts in northernmost parts of India and excessive rains in southern India (Griffiths et al., 2020). A study by Leuschner and Sirocko (2003) shows that precessional and obliquity cycles coincide with the major events observed in the insolation-based ISM index. Interestingly, a study by Li and Harrison (2008) suggest in their coupled model simulations, the orbital forcing mostly enhances the Asian summer precipitation but in contrast, the neighboring ocean reduces the orbitally-induced summer precipitation, leading to the postponement of the time of summer monsoon onset over the Asian monsoon region.

However, the above studies including the coupled modeling studies, have not specifically examined the relevance of the external forcings to the ISM during MH in detail. Furthermore, the relative variations in the ISM during MH and LM have been less-studied, particularly from the modeling perspective. Keeping this in mind, using the community atmospheric model version 5 (Hersbach et al., 2015), we carry out several time-slice experiments for MH, MWP, LIA, and Historical (deemed as "present-day") periods. Importantly, we explore the sensitivity of the simulations by changing the orbital parameters; a major external forcing said to be important for the MH climate period, as discussed in detail in the next section.

This manuscript is organized as follows. In the following section, we briefly describe the model, our experimental setup, and methodology. In section "Results," we present our results and discussion. We present our conclusions and future scope for related studies in the final section, which is section "Conclusions and Scope for Future Studies."

EXPERIMENTAL SETUP AND METHODOLOGY

The Community Atmospheric Model Version 5 (CAM5), is the atmospheric component of the well-known Community Earth System Model Version 1.2.0 (CESM1.2.0; Hersbach et al., 2015). The CESM1.2.0, formerly also known as CCSM4, is a fully coupled climate model used to generate simulations of the Earth's past, present, and future climate states. For our experiments, we configured the horizontal resolution of the CAM5 at 1.9° latitude × 2.5° longitude grids, with 30 vertical levels. This version of CAM is comparable and compared to the CESM simulations for the Coupled Model Intercomparison Project 5 (CMIP5) and the Paleo Model Intercomparison Project 3 (PMIP3) simulations. The PMIP3 is a collective initiative endorsed by the World Climate Research Programme (WCRP) and JSC/CLIVAR working group on coupled models and the International Geosphere and Biosphere Programme (IGBP; PAGES) (Braconnot et al., 2012).

We carried out four suites of multi-ensemble control simulations of a 30-year span for each of the MH, MWP, LIA, and Historical (Present day) periods. Each suite of the control experiments in turn contains three ensembles. Each ensemble simulation starts with January initial conditions that are different from one ensemble to another and continues for a year. The external boundary conditions used in this study are period-specific (i.e., MH, MWP, LIA, and HS), similar to those mentioned in the PMIP3 website https://pmip3.lsce.ipsl.fr/, and briefly presented in **Table 1**. The climatological SSTs used in this study for each period are adapted from the simulation outputs from the corresponding PMIP3 simulations that were generated with CCSM4 (**Figure 1**). Apart from the control simulations, we have also carried out multiple ensemble simulations for the MH period by forcing the model with different orbital forcings for different periods, e.g., present-day orbital, 8.2 kyr BP orbital, and LGM orbital forcings. The forcings are mentioned in **Table 2**. For comparison, the same set of initial conditions have been used in all the complementary experiments.

Further to these 30-year long control and orbital sensitivity simulations, we have also carried out suites of simulations of 1-year span (simulation starts in January and ends in December) with 10-ensembles each with the same set of initial conditions across various orbital forcings. The results from the 1-year length simulations are in very good agreement with those from the 30-year long simulations, as evidenced by the evolution of the seasonal cycles (**Supplementary Figure 2**). Therefore, we shall not discuss the results from these runs.

Apart from the control and orbital sensitivity experiments, we have also carried out two sensitivity experiments to gauge the potential relevance of the El Niños during MH, and two more to assess the impact of the La Niñas during the same period. This involved, for example in case of the La Niña sensitivity experiments, imposing the La Niña anomalies on the climatological SSTs over the tropical pacific ocean (120°E to 80°W and 30°S to 30°N) to obtain the lower boundary SSTs representing the La Niña SSTs during the MH, and in another experiment, imposing SST anomalies throughout the tropical Indo-pacific ocean (40°E to 80°W and 30°S to 30°N). The SST anomalies imposed in these SST sensitivity experiments for the MH period are shown in **Supplementary Figure 3**. The SST anomalies during the La Niñas (El Niños) were obtained by compositing monthly SST anomalies of all "typical" La Niñas (El Niños). These typical events are identified as those for which the magnitude of the simulated JJAS NINO3 index is above (below) one standard deviation.

In our analysis, the climatology is taken from the entire 30-year runs, because the initial conditions are taken from PMIP3 CCSM4 simulation, and they are therefore spun up well. As we are starting our simulation from January, the simulated atmosphere will adjust to the lower boundary SSTs within a couple of months. As it is, such experiments for the current day monsoonal season typically start in the month of May (e.g., Ashok et al., 2001, 2004, 2009, 2012; Guan et al., 2003).

We have calculated the monthly climatological cycles of rainfall and surface temperatures over the Indian land region bounded by 66.5°E–101.5°E; 6.5°N–39.5°N. We analyze the simulated fields of velocity potential-which represent divergence, vorticity, and moisture flux convergence. The moisture flux convergence has been computed as the sum of moisture convergence and advection. The fields of velocity potential, vorticity, and moisture convergence have been computed from the simulated outputs of horizontal winds and moisture through the application of spherical harmonics using the NCL routines. The details can be found at https://www.ncl.ucar.edu/Applications/wind.shtml. The orbital parameters are calculated using the PMIP3 protocol https://pmip3.lsce.ipsl.fr/ and are present in **Supplementary Table 1**.

RESULTS

Simulated Mean Summer Monsoon Rainfall and Surface Temperatures Over India

Before going any further, we have validated HS simulations with the observational and PMIP3 CCSM4 historical simulations and are presented in **Supplementary Figure 4**. We briefly validated the seasonal cycle evolution of rainfall and surface temperatures of these simulations (PMIP3 CCSM4 and AGCM CAM5) with the ERA-20CM skin temperature (SKT; Hersbach et al., 2015), Climate Prediction Center (CPC) Global Land Surface Air Temperature data (Fan and van den Dool, 2004) and the India Meteorological Department (IMD) gridded rainfall (Rajeevan et al., 2006). We present the seasonal cycle validation in **Supplementary Figure 4**. From **Supplementary Figure 4**, we can see that the seasonal cycle evolution of rainfall and surface temperatures are well captured in the AGCM HS.

TABLE 1 | Summary of boundary conditions used in different climate periods.

Boundary conditions	Historical (HS; present day)	LIA (0.3 kyr BP)	MWP (1 kyr BP)	Mid-Holocene (6 kyr BP)
Orbital parameters	ecc = 0.016724 obl = 23.446 peri-180 = 102.04 orb_iyear = 1,850	ecc = 0.016724 obl = 23.446 peri-180 = 102.04 orb_iyear = 1,850	ecc = 0.017093 obl = 23.569 peri-180 = 85.79 orb_iyear = 1,000	ecc = 0.018682 obl = 24.105 peri-180 = 0.87 orb_iyear = −4050
Date of vernal equinox	March 21 at noon	March 21 at noon	March 21 at noon	March 21 at noon
Trace gases	CO2 = 367 ppm CH4 = 1,760 ppb N2O = 316 ppb CFC11 = 653.45 ppt CFC12 = 535 ppt O3 = Modern-10DU	CO2 = 280 ppm CH4 = 760 ppb N2O = 270 ppb CFC11 = 0 CFC12 = 0 O3 = Modern-10DU	CO2 = 279.265 ppm CH4 = 674.6 ppb N2O = 266.9 ppb CFC11 = 12.48e−12 CFC12 = 0.0 O3 = same as in CMIP5 PI	CO2 = 280 ppm CH4 = 650 ppb N2O = 270 ppb CFC = 0 O3 = same as in CMIP5 PI
Climotological SST	Computed from CCSM4 CMIP5 historical simulation (CE 1901-1999)	Computed from CCSM4 CMIP5 last millennum simulation (CE 1750-1849)	Computed from CCSM4 CMIP5 last millennum simulation (CE 1000-1099)	Computed from CCSM4 PMIP3 MidHolocene simulation
Aerosols	Present day	Same as in CMIP5 PI	Same as in CMIP5 PI	Same as in CMIP5 PI
Solar constant	1,365 W/m^2	1,365 W/m^2	1361 W/m^2	1360.747 W/m^2
Vegetation	Interactive	Interactive	Interactive	Interactive
Topography and coastlines	Present day	Present day	PMIP3 Past1000	Same as in CMIP5 PI

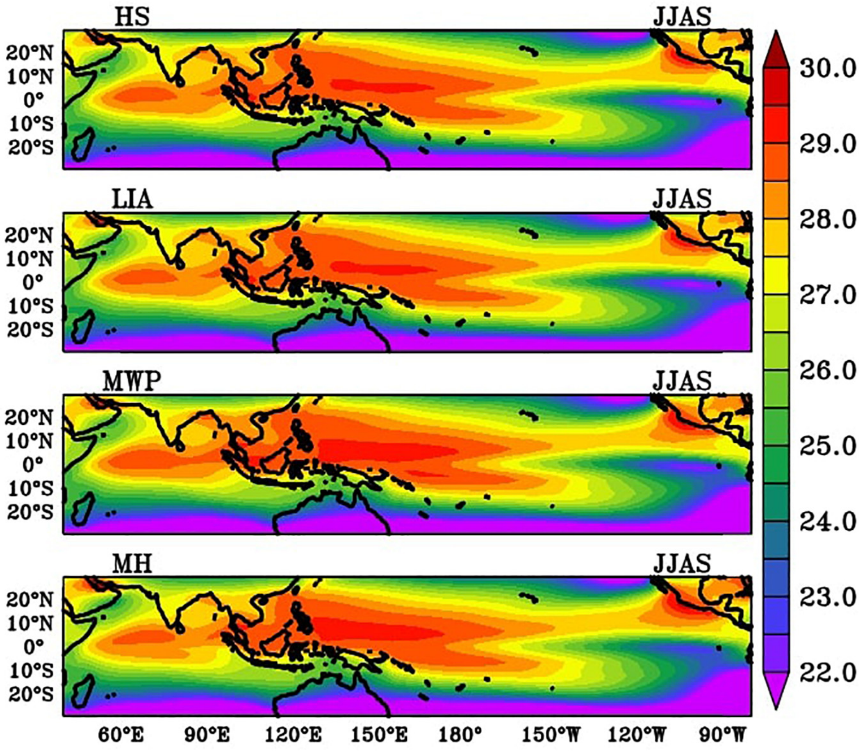

FIGURE 1 | Mean sea surface temperatures (°C) for the months of June to September used in the control simulations for MH, MWP, LIA, and HS periods.

Mid-Holocene

Figures 2A,C show that simulated summer monsoon rainfall during MH is higher than the HS. Note that we compute the area-averages over the Indian land region only (e.g., see the domain in **Figure 2C**). This simulated higher ISMR during MH, particularly around ∼ 6 kyr BP, agrees well with several coupled model simulations (Kumar et al., 2019; Tejavath et al., 2020), as well as with the proxy-based studies (Rawat et al., 2015; Band et al., 2018). The simulated area-averaged surface temperature found to be coldest during MH compared to the Present-day period

(**Figures 2B,D**), as also indicated by several coupled models of the PMIP3 vintage in Tejavath et al. (2020). The simulations suggest, during the MH, a relatively higher rainfall relative to the HS in the core monsoon region, northeast India, and foothills of the Himalayas (**Figure 2C**), and lower rainfall in the western part of India. Interestingly, despite being a major ISM rainfall region, the simulated rainfall over the western ghats is relatively less rainfall during the MH compared to the HS (**Figure 2C**). We have observed a similar kind of pattern in the southern part of western ghats (i.e., Kerala) in PMIP3 CCSM4 coupled model simulations also. This could be because, during the MH, the monsoon winds are weaker over the western ghats region and less moisture availability compared to the HS. While the monsoon circulation seems to be stronger relative to the HS during the MH (**Figure 5**), when the Indus civilization, encompassing the modern-day Rajasthan and neighboring Pakistan, etc., is said to have thrived. However, as can be conjectured from the 850 hPa circulation, the low-level circulation is weaker relative to the historical period. This of course may be also model-specific. We shall explore this aspect further making a detailed PMIP model analysis and sensitivity experiments with multiple AGCMs. Apart from them, comparatively low-resolution simulations and the atmospheric-only simulation could be the reasons behind it.

TABLE 2 | Orbital parameters of the different climatic periods.

Parameters	Time period			
	MH	HS	8.2 kyr BP	21 kyr BP
Eccentricity	0.018682	0.016724	0.019199	0.018994
Obliquity	24.105°	23.446°	24.222	22.949°
PERI-180	0.87°	102.04°	319.495°	114.42°

MWP and LIA

Figures 3A,C, show that the area-averaged summer monsoon rainfall during MWP is higher than LIA, in agreement with a majority of the PMIP3 simulations (e.g., Tejavath et al., 2019). **Figure 3B** confirms that the AGCM simulations reproduce the expected surface temperature response to increased greenhouse gases, from the perspective of increased GHGs in the present day when industrialization has begun (also see **Table 1**), and hence considered reliable. The simulated area-averaged surface temperature during the LIA is cooler compared to the MWP, again as simulated by the coupled models of the PMIP3 vintage (Tejavath et al., 2019). Interestingly, the rainfall difference over northeast India indicates a dipolar pattern during the MWP and LIA (**Figure 3C**). When area-averaged, these values are almost negligible, in agreement with results from three relatively high resolution PMIP3 simulations suggest that the area-averaged summer monsoon rainfall over northeastern India has not changed across the MWP, LIA, and historical periods (Ashok et al., 2020, under review).

Role of Tropical Ocean-Atmospheric Coupled Processes or the Lack Thereof

Apart from these, we compare the results from our simulations with the results from the corresponding past climate simulations

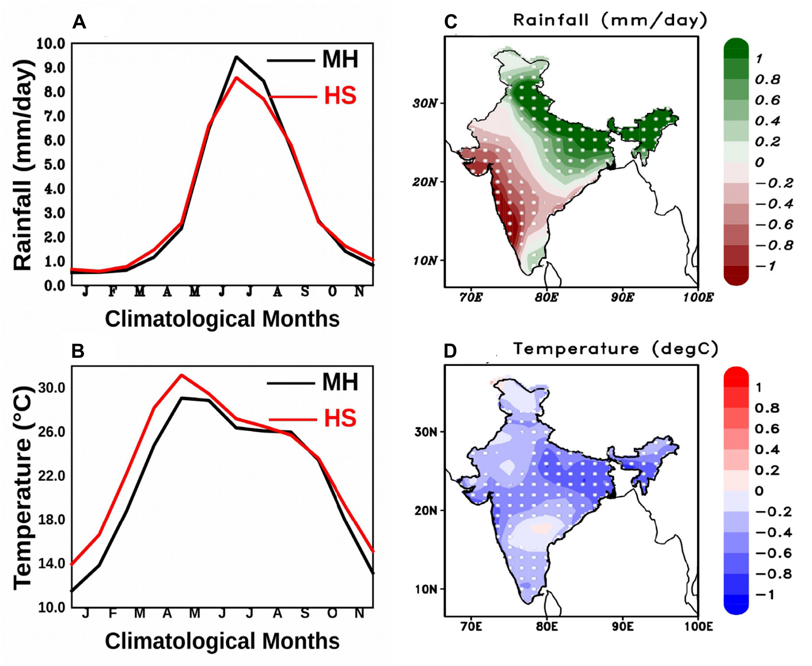

FIGURE 2 | Comparison between the area-averaged seasonal cycle of Mid-Holocene (MH) and Historical period, **(A)** is for the simulated rainfall and **(B)** is for the simulated surface temperature over Indian land region. Spatial distributions of the simulated summer monsoon rainfall (mm/day; **C**) and surface temperature (°C; **D**) for MH with the difference to HS. The dotted region represents a statistically significant region *at a 95%* confidence level from a two-tailed Student's *t*-test.

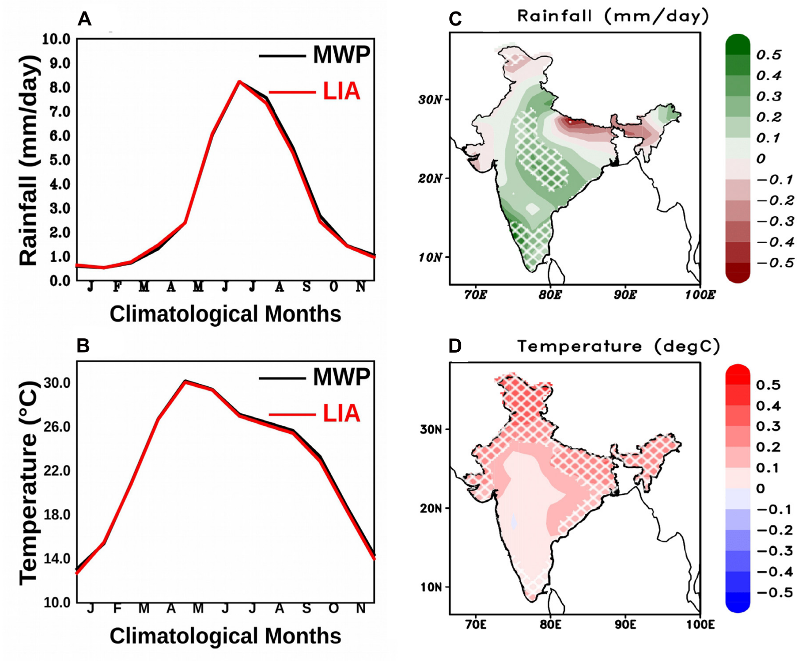

FIGURE 3 | Comparison between the area-averaged seasonal cycle of Medieval Warm Period (MWP) and Little Ice Age (LIA) period, **(A)** is for the simulated rainfall, and **(B)** is for the simulated surface temperature over Indian land region. Spatial distributions of the simulated summer monsoon rainfall (mm/day; **C**) and surface temperature (°C; **D**) for MWP with the difference to LIA. Hatched region represents a statistically significant region *at an 80%* confidence level from the two-tailed Student's *t*-test.

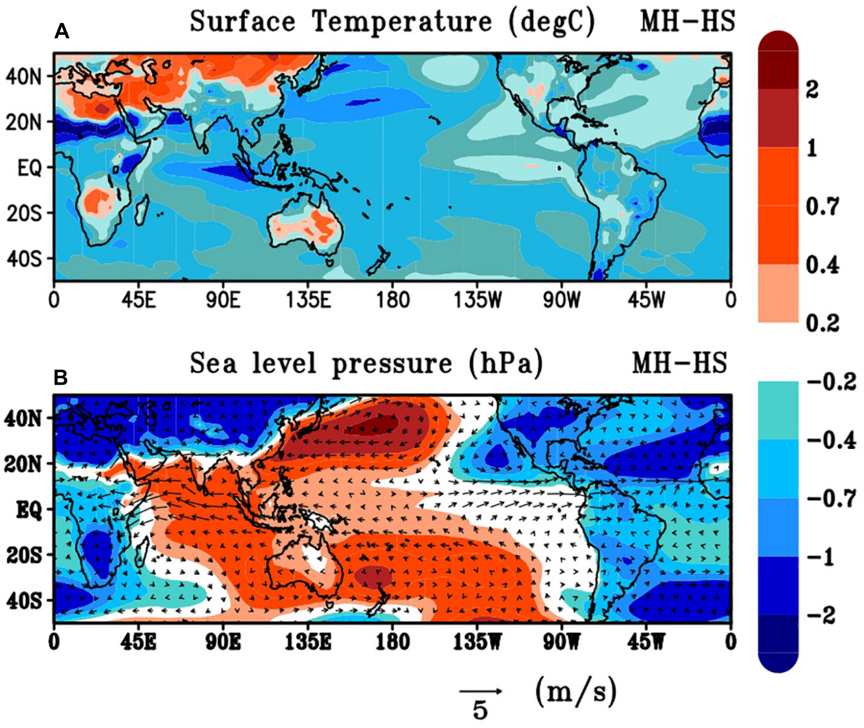

FIGURE 4 | (A) Spatial distribution of the simulated surface temperature (°C) difference in the time-averaged JJAS between MH and HS. **(B)** Spatial distribution of the simulated sea level pressure (hPa) and overlaid by the monsoon winds (m/s) at 850 hPa difference in the time-averaged JJAS between MH and HS.

by CCSM4 (**Supplementary Figure 5**), which are available as PMIP3 and CMIP5. Note that, these CCSM4, which have CAM as the atmospheric component, are fully coupled ocean-atmospheric simulations (Schmidt et al., 2012; Taylor et al., 2012). From **Supplementary Figure 5**, we see that simulated rainfall and surface temperature climatological cycles from our experiments with the CAM AGCM are comparable to those from the CCSM4 in terms of the evolution of the annual cycle. The AGCM simulations are relatively drier and warmer over India during the summer (**Supplementary Figures 5A–D**) across all the climate periods compared to the coupled CCSM4 simulations. Similarly, we see a warmer bias in AGCM surface temperatures compared to the coupled model simulations. The absence of air-sea coupled processes could be a probable reason behind the dry bias.

Simulated Circulation Changes Over India

Mid-Holocene

During the MH period, we see a stronger low pressure in the monsoon trough region northward from around 20°N relative to the HS (**Figure 4B**). This indicates the northward migration of the ITCZ, which is also seen in simulations by a few other AGCMs and coupled models of older vintage (e.g., Zhao and Harrison, 2012); strengthening of the subtropical high over the western pacific also apparently strengthens the monsoonal circulation over northern India (**Figure 4B**). Apart from these, the Indian subcontinent experienced relatively stronger low-level convergence associated with stronger monsoonal circulation and during MH (**Figure 5A**). Other factors such as a stronger zonal seasonal mean SST gradient in the tropical Indian Ocean, with a warmer (cooler) eastern (western) tropical Indian Ocean by 0.1∼0.2°C (**Figure 4A**) relative to the HS, which provides a positive IOD-like background, may have also contributed to the stronger mean ISM circulation and summer monsoon rainfall. Large-scale moisture convergence is seen during the MH (**Figure 5B**), consequently giving a relatively enhanced summer monsoon rainfall in the core monsoon region. Western India is associated with a relatively lower moisture convergence, manifesting as lower rainfall (also see **Figures 2A,C**). Earlier modeling studies also show that changes in the large-scale circulation facilitates the precipitation changes during the MH period and last millennium (e.g., Polanski et al., 2014; Tejavath et al., 2019; Ashok et al., 2020). Interestingly, the simulated pre-monsoon (MAM) land temperatures during the MH are cooler than the HS (**Supplementary Figure 6**). A similar kind of signal can be seen in general, the PMIP3 coupled simulations also (figures not shown). From this, it seems the pre-monsoon land warming may not be relatively so important. The land-sea gradient during the MH from our control run is also weak, suggesting that this may not be a major factor during the MH.

MWP and LIA

From **Figure 6A**, we clearly see that the Indian subcontinent experienced stronger low-level convergence, which is associated with stronger monsoonal circulation during the MWP compared to the LIA. The MWP climate period is associated with strong magnitudes of moisture convergence compared to the LIA (**Figure 6B**). These all resulted in a stronger ISM giving surplus rainfall over the Indian region during the MWP compared to the LIA (**Figure 6C**).

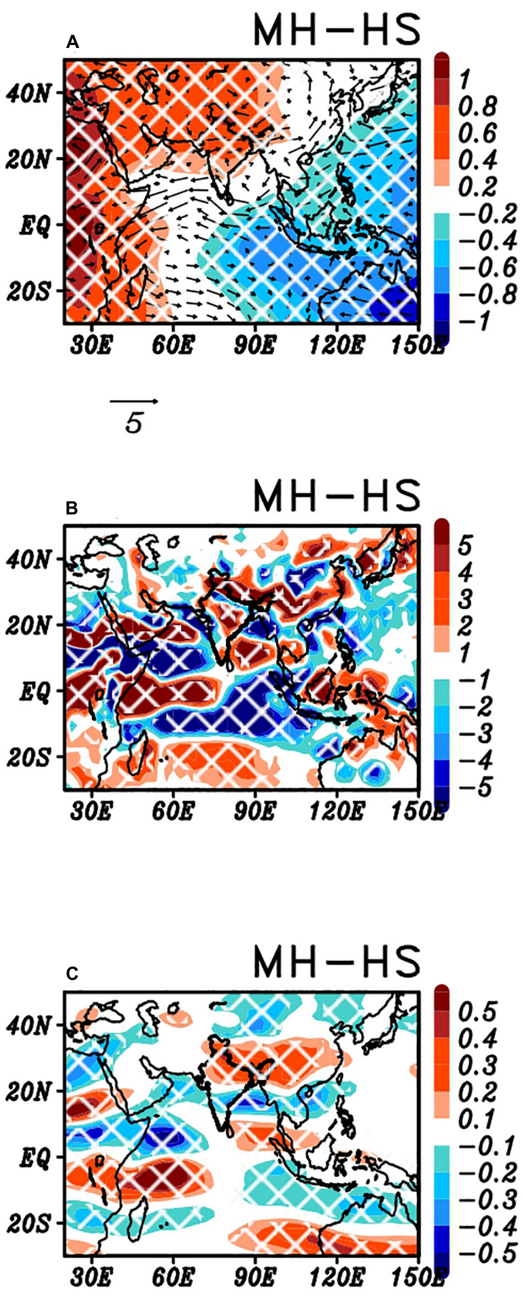

FIGURE 5 | (A) Spatial distribution of the simulated 850 hPa differences in the time-averaged JJAS velocity potential "χ 850" (m^2 s^{-1}; Shaded), and overlaid by the mean monsoon winds (m/s; Vectors) for MH period relative to that for the HS. **(B)** Show spatial distributions of simulated 600 hPa differences in the time-averaged JJAS Moisture Flux Convergence [10^{-5} g/(kg^{-s})]. **(C)** Shows spatial distributions of simulated 500 hPa relative vorticity (×10^{-5} S^{-1}) for the MH period relative to that for the HS. Hatched region represents a statistically significant region *at a 95%* confidence level from the two-tailed Student's *t*-test.

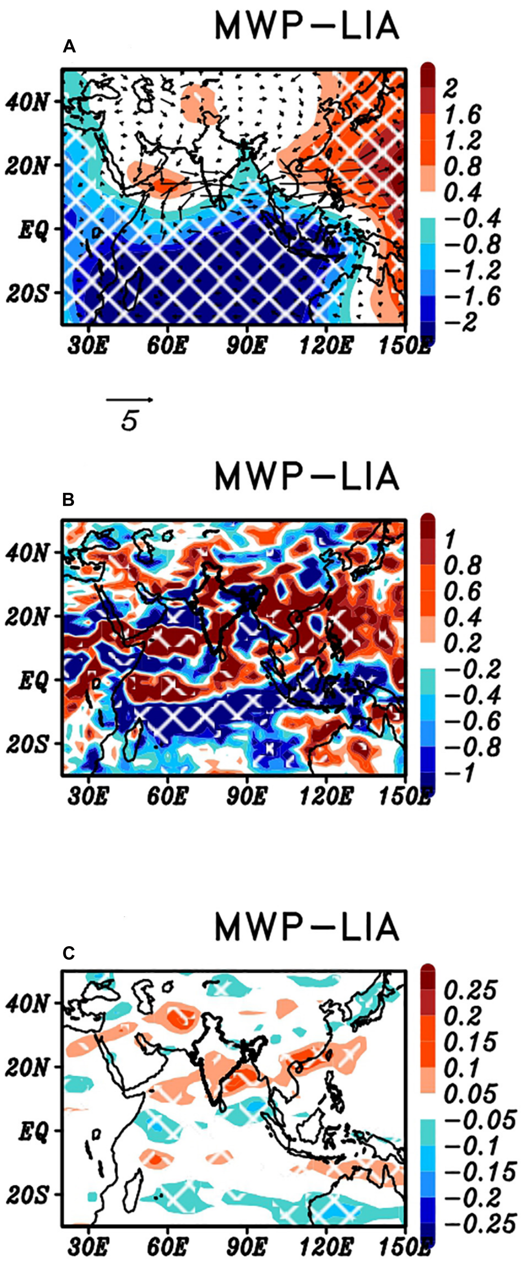

FIGURE 6 | (A) Spatial distribution of the simulated 850 hPa differences in the time-averaged JJAS velocity potential "χ 850" (m^2 s^{-1}; Shaded), and overlaid by the mean monsoon winds (m/s; Vectors) for MWP period relative to that for the LIA. **(B)** Show spatial distributions of simulated 600 hPa differences in the time-averaged JJAS Moisture Flux Convergence [10^{-5} g/(kg^{-s})]. **(C)** Shows spatial distributions of simulated 500 hPa relative vorticity ($\times 10^{-5}$ S^{-1}) for the MWP period relative to that for the LIA. Hatched region represents a statistically significant region *at a 95%* confidence level from the two-tailed Student's *t*-test.

Possible Mechanisms for the Stronger Mid-Holocene Summer Monsoon

In **Figure 7**, we show the differences in the simulated insolation between the MH and the HS climate periods, associated with the changes in the obliquity. From the perspective of the Milankovitch cycles, the obliquity (axial-tilt) of the Earth during the MH is 24.1°, and the HS is 23.4°. In other words, during the MH, the solar activity was more in the Northern hemisphere compared to the southern hemisphere (**Figure 7**). This shows that during the MH climate period, the Indian subcontinent has received more solar insolation than during the Historical climate period because of the changes in the orbital parameters (**Figure 7**). A few studies (Bosmans et al., 2012; Zhao and Harrison, 2012) suggest that this increased-insolation likely led to deeper thermal lows on the land region and resulted in a higher land-sea thermal gradient because of the difference in thermal inertia between land and ocean. In general, this can be expected to lead to stronger monsoonal winds into the Indian sub-continent with enhanced moisture flow toward the land region, giving more precipitation (Bosmans et al., 2012; Zhao and Harrison, 2012), at least during the onset phase when the land-sea thermal contrast is important. Indeed, the seasonal atmospheric circulation, in general, can also be expected to change as a result of the change in atmospheric energy balance prompted by the strengthening of the summer by stronger insolation (Merlis et al., 2013), and also eventually influence the rainfall. From this perspective, it is interesting to see how the Indian monsoon responded to the changes in orbital parameters, particularly for the mid-Holocene time period using the AGCM.

The Mid-Holocene ISM Response to Changes in Orbital Forcings

In this section, we examine the simulated ISM response to changes in orbital forcings through an analysis of our sensitivity experiments, which were discussed in section "Experimental Setup and Methodology."

We have carried out simulations for the MH climate period with different orbital forcings (e.g., present-day orbital, 8.2 kyr BP orbital, and LGM orbital forcings) are mentioned in **Table 2**. The motivation behind choosing the LGM and 8.2 kyr BP orbital parameters apart from HS follows: proxy-based studies suggest that during the LGM, the ISM was weaker and drier compared to the present-day (Pattanaik, 2012; Chabangborn et al., 2013). During the 8.2 kyr event, ISM had weakened abruptly (Dixit et al., 2018). Changes in orbital parameters are believed to have played a major role in weakening the ISM during the LGM (Bowen, 2009). It must be mentioned that Atlantic teleconnections also had a significant role in the weakening of ISM during the 8.2 kyr BP (Dixit et al., 2018). By applying the orbital parameters of LGM and 8.2 BP kyr for the MH gives an idea for the role of orbital parameters during MH compared to the other climatic periods, although they may possess characteristic differences in capturing the low/high rainfall patterns to these changes. The simulated MH solar irradiance over the Indian region during the summer monsoon season decreases when the orbital parameters are replaced by those observed during HS and LGM (**Figures 8A,C**). Furthermore, when the 8.2 kyr orbital parameters have been invoked, the simulated solar irradiance over the Indian region

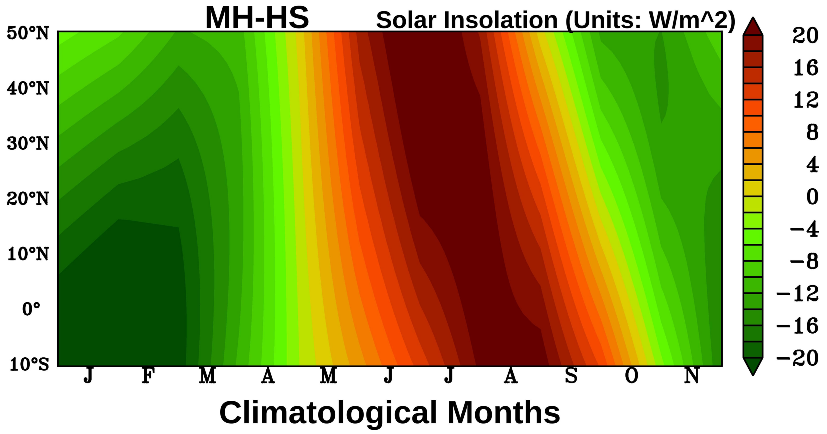

FIGURE 7 | Simulated insolation difference (W/m^2) between Mid-Holocene and HS (present-day). Averaged over all the longitudes (0°E to 360°E).

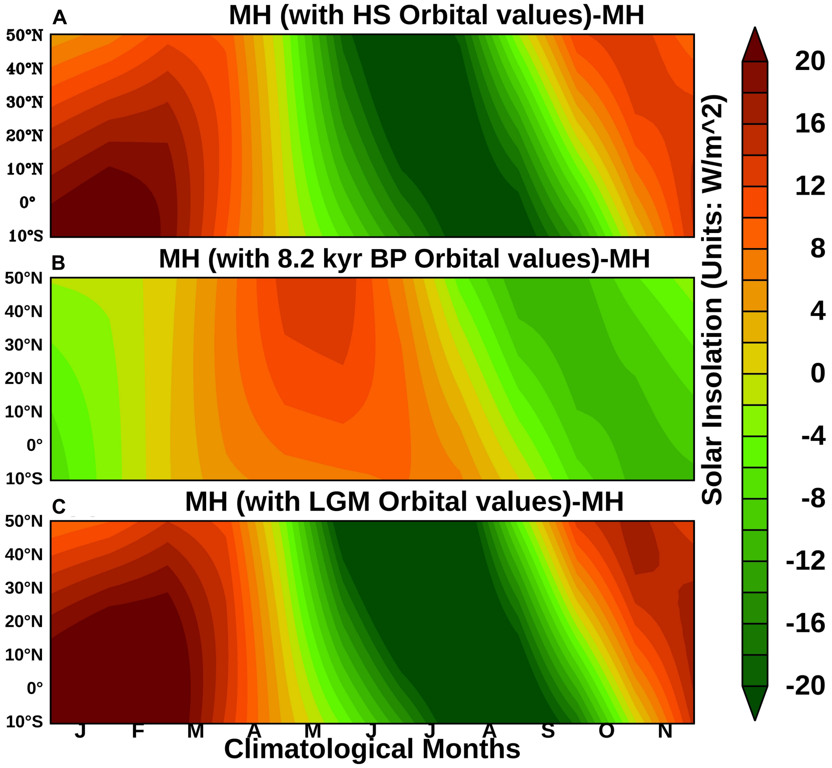

FIGURE 8 | Simulated insolation difference (W/m^2) between **(A)** MH sensitivity experiment with HS orbital parameters to MH control simulation, **(B)** MH sensitivity experiment with 8.2 kyr BP orbital parameters to MH control simulation, and **(C)** MH sensitivity experiment with LGM orbital parameters to MH control simulation. Averaged over all the longitudes (0°E to 360°E).

is seen to be slightly more compared to the MH control simulation (**Figure 8B**). The other simulated changes relative to these changes in orbital parameters are discussed in the following subsections.

Simulated Rainfall and Surface Temperature

Changing the orbital forcing to that of the HS, and to that of the LGM, reduces the simulated summer monsoon rainfall relative to the MH-control experiment (**Figure 9A**). Interestingly, the MH simulations with the orbital forcings pertaining to the 8.2 kyr BP resulted in relatively higher summer monsoon rainfall, contrary to proxy-based observations (Dixit et al., 2018). An earlier coupled model study also suggests that simulating the signatures of the 8.2 kyr BP event seen in proxy-observations is a difficult task (LeGrande and Schmidt, 2008). This tells us that apart from the orbital parameters, the North Atlantic teleconnections

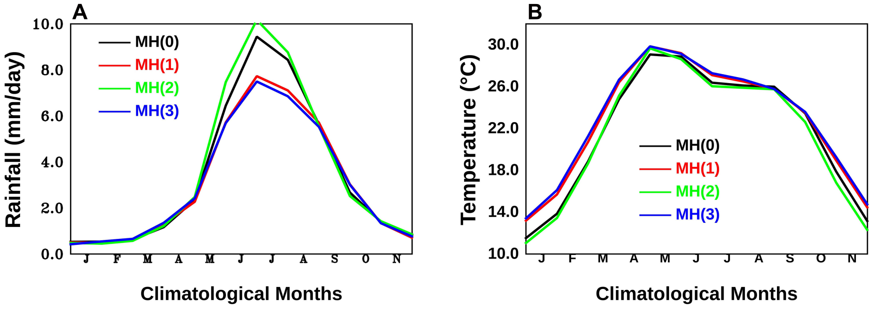

FIGURE 9 | Comparison between the area-averaged seasonal cycle of Mid-Holocene (MH) simulations, **(A)** is for the simulated rainfall, and **(B)** is for the simulated surface temperature over the Indian land region. Here, MH(0) is MH Control simulations; MH(1) is MH simulation with HS orbital values; MH(2) is MH simulation with 8.2 kyr BP orbital values; MH(3) is MH simulation with LGM orbital values.

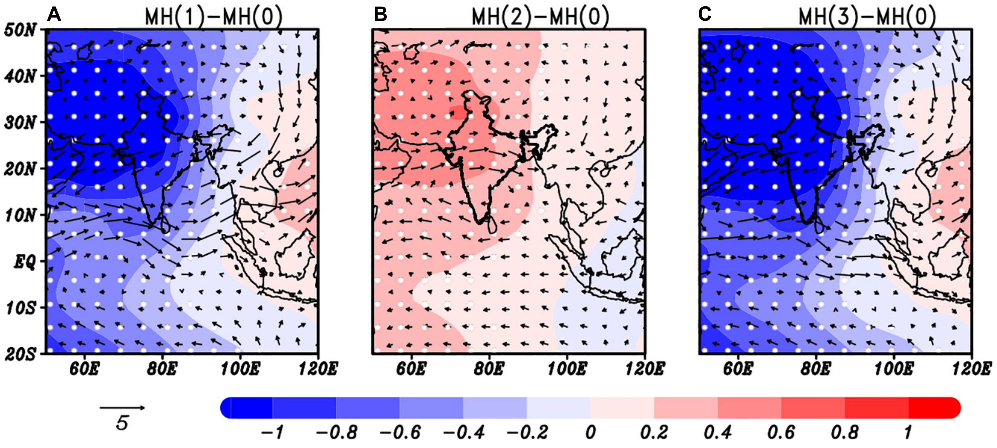

FIGURE 10 | Spatial distribution of the simulated 850 hPa differences in the time-averaged JJAS velocity potential 'χ 850' ($m^2\ s^{-1}$; Shaded), and overlaid by the mean monsoon winds (m/s; Vectors) for MH sensitivity experiments relative to that for the MH control simulation. **(A)** MH sensitivity experiment with HS orbital parameters to MH control simulation, **(B)** MH sensitivity experiment with 8.2 kyr BP orbital parameters to MH control simulation, and **(C)** MH sensitivity experiment with LGM orbital parameters to MH control simulation.

(Dixit et al., 2018) and, importantly, meltwater forcings (Renssen et al., 2001; Wiersma and Renssen, 2006; LeGrande and Schmidt, 2008) may have played a crucial role in the weakening of ISM 8.2 kyr BP event as seen in paleo-data based studies. In this context, the simulated relatively high ISMR with the 8.2 kyr BP may be due to a lack of suitable representation of the fresh-water perturbations, as our experiments are only AGCM-based.

Simulated Circulation Changes Over India

The changing of the orbital parameters to the current day, and in a parallel experiment to that in the LGM time period, caused the weakening of the mean monsoonal winds. This resulted in weakening large-scale low-level convergence over the Indian region (**Figures 10A,C**), and a deficit summer monsoon rainfall, particularly over the core monsoon region (**Figure 9**). From **Figures 9**, **10**, it is evident that the simulated ISMR during the MH has responded differently to changes in solar irradiance induced by changes in the orbital parameters. This suggests that enhanced solar insolation due to favorable orbital parameters during the MH time period played a crucial role in strengthening the ISM, compared to the HS and LGM, also supported by Crétat et al. (2020) This also suggests that changes in orbital parameters had a major role in the strengthening of ISM during the MH than the equatorial ocean-atmosphere dynamical processes at that time.

Potential Role of Concurrent ENSO

The simulated model response in the experiments carried out with El Niño-type of SSTs in the *tropical Pacific* for the MH period [Experiment ELP(MH)] resulted in negative summer rainfall anomalies over India (**Supplementary Figure 7**). However, the model response to the La Niña-like lower boundary forcing *in the tropical Pacific* [Experiment LNP(MH)] for the same period seems to be anomalous (**Supplementary Figure 7**), as it produces a negative summer monsoon rainfall anomaly over the Indian region. To be sure, studies such as that by Annamalai et al. (2005) suggest that some models may also need the ENSO-associated SST forcing in the tropical Indian Ocean to produce a realistic response over the Indian monsoon rainfall. In addition, recent research by Chowdary et al. (2017) suggests that the ENSO signal in the tropical Indian Ocean, in addition to its signal in the tropical Pacific may be relevant for the current day monsoon variability. In our model too, for the historical period, the Indian Ocean SST anomalies associated with La Niña, along with the Pacific SST anomalies, seem to produce above-normal summer monsoon rainfall at least from August for the *historical period* (**Supplementary Figure 7**). Interestingly, even when we introduce the La Niña-related SSTA in the tropical Indian Ocean to the tropical Pacific SST signals [LNPI(MH)] for the MH, the model does not simulate the above positive summer monsoon rainfall anomalies over India (**Supplementary Figure 7**). On the other hand, similar experiments carried out with the ENSO-SSTs in both basins simulate positive summer monsoon rainfall anomalies over India for the HS, MWP, and LIA at least from August through September.

All the exercises suggest that, at least in our model simulations, there may not be a contribution of the MH La Niñas to the wet MH summer monsoon rainfall. Their contribution to the ISM during MWP and LIA, however, is at least qualitatively palpable, in agreement with the PMIP3 results (Tejavath et al., 2019, 2020).

CONCLUSION AND SCOPE FOR FUTURE STUDIES

While several proxy studies, such as Rawat et al. (2015) and Band et al. (2018) suggest that the ISM during the mid-Holocene (MH; ∼6000 yr BP) was characterized by a wet climate relative to the modern time. The few modeling studies (Kumar et al., 2019; Tejavath et al., 2020, etc.) also suggest that the ISM was indeed stronger at that time. Interestingly, proxy-based (Mukherjee et al., 2016) and model-based studies suggest that external factors such as changes in the orbital parameters, changes in solar forcing induced by volcanic eruptions, land surface, and vegetation changes, etc., may have played an important role in evolving a distinct climate of the Earth during MH relative to the current day (Crétat et al., 2020). The present study, through various experiments with the Community Atmospheric Model (CAM5), examines the potential role that the distinct orbital parameters during the MH may have played in the manifestation of mean ISM conditions during the MH.

We have carried out 30-year long multiple ensemble simulations for MH, MWP, LIA, and Historical period (Present-day; HS) climate periods. The results show that the ISMR during the MWP is higher than that of the LIA, but lesser than that of the HS, in agreement with various PMIP3 coupled simulations (Tejavath et al., 2019). Our AGCM experiments simulate relatively higher surplus ISMR during the MH period relative to the HS, supporting proxy observation-based studies and from few modeling studies.

Results from our novel experiments show that the higher ISMR simulated in the MH is due to a stronger monsoon circulation, northward migration of the ITCZ, strengthening of the subtropical high over the western pacific relative to the HS. To examine the potential role of orbital parameters on the ISM variability during the MH, we carried out several sensitivity simulations for the MH period by changing the orbital parameter with those of the HS, LGM, and 8.2 kyr BP. These sensitivity experiments demonstrate that the higher orbital parameter during the MH, which meant more solar insolation in the northern hemisphere played a significant role in enhancing the ISM, and consequently, high ISMR.

This suggests that the higher insolation during the MH, around 6 kyr BP, associated with relatively favorable external forcings (e.g., orbital parameters) likely played a significant role in enhancing the ISM during the MH compared to the HS. Of course, this is by no means a complete explanation for the high MH rainfall simulated and recorded in several proxies. For example, we have not carried out any experiments to ascertain the potential role of land-surface and vegetation changes in the mid-Holocene, which is said to have facilitated the mid-Holocene climate in West Africa (Messori et al., 2018; Crétat et al., 2020; Griffiths et al., 2020). Such experiments need a model with an interactive land-surface and vegetation model. The other factors, such as the internal variability such as ENSO, whether generated due to internal coupled dynamics or forced by orbital forcings may have played their roles. In this context, a few sensitivity simulations carried out by us suggest that our AGCM simulates below normal ISM rainfall during the MH as a response to concurrent El Niño-like SSTs imposed in the tropical Pacific (e.g., Ashok et al., 2004). This is similar to the current day ENSO impact on ISM. But we elicit a relatively low Indian summer rainfall response during the months of June and July when we force the model La Niña type of SSTs in the tropical Pacific ocean or even when the La Niña-associated concurrent SST anomalies are also imposed in the tropical Indian Ocean. Importantly, similar La Niña experiments for the MWP and LIA result in a position ISMR anomaly. This suggests that, at least in our simulations, the La Ninas have not significantly contributed to the relatively wet ISM during the MH, and that the orbital forcings may be relatively more important.

To get a comprehensive idea of the relative roles of various internal and external factors and their influences on the ISM during the MH, a more extensive study with a fully coupled land-biosphere-ocean-atmospheric model will be carried out soon. We also plan to revisit the above results by repeating these experiments with multiple AGCMs in order to ascertain our claims in this paper.

DATA AVAILABILITY STATEMENT

The original contributions presented in the study are included in the article/**Supplementary Material**, further inquiries can be directed to the corresponding author/s.

AUTHOR CONTRIBUTIONS

CT took lead in carrying out the simulations, analyzed the data, and wrote the manuscript. KA and SC supervised and co-wrote the manuscript. All authors contributed to the article and approved the submitted version.

ACKNOWLEDGMENTS

The DST, Government of India is acknowledged for the Grant DST/19/1901/2017/01061. Partial financial support was provided by the IAEA through CRP F31004 to SC. The CAM model of NCAR (NOAA) has been downloaded from https://www.cesm.ucar.edu/models/. CT acknowledges help from the CESM working group in building the AGCM. KA and CT thank the IITM-Pune and MoES for the access to the Aditya HPC. The GrADS (COLA), Ferret (NOAA), NCL (NCAR), and CDO (MPI) tools have been used in this study. CT acknowledges a Ph.D. fellowship grant from the UGC, Govt. of India, to carry out this work.

SUPPLEMENTARY MATERIAL

The Supplementary Material for this article can be found online at: https://www.frontiersin.org/articles/10.3389/feart.2021.631310/full#supplementary-material

REFERENCES

An, S.-I., and Choi, J. (2014). Mid-Holocene tropical Pacific climate state, annual cycle, and ENSO in PMIP2 and PMIP3. *Clim. Dyn.* 43, 957–970. doi: 10.1007/s00382-013-1880-z

Annamalai, H., Lui, P., and Xie, S. P. (2005). Southwest Indian Ocean SST variability: Its local effect and remote influence on Asian monsoons. *J. Clim.* 18, 4150–4167. doi: 10.1175/jcli3533.1

Ashok, K., Bidyabati, S., Tejavath, C. T., and Cubasch, U. (2020). Summer monsoon over northeastern India during the last millennium. *Int. J. Climatol.* 70, 443–452.

Ashok, K., Feba, F., and Tejavath, C. T. (2019). The Indian summer monsoon rainfall and ENSO. *Mausam* 70, 443–452.

Ashok, K., Guan, Z., Saji, N. H., and Yamagata, T. (2004). Individual and combined influences of the ENSO and the Indian Ocean dipole on the Indian summer monsoon. *J. Climate* 17, 3141–3155. doi: 10.1175/1520-04422004017<3141:IACIOE<2.0.CO;2

Ashok, K., Guan, Z., and Yamagata, T. (2001). Impact of the Indian Ocean Dipole on the relationship between the Indian Monsoon rainfall and ENSO. *Geophys. Res. Lett.* 28, 4499–4502. doi: 10.1029/2001gl013294

Ashok, K., Iizuka, S., Rao, S. A., Saji, N. H., and Lee, W. J. (2009). Processes and boreal summer impacts of the 2004 El Niño Modoki: an AGCM study. *Geophys. Res. Lett.* 36:L04703.

Ashok, K., Sabin, T. P., Swapna, P., and Murtugudde, R. G. (2012). Is a global warming signature emerging in the tropical Pacific? *Geophys. Res. Lett.* 39:L02701.

Band, S., Yadava, M. G., Lone, M. A., Shen, C.-C., Sree, K., and Ramesh, R. (2018). High-resolution mid-Holocene Indian Summer Monsoon recorded in a stalagmite from the Kotumsar Cave, Central India. *Quat. Int.* 479, 19–24. doi: 10.1016/j.quaint.2018.01.026

Banerji, U. S., Arulbalaji, P., and Padmalal, D. (2020). Holocene climate variability and Indian summer monsoon: an overview. *Holocene* 30, 744–773. doi: 10.1177/0959683619895577

Bosmans, J. H. C., Drijfhout, S. S., Tuenter, E., Lourens, L. J., Hilgen, F. J., and Weber, S. L. (2012). Monsoonal response to mid- holocene orbital forcing in a high resolution GCM. *Clim. Past* 8, 723–740. doi: 10.5194/cp-8-723-2012

Bowen, D. Q. (2009). "Last glacial maximum," in *Encyclopedia of Paleoclimatology and Ancient Environments. Encyclopedia of Earth Sciences Series*, ed. V. Gornitz (Dordrecht: Springer), doi: 10.1007/978-1-4020-4411-3_122

Boyaj, A., Dasari, H. P., Hoteit, I., and Ashok, K. (2020). Increasing heavy rainfall events in South India due to changing land use land cover. *Q. J. R. Meteorol. Soc.* 146, 3064–3085. doi: 10.1002/qj.3826

Braconnot, P., Harrison, S. P., Kageyama, M., Bartlein, P. J., Masson-Delmotte, V., Abe-Ouchi, A., et al. (2012). Evaluation of climate models using palaeoclimatic data. *Nat. Clim. Change* 2, 417–424. doi: 10.1038/nclimate1456

Braconnot, P., Otto-Bliesner, B. L., Harrison, S., Joussaume, J., Peterchmitt, J. Y., Abe-Ouchi, A., et al. (2007a). Results of PMIP2 coupled simulations of the mid-Holocene and last glacial maximum. Part 1: experiments and large-scale features. *Clim. Past* 3, 261–277. doi: 10.5194/cp-3-261-2007

Braconnot, P., Otto-Bliesner, B. L., Harrison, S., Joussaume, J., Peterchmitt, J. Y., Abe-Ouchi, A., et al. (2007b). Results of PMIP2 coupled simulations of the mid-Holocene and last glacial maximum. Part 2: feedbacks with emphasis on the location of the ITCZ and mid-and high latitudes heat budget. *Clim. Past* 3, 279–296. doi: 10.5194/cp-3-279-2007

Chabangborn, A., Brandefelt, J., and Wohlfarth, B. (2013). Asian monsoon climate during the last glacial maximum: palaeo-data model comparisons. *Boreas* 43, 220–242. doi: 10.1111/bor.12032

Chakraborty, S., Goswami, B. N., and Dutta, K. (2012). Pacific coral oxygen isotope and the tropospheric temperature gradient over Asian monsoon region: a tool to reconstruct past Indian summer monsoon rainfall. *J. Quat. Sci.* 27, 269–278. doi: 10.1002/jqs.1541

Chen, L., Zheng, W., and Braconnot, P. (2019). Towards understanding the suppressed ENSO activity during mid-Holocene in PMIP2 and PMIP3 simulations. *Clim. Dyn.* 53, 1095–1110. doi: 10.1007/s00382-019-04637-z

Chowdary, J. S., Harsha, H. S., Gnanaseelan, C., Srinivas, G., Parekh, A., Pillai, P., et al. (2017). Indian summer monsoon rainfall variability in response to differences in the decay phase of El Niño. *Clim. Dyn.* 48, 2707–2727. doi: 10.1007/s00382-016-3233-1

Clemens, S. C., and Prell, W. L. (2007). The timing of orbital-scale Indian monsoon changes. *Quat. Sci. Rev.* 26, 275–278. doi: 10.1016/j.quascirev.2006.11.010

Cobb, K. M., Westphal, N., Sayani, H., Watson, J. T., Di Lorenzo, E., Cheng, H., et al. (2013). Highly variable El Niño-Southern oscillation throughout the holocene. *Science* 339, 67–70.

Crétat, J., Braconnot, P., Terray, P., Marti, O., and Falasca, F. (2020). Mid-Holocene to present-day evolution of the Indian monsoon in transient global simulations. *Clim. Dyn.* 55, 2761–2784. doi: 10.1007/s00382-020-05418-9

Dixit, Y., Hodell, D. A., Giesche, A., Tandon, S. K., Gázquez, F., Saini, H. S., et al. (2018) Intensified summer monsoon and the urbanization of Indus Civilization in northwest India. *Sci. Rep.* 8:4225. doi: 10.1038/s41598-018-22504-5

Dixit, Y., Hodell, D. A., and Petrie, C. A. (2014a). Abrupt weakening of the summer monsoon in northwest India ˜ 4100 yr ago. *Geology* 42, 339–342. doi: 10.1130/g35236.1

Dixit, Y., Hodell, D. A., Sinha, R., and Petrie, C. A. (2014b). Abrupt weakening of the Indian summer monsoon at 8.2 kyr BP. Earth Planet. *Sci. Lett* 391, 16–23. doi: 10.1016/j.epsl.2014.01.026

Dixit, Y., and Tandon, S. K. (2016). Earth-science reviews hydroclimatic variability on the Indian subcontinent in the past millennium? Review and assessment. *Earth Sci. Rev.* 161, 1–15. doi: 10.1016/j.earscirev.2016.08.001

Fan, Y., and van den Dool, H. (2004). Climate prediction center global monthly soil moisture data set at 0.5° resolution for 1948 to present. *J. Geophys. Res.* 109:D10102. doi: 10.1029/2003JD004345

Fleitmann, D., Burns, S. J., Mangini, A., Mudelsee, M., Kramers, J., Villa, I., et al. (2007). Holocene ITCZ and Indian monsoon dynamics recorded in stalagmites from Oman and Yemen (Socotra). *Quat. Sci. Rev.* 26, 170–188. doi: 10.1016/j.quascirev.2006.04.012

Gadgil, S., and Rupa Kumar, K. (2006). "The Asian Monsoon — Agriculture and economy," in *The Asian Monsoon. Springer Praxis Books*, ed. B. Wang (Berlin: Springer), doi: 10.1007/3-540-37722-0_18

Gill, E. C., Rajagopalan, B., Molnar, P., and Marchitto, T. M. (2016). Reduced-dimension reconstruction of the equatorial Pacific SST and zonal wind fields over the past 10,000 years using Mg/Ca and alkenone records. *Paleoceanography* 31, 928–952. doi: 10.1002/2016PA002948

Gill, E. C., Rajagopalan, B., Molnar, P. H., Kushnir, Y., and Marchitto, T. M. (2017). Reconstruction of Indian summer monsoon winds and precipitation over the past 10,000 years using equatorial pacific SST proxy records. *Paleoceanography* 32, 195–216. doi: 10.1002/2016PA002971

Griffiths, M. L., Johnson, K. R., Pausata, F. S. R., White, J. C., Henderson, G. M., Wood, C. T., et al. (2020). End of Green Sahara amplified mid- to late Holocene megadroughts in mainland Southeast Asia. *Nat. Commun.* 11:4204. doi: 10.1038/s41467-020-17927-6

Grove, J. M. (1988). *The Little Ice Age*. London: Menthuen.

Guan, Z., Ashok, K., and Yamagata, T. (2003). Summertime response of the tropical atmosphere to the Indian Ocean sea surface temperature anomalies. *J. Meteor. Soc. Jpn.* 81, 533–561. doi: 10.2151/jmsj.81.533

Gupta, A. K., Das, M., and Anderson, D. M. (2005). Solar influence on the Indian summer monsoon during the Holocene. *Geophys. Res. Lett.* 32:L17703. doi: 10.1029/2005GL022685

Hersbach, H., Peubey, C., Simmons, A., Berrisford, P., Poli, P., Dee, D., et al. (2015). ERA-20CM: a twentieth-century atmospheric model ensemble. *Q. J. R. Meteorol. Soc.* 141, 2350–2375. doi: 10.1002/qj.2528

Hu, F. S., Kaufman, D., Yoneji, S., Nelson, D., Shemesh, A., Huang, Y., et al. (2003). Cyclic variation and solar forcing of Holocene climate in the Alaskan Subarctic. *Science* 301, 1890–1893. doi: 10.1126/science.1088568

Kathayat, G., Cheng, H., Sinha, A., Yi, L., Li, X., Zhang, H., et al. (2017). The Indian monsoon variabil- ity and civilization changes in the Indian subcontinent. *Sci. Adv.* 3:e1701296. doi: 10.1126/sciadv.1701296

Krishnan, R., Sanjay, J., Gnanaseelan, C., Mujumdar, M., Kulkarni, A., and Chakraborty, S. (eds) (2020). *Assessment of Climate Change Over the Indian Region. A Report of the Ministry of Earth Sciences (MoES), Government of India*. Singapore: Springer. doi: 10.1007/978-981-15-4327-2

Kumar, P., Sanwal, J., Dimri, A. P., and Ramesh, R. (2019). Contribution of diverse monsoon precipitation over Central and Northern India during Mid to Late Holocene. *Quat. Int.* 507, 217–223. doi: 10.1016/j.quaint.2018.10.003

Kutzbach, J., and Guetter, P. J. (1986). The influence of changing orbital parameters and surface boundary conditions on climate simulations for the past 18 000 years. *J. Atmos. Sci.* 43, 1726–1759. doi: 10.1175/1520-0469(1986)043<1726:tiocop>2.0.co;2

Kutzbach, J., Liu, X., Liu, Z., and Chen, G. (2008). Simulation of the evolutionary response of global summer monsoons to orbital forcing over the past 280,000 years. *Clim. Dyn.* 30, 567–579. doi: 10.1007/s00382-007-0308-z

Kutzbach, J. E. (1981). Monsoon climate of the early Holocene: climate experiment with the earth's orbital parameters for 9000 years ago. *Science* 214, 59–61. doi: 10.1126/science.214.4516.59

Kutzbach, J. E., and Otto-Bliesner, B. L. (1982). The sensitivity of the African-Asian monsoonal climate to orbital parameter changes for 9000 years BP in a low-resolution general-circulation model. *J. Atmos. Sci.* 39, 1177–1188. doi: 10.1175/1520-0469(1982)039<1177:tsotaa>2.0.co;2

Lamb, H. H. (1965). The early medieval warm epoch and its sequel. *Palaeogeogr. Palaeoclimatol.* 1, 13–37. doi: 10.1016/0031-0182(65)90004-0

LeGrande, A. N., and Schmidt, G. A. (2008). Ensemble, water isotope–enabled, coupled general circulation modeling insights into the 8.2 ka event. *Paleoceanography* 23:A3207.

Leuschner, D. C., and Sirocko, F. (2003). Orbital insolation forcing of the Indian Monsoon–a motor for global climate changes? *Palaeogeogr. Palaeoclimatol. Palaeoecol.* 197, 83–95. doi: 10.1016/s0031-0182(03)00387-0

Li, Y., and Harrison, S. P. (2008). Simulations of the impact of orbital forcing and ocean on the Asian summer monsoon during the Holocene. *Glob. Planet. Change* 60, 505–522. doi: 10.1016/j.gloplacha.2007.06.002

Marzin, C., Braconnot, P., and Kageyama, M. (2013). Relative impacts of insolation changes, meltwater fluxes and ice sheets on African and Asian monsoons during the Holocene. *Clim. Dyn.* 41, 2267–2286. doi: 10.1007/s00382-013-1948-9

Merlis, T. M., Schneider, T., Bordoni, S., and Eisenman, I. (2013). Hadley circulation response to orbital precession. Part II: subtropical continent. *J. Clim.* 26, 754–771. doi: 10.1175/jcli-d-12-00149.1

Messori, G., Gaetani, M., Zhang, Q., Zhang, Q., and Pausata, F. S. R. (2018). The water cycle of the mid-Holocene West African monsoon: the role of vegetation and dust emission changes. *Int. J. Climatol.* 39, 1927–1939. doi: 10.1002/joc.5924

Mohanty, U. C., Mohapatra, M., Ashok, K., Krishnan, R., Chowdary, J. S., and Mukhopadhyay, P. (2020). Indian monsoons variability and extreme weather event: recent improvements in observations and modelling. *Proc. Indian Natl. Sci. Acad.* 86, 1442–1445.

Mukherjee, P., Sinha, N., and Chakraborty, S. (2016). Investigating the dynamical behavior of the Inter-tropical Convergence Zone since the last glacial maximum based on terrestrial and marine sedimentary records. *Quat. Int.* 443, 49–57. doi: 10.1016/j.quaint.2016.08.030

Pattanaik, D. R. (2012). Indian monsoon variability. *Meteorol. Monogr.* 2, 35–77.

Pokras, E. M., and Mix, A. C. (1987). Earth's precession cycle and Qua- ternary climatic change in tropical Africa. *Nature* 326, 486–487. doi: 10.1038/326486a0

Polanski, S., Fallah, B., Befort, D. J., Prasad, S., and Cubasch, U. (2014). Regional moisture change over India during the past Millennium: a comparison of multi-proxy reconstructions and climate model simulations. *Glob. Planet. Change* 122, 176–185. doi: 10.1016/j.gloplacha.2014.08.016

Polanski, S., Rinke, A., Dethloff, K., Lorenz, S. J., Wang, Y., and Herzschuh, U. (2012). Simulation of the mid-Holocene Indian summer monsoon circulation with a regional climate model. *Open Atmos. Sci. J.* 6, 42–48. doi: 10.2174/1874282301206010042

Rajeevan, M., Bhate, J., Kale, J. D., and Lal, B. (2006). High resolution daily gridded rainfall data for the Indian region? Anal. Break Active Monsoon Spells. *Curr.Sci.* 91, 296–306.

Ramesh, R., Tiwari, M., Chakraborty, S., Managave, S. R., Yadava, M. G., and Sinha, D. K. (2010). Retrieval of south asian monsoon variation during the holocene from natural climate archives. *Curr. Sci.* 99, 1770–1786.

Rawat, S., Gupta, A. K., Sangode, S. J., Srivastava, P., and Nainwal, H. C. (2015). Late Pleistocene–Holocene vegetation and Indian summer monsoon record from the Lahaul, Northwest Himalaya, India. *Quat. Sci. Rev.* 114, 167–181. doi: 10.1016/j.quascirev.2015.01.032

Renssen, H., Goosse, H., Fichefet, T., and Campin, J. M. (2001). The 8.2 kyr BP event simulated by a global atmosphere—sea—ice—ocean model. *Geophys.Res. Lett.* 28, 1567–1570. doi: 10.1029/2000gl012602

Rind, D., and Overpeck, J. T. (1993). Hypothesized causes of decade- to century-scale climatic variability: climate model results. *Quat. Sci. Rev.* 12, 357–374. doi: 10.1016/s0277-3791(05)80002-2

Schmidt, G. A., Jungclaus, J. H., Ammann, C. M., Bard, E., Braconnot, P., Crowley, T. J., et al. (2012). Climate forcing reconstructions for use in PMIP simulations of the Last Millennium (v1.1). *Geosci. Model Dev.* 5, 185–191. doi: 10.5194/gmd-5-185-2012

Shi, Z. (2016). Response of Asian summer monsoon duration to orbital forcing under glacial and interglacial conditions: implication for precipitation variability in geological records. *Quat. Sci. Rev.* 139, 30–42. doi: 10.1016/j.quascirev.2016.03.008

Shindell, D. T., Schmidt, G. A., Mann, M. E., Rind, D., and Waple, A. (2001). Solar forcing of regional climate change during the Maunder Minimum. *Science* 294, 2149–2152. doi: 10.1126/science.1064363

Staubwasser, M., Sirocko, F., Grootes, P. M., and Segl, M. (2003). Climate change at the 4.2 ka BP termination of the Indus valley civilization and Holocene south Asian monsoon variability. *Geophys. Res. Lett.* 30:1425. doi: 10.1029/2002GL016822

Taylor, K. E., Stouffer, R. J., and Meehl, G. A. (2012). An overview of CMIP5 and the experiment design. *Am. Meteor. Soc. B* 93, 485–498. doi: 10.1175/BAMS-D-11-00094.1

Tejavath, C. T., Ashok, K., Chakraborty, S., and Ramesh, R. (2019). A PMIP3 narrative of modulation of ENSO teleconnections to the Indian summer monsoon by background changes in the Last Millennium. *Clim. Dyn.* 53, 3445–3461. doi: 10.1007/s00382-019-04718-z

Tejavath, C. T., Pankaj, U., and Ashok, K. (2020). The past climate of the Indian region as seen from the modelling world. *Curr. Sci.* 119, 316–327.

Tuenter, E., Weber, S., Hilgen, F., Lourens, L., and Ganopolski, A. (2005). Simulation of climate phase lags in response to precession and obliquity forcing and the role of vegetation. *Clim. Dyn.* 24, 279–295. doi: 10.1007/s00382-004-0490-1

Wang, X., Auler, A. S., Edwards, R., Cheng, H., Ito, E., Wang, Y., et al. (2007). Millennial-scale precipitation changes in southern Brazil over the past 90,000 years. *Geophys. Res. Lett.* 34:L23701. doi: 10.1029/2007GL031149

Weber, S., and Tuenter, E. (2011). The impact of varying ice sheets and greenhouse gases on the intensity and timing of boreal summer monsoons. *Quat. Sci. Rev.* 30, 469–479. doi: 10.1016/j.quascirev.2010.12.009

Webster, P. J., Magana, V. O., Palmer, T. N., Shukla, J., Tomas, R. A., Yanai, M., et al. (1998). Monsoons: processes, predictability, and the prospects for prediction. *J. Geophys. Res.* 103, 14451–14510. doi: 10.1029/97jc02719

Wiersma, A. P., and Renssen, H. (2006). Model–data comparison for the 8.2 ka BP event: confirmation of a forcing mechanism by catastrophic drainage of Laurentide Lakes. *Quat. Sci. Rev.* 25, 63–88. doi: 10.1016/j.quascirev.2005.07.009

Zhao, Y., and Harrison, S. (2012). Mid-Holocene monsoons: a multi-model analysis of the inter-hemispheric differences in the responses to orbital forcing and ocean feedbacks. *Clim. Dyn* 39, 1457–1487. doi: 10.1007/s00382-011-1193-z

Zheng, W., Braconnot, P., Guilyardi, E., Merkel, U., and Yu, Y. (2008). ENSO at 6 ka and 21 ka from ocean-atmosphere coupled model simulations. *Clim. Dyn.* 30, 745–762. doi: 10.1007/s00382-007-0320-3

Conflict of Interest: The authors declare that the research was conducted in the absence of any commercial or financial relationships that could be construed as a potential conflict of interest.

frontiers
in Earth Science

ORIGINAL RESEARCH
published: 31 May 2021
doi: 10.3389/feart.2021.645959

Himalayan Blue Pine Deduced Precipitation Record from Cold Arid Lahaul–Spiti, Himachal Pradesh, India

Krishna G. Misra, Vikram Singh, Akhilesh K. Yadava, Sandhya Misra, Ravi S. Maurya and Sadhana Vishwakarma*

Birbal Sahni Institute of Palaeosciences, Lucknow, India

Ecologically Himalayan blue pine (*Pinus wallichiana* A. B. Jackson) is the most sensitive tree-species found across the high mountain ranges of Himalaya with deciphering tree-line for the region. Earlier studies showed the potential of Himalayan blue pine to reconstruct the past climate for extending observational data back to the centuries from orography-dominated Himalaya. However, tree-growth of the blue pine is largely found modulated by temperature in the western Himalayan region. In the present study, we attempted the first time to develop precipitation records using Himalayan blue pine chronology from cold arid Lahaul–Spiti, Himachal Pradesh, India. The blue pine chronology extends back to AD 1578 and showed significant relationship with the climatic variables. The bootstrap correlation analyses revealed previous year December to current year July precipitation plays significant role in tree-growth advancements. The previous year December to current year July (pDcJuly) precipitation has been reconstructed back to the AD 1730 for the Lahaul–Spiti region. The recorded individual and multi-year periods of low and high precipitation are consistent with existing hydro-climatic records from the western Himalaya. The five driest and wettest individual years are 1732, 1737, 1970, 2008, 1785, and 1730, 1771, 1758, 1734, 1736, respectively. The spatial correlation between gridded precipitation and reconstructed pDcJuly precipitation is significant for the region close to the sampling site. The study based on the Himalayan blue pine tree-ring chronology addressed its dendroclimatic utility for the semi-arid Lahaul–Spiti region and would be valuable to understand climatic variability over the past three centuries. The strong resemblance of the species with the Himalayan cedar growth patterns showed its promising viability to develop a network of multispecies for more robust climatic reconstruction in the future.

Keywords: Himalayan blue pine, tree-ring, precipitation, climatic variability, Lahaul–Spiti, Himachal Pradesh

Edited by:
Anoop Ambili,
Indian Institute of Science Education and Research Mohali, India

Reviewed by:
Zoltan Kern,
Hungarian Academy of Sciences (MTA), Hungary
José Darrozes,
UMR5563 Géosciences Environnement Toulouse (GET), France

****Correspondence:***
Krishna G. Misra
kgmisrabsip@gmail.com

Specialty section:
This article was submitted to Quaternary Science, Geomorphology and Paleoenvironment, a section of the journal Frontiers in Earth Science

Received: *24 December 2020*
Accepted: *18 May 2021*
Published: *31 May 2021*

Citation:
Misra KG, Singh V, Yadava AK, Misra S, Maurya RS and Vishwakarma S (2021) Himalayan Blue Pine Deduced Precipitation Record from Cold Arid Lahaul–Spiti, Himachal Pradesh, India. Front. Earth Sci. 9:645959. doi: 10.3389/feart.2021.645959

INTRODUCTION

The Himalayan mountain system is unique in the world due to its complex geographical distribution and young dynamic geology. The high elevated orogeny of the Himalaya in combination with the Tibetan plateau controls the climate over the region. The high-altitude Himalayan ecosystem and environment have significant effect on global climate change and the Himalayan ranges, outside the poles, contained the largest body of ice/snow in the form of glaciers and snow-caps. These glaciers and snow-caps are very sensitive to climate change and as per the IPCC report (IPCC, 2013) glaciers are retreating worldwide due to on-going atmospheric global warming. Global warming leads to the Earth's average temperature up to a critical level, where the average temperature showing an increase of 0.85°C for 1880–2012 and since 1850 each of the last three decades has been successively warmer (IPCC, 2013). The consequences of climate change-induced global warming are not only restricted to the rising global average temperature of the earth but also disturbing the precipitation pattern over the Himalayan region. Climate change and global warming results include the uncertainty in the pattern and intensity of precipitation which affects hydrogeological conditions over the region. Precipitation over India is mainly brought by the Indian summer monsoon (ISM), from the southern end and by western disturbances (WD) from the northern end of the sub-continent. ISM intensified in the Indian sub-continent during the period from June–September (JJAS), whereas WD reaches its optimum during December–March (DJFM). These two are the primary sources of precipitation over the whole Indian sub-continent in which 1/6th of the world population lives and depends on their livelihood. ISM directly helps the major part of peninsular India and Himalayan foothills by dropping down the temperature, recharging groundwater level by natural irrigation of the agricultural land. Whereas WD provides a major source for the feeding of glaciers and rivers of western and northwestern Himalaya and plays a significant role to maintain the hydro-climatic conditions (Yadav and Bhutyani, 2013). Based on the observation of meteorological data generated by India Meteorological Department (IMD) and gridded data in the recent past from 1901 to 2012 the summer monsoon rainfall has weakened over south Asia in general and this is very striking over the central-east and northern region of India (Roxy et al., 2015). Although a recent study from Kishtwar, Jammu & Kashmir indicates about pluvial phase prevailing in the recent few decades over the northwest Himalaya and Karakoram (Yadav et al., 2017). The reconstruction revealed the last 31-years (1984–2014) from the past 576 years being the wettest; indicate recent strengthening of the westerly's over northwest Himalaya and Karakoram. In an agrarian economy like India, where the 2/3rd population is associated directly or indirectly with the agriculture and related sectors, uncertainty in precipitation pattern becomes the cause of huge misery for the socio-economic lives.

To understand the precipitation variability over a region it is important to access meteorological data records, but unfortunately in the Himalayan region, meteorological records are sparse and patchy. These observational records are inadequate to explain the long-term climatic variability of the region in terms of precipitation, temperature, snowfall etc. Therefore, to fill the data void and extends the existing records back to the centuries, high-resolution proxies such as tree-ring, lake sediments, ice cores, and speleothems have been studied over the decades from the Himalaya (Overpeck et al., 2005; Joshi et al., 2017; Phartiyal et al., 2020; Dahe et al., 2021; Kumar et al., 2021). However, to develop high-resolution annually resolved climatic records from centuries to millennium tree-rings proved its utility among all other proxies in the past few decades (Yadav and Park, 2000; Cook et al., 2003; Yadav et al., 2004; Tredyte et al., 2006; Singh et al., 2006, 2009; Cook et al., 2010; Yadav, 2011a, b, 2012, 2013; Yadav and Bhutiyani, 2013; Yadava et al., 2016; Singh et al., 2017; Yadav et al., 2017). In view of the great importance of tree-ring records to provide the annually resolved climatic data, we have selected Lahaul–Spiti region in the present study for analyzing the past climate.

The Lahaul–Spiti is a semi-arid to arid cold desert situated in the northern part of Himachal Pradesh. A major portion of annual precipitation occurs in this region due to the moisture-laden westerlies from December to april. Due to topographic barriers of the Pir Panjal range, summer monsoon rainfall does not reach properly over Lahaul–Spiti and it only drizzles during the peak monsoon (Yadav, 2011b). Over the western Himalaya, Lahaul–Spiti accumulates the foremost portion of ice and snow (Bajpai, 2002) and in the presence of weak ISM in the higher Himalaya; westerlies provides vital feeding to the glaciers and Himalayan rivers. To understand the climatic variability, precipitation reconstruction (Yadav, 2011b) and snowfall records (Yadav and Bhutiyani, 2013), was developed using *Cedrus deodara* chronologies from the cold arid Lahaul Himalaya. The Lahaul–Spiti region in the Northwest Himalaya has unique environmental setting for tree-ring studies where over millennium-long old trees growing in natural conditions are very common (Yadav, 2012; Misra et al., 2020). The potential of tree-ring-based climate studies using *Cedrus deodara* and *Juniperus polycarpos* has been widely explored from the cold arid Lahaul–Spiti region (Yadav et al., 2006; Yadav, 2011b, 2012; Yadav and Bhutiyani, 2013). However, the dendroclimatic potential of *Pinus wallichiana* has not been taken into account for climatic reconstruction largely due to its patchy distribution in difficult terrains but the rate of tree-line migration was observed earlier from the region (Dubey et al., 2003; Yadava et al., 2017). Although, studies on Himalayan blue pine from different regions of the western Himalaya showed its utility in developing centuries-long chronologies, establishing tree-growth climate relationship and climatic reconstructions (Yadav et al., 1997; Singh and Yadav, 2000; Yadava et al., 2017; Shah et al., 2019). However, the climatic signals thus far reported in Himalayan blue pine chronologies in terms of moisture signal was weak and vary with the nature of the ecological settings of the tree-ring sampling sites. Here, in the present attempt, we for the first time used Himalayan blue pine from the Lahaul–Spiti region for the precipitation reconstruction.

MATERIAL AND METHODS

Tree-Ring Data

The Himalayan blue pine (*P. wallichiana* A. B. Jackson) is a tall evergreen tree that has needle-like leaves in the form of bundles with a bluish-green tinge and therefore also known as blue pine. Himalayan blue pine is native of Himalaya and distributed all along the Himalayan Mountains generally over an altitude of 1,800–3,900 m, starting from the east of Afghanistan to northeast India to Nepal and Bhutan (Sahni, 1990). For the present study, we collected tree-ring samples of Himalayan blue

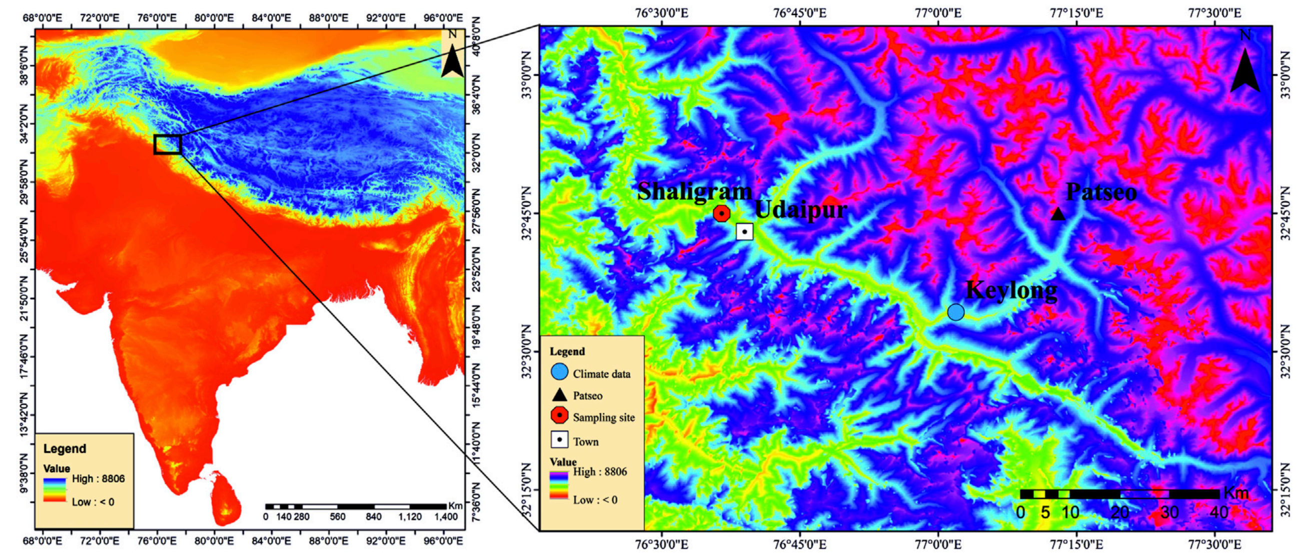

FIGURE 1 | Location of the study area, tree ring sampling site and meteorological station used in the present study.

pine from Shaligram, Lahaul–Spiti, Himachal Pradesh (**Figure 1**) over an altitude of 3,076 m asl. At this site, Himalayan blue pine trees are growing scattered and intermixed with Himalayan cedar trees. A detailed survey was done to collect the increment cores from healthy, old Himalayan blue Pine trees. Finally, 21 samples from 15 isolated and healthy trees were selected from the cold-arid moisture stressed site in the Lahaul Himalaya. Undisturbed samples were collected from the breast height (~1.4 m) of the stem in the direction perpendicular to the natural slope. Tree-ring increment cores were processed following the standard dendrochronological procedure (Stokes and Smiley, 1968), which includes mounting, surfacing, and polishing with different grades of abrasive. Growth ring sequences were dated using the skeleton plot method (Stokes and Smiley, 1968) and calendar age was assigned to each ring. To cross-date the tree-ring samples through the skeleton plotting method, signaling rings from each samples were plotted to the graph-strip to match the growth-ring patterns. Ring-widths in cross-dated samples were measured using linear encoder (LINTAB) attached to the personal computer (Rinn, 2003). The dating quality control program COFECHA was used to evaluate the accuracy of cross-dated samples which crosschecks the correlation between single measurement series and mean of all the series used in that particular segment (Holmes, 1983). Segments in the samples with problems or weak correlations were rechecked and errors corrected, if any, by comparing with master series. Samples were discarded if the correlation and cross-dating problems continue after re-examining the samples. COFECHA analyses revealed mean series intercorrelation between all individual samples is 0.64 and such good coherence among samples indicates strong year-to-year pattern matching. High correlation among all the individual series indicates the presence of common climatic signal in the tree-ring data. Except climate forcing, tree-ring sequence is also influenced by external and internal factors such as biological growth trend, disease and competition for nutrients among neighboring trees. These noises were removed and the climatic signal among all the series was maximized by curve fitting, called Standardization (Fritts, 1976) using ARSTAN program (Cook, 1985). The ring-width sequence of the Himalayan blue pine was observed cautiously for the selection of the appropriate detrending method. To detrend the ring-width measurements series 67% cubic smoothing spline with a 50% frequency response cut-off was used. Tree-ring-width series were power transformed before detrending to stabilize the variance in the individual series (Cook and Peters, 1997). After detrending, biweight robust mean (Cook, 1985) was calculated, and mean chronology (AD 1578–2016) was prepared by combining all the individual detrended series. 439 years long ring-width chronology of Himalayan blue pine was developed from the cold arid Lahaul–Spiti region (**Figure 2**). The chronology span for analysis depends on the threshold limit of expressed population signal (EPS) > 0.85 (Wigley et al., 1984). Replication of 21 samples from 15 trees was found to be sufficient for getting the desired EPS level. However, to stabilize the variance due to changing replication and inter-series correlation, variance adjustment (Osborn et al., 1997) was also tested but the effect was found to be insignificant so has not been applied on the calculation of the final mean ring-width index. The residual version of chronology (AD 1730–2016) based on EPS level >0.85 was taken into consideration for the further dendroclimatic analysis and climate reconstruction. Chronology statistics including chronology span, the number of samples used in the development of chronology, standard deviation, mean sensitivity and EPS threshold value are given in **Table 1**.

Climate Data

Instrumental climate records close to the sampling site are prerequisite for the tree-ring based climate reconstruction. Climate data from meteorological stations situated close to the

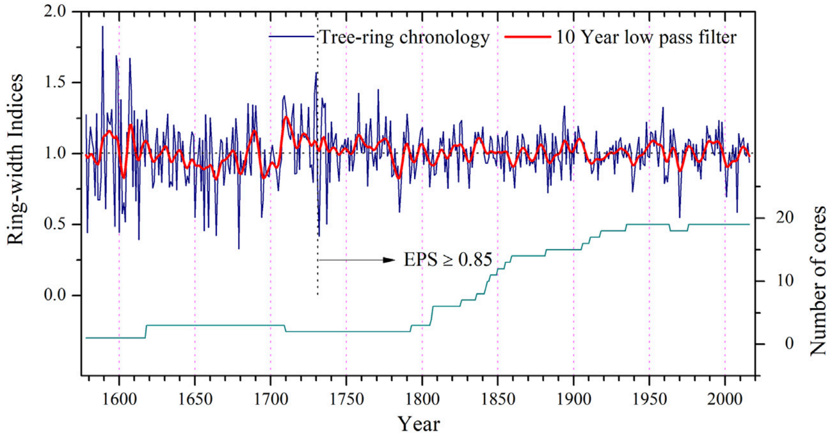

FIGURE 2 | Himalayan blue pine (*Pinus wallichiana*) chronology developed from Shaligram, Lahaul–Spiti, Himachal Pradesh, India (AD 1578–2016). EPS limit (0.85) of the chronology indicated by the vertical dotted line at AD 1730, after which chronology exceeds the threshold limit.

TABLE 1 | Himalayan blue pine chronology statistics developed from Shaligram, Lahaul–Spiti, Himachal Pradesh, India (AD 1578–2016).

Latitude (N)	Longitude (E)	Elevation (m asl)	Cores/ trees	Chronology span AD (yrs)	Chronology with EPS >0.85, AD	MI	MS	SD	AR1
32°44′58″–32°45′36″	76°36′30″–76°36′3″	3,076	21/15	1,578–2016 (439)	1730–2016	1.00	0.20	0.19	0.00

EPS, expressed population signal; MI, mean index; MS, mean sensitivity; SD, standard deviation; AR1, first-order autocorrelation.

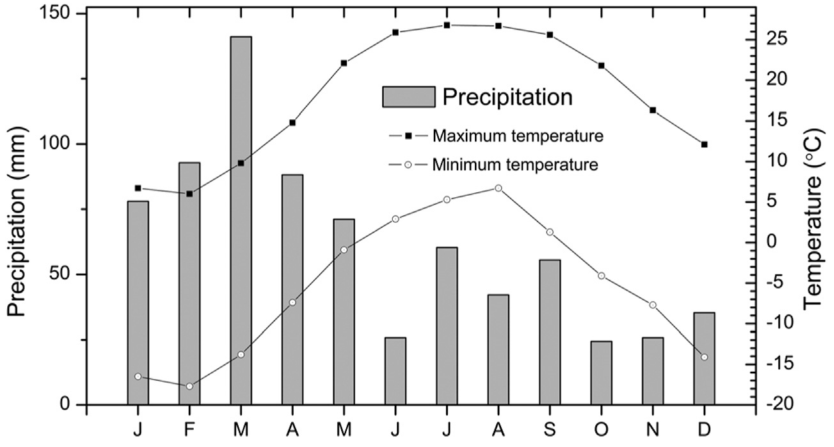

FIGURE 3 | The mean monthly precipitation pattern of Keylong and temperature of Srinagar meteorological stations used in the study.

tree-ring sampling sites explain the regional climatology better and are useful in calibration. The climate in orography dominated Himalayan region, changes within a very short distance due to altitudinal differences and mountain settings. Highly dissected orography restricts our understanding of climate variability over Himalaya on a regional scale and long-term spatial changes cannot be captured through sparsely located meteorological station data. Long and homogenous records of climate variables from the Himalaya are very few and mainly centered in the valley floors far away from the potential remote areas. Only very few stations in north India have data that extend more than a century and therefore difficulties always arise during the dendroclimatological studies (Yadav et al., 2004; Singh and Yadav, 2005). Keylong (33°34′N, 77°01′E, 3,054 m asl; AD 1933–1970) is the only station with precipitation data available close to the sampling site; with approximately 38 km nautical distance. The meteorological data of precipitation suggest that this cold desertic area receives maximum (about 80%) part of its

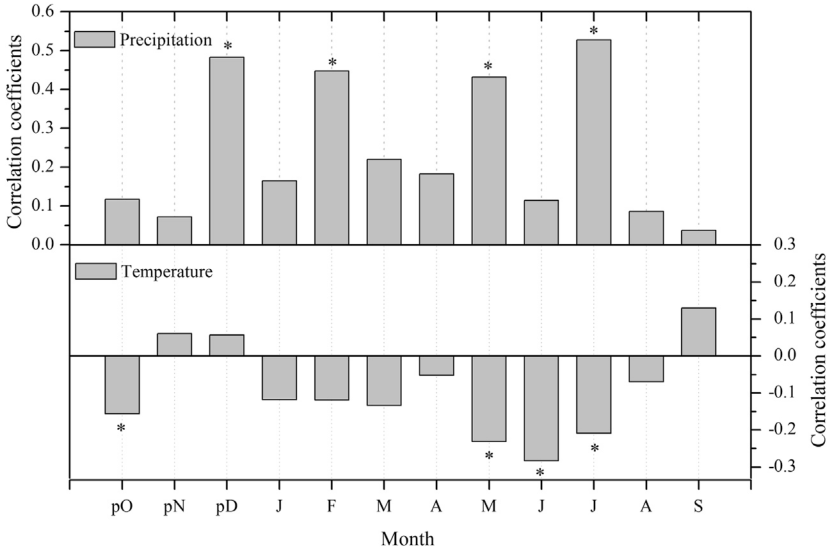

FIGURE 4 | Bootstrap correlation among residual tree-ring chronology and climate variables such as monthly precipitation of Keylong and temperature of Srinagar. The asterisk shows confidence level at 95%.

annual precipitation during the month of December–July by the WD and ISM does not play any significant role in contributing to its annual budget (**Figure 3**). Because large scale spatial variability in precipitation exist in the Himalaya due to complex mountain settings and therefore only the station close to the sampling site can explain the tree-growth-climate relationship clearly. Keylong is the only station close to the tree-ring sampling sites but unfortunately, the temperature record is not available from the station. In the absence of temperature data from Keylong, temperature data of Srinagar (34°08′N and 74°48′E, 1,587 m asl; 1900–2008) has been used in the present study which also shows strong consistency in similar climatic zones (Yadav et al., 2004).

Tree-Growth and Climate Relationship

To understand the climate signal in tree-ring chronology, tree-growth and climate relationship was established using response function analysis (Fritts, 1976). The residual chronology was used for the analysis with climatic variables like temperature and precipitation. Monthly precipitation (1933–1970) and temperature (1900–2008) data were used from previous year's October to the current year's September in correlation analysis using program DENDROCLIM 2002 (Biondi and Waikul, 2004). Bootstrap correlation analysis revealed that tree-growth has direct relationship with precipitation throughout the year (**Figure 4**). But the previous year's December to current year July (pDcJuly) precipitation plays significant role for tree-growth over the region with significant positive correlation for the previous year December and current year February, May and July months. The eight months (pDcJuly) period contributes ~80% of annual precipitation and mainly responsible for the tree-growth (**Figure 4**). Analysis with temperature data revealed an inverse relationship with tree-growth during the whole year except the previous year November, December and the current year September. The previous year October and current year May, June and July months have significantly negative effects on tree-growth (**Figure 4**), which indicates that increased temperature during these months reduces tree-growth. Overall correlation analysis revealed that cool and wet conditions in the cold-arid Lahaul Himalaya favor and warm and dry conditions hamper tree-growth. The correlation between tree-growth and the previous year's December to the current year's July (pDcJuly) precipitation was used for further analysis and climatic reconstruction.

Calibration, Verification and pDcJuly Precipitation Reconstruction

The residual chronology of Himalayan blue pine was used in developing the relationship between tree-ring data and climate variables. A strong and significant positive correlation was found with precipitation from the previous year's December to the current year's July. Earlier work by Yadav (2011a) also demonstrated the role of winter precipitation on the radial growth of *Cedrus deodara* over the cold-arid Lahaul Himalaya. Both studies from the cold-arid Lahaul Himalaya using two different species suggest that the winter precipitation provides vital and favourable conditions for tree-growth advancement. Using this strong relationship as a guide, the previous year's December to current year's July precipitation from AD 1933–1970 was used for the calibration and verification analyses and therefore regression approach has been adopted. Calibration and verification have been done for two different sub-periods using 1933–1970 precipitation data. Two sub-periods from 1933 to 1952 and 1953–1970 were successively used once for calibration and then verification. Due to the relatively shorter duration in two different sub-periods, the whole data from 1933 to 1970 was also separately used for calibration. For additional

TABLE 2 | Calibration and verification statistics of precipitation reconstruction; ar^2–r^2 adjusted after degrees of freedom, R-Pearson correlation, Sign test, RE (reduction of error), CE (coefficient of efficiency) and L1-Cross-validation using Leave-one-out method (Fritts, 1976; Cook et al., 1999).

Calibration		Verification					
Period	ar^2 (%)	Period	*R*	Sign test	*t* value	RE	CE
1933–1952	54.4	1953–1970	0.78 [0.0001]	$12^+/6^-$	2.61	0.23	0.024
1953–1970	59.5	1933–1952	0.75 [0.0001]	$13^+/7^-$	2.13	0.38	0.251
1933–1970	50.5						
1933–1970 L_1	44.8	1933–1970	0.68 [0.000002]	$26^+/12^-$	3.08	0.46	

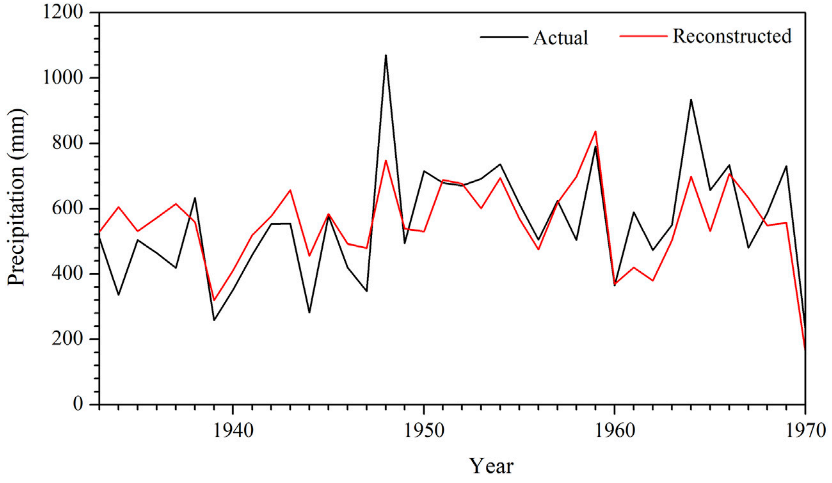

FIGURE 5 | Actual and reconstructed precipitation series plotted together for comparison ($r = 0.71$, 1933–1970, $p < 0.0001$).

verification, the leave-one-out cross-validation (Michaelsen, 1987) was also performed. The detailed statistics of calibration and verification of two different sub-periods 1933–1952, 1953–1970 and leave-one-out cross-validation, like Pearson correlation coefficients, Sign test, reduction of error (RE) and coefficient of efficiency (CE) (Fritts, 1976; Cook et al., 1999) were calculated to check reliability and utility of the reconstruction (**Table 2**). In verification analysis, RE and CE, the most rigorous analysis for validation of the model, values are positive which indicates reconstruction skills. The full period calibration model was used for reconstruction that captured 50% variance of the instrumental data. The significant correlation and strong year-to-year similarity of the reconstructed series with the monthly precipitation data of pDcJuly was observed ($r = 0.71$, 1933–1970, $p < 0.0001$) (**Figure 5**).

RESULTS AND DISCUSSION

Tree-Ring-Width Chronology

The Himalayan blue pine chronology developed from the cold-arid Lahaul Himalaya extends back to AD 1578 (439 years). Twenty-one increment cores from fifteen trees growing over moisture stressed sites at an altitude of 3,076 m asl, were used for chronology development. The tree-ring width chronology statistics including mean index, mean sensitivity and standard deviation for the chronology span 1730–2016 with EPS level >0.85 are shown in **Table 1**. The strong chronology statistics suggested high consistency among the growth pattern of trees used in the present study. In our field observation, we noted that Himalayan blue pine trees in the forest of Shaligram growing mixed with Himalayan cedar are in the proportion of 1:20. Favourable climatic conditions and ecological requirements of the Himalayan cedar could be the possible reason for such distribution of species. Interestingly, it was also noted that the Himalayan blue pine ring-width chronology also showed similar growth pattern as in Himalayan cedar (unpublished data) growing over the site.

Analyses of pDcJuly Precipitation Reconstruction

The pDcJuly precipitation reconstruction using the Himalayan blue pine ring-width chronology extends back to AD 1730 (287-years), revealed annual to decadal-scale variability (**Figure 6**). The present reconstruction from the cold-arid Lahaul Himalaya explains 50% of the variance in the recorded precipitation data of Keylong from the previous year December to the current year July. Such a good relationship among Himalayan blue pine and instrumental records reflected the importance of the species to

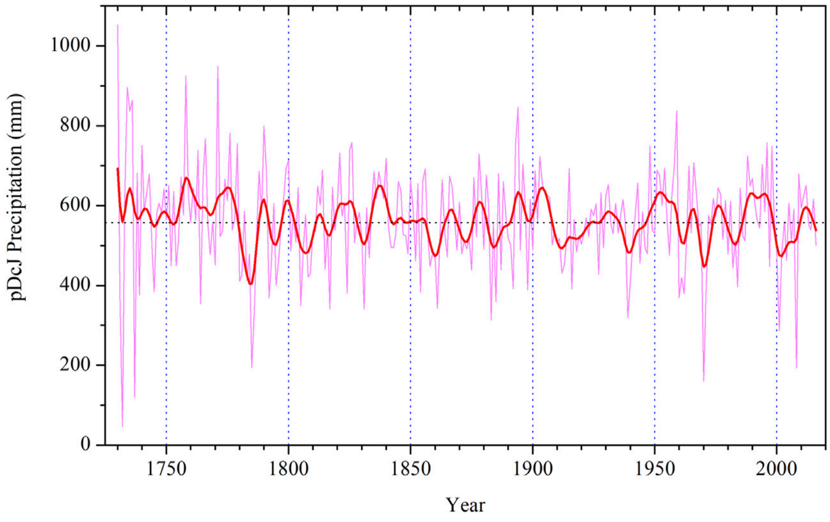

FIGURE 6 | pDcJuly Precipitation reconstruction series (AD 1730–2016) for Shaligram, Lahaul–Spiti, Himachal Pradesh, India. The 10-years low pass filter was applied to the reconstruction (thick superimposed line) to show the precipitation variability in 10 or more year periods. The dotted horizontal line is long term mean of the precipitation reconstruction.

TABLE 3 | The lowest and highest precipitation (mm) year obtained from precipitation reconstruction using the non-over lapping mean of 3-, 5- and 10-years.

3-years mean				5-years mean				10-years mean			
Wet		Dry		Wet		Dry		Wet		Dry	
Years	Prec.	Years	Prec.	Years	Prec.	Years	Prec.	Years	Prec.	Years	Prec.
1733–1735	782.1	1784–1786	335.7	1755–1759	662.6	1805–1809	453.6	1950–1959	638.9	1780–1789	463.2
1757–1759	709.3	1970–1972	369.2	1775–1779	651.4	1970–1974	455.7	1770–1779	638.3	2000–2009	486.1
1994–1996	682.0	1833–1835	409.0	1835–1839	650.0	2000–2004	456.0	1990–1999	617.5	1910–1919	509.6
1988–1990	680.5	2000–2002	418.9	1955–1959	639.9	1780–1784	462.8	1750–1759	606.2	1800–1809	520.3
1835–1837	662.8	1859–1861	430.6	1950–1954	637.9	1785–1789	463.7	1900–1909	603.1	1970–1979	525.2

reveal the climatic variability over the Lahaul–Spiti region, and our study also suggested that by adding more samples much strong relationship can be found. In the entire reconstructed period, the year 1732 showed the lowest (45.9 mm) and 1730 highest (1,053.3 mm) precipitation. Other individual driest and wettest year, those receive the lowest and highest precipitation are also recorded from the past 287-years reconstruction (**Table 3**). In the entire reconstruction, 1732 is the driest year followed by 1737, 1970, 2008, and 1785, all these years receive precipitation less than 200 mm in 8 months from the previous year December to the current year July. Similarly, the wettest year 1730 is followed by 1771, 1758, 1734, and 1736, which received precipitation more than 850 mm in the same period, while the long term mean of pDcJuly precipitation is 562.5 mm. Such high variability in precipitation records from the lowest 45.9 mm to the highest 1,053.3 mm in different individual years reveals that the cold desertic Lahaul Himalaya witnessed severe climatic challenges in the past three centuries.

Dry and wet individual years noted in the present reconstruction were matched with other western Himalayan hydrological records. The drought of 1785 and 1970 was also noted in Standardized Precipitation Index (SPI) reconstruction from Kishtwar, Jammu & Kashmir based on the Himalayan cedar (Singh et al., 2017) and it has been found that in the past 275 years, 1785 is the driest year (SPI −2.3) followed by 1971 (SPI −2.2) and 1970 (SPI −2.1). Both studies from two different regions also suggest the intensity of drought which is consistent from Lahaul, Himachal Pradesh to Kishtwar, Jammu & Kashmir. Low precipitation in 2008 and 1809 in the reconstruction was common with November to april snow water equivalent (SWE) reconstruction from Lahaul–Spiti, Himachal Pradesh (Yadav and Bhutiyani, 2013). Along with very low precipitation in the above mentioned years, some individual high precipitation years such as 1756 and 1730 were also noted in SWE reconstruction, developed from Himalayan cedar tree-ring chronologies, which is similar to the present reconstruction showing high precipitation for the

Lahaul Himalaya. Continuous low precipitation in two consecutive years revealed that 1731–1732 (214 mm) received lowest precipitation and 1734–1735 (866 mm) highest precipitation. Other biennial low and high precipitation years are 1970–1971, 1732–1733, 1784–1785, and 1758–1759, 1958–1959, 1790–1791, respectively. The drought of 1970–1971 was observed from different parts of western Himalaya such as from cold-arid Lahaul–Spiti, Himachal Pradesh (Yadav and Bhutiyani, 2013), Kumaun Himalaya (Yadav et al., 2015), Kinnaur, Himachal Pradesh (Yadava et al., 2016) and Kishtwar, Jammu & Kashmir (Singh et al., 2017; Yadav et al., 2017). Spatially such high-intensity drought which has a huge regional impact could be a cause of severe miseries for the socio-economic lives if happens again in the future. 1780–1781 and 2000–2001 drought was also consistent with earlier recorded low precipitation from Lahaul- Spiti, Himachal Pradesh (Yadav and Bhutiyani, 2013). Extreme individual and biennial years correlation with other existing hydrological records from the western Himalaya show utility and reliability of our present precipitation reconstruction. To understand the range of low/high precipitation in the longer timescale we used the non-overlapping mean of reconstructed data. 3-years non-overlapping mean indicated low precipitation in the years 1784–1786, 1970–1972, 1883–1885 and high precipitation in 1733–1735, 1757–1759, 1994–1996. The lowest precipitation of 1784–1786 was consistent with the Kumaun Himalayan drought obtained from 5 years (1782–1786) mean of SPI reconstruction (Yadav et al., 2015) and Kishtwar, Jammu & Kashmir drought (1784–1788) reconstruction (Singh et al., 2017) which indicate high resemblance in hydrological records from different regions of the western Himalaya.

The low precipitation recorded during the period 1784–1786 also coincided with the Laki volcanic event that occurred in Iceland in 1783. The Laki volcanic eruption in 1783 continued over 8 months and is considered the second largest volcano for producing pyroclastic flow. This eruption supplied a huge amount of aerosols to the atmosphere which created a thick blanket over the northern hemispheric troposphere/stratosphere for more than 5 months and changed the climatic thermal balance for the region (Thordarson and Self, 2003). We believe that the Laki volcanic eruption may be the cause behind such low precipitation between 1783 and 1786 over the western Himalayan region. The western Himalaya receives its largest part of the annual precipitation through westerlies carried moisture from the Atlantic Ocean and Mediterranean Sea. The changes associated with the volcanic events in the northern hemisphere or over Iceland could interrupt the normal atmospheric process/cycle of precipitation by changing the climatic thermal equation. Because of the proximal distance of Iceland to the Atlantic Ocean and Mediterranean Sea, the aerosols and pyroclastic materials produced through volcanoes can strongly disturb the pattern and impact of westerlies and thus precipitation and temperature over Himalaya. Similar to the precipitation, the impression of the Laki volcanic eruption is also marked in the tree-ring-based summer temperature record from Bhutan Himalaya (Krusic et al., 2015). Interestingly, 3-years non-overlapping means indicating low precipitation event from 1815 to 1817 coincided with another volcanic eruption which is Tambora volcano, which erupted in 1815. Tambora volcanic eruption is the largest recorded eruption (Stothers, 1984) which is mainly responsible for the huge destruction and unusual global cooling (Self et al., 2004). Signatures of Tambora volcanic eruption in the form of drought in the year 1816 was also recorded from the Kumaun Himalaya (Yadav et al., 2015) and the semi-arid region of Kinnaur Himalaya (Yadav, 2013). Whereas in Chinese history "Jiaqing famine" is one of the most severe famines that took place in the same period 1815–1817, associated with unusual cooling due to the Tambora volcanic eruption (Gao et al., 2017). Clues about droughts or famines associated with volcanic events offer a fascinating approach toward the understanding of long-term climatic changes and high-resolution tree-ring data from the moisture-stressed sites could provide vital tools to understand the nature of such past events. However, robust data would be required to precisely address the past volcanic episodes and their impact on the climate and societies in long-term perspective.

The reconstruction further revealed low and high episodes of precipitation for the Lahaul region with 5 and 10-years non-overlapping mean of precipitation reconstruction (**Table 3**). 1780–1789, 2000–2009, 1910–1919 are the driest decades with low precipitation in the reconstruction whereas, 1950–1959, 1770–1779, 1990–1999 are the pluvial decades. These high and low precipitation years were also consistent with exiting hydrological records from western Himalaya, India (Yadav and Bhutyani, 2013; Yadava et al., 2016; Singh et al., 2017). 50-years non-overlapping mean suggest that mid-twentieth (1930–1979) and mid-eighteenth (1730–1779) centuries were associated with pluvial phases with some annual droughts, while droughts due to low precipitation were recorded in the late 18th to early 19th century (1780–1829) and late 19th to early 20th (1880–1929) century with some individual wet years in the reconstruction.

We have also compared the present Himalayan blue pine based precipitation reconstruction (pDcJuly) with previous year August to current year July (pAcJuly) precipitation record of the Lahaul–Spiti region (Yadav, 2011b) to understand the consistency in two distinct precipitation records from the same region with different tree species. The earlier pAcJuly precipitation record was developed using Himalayan cedar samples and in the present study, we have used the Himalayan blue pine to develop the climatic record. The present precipitation record revealed significant correlation ($r = 0.49$, $p < 0.0001$, AD 1730–2008) and strong year-to-year consistency with the pAcJuly precipitation record based on the Himalayan cedar (**Figure 7**). Such a strong resemblance among both the records support the utility and strength of present precipitation reconstruction and advocate the sensitivity of Himalayan blue pine to develop hydroclimatic records from the high-altitudinal semi-arid region of Lahaul–Spiti to understand the long-term regional and global climatic significance.

We have also performed cross-field spatial correlation, using KNMI climate explorer, between reconstructed pDcJuly precipitation and gridded precipitation data CRU TS 4.04 (http://climexp.knmi.nl; Oldenborgh and Burgers, 2005) for the period 1970–2015 and significant positive correlation for the westerly dominated regions was observed for the previous year December to current year July (**Figure 8**). Negative correlations for the ISM dominated region of eastern Himalaya were also noteworthy in the gridded spatial correlation and indicate the

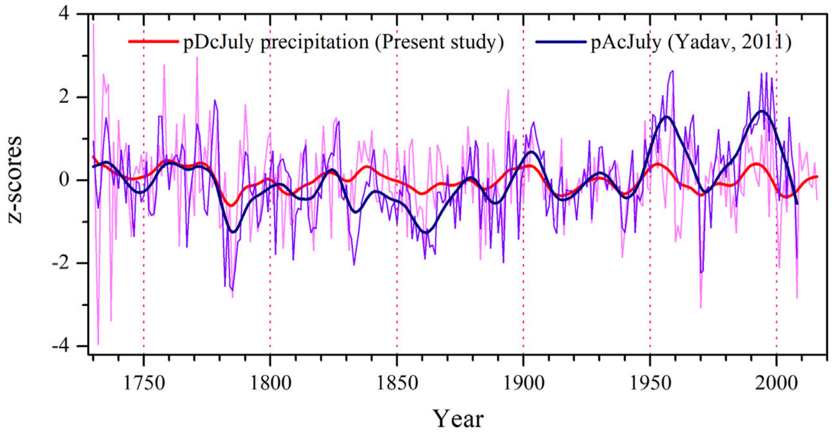

FIGURE 7 | Present pDcJuly precipitation based on Himalayan blue pine and pAcJuly precipitation reconstruction (Yadav, 2011b) developed using Himalayan cedar plotted together to show the consistency among them. The thick smoothed line over the reconstruction is 20-years low pass filter.

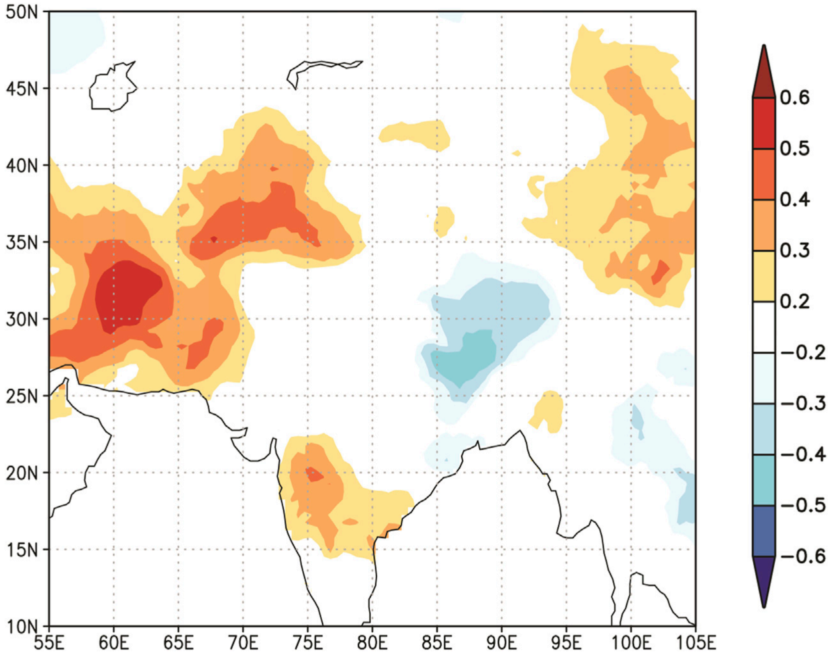

FIGURE 8 | Spatial correlation between gridded data available in http://climexp.knmi.nl (Oldenborgh and Burgers, 2005) and pDcJuly precipitation reconstruction for the period 1970–2015.

opposite relationship for two distinct precipitation regimes. We believe that a network of long and homogenous annually resolved moisture-sensitive Himalayan blue pine tree-ring data from the orography controlled western Himalaya will be very helpful in the future to understand such high variability in the climatic parameters.

Socioeconomic Implication

In the monsoon shadow zone of western Himalaya variability in winter or westerly influenced precipitation controls the agriculture-based production. In the absence of proper network of canals or other irrigation facilities in terraced farms over the hills of Lahaul Himalaya, winter precipitation becomes the only source to supply necessary moisture to the crops. To explore the socioeconomic implication, agricultural crop production relationship with the reconstructed precipitation data were analyzed. Wheat and barley data available for a limited period from 1987 to 2001 (Department of Agriculture, Himachal Pradesh) was correlated with reconstructed precipitation for the Lahaul–Spiti region

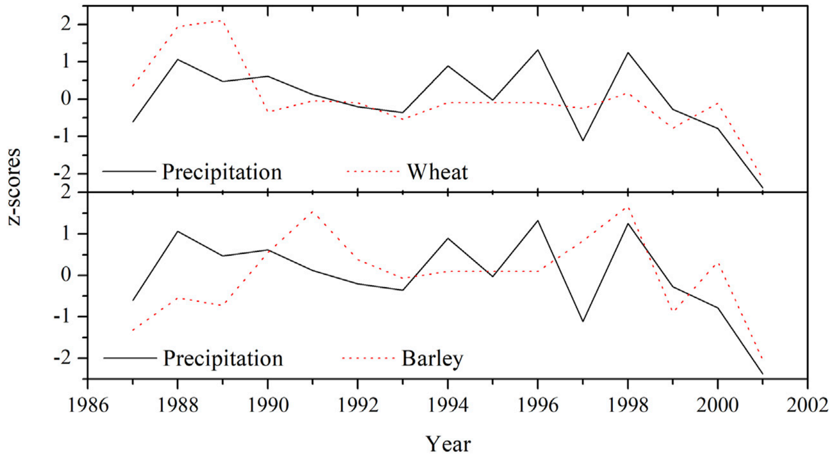

FIGURE 9 | pDcJuly Precipitation reconstruction and wheat-barley productivity from 1987 to 2001 of Lahaul–Spiti plotted together, the data were normalized with respect to mean and standard deviation for the period (1987–2001).

(**Figure 1**). The agriculture data of wheat and barley showed that in 2001 crop production was very low along with low precipitation in the same year. Due to the widespread drought over southwest central Asia in 1999–2000 decline of agriculture-based production was reported from the Lahaul region (DOA, 2009). 1987, 1993 and 2001 years recorded as dry years in Himachal Pradesh (Ray and Shewale, 2001; Chandel and Brar, 2013) and comparable with the reconstructed data which also showed low precipitation, due to which agricultural production decreased and are consistent with the present reconstruction. Crop production of wheat and barley was comparatively good during the year 1988 which is recorded a drought-free year (Ray and Shewale, 2001). Pearson correlation among reconstructed precipitation and crop production data for the period of 1987–2001 were positive. Wheat and barley data with the reconstruction showed 0.60 ($p = 0.01$, 1987–2001) and 0.47 ($p = 0.07$, 1987–2001) correlations, respectively (**Figure 9**). Such a good consistency between precipitation and crop productivity shows the strength of tree-ring based precipitation reconstruction to understand the relationship between climate and crop productivity.

CONCLUSIONS

The present study is the maiden attempt to develop tree-ring based climate reconstruction using tree-ring samples of Himalayan blue pine (*P. wallichiana*) from Shaligram, cold arid Lahaul, Himachal Pradesh. A 439-years long Himalayan blue pine chronology was developed extending back to AD 1578 and showed strong correlation with monthly climate variables. The ring-width chronology of Himalayan blue pine showed positive correlation with precipitation and negative correlation with temperature. It has been observed that the precipitation from the previous year December to current year July (pDcJuly) is directly associated with tree growth, whereas the temperature of May to July has negative effect on the radial tree-growth. Based on strong and significant correlation between pDcJuly precipitation and ring-width chronology, precipitation reconstruction was developed back to AD 1730. The reconstruction explains the 50% variance of the instrumental data over the period from 1933 to 1970. The 287-years precipitation reconstruction indicates year-to-year and decadal-scale variability in the entire reconstruction. The reconstruction revealed low precipitation in the year 1732, 1737, 1970, 2008, 1785 and high precipitation in 1730, 1771, 1758, 1734 and 1736. We also analyzed decades of low and high precipitation with the help of non-overlapping mean of the precipitation series, which showed the period of 1780–1789, 2000–2009 received low and 1950–1959, 1770–1779 high precipitation in the reconstruction. We identified the signature of Tambora and Laki volcanic eruptions induced low precipitation or drought in the reconstructed precipitation during 1815–1817 and 1783–1786, respectively. The spatial correlation between reconstructed precipitation and gridded precipitation data revealed significant correlation for the western Himalayan region. The reconstructed precipitation also showed good correlation with wheat and barley crop production data of Lahaul–Spiti, Himachal Pradesh. Good consistency among Himalayan blue pine induced precipitation reconstruction with earlier hydrological reconstruction from the western Himalaya showed its utility and reliability among other tree species. The large network of high-resolution Himalayan blue pine chronologies with large number of sample replication from the cold-arid Lahaul Himalaya could be very helpful to understand the utility of this species to develop the climatic records as well as its socioeconomic implications over the region in future.

DATA AVAILABILITY STATEMENT

The data supporting the conclusions of this article will be made available by the authors, without undue reservation.

AUTHOR CONTRIBUTIONS

KM and VS drafted the manuscript. KM, VS, and AY collected and cross dated the tee-ring samples. KM, VS, AY, SM, RM and SV evaluated the results. SM arranged the crop productivity data. All authors provided comments to improve the manuscript.

FUNDING

The research is partially supported by the Science and Engineering Research Board, New Delhi (SB/DGH-76/2013).

ACKNOWLEDGMENTS

We sincerely acknowledge Dr. Vandana Prasad, Director, Birbal Sahni Institute of Palaeosciences Lucknow for providing all the necessary facilities, support and permission to publish this work. We also thank the Department of Forest, Government of Himachal Pradesh, India for all necessary help and logistic support during the collection of tree-ring samples and India meteorological department (IMD) for providing climate data. KGM and VS are thankful to the SERB-DST, New Delhi for providing financial assistance (SB/DGH-76/2013). We sincerely thanks to both the reviewers for constructive suggestions which greatly improved the earlier version of the manuscript.

REFERENCES

Bajpai, S. C. (2002). *Lahaul–Spiti: A Forbidden Land in the Himalayas*. fourth edition. London: Indus Publishing Company.

Biondi, F., and Waikul, K. (2004). DENDROCLIM2002: a C++ Program for Statistical Calibration of Climate Signals in Tree-Ring Chronologies. *Comput. Geosci.* 30, 303–311. doi:10.1016/j.cageo.2003.11.004

Chandel, V. B. S., and Brar, K. K. (2013). Drought in Himachal Pradesh, India: A Historical-Geographical Perspective, 1901–2009. *Trans. Inst. Indian Geogr.* 35 (2), 259–273. doi:10.17501/icfow.2018.1102

Cook, E. R. (1985). A Time Series Analysis Approach to Tree-Ring Standardization. Ph.D. thesis. Tucson, Arizona, USA: University of Arizona.

Cook, E. R., Anchukaitis, K. J., Buckley, B. M., D'Arrigo, R. D., Jacoby, G. C., and Wright, W. E. (2010). Asian Monsoon Failure and Megadrought during the Last Millennium. *Science* 328, 486–489. doi:10.1126/science.1185188

Cook, E. R., Krusic, P. J., and Jones, P. D. (2003). Dendroclimatic Signals in Long Tree-Ring Chronologies from the Himalayas of Nepal. *Int. J. Climatol.* 23, 707–732. doi:10.1002/joc.911

Cook, E. R., Meko, D. M., Stahle, D. W., and Cleaveland, M. K. (1999). Drought Reconstructions for the Continental United States*. *J. Clim.* 12, 1145–1162. doi:10.1175/1520-0442

Cook, E. R., and Peters, K. (1997). Calculating Unbiased Tree-Ring Indices for the Study of Climatic and Environmental Change. *The Holocene* 7, 361–370. doi:10.1177/095968369700700314

Dahe, Q., Mayewski, P. A., Wake, C. P., Shichang, K., Jiawen, R., Shugui, H., et al. (2000). Evidence for Recent Climate Change from Ice Cores in the central Himalaya. *Ann. Glaciol.*, 31 153–158. doi:10.3189/172756400781819789

DOA (2009). *District Agriculture Plan: Lahaul–Spiti, H.P.* Department of Agriculture, Himachal Pradesh, 103.

Dubey, B., Yadav, R. R., Singh, J., and Chaturvedi, R. (2003). Upward Shift of Himalayan pine in Western Himalaya, India. *Curr. Sci.* 85 (8), 25. doi:10.1016/j.quaint.2016.07.032

Fritts, H. C. (1976). *Tree-rings and Climate*. London: Academic Press.

Gao, C., Gao, Y., Zhang, Q., and Shi, C. (2017). Climatic Aftermath of the 1815 Tambora Eruption in China. *J. Meteorol. Res.* 31, 28–38. doi:10.1007/s13351-017-6091-9

Holmes, R. L. (1983). Computer-assisted Quality Control in Tree-Ring Dating and Measurement. *Tree-ring Res.* 43, 69–78. doi:10.4324/9781315748689-14

IPCC (2013). *Climate Change 2013: The Physical Science Basis. Contribution of Working Group I to the Fifth Assessment Report of the Intergovernmental Panel on Climate Change. Summary for Policymakers*. London: Academic Press.

Joshi, L. M., Kotlia, B. S. Ahmad, S. M. Wu, C. C. Sanwal, J. Raja, M., et al. (2017). *Reconstruction of Indian Monsoon Precipitation Variability between 4.0 and 1.6 Ka BP Using Speleothem* $\delta^{18}0$ *Records from the central Lesser Himalaya*. India: Saudi Society for Geoscience.

Krusic, P. J., Cook, E. R., Dukpa, D., Putnam, A. E., Rupper, S., and Schaefer, J. (2015). Six Hundred Thirty-Eight Years of Summer Temperature Variability over the Bhutanese Himalaya. *Geophys. Res. Lett.* 42, 2988–2994. doi:10.1002/2015gl063566

Kumar, P., Dimri, A. P., and Tandon, S. K. (2021). Modeling of Indian Monsoon Extremes during 850-2000AD Using the Proxy-Data from Speleothems. *Quat. Int.* 12, 33. doi:10.1016/j.quaint.2021.02.009

Michaelsen, J. (1987). Cross-Validation in Statistical Climate Forecast Models. *J. Clim. Appl. Meteorol.* 26, 1589–1600. doi:10.1175/1520-0450(1987)026<1589:cviscf>2.0.co;2

Misra, K. G., Singh, V., Yadava, A. K., Misra, S., and Yadav, R. R. (2020). Treeline Migration and Settlement Recorded by Himalayan Pencil Cedar Tree-Rings in the Highest alpine Zone of Western Himalaya, India. *Curr. Sci.* 118, 192–195. doi:10.1016/j.quaint.2015.01.015

Oldenborgh, G. J., and Burgers, G. (2005). Searching for Decadal Variations in ENSO Precipitation Teleconnections. *Geophys. Res. Lett.* 32, L15701. doi:10.1029/2005GL023110

Osborn, T. J., Biffa, K. R., and Jones, P. D. (1997). Adjusting Variance for Sample-Size in Tree-Ring Chronologies and Other Regional-Mean Timeseries. *Dendrochronologia* 15, 89–99.

Overpeck, J., Liu, K. B., Morrill, C., Cole, J., Shen, C., Anderson, D., et al. (2005). Holocene Environmental Change in the Himalayan-Tibetan Plateau Region: Lake Sediments and the Future. *Glob. Chan Mount Reg.* 13, 83–92. doi:10.1007/1-4020-3508-x_9

Phartiyal, B., Singh, R., Joshi, P., and Nag, D. (2020). Late-Holocene Climatic Record from a Glacial lake in Ladakh Range, Trans-himalaya, India. *The Holocene* 30, 1029–1042. doi:10.1177/0959683620908660

Ray, K. C. S., and Shewale, M. P. (2001). Probability of Occurrence of Drought in Various Sub-divisions of India. *Mausam* 52, 541–546. doi:10.31142/ijtsrd19177

Rinn, F. (2003). *TSAP-win Time Series Analysis and Presentation for Dendrochronology and Related Applications, Version 0.53 for Microsoft Windows*. Heidelberg, Germany: Rinn Tech.

Roxy, M. K., Ritika, K., Terray, P., Murtugudde, R., Ashok, K., and Goswami, B. N. (2015). Drying of Indian Subcontinent by Rapid Indian Ocean Warming and a Weakening Land-Sea thermal Gradient. *Nat. Commun.* 6, 7423. doi:10.1038/ncomms8423

Sahni, K. C. (1990). *Gymnosperms of India and Adjacent Countries*. India: Shiva offset press Dehradun.

Self, S., Gertisser, R., Thordarson, T., Rampino, M. R., and Wolff, J. A. (2004). Magma Volume, Volatile Emissions, and Stratospheric Aerosols from the 1815 Eruption of Tambora. *Geophys. Res. Lett.* 31, L20608. doi:10.1029/2004gl020925

Shah, S. K., Pandey, U., Mehrotra, N., Wiles, G. C., and Chandra, R. (2019). A winter Temperature Reconstruction for the Lidder Valley, Kashmir, Northwest Himalaya Based on Tree-Rings of *Pinus Wallichiana*. *Clim. Dyn.* 53 (7-8), 4059–4075. doi:10.1007/s00382-019-04773-6

Singh, J., Park, W.-K., and Yadav, R. R. (2006). Tree-ring-based Hydrological Records for Western Himalaya, India, since a.D. 1560. *Clim. Dyn.* 26, 295–303. doi:10.1007/s00382-005-0089-1

Singh, J., and Yadav, R. R. (2005). Spring Precipitation Variations over the Western Himalaya, India, since A.D. 1731 as Deduced from Tree Rings. *J. Geophys. Res.* 110, D01110. doi:10.1029/2004JD004855

Singh, J., and Yadav, R. R. (2000). Tree-ring Indications of Recent Glacier Fluctuations in Gangotri, Western Himalaya, India. *Curr. Sci.* 79 (11), 1598–1601. doi:10.1016/j.dendro.2008.09.002

Singh, J., Yadav, R. R., and Wilmking, M. (2009). A 694-year Tree-Ring Based Rainfall Reconstruction from Himachal Pradesh, India. *Clim. Dyn.* 33, 1149–1158. doi:10.1007/s00382-009-0528-5

Singh, V., Yadav, R. R., Gupta, A. K., Kotlia, B. S., Singh, J., Yadava, A. K., et al. (2017). Tree Ring Drought Records from Kishtwar, Jammu and Kashmir, Northwest Himalaya, India. *Quat. Int.* 444, 53–64. doi:10.1016/j.quaint.2016.09.031

Stokes, M. A., and Smiley, T. L. (1968). *An Introduction to Tree-Ring Dating*. Chicago: University of Chicago Press.

Stothers, R. B. (1984). The Great Tambora Eruption in 1815 and its Aftermath. *Science* 224, 4654. doi:10.1126/science.224.4654.1191

Thordarson, T., and Self, S. (2003). Atmospheric and Environmental Effects of the 1783-1784 Laki Eruption: A Review and Reassessment. *J. Geophys. Res.* 108 (D1), 4011. doi:10.1029/2001JD002042

Treydte, K. S., Schleser, G. H., Helle, G., Frank, D. C., Winiger, M., Haug, G. H., et al. (2006). The Twentieth century Was the Wettest Period in Northern Pakistan over the Past Millennium. *Nature* 440, 1179–1182. doi:10.1038/nature04743

Wigley, T. M. L., Briffa, K. R., and Jones, P. D. (1984). On the Average Value of Correlated Time Series, with Applications in Dendroclimatology and Hydrometeorology. *J. Clim. Appl. Meteorol.* 23, 201–213. doi:10.1175/1520-0450(1984)023<0201:otavoc>2.0.co;2

Yadav, R. R. (2012). Over Two Millennia Long Ring-Width Chronology of Himalayan Pencil Cedar from Western Himalaya, India. *Curr. Sci.* 103, 1279–1280. doi:10.1007/bf02702206

Yadav, R. R. (2011b). Tree Ring Evidence of a 20th-century Precipitation Surge in the Monsoon Shadow Zone of the Western Himalaya, India. *J. Geophys. Res. Atmos.* 116 (DO2112). doi:10.1029/2010jd014647

Yadav, R. R., and Bhutiyani, M. R. (2013). Tree-ring-based Snowfall Record for Cold Arid Western Himalaya, India since A.D. 1460. *J. Geophys. Res. Atmos.* 118, 7516–7522. doi:10.1002/jgrd.50583

Yadav, R. R., Gupta, A. K., Kotlia, B. S., Singh, V., Misra, K. G., Yadava, A. K., et al. (2017). Recent Wetting and Glacier Expansion in the Northwest Himalaya and Karakoram. *Sci. Rep.* 7 (1), 1–8. doi:10.1038/s41598-017-06388-5

Yadav, R. R. (2011a). Long-term Hydroclimatic Variability in Monsoon Shadow Zone of Western Himalaya, India. *Clim. Dyn.* 36, 1453–1462. doi:10.1007/s00382-010-0800-8

Yadav, R. R., Misra, K. G., Yadava, A. K., Kotlia, B. S., and Misra, S. (2015). Tree-ring Footprints of Drought Variability in Last ~300 Years over Kumaun Himalaya, India and its Relationship with Crop Productivity. *Quat. Sci. Rev.* 117, 113–123. doi:10.1016/j.quascirev.2015.04.003

Yadav, R. R., Park, W-K., Singh, J., and Dubey, B. (2004). Do the Western Himalayas Defy Global Warming? *Geophys. Res. Lett.* 31, 12–18. doi:10.1029/2004GL020201

Yadav, R. R., Park, W.-K., and Bhattacharyya, A. (1997). Dendroclimatic Reconstruction of April-May Temperature Fluctuations in the Western Himalaya of India since A.D. 1698. *Quat. Res.* 48, 187–191. doi:10.1006/qres.1997.1919

Yadav, R. R., and Park, W.-K. (2000). Precipitation Reconstruction Using Ring-Width Chronology of Himalayan Cedar from Western Himalaya: Preliminary Results. *J. Earth Syst. Sci.* 109 (3), 339–345. doi:10.1007/bf02702206

Yadav, R. R., Singh, J., Dubey, B., and Mishra, K. G. (2006). A 1584-year Ring Width Chronology of Juniper from Lahul, Himachal Pradesh: Prospects of Developing Millennia Long Climate Records. *Curr. Sci.* 90, 1122–1126. doi:10.1007/bf02702206

Yadav, R. R. (2013). Tree Ring-Based Seven-century Drought Records for the Western Himalaya, India. *J. Geophys. Res. Atmos.* 118, 4318–4325. doi:10.1029/2012JD01866110.1002/jgrd.50265

Yadava, A. K., Bräuning, A., Singh, J., and Yadav, R. R. (2016). Boreal spring Precipitation Variability in the Cold Arid Western Himalaya during the Last Millennium, Regional Linkages, and Socio-Economic Implications. *Quat. Sci. Rev.* 144, 28–43. doi:10.1016/j.quascirev.2016.05.008

Yadava, A. K., Sharma, Y. K., Dubey, B., Singh, J., Singh, V., Bhutiyani, M. R., et al. (2017). Altitudinal Treeline Dynamics of Himalayan pine in Western Himalaya, India. *Quat. Int.* 444, 44–52. doi:10.1016/j.quaint.2016.07.032

Conflict of Interest: The authors declare that the research was conducted in the absence of any commercial or financial relationships that could be construed as a potential conflict of interest.

The handling editor declared a past co-authorship with one of the authors KM.

frontiers
in Earth Science

ORIGINAL RESEARCH
published: 04 June 2021
doi: 10.3389/feart.2021.656281

Holocene Lake Evolution and Glacial Fluctuations Indicated by Carbonate Minerals and Their Isotopic Compositions in the Sediments of a Glacial Melt Recharge Lake on the Northwestern Tibetan Plateau

***Minghui Li*[1,2], *Liping Zhu*[1,2,3]*, *Junbo Wang*[1,2], *Jianting Ju*[1], *Chong Liu*[1,3], *Qingfeng Ma*[1], *Teng Xu*[1,3], *Baojin Qiao*[4] and *Xiaoxiao Wang*[1,3]**

[1]Key Laboratory of Tibetan Environment Changes and Land Surface Processes, Institute of Tibetan Plateau Research, Chinese Academy of Sciences, Beijing, China, [2]CAS Center for Excellence in Tibetan Plateau Earth Sciences, Beijing, China, [3]University of Chinese Academy of Sciences, Beijing, China, [4]School of Geosciences and Technology, Zhengzhou University, Zhengzhou, China

Lakes and glaciers are widely distributed on the Tibetan Plateau and are linked via hydrological processes. They are experiencing rapid changes due to global warming, but their relationships during the Holocene are less well known due to limited coupled geological records. Here, we analyzed the $\delta^{13}C_{\text{-VPDB}}$ and $\delta^{18}O_{\text{-VPDB}}$ values and ion content of calcite and aragonite in a 407-cm-long sediment core from Guozha Co, a closed basin on the northwestern Tibetan Plateau supplied by glacial meltwater, in order to understand how the lake responded to glacier changes during the Holocene. Our results indicate that the glacial meltwater lowered the lake's temperature and the $\delta^{18}O_{\text{lake water}}$ and $\delta^{18}O_{\text{endogenic + authigenic carbonate}}$ values and diluted the ion concentrations in the lake water. Three stages of evolution, 8.7–4.0, 4.0–1.5, and 1.5 kyr BP to present, are distinguished based on the decrease in glacial meltwater recharge. Guozha Co has been a closed basin since at least 8.7 kyr BP, and it has changed from a fresh water lake during 8.7–1.5 kyr BP to a brackish lake from 1.5 kyr BP to present due to several climate events. The famous 4.2 kyr BP cold event was identified in the core at 4.0 kyr BP, while warm events occurred at 6.2, 3.9, 2.2, 0.9, and 0.4 kyr BP. Both glaciers and lakes in this area are controlled by climate, but they exhibit opposite changes, that is, glaciers retreat and lakes expand, and vice versa. Our results provide an accurate interpretation of the cold events based on carbonate minerals and carbon–oxygen isotopes in glacial meltwater–recharged lake sediments.

Keywords: carbonate minerals, oxygen and carbon isotopes, lake water temperature, glacial fluctuations, climatic events

OPEN ACCESS

Edited by:
Praveen K. Mishra,
Wadia Institute of Himalayan Geology,
India

Reviewed by:
Som Dutt,
Wadia Institute of Himalayan Geology,
India
Sayak Basu,
Indian Institute of Science Education
and Research Mohali, India

****Correspondence:***
Liping Zhu
lpzhu@itpcas.ac.cn

Specialty section:
This article was submitted to
Quaternary Science, Geomorphology
and Paleoenvironment,
a section of the journal
Frontiers in Earth Science

Received: *20 January 2021*
Accepted: *10 May 2021*
Published: *04 June 2021*

Citation:
Li M, Zhu L, Wang J, Ju J, Liu C, Ma Q,
Xu T, Qiao B and Wang X (2021)
Holocene Lake Evolution and Glacial
Fluctuations Indicated by Carbonate
Minerals and Their Isotopic
Compositions in the Sediments of a
Glacial Melt Recharge Lake on the
Northwestern Tibetan Plateau.
Front. Earth Sci. 9:656281.
doi: 10.3389/feart.2021.656281

HIGHLIGHTS

- Guozha Co has been a closed basin since at least 8.7 kyr BP, based on the high correlation coefficient noted between $\delta^{13}C_{\text{-VPDB}}$ and $\delta^{18}O_{\text{-VPDB}}$ for calcite.
- Climatic change is reflected in the influence of glacial meltwater on the lake water temperature and the oxygen isotopic values.
- Three stages (8.7–4.0, 4.0–1.5, and 1.5 kyr BP to present) can be distinguished based on the decrease in glacial meltwater recharge.
- The lake changed from a fresh lake during 8.7–1.5 kyr BP to a brackish lake from 1.5 kyr BP to present.

INTRODUCTION

Lakes and glaciers are widely distributed on the Tibetan Plateau (TP) (Yao et al., 2019), which is particularly sensitive to climatic changes and is currently experiencing significant warming (Chen et al., 2015). With climate warming, numerous glaciers on the TP are shrinking. These shrinkages have different temporal–spatial features (Yao et al., 2012) and make different contributions to lake expansions (Yang et al., 2017). On the northwestern TP, which is an extremely cold and dry area of the Eurasian continent (Zheng, 1996), the maintenance or expansion of lakes is mainly supported by glacial meltwater under conditions of severely low precipitation (e.g., 61.6 mm/yr) and when there are huge differences between precipitation and evaporation (e.g., 1,361 mm/yr) (Qiao and Zhu, 2019). However, several studies have reported that the glaciers on the northwestern TP are relatively stable, even perform advancing. This so-called Karakoram anomaly (Bolch et al., 2012; Kääb et al., 2012) is contradictory to the expansion of lakes in this area that have mainly been supplied by glacial meltwater in the recent years. Present-day lake water balance studies are important because they reveal the essential relationships between glaciers and lakes. Proxies in ice cores provide detailed climatic records for long geological periods (Thompson, 2000), but they contain less direct indicators of the glacier movement. Moraines are direct relics of glacial movement (Owen and Dortch, 2014), but due to their discontinuities and reformation following their deposition, continuous glacial movements are not well recorded (Xu and Yi, 2017).

The $\delta^{18}O$ and $\delta^{13}C$ values for aragonite and calcite (if autogenous) in lacustrine sediments are controlled by the isotopic composition and temperature of the lake water (Leng and Marshall, 2004; Horton et al., 2016). Thus, calcite and aragonite and their isotopic compositions ($\delta^{18}O$ and $\delta^{13}C$) in lake sediments are widely used to investigate past changes in temperature and the $\delta^{18}O$ of lake water, as well as the paleoenvironmental and paleoclimatic changes (Talbot, 1990; Leng and Marshall, 2004; Henderson et al., 2010; Deocampo and Tactikos, 2010; Hren and Sheldon, 2012; Bernasconi and McKenzie, 2013; Wang et al., 2013; He et al., 2016; and references therein). These proxies may indicate the degree of closure of a lake and may contain signals of glacial meltwater linked with glacier movement. In order to understand how a lake responded to glacier changes, we used a 407-cm-long sediment core to examine the relationship between the glaciers and lake changes. The core was drilled at Guozha Co on the northwestern TP, which is directly supplied by glacial meltwater from the Western Kunlun Mountains.

STUDY AREA

Guozha Co is a semi-closed lake located on the southern slope of the West Kunlun Mountains (**Figures 1A,B**). The lake is surrounded by bedrock slopes with undeveloped lake shore terraces (Li et al., 1991). The bedrock of the lake basin is primarily composed of clastic, metamorphic, and igneous rocks, mainly consisting of conglomerate, sandstone, siltstone, mudstone, limestone, shale, pyroclastic rock, granite, gneiss, diabase, and ophiolite (Bureau of Geology and Mineral resources of Xizang Autonomous Regions, 1993). The lake has an area of 248 km^2 with a maximum depth of 149.5 m and situated at an altitude of 5,080 m above sea level (asl) (Qiao et al., 2017). There are 62 glaciers in the catchment with a total glacier area of 544 km^2 (Li et al., 1993), the meltwater of these glaciers contributed the local hydrology of the lake. When the lake level is high, the lake water flows into Aksai Chin Lake via a channel in the western section (**Figure 1**). As the fresh glacial meltwater enters the lake through rivers in the east and north sections, the present lake's salinity exhibits spatial differences (**Figure 1C**; **Table 1**). Due to the high altitude, the lake region is characterized by cold and thin air with strong solar radiation and large temperature differences (Li et al., 1991; Yao et al., 2013). According to the China Meteorological Forcing Dataset, the mean annual precipitation and mean annual temperature were 90 mm and −12.9°C, respectively, from 1979 to 2013 (Qiao et al., 2017). The observed temperature of the surface water was 4.17°C in September 2015. Due to the low temperature and low amount of precipitation, the lake basin only contains sparsely distributed desert vegetation.

MATERIALS AND METHODS

Li et al. (2021) used the $\delta^{18}O_{\text{carbonate}}$ data from another core (GZHC 2014-1, 304.5-cm long) to quantitatively estimate the Holocene variations in the glacier meltwater in Guozha Co, but they did not discuss the influences of glacial meltwater on the chemical characteristics of the lake water and mineral precipitation in the lake. In addition, core GZHC 2014-1 was collected from a steep underwater slope in the southwestern part of the lake where the lake water is less influenced by the glacial meltwater (**Figure 1C**), and the sediments (including carbonate) are largely controlled by terrestrial debris input.

To more extensively determine the glacial meltwater's influence, using the core sediment and proxy data (carbonate minerals, $\delta^{18}O$ and $\delta^{13}C$, and geochemical characteristics of carbonates), this study is focusing on the evolution of the lake's status and the impact of glacial fluctuation on Guozha Co lake. In 2015, a 407-cm-long sediment core (GZLC15-1, 35°01′8.18″ N, 81°03′37.25″ E; 5,080 m asl; **Figure 1**) was retrieved from the center of Guozha Co using a piston corer.

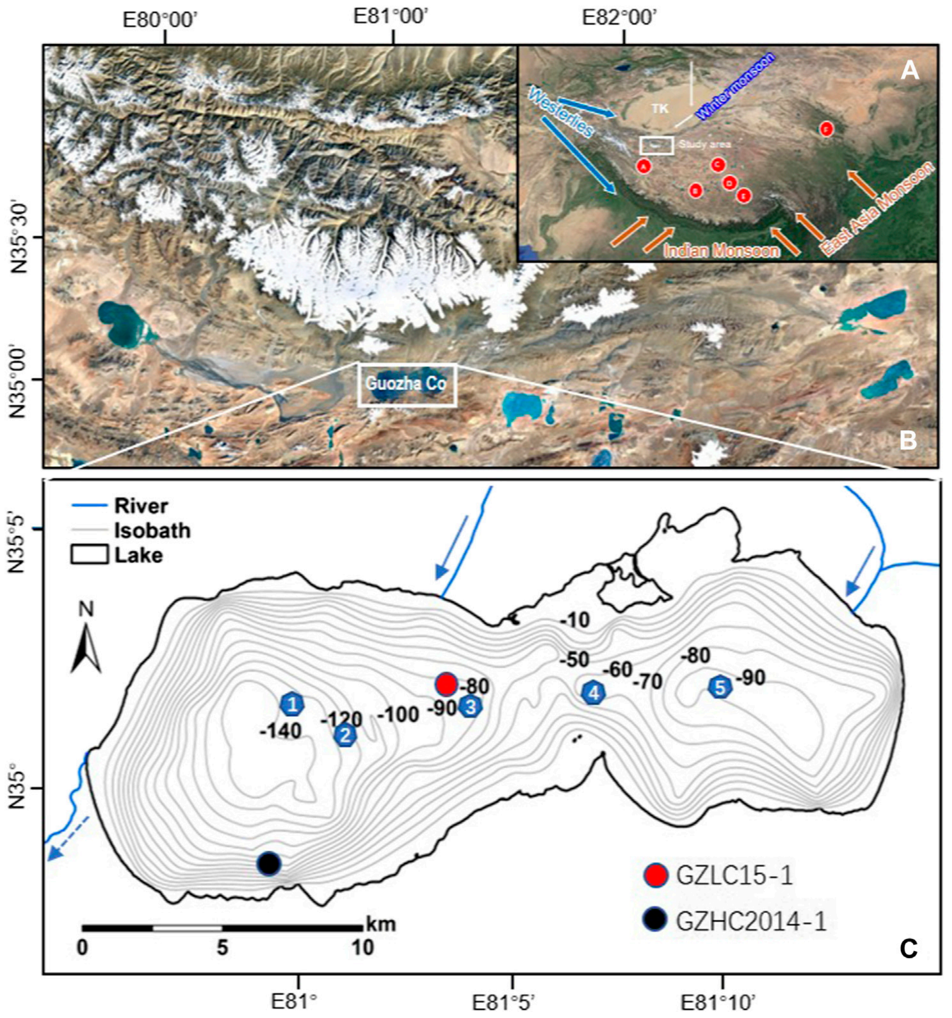

FIGURE 1 | **(A)** Location of Guozha Co and the other lakes referred to in this study. TK-Taklimakan Desert. A: Bangong Co; B: Taruo Co; C: Buro Co; D: Lingge Co; E: Selin Co; F: Qinghai Lake; **(B)** Relative positions between Guozha Co and glacier; **(C)** Isobath map showing sampling sites of surface lake water(blue number), the cores GZLC15-1, this study and the core GZHC2014-1 by Li et al. (2021).

TABLE 1 | Salinity, pH, ion concentrations (ppm), and temperature (°C) of Guozha Co water

Location	pH	Salinity (g/L)	CO_3^{2-}	HCO_3^-	Cl^-	SO_4^{2-}	Ca^{2+}	Mg^{2+}	K^+	Na^+	Mg/Ca (molar)	Temperature (°C)	References
Center	8.29	3.83	92.26	860	1,348	221	2.57	123	112	1,080	47.9		Li et al. (1993)
Southeast	8.94	2.46	86.49	776	1,180	238	6.51	113.4	96	960	17.5		
Site ①	9.08	3.32										4.34	This study
Site ②	9.11	3.28										4.25	
Site ③	9.08	3.24			1,667	198	19.2	154	82	989	8.02	4.64	
Site ④	9.08	3.19										4.86	
Site ⑤	9.06	3.21										5.03	

The water depth at the drilling site was about 88.3 m. The core contained continuous lacustrine accumulation of silt clay with carbonates. The sediment core was kept intact in the polycarbonate (PC) tube that was used for the core collection while it was transported to the laboratory, where it was sliced at 1-cm intervals. All of the samples were stored at 4–6°C.

Sediment Dating and the Depth–Age Model

The 407-cm-long core was dated using ^{14}C radioactivity. The samples were collected at different depths and each sample was divided into two parts for bulk organic carbon dating (D_{org}) and bulk inorganic carbon dating (D_{in}). A total of 21 effective dates were obtained (**Table 2**). InCal13 software was applied to convert

TABLE 2 | Conventional ^{14}C dating and calibration ages for core GZLC15-1 from Guozha Co

Depth (cm)	D_{org} (con yr BP)	Error	D_{in} (con yr BP)	Error	D_{org} (cal yr BP)	Error	D_{in} (cal yr BP)	Error	Age effect (yr)	Age (cal yr BP)
1	16,500	50	7,870	30	19,892	204	8,679	91	8,744	–65
70	20,620	60	13,640	40	24,828	311	16,450 (reversed)	205		-
110	17,210	50	9,420	-	20,760	188	10,650	-		1,906
150	15,630	40	-	-	18,872	107	-	-		-
180	17,730	50	11,460	30	21,470	240	13,313	89		4,569
260	17,360	60	12,060	30	20,945	234	13,907	133		5,163
310	17,760	50	12,850	40	21,521	232	15,352	193		6,608
335	14,850	40	13,760	40	17,767	168	16,632 (reversed)	238		-
360	16,830	40	13,400	40	20,295	187	16,114	170		7,370
395	15,670	40	13,770	40	18,907	112	16,650	238		7,906
407	17,960	50	12,880	40	21,749	191	15,392 (reversed)	193		-

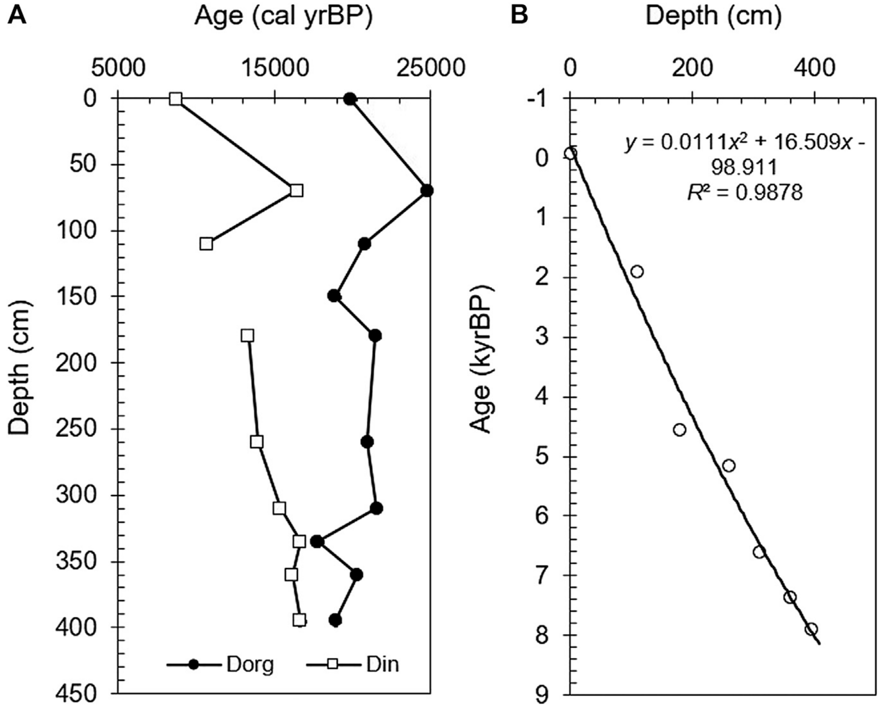

FIGURE 2 | (A) Changes in the bulk organic carbon and inorganic carbon calibrated ^{14}C dates and inorganic carbon age–depth curves with the authigenic carbonate effect removed. **(B)** Diagram of age-depth after removing carbon reservoir effect.

the conventional radiocarbon age to the calendar age (yr BP) (Reimer et al., 2013) and to draw a chrono-depth diagram (**Figure 2A**). The sample analysis was done at the Beta Analytic Radiocarbon Dating Laboratory in the United States.

Environmental Proxies

A total of 44 samples were air dried and ground into fine powder before the various mineral types were identified using an X-ray diffractometer (XRD) (a Rigaku D/MAX-2000, Cu, Kα1, 1.5406 Å, 40 kV, 40 mA, 3–65°, step 0.01°, 10°/min). The minerals were identified by the peak areas. The measurements were conducted at the Micro Structure Analytical Laboratory (MSAL), Peking University, in compliance with the Chinese oil and gas industry standard SY/T 5163-2010.

A total of 82 samples were collected at 5-cm intervals to determine their carbonate Ca and Mg contents. Approximately 0.2 g of each sample was placed in a 15-ml polyethylene centrifuge tube with 10 ml of ultra-pure water to leach the soluble ions from the pore water. Then, these samples were mixed using a vortex shaker, allowed to stand for 24 h at room temperature, and centrifuged, after which the liquid supernatant was extracted. Then, 10 ml of 1 M acetic acid (HAc) was added, and the samples were allowed to stand at room temperature for 24 h, with occasional shaking. Finally, the solid residues were separated by centrifugation, and the liquid supernatant was collected and analyzed. The Ca and Mg concentrations were determined using inductively coupled plasma optical emission spectroscopy (ICP-OES) at the Institute of Tibetan Plateau Research, Chinese Academy of Sciences (CAS).

A total of 44 bulk sediment samples were selected for carbonate δ^{13}C and δ^{18}O analyses, and three of these samples were sieved with a 400-mesh sieve (38-μm mesh) to compare the results of the bulk samples with fine particles. The samples were reacted with 100% phosphoric acid in reaction vessels for at least half an hour at 70°C to liberate the CO_2 gas, and then, the carbon and oxygen isotopes of the CO_2 were analyzed using an IsoPrime100 gas source stable isotope ratio mass spectrometer equipped with a MultiPrep system at the Institute of Earth Environment, CAS. The δ^{18}O and δ^{13}C values were normalized to the recommended values for international reference standards NBS-19 and SLAP. All of the δ^{18}O and δ^{13}C values have been reported in δ notation relative to Vienna Pee Dee Belemnite (VPDB). The standard results showed that the precision of the $\delta^{18}O_{\text{-VPDB}}$ and $\delta^{13}C_{\text{-VPDB}}$ analysis was better than 0.08 and 0.06‰ (2σ), respectively.

The $\delta^{18}O_{\text{calcite}}$ and $\delta^{18}O_{\text{aragonite}}$ values were calculated using the following equation (Wang et al., 2008):

$$\delta^{18}O_{\text{bulk carbonate}} = \delta^{18}O_{\text{calcite}} \times a + \delta^{18}O_{\text{aragonite}} \times b,$$

where a and b are the proportions of calcite and aragonite to the bulk carbonate (a + b = 1), respectively. Generally, the δ^{18}O of aragonite is about 0.6‰ more positive than that of calcite under the same conditions (Land, 1980; Grossman and Ku, 1986; Abell and Williams, 1989), that is, $\delta^{18}O_{\text{calcite}} + 0.6‰ = \delta^{18}O_{\text{aragonite}}$.

RESULTS

Sediment Dating

Generally, the bulk organic carbon is a mixture carbon from terrestrial plants, aquatic plants, and topsoil organics. Terrestrial plant carbon is related to the atmospheric CO_2 during plant growth; aquatic plant carbon utilizes the CO_2 dissolved in the water; and the topsoil organic carbon is related to the soil formation process. The atmospheric CO_2 is generally constant. The CO_2 in the water comes from the atmospheric CO_2 and is also released from clastic carbonates during their dissolution.

Terrestrial plant carbon comes from the assimilation of atmospheric CO_2 during the growth process, and exhibits obvious decay after a long period of burial. The relatively stable dating data for the bulk organic carbon from the bottom to the top of the GZLC15-1 core indicate that terrestrial organic carbon contributed less to the bulk organic carbon dating. In the arid/cold climatic condition, the soil formation processes are weak, resulting in less supply of topsoil organic carbon. Therefore, the bulk organic carbon dating data (D_{org}) of the GZLC15-1 core should be predominately influenced by the aquatic plant carbon. However, aquatic plants that used dissolved CO_2 in the water also did not change the stability of the bulk organic carbon dating data from the bottom to the top of the core. This indicates that the dissolved CO_2 in the lake water, although used by aquatic plants found at different burial depths (different burial times), was from the same period and less influenced by atmospheric CO_2 of the sedimentary period. In particular, the oldest date was around 20,000 years BP, which coincides with the Last Glacial Maximum (LGM), implying that CO_2 that was frozen and trapped in the glaciers during the LGM came into the lake with glacial meltwater.

The ^{14}C ages of the bulk organic carbon did not increase with depth. Therefore, the ^{14}C dates of the inorganic carbon, which are also related to the CO_2 dissolved in the lake, were considered when constructing the age sequence. As can be seen from **Figure 2A**, the inorganic carbon dates (D_{in}) gradually decrease from bottom to top, indicating that a rational sequence exists between the inorganic carbon dates (D_{in}) and the depositional depth. The inorganic carbon in the lake sediments is a mixture of authigenic carbonate and clastic carbonate. As the isotopes of fine-grained (<38 μm) carbonates are similar to those of the bulk carbonate, the bulk carbonate is concluded to be authigenic (see section "Origin of carbonate minerals and $\delta^{18}O_{\text{-VPDB}}$ and $\delta^{13}C_{\text{-VPDB}}$") based on the balance of Ca^{2+} in the equation $2HCO_3^- = CaCO_3 + CO_2 + H_2O$. Fontes et al. (1996) discussed the formation of lake authigenic calcite in Bangong Co, which is located in the same area as Guozha Co, and concluded that the authigenic calcite was mostly formed under the influence of dissolved carbonate from the basin's surface soil and the CO_2 released from deep fractures in the fault zones. It was further concluded that the CO_2 released from the deep fracture in the fault zones was roughly similar to the atmospheric CO_2 at the time. However, despite the extreme drought in the Guozha Co basin, the limited surface water produced by precipitation can still form carbonates in the surface soil, and thus, the surface soil contains atmospheric CO_2 information. After the carbonates in the surface soil are transported into the lake by the glacial meltwater, groundwater, and atmospheric precipitation, the carbon isotopes of these carbonates reflect the characteristics of the atmospheric CO_2 during its deposition into the lake. The deposition age can be obtained if the authigenic carbonate age effect (only using water CO_2) is removed from the inorganic carbon age results.

As we do not know the ratio of the surface soil carbonate to the lake water authigenic carbonate, it is simply assumed that the difference between the calendar age of the top layer of inorganic carbon and its actual age (1 year before sampling) is the age effect. Thus, the age effect can be eliminated by subtracting the age effect from the bulk inorganic carbon age of each depth. Based on this calculation, we constructed an age sequence for the entire core and plotted the core's depth–age curve (**Figure 2B**). The correlation between age and depth was obtained via quadratic multiphase fitting of the data, and the age corresponding to each depth was calculated.

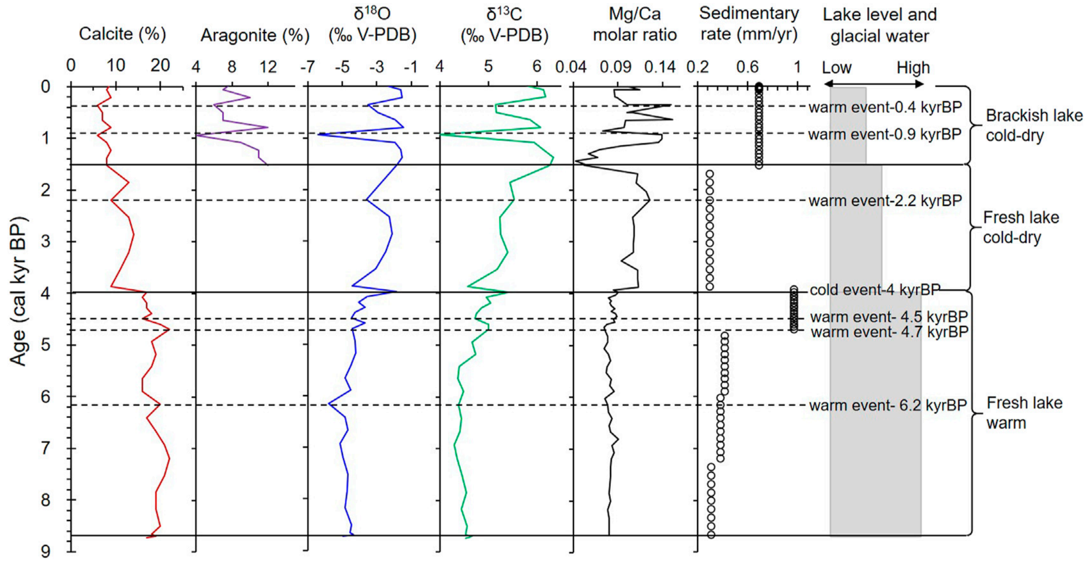

FIGURE 3 | Overview of the ages and multiple proxies for core GZLC15-1, showing the changes in the sedimentary environment and climate since 8.7 kyr BP.

Mineralogical Features

Two types of carbonate minerals were identified using X-ray diffraction. Calcite is the main carbonate phase, and it is continuous in the core with contents of 6–22% (average 14.5%; **Figure 3**). However, the aragonite is only present in the top part of the core (0–110 cm; until 1.5 kyr BP), and ranges between 4% and 12%. The minimum concentration (4%) of aragonite is observed at around 0.9 kyr BP. The $MgCO_3$ concentration of the calcite is less than 1%, indicating that it is low-Mg calcite. The calcite content shifts dramatically at a depth of 190 cm (4.0 kyr BP), after which it exhibits a decreasing trend. Dolomite is a minor component, accounting for less than 5% (**Table 3**).

Geochemistry, $\delta^{18}O_{\text{-VPDB}}$ and $\delta^{13}C_{\text{-VPDB}}$

Calcium is the main element in carbonate minerals, and the Ca content of the core ranges between 39.1 and 148.4 mg/g. Mg and Sr are minor elements that enter the carbonate mineral lattice to replace Ca, and their contents are 2.8–8.9 mg/g and 0.16–2.16 mg/g, respectively. Ca and Mg have similar curves at 8.7–4.0 kyr BP, and Ca and Sr have similar curves after 1.5 kyr BP. The Mg/Ca molar ratios are less than 0.16 (**Figure 4**). The K and Na curves are similar to those of Ca, Mg, and Sr after 4.0 kyr BP. The Na content increases with decreasing depth. Peaks in the element concentrations occur at 6.7, 6.2, 4.5, and 2.2 kyr BP, but they are not always consistent with those of the carbonate minerals (**Figure 4**).

At depths of 407–110 cm (8.7–1.5 kyr BP), calcite is the only carbonate mineral. The $\delta^{18}O_{\text{calcite}}$ values range from −5.79‰ to −1.87‰, while the $\delta^{13}C_{\text{calcite}}$ values range from 5.53‰ to 4.36‰. Little change was noted in the $\delta^{18}O_{\text{-VPDB}}$ and $\delta^{13}C_{\text{-VPDB}}$ values during 8.7–4.0 kyr BP, but the values of both distinctly increased during 4.0–1.5 kyr BP. After 1.5 kyr BP, the carbonate minerals consisted of calcite and aragonite. The $\delta^{18}O_{\text{calcite+aragonite}}$ values ranged from −6.39‰ to −1.43‰, while the $\delta^{13}C_{\text{calcite+aragonite}}$ values ranged from 3.98 to 6.34‰. The values of both $\delta^{18}O_{\text{-VPDB}}$ and $\delta^{13}C_{\text{-VPDB}}$ increased gradually and then shift dramatically from 4.0 to 0.9 kyr BP (**Figure 3**).

DISCUSSION

Origin of Carbonate Minerals and $\delta^{18}O_{\text{-VPDB}}$ and $\delta^{13}C_{\text{-VPDB}}$

Regardless of the lake water type, the first minerals to precipitate from water are alkaline earth carbonates, and their sequence is calcite followed by argonite and then dolomite. These carbonate minerals are also formed by the diagenetic action of the pore water during postdepositional processes and even during syndepositional diagenesis (Hardie et al., 1985; Warren, 1989). As the pore water is basically captured lake water, it is impossible to distinguish between the authigenic and endogenic carbonates.

Lacustrine aragonite is authigenic and/or endogenic because it is a metastable mineral and is never found in ancient carbonate rocks. Lacustrine aragonite is generally found in saline or brackish lakes (Fontes et al., 1996; Digerfeldt et al., 2000; Landmanna et al., 2002; Shapley et al., 2005; Murphy et al., 2014). In the process of seawater evaporation, aragonite begins to precipitate when the solution reaches 2–3 times the concentration of seawater (Warren, 1989). Therefore, the presence of aragonite generally suggests that the lake water was brackish during the depositional period. In the core, aragonite is only present in the upper 110 cm (1.5 kyr BP), with a content of less than 12% (**Table 3**). This indicates that the Guozha Co water became brackish at least 1.5 kyr BP ago according to the classification of lakes based on salinity (fresh lake: salinity <1 g/L; brackish: 1–35 g/L; saline lake: 35–50 g/L; salt/salar lake: >50 g/L; Zheng et al., 2002).

TABLE 3 | Mineral content (%) and isotopic composition (‰VPDB)

Depth (cm)	Calcite	Aragonite	Dolomite	δ^{18}O-bulk	δ^{13}C-bulk	δ^{18}O-calcite	δ^{18}O-aragonite
1	9	8	3	−2.92	5.51	−3.20	−2.60
10	8	7	5	−1.61	6.13	−1.89	−1.29
20	9	10	4	−1.54	6.18	−1.86	−1.26
30	6	6	3	−3.53	5.15	−3.83	−3.23
40	7	7	4	−2.94	5.16	−3.24	−2.64
50	7	7	4	−1.95	5.86	−2.25	−1.65
60	9	12	3	−1.43	6.08	−1.77	−1.17
70	6	4	3	−6.39	3.98	−6.63	−6.03
80	8	9	4	−1.92	5.94	−2.24	−1.64
90	9	11	3	−1.59	6.15	−1.92	−1.32
100	8	11	4	−1.52	6.34	−1.87	−1.27
110	8	12	4	−1.80	6.26	−2.16	−1.56
120	13		4	−2.73	5.44	−−2.73	
130	9		3	−3.60	5.53	−3.6	
140	13		2	−2.26	5.23	−2.26	
150	14		3	−2.12	5.25	−2.12	
160	13		4	−2.48	5.40	−2.48	
170	11		4	−3.05	5.17	−3.05	
180	9		3	−4.41	4.57	-4.41	
190	17		3	−1.87	5.41	−1.87	
200	16		3	−3.55	4.96	−3.55	
210	17		3	−4.05	5.05	−4.05	
220	17		3	−3.66	4.85	−3.66	
230	18		5	−4.27	4.75	−4.27	
240	16		3	−4.48	4.72	−4.48	
250	20		3	−3.69	5.00	−3.69	
260	22		3	−4.41	5.00	−4.41	
270	18		4	−4.26	4.67	-4.26	
280	19		4	−4.21	4.73	−4.21	
290	18		4	−4.51	4.40	−4.51	
300	16		3	−4.82	4.37	−4.82	
310	16		3	−4.51	4.49	−4.51	
320	20		4	−5.79	4.38	−5.79	
330	17		3	−4.85	4.45	−4.85	
340	19		4	−4.69	4.41	−4.69	
350	21		4	−5.12	4.29	−5.12	
360	22		3	−4.95	4.36	−4.95	
370	21		4	−4.65	4.46	−4.65	
380	19		3	−4.72	4.54	−4.72	
390	19		3	−4.83	4.45	−4.83	
400	20		3	−4.47	4.56	−4.47	
405	18		3	−4.54	4.53	-4.54	
406	19		3	−4.34	4.66	−4.34	
407	17		4	−4.95	4.53	−4.95	

Dolomite is common in ancient carbonates and is rare in Holocene sediments. As it is an evaporative mineral, laboratory experiments have shown that it is not able to precipitate in fresh water at Earth surface temperatures without bacterial mediation (Warren, 2000). It is very likely that the dolomite present in the section of the core deposited during the fresh water stage, that is, from the bottom (8.7 kyr BP) to 110 cm (1.5 kyr BP), was detrital and was transported by water from the surrounding catchment, most likely from the adjacent TK desert. Since the dolomite concentration was <5% in the core sediment, the bulk carbonates composition are dominantly controlled by the calcite.

At high altitudes, the wind contribution to sediments can usually not be ignored. In the Guozha Co sediments, the fine grain size (less than 38 μm) is dominant (Li et al., 2021), while the <75 μm fraction from the Chinese desert is less than 8% (Rao et al., 2009). This indicates that the amount of fine grains from the adjacent TK desert may be very small or trace, and the detrital sediments in Guozha Co are mainly from the local weathering of rocks and were transported by river water and wind.

There are three hypotheses regarding the formation of calcite: (1) chemical precipitation; (2) detrital sources; and (3) biological origin (Fontes et al., 1996; Digerfeldt et al., 2000; Landmanna et al., 2002; Shapley et al., 2005; Liu et al., 2009; Murphy et al., 2014; McCormack et al., 2019). The amount of calcite debris mainly depends on the chemical weathering and wind contribution. In the dry and cold climate of the Guozha Co area, the mean annual precipitation and temperature from 1979 to 2013 were 90 mm and −12.9°C, respectively (Qiao et al., 2017), which suggests that the intensity of chemical weathering in the

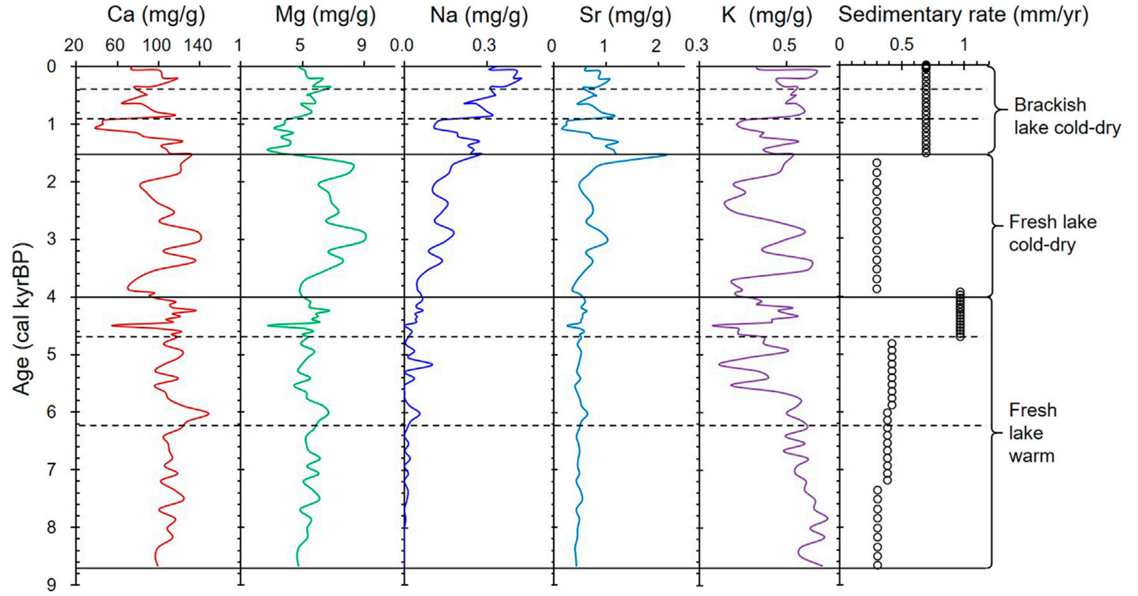

FIGURE 4 | Plot of ion content versus age showing the changes in the sedimentary environment and climate since 8.7 kyr BP.

TABLE 4 | Isotopic comparisons of bulk and fine-grained carbonates (‰VPDB)

Depth (cm)	Calcite in bulk	Aragonite in bulk	δ^{18}O-bulk	δ^{13}C-bulk	δ^{18}O-fine grain	δ^{13}C-fine grain	$\Delta\ \delta^{18}O_{(\text{fine grain-bulk})}$
70	6	4	−6.39	3.98	−4.82	4.69	1.57
150	14		−2.12	5.25	−1.63	5.49	0.49
330	17		−4.85	4.45	−4.25	4.9	0.6

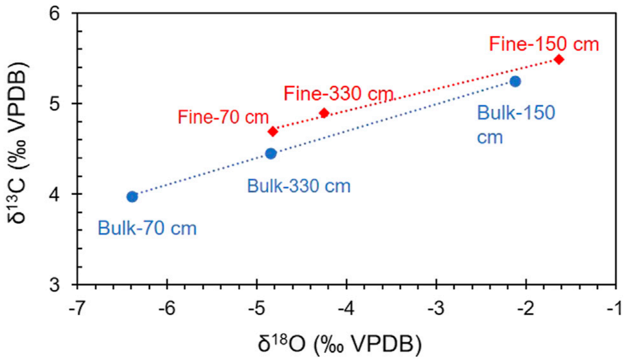

FIGURE 5 | Comparison of the δ^{18}O (‰VPDB) and δ^{13}C (‰VPDB) values of the fine-grained and bulk carbonates in core GZLC15-1 from Guozha Co.

lake basin was very weak and thus the clastic calcite content of the lake sediments should be low.

Biological shells such as ostracod shells normally weigh only a few micrograms and are only a minor component of lacustrine sediments (Liu et al., 2009; McCormack et al., 2019). Therefore, most of the calcite in the lake sediments must have been produced by chemical precipitation, and the bulk carbonate is mainly authigenic.

The isotopic composition of the bulk carbonate in the upper 110 cm may contain a contribution from both aragonite and calcite, while only calcite contributes to the isotopic composition of the bulk carbonate at depths of 110–407 cm. Although the δ^{18}O-$_{\text{VPDB}}$ and δ^{13}C-$_{\text{VPDB}}$ values of the calcite may contain contributions from chemical, minor detrital, and biological (mainly ostracods) calcite in the core, the detrital carbonate and the "vital offsets" from the ostracods have little influence on the isotopic composition of bulk calcite in cold–dry regions. This is due to the following reasons: 1) The δ^{18}O values of calcite with a biological origin, such as ostracod shells, are close to those of inorganic calcite, and they mainly reflect the isotopic variations of the water in the lake sediments, with a mean offset of +1.3‰ (Liu et al., 2009; Guo et al., 2016; Börner et al., 2017). Thus, the "vital offsets" from ostracods have little influence on the oxygen isotopes of bulk carbonate as they only weigh a few micrograms; and 2) the δ^{18}O values of the fine-grained carbonate (considered to be authigenic) in this study are close to those of the bulk carbonate and the correlation between δ^{18}O-$_{\text{VPDB}}$ and δ^{13}C-$_{\text{VPDB}}$ is linear (**Table 4**; **Figures 5**, **6**). The δ^{18}O-$_{\text{VPDB}}$ values of the fine-grained carbonate are only 0.49‰, 0.6‰, and 1.57‰ more positive than the bulk carbonate values at depths of 330, 150,

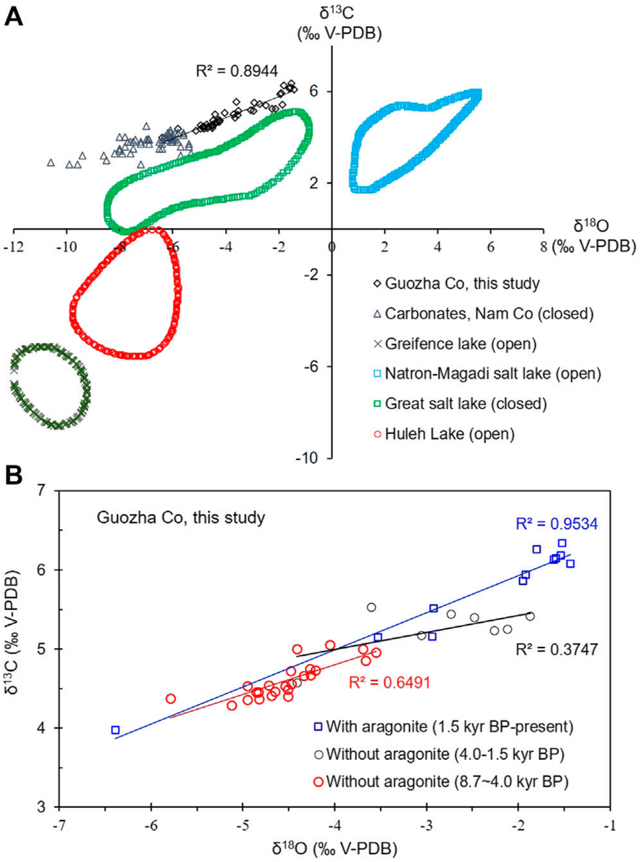

FIGURE 6 | Comparison of the $\delta^{18}O$ (‰VPDB) and $\delta^{13}C$ (‰VPDB) values from **(A)** Guozha Co and other lakes **(B)** from different stages in Guozha Co. The $\delta^{18}O$ and $\delta^{13}C$ data for Nam Co are from Li et al. (2012), and the data for the other lakes are from Talbot (1990).

and 70 cm, respectively (**Table 4**). The most positive value of 1.57‰ at a depth of 70 cm is due to the presence of aragonite because under the same conditions, the $\delta^{18}O$ of aragonite is about 0.6‰ more positive than that of calcite (Land, 1980; Grossman and Ku, 1986; Abell and Williams, 1989). These facts suggest that the isotopic compositions of the bulk and fine-grained carbonate were both controlled by the isotopic composition of the lake water. However, not all fine-grained carbonates are authigenic/endogenic. This is why many studies have used the isotopic composition of the bulk carbonate to trace paleoenvironmental changes in lakes (Keatings et al., 2002; Liu et al., 2009; Wünnemann et al., 2018; McCormack et al., 2019).

The $\delta^{18}O_{carbonate}$ is dependent on the oxygen isotopic composition of the water ($\delta^{18}O_{water}$) and the temperature at which the carbonate minerals formed. It is a function of water temperature (T_{water}) and follows the temperature-dependent fractionation equation: T_{water} (°C) = $13.8–4.58 \times (\delta^{18}O_{carbonate} - \delta^{18}O_{water}) + 0.08 \times (\delta^{18}O_{carbonate} - \delta^{18}O_{water})^2$ (Kim and O'Neil, 1997; Leng and Marshall, 2004). The influence of dolomite on the $\delta^{18}O_{carbonate}$ values can be ignored because CO_2 is generally released from dolomite at 90°C, but in this study, the $\delta^{18}O_{carbonate}$ was examined at 70°C. In the upper 110 cm, the $\delta^{18}O_{carbonate}$ values resulted from the mixing of the calcite and aragonite oxygen isotopic compositions. The fractionation factors of the inorganic calcite $\alpha_{calcite\text{-}water}$ and aragonite $\alpha_{aragonite\text{-}water}$ values are different, and under the same conditions, $\delta^{18}O_{aragonite}$ is enriched relative to $\delta^{18}O_{calcite}$ (Land, 1980; Grossman and Ku, 1986; Abell and Williams, 1989). Regardless of their fractionation factors, both the $\delta^{18}O_{calcite}$ and $\delta^{18}O_{aragonite}$ values are dependent upon the $\delta^{18}O_{water}$ and the T_{water}. A high T_{water} under warm conditions contributes to a high $\delta^{18}O_{carbonate}$ (i.e., ^{18}O enrichment). However, the recharge of glacial meltwater with very negative $\delta^{18}O$ values and a low temperature can decrease the temperature of the lake water and the $\delta^{18}O_{lake\ water}$ and $\delta^{18}O_{carbonate}$ values at the same time. Glacial melting occurs under warm climate conditions. As Guozha Co is a glacial melt recharge lake, the low $\delta^{18}O_{carbonate}$ values of core GZLC15-1 may represent a large amount of recharge by glacial water and a warm climate. This is further supported by the presence of similar trends in the $\delta^{18}O_{carbonate}$ of core GZLC15-1 and the $\delta^{18}O$ of an ice core (**Figure 7**) from the Guliya Ice Cape, the glacial meltwater of which directly supplies Guozha Co (**Figure 1**).

The $\delta^{18}O$ of glacial meltwater is also a sensitive proxy for temperature and climatic change (Yao et al., 2013; Yu et al., 2016; Thompson et al., 2018), and it is very negative compared with $\delta^{18}O_{carbonate}$ in lacustrine sediments. In addition to temperature, the latter is mainly controlled by the ratio of the water input to output, that is, evaporation and precipitation plus glacial meltwater. Consequently, the $\delta^{18}O_{carbonate}$ oscillations in core GZLC15-1 are not always consistent with the $\delta^{18}O$ records of the Guliya ice core (**Figure 7**).

Carbonate Elements and Glacial Effects

The chemical components of the lake water are the most crucial factors controlling the authigenic and/or endogenic carbonate mineral precipitation. A dry climate will increase the soluble ion concentrations in lake water, while glacial meltwater will reduce the soluble ion concentrations. Ca is the main element in carbonates, and it has an ionic radius similar to the ionic radii of Mg and Sr. Due to the different crystal structures of calcite and aragonite, the Ca in calcite is often replaced by Mg and Sr, while the Ca in aragonite is often replaced by Sr. This is why the correlation coefficients between Ca and Sr are high throughout the core, while a high coefficient between Ca and Mg is only evident during 8.7–1.5 kyr BP (**Figure 8**) when calcite was the dominant carbonate mineral, and there was no aragonite. In the inorganic precipitation of carbonates, when the Mg concentration in the lake water becomes high, calcite formation is inhibited and aragonite precipitation increases (Shapley et al., 2005; Rivadeneyra et al., 2006; Li et al., 2009). Thus, the correlation coefficient between Ca and Mg decreased from 8.7 to 4.0 kyr BP ($R^2 = 0.8607$) to 4.0–1.5 kyr BP ($R^2 = 0.7703$) and from 1.5 kyr BP to present ($R^2 = 0.0149$; **Figure 8**). This may be due to the increasing Mg concentration in the lake water as well as the presence of both calcite and aragonite during the last stage. These effects resulted from a dry climate and the reduced recharge from glacial meltwater.

Similarly, the changes noted in the correlation coefficient between Ca and Na (**Figure 8**) indicate that the Na content is related to the calcite content in the core. Unlike Mg and Sr, Na is

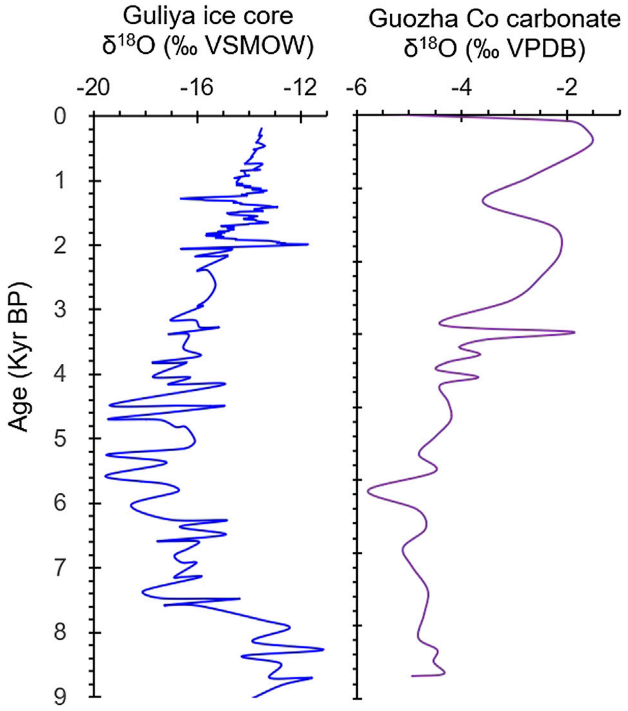

FIGURE 7 | Comparison of the oxygen isotopic compositions of the carbonates in core GZLC15-1 and the Guliya ice core. The $\delta^{18}O$ data for the ice core are from Yang et al. (2006) and Thompson et al. (2018).

more sensitive to changes in salinity. The increasing Na content indicates that the climate gradually became dry, and the recharge from glacial meltwater gradually decreased after 8.7 kyr BP. The Na content was very low (even zero) during 8.7–4.0 kyr BP (**Figure 4**), which may be due to the glacial meltwater. During this period, the correlation coefficient between Ca and K was also low and similar to that between Ca and Na. This indicates that K content was also mainly related to the calcite content. However, the K and Na curves depict different trends, and the K content is higher than the Na content (**Figure 4**). It is well known that in nature, the K content of water is lower than that of Na. It is difficult to judge the effect of climate and glacial meltwater on the K content of carbonates and lake water. One possible reason for this is that some of the K came from the acid dissolution of clay minerals, although we used acetic acid (HAc, weak acid).

Lake Status and Glacial Effects

Guozha Co has been a closed basin since at least 8.7 kyr BP, based on the high correlation coefficient noted between $\delta^{18}O$-$_{VPDB}$ and $\delta^{13}C$-$_{VPDB}$ values (R^2 = 0.89; **Figure 6**). In the $\delta^{18}O$–$\delta^{13}C$ plot, all of the data are distributed within the same quadrant, as similar to other closed lakes, such as Nam Co and Great Salt Lake (**Figure 6A**). In general, the relation between $\delta^{18}O$ and $\delta^{13}C$ show weak/insignificant correlation for the carbonates in open lakes, whereas in the closed basins, it shows a strong correlation (Talbot, 1990; Liu et al., 2001). This is because, the water in open lakes flows rapidly and has a short residence time, and as a result, the $\delta^{18}O$-$_{VPDB}$ and $\delta^{13}C$-$_{VPDB}$ values of the lake water reflect the isotopic characteristics of the inflowing water, including meltwater, groundwater and rain water, which are affected by different factors. However, in closed lakes, the residence time of the water is long, and evaporation plays a controlling role in the lake water's composition. Moreover, closed lakes contain large amounts of algae, which preferentially absorb lighter carbon, resulting in enriched $\delta^{13}C$ values (Kelts, 1988).

As Guozha Co is directly recharged by glacial meltwater, the glacial recharge influenced not only the $\delta^{18}O$-$_{VPDB}$ and $\delta^{13}C$-$_{VPDB}$ values of the calcite and aragonite minerals but also influence the lake level changes. The increase of glacial meltwater will reduce the $\delta^{18}O$ values of carbonate minerals and cause the lake level to rise. According to the variations in the carbonate minerals and the coefficients between $\delta^{18}O$-$_{VPDB}$ and the calcite content and between $\delta^{18}O$ and $\delta^{13}C$, the lake level was highest during 8.7–4.0 kyr BP and lowest from 1.5 kyr BP to present. As most of the calcite was inorganically precipitated from the lake water, in general, the changes in the calcite content and $\delta^{18}O$-$_{VPDB}$ values should be consistent (Li et al., 2008,2012; Liu et al., 2009; McCormack et al., 2019). However, there is no correlation between calcite content and $\delta^{18}O$-$_{VPDB}$ values during 8.7–4.0 kyr BP (R^2 = 0.1), whereas the correlation has a high coefficient during 4.0–1.5 kyr BP (R^2 = 0.85) and from 1.5 kyr BP to present (R^2 = 0.51; **Figure 9**). One possible reason for this is that the inflow of glacial meltwater, which had more negative $\delta^{18}O$-$_{VPDB}$ values than the lake water, was much higher during 8.7–4.0 kyr BP and from 4.0 kyr BP to present. The inflow of fresh meltwater is also supported by the low Na and high Ca

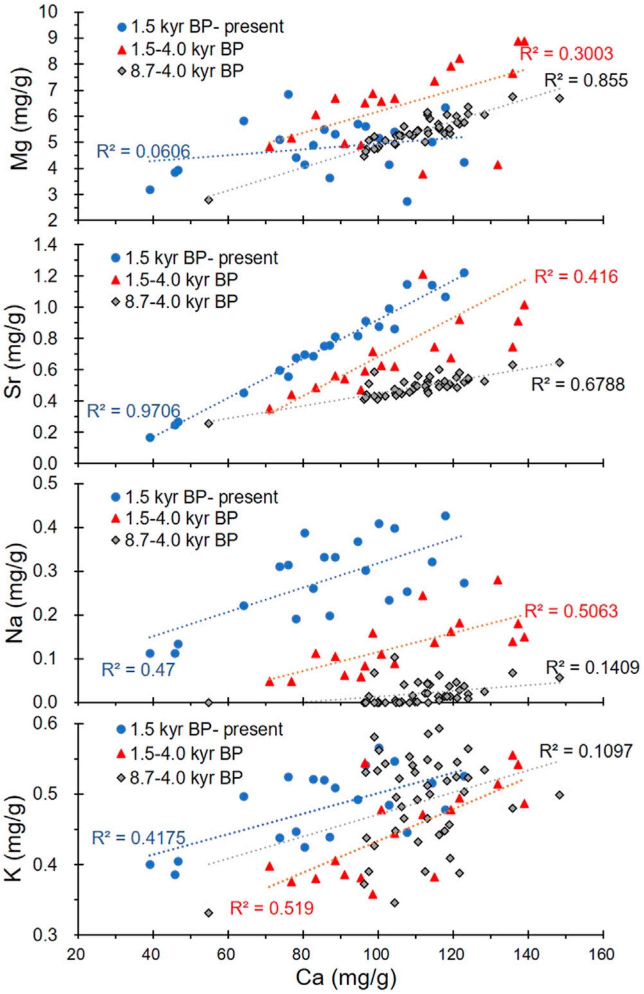

FIGURE 8 | Correlations between the Ca and Mg, Sr, Na, and K contents of the carbonates.

and Mg contents during 8.7–4.0 kyr BP (**Figure 4**). Owing to the very low rainfall and high evaporation in the study area (Qiao et al., 2017), the glacial meltwater is the main input to the lake, and the glacial recharge contributed to the lake level being highest during 8.7–4.0 kyr BP, as indicated by the core data (**Figure 3**).

The lake water level was lowest from 1.5 kyr BP to present based on the presence of aragonite, which is generally precipitated in brackish or saline lake water. The high Na content (**Figure 4**) and the high correlation coefficient between $\delta^{18}O_{\text{-VPDB}}$ and $\delta^{13}C_{\text{-VPDB}}$ (R^2 = 0.95; **Figure 6B**) from 1.5 kyr BP to present also suggest high evaporation, increasing lake water salinity, and a low water level with less glacial recharge (**Figure 3**). Therefore, the recharge from glacial meltwater in the aragonite stage (1.5 kyr BP to present) was less than in the calcite stage (8.7–1.5 kyr BP).

Climatic Change and Glacial Effect

The changes in the mineral composition and element contents of the sediment indicate that the lake water has gradually become more concentrated since 8.7 kyr BP. Three distinct stages can be identified, 8.7–4.0, 4.0–1.5, and from 1.5 kyr BP to present (**Figure 10**), which indicate that the recharge from glacial meltwater has continuously decreased.

Stage I (8.7–4.0 kyr BP): The climate was warm, which is consistent with the Holocene warm optimum and the high global temperature (**Figure 11**). The warm climate during this period has also been indicated by a variety of other land- and marine-based proxy data from all around the world (Marcott et al., 2013). Under these warmer conditions, the glaciers in the West Kunlun Mountains retreated, as corroborated by the $\delta^{18}O$ of ice core water and other climatic proxies (Li, 1996; Thompson et al., 1997; Pang et al., 2020). As a result, the lake's water level rose (**Figure 10**) and the lake water was fresh with low Na content (**Figure 3**). This suggests that the regional glacier was affected by the Holocene climate change, and the $T_{\text{lake water}}$ was mainly controlled by climate change and not glacial meltwater. The surface lake water temperature results for Guozha Co also support this conclusion. The water temperature in the eastern part of the basin was higher than in the western part of the basin (**Table 1**), despite the fact that the glacial meltwater entered the

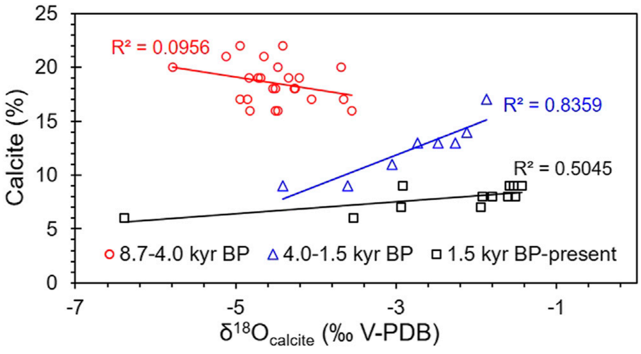

FIGURE 9 | Relationships between the calcite content and $\delta^{18}O_{calcite}$ (‰VPDB) during the different periods.

lake through the eastern part due to the direction of the blowing wind from west to east.

The low $\delta^{18}O$-$_{VPDB}$ values and the slight increasing contents of Ca, Mg, and Na at around 6.2 kyr BP (**Figures 3**, **4**) were also due to climatic change. The warm event at 6.2 kyr BP has also been identified in cores and paleoshorelines from the glacial recharge lakes on the TP, such as Nam Co (at around 6 kyr BP), Lingge Co (~6.1 kyr BP), and Bangong Co (around 6.3–6.0 kyr BP) (Frontes et al., 1996; Gasse et al., 1996; Zhu et al., 2008; Pan et al., 2012). Based on the abrupt increases in the sedimentary rates and high carbonate Mg/Ca molar ratios, there may have been a warm-dry event at 4.7 kyr BP (**Figure 3**). The event at 4.7 kyr BP has also been identified in a core from Ahung Co, a lake in central Tibet (Morrill et al., 2006).

Stage II (4.0–1.5 kyr BP): The climate was cold-dry, which is consistent with the decreasing global temperature (**Figure 10**). The cold climate during this time is well reflected by the famous "4.2 kyr cold event", which is considered to have marked the end of the Holocene warm optimum (Bond et al., 1997; 2001; Xiao et al., 2019; Mehrotra et al., 2019). This cold event has also been recorded in other lake sediments on the TP, such as the fresh-brackish Bangong Co in west Kunlun on the western TP (**Figure 11**) based on the $\delta^{18}O$, $\delta^{13}C$, geochemistry, and grains (Gasse et al., 1996; Wei and Gasse, 1999); Selin Co, a glacial recharge lake on the central TP (**Figure 11**) based on the $\delta^{18}O$ and $\delta^{13}C$ (Gu et al., 1993) and shorelines (Shi et al., 2017); and Qinghai Lake on the eastern TP based on the $\delta^{18}O$ and $\delta^{13}C$ of carbonates (Liu et al., 2003). This event was also observed in other places in the world, such as the Indo-Gangetic Plain (dominated by Indian Summer Monsoon [ISM]) based on the fluvial landscapes (MacDonald, 2011; Giosan et al., 2012), and the PT Tso Lake, Eastern Himalaya (dominated by ISM), based on pollen and carbon isotopes (Mehrotra et al., 2019). The reconstructed sea surface temperatures (SSTs) in the western Bay of Bengal (dominated by ISM) also start to cool off during this stage based on the $\delta^{18}O$ and Mg/Ca ratio of planktonic foraminifera (Govil and Naidu, 2011; **Figure 11**).

Under these cold conditions, the glaciers in the West Kunlun Mountains stopped retreating after 3 kyr BP, which is supported by the ^{10}Be ages of the moraines (Li, 1996; Pang et al., 2020; Chen et al., 2020) and proxies from ice cores (Thompson et al., 1997; Pang et al., 2020). Glacier advances also occurred frequently in the North Atlantic at 4.4–4.2, 3.8–3.4, 3.3–2.8, 2.6, and 2.3–2.1 kyr BP (Solomina et al., 2015). As a result, less meltwater entered Guozha Co and the lake level decreased (**Figure 10**). Although the lake water may still have been fresh, the increased Na content indicates that the lake water became more concentrated (**Figure 4**). Decreasing rainfall was observed in northern Australia (dominated by Australia–Indian summer monsoon [AISM]) during 4.1–1.5 kyr BP based on the $\delta^{18}O$ of stalagmite from Western Australia (Denniston et al., 2013) and southern China (Yuan et al., 2004), and the Ti/Ca ratio of bulk lacustrine sediments in the Lombok Basin in Indonesia (Steinke et al., 2014; **Figure 11**).

Similar to Stage I, the low $T_{lake\ water}$ in Stage II was controlled by the cold climate. The low $T_{lake\ water}$ and the cold climate (e.g., low precipitation/evaporation) driving the hydrochemical conditions (e.g., Mg/Ca ratio) influenced both the calcite precipitation and the $\delta^{18}O$ of the lake water. Thus, the coefficient between the calcite content and the $\delta^{18}O$-$_{VPDB}$ values was high (R^2 = 0.85; **Figure 9**).

In addition to the 4.0 kyr BP cold event, warm events also occurred at 3.9 and 2.2 kyr BP under arid-cold conditions (**Figure 3**). The 2.2 kyr BP event has also been identified in the Nam Co core based on rare earth element concentrations (Li et al., 2011). The 3.9 kyr BP warm event was coincident with a pronounced dry period at Nam Co around 3.7 kyr BP (Mügler et al., 2010), and at Lake Qinghai around 3.9 kyr BP (Shen et al., 2005).

Stage III: From 1.5 kyr BP to present, the climate was basically dry-cold and fluctuated, with two warm events at 0.9 and 0.4 kyr BP in the Guozha Co area (**Figure 3**). During this period, the global temperature also exhibited a decreasing and fluctuating trend (**Figure 11**). The deterioration and fluctuations in the climate during the Late Holocene occurred worldwide (Bond et al., 2001; Rasmussen et al., 2007; Zhu et al., 2009; Marcott et al., 2013). For example, lake shrinkage and salinization has also been observed in Nam Co during 1.4–0.8 kyr BP, and these climate variations have been identified in cores from other glacier-fed lakes, such as Lingge Co on the northern part of the TP based on the paleoshorelines (Pan et al., 2012), Taro Co based on the $\delta^{18}O$ values of ostracod shells (Guo et al., 2016), Buruo Co based on the

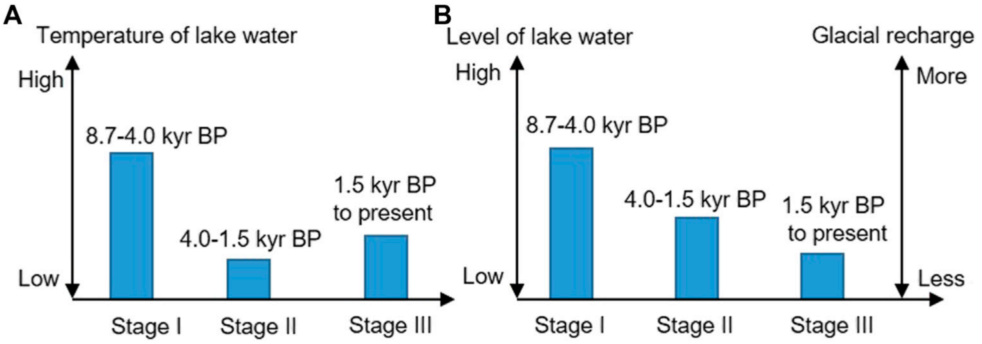

FIGURE 10 | Comparison of **(A)** the temperature changes of the lake water and **(B)** the lake water level changes (Left axis) and the glacial recharge changes (Right axis) during the three stages.

grain size and elements (Xu et al., 2019), and Selin Co based on the shorelines (Shi et al., 2017). The climatic fluctuations in the Late Holocene have also been observed in the western Bay of Bengal (dominated by ISM) based on the reconstructed sea surface temperature (Govil and Naidu, 2011) and in western Australia based on the $\delta^{18}O$ values of stalagmites (Denniston et al., 2013; **Figure 11**).

Based on the presence of aragonite, Guozha Co became a brackish lake at least by 1.5 kyr BP. This is consistent with the adjacent Bangong Co, in which aragonite was found at 1.3 kyr BP (**Figure 11**). Therefore, the recharge from glacial meltwater was low, and the glacier may not have retreated. In this stage, multiple glacier advances occurred in most regions during the Late Holocene (Owen, 2009), including the glaciers in the West Kunlun Mountains (Li, 1996; Thompson et al., 2018).

During the past century, the global temperature began to increase dramatically (**Figure 11**; Marcott et al., 2013). The glaciers in the West Kunlun Mountains retreated from 1976 to 2010 based on remote sensing and the expansion of the glacial lakes on the northern slope of the West Kunlun Mountains (Li et al., 2015). Corresponding to the glaciers retreating, a river flowing from Guozha Co was identified by Li et al. (2021), although the modern lake water in Guozha Co is still brackish (**Table 1**). Therefore, both of the glaciers and lakes in the West Kunlun Mountains are controlled by climatic change, but they exhibit opposite changes.

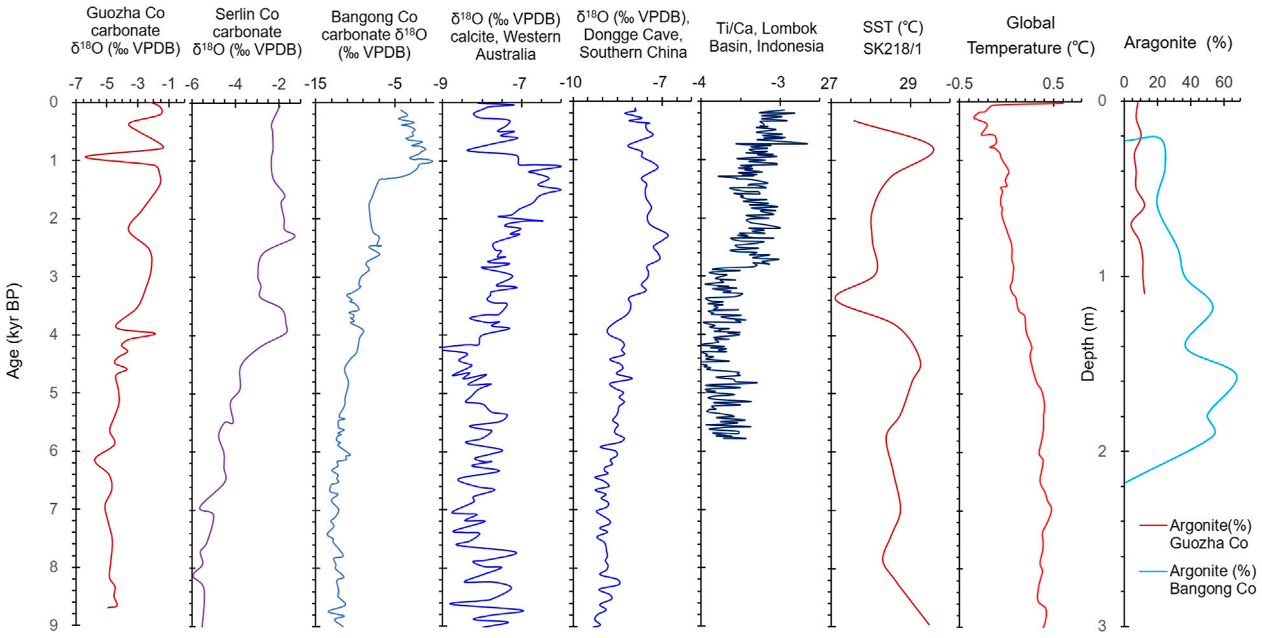

FIGURE 11 | Comparison of data from this study and other records. The $\delta^{18}O$ of sediments carbonate for Bangong Co and Selin Co are from Gasse et al. (1996) and Gu et al. (1993), respectively. The $\delta^{18}O$ of cave carbonate for Western Australia and southern China are from Denniston et al. (2013) and Yuan et al. (2004), respectively. Ti/Ca for Indonesia are from Steinke et al. (2014), the reconstructed SST of marine core SK218/1 from the western Bay of Bengal are from Govil and Naidu (2011), and the aragonite data for Bangong Co are from Fontes et al. (1996). The global temperature data are from Marcott et al. (2013).

CONCLUSION

The carbonates in the Guozha Co sediments are mainly authigenic/endogenic calcite and aragonite. The $\delta^{18}\mathrm{O}\text{-}_{\mathrm{VPDB}}$-$\delta^{13}\mathrm{C}\text{-}_{\mathrm{VPDB}}$ values of the fine-grained carbonates are slightly more positive than those of the bulk carbonate, and both are controlled by the isotopic composition of the lake water.

Proxies for calcite content, the $\delta^{18}\mathrm{O}\text{-}_{\mathrm{VPDB}}$ and $\delta^{13}\mathrm{C}\text{-}_{\mathrm{VPDB}}$ values, and their correlation coefficients suggest that three stages occurred at 8.7–4.0, 4.0–1.5, and from 1.5 kyr BP to present, during which the recharge from glacial meltwater decreased.

Guozha Co has been a closed basin since at least 8.7 kyr BP, and it changed from a fresh lake during 8.7–1.5 kyr BP to a brackish lake from 1.5 kyr BP to present, coincident with several climate events, despite the fact that the glacial meltwater diluted the ion concentrations in the lake water. The glacier and the lakes in the West Kunlun Mountains exhibit opposite changes, but both are controlled by climatic changes.

DATA AVAILABILITY STATEMENT

The original contributions presented in the study are included in the article/Supplementary Material. Further inquiries can be directed to the corresponding author.

AUTHOR CONTRIBUTIONS

LZ designs the research, constructs the dating, and writes the text. ML makes the minerals and isotope analyses and writes text. JW, JJ, CL, QM, TX, and BQ carried out field investigation and coring. XW participates in laboratory analyses.

FUNDING

This study was supported by the China Ministry of Science and Technology, the Second Tibetan Plateau Scientific Expedition and Research (grant no. 2019QZKK0202), the Key Project of the National Natural Science Foundation of China (grant no. 41831177), and the Strategic Priority Research Program of the Chinese Academy of Sciences (grant nos. XDA20020100 and XDA20070101).

ACKNOWLEDGMENTS

The authors thank LetPub (www.letpub.com) for its linguistic assistance during the preparation of this article.

REFERENCES

Abell, P. I., and Williams, M. A. J. (1989). Oxygen and Carbon Isotope Ratios in Gastropod Shells as Indicators of Paleoenvironments in the Afar Region of ethiopia. *Palaeogeogr. Palaeoclimatol. Palaeoecol.* 74, 265–278. doi:10.1016/0031-0182(89)90065-5

Bernasconi, S. M., and McKenzie, J. A. (2013). "Carbonate Stable Isotopes Lake Sediments", in *Encyclopedia of Quaternary Science*. Editors Elias, S. A., and Mock, C. J. 2nd Edn, (Elsevier), 333–340.

Bolch, T., Kulkarni, A., Kääb, A., Huggel, C., Paul, F., Cogley, J. G., et al. (2012). The State and Fate of Himalayan Glaciers. *Science* 336, 310–314. doi:10.1126/science.1215828

Bond, G., Kromer, B., Beer, J., Muscheler, R., Evans, M. N., Showers, W., et al. (2001). Persistent Solar Influence on north Atlantic Climate Change during Holocene. *Science* 294 (13), 2130–2135. doi:10.1126/science.1065680

Bond, G., Showers, W., Cheseby, M., Lotti, R., Almasi, P., deMenocal, P., et al. (1997). A Pervasive Millennial-Scale Cycle in North Atlantic Holocene and Glacial Climates. *Science* 278, 1257–1266. doi:10.1126/science.278.5341.1257

Börner, N., De Baere, B., Akita, L. G., Francois, R., Jochum, K. P., Frenzel, P., et al. (2017). Stable Isotopes and Trace Elements in Modern Ostracod Shells: Implications for Reconstructing Past Environments on the Tibetan Plateau, China. *J. Paleolimnol* 58, 191–211. doi:10.1007/s10933-017-9971-1

Bureau of Geology and Mineral resources of Xizang Autonomous Regions (1993). *Regional Geology of Xingzang(Tibet) Autonomous Region*. Beijing: Geological Publishing House.(in Chinese).

Chen, D. L., Xu, B. Q., Yao, T. D., Guo, Z. T., Cui, P., Chen, F. H., et al. (2015). Assessment of Past, Present and Future Environmental Changes on the Tibetan Plateau. *Chin. Sci. Bull.* 60, 3025–3035. doi:10.1360/n972015-00849

Chen, F., Zhang, J., Liu, J., Cao, X., Hou, J., Zhu, L., et al. (2020). Climate Change, Vegetation History, and Landscape Responses on the Tibetan Plateau during the Holocene: a Comprehensive Review. *Quat. Sci. Rev.* 243, 106444. doi:10.1016/j.quascirev.2020.106444

Denniston, R. F., Wyrwoll, K. H., Polyak, V. J., Brown, J. R., Asmerom, Y., Wanamaker, A. D., Jr., et al. (2013). A Stalagmite Record of Holocene Indonesiane Australian Summer Monsoon Variability from the Australian Tropics. *Quat. Sci. Rev.* 78, 155–168. doi:10.1016/j.quascirev.2013.08.004

Deocampo, D. M., and Tactikos, J. C. (2010). Geochemical gradients and artifact mass densities on the lowermost Bed II eastern lake margin (~1.8Ma), Olduvai Gorge, Tanzania. *Quat. Research* 74 (3), 411–423. doi:10.1016/j.yqres.2010.09.004

Digerfeldt, G., Olsson, S., and Sandgren, P. (2000). Reconstruction of lake-level Changes in lake Xinias, central Greece, during the Last 40 000 Years. *Palaeogeogr. Palaeoclimatol. Palaeoecol.* 158 (1), 65–82. doi:10.1016/s0031-0182(00)00029-8

Fontes, J.-C., Gasse, F., and Gibert, E. (1996). Holocene Environmental Changes in Lake Bangong Basin (Western Tibet). Part 1: Chronology and Stable Isotopes of Carbonates of a Holocene Lacustrine Core. *Palaeogeogr. Palaeoclimatol. Palaeoecol.* 120, 25–47. doi:10.1016/0031-0182(95)00032-1

Gasse, F., Fontes, J. C., Van Campo, E., and Wei, K. (1996). Holocene Environmental Changes in Bangong Co Basin (Western Tibet). Part 4: Discussion and Conclusions. *Palaeogeogr. Palaeoclimatol. Palaeoecol.* 120, 79–92. doi:10.1016/0031-0182(95)00035-6

Giosan, L., Clift, P. D., Macklin, M. G., Fuller, D. Q., Constantinescu, S., Durcan, J. A., et al. (2012). Fluvial Landscapes of the Harappan Civilization. *Proc. Natl. Acad. Sci.* 109 (26), E1688–E1694. doi:10.1073/pnas.1112743109

Govil, P., and Divakar Naidu, P. (2011). Variations of Indian Monsoon Precipitation during the Last 32kyr Reflected in the Surface Hydrography of the Western Bay of Bengal. *Quat. Sci. Rev.* 30, 3871–3879. doi:10.1016/j.quascirev.2011.10.004

Grossman, E. L., and Ku, T.-L. (1986). Oxygen and Carbon Isotope Fractionation in Biogenic Aragonite: Temperature Effects. *Chem. Geology. Isotope Geosci. section* 59, 59–74. doi:10.1016/0168-9622(86)90057-6

Gu, Z. Y., Liu, J, Q., Yuan, B. Y., Liu, T. S., Liu, R. M., Liu, Y., et al. (1993). Monsoon Variations of the Qinghai-Xizang Plateau during the Last 12 000 Years: Geochemical Evidences from the Sediments in the Siling Co (lake). *Chinense Sci. Bull.* 07.

Guo, Y., Zhu, L., Frenzel, P., Ma, Q., Ju, J., Peng, P., et al. (2016). Holocene lake Level Fluctuations and Environmental Changes at Taro Co, Southwestern Tibet, Based on Ostracod-Inferred Water Depth Reconstruction. *The Holocene* 26, 29–43. doi:10.1177/0959683615596829

Hardie, L. A., Lowenstein, T. K., and Spencer, R. J. (1985). The Problem of Distinguishing between Primary and Secondary Features in Evaporites. in *Sixth International Symposium on Salt*, 1. Alexandria: Salt Institute, 11–39.

He, Y., Zhao, C., Liu, Z., Wang, H., Liu, W., Yu, Z., et al. (2016). Holocene Climate Controls on Water Isotopic Variations on the Northeastern Tibetan Plateau. *Chem. Geology.* 440, 239–247. doi:10.1016/j.chemgeo.2016.07.024

Henderson, A. C. G., Holmes, J. A., and Leng, M. J. (2010). Late Holocene Isotope Hydrology of Lake Qinghai, NE Tibetan Plateau: Effective Moisture Variability and Atmospheric Circulation Changes. *Quat. Sci. Rev.* 29, 2215–2223. doi:10.1016/j.quascirev.2010.05.019

Horton, T. W., Defliese, W. F., Tripati, A. K., and Oze, C. (2016). Evaporation Induced 18O and 13C Enrichment in lake Systems: A Global Perspective on Hydrologic Balance Effects. *Quat. Sci. Rev.* 131, 365–379. doi:10.1016/j.quascirev.2015.06.030

Hren, M. T., and Sheldon, N. D. (2012). Temporal Variations in lake Water Temperature: Paleoenvironmental Implications of lake Carbonate δ18O and Temperature Records. *Earth Planet. Sci. Lett.* 337-338, 77–84. doi:10.1016/j.epsl.2012.05.019

Kääb, A., Berthier, E., Nuth, C., Gardelle, J., and Arnaud, Y. (2012). Contrasting Patterns of Early Twenty-First-Century Glacier Mass Change in the Himalayas. *Nature* 488, 495–498. doi:10.1038/nature11324

Keatings, K. W., Heaton, T. H. E., and Holmes, J. A. (2002). Carbon and Oxygen Isotope Fractionation in Non-marine Ostracods: Results from a 'natural Culture' Environment. *Geochimica et Cosmochimica Acta* 66, 1701–1711. doi:10.1016/s0016-7037(01)00894-8

Kelts, K. (1988). Environments of Deposition of Lacustrine Petroleum Source Rocks: an Introduction, in *Geological Society*, London, Special Publications 40. 3–26. doi:10.1144/gsl.sp.1988.040.01.02

Kim, S.-T., and O'Neil, J. R. (1997). Equilibrium and Nonequilibrium Oxygen Isotope Effects in Synthetic Carbonates. *Geochimica et Cosmochimica Acta* 61, 3461–3475. doi:10.1016/s0016-7037(97)00169-5

Land, L. S. (1980). The Isotopic and Trace Element Geochemistry of Dolomite: the State of the Art. In: D. H. Zenger, J. B. Dunham, and R. L. Ethington (Eds.), *Concepts and Models of Dolomitization 28*. Broken Arrow: SEPM Special Publication. *pp*. 87–110. doi:10.2110/pec.80.28.0087

Landmann, G., Abu Qudaira, G. M., Shawabkeh, K., Wrede, V., and Kempe, S. (2002). Geochemistry of the Lisan and Damya Formations in Jordan, and Implications for Palaeoclimate. *Quat. Int.* 89, 45–57. doi:10.1016/s1040-6182(01)00080-5

Leng, M. J., and Marshall, J. D. (2004). Palaeoclimate Interpretation of Stable Isotope Data from lake Sediment Archives. *Quat. Sci. Rev.* 23 (7), 811–831. doi:10.1016/j.quascirev.2003.06.012

Li, B. Y., Zhang, Q. S., and Wang, F. B. (1991). Evolution of the Lakes in the KARAKORUM-West Kunlun Mountains. *Quat. Sci.* (1), 64–71. (in Chinese with English abstract).

Li, C.-G., Wang, M., Liu, W., Lee, S.-Y., Chen, F., and Hou, J. (2021). Quantitative Estimates of Holocene Glacier Meltwater Variations on the Western Tibetan Plateau. *Earth Planet. Sci. Lett.* 559, 116766. doi:10.1016/j.epsl.2021.116766

Li, C. X., Yang, T. B., and Tian, H. Z. (2015). Variation of Western Kunlun Mountain Glaciers Monitored by Remote Sensing during 1976—2010. *Mountain Res.* 33 (2), 157–165. (In Chinese with English Abstract). doi:10.16089/j.cnki.1008-2786.000021

Li, J. J. (1996). Climatic Change in Arid Areas of China and Monsoon Fluctuations during the Past 10 K Years. *J. Arid Environ.* 32, 1–7.

Li, M., Kang, S., Zhu, L., Wang, F., Wang, J., Yi, C., et al. (2009). On the Unusual Holocene Carbonate Sediment in lake Nam Co, central Tibet. *J. Mt. Sci.* 6, 346–353. doi:10.1007/s11629-009-1020-8

Li, M., Kang, S., Zhu, L., You, Q., Zhang, Q., and Wang, J. (2008). Mineralogy and Geochemistry of the Holocene Lacustrine Sediments in Nam Co, Tibet. *Quat. Int.* 187, 105–116. doi:10.1016/j.quaint.2007.12.008

Li, M., Wang, J., Zhu, L., Wang, L., and Yi, C. (2012). Distribution and Formation of Monohydrocalcite from Surface Sediments in Nam Co Lake, Tibet. *Quat. Int.* 263, 85–92. doi:10.1016/j.quaint.2012.01.035

Li, M., Zhu, L., Wang, J., Wang, L., Yi, C., and Galy, A. (2011). Multiple Implications of Rare Earth Elements for Holocene Environmental Changes in Nam Co, Tibet. *Quat. Int.* 236, 96–106. doi:10.1016/j.quaint.2010.12.022

Li, S. J., Zheng, B. X., and Jiao, K. Q. (1993). Lakes in the Western Kunlun Moutain Areas. *Oceannol. Liminol. Sinica.* 24 (1), 37–44. (in Chinese with English abstract).

Li, S. J., Zheng, B. X., and Jiao, K. Q. (1991). Preliminary Research on Lacustrine deposit and lake Evolution on the South Slope of the Western Kunlun Mountains. *Scientia Geograp. Sinica.* 11 (4), 308–314. (in Chinese with English abstract). 10.13249/j.cnki.sgs.1991.04.306.

Liu, C., Zhao, Q., and Wang, P. (2001). Correlation between Carbon and Oxygen Isotopic Ratios of Lacustrine Carbonates and Types of Oil-Producing Paleolake. *Geochimica* 30 (4), 363–367. (In Chinese with English abstract). doi:10.19700/j.0379-1726.2001.04.009

Liu, W., Li, X., Zhang, L., An, Z., and Xu, L. (2009). Evaluation of Oxygen Isotopes in Carbonate as an Indicator of lake Evolution in Arid Areas: The Modern Qinghai Lake, Qinghai-Tibet Plateau. *Chem. Geology.* 268, 126–136. doi:10.1016/j.chemgeo.2009.08.004

Liu, X. Q., Shen, J., Wang, S. M., Zhang, E. L., and Cai, Y. F. (2003). A 16000-Year Paleoclimatic Record Derived from Authigenetic Carbonate of Lacustrine Sediment in Qinghai Lake. *Geolog. China Univer.* 9 (1), 38–46. (In Chinese with English abstract). doi:10.16108/j.issn1006-7493.2003.01.005

MacDonald, G. (2011). Potential Influence of the Pacific Ocean on the Indian Summer Monsoon and Harappan Decline. *Quat. Int.* 229 (1–2), 140–148. doi:10.1016/j.quaint.2009.11.012

Marcott, S. A., Shakun, J. D., Clark, P. U., and Mix, A. C. (2013). A Reconstruction of Regional and Global Temperature for the Past 11,300 Years. *Science* 339, 1198–1201. doi:10.1126/science.1228026

McCormack, J., Nehrke, G., Jöns, N., Immenhauser, A., and Kwiecien, O. (2019). Refining the Interpretation of Lacustrine Carbonate Isotope Records: Implications of a Mineralogy-specific Lake Van Case Study. *Chem. Geology.* 513, 167–183. doi:10.1016/j.chemgeo.2019.03.014

Mehrotra, N., Shah, S. K., Basavaiah, N., Laskar, A. H., and Yadava, M. G. (2019). Resonance of the '4.2ka Event' and Terminations of Global Civilizations during the Holocene, in the Palaeoclimate Records Around PT Tso Lake, Eastern Himalaya. *Quat. Int.* 507, 206–216. doi:10.1016/j.quaint.2018.09.027

Morrill, C., Overpeck, J. T., Cole, J. E., Liu, K.-b., Shen, C., and Tang, L. (2006). Holocene Variations in the Asian Monsoon Inferred from the Geochemistry of lake Sediments in central Tibet. *Quat. Res.* 65, 232–243. doi:10.1016/j.yqres.2005.02.014

Mügler, I., Gleixner, G., Günther, F., Mäusbacher, R., Daut, G., Schütt, B., et al. (2010). A Multi-Proxy Approach to Reconstruct Hydrological Changes and Holocene Climate Development of Nam Co, Central Tibet. *J. Paleolimnol* 43, 625–648. doi:10.1007/s10933-009-9357-0

Murphy, J. T., Lowenstein, T. K., and Pietras, J. T. (2014). Preservation of Primary lake Signatures in Alkaline Earth Carbonates of the Eocene Green River Wilkins Peak-Laney Member Transition Zone. *Sediment. Geology.* 314, 75–91. doi:10.1016/j.sedgeo.2014.09.005

Owen, L. A., and Dortch, J. M. (2014). Nature and Timing of Quaternary Glaciation in the Himalayan-Tibetan Orogen. *Quat. Sci. Rev.* 88, 14–54. doi:10.1016/j.quascirev.2013.11.016

Owen, L. A. (2009). Latest Pleistocene and Holocene Glacier Fluctuations in the Himalaya and Tibet. *Quatern. Sci. Rev.* 28 (21-22), 2150–2164. doi:10.1016/j.quascirev.2008.10.020

Pan, B., Yi, C., Jiang, T., Dong, G., Hu, G., and Jin, Y. (2012). Holocene lake-level Changes of Linggo Co in central Tibet. *Quat. Geochronol.* 10, 117–122. doi:10.1016/j.quageo.2012.03.009

Pang, H., Hou, S., Zhang, W., Wu, S., Jenk, T. M., Schwikowski, M., et al. (2020). Temperature Trends in the Northwestern Tibetan Plateau Constrained by Ice Core Water Isotopes over the Past 7,000 Years. *J. Geophys. Res. Atmos.* 125, e2020JD032560. doi:10.1029/2020jd032560

Qiao, B., and Zhu, L. (2019). Difference and Cause Analysis of Water Storage Changes for Glacier-Fed and Non-glacier-fed Lakes on the Tibetan Plateau. *Sci. Total Environ.* 693, 133399. doi:10.1016/j.scitotenv.2019.07.205

Qiao, B., Zhu, L., Wang, J., Ju, J., Ma, Q., and Liu, C. (2017). Estimation of Lakes Water Storage and Their Changes on the Northwestern Tibetan Plateau Based on Bathymetric and Landsat Data and Driving Force Analyses. *Quat. Int.* 454, 56–67. doi:10.1016/j.quaint.2017.08.005

Rao, W., Chen, J., Yang, J., Ji, J., and Zhang, G. (2009). Sr Isotopic and Elemental Characteristics of Calcites in the Chinese Deserts: Implications for Eolian Sr

Transport and Seawater Sr Evolution. *Geochimica et Cosmochimica Acta* 73, 5600–5618. doi:10.1016/j.gca.2009.06.028

Rasmussen, S. O., Vinther, B. M., Clausen, H. B., and Anderson, K. K. (2007). Early Holocene Climate Oscillations Recorded in Three Greenland Ice Cores. *Quat. Sci. Rev.* 26 (3), 1907–1914. doi:10.1016/j.quascirev.2007.06.015

Reimer, P. J., Bard, E., Bayliss, A., Beck, J. W., Blackwell, P. G., Ramsey, C. B., et al. (2013). IntCal13 and Marine13 Radiocarbon Age Calibration Curves 0-50,000 Years Cal BP. *Radiocarbon* 55 (4), 1869–1887. doi:10.2458/azu_js_rc.55.16947

Rivadeneyra, M. A., Martín-Algarra, A., Sánchez-Navas, A., and Martín-Ramos, D. (2006). Carbonate and Phosphate Precipitation byChromohalobacter Marismortui. *Geomicrobiology J.* 23 (1), 1–13. doi:10.1080/01490450500398245

Shapley, M. D., Ito, E., and Donovan, J. J. (2005). Authigenic Calcium Carbonate Flux in Groundwater-Controlled Lakes: Implications for Lacustrine Paleoclimate Records. *Geochimica et Cosmochimica Acta* 69 (10), 2517–2533. doi:10.1016/j.gca.2004.12.001

Shen, J., Liu, X. Q., aWang, S. M., and Matsumoto, R. (2005). Palaeoclimatic Changes in the Qinghai Lake Area during the Last 18,000 Years. *Quatern. Internat.* 136 (1), 131–140. doi:10.1016/j.quaint.2004.11.014

Shi, X., Kirby, E., Furlong, K. P., Meng, K., Robinson, R., Lu, H., et al. (2017). Rapid and Punctuated Late Holocene Recession of Siling Co, central Tibet. *Quat. Sci. Rev.* 172, 15–31. doi:10.1016/j.quascirev.2017.07.017

Solomina, O. N., Bradley, R. S., Hodgson, D. A., Ivy-Ochs, S., Jomelli, V., Mackintosh, A. N., et al. (2015). Holocene Glacier Fluctuations. *Quat. Sci. Rev.* 111, 9–34. doi:10.1016/j.quascirev.2014.11.018

Steinke, S., Mohtadi, M., Prange, M., Varma, V., Pittauerova, D., and Fischer, H. W. (2014). Mid- to Late-Holocene Australian-Indonesian Summer Monsoon Variability. *Quat. Sci. Rev.* 93, 142–154. doi:10.1016/j.quascirev.2014.04.006

Talbot, M. R. (1990). A Review of the Palaeohydrological Interpretation of Carbon and Oxygen Isotopic Ratios in Primary Lacustrine Carbonates. *Chem. Geology. Isotope Geosci. section* 80 (4), 261–279. doi:10.1016/0168-9622(90)90009-2

Thompson, L. G. (2000). Ice Core Evidence for Climate Change in the Tropics: Implications for Our Future. *Quat. Sci. Rev.* 19 (1–5), 19–35. doi:10.1016/s0277-3791(99)00052-9

Thompson, L. G., Yao, T., Davis, M. E., Henderson, K. A., Mosley-Thompson, E., Lin, P.-N., et al. (1997). Tropical Climate Instability: the Last Glacial Cycle from a Qinghai-Tibetan Ice Core. *Science* 276, 1821–1825. doi:10.1126/science.276.5320.1821

Thompson, L. G., Yao, T., Davis, M. E., Mosley-Thompson, E., Wu, G., Porter, S. E., et al. (2018). Ice Core Records of Climate Variability on the Third Pole with Emphasis on the Guliya Ice Cap, Western Kunlun Mountains. *Quat. Sci. Rev.* 188, 1–14. doi:10.1016/j.quascirev.2018.03.003

Wang, N., Liu, W. G., Xu, L. M., and An, Z. S. (2008). Oxygen Isotopic Compositions of Carbonates of Modern Surface Lacustrine Sediments and Their Affecting Factors in Tibet Plateau. *Quatern. Sci.* 28, 591–600.

Wang, Z., Gaetani, G., Liu, C., and Cohen, A. (2013). Oxygen Isotope Fractionation between Aragonite and Seawater: Developing a Novel Kinetic Oxygen Isotope Fractionation Model. *Geochimica et Cosmochimica Acta* 117, 232–251. doi:10.1016/j.gca.2013.04.025

Warren, J. (2000). Dolomite: Occurrence, Evolution and Economically Important Associations. *Earth Sci. Rev.* 52, 1–81. doi:10.1016/s0012-8252(00)00022-2

Warren, J. K. (1989). *Evaporite Sedimentology: Importance in Hydrocarbon Accumulation*. Englewood Cliffs, NJ: Prentice-Hall, 1–37.

Wei, K., and Gasse, F. (1999). Oxygen Isotopes in Lacustrine Carbonates of West China Revisited: Implications for post Glacial Changes in Summer Monsoon Circulation. *Quat. Sci. Rev.* 18, 1315–1334. doi:10.1016/s0277-3791(98)00115-2

Wünnemann, B., Yan, D., Andersen, N., Riedel, F., Zhang, Y., Sun, Q., et al. (2018). A 14 Ka High-Resolution δ18O lake Record Reveals a Paradigm Shift for the Process-Based Reconstruction of Hydroclimate on the Northern Tibetan Plateau. *Quat. Sci. Rev.* 200, 65–84. doi:10.1016/j.quascirev.2018.09.040

Xiao, J., Zhang, S., Fan, J., Wen, R., Xu, Q., Inouchi, Y., et al. (2019). The 4.2 Ka Event and its Resulting Cultural Interruption in the Daihai Lake basin at the East Asian Summer Monsoon Margin. *Quat. Int.* 527, 87–93. doi:10.1016/j.quaint.2018.06.025

Xu, T., Zhu, L., Lü, X., Ma, Q., Wang, J., Ju, J., et al. (2019). Mid- to Late-Holocene Paleoenvironmental Changes and Glacier Fluctuations Reconstructed from the Sediments of Proglacial lake Buruo Co, Northern Tibetan Plateau. *Palaeogeogr. Palaeoclimatol. Palaeoecol.* 517, 74–85. doi:10.1016/j.palaeo.2018.12.023

Xu, X., and Yi, C. (2017). Timing and Configuration of the Gongga II Glaciation in the Hailuogou valley, Eastern Tibetan Plateau: A Glacier-Climate Modeling Method. *Quat. Int.* 444, 151–156. doi:10.1016/j.quaint.2017.01.011

Yang, M., Yao, T., Wang, H., and Gou, X. (2006). Climatic Oscillations over the Past 120kyr Recorded in the Guliya Ice Core, China. *Quat. Int.* 154-155, 11–18. doi:10.1016/j.quaint.2006.02.015

Yang, R. M., Zhu, L. P., Wang, J. B., Ju, J. T., Ma, Q. F., Turner, F., et al. (2017). Spatiotemporal Variations in Volume of Closed Lakes on the Tibetan Plateau and Their Climatic Responses from 1976 to 2013. *Climatic Change* 140 (3-4), 621–633. doi:10.1007/s10584-016-1877-9

Yao, T., Masson-Delmotte, V., Gao, J., Yu, W., Yang, X., Risi, C., et al. (2013). A Review of Climatic Controls on δ18O in Precipitation over the Tibetan Plateau: Observations and Simulations. *Rev. Geophys.* 51, 525–548. doi:10.1002/rog.20023

Yao, T., Thompson, L., Yang, W., Yu, W., Gao, Y., Guo, X., et al. (2012). Different Glacier Status with Atmospheric Circulations in Tibetan Plateau and Surroundings. *Nat. Clim Change* 2 (9), 663–667. doi:10.1038/nclimate1580

Yao, T., Xue, Y., Chen, D., Chen, F., Thompson, L., Cui, P., et al. (2019). Recent Third Pole's Rapid Warming Accompanies Cryospheric Melt and Water Cycle Intensification and Interactions between Monsoon and Environment: Multidisciplinary Approach with Observations, Modeling, and Analysis. *Bull. Am. Meteorolog. Soc.* 100 (3), 423–444. doi:10.1175/bams-d-17-0057.1

Yu, W. S., Tian, L. D., Risi, C., Yao, T. D., Ma, Y. M., Zhao, H. B., et al. (2016). δ^{18}O Records in Water Vapor and an Ice Core from the Eastern Pamir Plateau: Implications for Paleoclimate Reconstructions. *Earth Planetary Sci. Lett.* 456, 146–156. doi:10.1016/j.epsl.2016.10.001

Yuan, D., Cheng, H., Edwards, R. L., Dykoski, C. A., Kelly, M. J., Zhang, M. L., et al. (2004). Timing, Duration, and Transitions of the Last Interglacial Asian Monsoon. *Science* 304, 575–578. doi:10.1126/science.1091220

Zheng, D. (1996). The System of Physico-Geographical Regions of the Qinghai-Xizang (Tibet) Plateau. *Sci. China Ser. D-Earth Sci.* 39 (4), 410–417.

Zheng, X. Y., Zhang, M. G., Xu, C., and Li, B. X. (2002). *Salt Lake of China*. Beijing: China Science Press.

Zhu, L., Wang, J., Lin, X., Ju, J. T., Xie, M. P., Li, M. H., et al. (2008). Environmental Changes Reflected by Core Sediments since 8.4 Ka in Nam Co, Central Tibet of China. *Holocene* 185, 831–839. doi:10.1177/0959683608091801

Zhu, L., Zhen, X., Wang, J., Lü, H., Xie, M., Kitagawa, H., et al. (2009). A ~30,000-year Record of Environmental Changes Inferred from Lake Chen Co, Southern Tibet. *J. Paleolimnol.* 42, 343–358. doi:10.1007/s10933-008-9280-9

Conflict of Interest: The authors declare that the research was conducted in the absence of any commercial or financial relationships that could be construed as a potential conflict of interest.

frontiers in Earth Science

ORIGINAL RESEARCH
published: 05 July 2021
doi: 10.3389/feart.2021.687376

Sources, Distribution and Paleoenvironmental Application of Fatty Acids in Speleothem Deposits From Krem Mawmluh, Northeast India

M. S. Kalpana[1], **Joyanto Routh**[2]*, **Susanne Fietz**[3], **Mahjoor A. Lone**[4,5] **and Augusto Mangini**[6]

[1]CSIR-National Geophysical Research Institute, Hyderabad, India, [2]Department of Thematic Studies-Environmental Change, Linköping University, Linköping, Sweden, [3]Department of Earth Sciences, Stellenbosch University, Stellenbosch, South Africa, [4]Department of Geosciences, National Taiwan University, Taipei, Taiwan, [5]Research Center for Future Earth, National Taiwan University, Taipei, Taiwan, [6]Institut für Umweltphysik, INF 229, Heidelberg, Germany

Edited by:
Steven L. Forman,
Baylor University, United States

Reviewed by:
James M. Fulton,
Baylor University, United States
Guoqiang Li,
Lanzhou University, China

***Correspondence:**
Joyanto Routh
joyanto.routh@liu.se

Specialty section:
This article was submitted to
Quaternary Science, Geomorphology,
and Paleoenvironment,
a section of the journal
Frontiers in Earth Science

Received: 29 March 2021
Accepted: 21 June 2021
Published: 05 July 2021

Citation:
Kalpana MS, Routh J, Fietz S, Lone MA
and Mangini A (2021) Sources,
Distribution and Paleoenvironmental
Application of Fatty Acids in
Speleothem Deposits From Krem
Mawmluh, Northeast India.
Front. Earth Sci. 9:687376.
doi: 10.3389/feart.2021.687376

Integrated multiproxy geochemical studies are essential to reconstruct the paleoenvironment through different time scales. Pristine terrestrial archives such as speleothems provide an excellent opportunity to study these changes by measuring the stable isotope and biomarker trends preserved in these records. Here, we investigated fatty acids in drip water, moonmilk, and a stalagmite (KM-1) retrieved from Krem Mawmluh in northeast India to constrain the sources and distribution of these compounds. Besides, we tested their compatibility with established glycerol dialkyl glycerol tetraethers and stable isotope proxies in KM-1 to probe the use of fatty acid-derived proxies for paleoclimate reconstruction. We observe a similar composition of fatty acids in drip water as well as the cave deposits with significantly higher concentrations of fatty acids in drip water (10.6–124 μg/L) and moonmilk (1.32–16.5 μg/g) compared to the stalagmite (0.67–2.09 μg/g). In KM-1 stalagmite, fatty acids and the presence of azelaic acid transported from surface soils indicate that these compounds are derived from bacterial activity both within the cave and the overlying soil cover. The branched C_{15} fatty acid index (*iso*+*anteiso* C_{15}/nC_{15}) increases during the Holocene, suggesting enhanced microbial production under warm/wet conditions. Fluctuations in the fatty acid indices coincide with abrupt shifts in the TEX_{86} and BIT proxies reflecting the warm/wet Holocene and cold/dry Late Pleistocene. These trends imply the potential use of fatty acids for reconstructing past climate changes in speleothems but need more analytical reference points to provide statistical data.

Keywords: drip water, moonmilk, stalagmite, fatty acids, paleoclimate, Indian monsson

INTRODUCTION

Stalagmites are promising terrestrial archives for past climate reconstructions. They are undisturbed by human activities, can be precisely dated, and record environmental information on the decadal, centennial, or millennial scales (Fleitmann et al., 2003; McDermott, 2004; Lachniet 2009). Stable oxygen isotope ($\delta^{18}O$) and trace element records in stalagmites from around the globe have been studied for climate reconstruction at very high temporal resolution (e.g., Fleitmann et al., 2003; Fairchild and Treble, 2009; Cheng et al., 2012; Dutt et al., 2015). As outcomes of these global efforts, large databases of oxygen and carbon isotope records have been created to provide detailed information to climate researchers (Atsawawaranunt et al., 2018; Comas-Bru et al., 2020).

Stalagmite based oxygen isotope investigations have been particularly successful in gaining new insights on climate variability in Southeast Asia and adjoining regions where monsoons play a dominant role (Lone et al., 2014; Dutt et al., 2015; Sinha et al., 2015; Band et al., 2018; Gautam et al., 2019). The $\delta^{18}O$ based climate signals recorded in stalagmites are, however, prone to alteration due to many interrelated factors such as continental effect, moisture source(s), air mass history, temperature, rainout, altitude, orographic effects, evaporation, and mixing of source waters (Lachniet 2009; Cheng et al., 2016). The actual impact of these effects on $\delta^{18}O$ trends is highly site-specific and shows varying sensitivities to global vs. local scale changes. Therefore, climate records generated using stalagmites must not be predominantly based on a single or few inter-dependent proxies. Instead, researchers should expand the scope by incorporating multiple independent proxies to make the emergent climate signals far more reliable (Blyth et al., 2008; Blyth et al., 2011; Apaéstegui et al., 2014).

The study of bulk and molecular organic proxies preserved in speleothems has gained momentum over the last 2 decades to infer spatiotemporal changes in the environment (Rousseau et al., 1995; McGarry and Baker, 2000; Xie et al., 2003; Blyth et al., 2007; Rushdi et al., 2011; Yang et al., 2011; Blyth and Schouten, 2013; Blyth et al., 2014; Blyth et al., 2016; Heidke et al., 2018; Baker et al., 2019). In particular, the application of various molecular organic proxies (lipids derived from microorganisms or transported from soil zone) in speleothems have shown promising outcomes (Blyth et al., 2016). This inference is based on the premise that microbial communities adapt to changing environmental conditions leaving distinct organic signatures. These communities inhabit either inside the caves or the overlying soil and epikarst zones. Researchers have focused on the optimization of various sample preparation methods that significantly improved the temporal resolution as well as yields of the targeted lipids to interpret more nuanced source changes (Blyth et al., 2006; Blyth et al., 2007; Huang et al., 2008; Wang et al., 2012; Bosle et al., 2014). Hence, regardless of the low abundance of organic matter (0.01–0.30% of total carbon) and large sample requirement, multiple organic molecular markers, viz. *n*-alkanes, *n*-alkanols, fatty acids, *n*-alkan-2-ones, lignin, and tetraether membrane lipids (glycerol dialkyl glycerol tetraethers; GDGT), have been analyzed in stalagmites and applied to understand the source signals and reconstruct past climatic and environmental changes (Blyth et al., 2016; Heidke et al., 2018).

Xie et al. (2003) were the first to assess the lipid biomarker variations in a stalagmite from the Heshang Cave (HS2 stalagmite) in southern China. They compared the biomarker variation with alkenone-derived sea surface temperatures spanning from 21 to 10 ka BP. They observed that the high molecular weight (HMW) *n*-alkanols and *n*-alkan-2-ones originated from the surrounding vegetation, while the low molecular weight (LMW) *n*-alkanols and *n*-alkan-2-ones originated from soil organisms. The distinct shifts in the LMW/HMW lipid ratio in the source signal followed the sea surface temperature records indicating a local soil ecosystem response to global climate patterns. Xie et al. (2005) subsequently reported fatty acids derived from various source organisms from the same stalagmite. They indicated recognizing short-scale events such as the cold North Atlantic Heinrich event 1 in the fatty acid composition, e.g., by observing reduced degradation of monounsaturated fatty acids. This event coincided with elevated monounsaturated to saturated $C_{16:1}$/$C_{16:0}$ and $C_{18:1}$/$C_{18:0}$ ratios and low microbial activity (Xie et al., 2005). Their findings implied a temperature-dependent imprint in the paleo-lipid biomarker composition. Consistent with this idea, monitoring modern drip water from the Heshang Cave revealed a temperature-dependent signal in the ratio of $C_{16:1}$/$C_{16:0}$ and $C_{18:1}$/$C_{18:0}$ fatty acids (Li et al., 2011).

Yang et al. (2011) reported the distribution of GDGTs in soil, drip water, and stalagmites from the same cave. This study established that most GDGTs in stalagmites are derived from *in situ* microbial communities within the cave or vadose zone. They indicated a predominance of the isoprenoid GDGT crenarchaeol in stalagmites and weathered rock surfaces, whereas branched GDGTs were more abundant in the overlying soils. The results implied that source and depositional signals could be disentangled based on the distinct GDGT signals that were so far difficult to resolve with confidence. Recently, Huguet et al. (2018) applied GDGT based proxies in combination with high-resolution stable isotope data in stalagmite KM-1 (same stalagmite studied in the present work) from Krem Mawmluh in northeast India. They reconstructed the precipitation pattern resulting from the Indian Summer Monsoon activity in response to paleo-temperature changes from 22 to 6 ka BP. The outcome was a reliable temperature and precipitation reconstruction in KM-1 against which other biomarker proxies could be tested in the same stalagmite as in the present study.

Fatty acids are the dominant and most commonly occurring lipid biomarkers reported in stalagmites (Blyth et al., 2006; Huang et al., 2008; Xie et al., 2003; Xie et al., 2005). In particular, the unsaturated and branched LMW fatty acids have been used to reconstruct past temperature changes (Xie et al., 2005; Blyth et al., 2011). These LMW fatty acids thought to be derived from bacteria, plants, and fungi, can be transported from the overlying soil cover. Bacteria, however, not only produce fatty acids in the cave and soil but also control their degradation. Hence, the distribution of fatty acids may be influenced by temperature or moisture content in the soil zone and inside the cave (Blyth et al., 2011). Consequently, fatty acids have not been pursued widely as robust environmental proxies compared to the more source-specific biomarkers viz., *n*-alkanes, *n*-alkanols, *n*-alkan-2-ones. This study reports for the first time fatty acids examined in an array of samples collected from a karst environment such as drip water, moonmilk, and a stalagmite (KM-1) retrieved from Krem Mawmluh. Further, we traced the compositional changes, distribution, and source(s) of these compounds in the speleothems. We related this information to the paleotemperature and paleohydrological changes inferred earlier based on the GDGT, $\delta^{18}O$, and $\delta^{13}C$ signals in the stalagmite KM-1 (Huguet et al., 2018) to provide insights into the complex environmental changes since the Late Pleistocene.

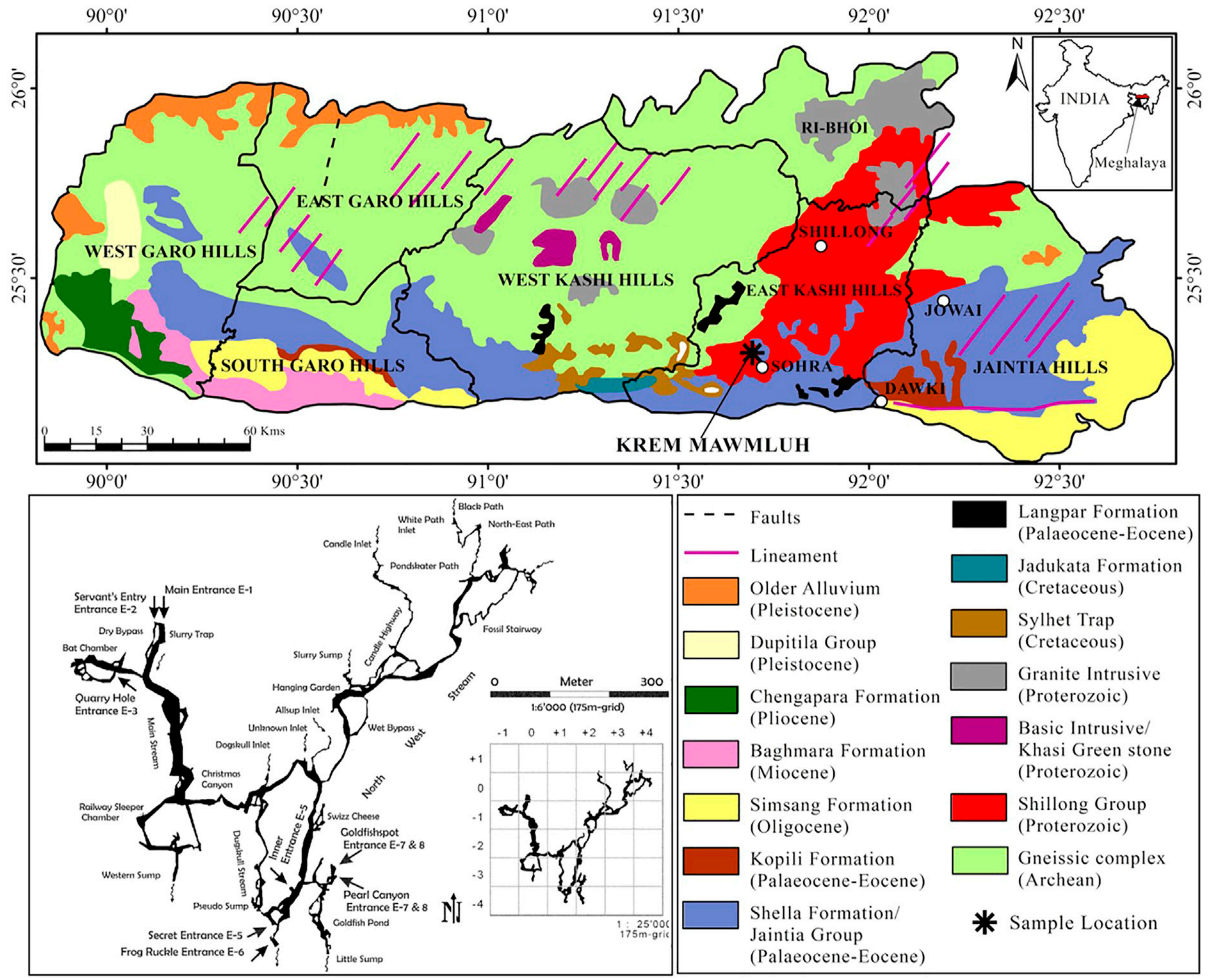

FIGURE 1 | Geological map showing the sampling location of KM-1 stalagmite and a sketch of Krem Mawmluh passageways inside the cave in Khasi Hills, Meghalaya (modified after the National Bureau of Soil Survey and Land Use Planning, 1996; Daly 2006).

Study Area

Some of the longest and deepest cave systems in the Indian subcontinent are located in Meghalaya in northeast India. Nearly 1,000 caves have developed in a 300 km long narrow belt of diverse sedimentary rocks along the state's southern and southeastern borders (Daly, 2006). Krem Mawmluh (Krem means cave in the local Khasi language) located in the Khasi Hills (25°07″; 25°41″N and 91°21″; 92°09″E, altitude 1,290 m) is one of these caves, which is ~7.1 km long and is listed as the fourth longest cave in India (**Figure 1**). The cave has been subject to many investigations in recent years (Baskar et al., 2011; Berkelhammer et al., 2012; Breitenbach et al., 2015; Dutt et al., 2015).

Lithologically, the Khasi Hills in Meghalaya consists of sandstone and conglomerate of the Jadukata formation (known for its rich uranium deposits) overlying the feldspathic sandstone of the Mahadek formation. The Sylhet limestone belt of the fossiliferous Eocene Shella formation (30–100 m thick) hosts Krem Mawmluh (**Figure 1**), overlain by a thin soil cover of 5–15 cm in thickness. The cave is overlain by 30–100 m thick and heavily karstified host rock consisting of limestone, sandstone, and a 40–100 cm thick coal layer. Krem Mawmluh is located near Sohra (Cherrapunji; **Figure 1**), the wettest place on Earth. The dominance of the Indian Summer Monsoon (ISM) characterizes this tropical region, receiving abundant rainfall (~12,000 mm) from June to September (Murata et al., 2007). The orographic rain results from clouds originating in the Bay of Bengal that drifts towards the Bangladesh plains. These clouds collide with the Khasi Hills and rise to the upper atmosphere to cool down and precipitate. Despite the heavy summer rainfall in Sohra, this region suffers from water shortage during most parts of the year, and precipitation in recent decades has decreased to 8,000–9,000 mm yr^{-1} (Bhaumik, 2009).

Krem Mawmluh has multiple entrances that lead inside the cave. The cave has beautiful ornamentation with many stalagmites and stalactite-filled hallways developed as a maze of sub-horizontal passageways. The secret entrance E-5 (**Figure 1**) offers a more accessible and safe path leading into a large chamber above the Goldfish Pond and remains isolated from floodwaters that fill large sections of the cave during heavy rainfall. In this large chamber, we retrieved the 87-cm long KM-1 stalagmite. Drip water seeps through the cracks or stalactites. A notable feature in the cave is the occurrence of sheer moonmilk and cave pearls, which are microcrystalline secondary mineral deposits found on the cave floor in isolated pockets (Baskar et al., 2011). Microbial analysis and scanning electron microscopy in KM moonmilk deposits indicated abundant bacterial population and calcified microbial filaments supporting the biogenic source of these deposits (ibid.). The cave also presents a unique habitat for bats, amphibians, insects, and plants (in the twilight zone). However, blasting of dynamite and pollution associated with intensive limestone mining by the cement factories near Krem Mawmluh have damaged several sections inside the cave (including the main entrance) and other nearby caves in Khasi Hills. Consequently, many of these caves and the unique and fragile ecosystems they support are very vulnerable to irreparable damage (Biswas, 2009).

MATERIALS AND METHODS

Sampling

We collected drip water samples in acid rinsed glass bottles from four locations on the way to the cave's inner chamber (near the Goldfish pond, **Figure 1**), representing both fast and slow drip rates. We made multiple trips to the cave within 1 week to transport speleothem samples and large volumes of water needed for lipid extraction. The total volume of drip water collected from the sites was 25 L in 3 days at S1, 24 L in 7 days at S2 and S4, and the total volume of water collected from site S3 was 2 L in 1 day. We also collected two moonmilk samples (MM-1 and MM-2) from the inner chamber where KM-1 was found and along the passageway leading into the Goldfish pond (**Figure 1**). The moonmilk slurry was collected with disposable gloves and forceps and then placed into sterilized 250 ml Schott Duran bottles in an icebox and transported to the lab. We stored the moonmilk samples at 4°C in the laboratory until analysis.

The stalagmite KM-1 was split along the growth axis from its center using a diamond drill. A detailed description of the stalagmite chronology and stable isotope analysis is reported in Huguet et al. (2018). Briefly, the U-Th dating of the sample was carried out by drilling samples at various intervals along its growth axis and analyzed on a Finnigan MAT 262 RPQ mass spectrometer. For stable C and O isotope analyses, samples were drilled at every 0.5 cm interval using a Proxxon dental drill and analyzed on a Delta Plus Advantage Isotope Ratio Mass Spectrometer coupled with a Kiel IV automatic carbonate device. The $\delta^{18}O$ and $\delta^{13}C$ values are reported in standard delta notation as per mil relative to the Vienna Pee Dee Belemnite (V-PDB) standard.

Lipid Extraction

Drip water: The water samples were processed the same day after returning from the cave. We used ENVI™–18 DSK Solid Phase Disk (glass fiber embedded with surface-modified silica (C18 bonded phase from Supelco) to extract lipid biomarkers from drip water samples. The disks were conditioned with dichloromethane (DCM) and ultra-pure water before passing the drip water. After passing the drip water, the ENVI™ disks were wrapped in aluminum foil and refrigerated at 4°C until further extraction. Within 2 weeks after all samples were taken to Sweden, the disks with organic matter sorbed to them were extracted with a mixture of DCM and methanol (9:1 v/v) using an automated solvent extractor (Dionex ASE 300) maintained at 1,000 psi and 100°C in the course of three extraction cycles. We then used the Buchi Syncore Solid Phase Extraction (SPE) module and Sigma Aldrich cartridges packed with 500 mg of aminopropyl stationary phase covered on the top and bottom with a PTFE frit (Russell and Werne, 2007) to separate the total lipid extracts (TLE) into neutral and acid fractions. The cartridges were pre-conditioned with four column volumes of 2:1 DCM: isopropanol mixture. After pre-conditioning, the TLE in DCM: isopropanol solution was loaded onto the cartridge and eluted with 15 ml of DCM: isopropanol (2: 1 v/v) and 15 ml of 2% acetic acid in diethyl ether for extracting the neutral and fatty acids, respectively. The neutral and fatty acid fractions were reduced under a gentle stream of nitrogen to dryness.

Moonmilk: We freeze-dried the moonmilk samples, and about 4 g of the sample was taken in the glass culture tubes to extract lipids following the Bligh and Dyer (BD) method (Bligh and Dyer, 1959). A mixture of 5 ml of chloroform, 10 ml methanol, and 4 ml deionized distilled water in the ratio of 1:2:0.8 was added and sonicated for 45 min. After sonication, the sample was centrifuged at 3,000 rpm for 5 min. The organic phase was pipetted into a fresh tube. Two more extractions were performed, and to the resultant extract, equal volumes of chloroform and water (5 ml) were added to separate the aqueous and organic phases. After removing the organic phase, the aqueous phase was extracted twice with 5 ml of chloroform. The organic phase containing the TLE was reduced under a gentle stream of nitrogen. Once the TLE was dry, it was re-dissolved in DCM and activated copper, and left overnight to remove elemental sulfur. The extract was transferred to a fresh vial, and the copper powder was rinsed with additional DCM to ensure that the TLE was recovered completely. After the lipid extraction, calcite was dissolved with 3 M HCl, and the dissolved lipids were extracted using 30 ml of DCM (30 ml × 5 times). The organic solvent in the lipid extract was concentrated by evaporation under reduced pressure using the Buchi Syncore concentrator. The lipids from dissolving the calcite and the TLE from the BD method were combined and further reduced under a nitrogen stream. The extract was fractionated using aminopropyl cartridges as described earlier for the drip water.

Stalagmite: The stalagmite was thoroughly cleaned in deionized filtered water followed by DCM to remove any surface contaminants. The samples for lipid analysis were drilled from the stalagmite along the growth axis using a Proxxon dental drill. We extracted the TLE from ~10 g of powdered sample drilled from 17 spots along the growth axis. The stalagmite powder was spiked with 20 µl of 500 mg/L deuterated-hexatriacontane as recovery standard, digested with 3 M HCl (70 ml), and reflux heated (see Blyth et al., 2006). After cooling, the total lipids were extracted in a separating funnel using 30 ml of DCM (30 ml × 5 times). The solvent evaporation was performed under reduced pressure using the Buchi Syncore concentrator.

Derivatisation and Quantification

The fatty acid fraction from drip waters and moonmilk and the TLE from stalagmite was reduced to 1 ml and methylated with 3 ml of 14% BF_3-methanol at 70°C for 2 h to convert the carboxylic groups to fatty acid methyl esters. After cooling overnight at room temperature and destruction of excessive BF_3 complex with ultra-pure deionized water (3 ml), the methylated solution was extracted with hexane (2 ml × 6 times). The hexane extract was reduced to near dryness under a high-grade nitrogen stream. The extract was then derivatized by heating at 70°C for 2 h in a sealed reaction vial with 30 µl of BSTFA (N, O-bis trimethylsilyl trifluoroacetamide) and left overnight (Blyth et al., 2006). The derivatized extract was reduced to dryness under nitrogen and reconstituted in 150 µl of DCM, spiked with deuterated-tetracosane and deuterated-eicosanoic acid methyl ester before analysis. The two procedural blanks and a $CaCO_3$ blank (from Merck) showed minor contamination from short-chain, mainly C_{16} and C_{18} fatty acids (**Supplementary Figure S3**). The average concentrations of C_{16} and C_{18} fatty acids in procedural blanks were 0.32 µg/g and 0.13 µg/g, respectively, and similar to the values reported by Blyth et al. (2006) and Huang et al. (2008). The $CaCO_3$ blanks indicated lower values of C_{16} and C_{18} fatty acids (0.02 µg/g and 0.01 µ/g, respectively).

Chronology

The age model for stalagmite KM-1 that was derived from twelve ^{230}Th data in stratigraphic sequence published previously in Huguet et al. (2018) is adopted here.

GCMS Analysis

We analyzed the biomarkers on an Agilent 6890N GC coupled to a 5,973 inert mass selective detector. The GC was equipped with a J&W DB-5 (5% phenyl, 95% dimethyl polysiloxane) fused silica capillary column (30 m length × 0.25 mm inner diameter × 0.25 µm film thickness). One microliter of the sample was injected in splitless mode using helium as a carrier gas; the injector temperature was set at 300°C. The operating conditions in the GC oven were as follows: the initial temperature was at 35°C with 1 min hold time followed by ramping from 35 to 130°C at 20°C/min; ramping from 130 to 320°C was at 4°C/min with 15 min hold time. The mass detector was operated in full scan mode with a mass range (*m/z*) of 50–600 Da under electron impact ionization. The ionization energy was set at 70 eV, source temperature at 230°C, quadrupole temperature at 150°C, and interface temperature at 310°C (Baker et al., 2016). The individual lipid compounds were identified based on their retention times using a standard mixture of fatty acid methyl esters from Sigma Aldrich and matching the mass spectra with the NIST and AOCS Lipid Library. Quantification of fatty acids was based on the GCMS response and comparison of peak areas with known quantities of deuterated eicosanoic acid methyl ester added to the samples before GCMS analysis.

The distribution of fatty acids was used to 1) differentiate the source inputs for organic matter derived from overlying vegetation, algae, as well as microbes including bacteria and fungi within the soil or cave (Ruess et al., 2002; Ouyang et al., 2015; Wang et al., 2019), and 2) reconstruct paleoenvironmental conditions such as temperature and precipitation (**Table 1**).

RESULTS AND DISCUSSION

Distribution and Sources of Fatty Acids

Drip Water

The total fatty acid concentration in drip water samples S1, S2, and S4 range from 10.6–14.6 µg/L. In contrast, S3 shows an anomalously high concentration of 123 µg/L (**Table 2**). Notably, concentrations of fatty acids in the Krem Mawmluh drip water S1, S2, and S4 are similar to the fatty acid concentrations previously reported for the Heshang cave ($\sum C_{12}$–C_{20} 13.8 µg/L; Li et al., 2011) and *Herbstlabyrinth-Adventhöhle Cave System* ($\sum C_{12}$–C_{20} 13.7 µg/L; Bosle et al., 2014) during November and January, respectively. The LMW fatty acids ($<C_{20}$) constitute 91–95% of the total fatty acid pool (**Table 2**). These LMW compounds are dominated by *n*-C_{16} and C_{18} fatty acids (**Supplementary Figure S1**). The total concentration of the LMW fatty acids is an order of magnitude higher than all HMW fatty acids ($>C_{20}$) in S2 and S4. In samples S1 and S3, LMW fatty acids concentration is two orders of magnitude higher than HMW fatty acids (**Table 2**).

We attribute the difference in concentration and composition of fatty acids in drip water to water flow (rate of discharge) at the sampling point. Rushdi et al. (2011) reported that slow infiltration of drip water (long duration) increases the residence time and microbial activity in the overlying soil cover resulting in higher input of soil organic matter indicated by the high concentrations of HMW and LMW fatty acids. Estimated drip rates in Krem Mawmluh are 2 L/d in S3, which increased to 3.4 L/d in S4, 4L/d in S2, and 8.3 L/d in S1 (**Table 2**). The slowest drip rate (S3) yielded the highest total fatty acid concentration, whereas the fastest drip rate (S1) produced the lowest total fatty acid concentration in Krem Mawmluh. The drip rate may also explain the abundance of regular n-C_{15} (843 ng/L, 871 ng/L) and n-C_{15} branched fatty acids (39 ng/L, 32 ng/L; **Supplementary Table S2**) in samples S2 and S4 (moderate drip rates) that are higher than in S1 (fastest drip rate), but lower than in S3 (slowest drip rate).

While the fatty acid concentration arguably results from infiltration rates, microbial activity during infiltration is also possible. For example, the regular *n*-C_{15} fatty acids and their branched homologs are derived from bacterial sources (Bianchi and Canuel, 2011; Zhao et al., 2014), and the microbial activity is expressed as the *n*-C_{15} fatty acid index, i.e., branched C_{15} fatty acid (cf. (*iso+anteiso*)C_{15}/*n*-C_{15}). This index shows higher values for S2 and S4 samples (0.05 and 0.04) than S1 and S3, suggesting higher microbial activity. In addition, certain *n*-alkanedioic acids point to a link between infiltration rate and microbial activity. The *n*-alkanedioic acids consist of suberic, azelaic, sebacic, and undecanedioic acids with a higher abundance of azelaic acid in S1

TABLE 1 | Fatty acid proxies and interpretation about organic matter sources and paleoenvironment conditions.

Fatty acid proxies	Source/paleoenvironment information	References
Carbon Preference Index (CPI) = $\sum C_{8–32}$ (even)/$\sum C_{9–31}$ (odd)	Low CPI–increased microbial activity-warm and wet climate High CPI–reduced microbial activity-cold and dry climate	Cranwell et al. (1987), Zhou et al. (2005), Zheng et al., 2007, Zhao et al. (2014)
LMW/HMW ratio = $\sum C_{8–18}$ (even)/$\sum C_{20–34}$ (even)	High LMW/HMW–algal or bacterial source with abundant short-chain n-fatty acids Low LMW/HMW–terrigenous higher plants dominated with long-chain fatty acids	Zheng et al., 2007, Zhou et al. (2005)
Average Chain Length ($ACL_{14–32}$) = $\sum (C_n \times n)/\sum C_n$	ACL = 16–17–algal/bacterial source ACL > 19–terrigenous and submerged plant sources	Ouyang et al. (2015), Liu and Liu (2017)
Algal/Terrigenous ratios $ATR_{14\text{-}18}$ = (C14+C16+C18)/(C14+C16+C18+C20+C22+C24+C26+C28+C30) $ATR_{26–30}$ = (C26+C28+C30)/(C14+C16+C18)	$ATR_{14–18}$ > 0.80–algal sources <0.80–terrestrial and submerged plant sources $ATR_{26–30}$ < 0.10 for algal sources >0.1 for terrestrial and submerged plant sources	Liu and Liu (2017)
$C_{16:1}/C_{16}$	Microbial source High ratio–reduced microbial alteration-cold and dry climate Low ratio–enhanced microbial alteration-warm and wet climate	Kawamura and Gagosian (1987), Xie et al. (2005), Zhou et al. (2005), Zhao et al. (2014)
$C_{18:1}/C_{18}$, $C_{18:2}/C_{18}$	Microbial source High ratio–reduced microbial alteration-cold and dry climate Low ratio–enhanced microbial alteration-warm and wet climate	Kawamura and Gagosian (1987), Xie et al. (2005), Zhou et al. (2005), Zhao et al. (2014), Wang et al. (2016)
(*iso*+*anteiso*)C_{15}/nC_{15}	Microbial source High ratio–enhanced microbial alteration-warm and wet climate Low ratio–reduced microbial alteration-cold and dry climate	Zhao et al. (2014), Bianchi and Canuel. (2011)
Azelaic Acid (1, 9 Nonanedioic Acid Dimethyl Ester	Bacterial oxidation of unsaturated fatty acids ($C_{18:1}$) High–enhanced microbial alteration-warm and wet climate Low–reduced microbial alteration-cold and dry climate	Kawamura and Gagosian. (1987), Kawamura et al. (1999), Volkman (2006), Pokhrel et al. (2015), Bianchi and Canuel. (2011)

(20.0 ng/L) compared to S2 (0.60 ng/L) and S4 (13.9 ng/L) (**Table 2**). In particular, the high concentrations of azelaic acid and $C_{18:1}$ in S1 (**Table 2**) imply a short residence time for infiltrating water due to the fast drip rate, which results in low microbial activity and rapid transport of azelaic acid from the epikarst zones or surface soils. Admittedly, this reasoning does not apply to the high azelaic acid (136 ng/L) and $C_{18:1}$ (8.9 ng/L) concentration observed in sample S3 (**Table 2**) that has the slowest drip rate. It appears that in S3, the azelaic acid and $C_{18:1}$ concentrations remain high (mostly undegraded) despite a relatively long residence time in the epikarst or surface soil.

The distribution and chain length of fatty acids can trace organic matter sources from a wide range such as bacteria, algae, and terrestrial higher plants in lakes and other aquatic environments (Ouyang et al., 2015; Liu and Liu 2017). An algal origin is less likely in speleothems, and the two main end-members for LMW fatty acids are microbes and higher plants (Wang et al., 2019). Due to lack of information, we could not differentiate bacterial vs. fungal sources of LMW fatty acids in the speleothems. Therefore, we refer to these compounds as having a microbial origin. We have included the values of different fatty acid indices in drip water samples in **Table 2**. In all four drip water samples, the carbon preference index (CPI; ranges between 8 and 12) and LMW/HMW ratio (ranges between 10 and 20) providing the first indication of dominant inputs of microbial fatty acids. The indices varied again between S1/S3 and S2/S4 samples, revealing possible links with the infiltration rate and organisms producing fatty acids. The CPI and LMW/HMW ratios in S2 and S4 (CPI: 8.2–8.8; LMW/HMW: 10.6–13.1) are low compared to S1 (CPI: 11.7; LMW/HMW: 20.1;

TABLE 2 | Total fatty acid concentrations (μg/L) and molecular indices of fatty acids in Krem Mawmluh Drip Water.

Drip water	S1	S2	S3	S4
Duration of drip water collection	3 days	6 days	1 day	7 days
Total volume of drip water	25 L	24 L	2 L	24 L
Drip water rate	8.3 L/d	4 L/d	2 L/d	3.4 L/d
Total lipid concentration (μg/L)	10.6	14.6	123.7	14.5
LMW-even	9,163	11,833	107,019	11,516
HMW-even	455	903	6,102	1,090
$\text{LMW}_{\text{even}}/\text{HMW}_{\text{even}}$	20.1	13.1	17.5	10.6
LMW-total	10.1	13.6	116.9	13.25
HMW-total	0.49	1.0	6.83	1.27
LMW%	95	93	94	91
HMW%	5	7	6	9
$\text{CPI}_{\text{Total}}$	11.7	8.8	12.5	8.2
$\text{ACL}_{8–32}$	16.5	16.7	16.6	16.9
$\text{ATR}_{14–18}$	0.95	0.92	0.95	0.91
$\text{ATR}_{26–30}$	0.00	0.02	0.01	0.02
Branched C_{15} fatty acid index	0.001	0.05	0.001	0.04
Azelaic acid (μg/L)	0.020	0.001	0.136	0.014

TABLE 3 | Molecular indices of fatty acids in Krem Mawmluh moonmilk.

n-Alkanoic acid indices	MM-1	MM-2
LMW_{even}	1.06	13.3
HMW_{even}	0.13	1.46
$\text{LMW}_{\text{even}}/\text{HMW}_{\text{even}}$	8.26	9.10
Total LMW	1.16	14.7
Total HMW	0.15	1.79
Total fatty acids (μg/g)	1.31	16.5
Totalfatty acids (ng/g)	1,310	16,500
LMW%	88.4	89.2
HMW%	11.6	10.8
$\text{ACL}_{8–32}$	17.4	17.5
$\text{ATR}_{14–18}$	0.89	0.9
$\text{ATR}_{26–30}$	0.08	0.05
$\text{CPI}_{\text{Total}}$	14.5	11.8

Table 2) drip water samples. The primary sources of short chain LMW fatty acids in drip water are most likely from *in situ* microbial production in the percolating surface/groundwater and soil zone, while the longer chain HMW fatty acids are mainly derived from surface vegetation (Blyth et al., 2016). Thus the low CPI and LMW/HMW ratios imply enhanced soil microbial activity and higher inputs of HMW fatty acids from the surface (Cranwell et al., 1987, Zheng et al., 2007), reflecting the slow drip rate and longer residence time at S2 and S4 sites. However, the high CPI and LMW/HMW ratio in the S3 sample (CPI: 12.5; LMW/HMW: 17.5; **Table 2**), which has the slowest drip rate, is puzzling and points to a differentiated link between source area, microorganisms, and residence time in this particular site.

In addition to the CPI and LMW/HMW ratio indices, we used the ratios $\text{ACL}_{14–32}$, $\text{ATR}_{14–18,}$ and $\text{ATR}_{26–30}$ (**Table 1**) to constrain fatty acids derived from surface algae relative to those from terrigenous higher plants. This differentiation will support our assessment of the source environment. In drip water samples, the values of $\text{ACL}_{14–32}$, $\text{ATR}_{14–18}$, and $\text{ATR}_{26–30}$ range from 16.5 to 17.0, 0.91–0.95, and 0–0.02, respectively (**Table 2**). If the $\text{ATR}_{14–18}$ and $\text{ATR}_{26–30}$ values are >0.80 and <0.10, respectively, along with low $\text{ACL}_{14–32}$ ratios, they indicate algal-derived organic matter in percolating drip water in Krem Mawmluh. Because algae need sunlight for photosynthesis and this cave is primarily aphotic, we postulate that the algal-derived fatty acids originated at the soil surface and percolated through the soil veneer and fractured limestone. The comparison of fatty acid profiles in the soil cover and drip water would have shed some light on the source of these compounds. However, access to soil profiles near the cave was limited because of the topographic barrier and issues with accessibility near Krem Mawmluh.

In summary, the drip water samples reflect that the organic matter is 1) mainly derived from microorganisms and added during the infiltration process, 2) partially derived from microorganisms at the photic surface, and 3) from surface vegetation. The amount of *ex situ* material (total lipid concentration) transported with drip water varies about an order of magnitude.

Moonmilk

A previous geomicrobiological study of moonmilk and moonmilk pool waters in Krem Mawmluh indicated many isolated bacterial strains that precipitate carbonates (Baskar et al., 2011). The microorganisms species identified in the moonmilk deposits belong to *Bacillus* and Actinomycetes, and the richness of species indicates a diverse microbial community inside the cave (ibid). The lipids in both our moonmilk samples (MM1 and MM2; **Supplementary Table S3**) are predominantly composed of fatty acids, consisting of ~89% LMW and 11% HMW fatty acids (**Table 3**). The samples are dominated by *n*-C_{16}, C_{18}, and C_{24} fatty acids (**Supplementary Figure S2**). The total lipid abundances are 16.5 μg/g and 1.3 μg/g in samples MM2 and MM1, respectively (**Table 3**), including the LMW suberic and azelaic acids (**Table 3**). Lipid biomarker abundances in Krem Mawmluh moonmilk are lower than the concentrations reported from moonmilk samples analyzed from other caves, such as the Paganella Massif in northeastern Italy (40–88 μg/g; Blyth et al., 2008), implying different biological and chemical processes in their genesis. The lipid biomarker indices (e.g., CPI, ACL, $\text{ATR}_{14–18,}$ and $\text{ATR}_{26–30}$) in the Krem Mawmluh moonmilk samples show a substantial similarity with drip water (**Table 2**). Drip water constrained by various physical and chemical parameters inside the cave can play a fundamental role in speleogenesis. The similarity between moonmilk and drip water in biomarker indices supports an important subaerial provenance of these compounds eventually incorporated in the modern speleothems (besides *in situ* production) in Krem Mawmluh.

Stalagmite

Modeled ^{230}Th dates indicated the age of stalagmite KM-1 extending from 22.7 ka B.P. (Last Glacial Maximum) to 6.6 ka B.P. (mid-Holocene), covering a period of ~16,000 years BP (Huguet et al., 2018). The modeled ages reveal a drastic change in growth rate with the onset of the Holocene interglacial climate (Huguet et al., 2018).

The total lipid concentrations in the moonmilk samples are one order of magnitude higher than in KM-1 (**Tables 3**, **4**). The

TABLE 4 | Total *n*-alkanoic acid concentrations (ng/g) and different molecular indices in KM-1 stalagmite.

Ages (ky)	Depth (cm)	Total *n*-fatty acids (ng/g)	LMW/ HMW	CPI	ACL	Total dicarboxylic acids (ng/g)	Azelaic acid (ng/g)	$C_{16:1}$/C_{16}	$C_{18:1}$/C_{18}	$C_{18:2}$/C_{18}	($isoC_{15}$+$anteisoC_{15}$)/ nC_{15} (branchedC_{15} fatty acid index)
6.7	4.5–5	2087	9.3	12.6	17.2	151	56	0.02	0.020	0.080	0.34
7.1	13.8–14.4	916	5.2	9.6	17.6	155	82	0.02	0.016	0.057	0.33
7.8	26–27	1947	6.9	8.9	17.2	134	20	0.02	0.011	0.035	0.40
8.2	33–33.5	961	5.0	10.6	18.0	184	121	0.02	0.111	0.040	0.30
8.8	44–44.5	1,227	9.0	8.0	16.8	237	8	0.013	0.018	0.063	0.31
8.9	46.5–47	999	6.3	9.0	17.3	66	9	0.003	0.176	0.084	0.48
9.3	52.8–53.5	1,477	5.5	7.7	17.5	168	48	0.014	0.017	0.079	0.29
9.8	59–59.5	1,068	7.9	7.7	17.0	116	12	0.02	0.012	0.033	0.33
10.4	62–62.5	928	8.8	10.7	17.0	45	17	0.01	0.023	0.059	0.37
12.0	67–67.5	1,612	5.7	10.1	17.6	255	0	0.01	0.009	0.027	0.30
12.3	71–71.5	666	10.0	6.2	18.0	8	2	0.02	0.001	0.000	0.22
13.5	73–74	1,204	6.2	8.2	17.2	72	14	0.013	0.014	0.027	0.58
14.3	74.5–75	1,234	5.8	7.4	17.0	74	25	0.03	0.004	0.080	0.37
16.0	77–78	920	9.1	7.7	17.0	19	5	0.05	0.020	0.000	0.26
16.9	78–79.5	1,512	10.9	11.6	17.0	411	318	0.02	0.008	0.023	0.33
18.3	80.5–81	850	8.0	8.5	17.1	12	2	0.04	0.003	0.000	0.18
21.3	84.5–85.5	1,071	6.1	9.0	17.5	13	2	0.05	0.004	0.000	0.21

internal standard added to the stalagmite samples indicated a recovery of ~85%; this suggests that the loss of lipid biomarkers during extraction was minimal. The total fatty acid contents observed in KM-1 (0.67–2.09 µg/g; **Table 4**) are similar to the total lipid contents in stalagmites from high-altitude caves in northeast Italy (<10 µg/g; Blyth et al., 2008), but low compared to the tropical Heshang Cave (>10 µg/g; Huang et al., 2008).

The distribution of lipids also differed in the different sample types. This change in lipid composition reflects provenance changes that are further illustrated and discussed below. Here, we first report the lipid composition in KM-1 contrasted with stalagmite lipid composition worldwide. The total lipid extracts from KM-1 mainly consist of monocarboxylic acids (**Supplementary Table S4**; **Supplementary Figure S4**) and dicarboxylic acids (**Supplementary Table S5**), along with traces of *n*-alkanes, alcohols, and sterols (data not shown). Similar observations of high concentrations of fatty acids vs. low concentrations or the complete absence of *n*-alkanes have been reported in other caves, e.g., stalagmites retrieved from the Oregon Caves National Monument (Rushdi et al., 2011) and the Heshang Cave (Huang et al., 2008). Other lipids, such as the *n*-alkan-2-ones, reported as major lipid components by Xie et al. (2003) in the Heshang cave, were absent in KM-1. The KM-1 samples were also devoid of 3-hydroxy and 2-hydroxy fatty acids that have been reported in stalagmites from Ethiopia, China, and Scotland (Blyth et al., 2006; Wang et al., 2012; Wang et al., 2018).

Short-chain (C_8 to C_{19}) LMW *n*-alkanoic and *n*-alkanedioic acids, including monounsaturated (C_{14}–C_{18}) and branched (*iso*- and *anteiso*-C_{15} and C_{17}) fatty acids account for ~88% of total fatty acids, whereas long-chain (C_{20}–C_{30}) HMW fatty acids and *n*-alkanedioic acids account for ~12% (**Supplementary Table S4**; **Table 4**). The LMW *n*-alkanoic acid concentrations in KM-1 (0.68–1.75 µg/g) are similar to the abundance of LMW compounds in stalagmites from the Herbstlabyrinth-Adventhöhle cave system in Germany (0.002–1.35 µg/g; Bosle et al., 2014). The ubiquitous palmitic (C_{16}) and stearic (C_{18}) acids dominate the LMW fractions, and C_{24} dominate the HMW fractions (**Supplementary Figure S4**). Consequently, the LMW/HMW ratios range from 5.0 to 11 in KM-1, and the CPI and ACL_{14-32} vary from 6 to 13 and 17–18, respectively (**Figure 2**).

Biomarker Provenance in Stalagmites

The distribution and composition of fatty acids in KM-1 stalagmite and their comparison with drip water and moonmilk and previously published studies help interpret their sources. Below we discuss whether these compounds in the stalagmite are derived from 1) bacteria, fungi, cyanobacteria, algae, or higher plants, 2) *in situ* microbial production, or 3) *ex-situ* production that is transported from the overlying soil cover *via* drip water.

Source Organisms

The long-chain fatty acids (>C_{20}) are typically derived from higher plant waxes, whereas short-chain fatty acids (<C_{20}) are produced by multiple sources, including algae, fungi, and bacteria (Meyers and Ishiwatari, 1993; Logan and Eglinton, 1994; Blyth et al., 2006; Liu and Liu 2017). The low ACL and ATR_{14-18} > 0.80 in KM-1 (**Table 4**) suggest a predominantly bacterial and/or algal source. ATR_{20-24} ≈ 0.1 in few samples from KM-1 imply minor inputs from higher plant-derived organic matter. To further constrain the sources as bacteria vs. algal-derived matter, we focus on the 3-hydroxy fatty acids. The 3-hydroxy fatty acids are derived from lipopolysaccharides present in cell walls of gram-negative bacteria, and 2-hydroxy fatty acids are derived from lipopolysaccharides in the cell walls of algae and cyanobacteria

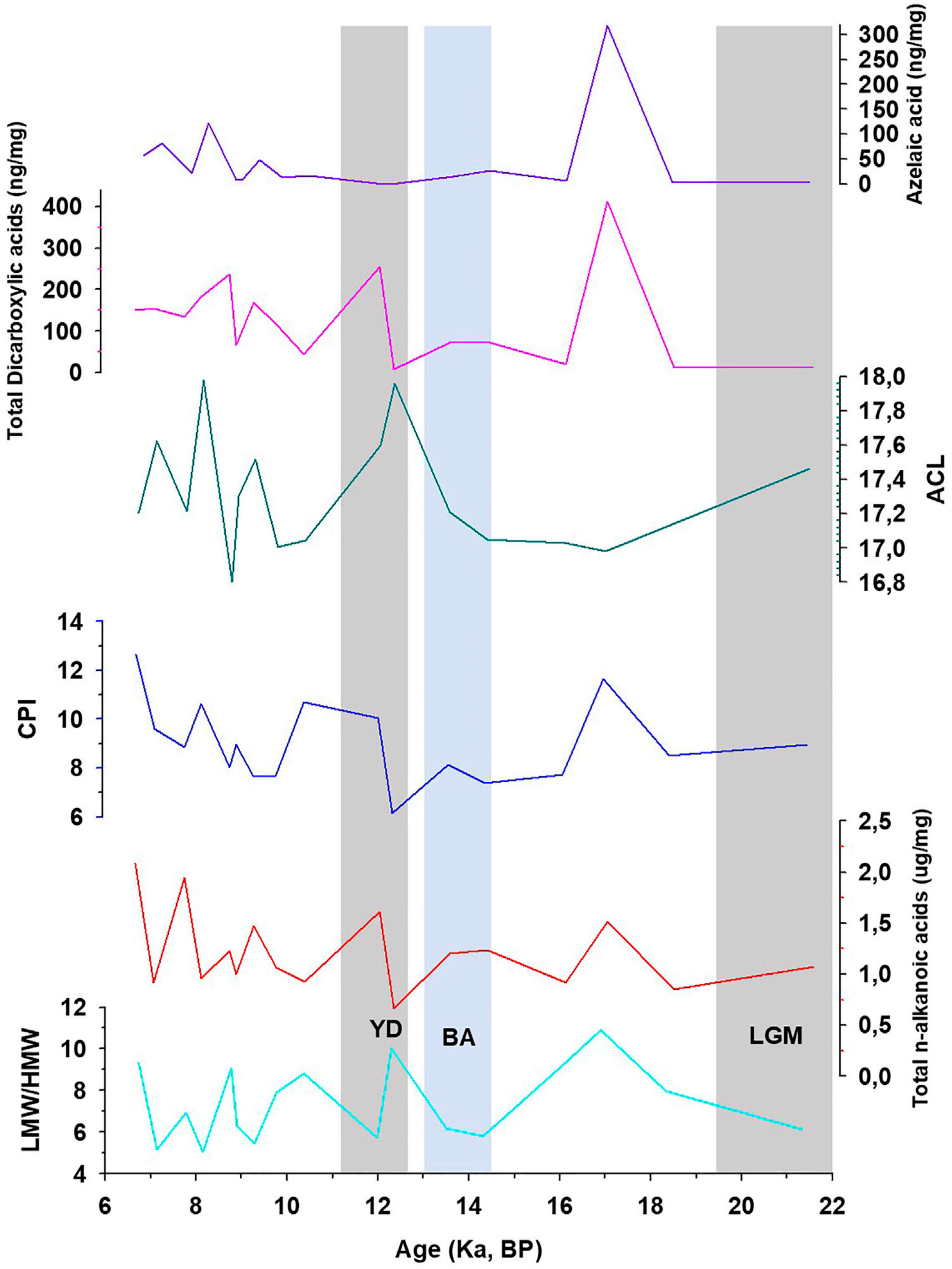

FIGURE 2 | Variation of low to high molecular weight ratio (LMW/HMW), total fatty acids Carbon Preference Index (CPI), Average Chain Length (ACL), total concentration of dicarboxylic acids, and azelaic acid in KM-1. LGM, Last Glacial Maximum; BA, Bolling-AllerØd; YD, Younger Dryas.

(Edlund et al., 1985; Mendoza et al., 1987; Wakeham, 1999). The absence of hydroxy acids in the KM-1 stalagmite is consistent with earlier suggestions of low occurrence or absence of gram-negative bacteria (Baskar et al., 2011). Besides, the KM-1 stalagmite was retrieved from the aphotic deep interior (**Figure 1**), making *in situ* production by photosynthetic organisms very unlikely. Further, we postulate the fatty acids (*iso*- and *anteiso*-C_{15}) identified in KM-1 (**Figure 3**) are most likely derived from bacterial sources based on the geomicrobiological analysis of KM moonmilk and moonmilk pool waters that have shown high microbial counts with many of the isolated strains precipitating carbonate mineral. The bacteria identified in these deposits belonged to *Bacillus* spp. and Actinomycetes (Baskar et al., 2011). Based on these trends, we conclude the abundance of palmitic acid (16:0) and stearic acid (18:0), presence of branched fatty acids, and low concentrations of HMW fatty acids in KM-1 stalagmite indicate a predominantly microbial signal. Detailed genetic fingerprinting can likely confirm the microbial diversity of the fatty acids in the future.

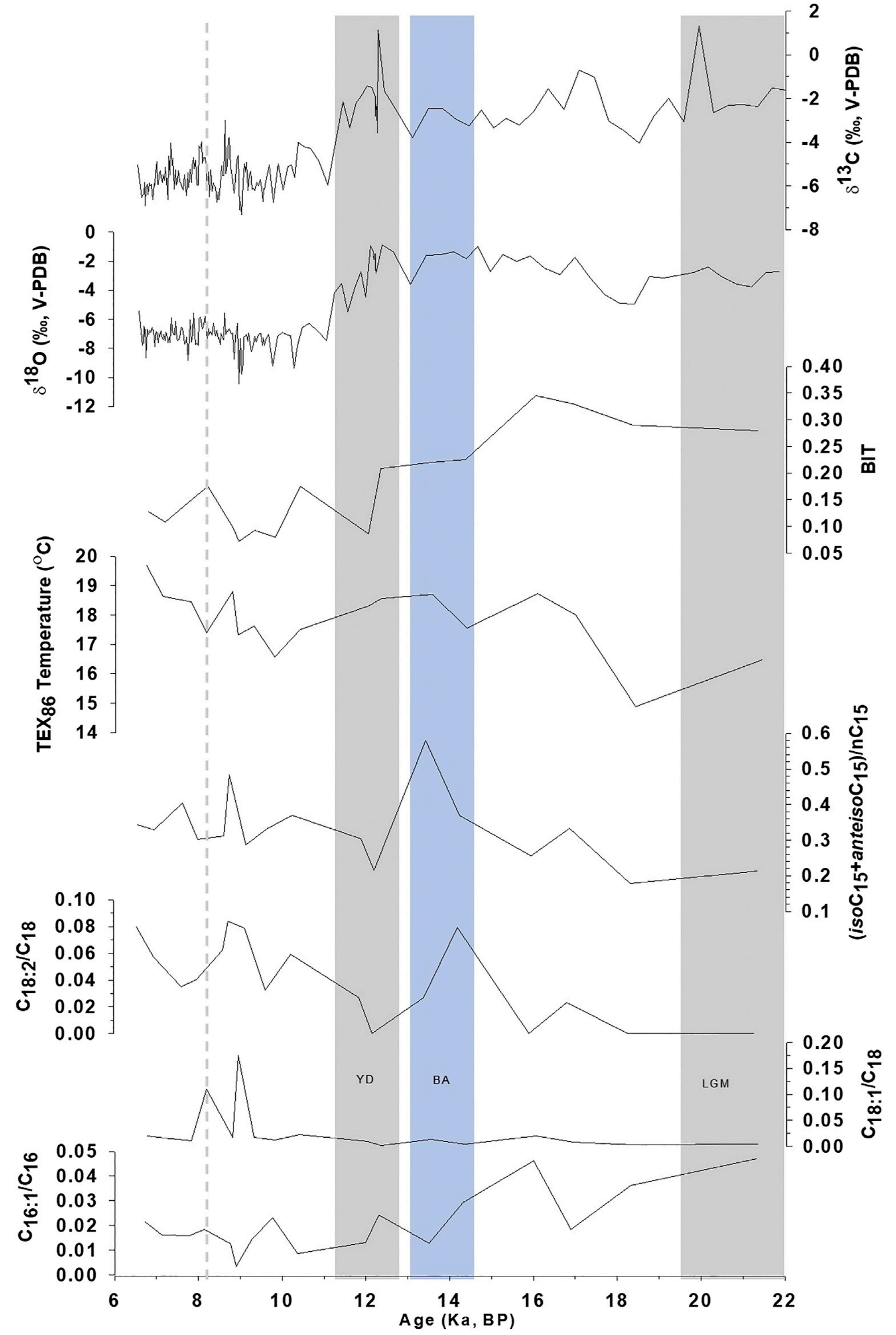

FIGURE 3 | Comparison of $C_{16:1}/C_{16:0}$, $C_{18:1}/C_{18:0}$, $C_{18:2}/C_{18:0}$, and Branched-nC_{15}index (*iso*+*anteiso*C_{15}/*n*C_{15}) in KM-1 stalagmite with TEX_{86}, BIT, $\delta^{18}O$, and $\delta^{13}C$ records from Huguet et al. (2018).

In-Cave Versus Out of Cave Biomarker Sources

The provenance of lipids in KM-1 is from microbes inhabiting the surface soils, percolating drip water, or compounds produced inside the cave. The lack of input for diagnostic vegetation markers in percolating drip water in the KM-1 samples indicates a predominant microbial origin. This assumption is reflected in the absence of *n*-alkanes and *n*-alkan-2-ones in KM-1, arguably due to their absence or low abundance in drip water samples from Krem Mawmluh. A filtration effect is likely to remove large colloidal organic matter seeping through the soil veneer and karst terrain or bind them with the soil matrix in the vadose zone. Perhaps this contributes to some of the loss, but this cannot be assessed in the present study.

Supporting evidence for the *ex situ* microbial origins of certain lipids in this study is provided by the similar distribution of fatty acids in moonmilk deposits and drip water. Notably, the occurrence of LMW dicarboxylic acids in KM-1, drip water, and moonmilk samples is characterized by the abundance of azelaic acid (C_9). Azelaic acid is derived from the photochemical oxidation of unsaturated fatty acids (C18:1) that predominantly have a double bond at the C_9 position (Kawamura and Gagosian, 1987). Krem Mawmluh, however, is a deep aphotic cave system with hardly any natural light. Therefore an *in situ* provenance of azelaic acid resulting from photochemical oxidation of unsaturated fatty acids seems unlikely. Instead, the production of these compounds in the overlying soil zone or pore waters is the most likely source. Thus, varying concentrations of azelaic acid in KM-1 may provide insights into local/regional hydrological changes or flow paths of the percolating rainwater around Krem Mawmluh. A significant concentration of sebacic acid (C_{10}, 26%) and undecanoic acid (C_{11}, 9%; **Supplementary Figure S4**) also occur in KM-1. These short-chain dicarboxylic acids along with azelaic acid have been reported in marine sediments, ice cores, and aerosols (Kawamura et al., 1999; Pokhrel et al., 2015), and their occurrence is attributed to the oxidative degradation of double bonds in unsaturated fatty acids (Volkman, 2006). The *n*-alkanedioic acids in KM-1 stalagmite most likely resulted from bacterial oxidation of lipids (Bianchi and Canuel, 2011) in soils that underwent further diagenetic changes before and during the transport of these lipids into the cave.

We compared the fatty acid trends with other proxies to constrain the variation in biomarker sources over time, especially in the stalagmite. Huguet et al. (2018) used isoprenoid and branched GDGTs in KM-1 to indicate a change in regional hydrological conditions. The GDGT-based indication of increasing moisture and in-cave over soil-derived signal during deglaciation is similar to the observed shifts in the fatty acids, particularly in azelaic acid. High concentrations of azelaic acid (360 ng/g; **Figure 2**) are recorded during the late glacial period (before 12 ka), which indicates that due to the weak monsoon, the drier conditions led to slow percolating waters, which increased the total lipid and azelaic acid levels in drip water. As a result, KM-1 is marked by less *in situ* production and more surface production, and a higher contribution of lipids from the overlying soils. This dynamic shifts to more vigorous monsoons, faster-percolating waters, and a decrease in total lipid and azelaic acid levels in the drip water occur during the deglacial. As a result, similar to the GDGT-based findings, the deglacial KM-1 is marked by stronger *in situ* production over the contribution of lipids from the overlying soils. Subsequently, another sharp increase in the concentration of azelaic acid (121 ng/g) occurs at c. 8.2 ka, which is again a dry period and reflects a higher contribution of soil-derived azelaic acid. In summary, the fatty acids 1) support the change in hydrological conditions derived from the GDGT-based proxies in Huguet et al. (2018), and 2) the primary source of these compounds in KM-1 appears to be subaerial pre-12 ka (and subsequent dry events), shifting to a primary *in situ* organic matter source signal during the wetter Holocene.

Fatty Acid Records in KM-1

C_{16} and C_{18} Unsaturation-Based Indices

Despite the low sampling frequency of the biomarker record in KM-1, some distinct variations can be related to paleoclimate changes (**Figure 2**). The average concentrations of fatty acids are 1.2 μg/g, with the maximum and minimum concentrations recorded during the mid-Holocene ~6.7 ka (2.1 μg/g) and the Younger Dryas ~12.3 ka (0.67 μg/g). The high concentrations indicate an increase in microbial activity during warm, wet conditions, while the low concentrations indicate a decrease in microbial activity during cold, dry periods. However, the molecular distribution of CPI and LMW/HMW ratios fluctuates within a narrow range. They do not seem to record explicitly the changes that follow known major climate patterns (e.g., the Last Glacial Maximum, Bolling-AllerØd, or Younger Dryas). In contrast, more distinct changes have been observed in the ratios of unsaturated vs. saturated fatty acids. In this context, the ratios $C_{16:1}/C_{16:0}$, $C_{18:2}/C_{18:0}$, and $C_{18:1}/C_{18:0}$ are sensitive to temperature changes and are considered more promising (Kawamura and Gagosian, 1987; Xie et al., 2005; Zhou et al., 2005; Zhao et al., 2014). For example, Wang et al. (2016) related the abrupt shifts (increase) in the sedimentary $C_{18:2}/C_{18:0}$ ratios ~4,400 years BP to climate change (cooling) and prehistoric cultural transition in Yuchisi, China. The unsaturation results from acclimation to ensure cell membrane stability and flexibility (Suutari and Laakso, 1994), but changes influence these trends during degradation or preservation. In KM-1, the $C_{16:1}/C_{16:0}$ ratio decreases from 0.05 to <0.01 through the glacial-interglacial continuum (**Figure 3**). The higher $C_{16:1}/C_{16:0}$ ratios before 12 ka indicate cell membrane acclimation and reduced degradation of the unsaturated acids consistent with the cold and dry conditions during the LGM. In contrast, lower $C_{16:1}/C_{16:0}$ ratios suggest cell membrane acclimation and increased microbial degradation at times of warmer and wetter conditions during the Holocene. In contrast to the decreasing trend in the $C_{16:1}/C_{16:0}$ ratios, the $C_{18:1}/C_{18:0}$ and $C_{18:2}/C_{18:0}$ ratios increase slightly from the late glacial (<0.01) to the Holocene (0.18). The C_{18} ratios experience sharp increases in $C_{18:1}/C_{18:0}$–8.9 ka (0.18) and 8.2 ka (0.11) and $C_{18:2}/C_{18:0}$–14.3 ka (0.08). These changes do not occur in the C_{16} ratio (**Figure 3**). These apparent contradictory trends are similar to the study by Blyth et al. (2011), whereby not all three unsaturated isomers show similar variation.

One reason for the observed mismatch in the fatty acid trends might be the source signal. From the drip water data, it is evident that the S1 sample with a fast drip rate shows $C_{18:1}$ (0.34 μg/g), but $C_{16:1}$ is absent or below the detection limit. In contrast, samples S2 and S4 with a slow drip rate indicate that $C_{16:1}$ occurs in appreciable concentration (3.80 μg/g and 3.20 μg/g, respectively), but $C_{18:1}$ is absent or below the detection limit. In the moon milk sample MM3, $C_{18:1}$ and $C_{18:2}$ are present in large concentrations, but $C_{16:1}$ is absent or below the detection limit. Based on these observations, it is assumed that the higher values of $C_{18:2}/C_{18:0}$ in KM-1 during the Holocene and in drip water sample S1 could be related to the fast inflow of drip water during the high monsoon season resulting in lower residence time and a decrease in surface production. This trend preferably leads to the higher inputs of $C_{18:1}$ compared to $C_{16:1}$ unsaturated acid. This trend implies that the C_{16} and C_{18} unsaturation indices reflect precipitation or moisture and infiltration rate rather than temperature. With the limited data, it is impossible to ascertain the effect of different factors like rate of reaction, temperature, and precipitation effects, influencing the decomposition of diagenetic changes in unsaturated fatty acids behooves further investigations.

C_{15} and Branched-Based Indices

The branched C_{15} fatty acid proxy (*iso+anteiso* C_{15}/nC_{15}) was applied to reconstruct the ISM variability in KM-1. This index was previously referred to as the Bacteria Invasion Index [$(iC_{15:0} + aC_{15:0})/nC_{15:0}$] by Zhao et al. (2014) in organic matter from penguin droppings in sediment cores to trace the historical changes in climate and environment. The C_{15} index indicated high values during warm periods due to increased contribution from bacterial activity. The basis for proposing the branched C_{15} fatty acid proxy is that variation in the distribution of C_{15} fatty acids, alcohols, and 3-hydroxy fatty acids are indicators of microbial activity that correlate with paleoclimatic changes (Huang et al., 2008; Wang et al., 2016; Zhang et al., 2017). Iso- and anteiso branched fatty acids are metabolic products of bacteria synthesized from amino acids (Willecke and Pardee, 1971; Kaneda, 1991; Wakeham and Beier, 1991). Their composition in the cell membrane is modified depending on the temperature to acclimate to changing environmental conditions. At low temperatures, to maintain membrane fluidity, most bacteria synthesize a higher proportion of unsaturated and branched fatty acids (Kaneda, 1991). A high value indicates this for the branched C_{15} fatty acid index under low temperature. However, some bacteria, such as *Bacillus cereus* reported in Krem Mawmluh (Baskar et al., 2011), reduce branched fatty acids and increase unsaturated fatty acids at low temperatures (Brillard et al., 2010; de Sarrau et al., 2012). Assuming *B. cereus* is an essential component of the microbial community, we expect contrary results, i.e., a low branched C_{15} fatty acid index reflecting low temperature, similar to the Bacteria Invasion Index. In KM-1, the distribution of C_{15}, iso- and anteiso branched fatty acids vary across the glacial-interglacial continuum (**Figure 3**). The branched C_{15} fatty acid index in KM-1 ranges from 0.18 to 0.58 with an average value of 0.33 (**Figure 3**). The average branched C_{15} fatty acid index values are <0.33 during the pre-12 ka and >0.33 during the post-12 ka intervals. The branched C_{15} fatty acid index values are the lowest (0.18) during the late glacial period (pre-12 ka) and highest during the Bølling-Allerød (0.58). The low value during the late-glacial period for branched C_{15} fatty acid index implies low bacterial activity and reduced production of branched fatty acids by *B. cereus* at low temperatures. Correspondingly, the high C_{15} fatty acid index during the Bølling-Allerød and Holocene periods implies higher bacterial activity and increased production of branched fatty acids by *B. cereus* at higher temperatures during the Holocene.

KM-1 Paleohydrological and Temperature Record

Biomarkers, Stable Isotopes, and the Glacial-Interglacial Continuum

We further evaluate the potential of azelaic acid and branched C_{15} fatty acid proxies from the present study in sync with previously published GDGT, $\delta^{18}O$, and $\delta^{13}C$ records (Huguet et al., 2018) to refine the paleotemperature and paleohydrological interpretation in the KM-1 stalagmite (**Figure 3**). Abrupt shifts of 4.70 and 3.42‰ in the $\delta^{18}O$ and $\delta^{13}C$ profile in KM-1 after the onset of Holocene imply more intense monsoon and change in vegetation cover during this period in contrast to the late glacial period (**Figure 3**). The KM-1 stalagmite $\delta^{18}O$ profile spanning from ~22 to 6 ka also concurs with other isotope records from the same cave extending from ~34 to 5.5 ka (Dutt et al., 2015) and ~12 to 3.6 ka (Berkelhammer et al., 2012). The branched C_{15} fatty acid index does not significantly correlate with $\delta^{18}O$ and $\delta^{13}C$ (**Supplementary Figure S6b**). Nevertheless, the branched - C_{15} fatty acid index shows a trend during the last glacial-interglacial periods tracking the shifts in ISM intensity delineated by $\delta^{18}O$ and $\delta^{13}C$.

The GDGT-based paleothermometry proxy TEX_{86} in KM-1 increased from the late glacial to the Holocene (**Figure 3**), indicating an increase in temperatures from 16.5 to 19.7°C (Huguet et al., 2018). The TEX_{86} based paleotemperature calibration of modern speleothems with surface temperatures was proposed in investigations led by Blyth and Schouten (2013), Blyth et al. (2016), and Baker et al. (2019). Huguet et al. (2018) indicated the possibility that in Krem Mawmluh, the GDGTs could have migrated inside the cave from overlying soils. This change most likely happened during the glacial to interglacial period, which indicated differences in hydrological conditions. Although branched C_{15} fatty acid index shows an overall weak correlation with TEX_{86} in KM-1 (22–6 ka), we observe a distinct relationship during the pre-glacial and post-glacial periods (**Supplementary Figure S6a**), pointing to a decoupling between TEX_{86} and branched C_{15} fatty acid index with shifts in hydrological conditions.

The BIT index (**Figure 3**) indicates the relative contribution of branched GDGTs produced by soil bacteria than iso-GDGTs produced by Thaumarchaeota (Hopmans et al., 2004). Though BIT vs. azelaic acid does not show a significant statistical correlation, their values show a good relationship during the glacial-interglacial periods. The average azelaic acid concentration (51.3 μg/g) during pre-12 ka is higher than the overall average concentration (46 μg/g; **Figure 2**). Higher BIT values (~0.35) indicating more substantial input from terrestrial sources than Thaumarcheotal source observed during the late glacial period coincide with higher azelaic acid concentrations indicating increased input of surface-derived organic matter during low monsoon intensity.

The branched C15 fatty acid index could not capture the short-lived abrupt cold Henrich 1 (H1) event at ~17 ka due to the low temporal resolution in sampling spanning this period. After ~16 ka, the branched C_{15} fatty acid index increases matching the low $\delta^{18}O$ values until ~13.5 ka. These changes result from increased drip water within the cave due to ISM's strengthening during the warmer Bølling-Allerød period. This finding is consistent with the $\delta^{18}O$ record from the Kailash Cave in central India, which refers to increased ISM precipitation during the Bølling-Allerød interstadial (~14.8–12.6 ka; Gautam et al., 2019). A sharp decline in branched C_{15} fatty acid index at ~12.3 ka corresponds to the cold/dry and weak monsoon during the Younger Dryas. The high $\delta^{18}O$ and $\delta^{13}C$ values at ~12 ka indicate low drip water input coinciding with a weak monsoon.

The branched C_{15} fatty acid profile (**Figure 3**) after ~12 ka changes drastically again coinciding with an abrupt shift of about ~5 and ~3.5‰ in $\delta^{18}O$ and $\delta^{13}C$ values, respectively (Huguet et al., 2018). This trend illustrates the transition from the cold and dry Younger Dryas to a warm and wet Holocene epoch. The early to mid-Holocene (~10 to 6.5 ka) is characterized by intense monsoon activity with few abrupt dry events reflected by the branched C_{15} fatty acid profile in KM-1. The highest branched C_{15} fatty acid ratio during the post-glacial period occurs ~8.9 ka along with higher TEX_{86} has lower $\delta^{18}O$ values indicating a warmer period owing to more robust ISM circulation. Likewise, the lower branched C_{15} fatty acid ratios at ~8.15 ka are consistent with lower TEX_{86} and slightly positive $\delta^{18}O$ values indicating a cold and dry event during the Holocene (Anderson et al., 2002; Staubwasser et al., 2002; Gupta et al., 2003; Prasad and Enzel, 2006).

Independent biomarker analyses in stalagmites provide a complementary tool to ascertain changes inferred based on stable isotopes and trace metals. This opportunity offers more precision and confidence in interpreting paleoclimate changes. The fatty acid ratios broadly overlap with paleoenvironmental inferred modifications based on other high-resolution proxies investigated in Krem Mawmluh (Berkelhammer et al., 2012; Dutt et al., 2015). However, one of the potential drawbacks is the low-resolution of all biomarker data investigated to date in speleothems retrieved from this cave (Huguet et al., 2018 and current study) and other cave systems too. This disadvantage is partly due to the high sample demand for traditional biomarker analyses implemented in stalagmite research. Hence, further investigations are recommended for alternative analytical methods involving less sample demand, even in low C deposits. For example, extraction-free lipid analyses at μm scale (Wörmer et al., 2014; Alfken et al., 2019) is a promising method that could be applied to selected samples for specific time intervals to deconvolute the nuanced changes in climate reconstruction.

CONCLUSION

The present study addresses the sources and distribution of fatty acids, the most dominant biomarker lipids found in drip water, moonmilk deposits, and a stalagmite retrieved from Krem Mawmluh in northeast India. The total lipid extracts in moonmilk samples are one order of magnitude higher than in the stalagmite. The composition of fatty acids is similar in all three types of cave deposits investigated in this study. The trends indicate an abundance of saturated palmitic acid (16:0) and stearic acid (18:0), the presence of branched fatty acids, and low concentrations of HMW fatty acids, indicating the microbial origin of these lipids from both *in situ* as well as surface production. Another important finding in these samples is the abundance of azelaic acid, a novel biomarker derived from unsaturated fatty acids ($C_{18:1}$), indicating the input of lipids from surface soils. We have also assessed the application of fatty acid proxies to reconstruct the paleoenvironment. The $C_{18:1}/C_{18:0}$ and $C_{18:2}/C_{18:0}$ ratios indicate high values during pre-12 ka and low values during the post-12 ka period. In contrast, $C_{16:1}/C_{16:0}$ shows a reverse trend implying warm climate events recorded by lower ratios. The weak correlation between unsaturated and saturated fatty acid ratios is a drawback in applying them for paleoclimate/paleotemperature reconstruction. This disadvantage is partly due to the low sampling resolution in this study. However, the branched C_{15} fatty acid proxy denoted as (*iso+anteiso* C_{15}/nC_{15}) appears to be more sensitive to the last glacial-interglacial climate change. Higher values of branched C_{15} fatty acid ratios during the Bølling-Allerød interstadial and Holocene suggest enhanced microbial production of branched (*iso+anteiso*) C_{15} under warmer/wetter conditions. During weak monsoon events, microbial activity in the cave is reduced due to slow drip water flow resulting in the higher input of soil-derived biomarkers such as azelaic acid from the overlaying karst system. This trend coincides with GDGT based BIT values. Thus, the source of fatty acids in KM-1 is predominantly *in situ,* with some terrestrial input from the overlying soil zone during intense monsoons. Branched C_{15} fatty acid ratios are comparable with $\delta^{18}O$, $\delta^{13}C$, and TEX_{86} paleoclimate reconstruction. The branched C_{15} fatty acid index unambiguously captures global climate patterns, namely, the LGM, Bølling-Allerød, Younger Dryas, and Holocene. However, more high-resolution studies are required to establish fatty acid-based proxies as a complementary tool for paleoclimate reconstruction.

DATA AVAILABILITY STATEMENT

The original contributions presented in the study are included in the article/**Supplementary Material**, further inquiries can be directed to the corresponding author.

AUTHOR CONTRIBUTIONS

JR has carried out the fieldwork and sample collection. Lipid extraction and analyses were led by MSK and JR. AM led the U/T dating. MSK led data interpretation and writing with JR, SF, and MAL. All authors have approved the final version of the paper.

FUNDING

The project was funded by a grant provided by SIDA to JR (Grant SWE 2009-089).

ACKNOWLEDGMENTS

We thank SIDA for funding the project. MK thanks Susanne Karlsson and Lena Lundman for their help in the laboratory. JR thanks “Teddy” Kharpam Daly for helping with sampling inside the cave. Suggestions from the reviewers helped in improving the manuscript. MK thanks the Director, CSIR-NGRI for the support extended to this study. SF acknowledges support from the South African National Research Foundation (Grant 93072, 98905). ML acknowledges support from the Ministry of Science and Technology.

SUPPLEMENTARY MATERIAL

The Supplementary Material for this article can be found online at: https://www.frontiersin.org/articles/10.3389/feart.2021.687376/full#supplementary-material

REFERENCES

Alfken, S., Wörmer, L., Lipp, J. S., Wendt, J., Taubner, H., Schimmelmann, A., et al. (2019). Micrometer Scale Imaging of Sedimentary Climate Archives – Sample Preparation for Combined Elemental and Lipid Biomarker Analysis. *Org. Geochem.* 127, 81–91. doi:10.1016/j.orggeochem.2018.11.002

Anderson, D. M., Overpeck, J. T., and Gupta, A. K. (2002). Increase in the Asian Southwest Monsoon during the Past Four Centuries. *Science* 297, 596–599. doi:10.1126/science.1072881

Apaéstegui, J., Cruz, F. W., Sifeddine, A., Vuille, M., Espinoza, J. C., Guyot, J. L., et al. (2014). Hydroclimate Variability of the Northwestern Amazon Basin Near the Andean Foothills of Peru Related to the South American Monsoon System during the Last 1600 Years. *Clim. Past* 10, 1967–1981. doi:10.5194/cp-10-1967-2014

Atsawawaranunt, K., Comas-Bru, L., Amirnezhad Mozhdehi, S., Deininger, M., Harrison, S. P., Baker, A., et al. (2018). The SISAL Database: A Global Resource to Document Oxygen and Carbon Isotope Records from Speleothems. *Earth Syst. Sci. Data* 10, 1687–1713. doi:10.5194/essd-10-1687-2018

Baker, A., Blyth, A. J., Jex, C. N., Mcdonald, J. A., Woltering, M., and Khan, S. J. (2019). Glycerol Dialkyl Glycerol Tetraethers (GDGT) Distributions from Soil to Cave: Refining the Speleothem Paleothermometer. *Org. Geochem.* 136, 103890. doi:10.1016/j.orggeochem.2019.06.011

Baker, A., Routh, J., and Roychoudhury, A. N. (2016). Biomarker Records of Palaeoenvironmental Variations in Subtropical Southern Africa since the Late Pleistocene: Evidences from a Coastal Peatland. *Palaeogeogr. Palaeoclimatol. Palaeoecol.* 451, 1–12. doi:10.1016/j.palaeo.2016.03.011

Band, S., Yadava, M. G., Lone, M. A., Shen, C.-C., Sree, K., and Ramesh, R. (2018). High-resolution Mid-holocene Indian Summer Monsoon Recorded in a Stalagmite from the Kotumsar Cave, central India. *Quat. Int.* 479, 19–24. doi:10.1016/j.quaint.2018.01.026

Baskar, S., Baskar, R., and Routh, J. (2011). Biogenic Evidences of Moonmilk Deposition in the Mawmluh Cave, Meghalaya, India. *Geomicrobiology J.* 28, 252–265. doi:10.1080/01490451.2010.494096

Berkelhammer, M., Sinha, A., Stott, L., Cheng, H., Pausata, F. S. R., and Yoshimura, K. (2012). An Abrupt Shift in the Indian Monsoon 4000 Years Ago. *Geophys. Monogr. Ser.* 198, 75–88. doi:10.1029/2012GM001207

Bhaumik, S. (2009). *India’s Wettest Place ‘Lacks Water’*. Sohra: BBC. Available at: http://news.bbc.co.uk/2/hi/south_asia/8378327.stm.

Bianchi, T. S., and Canuel, E. A. (2011). *Chemical Biomarkers in Aquatic Ecosystem*. New Jersey: Princeton University Press, 385.

Biswas, J. (2009). The Biodiversity of Krem Mawkhyrdop of Meghalaya, India, on the Verge of Extinction. *Curr. Sci.* 96, 904–910.

Bligh, E. G., and Dyer, W. J. (1959). A Rapid Method of Total Lipid Extraction and Purification. *Can. J. Biochem. Physiol.* 37, 911–917. doi:10.1139/o59-09910.1139/y59-099

Blyth, A. J., Asrat, A., Baker, A., Gulliver, P., Leng, M. J., and Genty, D. (2007). A New Approach to Detecting Vegetation and Land-Use Change Using High-Resolution Lipid Biomarker Records in Stalagmites. *Quat. Res.* 68, 314–324. doi:10.1016/j.yqres.2007.08.002

Blyth, A. J., Baker, A., Collins, M. J., Penkman, K. E. H., Gilmour, M. A., Moss, J. S., et al. (2008). Molecular Organic Matter in Speleothems and its Potential as an Environmental Proxy. *Quat. Sci. Rev.* 27, 905–921. doi:10.1016/j.quascirev.2008.02.002

Blyth, A. J., Baker, A., Thomas, L. E., and Van Calsteren, P. (2011). A 2000-year Lipid Biomarker Record Preserved in a Stalagmite from North-West Scotland. *J. Quat. Sci.* 26, 326–334. doi:10.1002/jqs.1457

Blyth, A. J., Farrimond, P., and Jones, M. (2006). An Optimised Method for the Extraction and Analysis of Lipid Biomarkers from Stalagmites. *Org. Geochem.* 37, 882–890. doi:10.1016/j.orggeochem.2006.05.003

Blyth, A. J., Hartland, A., and Baker, A. (2016). Organic Proxies in Speleothems - New Developments, Advantages and Limitations. *Quat. Sci. Rev.* 149, 1–17. doi:10.1016/j.quascirev.2016.07.001

Blyth, A. J., Jex, C. N., Baker, A., Khan, S. J., Schouten, S., and Schouten, S. (2014). Contrasting Distributions of Glycerol Dialkyl Glycerol Tetraethers (GDGTs) in Speleothems and Associated Soils. *Org. Geochem.* 69, 1–10. doi:10.1016/j.orggeochem.2014.01.013

Blyth, A. J., and Schouten, S. (2013). Calibrating the Glycerol Dialkyl Glycerol Tetraether Temperature Signal in Speleothems. *Geochimica et Cosmochimica Acta* 109, 312–328. doi:10.1016/j.gca.2013.02.009

Bosle, J. M., Mischel, S. A., Schulze, A.-L., Scholz, D., and Hoffmann, T. (2014). Quantification of Low Molecular Weight Fatty Acids in Cave Drip Water and Speleothems Using HPLC-ESI-IT/MS - Development and Validation of a Selective Method. *Anal. Bioanal. Chem.* 406, 3167–3177. doi:10.1007/s00216-014-7743-6

Breitenbach, S. F. M., Lechleitner, F. A., Meyer, H., Diengdoh, G., Mattey, D., and Marwan, N. (2015). Cave Ventilation and Rainfall Signals in Dripwater in a Monsoonal Setting - A Monitoring Study from NE India. *Chem. Geology* 402, 111–124. doi:10.1016/j.chemgeo.2015.03.011

Brillard, J., Jéhanno, I., Dargaignaratz, C., Barbosa, I., Ginies, C., Carlin, F., et al. (2010). Identification of *Bacillus Cereus* Genes Specifically Expressed during Growth at Low Temperatures. *Appl. Environ. Microbiol.* 76, 2562–2573. doi:10.1128/AEM.02348-09

Cheng, H., Edwards, R. L., Sinha, A., Spötl, C., Yi, L., Chen, S., et al. (2016). The Asian Monsoon over the Past 640,000 Years and Ice Age Terminations. *Nature* 534, 640–646. doi:10.1038/nature18591

Cheng, H., Sinha, A., Wang, X., Cruz, F. W., and Edwards, R. L. (2012). The Global Paleomonsoon as Seen through Speleothem Records from Asia and the Americas. *Clim. Dyn.* 39, 1045–1062. doi:10.1007/s00382-012-1363-7

Comas-Bru, L., Atsawawaranunt, K., and Harrison, S.SISAL working group members (2020). *SISAL (Speleothem Isotopes Synthesis and Analysis Working Group) Database Version 2.0*. England: University of Reading. Dataset. doi:10.17864/1947.256

Cranwell, P. A., Eglinton, G., and Robinson, N. (1987). Lipids of Aquatic Organisms as Potential Contributors to Lacustrine Sediments-II. *Org. Geochem.* 11, 513–527. doi:10.1016/0146-6380(87)90007-6

Daly, K. B. D. (2006). *The Caves of Meghalaya*. Shillong: The Directorate of Information and Public Relations Government of Meghalaya.

de Sarrau, B., Clavel, T., Clerté, C., Carlin, F., Giniès, C., and Nguyen-The, C. (2012). Influence of Anaerobiosis and Low Temperature on *Bacillus Cereus* Growth, Metabolism, and Membrane Properties. *Appl. Environ. Microbiol.* 78, 1715–1723. doi:10.1128/aem.06410-11

Dutt, S., Gupta, A. K., Clemens, S. C., Cheng, H., Singh, R. K., Kathayat, G., et al. (2015). Abrupt Changes in Indian Summer Monsoon Strength during 33,800 to 5500 Years B.P. *Geophys. Res. Lett.* 42, 5526–5532. doi:10.1002/2015GL064015

Edlund, A., Nichols, P. D., Roffey, R., and White, D. C. (1985). Extractable and Lipopolysaccharide Fatty Acid and Hydroxy Acid Profiles from *Desulfovibrio* Species. *J. Lipid Res.* 26, 982–988. doi:10.1016/s0022-2275(20)34302-9

Fairchild, I. J., and Treble, P. C. (2009). Trace Elements in Speleothems as Recorders of Environmental Change. *Quat. Sci. Rev.* 28, 449–468. doi:10.1016/j.quascirev.2008.11.007

Fleitmann, D., Burns, S. J., Mudelsee, M., Neff, U., Kramers, J., Mangini, A., et al. (2003). Holocene Forcing of the Indian Monsoon Recorded in a Stalagmite from Southern Oman. *Science* 300, 1737–1739. doi:10.1126/science.1083130

Gautam, P. K., Narayana, A. C., Band, S. T., Yadava, M. G., Ramesh, R., Wu, C.-C., et al. (2019). High-resolution Reconstruction of Indian Summer Monsoon during the Bølling-Allerød from a central Indian Stalagmite. *Palaeogeogr. Palaeoclimatol. Palaeoecol.* 514, 567–576. doi:10.1016/j.palaeo.2018.11.006

Gupta, A. K., Anderson, D. M., and Overpeck, J. T. (2003). Abrupt Changes in the Asian Southwest Monsoon during the Holocene and Their Links to the North Atlantic Ocean. *Nature* 421, 354–357. doi:10.1038/nature01340

Heidke, I., Scholz, D., and Hoffmann, T. (2018). Quantification of Lignin Oxidation Products as Vegetation Biomarkers in Speleothems and Cave Drip Water. *Biogeosciences* 15, 5831–5845. doi:10.5194/bg-15-5831-2018

Hopmans, E. C., Weijers, J. W. H., Schefuß, E., Herfort, L., Sinninghe Damsté, J. S., and Schouten, S. (2004). A Novel Proxy for Terrestrial Organic Matter in Sediments Based on Branched and Isoprenoid Tetraether Lipids. *Earth Planet. Sci. Lett.* 224, 107–116. doi:10.1016/j.epsl.2004.05.012

Huang, X., Cui, J., Pu, Y., Huang, J., and Blyth, A. J. (2008). Identifying “Free” and “Bound” Lipid Fractions in Stalagmite Samples: An Example from Heshang Cave, Southern China. *Appl. Geochem.* 23, 2589–2595. doi:10.1016/j.apgeochem.2008.05.008

Huguet, C., Routh, J., Fietz, S., Lone, M. A., Kalpana, M. S., Ghosh, P., et al. (2018). Temperature and Monsoon Tango in a Tropical Stalagmite: Last Glacial-Interglacial Climate Dynamics. *Sci. Rep.* 8, 23606. doi:10.1038/s41598-018-23606-w

Kaneda, T. (1991). Iso- and Anteiso-Fatty Acids in Bacteria: Biosynthesis, Function, and Taxonomic Significance. *Microbiol. Rev.* 55, 288–302. doi:10.1128/mr.55.2.288-302.1991

Kawamura, K., and Gagosian, R. B. (1987). Implications of ω-oxocarboxylic Acids in the Remote marine Atmosphere for Photo-Oxidation of Unsaturated Fatty Acids. *Nature* 325, 330–332. doi:10.1038/325330a0

Kawamura, K., Yokoyama, K., Fujii, Y., and Watanabe, O. (1999). Implication of Azelaic Acid in a Greenland Ice Core for Oceanic and Atmospheric Changes in High Latitudes. *Geophys. Res. Lett.* 26, 871–874. doi:10.1029/1999GL9000116

Lachniet, M. S. (2009). Climatic and Environmental Controls on Speleothem Oxygen-Isotope Values. *Quat. Sci. Rev.* 28, 412–432. doi:10.1016/j.quascirev.2008.10.021

Li, X., Wang, C., Huang, J., Hu, C., and Xie, S. (2011). Seasonal Variation of Fatty Acids from Drip Water in Heshang Cave, central China. *Appl. Geochem.* 26, 341–347. doi:10.1016/j.apgeochem.2010.12.007

Liu, H., and Liu, W. (2017). Concentration and Distributions of Fatty Acids in Algae, Submerged Plants and Terrestrial Plants from the Northeastern Tibetan Plateau. *Org. Geochem.* 113, 17–26. doi:10.1016/j.orggeochem.2017.08.008

Logan, G. A., and Eglinton, G. (1994). Biogeochemistry of the Miocene Lacustrine deposit, at Clarkia, Northern Idaho, U.S.A. *Org. Geochem.* 21, 857–870. doi:10.1016/0146-6380(94)90045-0

Lone, M. A., Ahmad, S. M., Dung, N. C., Shen, C.-C., Raza, W., and Kumar, A. (2014). Speleothem Based 1000-year High Resolution Record of Indian Monsoon Variability during the Last Deglaciation. *Palaeogeogr. Palaeoclimatol. Palaeoecol.* 395, 1–8. doi:10.1016/j.palaeo.2013.12.010

McDermott, F. (2004). Palaeo-climate Reconstruction from Stable Isotope Variations in Speleothems: A Review. *Quat. Sci. Rev.* 23, 901–918. doi:10.1016/j.quascirev.2003.06.021

McGarry, S. F., and Baker, A. (2000). Organic Acid Fluorescence: Applications to Speleothem Palaeoenvironmental Reconstruction. *Quat. Sci. Rev.* 19, 1087–1101. doi:10.1016/S0277-3791(99)00087-6

Mendoza, Y. A., Gülaçar, F. O., and Buchs, A. (1987). Comparison of Extraction Techniques for Bound Carboxylic Acids in Recent Sediments. *Chem. Geology* 62, 321–330. doi:10.1016/0009-2541(87)90094-5

Meyers, P. A., and Ishiwatari, R. (1993). Lacustrine Organic Geochemistry-An Overview of Indicators of Organic Matter Sources and Diagenesis in lake Sediments. *Org. Geochem.* 20, 867–900. doi:10.1016/0146-6380(93)90100-P

Murata, F., Hayashi, T., Matsumoto, J., and Asada, H. (2007). Rainfall on the Meghalaya Plateau in Northeastern India-one of the Rainiest Places in the World. *Nat. Hazards* 42, 391–399. doi:10.1007/s11069-006-9084-z

Ouyang, X., Guo, F., and Bu, H. (2015). Lipid Biomarkers and Pertinent Indices from Aquatic Environment Record Paleoclimate and Paleoenvironment Changes. *Quat. Sci. Rev.* 123, 180–192. doi:10.1016/j.quascirev.2015.06.029

Pokhrel, A., Kawamura, K., Seki, O., Matoba, S., and Shiraiwa, T. (2015). Ice Core Profiles of Saturated Fatty Acids (C 12:0 -C 30:0) and Oleic Acid (C 18:1) from Southern Alaska since 1734 AD: A Link to Climate Change in the Northern Hemisphere. *Atmos. Environ.* 100, 202–209. doi:10.1016/j.atmosenv.2014.11.007

Prasad, S., and Enzel, Y. (2006). Holocene Paleoclimates of India. *Quat. Res.* 66, 442–453. doi:10.1016/j.yqres.2006.05.008

Rousseau, L., Laafar, S., Pèpe, C., and de Lumley, H. (1995). Sterols as biogeochemical markers: Results from ensemble E of the stalagmitic floor, Grotte du Lazaret, Nice, France. *Quat. Sci. Rev.* 14, 51–59. doi:10.1016/0277-3791(94)00111-N

Ruess, L., Häggblom, M. M., Garcı́a Zapata, E. J., and Dighton, J. (2002). Fatty Acids of Fungi and Nematodes-Possible Biomarkers in the Soil Food Chain?. *Soil Biol. Biochem.* 34 (6), 745–756. doi:10.1016/S0038-0717(01)00231-0

Rushdi, A. I., Clark, P. U., Mix, A. C., Ersek, V., Simoneit, B. R. T., Cheng, H., et al. (2011). Composition and Sources of Lipid Compounds in Speleothem Calcite from Southwestern Oregon and Their Paleoenvironmental Implications. *Environ. Earth Sci.* 62, 1245–1261. doi:10.1007/s12665-010-0613-4

Russell, J. M., and Werne, J. P. (2007). The Use of Solid Phase Extraction Columns in Fatty Acid Purification. *Org. Geochem.* 38, 48–51. doi:10.1016/j.orggeochem.2006.09.003

Sinha, A., Kathayat, G., Cheng, H., Breitenbach, S. F. M., Berkelhammer, M., Mudelsee, M., et al. (2015). Trends and Oscillations in the Indian Summer Monsoon Rainfall over the Last Two Millennia. *Nat. Commun.* 6, 7309. doi:10.1038/ncomms7309

Staubwasser, M., Sirocko, F., Grootes, P. M., and Erlenkeuser, H. (2002). South Asian Monsoon Climate Change and Radiocarbon in the Arabian Sea during Early and Middle Holocene. *Paleoceanography* 17, 15. doi:10.1029/2000pa000608

Suutari, M., and Laakso, S. (1994). Microbial Fatty Acids and thermal Adaptation. *Crit. Rev. Microbiol.* 20, 285–328. doi:10.3109/10408419409113560

Volkman, J. K. (2006). Lipid Markers for marine Organic Matter. *Handbook Environ. Chem.* 2, 27–70. doi:10.1007/698_2_002

Wakeham, S. G. (1999). Monocarboxylic, Dicarboxylic and Hydroxy Acids Released by Sequential Treatments of Suspended Particles and Sediments of the Black Sea. *Org. Geochem.* 30, 1059–1074. doi:10.1016/S0146-6380(99)00084-4

Wakeham, S. G., and Beier, J. A.(1991). Fatty Acid and Sterol Biomarkers as Indicators of Particulate Matter Source and Alteration Processes in the Black Sea. *Deep-Sea Res.* 38, 5943–5968.

Wang, C., Bendle, J. A., Greene, S. E., Griffiths, M. L., Huang, J., Moossen, H., et al. (2019). Speleothem Biomarker Evidence for a Negative Terrestrial Feedback on Climate during Holocene Warm Periods. *Earth Planet. Sci. Lett.* 525, 115754. doi:10.1016/j.epsl.2019.1157542019

Wang, C., Bendle, J. A., Zhang, H., Yang, Y., Liu, D., Huang, J., et al. (2018). Holocene Temperature and Hydrological Changes Reconstructed by Bacterial 3-hydroxy Fatty Acids in a Stalagmite from central China. *Quat. Sci. Rev.* 192, 97–105. doi:10.1016/j.quascirev.2018.05.030

Wang, C., Zhang, H., Huang, X., Huang, J., and Xie, S. (2012). Optimization of Acid Digestion Conditions on the Extraction of Fatty Acids from Stalagmites. *Front. Earth Sci.* 6, 109–114. doi:10.1007/s11707-012-0311-5

Wang, J., Sun, L., Chen, L., Xu, L., Wang, Y., and Wang, X. (2016). The Abrupt Climate Change Near 4,400 Yr BP on the Cultural Transition in Yuchisi, China and its Global Linkage. *Sci. Rep.* 6, 27723. doi:10.1038/srep27723

Willecke, K., and Pardee, A. B. (1971). Fatty Acid-Requiring Mutant of Bacillus Subtilis Defective in Branched Chain α-Keto Acid Dehydrogenase. *J. Biol. Chem.* 246, 5264–5272. doi:10.1016/s0021-9258(18)61902-7

Wörmer, L., Elvert, M., Fuchser, J., Lipp, J. S., Buttigieg, P. L., Zabel, M., et al. (2014). Ultra-high-resolution Paleoenvironmental Records via Direct Laser-

Based Analysis of Lipid Biomarkers in Sediment Core Samples. *Proc. Nat. Acad. Sci.* 111, 15669–15674. doi:10.1073/pnas.1405237111

Xie, S., Huang, J., Wang, H., Yi, Y., Hu, C., Cai, Y., et al. (2005). Distributions of Fatty Acids in a Stalagmite Related to Paleoclimate Change at Qingjiang in Hubei, Southern China. *Sci. China Ser. D-earth Sci.* 48, 1463. doi:10.1360/04yd0155

Xie, S., Yi, Y., Huang, J., Hu, C., Cai, Y., Collins, M., et al. (2003). Lipid Distribution in a Subtropical Southern China Stalagmite as a Record of Soil Ecosystem Response to Paleoclimate Change. *Quat. Res.* 60, 340–347. doi:10.1016/j.yqres.2003.07.010

Yang, H., Ding, W., Zhang, C. L., Wu, X., Ma, X., He, G., et al. (2011). Occurrence of Tetraether Lipids in Stalagmites: Implications for Sources and GDGT-Based Proxies. *Org. Geochem.* 42, 108–115. doi:10.1016/j.orggeochem.2010.11.006

Zhang, Y., Meyers, P. A., Gao, C., Liu, X., Wang, J., and Wang, G. (2017). Holocene Climate Change in Northeastern China Reconstructed from Lipid Biomarkers in a Peat Sequence from the Sanjiang Plain. *Org. Geochem.* 113, 105–114. doi:10.1016/j.orggeochem.2017.07.018

Zhao, J., Zhang, H., Han, Z., Liu, G., and Lu, B. (2014). The Vicissitudes of Microorganism and Vegetation Recorded by Lipid Biomarkers in the Antarctic Penguin Habitat and Their Implications for Climate Change. *Acta Ecologica Sinica* 34, 277–283. doi:10.1016/j.chnaes.2014.07.001

Zheng, Y., Zhou, W., Meyers, P. A., and Xie, S. (2007). Lipid Biomarkers in the Zoigê-Hongyuan Peat Deposit: Indicators of Holocene Climate Changes in West China. *Org. Geochem.*, 38 1927–1940.

Zhou, W., Xie, S., Meyers, P. A., and Zheng, Y. (2005). Reconstruction of Late Glacial and Holocene Climate Evolution in Southern China from Geolipids and Pollen in the Dingnan Peat Sequence. *Org. Geochem.* 36, 1272–1284. doi:10.1016/j.orggeochem.2005.04.005

Conflict of Interest: The authors declare that the research was conducted in the absence of any commercial or financial relationships that could be construed as a potential conflict of interest.

frontiers in Earth Science

ORIGINAL RESEARCH
published: 30 August 2021
doi: 10.3389/feart.2021.689508

Sedimentary Dynamics of the Central South Yellow Sea Revealing the Relation Between East Asian Summer and Winter Monsoon Over the Past 6000 years

Wenzhe Lyu[1,2], *Tengfei Fu*[2,3], *Zhangxi Hu*[4], *Ying Zhong Tang*[4], *Guangquan Chen*[2,3], *Xingyong Xu*[2,3], *Yanping Chen*[5] *and Shenliang Chen*[1]*

[1]*State Key Laboratory of Estuarine and Coastal Research, East China Normal University, Shanghai, China,* [2]*Key Laboratory of Marine Geology and Metallogeny, First Institute of Oceanography, Ministry of Natural Resources, Qingdao, China,* [3]*Laboratory of Marine Ecology and Environmental Science, Qingdao National Laboratory for Marine Science and Technology, Qingdao, China,* [4]*CAS Key Laboratory of Marine Ecology and Environmental Sciences, Institute of Oceanology, Chinese Academy of Sciences, Qingdao, China,* [5]*Key Laboratory of Engineering Oceanography, Second Institute of Oceanography, Ministry of Natural Resources, Hangzhou, China*

Edited by:
Praveen K. Mishra,
Wadia Institute of Himalayan Geology,
India

Reviewed by:
Xiaodong Miao,
Linyi University, China
Kizhur Sandeep,
Central University of Kerala, India

***Correspondence:**
Shenliang Chen
slchen@sklec.ecnu.edu.cn

Specialty section:
This article was submitted to
Quaternary Science, Geomorphology
and Paleoenvironment,
a section of the journal
Frontiers in Earth Science

Received: *01 April 2021*
Accepted: *18 August 2021*
Published: *30 August 2021*

Citation:
Lyu W, Fu T, Hu Z, Tang YZ, Chen G, Xu X, Chen Y and Chen S (2021) Sedimentary Dynamics of the Central South Yellow Sea Revealing the Relation Between East Asian Summer and Winter Monsoon Over the Past 6000 years.
Front. Earth Sci. 9:689508.
doi: 10.3389/feart.2021.689508

The mud areas of East Asian marginal seas record considerable information about regional environmental evolution. However, debate continues regarding the relative importance of the major factors in regional sedimentary dynamics, i.e., the East Asian summer monsoon, East Asian winter monsoon, and oceanic circulation. In this study, we investigated the characteristics of grain size from a gravity core obtained in the South Yellow Sea to reveal changes in sedimentary dynamics since 6,000 years BP, and to elucidate the relationship between the East Asian summer monsoon and the East Asian winter monsoon. We found that the mean grain size was in the range of 6.9–7.8 Φ, the sediment was poorly sorted within a small range (1.2, 1.5), and the M values from 4.7 to 6.7 μm and most of the C values from 24 to 65 μm suggested pelagic suspension transport. Results indicated that the intensity of both the East Asian summer monsoon and the East Asian winter monsoon showed a fluctuating trend of decrease after approximately 6,000 years BP, and that the relationship between them was generally anticorrelated. Based on these results, we suggest that positive correlation between the East Asian summer monsoon and the East Asian winter monsoon usually results in the fall or establishment of ancient dynasties in the Central Plains of China and that negative correlation between them is controlled by strong solar radiation. Weakening of solar radiation diminishes its control of the intensity of (and thus the correlation between) the East Asian summer monsoon and the East Asian winter monsoon, at which time the North Atlantic Oscillation plays a modulating role.

Keywords: South Yellow Sea (SYS), continental mud area, sedimentary evolution, East Asian Winter Monsoon (EAWM), East Asian Summer Monsoon (EASM)

HIGHLIGHTS

1) Trends for the EASM and the EAWM and for their relationship since 6,000 years BP were extracted.
2) Negative correlation between the EASM and the EAWM is controlled by strong solar radiation.

INTRODUCTION

In recent years, the South Yellow Sea (SYS) has become an area of active research for paleoclimate, sedimentary environment, and marine current/hydrodynamics studies (Kong et al., 2006; Xiang et al., 2008; Zhao et al., 2013; Liu et al., 2014; Yang et al., 2018; Zhang et al., 2018; Wang et al., 2019). As a typical shelf sea, the SYS is an important reservoir of and transportation channel for sediments from the Yellow River, Yangtze River, and some local rivers. It has the largest area of mud in the shelf area of the eastern China Seas, and its sediments are sensitive to changes of sea level and climate (Yang and Youn, 2007). Many studies have shown that the volume of river input into the SYS is determined mainly by precipitation that is controlled by the East Asian summer monsoon (EASM) (Dykoski et al., 2005; Ding et al., 2008; Hu et al., 2008; Zhou et al., 2012). Recent studies have also revealed that the modern circulation system of the SYS, which largely comprises the Yellow Sea Warm Current (YSWC) and the Yellow Sea Coastal Currents (YSCC), was established approximately 6,000 years BP and that it has a relationship with the East Asian winter monsoon (EAWM) (Yuan and Hsueh, 2010; Xing et al., 2012; Zhao et al., 2013). Therefore, studies on the sediment sources and current systems of the SYS are actually linked to the East Asian monsoon (EAM).

The EAM climate system is an important component of the global climate system. Thus, further study of the patterns and forcing mechanisms associated with the EAM will help explain global climate change. Previous studies have used multiple proxies archived in lakes (Yancheva et al., 2007; Li et al., 2015; Li et al., 2018), peat (Hong et al., 2001; Hong et al., 2009), stalagmites (Hu et al., 2008; Wang K. et al., 2008; Cheng et al., 2019; Liu et al., 2020), ice cores (Thompson, 1997), and loess (Sun et al., 2006; Song et al., 2014; Beck et al., 2018) to reveal the long-term change of the EAM system and its effects. With the extension of the research effort toward the ocean, the extraction of EAM information from continental shelves has increased (Wang Y. et al., 2008; Zheng et al., 2010; Qiao et al., 2011; Hu et al., 2012; Zhou et al., 2012) and the most extensive proxy is the grain size of shelf sediment. However, it remains to be confirmed whether the winter monsoon or the summer monsoon is the dominant factor controlling grain size. For example, Xiao et al. (2006) used the sensitive grain size from the mud area of the inner shelf of the East China Sea to reconstruct a high-resolution record of the EAWM. Qiao et al. (2011) used the key grain size component from the East China Sea to reconstruct the record of the late Holocene EAWM. Hu et al. (2012) suggested that the grain size parameters of cores from the central mud area of the SYS are controlled mainly by the EAWM, and thus they recurved the variations of the EAWM since the middle Holocene. However, Wang Y. et al. (2008) suggested that the mean grain size of a sediment core obtained from the inner shelf of the East China Sea had no direct link to the EAWM, but that the rate of deposition exhibited a trend consistent with the EASM. Based on high-resolution magnetic analysis, Zheng et al. (2010) also believed that the sediment from the same core contains information relating to the EASM. Zhou et al. (2012) found that the sedimentary characteristics of a sediment core from the mud area of the Northern Yellow Sea correlated well with spatially averaged precipitation around the Yellow River, which could serve as reasonable proxies for summer monsoon strength. Therefore, it is necessary to confirm the role of EASM and EAWM in the sediment change.

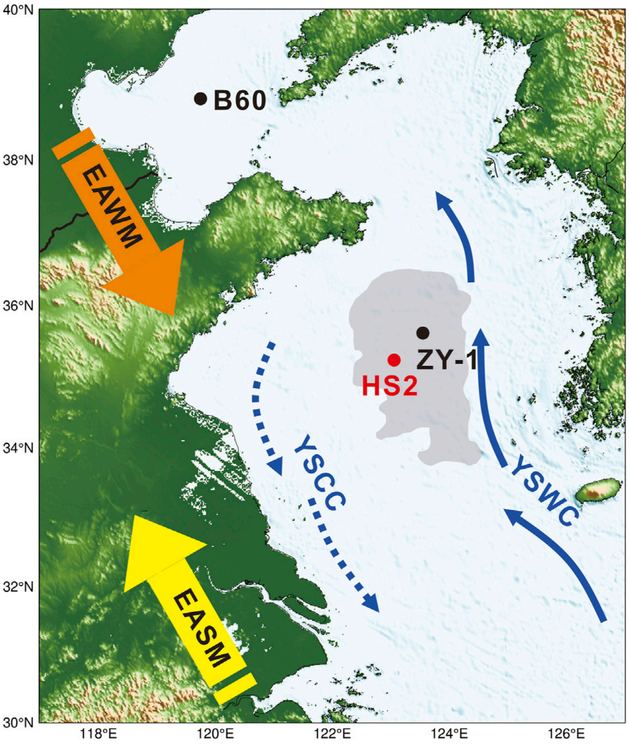

FIGURE 1 | Schematic illustration of the EAM and currents, the location of cores HS2 (used in this study), B60 (Lyu et al., 2020), and ZY-1 (Hu et al., 2012), and the central mud area in the South Yellow Sea (shaded area). (Modified from Li G. et al., 2016; Wessel et al., 2019; Ding et al., 2017).

It is also important to investigate the relationship between EASM and EAWM. Previous studies have shown that the EAM has an important impact on East Asia, especially China, and that there is negative correlation between the EAWM and temperature in winter and positive correlation between the EASM and precipitation in summer (Wu and Chan, 2005; Huang et al., 2007; Ding et al., 2008; Ding et al., 2009; Li and Wang, 2012). Thus, strong positive correlation often results in an anomalously strong or weak EASM and EAWM, which can lead to serious flood and drought disasters in different regions of China (Ding et al., 2008; Ding et al., 2009).

The nature of the relationship between the EASM and the EAWM during the Holocene remains controversial (Xiao et al.,

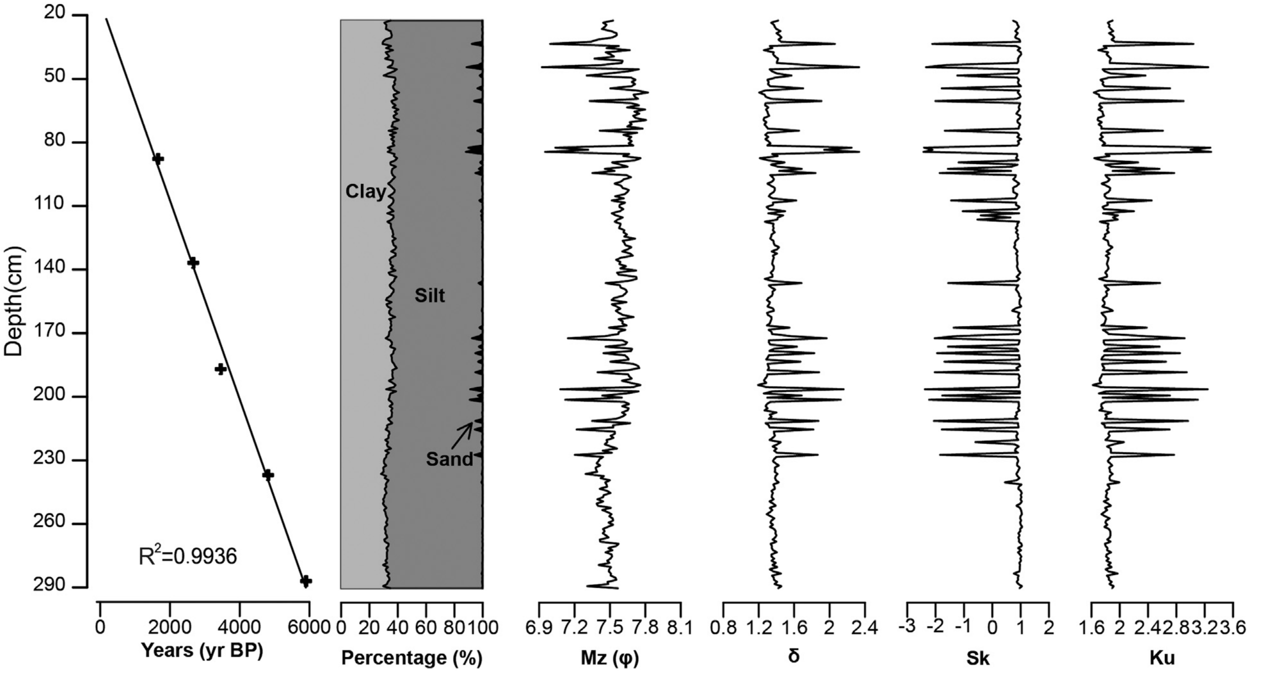

FIGURE 2 | Age model and profiles of core HS2 with grain size changes: clay, silt, and sand content, mean grain size, sorting, skewness, and kurtosis.

2006; Yancheva et al., 2007; Zhang and Lu, 2007; Zhou and Zhao, 2009; Steinke et al., 2011; Ge et al., 2017), although antiphase correlation has been identified on orbital timescales (Ding et al., 1995). The main reasons for ambiguity could include dating issues, the extraction of proxies, and different resolutions used in different studies. Therefore, it is vital to document monsoonal variability from different sedimentary sequences to clarify the factors controlling sedimentation on the continental shelves of the SYS, and thus to elucidate the relationship between the EASM and the EAWM.

In the current study, we analyzed the sediment grain size of core HS2, which was obtained in the central mud area of the SYS, and we reconstructed the EASM and EAWM records in the SYS for the period since 6,000 years BP. Based on the results, the dominant sedimentary dynamics within the study area and the relationship between the EASM and the EAWM were investigated.

MATERIALS AND METHODS

Core HS2

The studied core (HS2) was collected from the central mud area of the SYS (35°30.0′N, 122°59.9′E; water depth: 88 m) in September 2015 during a research cruise of the R/V *DONG FANG HONG ER HAO* (**Figure 1**), which was organized by the National Natural Science Foundation of China. The length of core obtained from the drill site was 290 cm, and the section of 22–290 cm below the core top, which was undisturbed and well constrained by radiocarbon dating, was selected for this study. This 269-cm-thick interval was sampled into 1-cm sections for analyses that included accelerator mass spectrometry (AMS) ^{14}C dating and sediment grain size measurements.

Age Model

Five foraminiferal samples were collected for AMS ^{14}C dating at the Beta Analytic Radiocarbon Dating Laboratory, Miami, United States. We converted the radiocarbon ages to calibrated calendar ages using the Calib 7.0 program (Stuiver and Reimer, 1993) and by applying the regional marine reservoir effect (ΔR value = −81 ± 60 years) chosen from the Marine Reservoir Correction Database (**Table 1**).

The age–depth correlation for the core record is shown in **Figure 2**. According to Qiao et al. (2017), the average modern sedimentation rate of the central Yellow Sea mud area is 1.4 mm/year, and that the mixed section of our core from 0 to 22 cm might have accumulated over approximately 157 years. Comparison of the modern sedimentation rate ages at the depth of 13 cm (1950 AD or 0 year BP) with the age at the same level determined from interpolation between the five AMS ^{14}C dates suggests that the radiocarbon age is in excess of the modern sedimentation rate age by 500 years. In consideration of both the benthic foraminiferal effect and the reservoir effect on the measurements of bulk organic carbon, we subtracted a value of 500 years from all ^{14}C ages prior to calibration.

Sediment Grain Size

In all, 269 grain size samples were measured at 1-cm intervals. An amount of approximately 0.5 g of material was collected from each sample, which was then pretreated with both a 10–20 ml

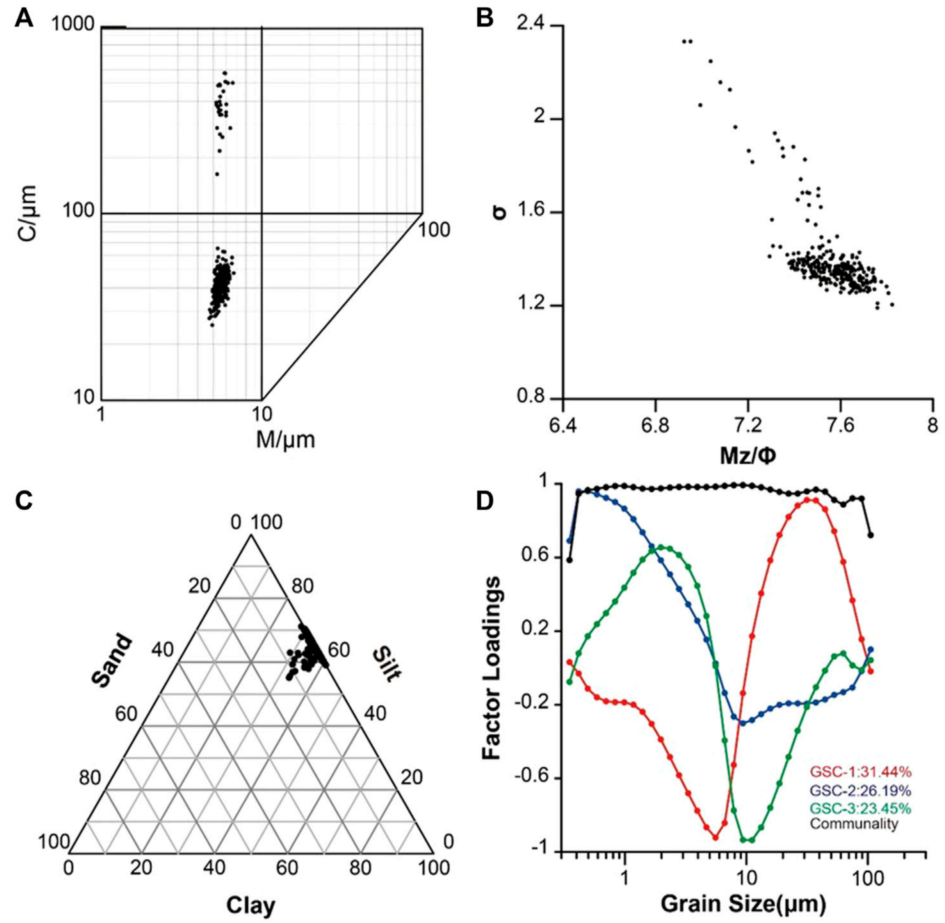

FIGURE 3 | Sediment grain size analysis of core HS2 samples: **(A)** relationship between C (the one percentile) and M (the median diameter), **(B)** relationship between mean grain size (represented by Mz, Φ values) and sorting (represented by σ, nondimensional parameters), **(C)** ternary diagrams for clay, silt, and sand components, and **(D)** VPCA results of core HS2

H_2O_2 solution (30%) to remove organic matter and a 10 ml HCl solution (10%) for 12 h to remove carbonates. Prior to measurement, all samples were rinsed with deionized water in a centrifuge at a rotation speed of 4,000 rpm and dispersed by ultrasonic treatment over a 10-min period. Measurements were obtained using a Malvern Mastersizer 2000 laser particle size analyzer (Malvern Panalytical Ltd., United Kingdom) at the Key Laboratory of Marine Sedimentology and Environmental Geology, First Institute of Oceanography, MNR. Fifty grain size classes in the range 0.3–2000 µm were selected for further analysis.

RESULTS AND ANALYSES

We chose the moment method of McManus (1988) to calculate grain size parameters, including mean grain size (Mz), sorting (σ), skewness (Sk), and kurtosis (Ku), as follows:

$$\text{mean grain size}: \ Mz = \frac{\sum f m_\phi}{100}, \tag{1}$$

$$\text{sorting}: \sigma = \sqrt{\frac{\sum f\left(m_\phi - Mz\right)^2}{100}}, \tag{2}$$

$$\text{skewness}: \mathrm{SK} = \frac{\sum f\left[m_\phi - Mz\right]^3}{100\sigma^3}, \tag{3}$$

$$kurtosis: Ku = \frac{\sum f\left[m_\phi - Mz\right]^4}{100\sigma^4}, \tag{4}$$

where m_Φ represents grain size (unit: Φ), f represents the percentage content of each grain grade, $\sum f = 100$, and σ, Sk, and Ku are nondimensional parameters.

In addition, we selected one coupled parameter, i.e., the C-M pattern (Passega, 1957; 1964), where the one percentile C reflects the initial hydrodynamic energy and the median diameter M reflects the average hydrodynamic energy.

As a result, the range of Mz was 6.9–7.8 Φ, most of which was between 7.4 and 7.8 Φ, and the material was poorly sorted within a small range (1.2, 1.5) (**Figures 2**, **3B**). There was negative correlation between Mz and σ, which could be divided into two parts with different slopes (**Figure 3B**). For most samples,

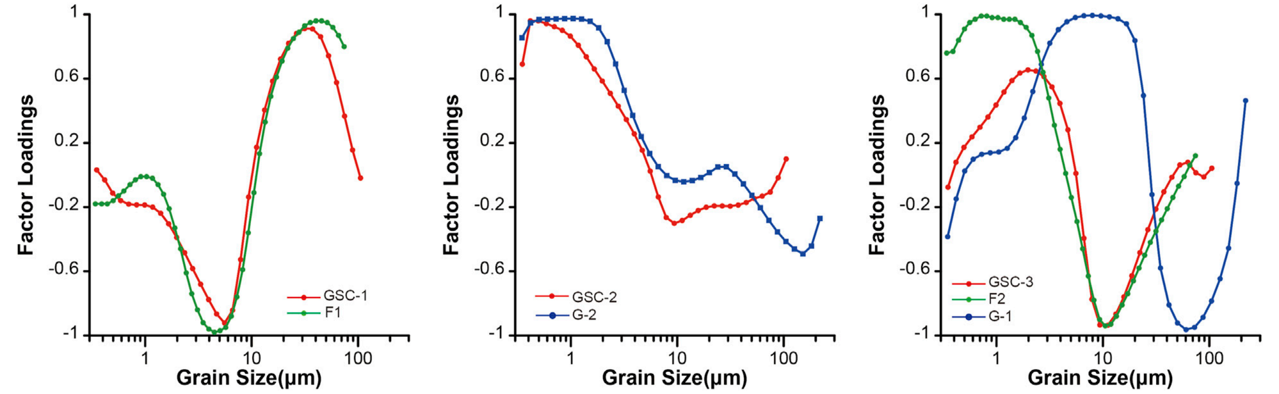

FIGURE 4 | VPCA results from different types of samples: GSC-1, GSC-2 and GSC-3 of core HS2 (this study), F1 and F2 of core ZY-1 (Hu et al., 2012) and G-1 and G-2 of core B60 (Lyu et al., 2020).

sediment sorting improved slowly with the decrease of Mz. The values of Sk and Ku were largely in the range of 0.6–1.0 and 1.5–1.9, respectively (**Figure 2**), indicating that the samples had positive skewness and normal kurtosis. The contents of silt (55–70%) and clay (30–40%) particles changed little, while the content of sand particles was mostly <1%, except for a small number of layers in which it was <10% (**Figures 2**, **3C**). As shown in the ternary diagrams and parameter scatter plots (**Figure 3C**), the sedimentary environment was reasonably stable with no significant change.

The C-M pattern is useful for analyzing both the mode of sediment transport and the hydrodynamic intensity. As shown, the M values from 4.7 to 6.7 μm indicate that the average hydrodynamic energy was stable and weak, while the C values varied widely from 25 to 600 μm (**Figure 3A**). Most points are located in a small area in which the C values are in the range of 25–65 μm (**Figure 3A**), indicating that the initial hydrodynamic energy was weak. However, the C values in the range of 125–600 μm indicate a wide range of unstable initial hydrodynamic energy, which might be related to a change of sediment source or to a highly dynamic sedimentary event. According to Passega (1957, 1964), the points located in the range of 25–65 μm suggest pelagic suspension transport. These results showed that the sedimentary environment was reasonably stable, and the sediments can be used to extract paleoenvironmental information.

For further analysis of grain size, we used a varimax-rotated principal component analysis (VPCA) method based on a correlation matrix for grain size spectra. Because the content of grain sizes >105.6 μm is usually <0.01%, we extracted 34 grain size classes in the range of 0.3–105.6 μm for the VPCA. Three components extracted from the VPCA procedure, i.e., GSC-1, GSC-2, and GSC-3, accounted for 81.08% of the total variance (**Figure 4D**). GSC-1 (31.44% of the data variance) consisted of two groups (2.8–7.9 and 15.8–62.8 μm), of which the fine part and the coarse part provided high negative and positive loading, respectively. Conversely, for GSC-2 (26.19% of the data variance) and GSC-3 (23.45% of the data variance), the fine part (GSC-2: 0.35–1.97 μm, GSC-3: 1.18–3.32 μm) and the coarse part (GSC-2: 7.88–13.24 μm, GSC-3: 7.88–18.72 μm) provided positive and negative loading, respectively.

To integrate the information on various sedimentary dynamics, we obtained a new series (i.e., GSC-23) according to the data variance of GSC-2 and GSC-3:

$$GSC-23 = GSC-2 \times 26.19 + GSC-3 \times 23.45 \qquad (5)$$

DISCUSSION

Variability of the East Asian Monsoon

For the study of the EAM, a reliable information carrier is crucial. Generally, fine-grained sediments can be used as an effective carrier, but the premise is that their sedimentary records are complete, continuous and can be extracted smoothly. The temporal variability of grain size parameters, along with C-M pattern, ternary diagrams, and the relationship between sorting and mean grain size, confirms a relatively stable depositional environment (**Figures 2**, **3A–C–C**). Thus, the sediments from core HS2 are well-suited for extracting paleoenvironmental information, e.g., monsoonal variability, sedimentary dynamics.

Based on previous studies (Yang et al., 2003; Yang and Youn, 2007; Zhou et al., 2015), it is known that the development of the mud area in the SYS is affected primarily by oceanic currents and the supply of sediment, both of which have obvious seasonal differences. In combination with the VPCA results shown in **Figure 3D**, i.e., the different loadings of fine and coarse particles between GSC-1, GSC-2, and GSC-3, we infer that GSC-2 and GSC-3 mostly represent the influence of weaker hydrodynamic conditions in summer, when the change of grain size is controlled principally by sediment supply. Conversely, GSC-1 most likely reflects the sedimentary processes in winter, when the study area is influenced primarily by the YSCC and YSWC.

It is usually considered that finer sediments on the continental shelves of East Asian marginal seas can be used as a proxy for the EASM because sediments dominated by the EAWM are relatively coarser. For example, the median grain size (8–14 μm) of core

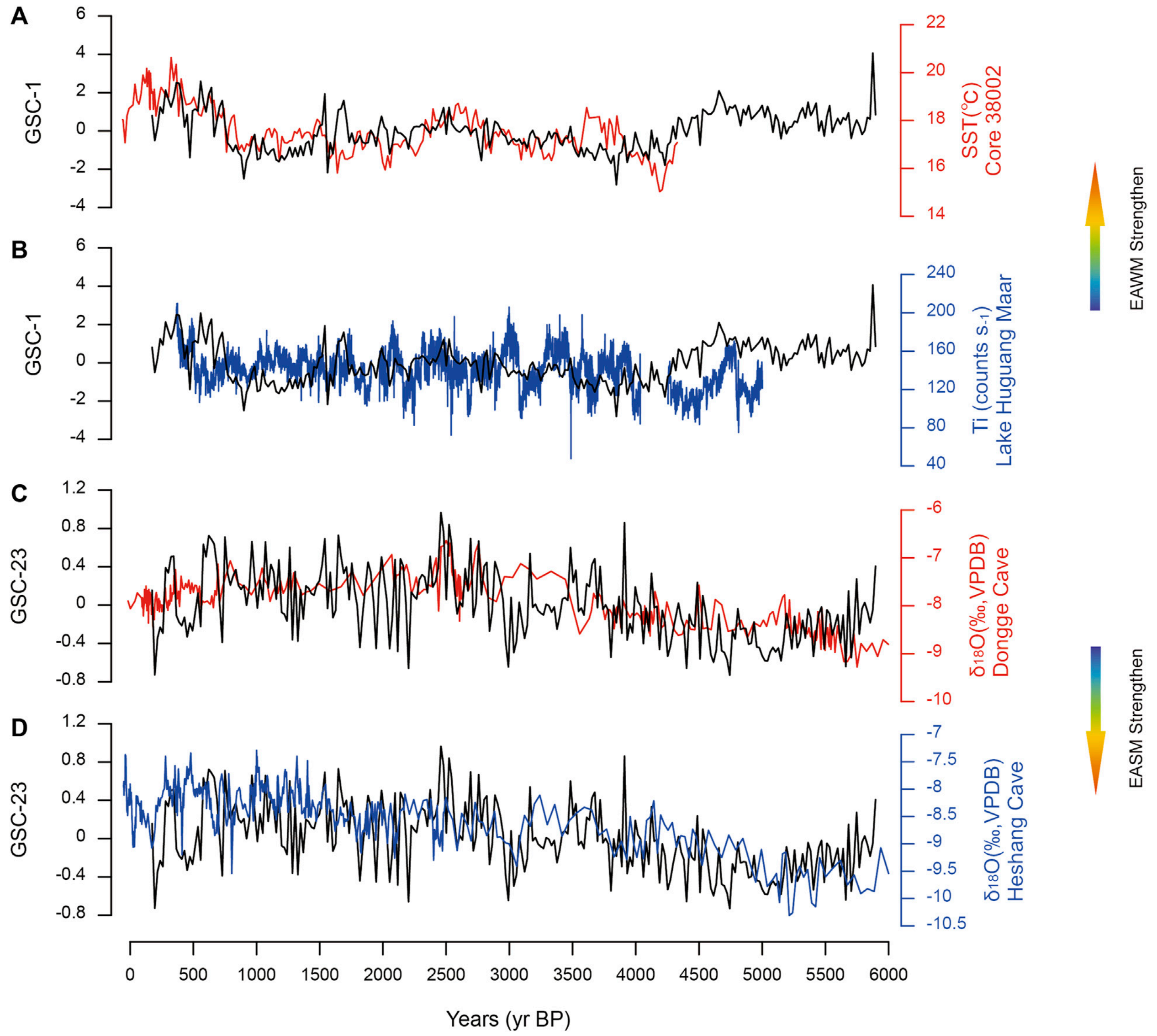

FIGURE 5 | Comparison between various paleoenvironmental proxies since 6,000 years BP: **(A)** the GSC-1 curve and sea surface temperature (SST) records of sediment core 38,002 in the North Yellow Sea (Zhang et al., 2019), **(B)** the GSC-1 curve and Ti content records of Lake Huguang Maar (Yancheva et al., 2007), and **(C,D)** the GSC-23 curve and stalagmite δ^{18}O series of Heshang Cave (Hu et al., 2008) and Dongge Cave (Dykoski et al., 2005), indicating EASM intensity.

M38002 from the North Yellow Sea (Zhou et al., 2012) and the grain size VPCA results (10–40 μm) of core B60 from the Bohai Sea (Lyu et al., 2020) were extracted as proxies for the EASM, whereas in a record of the EAWM, a sandy component contributes substantially to sediment grain size variation (Qiao et al., 2011; Hu et al., 2012; Zhang S. et al., 2020). We chose the grain size VPCA results of core ZY-1 from the SYS (Hu et al., 2012) and core B60 for comparison with our results (**Figure 4**). The same structure of data is evident between GSC-1 of core HS2 and F1 of core ZY-1, which was a proxy for the EAWM. The same structure of data also exists between GSC-2 of core HS2 and G-2 of core B60, as well as GSC-3 and G-1, GSC-3 and F2 of core ZY-1. It is also confirmed that G-12 of core B60 (combination of G-1 and G-2 according to their variance percentages) is a proxy for the EASM, F2 of core ZY-1 is speculated to reflect sedimentary processes in summer. Thus, we conclude that GSC-1 and GSC-23 of core HS2 could be used as proxies for the EAWM and the EASM, respectively. Furthermore, we find that GSC-2 of core HS2 has the same factor loadings in different grain sizes as G-2 of core B60, while the grain size of GSC-3 is finer than that of G-1 of core B60. The fine part plays a dominant role in GSC-2, which represent the weaker hydrodynamic conditions in summer. Through the comparison between GSC-3, F2 and G-1, considering the distance from the Yellow River Estuary (the main source area), it is consistent with the characteristics that the grain size gradually becomes finer after long-distance transportation. Thus, we infer that GSC-2 of core HS2 might represent

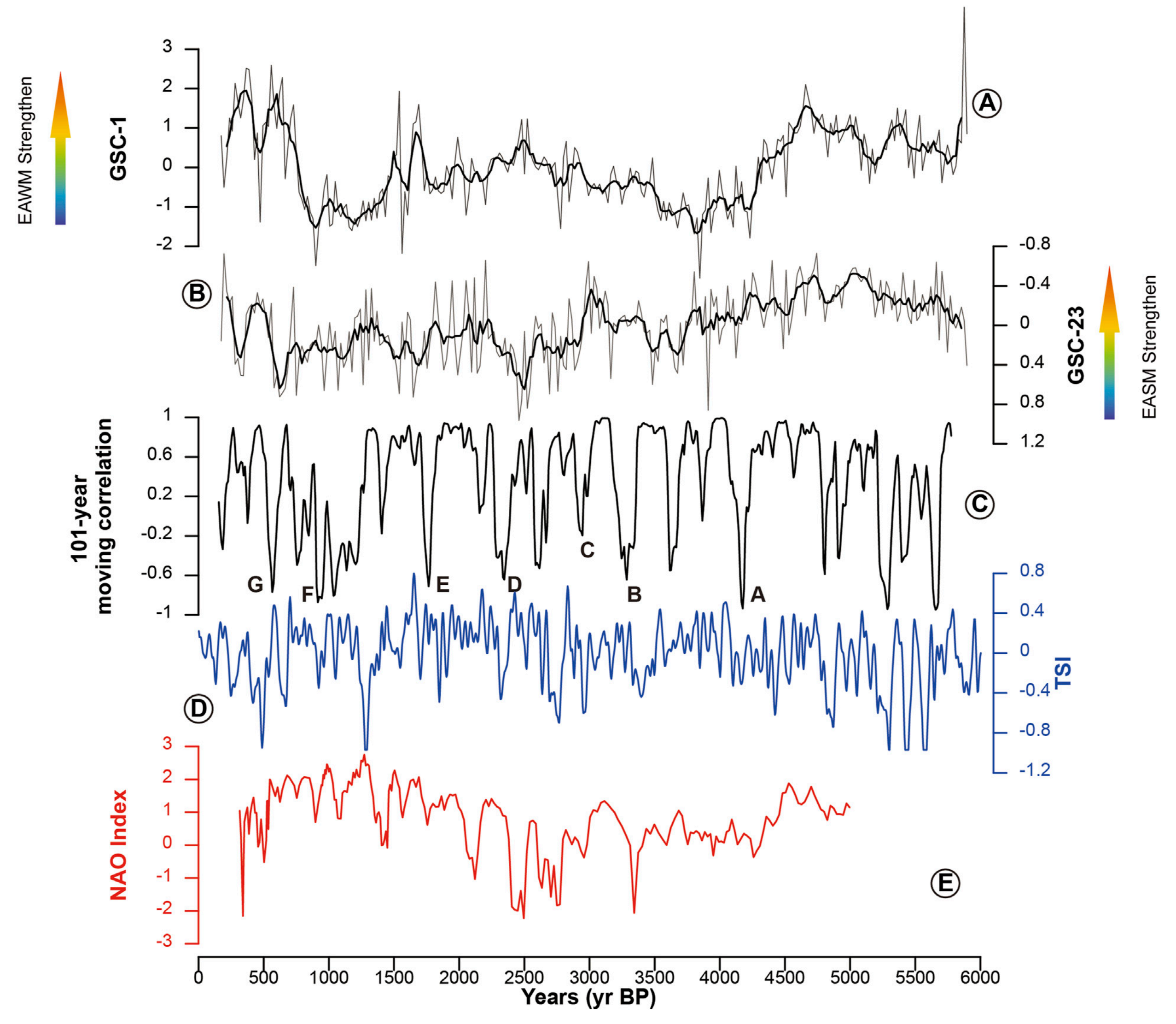

FIGURE 6 | (A,B) Variations of the EASM and the EAWM. The black lines represent the 5-point running average. **(C)** The 101-years moving correlation between the EASM and the EAWM (capital letters represent the times when certain ancient Chinese regimes were established, i.e., A: Xia Dynasty, B: Shang Dynasty, C: Eastern Zhou Dynasty, D: Han Dynasty, E: Xin Dynasty, F: Ming Dynasty, and G: Qing Dynasty). **(D)** Total solar irradiance (Steinhilber et al., 2009). **(E)** North Atlantic Oscillation index reconstructed from Lake SS1220 (Olsen et al., 2012).

sedimentary dynamics, and that GSC-3 represents river supply in summer.

In East Asia, a stronger EASM often brings increased precipitation. This can lead to augmentation of the transport capacity of rivers, which in turn leads to increase in both the sediment supply and the grain size values in the SYS. Given that the coarse part indicates negative loading in GSC-2 and GSC-3, but the fine part indicates positive loading, the low (high) values indicate greater (less) impact of coarse part, thus denote a strong (weak) EASM. In winter, the sedimentary processes are dominated mainly by the EAWM. A stronger EAWM would lead to resuspension of more coarse sediment and to an increase of the suspended sediment concentration. Meanwhile, the YSCC and YSWC would also both be strengthened by a stronger EAWM, which would lead to enhancement of the transport of the coarser part to the central mud area. Given that the coarse part indicates positive loading in GSC-1, the low (high) values denote a weak (strong) EAWM. In summary, of the factors extracted by VPCA, we conclude that GSC-1 and GSC-23 could be used as proxies for the EAWM and the EASM, respectively.

To validate our inference, we compared our proxies with other published proxies of the EAM (**Figure 5**). It can be seen that our proxy for the EASM (GSC-23) has reasonable correspondence with stalagmite $\delta^{18}O$ from Heshang Cave (Hu et al., 2008) and Dongge Cave (Dykoski et al., 2005), which are generally accepted as proxies for the EASM. Lower (higher) values of stalagmite $\delta^{18}O$ that reflect an enhanced (a weakened) EASM correspond to lower (higher) values of GSC-23. Additionally, GSC-1 has reasonable correspondence with both the Ti content records from Lake Huguang Maar (Yancheva et al., 2007) and the sea surface temperature (SST) records from sediment core 38,002 in the North Yellow Sea (Zhang et al., 2019). The Ti content records could be used as an indicator of the and Zhou et al. (2012) have suggested that SST records from the Yellow Sea reflect the intensity of the YSWC, which is controlled by the EAWM. Thus, the SST records could also be used as an indicator of the EAWM. Higher (lower) values of Ti content and SST that reflect an enhanced (a weakened) EAWM correspond to higher (lower) values of GSC-1. Moreover, we compared our proxies with proxies from core ZY-1 and B60, and proxies documented in more recent studies in central mud area in the South Yellow Sea and nearby regions (Hu et al., 2012; Li and Morrill, 2014; Lyu et al., 2020; Wang et al., 2020; Chen et al., 2021; Zhong et al., 2021), the results showed that there are corresponding relationships between proxies of EASM and EAWM, respectively (**Supplementary Figure S1**).

Using the proxies, we recovered the variability of the EAM and confirmed the main factor controlling the sedimentary process on the continental shelves of the SYS. Generally, the intensity of both the EASM and the EAWM has shown a fluctuating trend of decrease since approximately 6,000 years BP. Moreover, EAWM intensity can be divided into three periods: strong and relatively stable during approximately 6,000–4,000 years BP, weakened during approximately 4,000–700 years BP, and strong and highly fluctuating since approximately 700 years BP. Conversely, EASM intensity can be divided into just two parts: strong and relatively stable during approximately 6,000–3,700 years BP (similar to the EAWM), and weakened and highly fluctuating since approximately 3,700 years BP.

Relationship Between the East Asian Winter Monsoon and the East Asian Summer Monsoon and Possible Paleoenvironmental Mechanisms

The nature of the relationship between the EASM and the EAWM during the Holocene remains controversial. One of the main reasons for this uncertainty is the lack of an appropriate archive that could represent the intensity of the two monsoon systems simultaneously (Ge et al., 2017). The proxies for the EASM and the EAWM extracted from the same sedimentary record of core HS2, which remove the influence of dating, provide an excellent opportunity to test their relationship. In this study, the evolutionary history of the EASM and the EAWM showed a similar downward trend on the millennial timescale (**Figures 6A,B**); however, on the centennial timescale, their relationship was mostly anticorrelated (**Figures 6A,B**). This finding supports the results of Zhou and Zhao (2009), who concluded that the variability of the EAM during the Holocene was more complex than the simple antiphase relationship between the EASM and the EAWM that has been assumed previously (Xiao et al., 1995; Yancheva et al., 2007).

Moving correlation techniques have been applied widely in the field of climate research (Xu et al., 1997; Zong et al., 2010; Lyu et al., 2020) After comparison of various methods, we chose the 101-years moving correlation between the EAWM (GSC-1) and the EASM (GSC-23) to examine the relationship with global climate change. In addition, we also explored the driving factors of the relationship between the EASM and the EAWM and found reasonable correlation with the total solar irradiance reconstructed from ice cores (Steinhilber et al., 2009) (**Figure 6D**).

The results showed positive correlation of the value of total solar irradiance to the value of the correlation between the EASM and the EAWM, i.e., high (low) intensity of solar radiation corresponded to negative (positive) correlation between the EASM and the EAWM. Previous studies (Yan et al., 2011; Zhou et al., 2011; Li and Xu, 2016; Li Y. et al., 2016; Xiao and Huo, 2016) have suggested that the EAM is caused by the thermal difference between land and sea. When solar radiation is strong in summer (winter), the thermal difference between land and sea increases (reduces) owing to the faster rate of increase (slower rate of reduction) of the land surface temperature, which leads to the strengthening (weakening) of the EASM (EAWM). Thus, we can conclude that the negative correlation between the EASM and the EAWM is controlled by strong solar radiation. However, we believe that the weakening of solar radiation diminishes the contribution of solar radiation to the thermal difference between land and sea, which in turn leads to the weakening of its ability to control the intensity of the EASM and EAWM. Therefore, without the regulation of strong solar radiation, the EAM exhibits the original correlation, i.e., positive correlation between the EASM and the EAWM, which supports the conclusions of many previous studies (Chen et al., 2000; Yan et al., 2003; Yan et al., 2011).

We also found that the North Atlantic Oscillation (NAO) correlated negatively with the relationship between the EASM and the EAWM (**Figure 6E**). Previous studies have identified strong links between the EAM system and the NAO; however, these links can change substantially depending on the phase and intensity of the NAO (Sung et al., 2006; Jia and Lin, 2011; Qiao and Feng, 2016; Zuo et al., 2016). Ignoring dating errors, we believe that the NAO has a distinct modulating effect on the relationship between the EASM and the EAWM, particularly the positive correlation during significantly positive NAO phases (**Figure 6E**). Thus, we conclude that when solar radiation is weak, the correlation between the EASM and the EAWM is modulated by the NAO.

Influence of the East Asian Monsoon on Ancient Civilizations

We used the 101-years moving correlations between the EAWM (GSC-1) and the EASM (GSC-23) to examine the relationship with the evolution of ancient Chinese civilizations.

Through comparison with a table of Chinese historical dynasties, we found that the correlation between the EASM and the EAWM correspond to the fall or establishment of certain dynasties (**Figure 6C**). Moreover, all the dynasties represnted by letters in **Figure 6C** had a similar background of an arid climate and a peasant uprising. Peasant uprisings that

TABLE 1 | AMS^{14}C ages and calendar ages of core HS2.

Depth (cm)	Conventional ^{14}C age (a BP)	Calendar age (cal a BP)	2δ age range (cal a BP)
86–90	2,430 ± 30	2,161	1996–2,325
136–138	3,250 ± 30	3,169	2,986–3,352
186–188	3,880 ± 30	3,957	3,761–4,152
236–238	4,900 ± 30	5,316	5,114–5,514
286–288	5,890 ± 30	6,404	6,256–6,551

cause regime change often happen when people have experienced prolonged periods of serious drought. Thus, we infer that sustained and serious drought occurs in China as a result of positive correlation between the EASM and the EAWM, rather than simply as the consequence of the role of the EASM. Furthermore, we found positive correlation between the EASM and the EAWM at approximately 4,200 years BP that corresponds to the 4.2-ka cooling event recorded in historical archives (Zhang X. et al., 2020). Previous studies have shown that the 4.2-ka cooling event, with the background of a population explosion in the Holocene Warm Period, promoted the formation of the Chinese civilization (Wu and Liu, 2001; Wang, 2005; Ma et al., 2008). On this basis, our results showed that the EASM and the EAWM weakened simultaneously during 4,700–4,000 years BP. Thus, the concentration of the population in Central China caused by the EAWM and the flooding caused by the EASM led to the establishment of the Xia Dynasty, which is regarded symbolically as the beginning of the Chinese civilization.

CONCLUSION

Through establishment of an age model and grain size analysis, we extracted proxies for the EASM and the EAWM, and we investigated the main factors controlling the sedimentary dynamics in the SYS and the relationship between the EASM and the EAWM. Results suggested that the intensity of both the EASM and the EAWM showed a fluctuating trend of decrease after approximately 6,000 years BP. It was established that the intensity of the EAWM could be divided into three periods: strong and relatively stable during approximately 6,000–40,000 years BP, weakened during approximately 4,000–700 years BP, and strong and highly fluctuating since approximately 700 years BP. Conversely, the EASM intensity could be divided into only two parts: strong and relatively stable during approximately 6,000–3,700 years BP, and weakened and highly fluctuating since approximately 3,200 years BP.

The evolutionary history of the EASM and the EAWM showed a similar downward trend at the millennial timescale; however, on the centennial timescale, their relationship was mostly anticorrelated. Moreover, it was determined that periods of positive correlation usually coincided with the fall or establishment of ancient dynasties on the Central Plains of China. It was established that negative correlation between the EASM and the EAWM is controlled by strong solar radiation. Weakening solar radiation leads to weakening of the ability to regulate the correlation between the EASM and the EAWM, at which time the NAO plays a modulating role.

DATA AVAILABILITY STATEMENT

The original contributions presented in the study are included in the article/**Supplementary Material**, further inquiries can be directed to the corresponding author.

AUTHOR CONTRIBUTIONS

Conceptualization, SC; methodology, WL and TF; formal analysis, WL, ZH, YT, GC, and XX; original draft preparation, WL and TF; review and editing, WL and SC. All authors have read and agreed to the published version of the manuscript.

FUNDING

This research was supported by the National Natural Science Foundation of China (No. U1706214 and 41706068), Basic Scientific Fund for National Public Research Institutes of China (2019Q01), the China Scholarship Council (No. 201906140151).

ACKNOWLEDGMENTS

The authors thank the captain and crew of the 2015 public cruise of R/V DONG FANG HONG ER HAO organized by the National Natural Science Foundation of China. We thank James Buxton MSc from Liwen Bianji, Edanz Group China (www.liwenbianji.cn/ac), for editing the English text of this manuscript.

SUPPLEMENTARY MATERIAL

The Supplementary Material for this article can be found online at: https://www.frontiersin.org/articles/10.3389/feart.2021.689508/full#supplementary-material

REFERENCES

Beck, J. W., Zhou, W., Li, C., Wu, Z., White, L., Xian, F., et al. (2018). A 550,000-year Record of East Asian Monsoon Rainfall from10Be in Loess. *Science* 360 (6391), 877–881. doi:10.1126/science.aam5825

Chen, W., Graf, H. F., and Ronghui, H. (2000). The Interannual Variability of East Asian Winter Monsoon and its Relation to the Summer Monsoon. *Adv. Atmos. Sci.* 17 (1), 48–60. doi:10.1007/s00376-000-0042-5

Chen, Y., Lyu, W., Fu, T., Li, Y., and Yi, L. (2021). Centennial Impacts of the East Asian Summer Monsoon on Holocene Deltaic Evolution of the Huanghe River, China. *Appl. Sci.* 11, 2799. doi:10.3390/app11062799

Cheng, H., Zhang, H., Zhao, J., Li, H., Ning, Y., and Kathayat, G. (2019). Chinese Stalagmite Paleoclimate Researches: A Review and Perspective. *Sci. China Earth Sci.* 62 (10), 1489–1513. doi:10.1007/s11430-019-9478-3

Ding, Z., Liu, T., Rutter, N. W., Yu, Z., Guo, Z., and Zhu, R. (1995). Ice-Volume Forcing of East Asian Winter Monsoon Variations in the Past 800,000 Years. *Quat. Res.* 44 (2), 149–159. doi:10.1006/qres.1995.1059

Ding, Y., Wang, Z., and Sun, Y. (2008). Inter-decadal Variation of the Summer Precipitation in East China and its Association with Decreasing Asian Summer monsoon.Part I: Observed Evidences. *Int. J. Climatol.* 28 (9), 1139–1161. doi:10.1002/joc.1615

Ding, Y., Sun, Y., Wang, Z., Zhu, Y., and Song, Y. (2009). Inter-decadal Variation of the Summer Precipitation in China and its Association with Decreasing Asian Summer Monsoon Part II: Possible Causes. *Int. J. Climatol.* 29 (13), 1926–1944. doi:10.1002/joc.1759

Ding, D. L., Li, G. X., Xu, J. S., Ding, D., Li, Q., Wang, L. Y., et al. (2017). Evolution of the Asian Monsoon during the Holocene. *Earth Sci. Front.* 24 (04), 114–123. (in Chinese with English Abstract). doi:10.13745/j.esf.yx.2017-4-12

Dykoski, C. A., Edwards, R., Cheng, H., Yuan, D., Cai, Y., Zhang, M., et al. (2005). A High-Resolution, Absolute-Dated Holocene and Deglacial Asian Monsoon Record from Dongge Cave, China. *Earth Planet. Sci. Lett.* 233 (1-2), 71–86. doi:10.1016/j.epsl.2005.01.036

Ge, Q., Xue, Z., Yao, Z., Zang, Z., and Chu, F. (2017). Anti-phase Relationship between the East Asian winter Monsoon and Summer Monsoon during the Holocene? *J. Ocean Univ. China* 16 (2), 175–183. doi:10.1007/s11802-017-3098-x

Hong, Y. T., Wang, Z. G., Jiang, H. B., Lin, Q. H., and Li, H. D. (2001). A 6000-year Record of Changes in Drought and Precipitation in Northeastern China Based on a δ 13C Time Series from Peat Cellulose. *Earth Planet. Sci. Lett.* 185 (1–2), 111–119. doi:10.1016/s0012-821x(00)00367-8

Hong, Y. T., Hong, B., Lin, Q. H., Shibata, Y., Zhu, Y. X., Leng, X. T., et al. (2009). Synchronous Climate Anomalies in the Western North Pacific and North Atlantic Regions during the Last 14,000 Years. *Quat. Sci. Rev.* 28 (9-10), 840–849. doi:10.1016/j.quascirev.2008.11.011

Hu, C., Henderson, G. M., Huang, J., Xie, S., Sun, Y., and Johnson, K. R. (2008). Quantification of Holocene Asian Monsoon Rainfall from Spatially Separated Cave Records. *Earth Planet. Sci. Lett.* 266 (3-4), 221–232. doi:10.1016/j.epsl.2007.10.015

Hu, B., Yang, Z., Zhao, M., Saito, Y., Fan, D., and Wang, L. (2012). Grain Size Records Reveal Variability of the East Asian Winter Monsoon since the Middle Holocene in the Central Yellow Sea Mud Area, China. *Sci. China Earth Sci.* 55 (10), 1656–1668. doi:10.1007/s11430-012-4447-7

Huang, R., Chen, J., and Huang, G. (2007). Characteristics and Variations of the East Asian Monsoon System and its Impacts on Climate Disasters in China. *Adv. Atmos. Sci.* 24 (6), 993–1023. doi:10.1007/s00376-007-0993-x

Jia, X., and Lin, H. (2011). Influence of Forced Large-Scale Atmospheric Patterns on Surface Air Temperature in China. *Monthly Weather Rev.* 139 (3), 830–852. doi:10.1175/2010mwr3348.1

Kong, G. S., Park, S. C., Han, H. C., Chang, J. H., and Mackensen, A. (2006). Late Quaternary Paleoenvironmental Changes in the Southeastern Yellow Sea, Korea. *Quat. Int.* 144, 38–52. doi:10.1016/j.quaint.2005.05.011

Li, Y., and Morrill, C. (2014). A Holocene East Asian Winter Monsoon Record at the Southern Edge of the Gobi Desert and its Comparison with a Transient Simulation. *Clim. Dyn.* 45, 1219–1234. doi:10.1007/s00382-014-2372-5

Li, F., and Wang, H. (2012). Predictability of the East Asian Winter Monsoon Interannual Variability as Indicated by the DEMETER CGCMS. *Adv. Atmos. Sci.* 29 (3), 441–454. doi:10.1007/s00376-011-1115-3

Li, Y., and Xu, L. (2016). Asynchronous Holocene Asian Monsoon Vapor Transport and Precipitation. *Palaeogeogr. Palaeoclimatol. Palaeoecol.* 461, 195–200. doi:10.1016/j.palaeo.2016.08.024

Li, C., Fu, J., Yi, L., Zhou, X., Wang, S., and Jiang, F. (2015). Millennial-Scale Asian Monsoon Influenced Longjie Lake Evolution during Marine Isotope Stage 3, Upper Stream of Changjiang (Yangtze) River, China. *Adv. Meteorol.* 2015, 1–10. doi:10.1155/2015/592894

Li, X., Liu, X., He, Y., Liu, W., Zhou, X., and Wang, Z. (2018). Summer Moisture Changes in the Lake Qinghai Area on the Northeastern Tibetan Plateau Recorded from a Meadow Section over the Past 8400 Yrs. *Glob. Planet. Change* 161, 1–9. doi:10.1016/j.gloplacha.2017.11.016

Li, G., Qiao, L., Dong, P., Ma, Y., Xu, J., Liu, S., et al. (2016). Hydrodynamic Condition and Suspended Sediment Diffusion in the Yellow Sea and East China Sea. *J. Geophys. Res. Oceans* 121 (8), 6204–6222. doi:10.1002/2015jc011442

Li, Y., Zhang, C., and Wang, Y. (2016). The Verification of Millennial-Scale Monsoon Water Vapor Transport Channel in Northwest China. *J. Hydrol.* 536, 273–283. doi:10.1016/j.jhydrol.2016.03.006

Liu, G., Li, X., Chiang, H.-W., Cheng, H., Yuan, S., Chawchai, S., et al. (2020). On the Glacial-Interglacial Variability of the Asian Monsoon in Speleothem δ18O Records. *Sci. Adv.* 6 (7), eaay8189. doi:10.1126/sciadv.aay8189

Liu, J., Shi, X., Liu, Q., Ge, S., Liu, Y., Yao, Z., et al. (2014). Magnetostratigraphy of a Greigitebearing Core from the South Yellow Sea: Implications for Remagnetization and Sedimentation. *J. Geophys. Res. Solid Earth* 119 (10), 7425–7441. doi:10.1002/2014JB011206

Lyu, W., Yang, J., Fu, T., Chen, Y., Hu, Z., Tang, Y. Z., et al. (2020). Asian Monsoon and Oceanic Circulation Paced Sedimentary Evolution over the Past 1,500 years in the central Mud Area of the Bohai Sea, China. *Geol. J.* 55 (7), 5606–5618. doi:10.1002/gj.3758

Ma, C. M., Zhu, C., Zheng, C. G., Wu, C. L., Guan, Y., Zhao, Z. P., et al. (2008). High-resolution Geochemistry Records of Climate Changes since Late-Glacial from Dajiuhu Peat in Shennongjia Mountains, Central China. *Chin. Sci. Bull.* 53 (S1), 26–37. doi:10.1007/s11434-008-5007-6

McManus, J. (1988). "Grain Size Determination and Interpretation," *Techniques in Sedimentology*. Editors M. Tucker (Oxford: Blackwell), 63–85.

Olsen, J., Anderson, N. J., and Knudsen, M. F. (2012). Variability of the North Atlantic Oscillation over the Past 5,200 Years. *Nat. Geosci.* 5 (11), 808–812. doi:10.1038/ngeo1589

Passega, R. (1964). Grain Size Representation by CM Patterns as a Geologic Tool. *J. Sediment. Res.* 34, 830–847.

Passega, R. (1957). Texture as Characteristic of Clastic Deposition. *AAPG Bull.*, 1952–1984.

Qiao, S., and Feng, G. (2016). Impact of the December North Atlantic Oscillation on the Following February East Asian Trough. *J. Geophys. Res. Atmos.* 121 (17), 10,074–10,088. doi:10.1002/2016jd025007

Qiao, S., Yang, Z., Liu, J., Sun, X., Xiang, R., Shi, X., et al. (2011). Records of Late-Holocene East Asian winter Monsoon in the East China Sea: Key Grain-Size Component of Quartz versus Bulk Sediments. *Quat. Int.* 230 (1), 106–114. doi:10.1016/j.quaint.2010.01.020

Qiao, S., Shi, X., Wang, G., Zhou, L., Hu, B., Hu, L., et al. (2017). Sediment Accumulation and Budget in the Bohai Sea, Yellow Sea and East China Sea. *Mar. Geology.* 390, 270–281. doi:10.1016/j.margeo.2017.06.004

Song, Y., Hao, Q., Ge, J., Zhao, D. a., Zhang, Y., Li, Q., et al. (2014). Quantitative Relationships between Magnetic Enhancement of Modern Soils and Climatic Variables over the Chinese Loess Plateau. *Quat. Int.* 334-335, 119–131. doi:10.1016/j.quaint.2013.12.010

Steinhilber, F., Beer, J., and Fröhlich, C. (2009). Total Solar Irradiance during the Holocene. *Geophys. Res. Lett.* 36, L19704. doi:10.1029/2009gl040142

Steinke, S., Glatz, C., Mohtadi, M., Groeneveld, J., Li, Q., and Jian, Z. (2011). Past Dynamics of the East Asian Monsoon: No Inverse Behaviour between the Summer and winter Monsoon during the Holocene. *Glob. Planet. Change* 78 (3-4), 170–177. doi:10.1016/j.gloplacha.2011.06.006

Stuiver, M., and Reimer, P. J. (1993). Extended 14C Data Base and Revised CALIB 3.0 14C Age Calibration Program. *Radiocarbon* 35 (1), 215–230. doi:10.1017/S0033822200013904

Sun, Y., Clemens, S. C., An, Z., and Yu, Z. (2006). Astronomical Timescale and Palaeoclimatic Implication of Stacked 3.6-Myr Monsoon Records from the Chinese Loess Plateau. *Quat. Sci. Rev.* 25 (1-2), 33–48. doi:10.1016/j.quascirev.2005.07.005

Sung, M. K., Kwon, W. T., Baek, H. J., Boo, K. O., Lim, G. H., and Kug, J. S. (2006). A Possible Impact of the North Atlantic Oscillation on the East Asian Summer Monsoon Precipitation. *Geophys. Res. Lett.* 33 (21). doi:10.1029/2006gl027253

Thompson, L. G. (1997). Tropical Climate Instability: The Last Glacial Cycle from a Qinghai-Tibetan Ice Core. *Science* 276 (5320), 1821–1825. doi:10.1126/science.276.5320.1821

Wang, H., Li, G., Zhang, Y., Liu, Y., Liu, D., Ding, D., et al. (2020). Evolution of Palaeoenvironment of the South Yellow Sea since the Last Deglaciation. *J. Ocean Univ. China* 19 (4), 827–836. doi:10.1007/s11802-020-4213-y

Wang, K., Zheng, H. B., Maarten, P., and Zheng, Y. (2008). High-resolution Paleoenvironmental Record of the Mud Sediments of the East China Sea Inner Shelf. *Mar. Geol. Quat. Geol.* 28 (4), 1–10. (in Chinese with English Abstract). doi:10.3724/SP.J.1140.2008.03001

Wang, L., Li, G., Xu, J., Liu, Y., Lu, Q., Ding, D., et al. (2019). Strata Sequence and Paleochannel Response to Tectonic, Sea-Level, and Asian Monsoon Variability Since the Late Pleistocene in the South Yellow Sea. *Quat. Res.* 1–19. doi:10.1017/qua.2019.29

Wang, Y., Cheng, H., Edwards, R. L., Kong, X., Shao, X., Chen, S., et al. (2008). Millennial- and Orbital-Scale Changes in the East Asian Monsoon over the Past 224,000 Years. *Nature* 451 (7182), 1090–1093. doi:10.1038/nature06692

Wang, S. W. (2005). Abrupt Climate Change and Collapse of Ancient Civilizations at 2200BC-2000BC. *Prog. Nat. Sci.* 15 (9), 1094–1099. (in Chinese with English Abstract). doi:10.3321/j.issn:1002-008X.2005.09.010

Wessel, P., Luis, J. F., Uieda, L., Scharroo, R., Wobbe, F., Smith, W. H. F., et al. (2019). The Generic Mapping Tools Version 6. *Geochem. Geophys. Geosyst.* 20 (11), 5556–5564. doi:10.1029/2019gc008515

Wu, M. C., and Chan, J. C. L. (2005). Observational Relationships between Summer and winter Monsoons over East Asia. Part II: Results. *Int. J. Climatol.* 25 (4), 453–468. doi:10.1002/joc.1153

Wu, W. X., and Liu, D. S. (2001). 4000 a B.P. Event and its Implications for the Origin of Ancient Chinese Civilization. *Quat. Sci.* 21 (5), 443–451. (in Chinese with English Abstract). doi:10.3321/j.issn:1001-7410.2001.05.008

Xiang, R., Yang, Z., Saito, Y., Fan, D., Chen, M., Guo, Z., et al. (2008). Paleoenvironmental Changes During the Last 8400 Years in the Southern Yellow Sea: Benthic Foraminiferal and Stable Isotopic Evidence. *Mar. Micropaleontol.* 67 (1-2), 104–119. doi:10.1016/j.marmicro.2007.11.002

Xiao, Z. N., and Huo, W. J. (2016). Influences of Solar Activity on Climate: the Spatio-Temporal Selectivity of the Amplification Process. *Adv. Meteorol. Sci. Technol.* 6 (3), 141–147. (in Chinese with English Abstract). doi:10.3969/j.issn.2095-1973.2016.03.019

Xiao, J., Porter, S. C., An, Z., Kumai, H., and Yoshikawa, S. (1995). Grain Size of Quartz as an Indicator of Winter Monsoon Strength on the Loess Plateau of Central China during the Last 130,000 Yr. *Quat. Res.* 43 (1), 22–29. doi:10.1006/qres.1995.1003

Xiao, S., Li, A., Liu, J. P., Chen, M., Xie, Q., Jiang, F., et al. (2006). Coherence between Solar Activity and the East Asian winter Monsoon Variability in the Past 8000 Years from Yangtze River-Derived Mud in the East China Sea. *Palaeogeogr. Palaeoclimatol. Palaeoecol.* 237 (2-4), 293–304. doi:10.1016/j.palaeo.2005.12.003

Xing, L., Zhao, M., Zhang, H., Zhao, X., Zhao, X., Yang, Z., et al. (2012). Biomarker Evidence for Paleoenvironmental Changes in the Southern Yellow Sea over the Last 8200 Years. *Chin. J. Ocean. Limnol.* 30 (1), 1–11. doi:10.1007/s00343-012-1045-7

Xu, J. J., Zhu, Q. G., and Shi, N. (1997). The Interaction of East Asian Winter Monsoon with ENSO Cycle and their Interdecadal Variations in Last Century. *Sci. Sin.* 21, 641–648. doi:10.3878/j.issn.1006-9895.1997.06.01

Yan, H. M., Duan, W., and Xiao, Z. N. (2003). A Study on Relation between East Asian Winter Monsoon and Climate Change during Raining Season in China. *J. Trop. meteorology* 19 (4), 367–376. (in Chinese with English Abstract). doi:10.3969/j.issn.1004-4965.2003.04.004

Yan, H., Yang, H., Yuan, Y., and Li, C. (2011). Relationship between East Asian Winter Monsoon and Summer Monsoon. *Adv. Atmos. Sci.* 28 (6), 1345–1356. doi:10.1007/s00376-011-0014-y

Yancheva, G., Nowaczyk, N. R., Mingram, J., Dulski, P., Schettler, G., Negendank, J. F. W., et al. (2007). Influence of the Intertropical Convergence Zone on the East Asian Monsoon. *Nature* 445 (7123), 74–77. doi:10.1038/nature05431

Yang, J., Li, G., Liu, Y., Dada, O. A., Zhao, M., Ma, Z., et al. (2018). Evolution of Sedimentary Mode Since Pleistocene in the Central South Yellow Sea, China, Based on Seismic Stratigraphy Analysis. *Quta. Int.* 482, 157–170. doi:10.1016/j.quaint.2018.03.018

Yang, S., and Youn, J. (2007). Geochemical Compositions and Provenance Discrimination of the central South Yellow Sea Sediments. *Mar. Geology.* 243 (1-4), 229–241. doi:10.1016/j.margeo.2007.05.001

Yang, S. Y., Jung, H. S., Lim, D. I., and Li, C. X. (2003). A Review on the Provenance Discrimination of Sediments in the Yellow Sea. *Earth-Science Rev.* 63 (1-2), 93–120. doi:10.1016/s0012-8252(03)00033-3

Yuan, D., and Hsueh, Y., 2010. Dynamics of the Cross-Shelf Circulation in the Yellow and East China Seas in winter., 57(19-20): 1745–1761. doi:10.1016/j.dsr2.2010.04.002

Zhang, D. e., and Lu, L. (2007). Anti-correlation of Summer/winter Monsoons? *Nature* 450 (7168), E7,8–E8-E9. doi:10.1038/nature06338

Zhang, Y., Li, G., Guo, H., Yong, L., Wang, H., Xu, J., et al. (2018). Sedimentary Characteristics of the Second Marine Layer During the Late Marine Isotope Stage 3 in Southern Yellow Sea and Their Response to the East Asian Monsoon. *J. Ocean Univ. China* 17 (5), 1103–1113. doi:10.1007/s11802-018-3527-5

Zhang, Y., Zhou, X., He, Y., Jiang, Y., Liu, Y., Xie, Z., et al. (2019). Persistent Intensification of the Kuroshio Current during Late Holocene Cool Intervals. *Earth Planet. Sci. Lett.* 506, 15–22. doi:10.1016/j.epsl.2018.10.018

Zhang, S., Xiao, J., Xu, Q., Wen, R., Fan, J., Huang, Y., et al. (2020). Contrasting Impacts of the 8.2- and 4.2-ka Abrupt Climatic Events on the Regional Vegetation of the Hulun Lake Region in north-eastern China. *J. Quat. Sci* 35 (6), 831–840. doi:10.1002/jqs.3231

Zhang, X., Fan, D., Tian, Y., Sun, Z., Zhai, B., Liu, M., et al. (2020). Quantitative Reconstruction of the East Asian Winter Monsoon Evolution over the Past 100 years: Evidence from High-Resolution Sedimentary Records of the Inner continental Shelf of the East China Sea. *The Holocene* 30, 1053–1062. doi:10.1177/0959683620908661

Zhao, X., Tao, S., Zhang, R., Zhang, H., Yang, Z., and Zhao, M. (2013). Biomarker Records of Phytoplankton Productivity and Community Structure Changes in the Central Yellow Sea Mud Area during the Mid-late Holocene. *J. Ocean Univ. China* 12 (4), 639–646. doi:10.1007/s11802-013-2271-0

Zheng, Y., Kissel, C., Zheng, H. B., Laj, C., and Wang, K. (2010). Sedimentation on the Inner Shelf of the East China Sea: Magnetic Properties, Diagenesis and Paleoclimate Implications. *Mar. Geology.* 268 (1-4), 34–42. doi:10.1016/j.margeo.2009.10.009

Zhong, F., Xiang, R., Zhang, L., Yang, Y., Zhao, M., and Zhou, L. (2021). A Synthesized Study of the Spatiotemporal Evolution of Central Yellow Sea Mud Depositional Processes during the Holocene. *Front. Earth Sci.* 9, 687344. doi:10.3389/feart.2021.687344

Zhou, B., and Zhao, P. (2009). Inverse Correlation between Ancient winter and Summer Monsoons in East Asia? *Chin. Sci. Bull.* 54 (20), 3760–3767. doi:10.1007/s11434-009-0583-7

Zhou, T., Li, B., Man, W., Zhang, L., and Zhang, J. (2011). A Comparison of the Medieval Warm Period, Little Ice Age and 20th century Warming Simulated by the FGOALS Climate System Model. *Chin. Sci. Bull.* 56 (28-29), 3028–3041. doi:10.1007/s11434-011-4641-6

Zhou, X., Sun, L., Huang, W., Cheng, W., and Jia, N. (2012). Precipitation in the Yellow River Drainage basin and East Asian Monsoon Strength on a Decadal Time Scale. *Quat. Res.* 78 (3), 486–491. doi:10.1016/j.yqres.2012.07.008

Zhou, C., Dong, P., and Li, G. (2015). Hydrodynamic Processes and Their Impacts on the Mud deposit in the Southern Yellow Sea. *Mar. Geology.* 360, 1–16. doi:10.1016/j.margeo.2014.11.012

Zong, H. F., Chen, L. T., and Zhang, Q. Y. (2010). The Instability of the Interannual Relationship Between ENSO and the Summer Rainfall in China. *Chin. J. Atmos. Sci.* 34, 184–192. doi:10.3878/j.issn.1006-9895.2010.01.17

Zuo, J., Ren, H.-L., Li, W., and Wang, L. (2016). Interdecadal Variations in the Relationship between the Winter North Atlantic Oscillation and Temperature in South-Central China. *J. Clim.* 29 (20), 7477–7493. doi:10.1175/jcli-d-15-0873.1

Conflict of Interest: The authors declare that the research was conducted in the absence of any commercial or financial relationships that could be construed as a potential conflict of interest.

frontiers in Earth Science

ORIGINAL RESEARCH
published: 06 September 2021
doi: 10.3389/feart.2021.703362

Vegetation History in a Peat Succession Over the Past 8,000 years in the ISM-Controlled Kedarnath Region, Garhwal Himalaya: Reconstruction Using Molecular Fossils

Sharmila Bhattacharya[1]*, *Harsh Kishor*[1], *Yadav Ankit*[1], *Praveen K. Mishra*[2] *and Pradeep Srivastava*[2]

[1]*Department of Earth and Environmental Sciences, Indian Institute of Science Education and Research Mohali, Mohali, India,* [2]*Wadia Institute of Himalayan Geology, Dehradun, India*

The Holocene epoch has witnessed several natural climate variations and these are well encoded in various geological archives. The present biomarker investigation in conjunction with previously published multi-proxy records was applied to reconstruct organic matter (OM) sources forming the peat succession spanning the last 8000 cal yr BP and shift in hydrological conditions from the Kedarnath region, Garhwal Himalaya. Intensified monsoon prevailed from ~7515 until ~2300 cal yr BP but with reversal to transient arid period particularly between ~5200 and ~3600 cal yr BP as revealed by the variability in n-C_{23}/n-C_{31}, ACL (average chain length of n-alkanes) and P_{aq} (P-aqueous) values. A prolonged arid phase is recognizable during the interval between ~2200 and ~370 cal yr BP suggested by the n-alkane proxies. Regional scale heterogeneity in the monsoonal pattern is known in the studied temporal range of mid to late Holocene across the Indian subcontinent that is probably a result of complex climate dynamics, sensitivity of proxies and impact of teleconnections. The biomarker signatures deduced from gas chromatography mass spectrometry (GCMS) analysis are suggestive of a mixed biotic input that includes prokaryotes, *Sphagnum* spp. and gymnosperm flora. The mid chain alkanes viz. n-C_{23} and n-C_{25} denote the presence of typical peat forming *Sphagnum* moss that preferentially grows in humid and waterlogged conditions. Diterpane marker such as *ent*-kaurane indicates contribution of gymnosperms, whereas the hopanes are signatures of microbial input. The preservation of organic matter is attributed to little microbial degradation in a largely suboxic depositional environment. Our study strengthens the applicability of organic geochemical proxies for the reconstruction of past climate history and indicates their suitability for use on longer timescales given the high preservation potential of the molecular remains.

Keywords: lipid biomarkers, peat, vegetation shift, Kedarnath, Garhwal Himalaya, palaeohydrological conditions

Edited by:
Steven L. Forman,
Baylor University, United States

Reviewed by:
Nadia Solovieva,
University College London,
United Kingdom
Francien Peterse,
Utrecht University, Netherlands

***Correspondence:**
Sharmila Bhattacharya
sbhattacharya@iisermohali.ac.in

Specialty section:
This article was submitted to
Quaternary Science, Geomorphology
and Paleoenvironment,
a section of the journal
Frontiers in Earth Science

Received: *30 April 2021*
Accepted: *19 August 2021*
Published: *06 September 2021*

Citation:
Bhattacharya S, Kishor H, Ankit Y,
Mishra PK and Srivastava P (2021)
Vegetation History in a Peat
Succession Over the Past 8,000 years
in the ISM-Controlled Kedarnath
Region, Garhwal Himalaya:
Reconstruction Using
Molecular Fossils.
Front. Earth Sci. 9:703362.
doi: 10.3389/feart.2021.703362

INTRODUCTION

Peatlands are highly dynamic ecosystems providing diverse ecological niches for a variety of biota and can be utilised to understand the past environmental conditions (Gorham et al., 2003; Chambers et al., 2012; Kumaran et al., 2016; Naafs et al., 2019). Peats form in a specific geomorphological environment mostly concentrated in mid to high latitudes in the Northern Hemisphere covering about 2–3% of land surface on Earth (Kayranli et al., 2010; Naafs et al., 2019; Dai et al., 2020). Rapid deposition of clastic sediments facilitates the burial of plant remains in wetlands, such as bogs and fens, resulting into the formation of peat layers through compaction over time (Zhang et al., 2017; Dai et al., 2020). The accumulation and preservation of the decomposed plant matter is a complex interplay of biological, physico-chemical, geomorphological and hydrological processes (Middleton, 1973; Finlayson and Milton, 2016). Most importantly, precipitation is a significant controlling factor in the development of the peat deposits. Increased precipitation (or high groundwater level) is a necessity for the growth of peatlands, whereas drier environmental conditions negatively impact peat ecosystem (Marcisz et al., 2016).

Recent advances in the application of lipid biomarkers have shaped our understanding on key aspects of past ecological and climatic dynamics (Nott et al., 2000; Bingham et al., 2010; Jordan et al., 2017; Baker et al., 2018; Jiang et al., 2020). Biomarkers (such as *n*-alkanes, acyclic and cyclic terpenoids) have been frequently used for biotic and palaeoenvironmental reconstruction in lacustrine and marine settings (Chen and Summons, 2001; Kelly et al., 2011; Dutta et al., 2013; Tulipani et al., 2015; French et al., 2020; Ankit et al., 2021). The *n*-alkanes and its proxies are widely used to understand the organic source inputs and past environmental conditions (Eglinton and Hamilton, 1967; Eglinton and Eglinton, 2008; Bush and Mclnerney, 2013; Tipple and Pagani, 2013). However, the utilization of biomarkers in peat deposits for understanding the palaeovegetational changes is limited (Ficken et al., 1998; Nott et al., 2000; Pancost et al., 2002; Bingham et al., 2010; Schellekens et al., 2015; Naafs et al., 2019). A variety of peat-forming plants producing distinct carbon chain lengths in the lipid fraction is known (Cranwell, 1973; Ficken et al., 1998; Nott et al., 2000; Bingham et al., 2010). For example, the mid-chain alkanes (n-C_{23} and n-C_{25}) are dominant components in peat-forming wetland plants, whereas the higher plants on land mainly comprise longer chain lengths such as n-C_{27}, n-C_{29} and n-C_{31}. Further, the ratio of acyclic terpenoids such as pristane (Pr) and phytane (Ph) (products of chlorophyll side chain of phototrophic organisms) can also be used to understand the redox potential of ambient environment (Didyk et al., 1978; Bechtel et al., 2003). Higher Pr/Ph ratios indicate oxic condition, whereas lower values are suggestive of a reducing environment. Additionally, specific cyclic terpenoids such as hopanoids (derived from prokaryotes) and diterpenoids (produced by gymnosperm vascular plants) are robust tools that specify the organisms contributing into sedimentary organic matter and provide useful information on their habitat (Brocks et al., 2003; Peters et al., 2005).

The Indian Summer Monsoon (ISM) is an important climatic element in the Indian subcontinent and provides the main water resources to the South Asian countries (Benn and Owen, 1998; Kumar et al., 2020). In recent years in the Himalaya, anomalous patterns of extreme rain events have caused huge socio-economic impacts on the human populations. Palaeoclimate studies from the region have utilized multiarchive-multiproxy approach for climate reconstructions (Anoop et al., 2013; Mishra et al., 2015; Bhushan et al., 2018; Kumar et al., 2020; Misra et al., 2020; Rawat et al., 2021). However, only a limited number of studies have targeted peat sediments for understanding the palaeovegetation and environmental and depositional conditions (Phadtare, 2000; Rawat et al., 2015; Srivastava et al., 2017). These studies have used several established climate proxies such as pollen, mineral magnetism, stable isotopes of C, N and elemental geochemistry to reconstruct the Holocene climatic changes. Sedimentary biomarkers that are now established as a strong molecular tool have so far not been explored in Indian Himalaya. Here, we utilize a well-dated peat succession spanning the past 8000 cal yr BP that was previously studied from the Kedarnath region, and analyze the succession for hydrocarbon biomarkers. This allows 1) an opportunity to provide a climate record using an independent proxy and also 2) to analyze how a molecular-based proxy relates and compares to already existing pollen and isotope-based proxy record. We have also compared the monsoonal changes in the Kedarnath region with previous records of variability pattern for clearer perspectives of the complexity of climate dynamics. Our study highlights the excellent applicability of biomarkers in improving the understanding of longer time-scale climatic fluctuations and thus can be utilized to address wider aspects in palaeoclimate research.

STUDY AREA

The study area (**Figures 1A,B**) is located at an altitude of 3525 m above mean sea level at northwestern Himalaya in Kedarnath, Uttarakhand, India (30.73°N; 79.07°E) (Srivastava et al., 2017). The region is a climatically sensitive zone located at the periphery domain of the ISM rainfall. The peat succession formed in a glacio-fluvial environment between two lateral moraines close to the Chorabari Glacier and north of the Pindari Thrust. The moraines are the only source of sediments into the depression. Geologically, the region is situated in Pindari formation which is characterized by calc-silicate, schist, and granitic formations (Valdiya et al., 1999) (**Figure 1B**). The long-term precipitation data of Kedarnath region from Climate Research Unit (CRU TS v4.03) for the period 1901–2019 interpolated into 0.5° latitude/longitude gridded cell (1901–2019) (Harris et al., 2020) shows a decreasing trend with mean precipitation of 7.2 mm per decade (**Figure 1C**) and an increasing trend in mean temperature (0.06°C per decade) (**Figure 1D**). The region is typically characterized by a temperate climate (Kar et al., 2016) and receives heavy rainfall during the months of June to September primarily under the influence of the Indian Summer Monsoon (ISM) (~71% of the mean annual rainfall). Winter precipitation comprises snowfall between the months of December to March due to intensification of the westerly winds. The temperature in the region fluctuates from a freezing −1°C to a maximum of 15°C during the months of June, July and August. The vegetation in the area is dominated by broadleaved

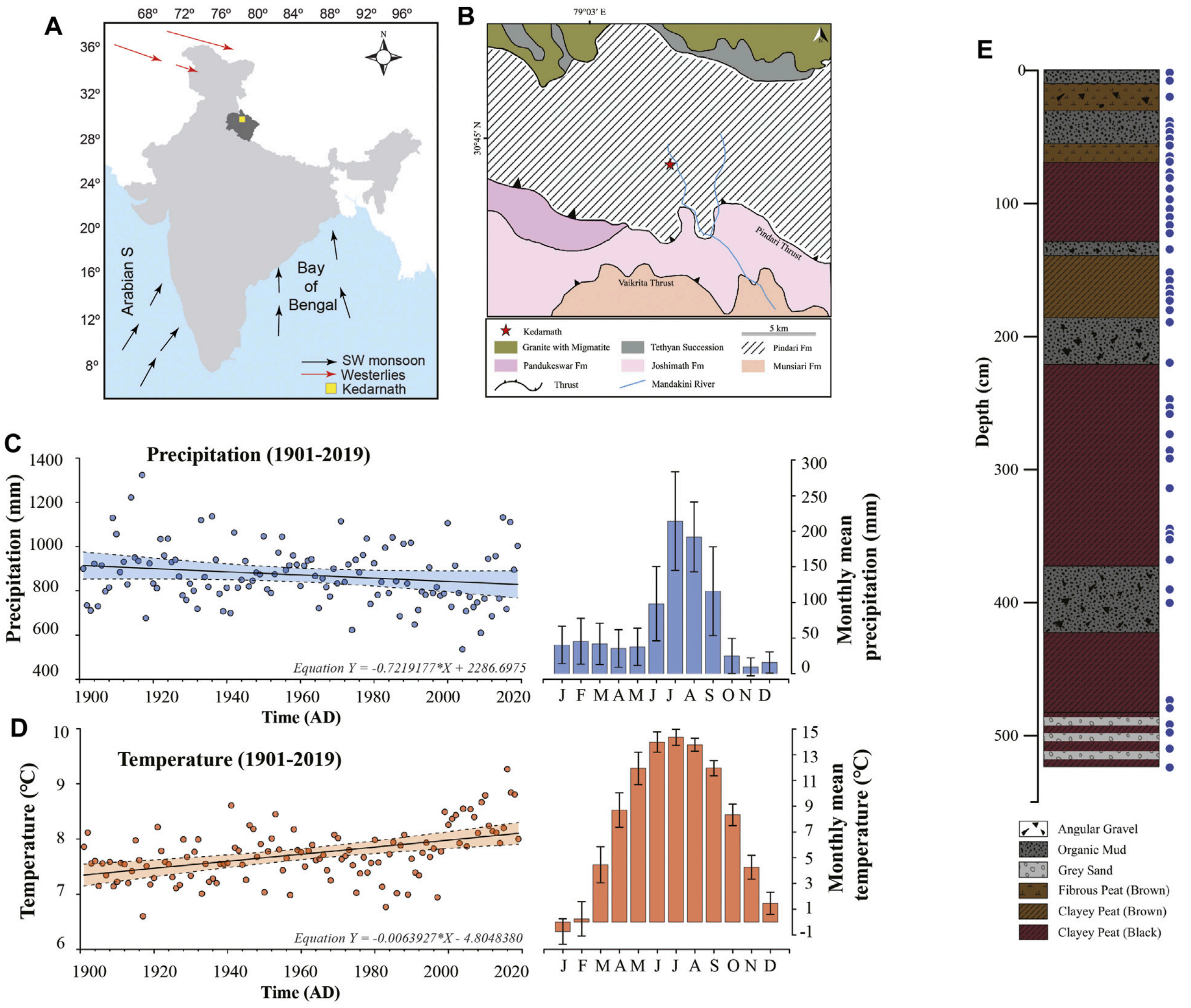

FIGURE 1 | (A) Location of the study area in the Indian subcontinent. **(B)** The geological map showing the sampling location of the peat succession in the Kedarnath region of Uttarakhand (marked with the red star). **(C)** The long term decreasing trend in the mean precipitation in Kedarnath region from Climate Research Unit (CRU TS v4.03) for the period 1901–2019 interpolated into 0.5° latitude/longitude gridded cell. The shaded region represents 99% confidence interval. **(D)** The long term increasing trend in the mean temperature in Kedarnath region from Climate Research Unit (CRU TS v4.03) for the period 1901–2019 interpolated into 0.5° latitude/longitude gridded cell. The shaded region represents 99% confidence interval. **(E)** The litho-column depicting the sedimentary layers across the studied depth along with the analyzed samples marked with solid blue circles.

species and conifer biota (Kar et al., 2016). Conifers are particularly abundant followed by a few broad-leaved taxa such as *Quercus*, *Alnus* and *Ulmus*. The most prominent herbaceous taxa include Lamiaceae, Rosaceae, Polygonaceae and Rutaceae. Few steppe elements such as Amarantheceae and sub-families of Asteraceae are also well represented (Kar et al., 2016).

MATERIALS AND METHODS

Samples

The studied sediments were collected from a ~5 m long peat succession (Srivastava et al., 2017). The section was dated using radiocarbon dating from seven bulk samples by accelerator mass spectrometry (AMS) and the detailed description is provided in the previous study (Srivastava et al., 2017). The ^{14}C dated succession covers the last ~8,000 years. A total of 46 sediment samples from various time intervals covering the section have been employed for the present biomarker analysis (**Figure 1E**). A detailed litholog (**Figure 1E**) depicting the various sedimentary layers of the studied section along with the sampling points is provided.

Sample Processing

The sediments were powdered and homogenized using mortar and pestle. The powdered samples were introduced into the speed extractor (Buchi, E-914) for recovering the soluble fraction of the organic matter (total extract) using a solution of dichloromethane and methanol (9:1 ratio, respectively; v/v) at 100°C and 70 bar pressure. For removing the insoluble polar fraction, *n*-pentane was added to the total extract and left for 12 h. Upon precipitation of the heavier and primarily unsaturated polar constituents, the supernatant fraction was decanted and dried overnight in fume-hood. Saturated hydrocarbon fractions were isolated using column chromatography (activated silica gel; 100–200 mesh; eluent *n*-hexane) and analyzed by gas chromatography mass spectrometry (GC-MS).

Gas Chromatography Mass Spectrometry

The aliquots of saturated hydrocarbon fraction were dissolved in dichloromethane and analyzed using an Agilent 5977C mass spectrometer interfaced to a 7890B gas chromatograph. The samples were injected by auto sampler in pulsed splitless mode. The GC is equipped with an HP-5MS capillary column (30 m × 0.25 i.d. × 0.25 µm film thickness). Helium was used as the carrier gas with a flow rate of 1 ml/min. The analysis was done in full scan mode over a mass range of 40–600 Da. The ion source operated in the electron ionization mode at 70 eV. The initial temperature of the GC oven was programmed to 40°C (isothermal for 5 min) and then ramped to 310°C (isothermal for 5.5 min) at 4°C/min. Data was processed using Mass Hunter software and the compounds were identified by comparing the elution pattern and mass spectra from published literature.

n-Alkane and Terpenoid Proxies

Based on carbon chain lengths, various *n*-alkane indices have been assessed to understand the possible organic matter sources. The short chain *n*-alkanes (n-C$_{15}$–n-C$_{21}$) are attributed to microbial input such as algae and prokaryotes, whereas higher order terrestrial plants are dominated by the long chain (n-C$_{27}$–n-C$_{33}$) homologues (Eglinton and Hamilton, 1967; Eglinton and Eglinton, 2008). The aquatic plants (submerged/floating) and *Sphagnum* moss species are characterized by a predominance of the mid-chain lengths typically the n-C$_{23}$ and n-C$_{25}$ (Ficken et al., 2000).

The *n*-alkane based indices [carbon preference index (CPI), P-aqueous (P_{aq}) and average chain length (ACL)] have been calculated to characterize the distribution pattern of normal alkanes in the studied Kedarnath sediment samples. The CPI, P_{aq} and ACL are calculated based on the following equations:

$$CPI = \frac{1}{2} * \left[\left(\frac{C_{23} + C_{25} + C_{27}}{C_{24} + C_{26} + C_{28}}\right) + \left(\frac{C_{25} + C_{27} + C_{29}}{C_{24} + C_{26} + C_{28}}\right)\right]$$

(Marzi et al., 1993)

$$P_{aq} = \frac{(C_{23} + C_{25})}{(C_{23} + C_{25} + C_{29} + C_{31})}$$

(Ficken et al., 2000)

$$ACL = \frac{23 \times C_{23} + 25 \times C_{25} + 27 \times C_{27} + 29 \times C_{29} + 31 \times C_{31}}{C_{23} + C_{25} + C_{27} + C_{29} + C_{31}}$$

(Wang et al., 2015)

CPI is used to understand the origin of hydrocarbon biomarkers and degree of molecular taphonomic alterations post deposition. Generally, CPI values tend to be higher on occasions of heavy influx of terrestrial plant matter and lower when derived from microbial biota such as algae and bacteria (Cranwell et al., 1987; Bulbul et al., 2021). In addition, significant microbial reworking and/or increasing thermal maturity also lower the CPI values. The P_{aq} denotes the relative proportion of submerged, floating and terrestrial biota and can successfully indicate the water level history especially in peat-forming environments (Zhou et al., 2010). The ACL which is the weighted mean of chain lengths is a crucial proxy that reveals the ambient climatic conditions (Sarkar et al., 2014). The underlying principle of ACL is that arid conditions induce increased production of the longer chain *n*-alkanes in terrestrial plants (Andrae et al., 2019). Other *n*-alkane ratio such as n-C$_{23}$/n-C$_{31}$ has been evaluated to decipher the shift in the biotic input in response to changing environmental conditions. The ratio n-C$_{23}$/n-C$_{31}$ is particularly applied to trace the changes in input of *Sphagnum vs.* non-*Sphagnum* species into the preserved organic matter in sediments.

Pr/Ph has been used to reconstruct redox potential of the depositional environment (Didyk et al., 1978). The Pr/Ph values are sufficiently high (>3) in oxic environments, whereas values <0.8 pertain to suboxic to reducing conditions. Furthermore, the acyclic terpenoid/*n*-alkane ratios viz. Pr/n-C$_{17}$ and Ph/n-C$_{18}$ are used to explain the relative contributions of aquatic and terrestrial biota and also the biodegradation status since the normal alkanes are generally consumed faster than the terpenoids during microbial degradation thus increasing the Pr/n-C$_{17}$ and Ph/n-C$_{18}$ values.

Diterpenoid compound is identified using base peak in the selected ion chromatogram at *m/z* 123 (Noble et al., 1985) and hopanoids with base peak in the selected ion chromatogram at *m/z* 191 (Waples and Machihara, 1991; Sessions et al., 2013; Nizar et al., 2021).

RESULTS

GCMS traces reveal the presence of *n*-alkanes, acyclic and cyclic terpenoids in the total ion chromatograms (**Figure 2**).

n-Alkanes

The *n*-alkanes, detected in selected ion chromatogram at *m/z* 57, in the saturated hydrocarbon fractions of the studied sediments comprise a homologous series ranging from n-C$_{16}$ to n-C$_{33}$ (**Figure 3**). The short-chain *n*-alkanes depict a moderate abundance of n-C$_{16}$, n-C$_{17}$ and n-C$_{18}$, whereas n-C$_{27}$, n-C$_{29}$ and n-C$_{31}$ generally dominate the longer-chain range. The mid-chain *n*-alkanes comprise relatively high abundance of n-C$_{23}$ and n-C$_{25}$. The *n*-alkane series exhibits a bimodal distribution with two distinct centers at n-C$_{16}$– n-C$_{18}$ and a dominant n-C$_{23}$– n-C$_{31}$ range. A strong odd-over-even carbon predominance is observed in the range of n-C$_{23}$–n-C$_{31}$ homologues.

CPI values for the n-C$_{23}$–n-C$_{29}$ homologues are characterized by a wide spread ranging between 1.0 and 11.4 and averaging at 3.3 (**Figure 4**; **Table 1**). Values are seen to fluctuate throughout

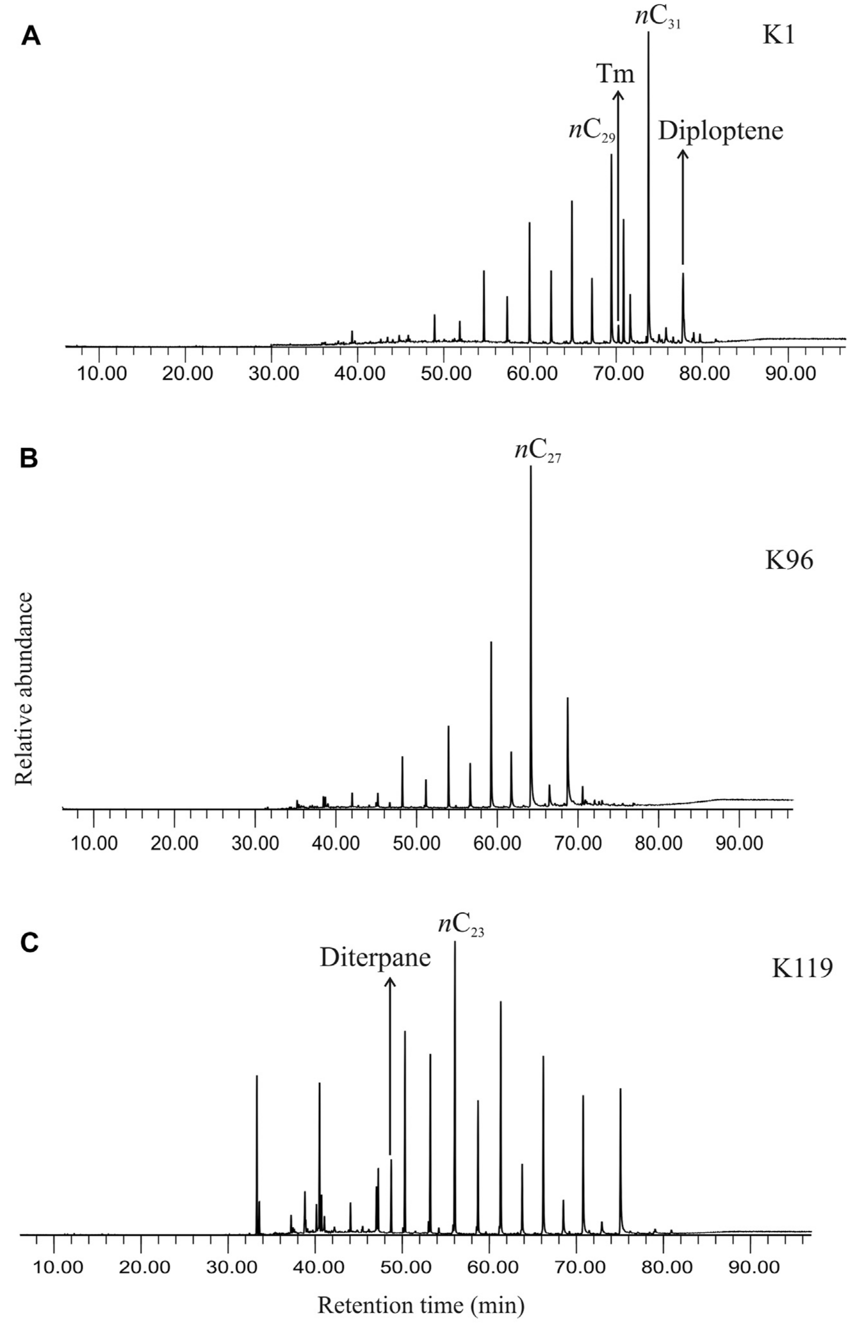

FIGURE 2 | (A) Total ion chromatogram showing the distribution of biomarkers, both linear chain and cyclic compounds, in the saturated hydrocarbon fraction extracted from the studied sediment (K1, ~369 cal yr BP). **(B)** Total ion chromatogram showing the distribution of biomarkers, both linear chain and cyclic compounds, in the saturated hydrocarbon fraction extracted from the studied sediment (K96, ~4842 cal yr BP). **(C)** Total ion chromatogram showing the distribution of biomarkers, both linear chain and cyclic compounds, in the saturated hydrocarbon fraction extracted from the studied sediment (K119, ~5655 cal yr BP).

the studied succession and no systematic trend could be discerned. However, a short interval between ~4900 and ~4400 cal yr BP distinctly displays considerably high CPI values between 3.7 and 8.0 (**Figure 4**).

The ACL values also vary throughout the Kedarnath peat succession between 25.9 and 29.1. Generally, lower values are observed in the interval between ~7515 and ~2300 cal yr BP and the ACL fluctuates between 25.9 and 28.9 averaging at 27.3 (**Figure 4**). In the above-mentioned interval, the temporal range between ~5300 and ~3600 cal yr BP shows many minor and short-lived fluctuations (**Figure 4**). During the period between ~3600 and ~2300 cal yr BP, the ACL shows minimum values (between 26.0 and 28.8 with a mean value of 27.1) followed by a sharp increasing trend

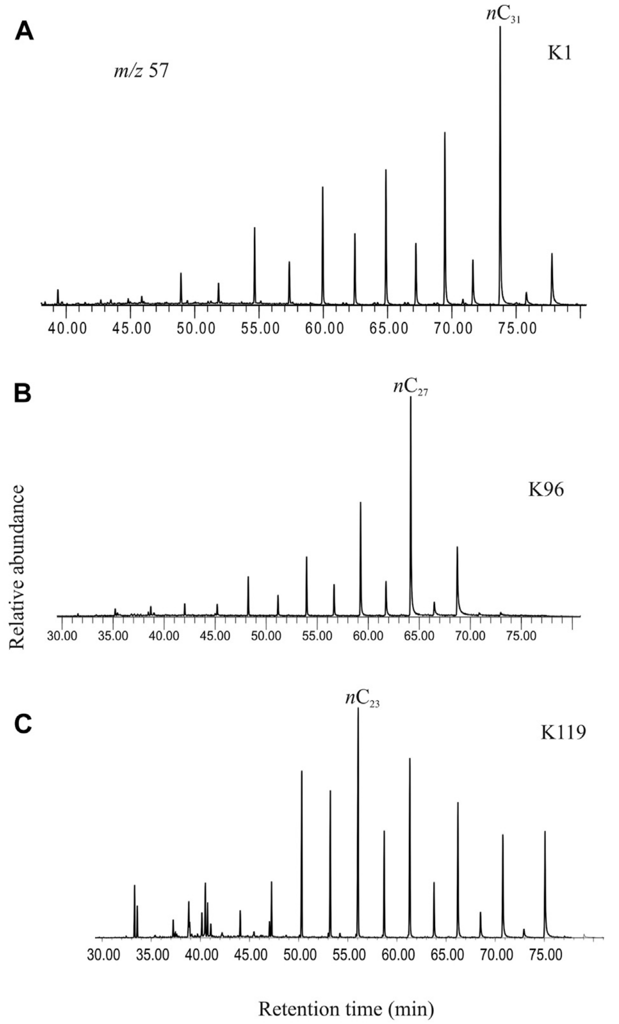

FIGURE 3 | (A) Selected ion chromatogram at *m/z* 57 showing the chain length distributions of the *n*-alkanes in the saturated hydrocarbon fraction extracted from the studied sediment (K1, ~369 cal yr BP). **(B)** Selected ion chromatogram at *m/z* 57 showing the chain length distributions of the *n*-alkanes in the saturated hydrocarbon fraction extracted from the studied sediment (K96, ~4842 cal yr BP). **(C)** Selected ion chromatogram at *m/z* 57 showing the chain length distributions of the *n*-alkanes in the saturated hydrocarbon fraction extracted from the studied sediment (K119, ~5655 cal yr BP). A clear shift in the predominant chain length in the sediments from different age intervals is observed. The changeover is a clear signature of response of the ambient vegetation to changing climatic conditions.

until ~370 cal yr BP (between 26.9 and 29.1 and averaging at 28.3) (**Figure 4**).

P_{aq} is generally characterized by higher values between ~7515 and ~2300 cal yr BP varying between 0.21 and 0.80 (averaging at 0.54) and relatively lower values in the range ~2300 to ~370 cal yr BP fluctuating between 0.16 and 0.53 (averaging at 0.28). Similar to ACL, fluctuations are clearly discernible in the range between ~5300 and ~3600 cal yr BP (**Figure 4**). Notably, the P_{aq} values exhibit a negative correlation (r = −0.91) with the ACL wherein higher values of ACL are accompanied by lower values of P_{aq} and vice versa in the studied succession.

Another parameter namely the n-C_{23}/n-C_{31} has been calculated to evaluate the distribution pattern of the *n*-alkanes. Typically, higher values, with a mean value of 3.10 are observed during the sufficiently long period between ~7500 and ~2400 cal yr BP (**Figure 4**; **Table 1**). A significant drop in the n-C_{23}/n-C_{31} ratio values is observed in the range between ~2300 and ~370 cal yr BP ranging between 0.11 and 0.67 (mean value 0.35). It is noteworthy that a concomitant decrease in the ACL is also observed during this time interval.

Acyclic Terpenoids

Pristane (Pr) and phytane (Ph), the C_{19} and C_{20} acyclic terpenoids, respectively are monitored by selected ion chromatogram at *m/z* 57 and detected by major fragments at *m/z* 183 and *m/z* 197 in the sediment samples. The Pr/Ph ranges between 0.37 and 1.35 with a mean of 0.83. Frequent oscillations in the Pr/Ph are observed over the studied sedimentary section and no distinct trend could be discerned. Similarly, fluctuations are observed for Pr/n-C_{17} and Ph/n-C_{18} (**Table 1**).

Diterpenoids

Diterpane is identified in selected ion chromatogram at *m/z* 123 in all the sediment samples (Noble et al., 1985). Other major fragments include *m/z* 231, 259 and 274. Tetracyclic diterpanes such as *ent*-phyllocladane and *ent*-kaurane have a very similar mass fragmentogram with major fragments at *m/z* 231, 259 and 274. However, these two compounds can be readily distinguished by the *m/z* 259/274 ion ratio wherein *ent*-kaurane is characterized by higher relative intensity of *m/z* 259 as compared to *m/z* 274. In our study, the diterpane peak is identified as *ent*-kaurane based on the higher *m/z* 259/274 ion ratio (**Figure 5**).

Hopanoids

Hopanoids are identified in selected ion chromatogram at *m/z* 191 in saturated hydrocarbon fractions of the studied sediments (**Figure 6**). The spectrum comprises both saturated and unsaturated compounds. 22, 29, 30-Trisnorhop-17(21)-ene (Te) is identified from the characteristic mass fragment at *m/z* 368 and other major diagnostic fragments at *m/z* 191 and *m/z* 231 (Nizar et al., 2021). The molecular ion fragment at *m/z* 368 (M^+ -$2H^+$) indicates unsaturation in the cyclic structure. C_{30} Diploptene [hop-22(29)-ene] is identified by the molecular ion at *m/z* 410 and characteristic mass fragments at *m/z* 191, 395, 299 (Sessions et al., 2013). 17α(H)-22, 29, 30-Trisnorhopane (Tm), a saturated C_{27} hopane, is identified based on the typical mass fragments in selected ion chromatogram at *m/z* 149 and major ions at *m/z* 191, 355 and 370 (Waples and Machihara, 1991). Other saturated hopanes include C_{29} norhopane and its isomer detected in selected ion chromatogram at *m/z* 177, C_{30} hopane and C_{31} hopane. Additionally, C_{31} methyl hopane, in selected ion chromatogram at *m/z* 205 is found to be present in the sediment samples. The mass fragment at *m/z* 177 signifies loss of a methyl group from the pentacyclic structure of hopane, whereas the presence of the fragment at *m/z* 205 indicates presence of a methyl group in the A-ring.

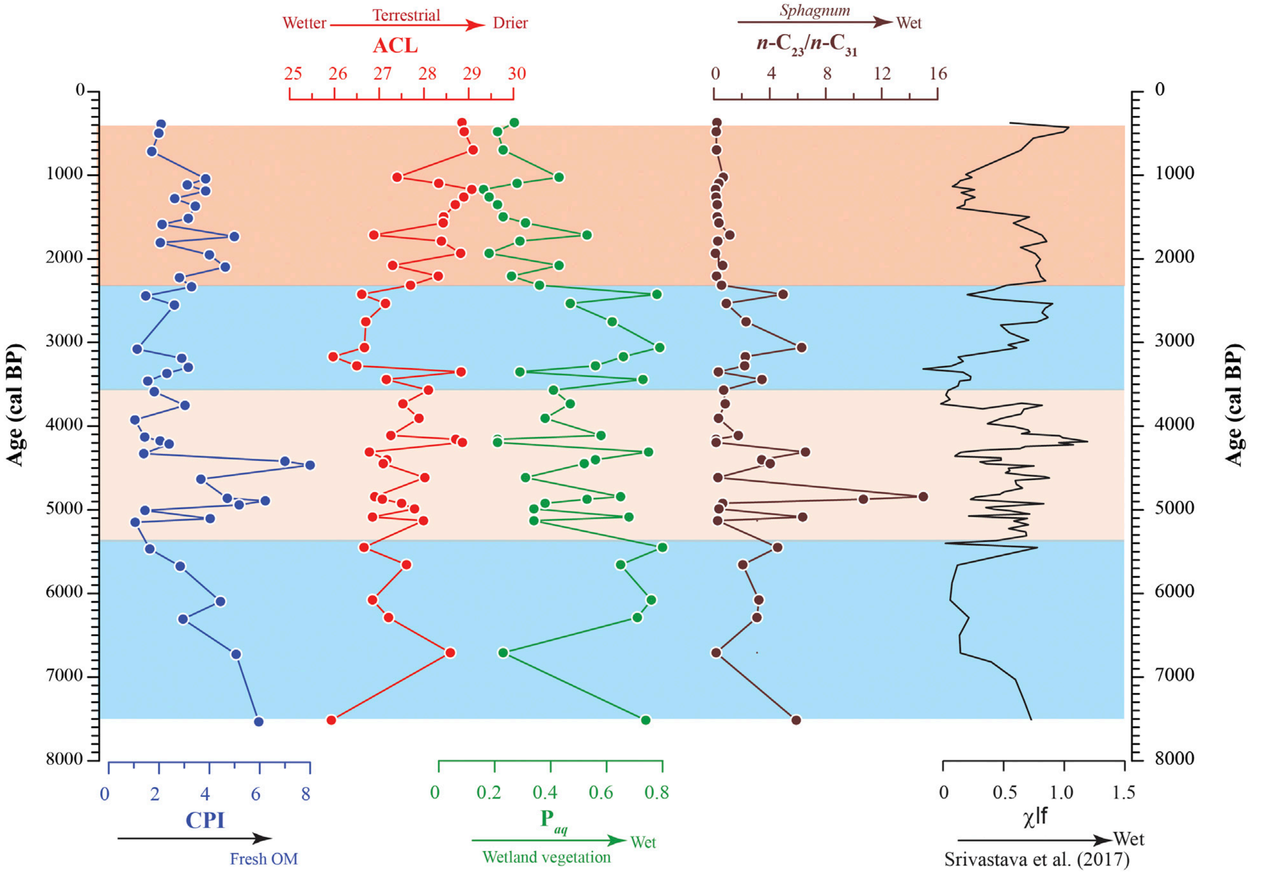

FIGURE 4 | The temporal variation of the CPI, ACL, P_{aq} and n-C_{23}/n-C_{31} across the studied ~8000 cal yr BP sedimentary succession. The P_{aq} and n-C_{23}/n-C_{31} reflect the influx of wetland vegetation and ACL indicates wetter or drier hydrological conditions. The palaeohydrological reconstruction by Srivastava et al. (2017) based on multiproxy records has been incorporated on the right representing the changing dry and wet phases across the studied succession as deduced from the previous work.

DISCUSSION

Depositional Conditions and Preservation of Organic Matter

Depositional Condition of the Environment

A significantly well-preserved organic matter transforming into the peat layers is evident from the high CPI values indicating limited microbial breakdown and diagenetic alterations (Alexander et al., 1981; Marzi et al., 1993; Peters et al., 2005). Further, low degree of biodegradation and relatively mild diagenesis are confirmed by the relation between Pr/n-C_{17} and Ph/n-C_{18} (Peters et al., 1999) (**Figure 7**) and presence of the unsaturated hopanes such as 22, 29, 30-trisnorhop-17(21)-ene (Te), and hop-22(29)-ene (diploptene). With increasing microbial degradation, values for the ratios Pr/n-C_{17} and Ph/n-C_{18} increase (>1) since normal alkanes are consumed faster than acyclic terpenoids. The structural similarity between 22, 29, 30-trisnorhop-17(21)-ene (Te) and 17α(H)-22, 29, 30-trisnorhopane (Tm) suggests that Te is the biogenic precursor of Tm and that the latter is produced during early diagenetic conditions in the sediment matrix. Further, the unsaturated hopanes indicate that the depositional condition was favorable towards inhibiting complete oxidation and degradation of the hopanoid class of compounds. Moderate degeneration of the organic matter and little taphonomic changes of the molecular fossils are plausibly consequential to the suboxic depositional condition of the environment as evident from low Pr/Ph values (**Table 1**) and corroborated by the relation between Pr/n-C_{17} and Ph/n-C_{18} (**Figure 7**).

Organic Matter Sources

Further, to understand the OM sources, biomarker signatures have been utilized here. The reconstruction of organic matter input is important to understand the endemic vegetation forming peat layers in the region (discussed herein) as well as to detect any biotic changes induced due to climatic and/or environmental shifts (see *Changes in Monsoonal Intensity as Inferred From Molecular Markers*). The ratio between Pr/n-C_{17}

TABLE 1 | A list of *n*-alkane (CPI, ACL, P_{aq} and n-C_{23}/n-C_{31}) and acyclic terpenoid (Pr/n-C_{17}, Ph/n-C_{18} and Pr/Ph) proxies across the studied sedimentary succession from the Kedarnath region, Garhwal Himalaya.

Samples	Age (cal yr BP)	CPI	ACL	P_{aq}	n-C_{23}/n-C_{31}	Pr/n-C_{17}	Ph/n-C_{18}	Pr/Ph
K-1	369.6	2.1	28.8	0.27	0.22	0.99	0.33	0.54
K-3	478.7	2.0	28.9	0.21	0.17	1.21	1.38	0.82
K-5	696.9	1.7	29.1	0.23	0.19	1.25	0.94	0.85
K-7	1024.2	3.8	27.4	0.43	0.67	0.77	0.21	1.35
K-9	1096.9	3.1	28.3	0.28	0.35	0.60	0.21	1.29
K-11	1169.6	3.8	29.1	0.16	0.12	0.70	0.37	0.87
K-13	1260.5	2.6	28.9	0.18	0.15	0.47	0.13	1.11
K-15	1351.5	3.4	28.7	0.21	0.24	0.55	0.09	1.40
K-17	1496.9	3.2	28.4	0.23	0.24	1.66	0.89	0.96
K-18	1569.6	2.1	28.4	0.31	0.36	0.80	0.86	0.89
K-20	1715.1	5.0	26.9	0.53	1.14	1.66	0.82	1.04
K-21	1787.8	2.0	28.4	0.29	0.28	1.02	1.01	0.62
K-23	1933.3	4.0	28.8	0.18	0.11	1.07	0.70	1.01
K-25	2078.7	4.6	27.3	0.43	0.63	1.17	0.47	1.21
K-27	2206.0	2.8	28.3	0.26	0.19	0.95	1.05	0.58
K-29	2315.1	3.3	27.7	0.36	0.55	0.82	0.30	0.76
K-31	2424.2	1.5	26.6	0.78	4.95	0.49	0.26	0.88
K-33	2533.3	2.6	27.1	0.47	0.89	1.17	0.88	1.00
K-37	2751.5	11.4	26.7	0.62	2.30	1.21	0.67	0.79
K-42	3060.5	1.1	26.7	0.79	6.28	0.38	0.07	0.50
K-44	3169.6	2.9	26.0	0.66	2.25	0.79	0.15	1.22
K-46	3278.7	3.2	26.5	0.56	2.20	0.95	0.22	1.08
K-48	3351.5	2.3	28.8	0.29	0.32	0.43	0.64	0.47
K-50	3442.4	1.5	27.2	0.73	3.44	0.47	0.45	1.16
K-53	3569.6	1.8	28.1	0.41	0.70	0.46	0.61	0.64
K-56	3733.3	3.0	27.5	0.47	0.81	0.46	0.55	0.57
K-62	3906.3	1.0	27.9	0.38	0.33	1.03	0.89	0.70
K-68	4111.8	1.4	27.3	0.58	1.75	0.29	0.43	0.38
K-70	4157.4	2.0	28.7	0.21	0.15	1.32	1.02	0.74
K-72	4195.5	2.4	28.9	0.21	0.16	1.49	1.83	0.81
K-77	4309.6	1.4	26.8	0.75	6.55	0.47	0.37	0.86
K-81	4401	7.0	27.2	0.56	3.42	0.52	0.53	0.47
K-83	4446.6	8.0	27.1	0.52	4.03	0.38	0.46	0.37
K-90	4614	3.7	28.0	0.31	0.29	1.17	1.25	0.78
K-96	4842.4	4.7	26.9	0.65	14.98	0.60	0.48	0.95
K-98	4872.8	6.2	27.1	0.53	10.69	0.48	0.35	1.19
K-99	4921.5	5.2	27.5	0.38	0.63	0.56	0.71	0.69
K-102	4987.9	1.4	27.8	0.34	0.36			
K-108	5085.4	4.0	26.8	0.68	6.35	0.44	0.39	1.15
K-110	5129.7	1.0	28.0	0.34	0.27	0.88	0.87	0.87
K-118	5448.7	1.6	26.7	0.80	4.56	0.36	0.10	0.53
K-119	5655.9	2.8	27.6	0.65	2.07	0.36	0.43	0.44
K-121	6077	4.4	26.8	0.76	3.22	0.56	0.51	0.69
K-122	6287.5	2.9	27.2	0.71	3.08	0.30	0.05	1.22
K-124	6708.5	5.1	28.6	0.23	0.16	0.33	0.07	0.93
K-128	7515.5	6.0	25.9	0.74	5.89	0.97	0.39	0.88

and Ph/n-C_{18} indicates that most of the samples lie in the zone of mixed organic matter, whereas only a few of them are exclusively characterized in land plants-derived organic matter (terrestrial vascular plants) (**Figure 7**). The sediment samples in the "mixed OM" zone are those that comprise OM formed from both wetland biota and terrestrial vascular plant. These samples characteristically have moderate to high P_{aq} and n-C_{23}/n-C_{31} and low ACL (signifying higher water levels and stronger precipitation). Conversely, the samples in "terrestrial vascular plants" zone represent the ones that have low P_{aq} and n-C_{23}/n-C_{31} and high ACL (indicating lowering of water levels that reduced the aquatic vegetation cover possibly consequential to decreased precipitation). The high molecular weight alkanes and strong odd-over-even carbon predominance also primarily indicate the contribution of vascular plants in the formation of the peat deposits. *Sphagnum* moss, a bryophyte, generally thrives in submerged/floating conditions and is one of the quintessential peat-forming aquatic biota (Cranwell, 1973; Ficken et al., 1998; Nott et al., 2000; Bingham et al., 2010).

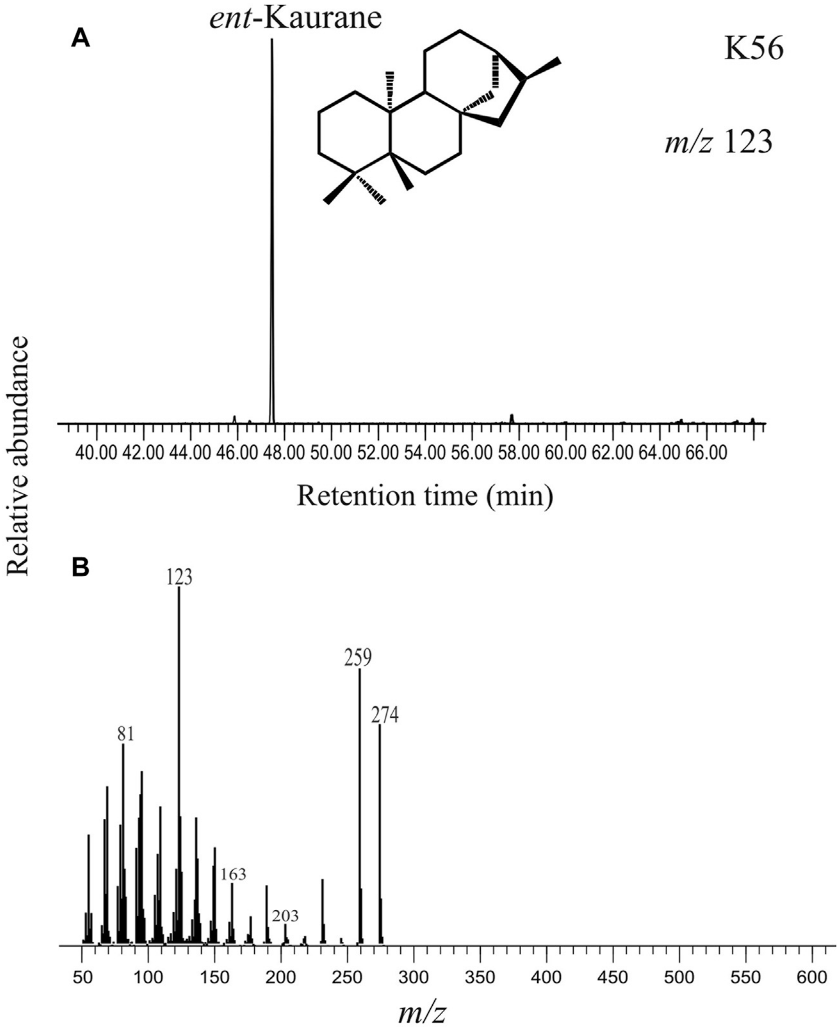

FIGURE 5 | (A) Selected ion chromatogram at *m/z* 123 depicting the peak for the diterpane compound detected as *ent*-kaurane in the saturated hydrocarbon fraction extracted from the studied sediment (K56, ~3733 cal yr BP). The structure of *ent*-kaurane is provided. **(B)** The mass spectrum of *ent*-kaurane with the base peak at *m/z* 123 and major mass fragments at *m/z* 259 and *m/z* 274 are given.

The *Sphagnum* species are dominant producers of the mid-chain lengths, typically the n-C_{23} and n-C_{25} (Bingham et al., 2010; Zhang et al., 2017). Therefore, the periodic enrichment of n-C_{23}/n-C_{31} ratio in the studied succession indicates contribution of *Sphagnum*-rich vegetation into formation of the peat layers. Further, the higher order terrestrial plants are dominated by the long chain (n-C_{27}–n-C_{33}) homologues. Notably, the modern arboreal vegetation cover in the study area is dominated by a preponderance of conifer elements (Kar et al., 2016; Srivastava et al., 2017). In particular, the vascular plant input includes gymnosperms as reflected by the presence of specific *ent*-kaurane diterpane compound. The compound *ent*-kaurene, which is the precursor for *ent*-kaurane is produced abundantly in conifer resins. Additionally, microbial biota such as bacteria also contributed into the peat-forming OM as revealed by the presence of the hopanoids. These compounds are produced as an integral part of the cellular membrane by prokaryotes of diverse taxonomic clades (Ourisson and Albrecht, 1992). The presence of the mono-unsaturated hopanoid compounds viz. 22, 29, 30-trisnorhop-17(21)-ene (Te), and C_{30} diploptene, i.e., hop-22(29)-ene are tracers of bacterial input into the organic matter (Ochs et al., 1992). A possible cyanobacterial source for 17α(H)-22, 29, 30-trisnorhopane (Tm) is suggested by Freeman et al. (1994). The C_{31} methylhopane is also known to be produced by cyanobacteria (Brocks et al., 2003). Likewise, the short chain n-alkanes (n-C_{15}–n-C_{21}) in the present study could be attributed to microbial input such as prokaryotes or algae (Cranwell et al., 1987). Concentrations of the shorter chain alkanes viz. n-C_{17}, n-C_{19} are relatively low as compared to the mid- and long-chain alkanes throughout our studied sedimentary record suggesting subdued presence of microbial biota. The acyclic terpenoids pristane and the phytane, produced from the phytyl side chain of chlorophyll upon diagenetic alterations in the sediments, could also be derivatives of microbial organisms or vascular higher plants.

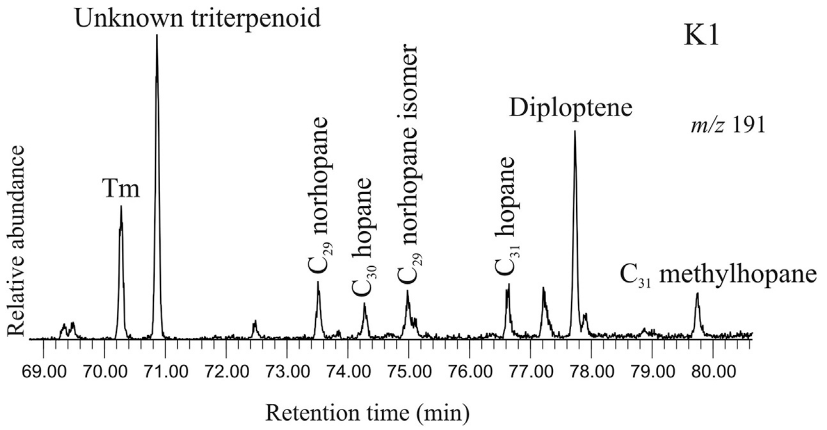

FIGURE 6 | Selected ion chromatogram at *m/z* 191 depicting the peaks for the hopanoids in the saturated hydrocarbon fraction extracted from the studied sediment (K1, ~369 cal yr BP). The hopanoid spectrum comprises both unsaturated (diploptene) and saturated compounds viz. Tm, C_{29} norhopane and its isomer, C_{30} hopane, C_{31} hopane and C_{31} methylhopane.

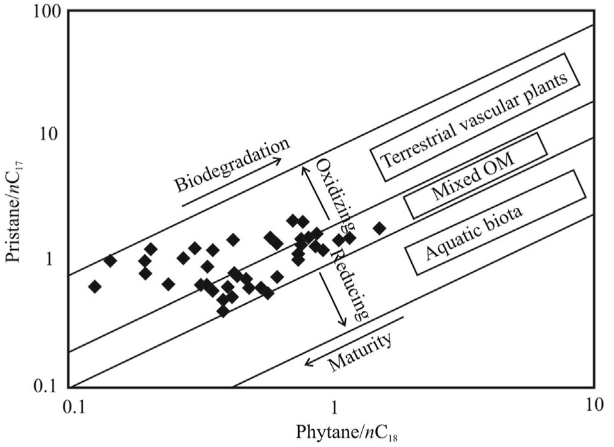

FIGURE 7 | Cross plot between pristane/n-C_{17} and phytane/n-C_{18} describing the type of biota forming the peat and organic rich layers in the studied section. The cross plot also indicates the extent of biodegradation of the preserved organic matter in the sediments, level of thermal maturity and the redox condition [modified after Alexander et al. (1981)].

Changes in Monsoonal Intensity as Inferred From Molecular Markers

Various *n*-alkane proxies derived from sedimentary records are robust indicators of source biota in peat along with the palaeohydrological conditions (Baker et al., 2016; Basu et al., 2017; He et al., 2019). For e.g., higher ACL values reflect the modification of wax lipid composition by plants as an adaptive measure to changing climatic conditions. The longer chain *n*-alkanes are hydrophobic in nature and hence increasingly produced in arid condition. Being hydrophobic, the longer chain *n*-alkanes create an impermeable layer that minimizes desiccation in drier environment. Hence, greater synthesis of the longer chain *n*-alkanes, reflected by higher ACL and lower n-C_{23}/n-C_{31} values, is one of the survival strategies of vascular land plants to combat dry spells and protect the cellular apparatus (Sarkar et al., 2014; Andrae et al., 2019). Marked variations are observed for CPI values in the studied section and higher values (>2) are reflective of preservation of fresh organic matter in the region (**Figure 4**). Further, the relative contribution of *Sphagnum* spp. and other vascular land plants has been assessed by the n-C_{23}/n-C_{31} and P_{aq} ratios wherein higher values are corelatable with expansion of wetland biota The trend in the n-C_{23}/n-C_{31} ratios complements the variability in ACL values as deduced from the studied sediments and a clear inverse correlation could be established between the ACL and n-C_{23}/n-C_{31} ratios (**Figure 4**; **Table 1**). Likewise, higher values of P_{aq} across the studied succession, related to increased aquatic taxa input, correlates well with higher range of n-C_{23}/n-C_{31} (**Figure 4**; **Table 1**). In terms of the *n*-alkanes proxy variables, climate variability in Kedarnath region can be divided into four distinct intervals: 1) ~7515 to ~5300 cal yr BP depicting higher P_{aq} and n-C_{23}/n-C_{31} and lower ACL values 2) ~5300 to ~3600 cal yr BP characterized by oscillating ACL and P_{aq} (also n-C_{23}/n-C_{31}) 3) ~3600 to ~2300 cal yr BP with reversal to higher P_{aq} and n-C_{23}/n-C_{31} 4) ~2300 to ~370 cal yr BP characterized by lower n-C_{23}/n-C_{31}, P_{aq} and increase in ACL index (**Figure 4**). During the time span between ~7515 and ~2300 cal yr BP, the higher n-C_{23}/n-C_{31} values are accompanied by lower ACL (and higher P_{aq}) and vice versa (**Figure 4**). This is reflective of a generally enhanced monsoonal phase and wetter hydrological condition that facilitates the proliferation of the hygrophilic *Sphagnum* moss biota. Despite generally intensified monsoon, there were brief periods of aridity during the time span between ~5300 and ~3600 cal yr BP. Further, a significant deviation towards lower ACL and higher n-C_{23}/n-C_{31} is observed for a short interval between ~3600 and ~2300 cal yr BP (**Figure 4**). This reflects return of humid condition briefly consequential to strengthening of monsoon that again resulted into proliferation of aquatic vegetation in the area. The increased precipitation facilitated expansion of waterlogged condition that is highly desirable for expansion of *Sphagnum* flora (Inglis et al., 2015). Conversely,

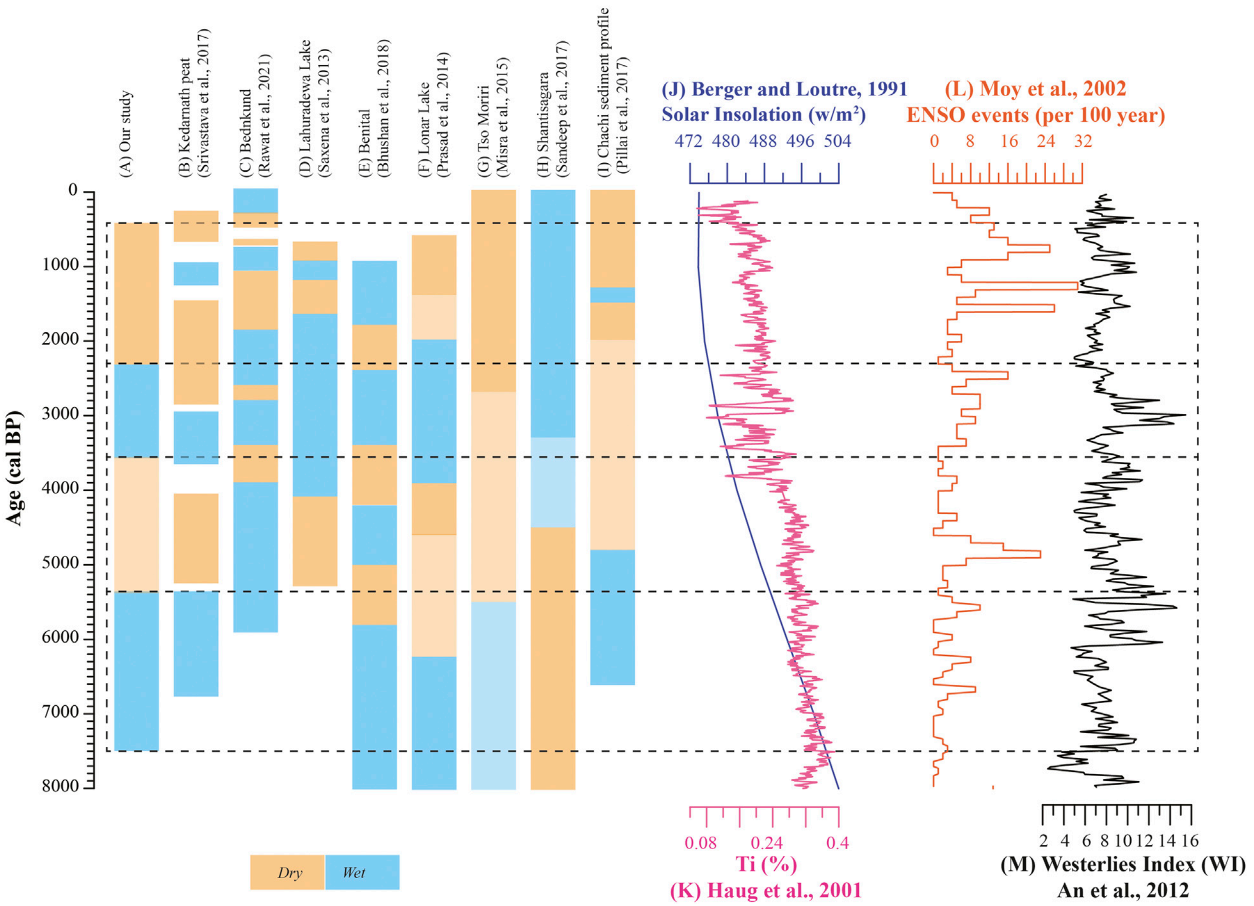

FIGURE 8 | Regional comparison of palaeoclimate data **(A–I)** with major teleconnections **(J–M)**.

lower values for the n-C$_{23}$/n-C$_{31}$ are co-relatable with higher ACL values between the interval ~2300 and ~370 cal yr BP (**Figure 4**). This observation suggests arid conditions resulting into sparse cover of *Sphagnum*-dominated vegetation during the period.

Palaeohydrological Changes in Kedarnath and a Regional Comparison

The present study based on n-alkane proxies from Kedarnath peat succession clearly demonstrates a shift in the biotic composition in response to a change in the hydrological conditions since mid-Holocene (ca. 7500 cal yr BP).

The wetter climatic condition during ~7515 to ~5300 cal yr BP inferred by n-alkane proxies is in agreement with previous geochemical and bulk organic proxy-based data from the region which shows warmer and wetter condition during mid-Holocene (~6500 to ~5400 cal yr BP) (Srivastava et al., 2017). Likewise, the pollen-based investigations from Bednikund and Tso Kar lakes (NW Himalaya) shows a short-term mid-Holocene climate optimum and intensified ISM (Demske et al., 2009; Rawat et al., 2021). In contrast, the terrestrial records from the Himalayan region (Tso Moriri and Benital lakes), southern India (Shantisagara Lake) and the central India (Lonar and Nonia Tal lakes) demonstrate early Holocene intensification followed by general weakening in monsoonal precipitation during the mid-Holocene (Prasad et al., 2014; Mishra et al., 2015; Sandeep et al., 2017; Bhushan et al., 2018; Kumar et al., 2019). Similarly, the *Globigerina bulloides*-based study from Arabian Sea (Gupta et al., 2003) and *Globigerinoides ruber* from Bay of Bengal (Rashid et al., 2011) have also portrayed an early Holocene intensification in response to the Northern Hemispheric solar insolation (Berger and Loutre, 1991) (**Figure 8**). Conversely, the pollen-based palaeorecord from Indo-Gangetic plain (Lahuradewa Lake) indicate a prolonged ISM intensification during ~9200 to ~5300 cal yr BP (Saxena et al., 2013). The δ^{18}O record from Kotumsar cave in central India represent mid-Holocene wetter climatic condition punctuated by series of megadroughts probably linked to increased frequency of El Nino events and weaker North Atlantic circulations (Band et al., 2018).

Further, a major shift in climatic pattern in the Kedarnath region is observed between ~5300 and 3600 cal yr BP. This brief period of generally weakened monsoon with high frequency climate variability is clearly visible in both our proxy records and the previous study by Srivastava et al. (2017). Such a scenario is well recorded in several other studies from the Indian subcontinent (e.g., Lahuradewa in central India, Benital and Tso Moriri in NW Himalaya, Lonar Lake in central India, and Chachi sediment profile in the western India) (Saxena et al., 2013; Prasad et al., 2014; Mishra et al., 2015; Pillai et al., 2017; Bhushan et al., 2018). Further, low ACL and high *P*aq and n-C_{23}/n-C_{31} values between ~3600 and ~2300 cal yr BP reflect wetter climatic condition due to increased monsoonal precipitation in the studied region. The NW Himalayan region (Bednikund Lake during ~3300 to ~2800 cal yr BP and Benital Lake between ~3500 and ~2400 cal yr BP) have also recorded wetter climatic condition in response to Northern Hemisphere temperature variability and increased solar irradiance (Bhushan et al., 2018; Rawat et al., 2021). In contrast, the record from central and southern India shows drier (weak monsoon) climatic condition due to weakening of ISM precipitation (Prasad et al., 2014; Sandeep et al., 2017). This discrepancy might be attributed to increased contribution of Westerlies as the region receives precipitation from dual sources (both ISM and Westerlies). This is supported by increased westerly contribution during ~3600 to ~2300 cal yr BP (An et al., 2012) (**Figure 8**).

Lastly, the period between ~2300 and ~370 cal yr BP exhibit low n-C_{23}/n-C_{31} and P_{aq} and high ACL suggesting progressive weakening of monsoonal condition in the region. Other signatures such as subdued presence of broad-leaved taxa and marshy flora also confirms the prevalence of drier conditions (Bingham et al., 2010; Inglis et al., 2015). The previous study has revealed two short-term centennial scale climatic events such as Medieval Climate Anomaly (during ~1250 to ~800 cal yr BP) and Little Ice Age (~600 and ~250 cal yr BP) (Srivastava et al., 2017). However, in our present proxy study, the identification of these events is beyond the scope due to relatively low sample resolution as a result of unavailability of sediments in these intervals that are most appropriate for organic geochemical analyses. Moreover, with the exception of these short term events, the majority of palaeoclimate records demonstrate depreciating monsoonal condition over the Indian subcontinent. This progressive decrease in monsoonal precipitation is mostly interpreted in terms of southern migration of the Intertropical Convergence Zone (ITCZ) coupled with increased frequency of El Niño events (Haug et al., 2001; Moy et al., 2002; Kumar et al., 2019; Singh et al., 2020). For example, the proxy records from Bednikund suggest intermittent weak monsoonal condition (1860–1050 cal yr BP followed by 760 to 580 cal yr BP and 500 to 320 cal yr BP) punctuated by several short term wet phase (Rawat et al., 2021). The study suggests the role of solar insolation and Northern Hemisphere temperature effects in controlling the climatic condition in the NW Himalaya. Likewise, the evaporative carbonates from Tso Moriri Lake indicate weakest monsoon (2700 cal yr BP to present) in response to reduced solar insolation (Mishra et al., 2015).

Thus succinctly, similar multiproxy studies from different climatic sensitive region are warranted to further understand the mechanisms for the spatial and temporal heterogeneity and the impact of teleconnections in monsoon variability (e.g., El Nino) (**Figure 8**).

CONCLUSION

A sedimentary succession with peat layers from the Kedarnath region, Garhwal Himalaya spanning the last 8000 cal yr BP has been investigated for lipid biomarkers. The peat-forming organic constituents include gymnosperms and *Sphagnum* moss as evident from the presence of *ent*-kaurane and high abundance of the n-C_{23} alkane, respectively. A variety of hopanoid compounds both unsaturated including hop-22(29)-ene and 22, 29, 30-trisnorhop-17(21)-ene (Te) and saturated such as the 17α(H)-22, 29, 30-trisnorhopane (Tm), C_{29} norhopanes, C_{30} hopane, C_{31} hopane and C_{31} methyl hopane reveal the suite of microbially derived lipid constituents. The *n*-alkane proxies used in the present study (P_{aq}, ACL, n-C_{23}/n-C_{31}) and previously published records clearly reveal shift in the intensity of monsoon and a concomitant changeover in the vegetation cover. The relatively high abundance of mid-chain alkane homologues during the interval between ~7515 and ~2300 cal yr BP suggests significant aquatic vegetation cover. The palaeohydrologic condition is established as wetter during the aforementioned interval although interlude periods of aridity had prevailed as evident from frequent shifts towards the longer *n*-alkane chain lengths, typically during ~5300 to ~3600 cal yr BP. Beginning at around 2300 cal yr BP until around 370 cal yr BP, the climate entered a prolonged phase of aridity triggering the synthesis of longer chain *n*-alkanes as a protective measure by the terrestrial plants to combat the dry spells. The climate reconstruction as inferred from the *n*-alkane proxies is consistent with the previously determined multiproxy records and attests the applicability of hydrocarbon biomarkers for past climatic reconstructions in sedimentary successions. The overall comparison of palaeoclimate data from the Kedarnath peat succession with other regional records reveals temporal and spatial heterogeneity in monsoonal pattern over the Indian sub-continent during mid to late Holocene.

DATA AVAILABILITY STATEMENT

The original contributions presented in the study are included in the article/supplementary material, further inquiries can be directed to the corresponding author.

AUTHOR CONTRIBUTIONS

SB, PM, and PS designed the research; PS collected the samples; HK and YA performed the analyses; SB and PM interpreted the data; SB and PM wrote the manuscript; YA and PS provided useful comments on the draft manuscript.

FUNDING

We thank Department of Science and Technology (DST) for the financial support (INSPIRE-18-149 and INSPIRE-15-2769).

ACKNOWLEDGMENTS

The authors gratefully acknowledge Anoop Ambili for the access to speed extractor and GC-MS at his laboratory and useful discussion and all the members of PRISM lab for technical support. SB greatly appreciates Department of Earth and Environmental Sciences, IISER Mohali for the necessary infrastructure and facilities provided for accomplishing the research.

REFERENCES

Alexander, R., Kagi, R., and Woodhouse, G. W. (1981). Geochemical Correlation of Windalia Oil and Extracts of Winning Group (Cretaceous) Potential Source Rocks, Barrow Subbasin, Western Australia. *AAPG Bull.* 65, 235–250. doi:10.1306/2f9197b0-16ce-11d7-8645000102c1865d

An, Z., Colman, S. M., Zhou, W., Li, X., Brown, E. T., Jull, A. J. T., et al. (2012). Interplay between the Westerlies and Asian Monsoon Recorded in Lake Qinghai Sediments since 32 Ka. *Sci. Rep.* 2, 1–7. doi:10.1038/srep00619

Andrae, J. W., McInerney, F. A., Tibby, J., Henderson, A. C. G., Hall, P. A., Marshall, J. C., et al. (2019). Variation in Leaf Wax *N*-Alkane Characteristics with Climate in the Broad-Leaved Paperbark (*Melaleuca Quinquenervia*). *Org. Geochem.* 130, 33–42. doi:10.1016/j.orggeochem.2019.02.004

Ankit, Y., Muneer, W., Lahajnar, N., Gaye, B., Misra, S., Jehangir, A., et al. (2021). Long Term Natural and Anthropogenic Forcing on Aquatic System - Evidence Based on Biogeochemical and Pollen Proxies from lake Sediments in Kashmir Himalaya, India. *Appl. Geochem.* 131, 105046. doi:10.1016/j.apgeochem.2021.105046

Anoop, A., Prasad, S., Krishnan, R., Naumann, R., and Dulski, P. (2013). Intensified Monsoon and Spatiotemporal Changes in Precipitation Patterns in the NW Himalaya during the Early-Mid Holocene. *Quat. Int.* 313-314, 74–84. doi:10.1016/j.quaint.2013.08.014

Baker, A., Routh, J., and Roychoudhury, A. N. (2018). *n*-Alkan-2-one Biomarkers as a Proxy for Palaeoclimate Reconstruction in the Mfabeni Fen, South Africa. *Org. Geochem.* 120, 75–85. doi:10.1016/j.orggeochem.2018.03.001

Baker, A., Routh, J., and Roychoudhury, A. N. (2016). Biomarker Records of Palaeoenvironmental Variations in Subtropical Southern Africa since the Late Pleistocene: Evidences from a Coastal Peatland. *Palaeogeogr. Palaeoclimatol. Palaeoecol.* 451, 1–12. doi:10.1016/j.palaeo.2016.03.011

Band, S., Yadava, M. G., Lone, M. A., Shen, C.-C., Sree, K., and Ramesh, R. (2018). High-resolution Mid-holocene Indian Summer Monsoon Recorded in a Stalagmite from the Kotumsar Cave, Central India. *Quat. Int.* 479, 19–24. doi:10.1016/j.quaint.2018.01.026

Basu, S., Anoop, A., Sanyal, P., and Singh, P. (2017). Lipid Distribution in the lake Ennamangalam, South India: Indicators of Organic Matter Sources and Paleoclimatic History. *Quat. Int.* 443, 238–247. doi:10.1016/j.quaint.2016.08.045

Bechtel, A., Sachsenhofer, R. F., Markic, M., Gratzer, R., Lücke, A., and Püttmann, W. (2003). Paleoenvironmental Implications from Biomarker and Stable Isotope Investigations on the Pliocene Velenje lignite Seam (Slovenia). *Org. Geochem.* 34, 1277–1298. doi:10.1016/s0146-6380(03)00114-1

Benn, D. I., and Owen, L. A. (1998). The Role of the Indian Summer Monsoon and the Mid-latitude Westerlies in Himalayan Glaciation: Review and Speculative Discussion. *J. Geol. Soc.* 155, 353–363. doi:10.1144/gsjgs.155.2.0353

Berger, A., and Loutre, M. F. (1991). Insolation Values for the Climate of the Last 10 Million Years. *Quat. Sci. Rev.* 10, 297–317. doi:10.1016/0277-3791(91)90033-Q

Bhushan, R., Sati, S. P., Rana, N., Shukla, A. D., Mazumdar, A. S., and Juyal, N. (2018). High-resolution Millennial and Centennial Scale Holocene Monsoon Variability in the Higher Central Himalayas. *Palaeogeogr. Palaeoclimatol. Palaeoecol.* 489, 95–104. doi:10.1016/j.palaeo.2017.09.032

Bingham, E. M., McClymont, E. L., Väliranta, M., Mauquoy, D., Roberts, Z., Chambers, F. M., et al. (2010). Conservative Composition of *N*-Alkane Biomarkers in Sphagnum Species: Implications for Palaeoclimate Reconstruction in Ombrotrophic Peat Bogs. *Org. Geochem.* 41, 214–220. doi:10.1016/j.orggeochem.2009.06.010

Brocks, J. J., Buick, R., Logan, G. A., and Summons, R. E. (2003). Composition and Syngeneity of Molecular Fossils from the 2.78 to 2.45 Billion-Year-Old Mount Bruce Supergroup, Pilbara Craton, Western Australia. *Geochimica et Cosmochimica Acta* 67, 4289–4319. doi:10.1016/S0016-7037(03)00208-4

Bulbul, M., Ankit, Y., Basu, S., and Anoop, A. (2021). Characterization of Sedimentary Organic Matter and Depositional Processes in Mandovi Estuary, Western India: An Integrated Lipid Biomarker, Sedimentological and Stable Isotope Approach. *Appl. Geochem.* 131, 105041. doi:10.1016/j.apgeochem.2021.105041

Bush, R. T., and McInerney, F. A. (2013). Leaf Wax *N*-Alkane Distributions in and across Modern Plants: Implications for Paleoecology and Chemotaxonomy. *Geochimica et Cosmochimica Acta* 117, 161–179. doi:10.1016/j.gca.2013.04.016

Chambers, F. M., Booth, R. K., De Vleeschouwer, F., Lamentowicz, M., Le Roux, G., Mauquoy, D., et al. (2012). Development and Refinement of Proxy-Climate Indicators from Peats. *Quat. Int.* 268, 21–33. doi:10.1016/j.quaint.2011.04.039

Chen, J., and Summons, R. E. (2001). Complex Patterns of Steroidal Biomarkers in Tertiary Lacustrine Sediments of the Biyang Basin, China. *Org. Geochem.* 32, 115–126. doi:10.1016/s0146-6380(00)00145-5

Cranwell, P. A. (1973). Chain-length Distribution of N-Alkanes from lake Sediments in Relation to post-glacial Environmental Change. *Freshw. Biol* 3, 259–265. doi:10.1111/j.1365-2427.1973.tb00921.x

Cranwell, P. A., Eglinton, G., and Robinson, N. (1987). Lipids of Aquatic Organisms as Potential Contributors to Lacustrine Sediments-II. *Org. Geochem.* 11, 513–527. doi:10.1016/0146-6380(87)90007-6

Dai, S., Bechtel, A., Eble, C. F., Flores, R. M., French, D., Graham, I. T., et al. (2020). Recognition of Peat Depositional Environments in Coal: A Review. *Int. J. Coal Geology.* 219, 103383. doi:10.1016/j.coal.2019.103383

Demske, D., Tarasov, P. E., Wünnemann, B., and Riedel, F. (2009). Late Glacial and Holocene Vegetation, Indian Monsoon and westerly Circulation in the Trans-himalaya Recorded in the Lacustrine Pollen Sequence from Tso Kar, Ladakh, NW India. *Palaeogeogr. Palaeoclimatol. Palaeoecol.* 279, 172–185. doi:10.1016/j.palaeo.2009.05.008

Didyk, B. M., Simoneit, B. R. T., Brassell, S. C., and Eglinton, G. (1978). Organic Geochemical Indicators of Palaeoenvironmental Conditions of Sedimentation. *Nature* 272, 216–222. doi:10.1038/272216a0

Dutta, S., Bhattacharya, S., and Raju, S. V. (2013). Biomarker Signatures from Neoproterozoic-Early Cambrian Oil, Western India. *Org. Geochem.* 56, 68–80. doi:10.1016/j.orggeochem.2012.12.007

Eglinton, G., and Hamilton, R. J. (1967). Leaf Epicuticular Waxes. *Science* 156, 1322–1335. doi:10.1126/science.156.3780.1322

Eglinton, T. I., and Eglinton, G. (2008). Molecular Proxies for Paleoclimatology. *Earth Planet. Sci. Lett.* 275, 1–16. doi:10.1016/j.epsl.2008.07.012

Ficken, K. J., Barber, K. E., and Eglinton, G. (1998). Lipid Biomarker, δ13C and Plant Macrofossil Stratigraphy of a Scottish Montane Peat Bog over the Last Two Millennia. *Org. Geochem.* 28, 217–237. doi:10.1016/S0146-6380(97)00126-5

Ficken, K. J., Li, B., Swain, D. L., and Eglinton, G. (2000). An *N*-Alkane Proxy for the Sedimentary Input of Submerged/floating Freshwater Aquatic Macrophytes. *Org. Geochem.* 31, 745–749. doi:10.1016/S0146-6380(00)00081-4

Finlayson, C. M., and Milton, G. R. (2016). "Peatlands," in *The Wetland Book*. Editors C. Finlayson, G. Milton, R. Prentice, and N Davidson (Dordrecht, Netherlands: Springer Science+Business Media), 227–244. doi:10.1007/978-94-007-6173-5_202-1

Freeman, K. H., Wakeham, S. G., and Hayes, J. M. (1994). Predictive Isotopic Biogeochemistry: Hydrocarbons from Anoxic marine Basins. *Org. Geochem.* 21, 629–644. doi:10.1016/0146-6380(94)90009-4

French, K. L., Birdwell, J. E., and Vanden Berg, M. D. (2020). Biomarker Similarities between the saline Lacustrine Eocene Green River and the Paleoproterozoic Barney Creek Formations. *Geochimica et Cosmochimica Acta* 274, 228–245. doi:10.1016/j.gca.2020.01.053

Gorham, E., Janssens, J. A., and Glaser, P. H. (2003). Rates of Peat Accumulation during the Postglacial Period in 32 Sites from Alaska to Newfoundland, with Special Emphasis on Northern Minnesota. *Can. J. Bot.* 81, 429–438. doi:10.1139/b03-036

Gupta, A. K., Anderson, D. M., and Overpeck, J. T. (2003). Abrupt Changes in the Asian Southwest Monsoon during the Holocene and Their Links to the North Atlantic Ocean. *Nature* 421, 354–357. doi:10.1038/nature01340

Harris, I., Osborn, T. J., Jones, P., and Lister, D. (2020). Version 4 of the CRU TS Monthly High-Resolution Gridded Multivariate Climate Dataset. *Sci. Data* 7, 1–18. doi:10.1038/s41597-020-0453-3

Haug, G. H., Hughen, K. A., Sigman, D. M., Peterson, L. C., and Röhl, U. (2001). Southward Migration of the Intertropical Convergence Zone through the Holocene. *Science* 293, 1304–1308. doi:10.1126/science.1059725

He, D., Huang, H., and Arismendi, G. G. (2019). *n*-Alkane Distribution in Ombrotrophic Peatlands from the Northeastern Alberta, Canada, and its Paleoclimatic Implications. *Palaeogeogr. Palaeoclimatol. Palaeoecol.* 528, 247–257. doi:10.1016/j.palaeo.2019.05.018

Inglis, G. N., Collinson, M. E., Riegel, W., Wilde, V., Robson, B. E., Lenz, O. K., et al. (2015). Ecological and Biogeochemical Change in an Early Paleogene Peat-Forming Environment: Linking Biomarkers and Palynology. *Palaeogeogr. Palaeoclimatol. Palaeoecol.* 438, 245–255. doi:10.1016/j.palaeo.2015.08.001

Jiang, L., Ding, W., and George, S. C. (2020). Late Cretaceous-Paleogene Palaeoclimate Reconstruction of the Gippsland Basin, SE Australia. *Palaeogeogr. Palaeoclimatol. Palaeoecol.* 556, 109885. doi:10.1016/j.palaeo.2020.109885

Jordan, S. F., Murphy, B. T., O'Reilly, S. S., Doyle, K. P., Williams, M. D., Grey, A., et al. (2017). Mid-Holocene Climate Change and Landscape Formation in Ireland: Evidence from a Geochemical Investigation of a Coastal Peat Bog. *Org. Geochem.* 109, 67–76. doi:10.1016/j.orggeochem.2017.02.004

Kar, R., Bajpai, R., and Mishra, K. (2016). Modern Pollen Rain in Kedarnath: Implications for Past Vegetation and Climate. *Curr. Sci.* 110, 296–298. doi:10.18520/cs/Fv110/Fi/2F296-298

Kayranli, B., Scholz, M., Mustafa, A., and Hedmark, Å. (2010). Carbon Storage and Fluxes within Freshwater Wetlands: A Critical Review. *Wetlands* 30, 111–124. doi:10.1007/s13157-009-0003-4

Kelly, A. E., Love, G. D., Zumberge, J. E., and Summons, R. E. (2011). Hydrocarbon Biomarkers of Neoproterozoic to Lower Cambrian Oils from Eastern Siberia. *Org. Geochem.* 42, 640–654. doi:10.1016/j.orggeochem.2011.03.028

Kumar, K., Agrawal, S., Sharma, A., and Pandey, S. (2019). Indian Summer Monsoon Variability and Vegetation Changes in the Core Monsoon Zone, India, during the Holocene: A Multiproxy Study. *The Holocene* 29, 110–119. doi:10.1177/0959683618804641

Kumar, O., Ramanathan, A., Bakke, J., Kotlia, B. S., Shrivastava, J. P., Kumar, P., et al. (2021). Role of Indian Summer Monsoon and Westerlies on Glacier Variability in the Himalaya and East Africa during Late Quaternary: Review and New Data. *Earth-Science Rev.* 212, 103431. doi:10.1016/j.earscirev.2020.103431

Kumaran, N. K. P., Padmalal, D., Limaye, R. B., S., V. M., Jennerjahn, T., and Gamre, P. G. (2016). Tropical Peat and Peatland Development in the Floodplains of the Greater Pamba Basin, South-Western India during the Holocene. *PLoS One* 11, e0154297–21. doi:10.1371/journal.pone.0154297

Marcisz, K., Colombaroli, D., Jassey, V. E. J., Tinner, W., Kołaczek, P., Gałka, M., et al. (2016). A Novel Testate Amoebae Trait-Based Approach to Infer Environmental Disturbance in *Sphagnum* Peatlands. *Sci. Rep.* 6, 1–11. doi:10.1038/srep33907

Marzi, R., Torkelson, B. E., and Olson, R. K. (1993). A Revised Carbon Preference index. *Org. Geochem.* 20, 1303–1306. doi:10.1016/0146-6380(93)90016-5

Middleton, G. V. (1973). Johannes Walther's Law of the Correlation of Facies. *Geol. Soc. America Bull.* 84, 979–988. doi:10.1130/0016-7606(1973)84<979:JWLOTC>2.0.CO;2

Mishra, P. K., Anoop, A., Schettler, G., Prasad, S., Jehangir, A., Menzel, P., et al. (2015). Reconstructed Late Quaternary Hydrological Changes from Lake Tso Moriri, NW Himalaya. *Quat. Int.* 371, 76–86. doi:10.1016/j.quaint.2014.11.040

Misra, S., Bhattacharya, S., Mishra, P. K., Misra, K. G., Agrawal, S., and Anoop, A. (2020). Vegetational Responses to Monsoon Variability during Late Holocene: Inferences Based on Carbon Isotope and Pollen Record from the Sedimentary Sequence in Dzukou valley, NE India. *Catena* 194, 104697. doi:10.1016/j.catena.2020.104697

Moy, C. M., Seltzer, G. O., Rodbell, D. T., and Anderson, D. M. (2002). Variability of El Niño/Southern Oscillation Activity at Millennial Timescales during the Holocene Epoch. *Nature* 420, 162–165. doi:10.1038/nature01194

Naafs, B. D. A., Inglis, G. N., Blewett, J., McClymont, E. L., Lauretano, V., Xie, S., et al. (2019). The Potential of Biomarker Proxies to Trace Climate, Vegetation, and Biogeochemical Processes in Peat: A Review. *Glob. Planet. Change* 179, 57–79. doi:10.1016/j.gloplacha.2019.05.006

Nizar, O., Jean-Pierre, G., and Habib, B. (2021). Significance of 2-methylhopane and 22,29,30Trisnorhop17(21)-Ene Biomarkers in Holocene Sediments from the Gulf of Tunis - Southern Mediterranean Sea. *J. Afr. Earth Sci.* 173, 104043. doi:10.1016/j.jafrearsci.2020.104043

Noble, R. A., Alexander, R., Kagi, R. I., and Knox, J. (1985). Tetracyclic Diterpenoid Hydrocarbons in Some Australian Coals, Sediments and Crude Oils. *Geochimica et Cosmochimica Acta* 49, 2141–2147. doi:10.1016/0016-7037(85)90072-9

Nott, C. J., Xie, S., Avsejs, L. A., Maddy, D., Chambers, F. M., and Evershed, R. P. (2000). *n*-Alkane Distributions in Ombrotrophic Mires as Indicators of Vegetation Change Related to Climatic Variation. *Org. Geochem.* 31, 231–235. doi:10.1016/S0146-6380(99)00153-9

Ochs, D., Kaletta, C., Entian, K. D., Beck-Sickinger, A., and Poralla, K. (1992). Cloning, Expression, and Sequencing of Squalene-Hopene Cyclase, a Key Enzyme in Triterpenoid Metabolism. *J. Bacteriol.* 174, 298–302. doi:10.1128/jb.174.1.298-302.1992

Ourisson, G., and Albrecht, P. (1992). Hopanoids. 1. Geohopanoids: the Most Abundant Natural Products on Earth? *Acc. Chem. Res.* 25, 398–402. doi:10.1021/ar00021a003

Pancost, R. D., Baas, M., van Geel, B., and Sinninghe Damsté, J. S. (2002). Biomarkers as Proxies for Plant Inputs to Peats: an Example from a Sub-boreal Ombrotrophic Bog. *Org. Geochem.* 33, 675–690. doi:10.1016/S0146-6380(02)00048-7

Peters, K. E., Fraser, T. H., Amris, W., Rustanto, B., and Hermanto, E. (1999). Geochemistry of Crude Oils from Eastern Indonesia. *AAPG Bull.* 83, 1927–1942. doi:10.1306/e4fd4643-1732-11d7-8645000102c1865d

Peters, K. E., Walters, C. C., and Moldowan, J. M. (2005). "The Biomarker Guide," in *Volume 2: Biomarkers and Isotopes in the Petroleum Exploration and Earth History*. Second Edition (Cambridge, UK: Cambridge University Press).

Phadtare, N. R. (2000). Sharp Decrease in Summer Monsoon Strength 4000-3500 Cal Yr B.P. In the Central Higher Himalaya of India Based on Pollen Evidence from Alpine Peat. *Quat. Res.* 53, 122–129. doi:10.1006/qres.1999.2108

Pillai, A. A. S., Anoop, A., Sankaran, M., Sanyal, P., Jha, D. K., and Ratnam, J. (2017). Mid-late Holocene Vegetation Response to Climatic Drivers and Biotic Disturbances in the Banni Grasslands of Western India. *Palaeogeogr. Palaeoclimatol. Palaeoecol.* 485, 869–878. doi:10.1016/j.palaeo.2017.07.036

Prasad, S., Anoop, A., Riedel, N., Sarkar, S., Menzel, P., Basavaiah, N., et al. (2014). Prolonged Monsoon Droughts and Links to Indo-Pacific Warm Pool: A Holocene Record from Lonar Lake, central India. *Earth Planet. Sci. Lett.* 391, 171–182. doi:10.1016/j.epsl.2014.01.043

Rashid, H., England, E., Thompson, L., and Polyak, L. (2011). Late Glacial to Holocene Indian Summer Monsoon Variability Based upon Sediment Records Taken from the Bay of Bengal. *Terr. Atmos. Ocean. Sci.* 22, 215–228. doi:10.3319/TAO.2010.09.17.02(TibXS)

Rawat, S., Gupta, A. K., Sangode, S. J., Srivastava, P., and Nainwal, H. C. (2015). Late Pleistocene-Holocene Vegetation and Indian Summer Monsoon Record from the Lahaul, Northwest Himalaya, India. *Quat. Sci. Rev.* 114, 167–181. doi:10.1016/j.quascirev.2015.01.032

Rawat, V., Rawat, S., Srivastava, P., Negi, P. S., Prakasam, M., and Kotlia, B. S. (2021). Middle Holocene Indian Summer Monsoon Variability and its Impact on Cultural Changes in the Indian Subcontinent. *Quat. Sci. Rev.* 255, 106825. doi:10.1016/j.quascirev.2021.106825

Sandeep, K., Shankar, R., Warrier, A. K., Yadava, M. G., Ramesh, R., Jani, R. A., et al. (2017). A Multi-Proxy lake Sediment Record of Indian Summer Monsoon Variability during the Holocene in Southern India. *Palaeogeogr. Palaeoclimatol. Palaeoecol.* 476, 1–14. doi:10.1016/j.palaeo.2017.03.021

Sarkar, S., Wilkes, H., Prasad, S., Brauer, A., Riedel, N., Stebich, M., et al. (2014). Spatial Heterogeneity in Lipid Biomarker Distributions in the Catchment and Sediments of a Crater lake in central India. *Org. Geochem.* 66, 125–136. doi:10.1016/j.orggeochem.2013.11.009

Saxena, A., Prasad, V., and Singh, I. B. (2013). Holocene Palaeoclimate Reconstruction from the Phytoliths of the lake-fill Sequence of Ganga plain. *Curr. Sci.* 104, 1054–1062.

Schellekens, J., Bradley, J. A., Kuyper, T. W., Fraga, I., Pontevedra-Pombal, X., Vidal-Torrado, P., et al. (2015). The Use of Plant-specific Pyrolysis Products as Biomarkers in Peat Deposits. *Quat. Sci. Rev.* 123, 254–264. doi:10.1016/j.quascirev.2015.06.028

Sessions, A. L., Zhang, L., Welander, P. V., Doughty, D., Summons, R. E., and Newman, D. K. (2013). Identification and Quantification of Polyfunctionalized Hopanoids by High Temperature Gas Chromatography-Mass Spectrometry. *Org. Geochem.* 56, 120–130. doi:10.1016/j.orggeochem.2012.12.009

Singh, S., Gupta, A. K., Dutt, S., Bhaumik, A. K., and Anderson, D. M. (2020). Abrupt Shifts in the Indian Summer Monsoon during the Last Three Millennia. *Quat. Int.* 558, 59–65. doi:10.1016/j.quaint.2020.08.033

Srivastava, P., Agnihotri, R., Sharma, D., Meena, N., Sundriyal, Y. P., Saxena, A., et al. (2017). 8000-year Monsoonal Record from Himalaya Revealing Reinforcement of Tropical and Global Climate Systems since Mid-holocene. *Sci. Rep.* 7, 14515. doi:10.1038/s41598-017-15143-9

Tipple, B. J., and Pagani, M. (2013). Environmental Control on Eastern Broadleaf forest Species' Leaf Wax Distributions and D/H Ratios. *Geochimica et Cosmochimica Acta* 111, 64–77. doi:10.1016/j.gca.2012.10.042

Tulipani, S., Grice, K., Greenwood, P. F., Haines, P. W., Sauer, P. E., Schimmelmann, A., et al. (2015). Changes of Palaeoenvironmental Conditions Recorded in Late Devonian Reef Systems from the Canning Basin, Western Australia: a Biomarker and Stable Isotope Approach. *Gondwana Res.* 28, 1500–1515. doi:10.1016/j.gr.2014.10.003

Valdiya, K. S., Paul, S. K., Chandra, T., Bhakuni, S. S., and Upadhyaya, R. C. (1999). Tectonic and Lithological Characterization of Himardri (Great Himalayan) between Kali and Yamuna Rivers, central Himalaya. *Himal Geol.* 20, 1–17.

Wang, M., Zhang, W., and Hou, J. (2015). Is Average Chain Length of Plant Lipids a Potential Proxy for Vegetation, Environment and Climate Changes? *Biogeosciences Discuss.* 12, 5477–5501. doi:10.5194/bgd-12-5477-2015

Waples, D. W., and Machihara, T. (1991). *Biomarkers for Geologists*. Tulsa, OK: American Association of Petroleum Geologists.

Zhang, Y., Meyers, P. A., Gao, C., Liu, X., Wang, J., and Wang, G. (2017). Holocene Climate Change in Northeastern China Reconstructed from Lipid Biomarkers in a Peat Sequence from the Sanjiang Plain. *Org. Geochem.* 113, 105–114. doi:10.1016/j.orggeochem.2017.07.018

Zhou, W., Zheng, Y., Meyers, P. A., Jull, A. J. T., and Xie, S. (2010). Postglacial Climate-Change Record in Biomarker Lipid Compositions of the Hani Peat Sequence, Northeastern China. *Earth Planet. Sci. Lett.* 294, 37–46. doi:10.1016/j.epsl.2010.02.035

Conflict of Interest: The authors declare that the research was conducted in the absence of any commercial or financial relationships that could be construed as a potential conflict of interest.

frontiers
in Earth Science

SYSTEMATIC REVIEW
published: 06 September 2021
doi: 10.3389/feart.2021.709455

Impact of Indian Summer Monsoon Change on Ancient Indian Civilizations During the Holocene

Amzad Hussain Laskar[1]* *and Archna Bohra*[2]

[1]*Geosciences Division, Physical Research Laboratory, Ahmedabad, India,* [2]*CSIR-National Geophysical Research Institute, Hyderabad, India*

A large part of South Asia receives rainfall mainly during the Indian Summer Monsoon (ISM) season of the year (Jun–Sep). The socioeconomic conditions of most of the developing countries in this region largely depend on the ISM rains. It also played important roles in rise and collapse of ancient civilizations in this region. However, the influence of the ISM on Indian ancient civilizations has not yet been fully explored though there were some attempts to correlate monsoon variation with their rise and fall. For example, in the mid to late Holocene period, Indus Valley or Harappan Civilization flourished in the western part of India from its early development, through its urbanization and eventual transformation into a rural society. Probably a prolonged decrease in the ISM rainfall caused the decline in the urban phase of the Indus Civilization around the 4.2 kyr BP global climate event. Another well-recorded early Holocene global climate event is the 8.2 kyr BP cooling event which also reportedly influenced ISM significantly, but its impact on human settlement is not clear in this region. The present study is a comprehensive review of the archaeological and climatological researches carried out on the role of ISM variability on the rise and fall of ancient Indian civilizations for the most part of the ongoing interglacial period, the Holocene. The review covers the studies on the period of the last 10 kyr as evidence suggests that human settlement and cultural developments in this region started around the beginning of this period. We have noted that the existing studies are mostly restricted to vague qualitative analysis of the weakening/strengthening of the ISM, and researches related to quantitative estimations of changes of the monsoon strengths and durations of drought events that caused collapse of civilizations are limited. Therefore, in the present analysis, emphasis has also been given on the requirement of estimating the absolute changes that might have caused cultural shifts. Some possible ways to quantitatively estimate the changes of some climate parameters are discussed.

Keywords: ancient civilization, Indian summer monsoon, paleoclimate records, stable isotopes, Holocene

Edited by:
Anoop Ambili,
Indian Institute of Science Education and Research Mohali, India

Reviewed by:
John Dodson,
Institute of Earth Environment (CAS), China
Mahesh Thakkar,
Krantiguru Shyamji Krishna Verma Kachchh University, India

***Correspondence:**
Amzad Hussain Laskar
amzad@prl.res.in

Specialty section:
This article was submitted to Interdisciplinary Climate Studies, a section of the journal Frontiers in Earth Science

Received: *13 May 2021*
Accepted: *20 July 2021*
Published: *06 September 2021*

Citation:
Laskar AH and Bohra A (2021) Impact of Indian Summer Monsoon Change on Ancient Indian Civilizations During the Holocene.
Front. Earth Sci. 9:709455.
doi: 10.3389/feart.2021.709455

INTRODUCTION

A Brief History of Ancient Civilizations in the Indian Subcontinent

There is a long history of rise and fall of civilizations in the Indian subcontinent. The existing records indicate that there was human occupation in North India about 30 kyr BP (Singh et al., 1999) though settled life probably started around early Holocene time. The old Indian civilizations were mostly developed on alluvium (Giosan et al., 2012; Macklin and Lewin, 2015), in dry environments with their farming dependent on natural inundation or controlled irrigation from river water. These early civilizations were vulnerable to political as well as environmental stresses, and the factors responsible for the decline and collapse of many of them have been debated (McAnany and Yoffee, 2010; Butzer, 2012). From the climatological point of view, some major causes of cultural abandonment were prolonged drought, e.g., the Indus (Staubwasser et al., 2003; Giosan et al., 2012; Kathayat et al., 2017), destructive floods, e.g., Huang He (Kidder et al., 2012), abrupt reductions in river flow and river water availability, e.g., Nile in Nubia (Macklin et al., 2013), and prolonged salinization of soil, e.g., Euphrates (Jacobsen and Adams, 1958). Available studies mostly point to climate change or, more precisely, significantly low ISM rainfall for a prolonged period of many years as the cause of the collapse of the ancient Indian civilizations.

Agricultural practices in Central India probably started around early Holocene. Based on pollen analysis, Quade et al. (2013) suggested that the agricultural activity in Madhya Pradesh, India, started about 9 kyr BP. The authors also observed humid conditions and increased agricultural activities between 7 and 4 kyr. Evidence of transformation from hunter-gathering to communities with settled agriculture and domestication of animals was reported at Mehrgarh (now in Pakistan) around the early phase of Holocene. The earliest available settlement at Mehrgarh dates back to ~ 9 kyr BP (Jarrige and Lechevallier, 1979; Jarrig, 1981; Jarrig, 1993) which coincides with a humid phase of the ISM (Fleitmann et al., 2003; Gupta, 2004). Existence of agricultural activity in central India about 7 kyr BP was also reported by Yadava et al. (2007) based on earth burns, charcoals, and plant remains observed in a limestone cave located in Chhattisgarh, India. Archaeological evidence of cultivation of grains in southern Asia around 9 kyr BP was reported by Kulke and Rothermund (2004). Therefore, settled life at least in some parts of India and transition from foraging to farming and pastoralism started in early Holocene time. However, it is very complex to identify the transition time from foraging to farming in south Asia as pointed out by BarkerRichards et al. (2013) particularly due to scarcity of archaeological data. Relatively more proxy data and extensive analysis are available from the mid Holocene onward during which the region witnessed many interesting phenomena related to both climate change and archaeology as discussed below.

One of the most well-documented advanced civilizations in the subcontinent is the Harappan or Indus Valley Civilization (Kenoyer, 1997; Kenoyer, 1998; Possehl, 2002a; Madella and Fuller, 2006; Wright, 2009; Gangal et al., 2010; MacDonald, 2011; Giosan et al., 2012; Sarkar et al., 2016; Sengupta et al., 2019) which developed at the arid outer belt of ISM dominated region (**Figure 1**). The Harappan Civilization that flourished in the north western part of the Indian subcontinent was probably the largest among the 10 kyr Bronze Age Civilizations. The Harappan culture started evolving from ~5.5 kyr BP from preceding agricultural communities in the Indus alluvial plain and reached to its urban peak, i.e., mature phase during 4.5–3.9 kyr BP (Sengupta et al., 2019). The Harappans were agrarian though they were advanced in trading and architecture and designed sophisticated materials including weapons. Unlike other contemporary civilizations, Harappans probably did not attempt to control water resources by large-scale canal irrigation (Schumm, 2007). Deurbanization of Harappa or dispersion into smaller groups happened after ~3.9 kyr BP, indicated by disappearance of the special Harappan script and appearance of regional artefact and trading activities (Kenoyer, 1998; Possehl, 2002a; Kenoyer, 2006; Wright, 2009; Sengupta et al., 2019). This is often referred to as the collapse of the Harappan Civilization. The Harappan Civilization perhaps flourished on the bank of the mythological river Saraswati. The existence of the Saraswati/Ghaggar has been established recently by Chatterjee et al. (2019) using geochemical and isotopic proxies. The authors inferred that the river was active in the region for two periods in the past, namely, 80–20 and 9.4–4.5 kyr, the timing of the ultimate decline of the river coincides with the collapse of the Harappan Civilization around the beginning of the Meghalayan Stage. Causes of decline of civilizations are elaborated in *Influences of ISM on the Ancient Civilizations in Indian Subcontinent*.

After Harappa or contemporary to it, another civilization flourished in the Indian subcontinent called the Vedic Civilization approximately between 4 and 2.5 kyr BP (Pruti, 2004). Some researchers argued that the Vedic Civilization also existed in the banks of the mythological river Saraswati that was flowing in the region between Indus River in the west and Aravalli Mountain range (Singhvi and Kar, 1992; Chauhan, 1999) and claimed to be even older than the Harappa (e.g., Radhakrishna and Merh, 1999; Paliwal, 2011). However, most consensus is that the Vedic Civilization flourished between 3.5 and 2.5 kyr BP (Samanta et al., 2011). Vedic is the first historic civilization which has some written records and the name Vedic came from *Vedas*, the early literature of Vedic people. Unfortunately, its relation with Harappan is not well established. Initial Vedic culture was nomadic in nature with cattle rearing as their main occupation along with cropping practices. The later phase was dominated by agricultural activities governing the economy with decline in cattle rearing and emergence of relatively large kingdoms (Pruti, 2004).

Indian Summer Monsson, Its Importance, Causes, and Consequences of Its Variation

The Indian Summer Monsoon (ISM) is a synoptic scale weather system and strongly impacts and contributes to shaping the socioeconomic and cultural advancement in South Asia. It is a manifestation of the seasonal migration of the Intertropical Convergence Zone (ITCZ) (Webster et al., 1998; Gadgil, 2018). It strongly affects the hydroclimatic conditions which in turn strongly impacts the food-grain production and the Gross Domestic Product (Gadgil and Gadgil, 2006) of nearly a quarter of the global human population living in this region. Slight variations in ISM strength or its delay in the historic past caused many serious impacts on humans in economic as well as ecological aspects caused by floods and droughts (Shewale and Kumar, 2005; Cook et al., 2010; Laskar et al., 2010, Laskar A. et al., 2013a; Sridhar et al., 2015; Dutt et al., 2018; Dutt et al., 2019; Kotlia et al., 2018; Gupta et al., 2020). In the Holocene, the region experienced many droughts, mega droughts, and extreme

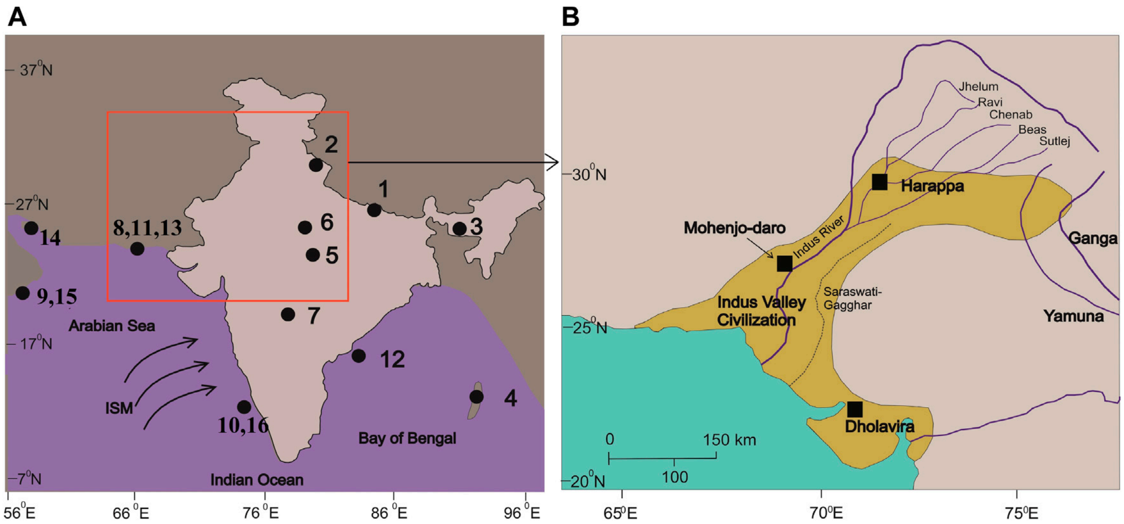

FIGURE 1 | (A) Map of India and its surroundings with filled circles showing the approximate locations of the sites from which the data of the proxy records are presented in **Figures 2**, **3**: 1) Ali et al. (2018), 2) Kathayat et al. (2016), 3) Berkelhammer et al. (2012), 4) Laskar A. H. et al. (2013b), 5) Dixit et al. (2014a), 6) Dixit et al. (2014b), 7) Prasad et al. (2014), 8) Staubwasser et al. (2002), 9) Gupta et al. (2003), 10) Tiwari et al. (2015), 11) von Rad et al. (1999), 12) Ponton et al. (2012), 13) Pichevin et al. (2007), 14) Sirocko et al. (1993), 15) (Altabet et al., 2002), and 16) Saraswat et al. (2013). **(B)** Regions showing the Indus Valley Civilization settlement along with major rivers. Some major excavation sites are shown by filled squares. Redrawn following Green (2021).

flooding observed by many paleoclimate researchers (Berkelhammer et al., 2010; Buckley et al., 2010; Cook et al., 2010; Sinha et al., 2011; Dixit and Tandon, 2016; Kathayat et al., 2018; Sharma et al., 2021). Many of these major climatic events are believed to cause collapse of ancient civilizations. Even in the last decade many such extreme events such as the Kedarnath flood in 2013; Kerala flood in 2019; and floods in Assam, Maharashtra, and Gujarat and glacier burst in Uttarakhand in 2021 caused severe human and financial loss (Dobhal et al., 2013; Singh et al., 2014; Rana et al., 2021). These extreme events may further intensify with greater magnitude in different geographical localities in the future with global warming (IPCC, 2013), thus jeopardizing planning strategies. Therefore, detailed analyses of the ISM in the past and how it influenced ancient inhabitants are required to understand its possible impacts. Though model forecasting and better technology would help to take preparation and minimization of loss in case any such situation arises in future, still a better understanding of the past may help to handle possible impacts in the future.

The Holocene is the current warm geological epoch, established around 11.5 kyr BP after the last glacial period. Warming during the Holocene has been associated with the increased solar insolation also termed as the Holocene Thermal Maxima (HTM). However, the temperature increase was punctured by some global cooling events. For example, events at 8.2 and 4.2 ka are identified as globally dry cool climates (Staubwasser et al., 2003; Liu et al., 2013; Dixit et al., 2014a; Dixit et al., 2014b; Banerji et al., 2020) though the exact reason for these relatively abrupt climate events remain elusive. The 8.2 kyr even was probably caused by weakening of the North Atlantic Deep Water formation resulting in the change in the Atlantic Meridional Overturn Circulation (Barber et al., 1999). The driving force behind the weakening of the North Atlantic Deep water formation was probably the glacial outburst of freshwater from Lake Agassiz into the North Atlantic (Bauer et al., 2004). The 4.2 kyr event, a multidecadal to century scale event over an extensive region (e.g., Cullen et al., 2000; Drysdale et al., 2006; Dixit et al., 2014a; Mehrotra et al., 2018), points to a global megadrought (Weiss, 2016). This event has been accepted as the formal boundary of late and middle Holocene at the global scale and the period after 4.2 kyr is called the Meghalayan age. Despite its wide spread recognition, the timing, duration, its origin in terms of changes in ocean and atmospheric circulation remain intangible. Moreover, many of the paleoclimate records do not show the evidence of the 4.2 ka event, at least as a major event of the mid-late Holocene (e.g., Seppa et al., 2009; Roland et al., 2014) and not necessarily as a cold and dry event (e.g., Railsback et al., 2018) indicating spatial variation in its impact. For example, in the regions affected by ISM, the 4.2 kyr event is not obvious in all proxy records and in the records where it is observed is mostly shown as weak ISM rather than cooling (e.g., Siroko et al., 1993). Some researchers suggested that this event is not just a single long dry event but a complex succession of dry/wet events, (Magny et al., 2009; Railsback et al., 2018). In the Mediterranean region, it is mostly considered as a dry interval as observed in many proxy records in speleothems (Drysdale et al., 2006; Zanchetta et al., 2016; Finné et al., 2017), pollen (e.g., Magri and Parra, 2002; Di Rita and Magri, 2009; Kaniewski et al., 2013), lake sediments (e.g., Zanchetta et al., 2012), and marine sediments (e.g., Margaritelli et al., 2016). Moreover, the exact timing of the event differs across proxy records (Finné et al., 2011), challenging the view that it is a global period of significant drought. Other regional to global climate events observed during the late Holocene period include the Roman Warm Period, Medieval Warm Anomaly, the Little Ice Age, and the modern warm period that influenced ISM rainfall significantly (Laskar A. H. et al., 2013b; Liang et al., 2015; Kotlia et al., 2017). Some of these events are consistent in many proxy records while some others are missing in some archives indicating their variations from region to region and nonuniform effects on different proxies. These seasonal to multidecadal climate anomalies are associated with El-Nino Southern Oscillation, Indian Ocean Dipole, North Atlantic Oscillation, Pacific Decadal Oscillation, Inter Decadal Pacific Oscillation, and Indo-Pacific Warm Pool. However, the effects of most of these forces on ISM are nonstationary (e.g., Krishna Kumar et al., 2006). Though these late Holocene climatic phenomena have drastic influence on the socioeconomy of the subcontinent and south Asian countries as discussed earlier, their effect on settlement/displacement of human civilization is probably not that severe to cause collapse of a civilizations as happened in the early to mid Holocene and hence not discussed in detail here.

The present work is an attempt to assess the details of the ISM variation in the last 10 kyr to understand its role on the rise and fall of civilizations in the north-western region of the Indian subcontinent. This is carried out by compiling the major available studies from the regions influenced by ISM during the Holocene. This study will serve to identify gaps in the regional coverage, to determine if coherent regional/subregional climatic patterns are present and expose aspects that should be addressed in future research on this topic. Another important purpose of the study is to explore the possibility of estimating quantitatively the variations of some of the past climate parameters using some recently developed proxies.

PROXY CLIMATE RECORDS

There are multiple terrestrial and marine paleoclimate records, sensitive to changes in climate parameters available in the Indian subcontinent and surrounding regions. The present review is mainly focused on stable isotope-based proxy records obtained from oceanic and terrestrial sediments, alluvial deposits, and speleothems. The proxy records used in this review are selected on the basis of length, temporal resolution, dating quality, data interpretability, and geographic distribution. Preferences are given to the records with a full Holocene coverage that attempted to quantitatively estimate climate parameters (e.g., rainfall for ISM strength), better temporally resolving data with relatively better constrains in chronology, directly associated with one or more climate variables and geographical distribution. Locations of the proxy records included and analysed in this review are shown in **Figure 1**. All records that suit the foregoing requirements are not included, but this collection represents a substantial set of data that can serve as a base for furthering a focused study related to climate change and archaeology.

RESPONSE OF INDIAN SUMMER MONSOON TO GLOBAL AND LOCAL CLIMATIC EVENTS DURING THE HOLOCENE

Although climate variability during the Holocene is smaller in amplitude compared to the large shifts of the last glacial cycle, they are large enough to play a major role in rise and collapse the human civilizations in various parts of the globe (e.g., Staubwasser et al., 2003; Prasad et al., 2014; Pokharia et al., 2014; Kathayat et al., 2017). A number of climate perturbations have been identified during the Holocene. For example, the early Holocene atmospheric warming, the 8.2 kyr event, the 4.2 kyr event, the Medieval Climate Anomaly, the Roman Warm Period, the Little Ice Age, and the current warm period are widely recognized climate phenomena observed during the Holocene (Gupta et al., 2003; Mayewski et al., 2004; Cheng et al., 2009; Buckley et al., 2010; Laskar et al., 2013b; Dixit et al., 2014a; Dixit et al., 2014b; Dutt et al., 2015; Kathayat et al., 2018; Kotlia et al., 2018). Based on major global abrupt climate events, the Holocene period has been divided into three substages, namely, Greenlandian (11.5–8.2 kyr), Northgrippian (8.2–4.2 kyr), and Meghalayan (4.2 kyr to AD 1950) (Walker et al., 2018; Walker et al., 2019). ISM rainfall during the early Holocene (11–7 kyr BP) was significantly higher than present and was linked to Himalayan snow cover and North Atlantic sea surface temperature along with the northward migration of the ITCZ (Wang et al., 2005; Fleitmann et al., 2007). ISM weakened around 8.2 kyr with retreat of the ITCZ southwards, reduction of the northern hemisphere ice sheet, and stabilization of the Thermohaline circulation. The subsequent monsoon strength was mainly controlled by solar insolation and position of the ITCZ. Different oceanic basins modulate ISM through ocean-atmosphere teleconnections. ISM rainfall exhibited a multidecadal oscillation mode with a significant coherence with that of the Atlantic Multidecadal Oscillation (Goswami et al., 2006).

The two well-documented global events at 8.2 and 4.2 kyr BP are identified as dry or cool climates, the onset of Northgrippian and Meghalayan stages, respectively (Barber et al., 1999). The cooling event at 8.2 kyr BP affected climate throughout the Northern Hemisphere and in Greenland (Thomas et al., 2007; Cheng et al., 2009; Liu et al., 2013; Banerji et al., 2020). Using $\delta^{18}O$ and Mg/Ca measurements of a speleothem, Liu et al. (2013) showed that climate was significantly drier ~8.2 kyr ago and lasted for 150 years, with 70 years of pronounced aridity. The timing and duration of the event corresponded with that observed in the Greenland ice cores, indicating a rapid atmospheric teleconnection between the North Atlantic and the ISM. Oxygen isotope ratios ($\delta^{18}O$) in speleothems from the ISM impacted regions also indicated a pronounced weakening of the Asian and Indian monsoons at 8.2 kyr BP that probably lasted for 100–150 years (Fleitmann et al., 2003; Cheng et al., 2009; Liu et al., 2013). Lake sediment biogenic carbonate $\delta^{18}O$ values from north-western India indicated weakening of the ISM around 8.2 kyr BP (Dixit et al., 2014b). This weakening was linked to the cooling of the North Atlantic (Staubwasser et al., 2002; Gupta et al., 2003; Cai et al., 2012) when temperatures fell by ~3°C within a couple of decades (Kobashi et al., 2007).

The cooling and arid event around 4.2 kyr BP has also been reported from various parts of the globe (e.g., Cullen et al., 2000; Staubwasser et al., 2003; Drysdale et al., 2006; Berkelhammer et al., 2012; Dixit et al., 2014a; Kathayat et al., 2018; Railsback et al., 2018). This event has been recognized in middle low latitude regions in many paleo climate records from North America, South America, Africa, China, and Antarctica

(Mayewski et al., 2004; Staubwasser and Weiss, 2006). Many archaeological studies also indicated that the 4.2 kyr event was associated with cultural shifts in Africa, the Mediterranean, Middle East, and South and East Asia (e.g., Weiss et al., 1993; Enzel et al., 1999; Cullen et al., 2000; Staubwasser et al., 2003; Liu and Feng, 2012; Weiss, 2016; Kathayat et al., 2017). It is believed that the 4.2 kyr event played a major role in the decline of the Bronze Age Civilizations, including the Egyptian Old Kingdom (Stanley et al., 2003; Ramsey et al., 2010), the Akkadian Empire in Mesopotamia (Weiss et al., 1993; Cullen et al., 2000; Weiss et al., 2012), Longshan culture in China (Chauhan, 1999; Liu and Feng, 2012), and Harappan Civilization in the Indian subcontinent (Staubwasser et al., 2003; Berkelhammer et al., 2012; Dixit et al., 2014a; Kathayat et al., 2017; Sengupta et al., 2019). The 4.2 kyr event from the ISM domain has been observed in speleothem $\delta^{18}O$ measurements from Mawmluh Cave, Meghalaya, and Northeast India (Berkelhammer et al., 2012). This record was used to define the period after 4.2 kyr as the Meghalayan Age (Walker et al., 2018). A number of proxy records from the Indian subcontinent suggest that a major weakening of the ISM occurred around or after the 4.2 kyr event (Staubwasser et al., 2003; Berkelhammer et al., 2012; Laskar A. H. et al., 2013b; Dixit et al., 2014a; Nakamura et al., 2016; Kathayat et al., 2017). The 4.2 ka event was generally described as drought for a duration of two to three centuries (e.g., Berkelhammer et al., 2012; Dixit et al., 2014b; Nakamura et al., 2016). The influence of 4.2 kyr event on ISM is discussed in more detail in *Discussion*.

Many other relatively smaller magnitude climate events impacted the ISM during the late Holocene (Laskar et al., 2010; Laskar et al., 2013a; Laskar et al., 2013b). For example, over the Bay of Bengal region, speleothem $\delta^{18}O$ records suggest a declining trend of ISM strength during 4–2.1 kyr BP and enhancement during 2.1–0.8 kyr BP, and during the transition from Medieval Climate Anomaly to the Little Ice Age (0.8–0.4 kyr BP) (Laskar A. H. et al., 2013b). The Central Himalayan region experienced a decline of ISM strength during 4–3 kyr BP and enhancement during 3–2 kyr and large fluctuations during 2.0–0.8 kyr BP and then an increase after 0.8 kyr BP (Kotlia et al., 2017; Kotlia et al., 2018). These studies suggest that the global climatic epochs have a varying degree of influence on monsoonal activity over different Indian regions. However, assessment of their influences on the human settlement/dispersion needs both high resolution archaeological and climate change data.

INFLUENCES OF INDIAN SUMMER MONSOON ON THE ANCIENT CIVILIZATIONS IN INDIAN SUBCONTINENT

The previous perspective that Holocene climate was stable has changed with the availability of high-resolution paleoclimate records (Fleitmann et al., 2003; Gupta et al., 2003; Buckley et al., 2010; Laskar A. H. et al., 2013b). As discussed before, the Holocene witnessed many climatic events which largely impacted the human societies, vegetation, and ecology. Researchers linked many of these climatic events with the shifts of cultures in different parts of the world. However, such linkage of climate with the establishment and collapse/displacement is intensely debated due to lack of direct evidence. It is believed that abrupt and/or prolonged drought conditions led the collapse or forceful migration of many cultures mainly by affecting food and water availability (Cullen et al., 2000; Buckley et al., 2010; Liu and Feng, 2012; Dixit et al., 2014a; Kathayat et al., 2017). For example, in Tell Sabi Abyad, a Neolithic archaeological site in northern Syria, a significant cultural change was observed around 6200 BC (~8.2 kyr BP) (Balter 2010; van der Plicht et al., 2011). Evidence of many such cultural shifts has been reported in Europe and Near East associated with the aridification around the 8.2 kyr event (e.g., Migowski et al., 2006; Staubwasser and Weiss, 2006; Weninger et al., 2006; Budja, 2007; Berger and Guilaine, 2009; Gronenborn, 2009; Wicks and Mithen, 2014). However, evidence of cultural changes related to the 8.2 kyr event in the Indian subcontinent is limited by the lack of data. Though there is evidence of changes in the ISM rainfall around 8.2 kyr and some sparse evidence of human settlements in the Indian subcontinent during the early Holocene as discussed earlier, the impact of the reduction of ISM strength around the 8.2 kyr event on early Holocene human settlements is unclear.

Impacts of ISM on the mid to late Holocene Indian civilizations are generally accepted as fact. The Harappan Civilization, established around the early-mid Holocene in the Indian subcontinent, was one of the most advanced Bronze Age Civilizations. The establishment and growth of this civilization started during the phase of higher precipitation from a strong ISM. Kathayat et al. (2017), based on speleothem $\delta^{18}O$ record from Sahiya cave, showed that the mature phase of Harappan culture was the period between 4.5 and 3.9 kyr BP, occurred during a wet and warm climate. Probably the optimum climate helped in agricultural activities and urban developments for the Harappans. However, the disappearance of this civilization has been a long debated subject. Evidence suggests that the decline/displacement of the civilization started around 4.2 kyr B.P probably caused by a significant decrease in ISM precipitation resulting in insufficient moisture availability in the region to support the agricultural needs of the population (Enzel et al., 1999; Staubwasser et al., 2003; Berkelhammer et al., 2012; Dixit et al., 2014a). The deurbanization of the Harappan Civilization after the 4.2 kyr event has been discussed widely (e.g., Possehl, 2002b; Ratnagar, 2002; Kulke and Rothermund, 2004; Lawler, 2008; Wright, 2009; Petrie et al., 2017). Some initial researchers also suggested foreign invasions (e.g., Aryan invasions) into India, societal instabilities, and a decline of trade (Possehl, 2002b) as causes, but no strong evidence supporting them exists (Fitzsimons, 1970). Environmental factors such as regional aridification, hydrological changes such as reduction in water flow in the main river channel, the Ghaggar-Hakra system (Kenoyer, 1998; Radhakrishna and Merh 1999; Possehl, 2002a; Fuller and Madella, 2002; Wright et al., 2008; Sengupta et al., 2019), and land degradation due to human activity (Fairservis, 1967; Atkins et al., 1998) were also suggested to play major roles in the decline of Harappan Civilization (Kenoyer, 1998; Possehl, 2002b; MacDonald, 2011). Kathayat et al. (2017) argued that a multicentennial trend of relatively drier and cooler conditions in the Harappan region that started ~4.1 kyr ago was associated with the deurbanization phase during 3.8–3.3 kyr BP. In addition, reduced river flows in the region around this time in response to decrease in ISM rainfall over the Himalayan region were also observed (Singh et al., 1990; Phadtare, 2000). Therefore, the most plausible reason for the deurbanization/decline of the Harappan Civilization is related to climate rather than other societal related causes. Probably a combined influence of the reduction of ISM rainfall and reduced discharge from the Himalayan glaciers due to colder condition and weak ISM caused decline and forceful migrations of the Harappan settlers. Many groups probably continued after 3.9 kyr BP but in reduced sizes (Mughal, 1997; Kenoyer, 1998; Possehl, 2002a). The post-Harappan urban phase witnessed establishment of smaller agricultural and pastoral communities especially in the Himalayan foothills and western part of the Ganges basin as indicated by abundant Neolithic and Chalcolithic settlements (Kenoyer, 1998; Possehl, 2002b; Korisettar et al., 2002; Panja, 2002; Singh, 2002; Kumar, 2009; Wright, 2009; Gangal et al., 2010).

The Vedic Civilization probably ended around 2.4 kyr BP and was marked by linguistic, cultural, and political changes, as well as eastward migrations (Witzel, 1987; Kulke and Rothermund, 2004). However, it is not well established how Vedic Civilization collapsed. According to Paliwal (2011), the Vedic Civilization collapsed due to climate changes and neotectonic activities that caused wide-spread salinization of soils and formation of saline lakes in the green fertile regions of the Vedic settlements. The weak ISM during the Roman Warm Period around 2 kyr BP (e.g., Laskar A. H. et al., 2013b) could be one of the causes of the decline of the Vedic Civilization. There is some speculation that the great war of Mahabharata caused the collapse of Vedic Civilization around 2 kyr BP, though evidence to support this is unreliable.

DISCUSSION

Some available prominent proxy records from terrestrial and oceanic archives in and around the Indian subcontinent that are sensitive to changes in the ISM strengths along with solar changes are discussed here. The major changes of the ISM observed in the proxy records and that coincided with the global climate events and collapse of civilizations are highlighted. Solar insolation data at 65° N, tropical temperature anomaly between 30° S and 30° N, and some continental proxy records from regions affected by ISM are shown in **Figure 2** (see **Figure 1** for locations of proxy records). The rainfall variation, derived using $\delta^{13}C$ in soil organic matter from a site from North Sikkim of Himalayan region, influenced by ISM strength is shown in **Figure 2C** (Ali et al., 2018). The annual rainfall is reconstructed based on an inverse relation between $\delta^{13}C$ values of the plants and rainfall (Kohn, 2010). In the Ganga plain, it is observed that the $\delta^{13}C$ values in modern C_3 vegetation increase by ~0.4‰ for a decrease in annual rainfall of 100 mm (Basu et al., 2015). For the last 10 kyr, it is clear that the ISM rainfall was high during the early Holocene (10.0–8.5 kyr) and decreased after 8.5 kyr BP. The annual rainfall was relatively low during the mid Holocene and again increased in the late Holocene from 3 kyr BP onward. The lowest rainfall observed during 4.8–3.9 kyr BP (~25% lower compared to the average of the last 1 kyr) probably coincides with the global 4.2 kyr event. The significantly lower rainfall probably caused the collapse/migration of the Harappan settlers. Also the strong decrease in annual rainfall after 8.5 kyr BP probably coincides with the global 8.2 kyr event. **Figure 3D** shows the stalagmite $\delta^{18}O$ variation from Sahiya cave, Uttarakhand, North India for the last 5.7 kyr (Kathayat et al., 2017). Speleothem $\delta^{18}O$ is sensitive to the changes in the ISM derived rainfall in the region (Yadava et al., 2004; Sinha et al., 2015; Band et al., 2018). A sharp increase in the $\delta^{18}O$ values after ~4 kyr BP is probably related to the decrease in the rainfall in response to the 4.2 kyr event. A slight difference in timing could be due to spatial variation of the influences of the ISM and differences in chronological precision. A decrease in rainfall around 4.2 kyr BP is also evident from the stalagmite $\delta^{18}O$ values from Mawmluh cave, Meghalaya, NE India (**Figure 2E**) (Berkelhammer et al., 2012). This indicates that the 4.2 kyr event was wide spread in the ISM-dominated regions. However, around the 8.2 kyr event, the $\delta^{18}O$ values indicate an increase in the ISM strength from the same cave unlike many other parts of the subcontinent. This region, having the highest rainfall in the world (Cherrapunji and Mawsynram are located here), due to its orography, has a different rainfall pattern than the ISM alone and probably from ISM rainfall pattern in the past as well. Influences of various climate events on ISM strength during late Holocene are shown in **Figure 2F** with high resolution stalagmite $\delta^{18}O$ values from Andaman Islands (Laskar A. H. et al., 2013b). All the major climate anomalies are reflected in the speleothem $\delta^{18}O$ values. These include decrease in ISM rainfall during Roman Warm Period (2.1–1.8 kyr BP) and transition from Medieval Warm Climate to the Little Ice Age (0.8–0.4 kyr BP) and increase during Medieval Warm Climate (1.2–0.8 kyr BP). The decreased rainfall around 4.2 kyr BP and a sharp increase after that is also evident in the $\delta^{18}O$ values in gastropod aragonite in paleo-lake sediments from Kotla Dahar, North India (**Figure 2G**) (Dixit et al., 2014a). Also the weakening in the ISM around ~8.2 kyr is visible in the biogenic carbonate $\delta^{18}O$ data from another north Indian Paleolake Riwasa (Haryana, India) (Dixit et al., 2014b). Within the Holocene, two prolonged dry periods during 4.3–4.0 kyr BP and 2.0–0.6 kyr BP were observed with multiple proxy records including $\delta^{13}C$ in carbonates and organic matter in the sediments from Lonar Lake, located in the core monsoon zone of central India (**Figure 2H**) (Prasad et al., 2014). The prolonged drought event during 4.3–4.0 kyr BP coincides with the 4.2 kyr event. Another prolonged dry period was observed between 2 and 0.6 kyr BP in the Lonar lake records. Along with other proxy records, a decrease in the $\delta^{13}C$ values in organic matter and carbonate was observed around the drought periods (**Figures 2H,I**) and was attributed to changes in phytoplankton metabolism from CO_2 to HCO_3^- under reduced CO_2 conditions. This caused enrichment in ^{13}C in organic matter and preferential degassing of ^{12}C from the supersaturated carbonates in lake water. The

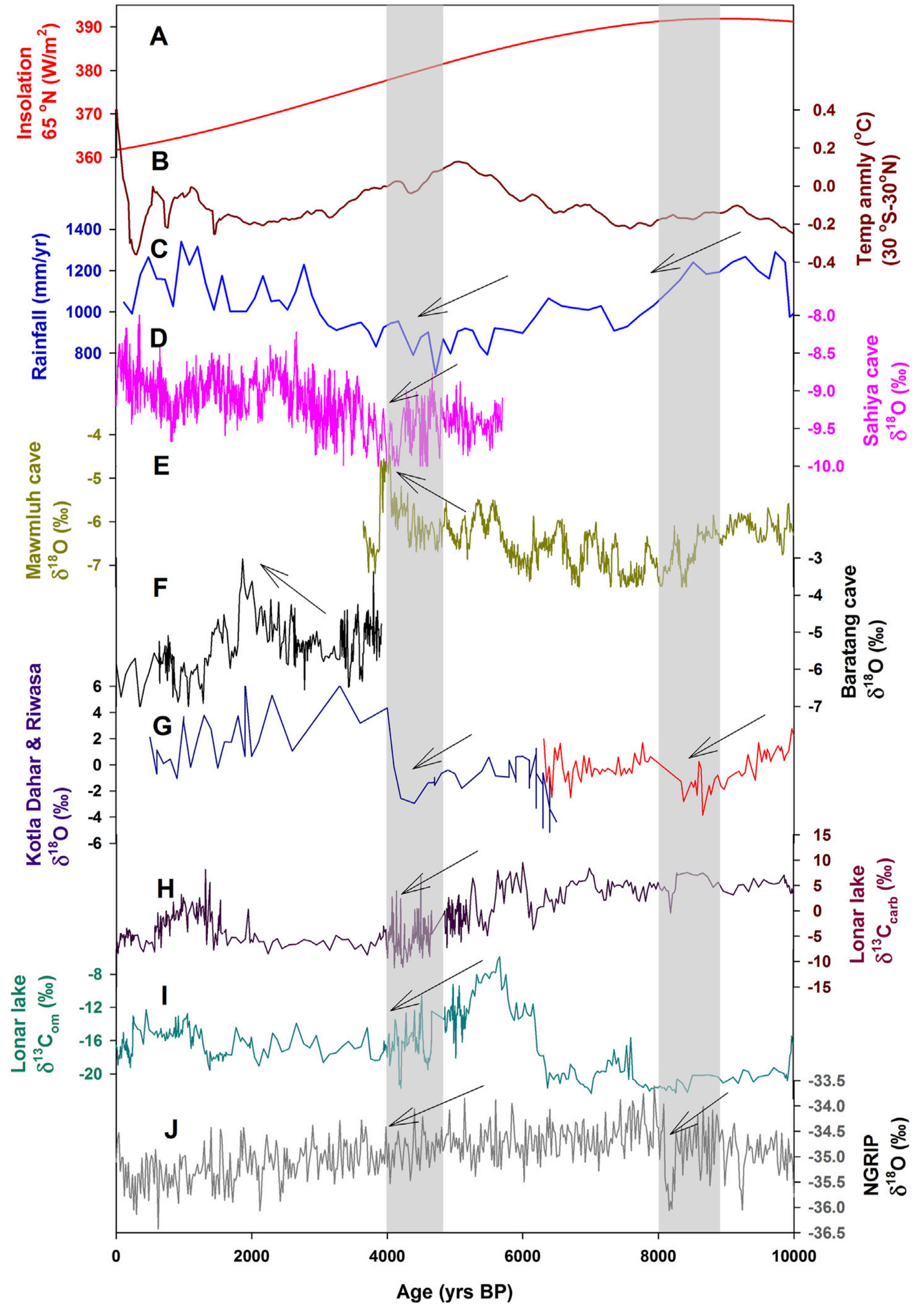

FIGURE 2 | (A) Solar insolation at 65°N (Laskar et al., 2006). **(B)** Temperature anomaly in the tropics (30°S–30°N) (Marcott et al., 2013). **(C)** Mean annual rainfall in the Himalayan region (Ali et al., 2018). **(D)** Sahiya cave oxygen isotope record (Kathayat et al., 2017). **(E)** Mawmluh cave speleothem $\delta^{18}O$ values from Meghalaya, NE India (Berkelhammer et al., 2012). **(F)** Speleothem $\delta^{18}O$ values from Baratang, Andaman Islands (Laskar A. H. et al., 2013b). **(G)** Lake sediment biogenic carbonate and gastropod aragonite $\delta^{18}O$ values from Riwasa and Kotla Dahar respectively (Dixit et al., 2014a,b). **(H,I)** Lonar lake $\delta^{13}C$ in carbonate and organic matter (Prasad et al., 2014). **(J)** North Greenland Ice Core $\delta^{18}O$ record for the last 10 kyr (Wolff et al., 2010). The shaded regions indicate the two global climate events around 8.2 and 4.2 kyr. The events are associated with significant changes in the ISM strengths and rise and fall of Indian ancient civilizations particularly around the 4.2 kyr event.

$\delta^{18}O$ data of North Greenland ice core (Wolff et al., 2010) are also plotted for comparison (**Figure 2J**) to assist in understanding the teleconnection with different proxy records from the ISM regions.

Figure 3 presents some prominent paleoclimate proxy records obtained from marine sediments from the Arabian sea and Bay of Bengal, i.e., the regions affected by ISM (see **Figure 1** for locations). Oxygen isotope ratios ($\delta^{18}O$) in planktonic

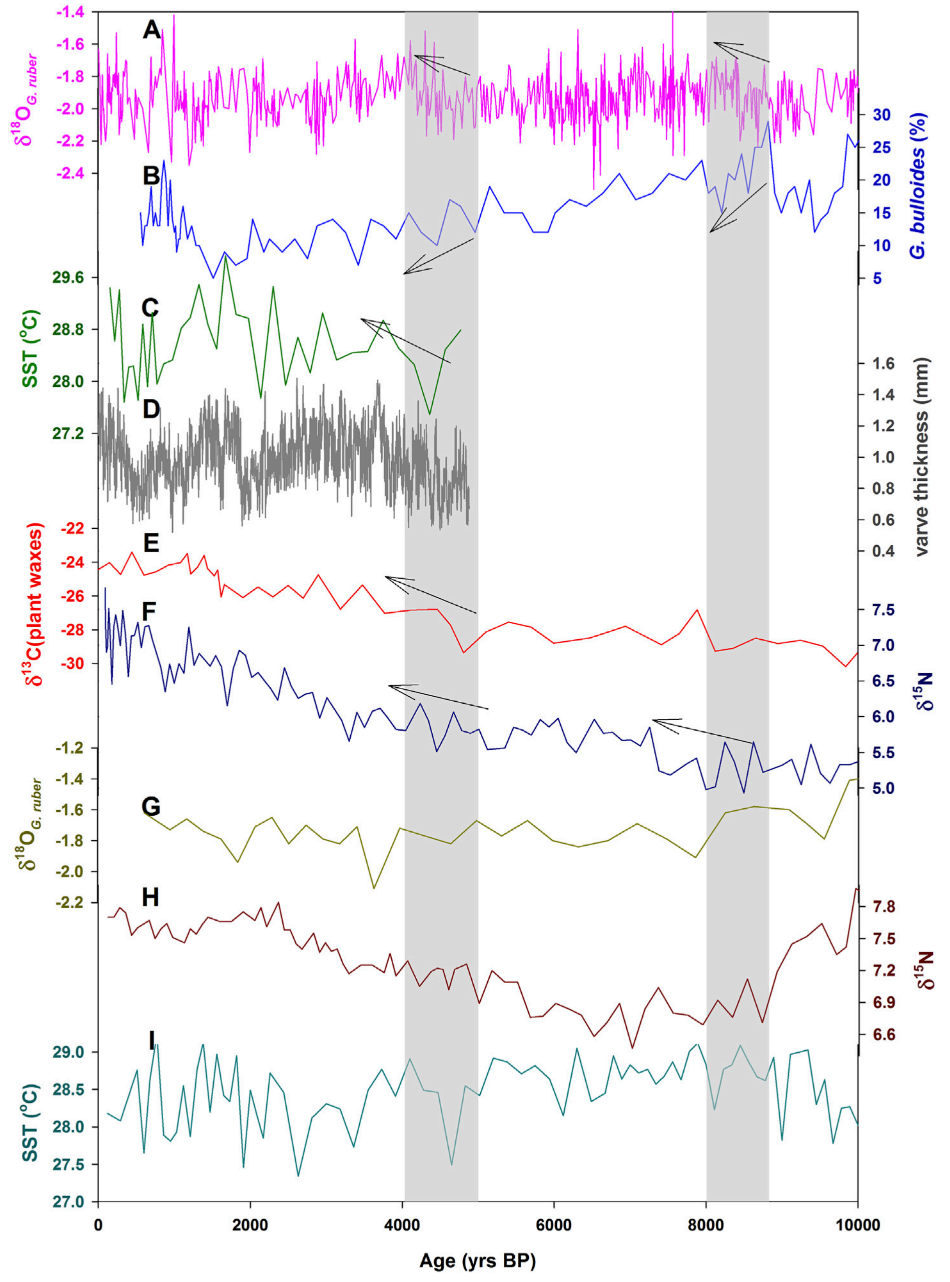

FIGURE 3 | Holocene marine proxy records from northern India ocean: **(A)** oxygen isotopic ratios in *G. ruber* from northern Arabian sea (Staubwasser et al., 2002). **(B)** Percentage abundance of *G. bulloides* from north-western Arabian sea (Gupta et al., 2003). **(C)** Sea surface temperature variation from Mg/Ca in the south-eastern Arabian sea (Tiwari et al., 2015). **(D)** Varve thickness from Northern Arabian Sea (von Rad et al., 1999). **(E)** Carbon isotope ratio in plant waxes from northern Bay of Bengal (Ponton et al., 2012). **(F)** Nitrogen isotope ratio in sediment as an indicator of denitrification and nitrous oxide emission in Arabian Sea (Pichevin et al., 2007). **(G)** Oxygen isotope ratio in *G. ruber* from Arabian Sea (Sirocko et al., 1993). **(H)** Nitrogen isotope ratio in sediment as an indicator of denitrification in Arabian Sea (Altabet et al., 2002). **(I)** Sea surface temperature reconstructed from Mg/Ca in foraminifera from south-eastern Arabian Sea (Saraswat et al., 2013). The shaded portions highlight the time periods during which the two major Holocene global climate events were reported by many researchers.

foraminifera *G. ruber* from the northern Arabian Sea sediment core 63 KA for the last 10 kyr are shown in **Figure 3A** (Staubwasser et al., 2002). At this location, the variations in the $\delta^{18}O$ value in planktonic foraminifera depend on the Indus River discharge, and the latter is largely governed by the ISM strength. During strong ISM episodes, high discharge of the Indus water with lower $\delta^{18}O$ value drags down the $\delta^{18}O$ values of the surface ocean water in the coastal region and hence the corresponding values in the planktonic foraminifera decrease. Clear increasing trends of $\delta^{18}O$ values in *G. ruber* around 8.2 and at 4.2 kyr BP indicate weakening of ISM strength around these climate events. **Figure 3B** shows the foraminifer *G. bulloides* concentration variation from a sediment core recovered from an oxygen minimum zone of the continental margin of Oman in the Arabian sea. The abundance variation of *G. bulloides* has been linked with the variation of ISM. Its abundance is associated with the wind-driven upwelling and strong sensitivity to wind speed and monsoonal atmospheric pressure gradient making it a suitable monsoon indicator (Gupta et al., 2003). Sharply decreasing trends in the concentration of *G. bulloides* around 8.2 kyr event indicate a weakening of the ISM. Similarly, around the 4.2 kyr event, decreasing trend in the *G. bulloides* indicates a weakening of the ISM strength. These are correlated with the North Atlantic Oscillations. Mid Holocene to the recent sea surface temperature (SST) reconstructed from Mg/Ca ratio in planktic foraminifera in the south-eastern Arabian sea is shown in **Figure 3C** (Tiwari et al., 2015). It is observed that the SST is significantly positively correlated with the sea surface salinity and negatively with monsoon intensity with value of coefficient of determination (R^2) of ~0.41 for 36 data points. Stronger monsoon causes reduced salinity and SST. Increasing SST trend after 4.3 kyr BP indicates significant reduction in ISM intensity which probably coincides with the 4.2 kyr event. ISM strength that started decreasing around 4.3 kyr was low until 1.3 kyr since when it increased significantly, as indicated by the SST values. **Figure 3D** shows the varve thickness record in a continuously laminated sediment core for the last 5 kyr from an oxygen minimum zone of the northern Arabian sea (von Rad et al., 1999). Their varve thickness is an indicator of the Indus River discharge and hence ISM strength. Relatively low varve thickness before 4 kyr BP indicates weak ISM around the 4.2 kyr event. Reduced varve thickness is also observed during the Roman Warm Period (~2 kyr BP) and Little Ice Age (0.5 kyr BP). **Figure 3E** shows the carbon isotopic composition ($\delta^{13}C$) in sedimentary leaf waxes in a core collected from offshore Godavari river estuary, north-western Bay of Bengal. $\delta^{13}C$ in leaf waxes is an indicator of the proportion of C3 and C4 vegetation in the Godavari River catchments (Ponton et al., 2012). A shift in the $\delta^{13}C$ values after 4.5 kyr BP indicates an increase in the proportion of C4 vegetation in the river catchments. C4 vegetation increases with increase in aridity. Therefore, the central Indian region experienced aridity after 4 kyr BP. **Figure 3F** shows nitrogen isotopic ratios ($\delta^{15}N$) from the oxygen minimum zone of the Northern Arabian sea reflecting the denitrification and plant productivity in the region (Pichevin et al., 2007). Denitrification occurs under suboxic conditions and causes large nitrogen isotopic fractionation. Denitrification varies with local productivity and downward particle flux which in turn is linked to the strong summer time monsoon winds causing upwelling of the nutrient rich water in the northern Arabian sea. Therefore, under strong ISM conditions, denitrification increases, which leads to an increase in $\delta^{15}N$ values as more denitrification would enrich the remaining nitrate reservoir in ^{15}N. An increasing trend of $\delta^{15}N$ after 8.1 and 4.4 kyr BP indicates weakening of ISM around these two climatic events. **Figure 3G** shows $\delta^{18}O$ values of *G. ruber* from a sediment core recovered from the upwelling region of the western Arabian sea (Sirocko et al., 1993). The change in the foraminiferal $\delta^{18}O$ is attributed to the change in ISM. A shift towards lower $\delta^{18}O$ values can be due to one or more of the following reasons: an increase in precipitation or decrease in evaporation, an increase in the proportion of Gulf outflow water with relatively lower $\delta^{18}O$ values, a change in the seasonal growth of the *G. ruber* species, or an increase in the SST (Sirocko et al., 1993). Relatively higher $\delta^{18}O$ values around 8.2 kyr probably indicated weaker ISM precipitation though the other factors mentioned above can also be partly responsible for the increased $\delta^{18}O$ values. However, the change around the 4.2 kyr event is not obvious in this sediment isotope record probably due to coarser time resolution. **Figure 3H** shows $\delta^{15}N$ values in a sediment core recovered from the Oman continental margin of the Arabian Sea reflecting the denitrification and productivity in the region. As mentioned before, denitrification in Arabian sea is controlled by ISM strength. For the period of last 10 kyr, weaker ISM was observed during 8.7–5.7 kyr BP indicated by low $\delta^{15}N$ values. The $\delta^{15}N$ values started increasing from 5.7 kyr BP indicating strengthening of ISM. **Figure 3G** shows centennial scale SST reconstructed from foraminiferal Mg/Ca ratio in a sediment core from south-eastern Arabian Sea. However, the sharp Holocene climatic events such as those observed around 8.2 and 4.2 kyr BP are not very clear in this sediment record probably because of its relatively coarser time resolution and core location.

A number of global climate events influenced the Holocene ISM rainfall including the two major events around 8.2 and 4.2 kyr BP and are evident in most of the terrestrial and oceanic proxy climate records. The changes in the proxy records in the terrestrial archives are larger in magnitude due to direct influence from ISM rainfall, and the signals are dampened in the oceanic reservoir due to its large size and slow response. It is to be noted that the two climatic events are not obvious in all the climate proxy records obtained in different geographical locations and, as mentioned before, there are differences in the timing of the events indicating spatial variation of the influences of ISM. We also note that there are climatic events comparable to the 8.2 or 4.2 kyr BP in some of the proxy records but not highlighted as much as these two events. Probably those events were confined to regional scale and are not reflected at global scale. It is also important to address how these local climate events influenced the human settlements. This needs further focused studies with better constrained chronology, wider geographic distribution, and quantitative analysis. Some possibilities for quantitative studies are discussed below.

OUTLOOK

There are two important aspects that need to be addressed to better understand the timing and causes of falls of ancient Indian civilizations. First, more archaeological data from the existing and new archaeological sites are required for understanding the timing of evolution of various civilizations and their terminations. There are many unexplored archaeological sites in the subcontinent and they can be used for this purpose though the majority are not easily accessible for political reasons. Second, more focused studies on quantitative estimates of the changes in climate parameters such as temperature and rainfall that favored/disfavored the ancient settlers with better chronological constraints are required. Most of the available studies used strengthening/weakening of the Indian Summer Monsoon qualitatively. It is important to obtain quantitative estimates of the extent of increase/decrease of the monsoon strengths at different ancient periods that are societally relevant. This would help to better manage future climate catastrophes. The role of change in air temperature might have influences on human settlements as well. It is important to see if prolonged drought periods were associated with any increase in regional air temperatures significantly. Tree ring is one of the best terrestrial paleoclimate records and can improve our understanding of the past monsoon and temperature variation. Unfortunately, the available dendroclimatology studies from India and surrounding regions do not cover the time periods of most of the ancient civilizations (Yadav, 2009; Yadav, 2013). With tree ring data covering the periods of interest, it is probably possible to better understand the monsoon variability at higher temporal resolutions.

Many of the aforementioned proxy records are controlled by combined influences of rainfall, evaporation, and temperature (e.g., $\delta^{18}O$ in speleothems, foraminifera, and lake sediment carbonates), and it is difficult to disentangle the signatures. For example, tropical speleothem $\delta^{18}O$ values are interpreted based on amount effect in many studies (Yadava and Ramesh, 2005; Laskar A. H. et al., 2013b), but this effect is absent or feeble in many ISM dominated regions (Laskar et al., 2015; Lekshmy et al., 2014). Even in the regions influenced by the amount effect, the rainfall variation explains the $\delta^{18}O$ variability partially making it difficult for a quantitative reconstruction of past rainfall. Therefore, it is important to look into new experimental and modelling techniques for quantitative reconstruction of paleomonsoon and temperature. Carbonate clumped isotope thermometry (e.g., Ghosh et al., 2006; Laskar et al., 2016) has the potential to independently constrain the temperature and can be combined with conventional oxygen isotope ratios to quantitatively estimate the rainfall variation in some paleoarchives. However, the thermometer has not been successfully applied to reconstruct temperatures from cave carbonates, but it has potentials in sediment carbonates (e.g., Quade et al., 2013; Beverly et al., 2021). With the advances of techniques, it is possible to constrain the absolute changes in temperature to a precision of 1–2°C (Thiagarajan et al., 2014; Tripati et al., 2014). Once temperature is constrained, the changes in the $\delta^{18}O$ values probably would help to quantitatively estimate the changes in the rainfall. Another recently developed proxy is the triple oxygen isotopic composition which can also be applied in carbonate archives (Passey et al., 2014; Sha et al., 2020). It depends on the extent of kinetic isotopic fractionation during carbonate precipitation, which in turn depends on the ambient relative humidity. The new experimental measurements can be combined with model data to quantitatively reconstruct the past rainfall and temperature variation.

SUMMARY

We have discussed the cultural shifts in the Indian subcontinent and reviewed some important marine and terrestrial climate data for the last 10 kyr from the ISM dominated regions to understand the role of monsoon on rise and collapse of the ancient Indian civilizations. The human settlement and agricultural activity in Indian subcontinent probably started around 9 kyr BP as evident from multiple archaeological findings. The two major climate events at 8.2 kyr and 4.2 kyr BP are evident in most of the climate proxies. Though the 8.2 kyr event influenced the ISM significantly, but its role on the civilization is not obvious mainly due to lack of early Holocene archaeological data in the Indian subcontinent. The collapse of the Harappan Civilization was probably due to the weakening of the Indian Summer Monsoon after 4.2 kyr BP as indicated by many climate proxies. We observed that most of the available paleoclimate records discussed the monsoon rainfall change qualitatively. It is extremely important to quantitatively obtain estimates of the various climate parameters including change in rainfall and temperature that probably caused the collapse of the civilizations. Some recently established paleoclimate proxies such as carbonate clumped isotope thermometry along with conventional oxygen isotope ratios in carbonate archives can probably disentangle the temperature and rainfall signature and help to estimate the rainfall variation quantitatively. Further combined analysis of multiple proxies in high resolution paleoclimate archives, precise dates of diverse archaeological samples, and more extensive paleoclimate model studies may help enhance our understanding of the rise, evolution, and collapse of early human civilizations and impacts of climate change on them.

DATA AVAILABILITY STATEMENT

The data reviewed in the present study are available with the original publications and are cited at the appropriate places of the article; further inquiries can be directed to the corresponding author.

AUTHOR CONTRIBUTIONS

AL formulated the study and wrote the manuscript in discussion with AB. AB reviewed the manuscript.

ACKNOWLEDGMENTS

The authors thank the Director of the Physical Research Laboratory for his support and encouragement to conduct the present study. AHL thanks Dr. Anoop Ambili for inviting him to contribute to this article. AB acknowledges CSIR for funding through SRA fellowship (13(9024-A)/2019-POOL).

REFERENCES

Ali, S. N., Dubey, J., Ghosh, R., Quamar, M. F., Sharma, A., Morthekai, P., et al. (2018). High Frequency Abrupt Shifts in the Indian Summer Monsoon since Younger Dryas in the Himalaya. *Sci. Rep.* 8, 9287. doi:10.1038/s41598-018-27597-6

Altabet, M. A., Higginson, M. J., and Murray, D. W. (2002). The Effect of Millennial-Scale Changes in Arabian Sea Denitrification on Atmospheric CO2. *Nature* 415, 159–162. doi:10.1038/415159a

Atkins, P. J., Simmons, I., and Roberts, B. K. (1998). "Environmental Degradation and the Collapse of Civilizations," in *People, Land and Time: An Historical Introduction to the Relations between Landscape, Culture and Environment*. Editors P. Atkins, I. Simmons, and B. Roberts (New York and London: Routledge, Taylor and Fransis Group).

Balter, M. (2010). In a Cold Snap, Farmers Turned to Milk. *Science* 329 (5998), 1465. doi:10.1126/science.329.5998.1465

Band, S., Yadava, M. G., Lone, M. A., Shen, C.-C., Sree, K., and Ramesh, R. (2018). High-resolution Mid-holocene Indian Summer Monsoon Recorded in a Stalagmite from the Kotumsar Cave, Central India. *Quat. Int.* 479, 19–24. doi:10.1016/j.quaint.2018.01.026

Banerji, U. S., Arulbalaji, P., and Padmalal, D. (2020). Holocene Climate Variability and Indian Summer Monsoon: An Overview. *The Holocene* 30 (5), 744–773. doi:10.1177/0959683619895577

Barber, D. C., Dyke, A., Hillaire-Marcel, C., Jennings, A. E., Andrews, J. T., Kerwin, M. W., et al. (1999). Forcing of the Cold Event of 8,200 Years Ago by Catastrophic Drainage of Laurentide Lakes. *Nature* 400 (6742), 344–348. doi:10.1038/22504

BarkerRichards, G. M. B., and Richards, M. B. (2013). Foraging-Farming Transitions in Island Southeast Asia. *J. Archaeol. Method Theor.* 20, 256–280. doi:10.1007/s10816-012-9150-7

Basu, S., Agrawal, S., Sanyal, P., Mahato, P., Kumar, S., and Sarkar, A. (2015). Carbon Isotopic Ratios of Modern C3-C4 Plants from the Gangetic Plain, India and its Implications to Paleovegetational Reconstruction. *Palaeogeogr. Palaeoclimatol. Palaeoecol.* 440, 22–32. doi:10.1016/j.palaeo.2015.08.012

Bauer, E., Ganopolski, A., and Montoya, M. (2004). Simulation of the Cold Climate Event 8200 Years Ago by Meltwater Outburst from Lake Agassiz. *Paleoceanogr. Paleoclim.* 19 (3), 001030. doi:10.1029/2004pa001030

Berger, J.-F., and Guilaine, J. (2009). The 8200calBP Abrupt Environmental Change and the Neolithic Transition: A Mediterranean Perspective. *Quat. Int.* 200, 31–49. doi:10.1016/j.quaint.2008.05.013

Berkelhammer, M., Sinha, A., Mudelsee, M., Cheng, H., Edwards, R. L., and Cannariato, K. (2010). Persistent Multidecadal Power of the Indian Summer Monsoon. *Earth Planet. Sci. Lett.* 290, 166–172. doi:10.1016/j.epsl.2009.12.017

Berkelhammer, M., Sinha, A., Stott, L., Cheng, H., Pausata, F., and Yoshimura, K. (2012). An Abrupt Shift in the Indian Monsoon 4000 Years Ago. *Geophys. Monogr. Ser.* 198, 75–88.

Beverly, E. J., Levin, N. E., Passey, B. H., Aron, P. G., Yarian, D. A., Page, M., et al. (2021). Triple Oxygen and Clumped Isotopes in Modern Soil Carbonate along an Aridity Gradient in the Serengeti, Tanzania. *Earth Planet. Sci. Lett.* 567, 116952. doi:10.1016/j.epsl.2021.116952

Buckley, B. M., Anchukaitis, K. J., Penny, D., Fletcher, R., Cook, E. R., Sano, M., et al. (2010). Climate as a Contributing Factor in the Demise of Angkor, Cambodia. *Proc. Natl. Acad. Sci.* 107, 6748–6752. doi:10.1073/pnas.0910827107

Budja, M. (2007). The 8200 calBP 'climate Event' and the Process of Neolithisation in South-Eastern Europe. *Doc. Praeh.* 34, 191–201. doi:10.4312/dp.34.14

Butzer, K. W. (2012). Collapse, Environment, and Society. *Proc. Natl. Acad. Sci.* 109, 3632–3639. doi:10.1073/pnas.1114845109

Cai, Y., Zhang, H., Cheng, H., An, Z., Lawrence Edwards, R., Wang, X., et al. (2012). The Holocene Indian Monsoon Variability over the Southern Tibetan Plateau and its Teleconnections. *Earth Planet. Sci. Lett.* 335-336, 135–144. doi:10.1016/j.epsl.2012.04.035

Chatterjee, A., Ray, J. S., Shukla, A. D., and Pande, K. (2019). On the Existence of a Perennial River in the Harappan Heartland. *Sci. Rep.* 9, 17221. doi:10.1038/s41598-019-53489-4

Chauhan, D. S. (1999). "Mythological Observations and Scientific Evaluation of the Lost Sarasvati River,". *Vedic Sarasvati*. Editors B. P. Radhakrishna and S. S. Merh (Bangalore, India: Memoir Geol. Soc. India), 42, 35–45.

Cheng, H., Fleitmann, D., Edwards, R. L., Wang, X., Cruz, F. W., Auler, A. S., et al. (2009). Timing and Structure of the 8.2 Kyr B.P. Event Inferred from δ18O Records of Stalagmites from China, Oman, and Brazil. *Geology* 37 (11), 1007–1010. doi:10.1130/g30126a.1

Cook, E. R., Anchukaitis, K. J., Buckley, B. M., D'Arrigo, R. D., Jacoby, G. C., and Wright, W. E. (2010). Asian Monsoon Failure and Megadrought during the Last Millennium. *Science* 328 (5977), 486–489. doi:10.1126/science.1185188

Cullen, H. M., deMenocal, P. B., Hemming, S., Hemming, G., Brown, F. H., Guilderson, T., et al. (2000). Climate Change and the Collapse of the Akkadian empire: Evidence from the Deep Sea. *Geology* 28, 379–382. doi:10.1130/0091-7613(2000)028<0379:ccatco>2.3.co;2

Di Rita, F., and Magri, D. (2009). Holocene Drought, Deforestation and evergreen Vegetation Development in the central Mediterranean: a 5500 Year Record from Lago Alimini Piccolo, Apulia, Southeast Italy. *The Holocene* 19, 295–306. doi:10.1177/0959683608100574

Dixit, Y., Hodell, D. A., and Petrie, C. A. (2014a). Abrupt Weakening of the Summer Monsoon in Northwest India 4100 Yr Ago. *Geology* 42 (4), 339–342. doi:10.1130/g35236.1

Dixit, Y., Hodell, D. A., SinhaPetrie, R. C. A., and Petrie, C. A. (2014b). Abrupt Weakening of the Indian Summer Monsoon at 8.2 Kyr B.P. *Earth Planet. Sci. Lett.* 391, 16–23. doi:10.1016/j.epsl.2014.01.026

Dixit, Y., and Tandon, S. K. (2016). Hydroclimatic Variability on the Indian Subcontinent in the Past Millennium: Review and Assessment. *Earth-Science Rev.* 161, 1–15. doi:10.1016/j.earscirev.2016.08.001

Dobhal, D. P., Gupta, A. K., Mehta, M., and Khandelwal, D. D. (2013). Kedarnath Disaster: Facts and Plausible Causes. *Curr. Sci.* 105 (2), 171–174.

Drysdale, R., Zanchetta, G., Hellstrom, J., Maas, R., Fallick, A., Pickett, M., et al. (2006). Late Holocene Drought Responsible for the Collapse of Old World Civilizations Is Recorded in an Italian Cave Flowstone. *Geol* 34, 101–104. doi:10.1130/g22103.1

Dutt, S., Gupta, A. K., Clemens, S. C., Cheng, H., Singh, R. K., Kathayat, G., et al. (2015). Abrupt Changes in Indian Summer Monsoon Strength during 33,800 to 5500 Years B.P. *Geophys. Res. Lett.* 42 (13), 5526–5532. doi:10.1002/2015gl064015

Dutt, S., Gupta, A. K., Singh, M., Jaglan, S., Saravanan, P., Balachandiran, P., et al. (2019). Climate Variability and Evolution of the Indus Civilization. *Quat. Int.* 507, 15–23. doi:10.1016/j.quaint.2018.11.012

Dutt, S., Gupta, A. K., Wünnemann, B., and Yan, D. (2018). A Long Arid Interlude in the Indian Summer Monsoon during ~4,350 to 3,450 Cal. Yr BP Contemporaneous to Displacement of the Indus valley Civilization. *Quat. Int.* 482, 83–92. doi:10.1016/j.quaint.2018.04.005

Enzel, Y., Ely, L. L., Mishra, S., Amit, R., Ramesh, R., Lazar, B., et al. (1999). High-Resolution Holocene Environmental Changes in the Thar Desert, Northwestern India. *Science* 284 (5411), 125–128. doi:10.1126/science.284.5411.125

Fairservis, W. A. (1967). The Origins, Character and Decline of an Early Civilization. *Am. Mus. Novit.* 2302, 1–48.

Finné, M., Holmgren, K., Shen, C. C., Hu, H.-M., Boyd, M., and Stocker, S. (2017). Late Bronze Age Climate Change and Descrution of the Mycenaean Palace of Nestor at Pylos. *PLoS ONE* 12, e0189447. doi:10.1371/journal.pone.0189447

Finné, M., Holmgren, K., Sundqvist, H. S., Weiberg, E., and Lindblom, M. (2011). Climate in the Eastern Mediterranean, and Adjacent Regions, during the Past 6000 Years - A Review. *J. Archaeological Sci.* 38, 3153–3173. doi:10.1016/j.jas.2011.05.007

Fitzsimons, M. A. (1970). The Indus Valley Civilization. *Hist. Teach.* 4 (1), 9–22. doi:10.2307/492135

Fleitmann, D., Burns, S. J., Mangini, A., Mudelsee, M., Kramers, J., Villa, I., et al. (2007). Holocene ITCZ and Indian Monsoon Dynamics Recorded in Stalagmites from Oman and Yemen (Socotra). *Quat. Sci. Rev.* 26 (1), 170–188. doi:10.1016/j.quascirev.2006.04.012

Fleitmann, D., Burns, S. J., Mudelsee, M., Neff, U., Kramers, J., Mangini, A., et al. (2003). Holocene Forcing of the Indian Monsoon Recorded in a Stalagmite from Southern Oman. *Science* 300, 1737–1739. doi:10.1126/science.1083130

Fuller, D. Q., and Madella, M. (2002). *Indian Archaeology in Retrospect. Protohistory*. Editors S. Settar and R. Korisettar (New Delhi: Manohar Publishers), Vol. II, 317–390.

Gadgil, S., and Gadgil, S. (2006). The Indian Monsoon, GDP and Agriculture. *Econ. Polit. Weekly* XLI (47), 4887–4895.

Gadgil, S. (2018). The Monsoon System: Land-Sea Breeze or the ITCZ? *J. Earth Syst. Sci.* 127 (1). doi:10.1007/s12040-017-0916-x

Gangal, K., Vahia, M., and Adhikari, R. (2010). Spatio-temporal Analysis of the Indus Urbanization. *Curr. Sci* 98, 846–852.

Ghosh, P., Adkins, J., Affek, H., Balta, B., Guo, W., Schauble, E. A., et al. (2006). 13C-18O Bonds in Carbonate Minerals: A New Kind of Paleothermometer. *Geochimica et Cosmochimica Acta* 70, 1439–1456. doi:10.1016/j.gca.2005.11.014

Giosan, L., Clift, P. D., Macklin, M. G., Fuller, D. Q., Constantinescu, S., Durcan, J. A., et al. (2012). Fluvial Landscapes of the Harappan Civilization. *Proc. Natl. Acad. Sci.* 109 (26), E1688–E1694. doi:10.1073/pnas.1112743109

Goswami, B. N., Madhusoodanan, M. S., Neema, C. P., and Sengupta, D. (2006). A Physical Mechanism for North Atlantic SST Influence on the Indian Summer Monsoon. *Geophys. Res. Lett.* 33 (2), 024803. doi:10.1029/2005gl024803

Green, A. S. (2021). Killing the Priest-King: Addressing Egalitarianism in the Indus Civilization. *J. Archaeol Res.* 29, 153–202. doi:10.1007/s10814-020-09147-9

Gronenborn, D. (2009). Climate Fluctuations and Trajectories to Complexity in the Neolithic: towards a Theoryfluctuations and Trajectories to Complexity in the Neolithic: towards a Theory. *Doc. Praeh.* 36, 97–110. doi:10.4312/dp.36.5

Gupta, A. K., Anderson, D. M., and Overpeck, J. T. (2003). Abrupt Changes in the Asian Southwest Monsoon during the Holocene and Their Links to the North Atlantic Ocean. *Nature* 421, 354–357. doi:10.1038/nature01340

Gupta, A. K., Dutt, S., Cheng, H., and Singh, R. K. (2020). Abrupt Changes in Indian Summer Monsoon Strength during the Last ~900 years and Their Linkages to Socio-Economic Conditions in the Indian Subcontinent. *Palaeogeogr. Palaeoclimatol. Palaeoecol.* 536, 109347.

Gupta, V. (2004). Global Climate Change: India's Local Concerns. *Ier* 6 (1), 54–59. doi:10.1504/ier.2004.053917

IPCC AR5 (2013). *Climate Change 2013: The Physical Science Basis*.

Jacobsen, T., and Adams, R. M. (1958). Salt and Silt in Ancient Mesopotamian Agriculture: Progressive Changes in Soil Salinity and Sedimentation Contributed to the Breakup of Past Civilizations. *Science* 128 (3334), 1251–1258. doi:10.1126/science.128.3334.1251

Jarrige, J. F. (1981). "Chronology of the Earlier Periods of the Greater Indus as Seen from Mehrgarh, Pakistan," in *South Asian Archaeology 1981*. Editor B. Allchin (Cambridge: Cambridge University Press).

Jarrige, J. F., and Lechevallier, M. (1979). "Excavations at Mehrgarh, Baluchistan," in *South Asian Archaeology 1977. Insti-tuto Universitario Orientale, Naples*. Editor M. Taddei.

Jarrige, J. F. (1993). *The Early Architectural Traditions of Greater Indus as Seen from Mehrgarh, Baluchistan*. New England: University Press of.

Kaniewski, D., Van Campo, E., Morhange, C., Guiot, J., Zviely, D., Shaked, I., et al. (2013). Early Urban Impact on Mediterranean Coastal Environments. *Sci. Rep.* 3, 3540. doi:10.1038/srep03540

Kathayat, G., Cheng, H., Sinha, A., Berkelhammer, M., Zhang, H., Duan, P., et al. (2018). Evaluating the Timing and Structure of the 4.2 Ka Event in the Indian Summer Monsoon Domain from an Annually Resolved Speleothem Record from Northeast India. *Clim. Past* 14 (12), 1869–1879. doi:10.5194/cp-14-1869-2018

Kathayat, G., Cheng, H., Sinha, A., Spötl, C., Edwards, R. L., Zhang, H., et al. (2016). Indian Monsoon Variability on Millennial-Orbital Timescales. *Sci. Rep.* 6, 24374. doi:10.1038/srep24374

Kathayat, G., Cheng, H., Sinha, A., Yi, L., Li, X., Zhang, H., et al. (2017). The Indian Monsoon Variability and Civilization Changes in the Indian Subcontinent. *Sci. Adv.* 3 (12), e1701296. doi:10.1126/sciadv.1701296

Kenoyer, J. M. (2006). in *Historical Roots in the Making of 'the Aryan'*. Editor R. Thapar (New Delhi: National Book Trust).

Kenoyer, J. M. (1998). *Ancient Cities of the Indus Valley Civilization*. Oxford: Oxford University Press.

Kenoyer, J. M. (1997). Trade and Technology of the Indus valley: New Insights from Harappa, Pakistan. *World Archaeology* 29 (2), 262–280. doi:10.1080/00438243.1997.9980377

Kidder, T., Liu, H., Xu, Q., and Li, M. (2012). The Alluvial Geoarchaeology of the Sanyangzhuang Site on the Yellow River Floodplain, Henan Province, China. *Geoarchaeology* 27, 324–343. doi:10.1002/gea.21411

Kobashi, T., Severinghaus, J. P., Brook, E. J., Barnola, J.-M., and Grachev, A. M. (2007). Precise Timing and Characterization of Abrupt Climate Change 8200 Years Ago from Air Trapped in Polar Ice. *Quat. Sci. Rev.* 26, 1212–1222. doi:10.1016/j.quascirev.2007.01.009

Kohn, M. J. (2010). Carbon Isotope Compositions of Terrestrial C3 Plants as Indicators of (Paleo)ecology and (Paleo)climate. *Proc. Natl. Acad. Sci.* 107, 19691–19695. doi:10.1073/pnas.1004933107

Korisettar, R., Venkatasubbaiah, P. C., and Fuller, D. Q. (2002). "Brahmagiri and beyond: the Archaeology of the Southern Neolithic,". *Indian Archaeology in Retrospect: Prehistory*. Editors S. Settar and R. Korisettar (New Delhi: Indian Council of Historical Research and Manohar Publishers), Vol. 1, 150–237.

Kotlia, B. S., Singh, A. K., Joshi, L. M., and Bisht, K. (2018). Precipitation Variability over Northwest Himalaya from ~4.0 to 1.9 Ka BP with Likely Impact on Civilization in the Foreland Areas. *J. Asian Earth Sci.* 162, 148–159. doi:10.1016/j.jseaes.2017.11.025

Kotlia, B. S., Singh, A. K., Zhao, J.-X., Duan, W., Tan, M., Sharma, A. K., et al. (2017). Stalagmite Based High Resolution Precipitation Variability for Past Four Centuries in the Indian Central Himalaya: Chulerasim Cave Re-visited and Data Re-interpretation. *Quat. Int.* 444, 35–43. doi:10.1016/j.quaint.2016.04.007

Kulke, H., and Rothermund, D. (2004). *A History of India*. fourth Edition. London and New York: Routledge Taylor and Francis Group.

Kumar, K. K., Rajagopalan, B., Hoerling, M., Bates, G., and Cane, M. (2006). Unraveling the Mystery of Indian Monsoon Failure during El Nino. *Science* 314, 115–119. doi:10.1126/science.1131152

Kumar, M. (2009). in *Linguistics, Archaeology and the Human Past, Occasional Paper 7. Research Institute for Humanity and Nature*. Editors T. Osada and A. Uesugi (Kyoto): Nakanishi Printing Co. Ltd), 1–75.

Laskar, A. H., Ramesh, R., Burman, J., Midhun, M., Jani, R. A., Yadva, M. G., et al. (2015). Stable Water Isotopic Characterization in Nor'westers in the South Assam, Northeast India. *J. Clim. Change* 1 (1-2), 75–87. doi:10.3233/jcc-150006

Laskar, A. H., Sharma, N., Ramesh, R., Jani, R. A., and Yadava, M. G. (2010). Paleoclimate and Paleovegetation of Lower Narmada Basin, Gujarat, Western India, Inferred from Stable Carbon and Oxygen Isotopes. *Quat. Int.* 227, 183–189. doi:10.1016/j.quaint.2010.05.020

Laskar, A., Yadava, M., Sharma, N., and Ramesh, R. (2013a). Late-Holocene Climate in the Lower Narmada valley, Gujarat, Western India, Inferred Using Sedimentary Carbon and Oxygen Isotope Ratios. *The Holocene* 23 (8), 1115–1122. doi:10.1177/0959683613483621

Laskar, A. H., Yadava, M. G., Ramesh, R., Polyak, V. J., and Asmerom, Y. (2013b). A 4 Kyr Stalagmite Oxygen Isotopic Record of the Past Indian Summer Monsoon in the Andaman Islands. *Geochem. Geophys. Geosyst.* 14 (9), 3555–3566. doi:10.1002/ggge.20203

Laskar, A. H., Yui, T.-F., and Liang, M.-C. (2016). Clumped Isotope Composition of Marbles from the Backbone Range of Taiwan. *Terra Nova* 28 (4), 265–270. doi:10.1111/ter.12217

Laskar, J., Robutel, P., Joutel, F., Gastineau, M., Correia, A. C. M., and Levrard, B. (2006). Long-term Solution for the Insolation Quantities of the Earth. *Proc. IAU* 2 (14), 465. doi:10.1017/s1743921307011404

Lawler, A. (2008). UNMASKING the INDUS: Trench Warfare: Modern Borders Split the Indus. *Science* 320, 1282–1283. doi:10.1126/science.320.5881.1282

Lekshmy, P. R., Midhun, M., Ramesh, R., Jani, R. A., et al. (2014). 18O Depletion in Monsoon Rain Relates to Large Scale Organized Convection Rather than the Amount of Rainfall. *Sci. Rep.* 4, 5661. doi:10.1038/srep05661

Liang, F., Brook, G. A., Kotlia, B. S., Railsback, L. B., Hardt, B., Cheng, H., et al. (2015). Panigarh Cave stalagmite Evidence of Climate Change in the Indian Central Himalaya since AD 1256: Monsoon Breaks and Winter Southern Jet Depressions. *Quat. Sci. Rev.* 124, 145–161. doi:10.1016/j.quascirev.2015.07.017

Liu, F., and Feng, Z. (2012). A Dramatic Climatic Transition at ~4000 Cal. Yr BP and its Cultural Responses in Chinese Cultural Domains. *The Holocene* 22 (10), 1181–1197. doi:10.1177/0959683612441839

Liu, Y.-H., Henderson, G. M., Hu, C.-Y., Mason, A. J., Charnley, N., Johnson, K. R., et al. (2013). Links between the East Asian Monsoon and North Atlantic Climate during the 8,200 Year Event. *Nat. Geosci* 6, 117–120. doi:10.1038/ngeo1708

MacDonald, G. (2011). Potential Influence of the Pacific Ocean on the Indian Summer Monsoon and Harappan Decline. *Quat. Int.* 229, 140–148. doi:10.1016/j.quaint.2009.11.012

Macklin, M. G., and Lewin, J. (2015). The Rivers of Civilization. *Quat. Sci. Rev.* 114, 228–244. doi:10.1016/j.quascirev.2015.02.004

Macklin, M. G., Woodward, J. C., Welsby, D. A., Duller, G. A. T., Williams, F. M., and Williams, M. A. J. (2013). Reach-scale River Dynamics Moderate the Impact of Rapid Holocene Climate Change on Floodwater Farming in the Desert Nile. *Geology* 41 (6), 695–698. doi:10.1130/g34037.1

Madella, M., and Fuller, D. Q. (2006). Palaeoecology and the Harappan Civilisation of South Asia: a Reconsideration. *Quat. Sci. Rev.* 25, 1283–1301. doi:10.1016/j.quascirev.2005.10.012

Magny, M., Vanniere, B., Zanchetta, G., Fouache, E., Touchias, G., Petrika, L., et al. (2009). Possible Complexity of the Climatic Event Around 4300–3800 Cal. BP in the central and Western Mediterranean. *The Holocene* 19, 1–11. doi:10.1177/0959683609337360

Magri, D., and Parra, I. (2002). Late Quaternary Western Mediterranean Pollen Records and African Winds. *Earth Planet. Sci. Lett.* 200, 401–408. doi:10.1016/s0012-821x(02)00619-2

Marcott, S. A., Shakun, J. D., Clark, P. U., and Mix, A. C. (2013). A Reconstruction of Regional and Global Temperature for the Past 11,300 Years. *Science* 339, 1198–1201. doi:10.1126/science.1228026

Margaritelli, G., Vallefuoco, M., Di Rita, F., Capotondi, L., Bellucci, L. G., Insinga, D., et al. (2016). Marine response to climate changes during the last five millennia in the central Mediterranean Sea. *Global Planet. Change* 142, 53–72.

Mayewski, P. A., Rohling, E. E., Curt Stager, J., Karlén, W., Maasch, K. A., Meeker, L. D., et al. (2004). Holocene Climate Variability. *Quat. Res.* 62 (3), 243–255. doi:10.1016/j.yqres.2004.07.001

Mehrotra, N., Shah, S. K., Basavaiah, N., Laskar, A. H., Yadava, M. G., and Yadava, M. G. (2019). Resonance of the '4.2ka Event' and Terminations of Global Civilizations during the Holocene, in the Palaeoclimate Records Around PT Tso Lake, Eastern Himalaya. *Quat. Int.* 507, 206–216. doi:10.1016/j.quaint.2018.09.027

Migowski, C., Stein, M., Prasad, S., Negendank, J. F. W., and Agnon, A. (2006). Holocene Climate Variability and Cultural Evolution in the Near East from the Dead Sea Sedimentary Record. *Quat. Res.* 66, 421–431. doi:10.1016/j.yqres.2006.06.010

Mughal, M. R. (1997). *Ancient Cholistan: Archaeology and Architecture*. Lahore: Ferozsons.

Nakamura, A., Yokoyama, Y., Maemoku, H., Yagi, H., Okamura, M., Matsuoka, H., et al. (2016). Weak Monsoon Event at 4.2 ka Recorded in Sediment From Lake Rara, Himalayas. *Quat. Int.* 397, 349–359. doi:10.1016/j.quaint.2015.05.053

Paliwal, B. S. (2011). Abrupt Holocene Climatic Change in Northwestern India: Disappearance of the Sarasvati River and the End of Vedic Civilization. *Geophys. Monogr. Ser.* 193, 185–194. doi:10.1029/2010GM001028

P. A. McAnany and N. Yoffee (Editors) (2010) *Questioning Collapse: Human Resilience, Ecological Vulnerability, and the Aftermath of Empire* (Cambridge: Cambridge University Press).

Panja, S. (2002). "Research on the Deccan Chalcolithic,". *Indian Archaeology in Retrospect: Prehistory*. Editors S. Settar and R. Korisettar (New Delhi: Indian Council of Historical Research and Manohar Publishers), Vol. 1, 263–276.

Passey, B. H., Hu, H., Ji, H., Montanari, S., Li, S., Henkes, G. A., et al. (2014). Triple Oxygen Isotopes in Biogenic and Sedimentary Carbonates. *Geochimica et Cosmochimica Acta* 141, 1–25. doi:10.1016/j.gca.2014.06.006

Petrie, C. A., Singh, R. N., Bates, J., Dixit, Y., French, C. A. I., Hodell, D. A., et al. (2017). Adaptation to Variable Environments, Resilience to Climate Change: InvestigatingLand, Water and Settlementin Indus Northwest India. *Curr. Anthropol.* 58, 1–30. doi:10.1086/690112

Phadtare, N. R. (2000). Sharp Decrease in Summer Monsoon Strength 4000-3500 Cal Yr B.P. In the Central Higher Himalaya of India Based on Pollen Evidence from Alpine Peat. *Quat. Res.* 53, 122–129. doi:10.1006/qres.1999.2108

Pichevin, L., Bard, E., Martinez, P., and Billy, I. (2007). Evidence of Ventilation Changes in the Arabian Sea during the Late Quaternary: Implication for Denitrification and Nitrous Oxide Emission. *Glob. Biogeochem. Cycles* 21, GB4008. doi:10.1029/2006gb002852

Pokharia, A. K., Kharakwal, J. S., and Srivastava, A. (2014). Archaeobotanical evidence of millets in the Indian subcontinent with some observations on their role in the Indus civilization. *Journal of Archaeological Science* 42, 442–455.

Ponton, C., Giosan, L., EglintonFuller, T. I. D. Q., Johnson, J. E., Kumar, P., and Collett, T. S. (2012). Holocene Aridification of India. *Geophys. Res. Lett.* 39 (3), 050722. doi:10.1029/2011gl050722

Possehl, G. L. (2002a). *The Indus Civilization: A Contemporary Perspective*. Oxford: Rowman & Littlefield Publishers, Inc.

Possehl, G. L. (2002b). *The Indus Civilization: A Contemporary Perspective*. Altamira Press.

Prasad, S., Anoop, A., Riedel, N., Sarkar, S., Menzel, P., Basavaiah, N., et al. (2014). Prolonged Monsoon Droughts and Links to Indo-Pacific Warm Pool: A Holocene Record from Lonar Lake, central Indiac Warm Pool: A Holocene Record from Lonar Lake, central India. *Earth Planet. Sci. Lett.* 391, 171–182. doi:10.1016/j.epsl.2014.01.043

Pruti, R. K. (2004). *Culture and Civilization Series Vedic Civilization*. New Delhi: Discovery Publishing House.

Quade, J., Eiler, J., Daëron, M., and Achyuthan, H. (2013). The Clumped Isotope Geothermometer in Soil and Paleosol Carbonate. *Geochimica et Cosmochimica Acta* 105, 92–107. doi:10.1016/j.gca.2012.11.031

Radhakrishna, B. P., and Merh, S. S. (1999). Vedic Saraswati. *Memoir. Geol. Soc.* India 42.

Railsback, L. B., Liang, F., Brook, G. A., Voarintsoa, N. R. G., Sletten, H. R., Marais, E., et al. (2018). The Timing, Two-Pulsed Nature, and Variable Climatic Expression of the 4.2 Ka Event: A Review and New High-Resolution Stalagmite Data from Namibia. *Quat. Sci. Rev.* 186, 78–90. doi:10.1016/j.quascirev.2018.02.015

Ramsey, C. B., Dee, M. W., Rowland, J. M., Higham, T. F. G., Harris, S. A., Brock, F., et al. (2010). Radiocarbon-Based Chronology for Dynastic Egypt. *Science* 328, 1554–1557. doi:10.1126/science.1189395

Rana, N., Sharma, S., Sundriyal, Y., Kaushik, S., Pradhan, S., Tiwari, G., et al. (2021). A Preliminary Assessment of the 7th February 2021 Flashflood in Lower Dhauli Ganga valley, Central Himalaya, India. *J. Earth Syst. Sci.* 130, 78. doi:10.1007/s12040-021-01608-z

Ratnagar, S. (2002). *The End of the Great Harappan Tradition*. New Delhi, India: Manohar Publishers and Distributors.

Roland, T. P., Caseldine, C. J., Charman, D. J., Turney, C. S. M., and Amesbury, M. J. (2014). Was There a '4.2 Ka Event' in Great Britain and Ireland? Evidence from the Peatland Record. *Quat. Sci. Rev.* 83, 11–27. doi:10.1016/j.quascirev.2013.10.024

Samanta, A. K., Kolte, A. P., Senani, S., Sridhar, M., and Jayapal, N. (2011). Prebiotics in Ancient Indian Diets. *Curr. Sci.* 101 (1), 43–46.

Saraswat, R., Lea, D. W., Nigam, R., Mackensen, A., and Naik, D. K. (2013). Deglaciation in the Tropical Indian Ocean Driven by Interplay between the Regional Monsoon and Global Teleconnections. *Earth Planet. Sci. Lett.* 375, 166–175. doi:10.1016/j.epsl.2013.05.022

Sarkar, A., Mukherjee, A. D., Bera, M. K., Das, B., Juyal, N., Morthekai, P., et al. (2016). Oxygen Isotope in Archaeological Bioapatites from India: Implications to Climate Change and Decline of Bronze Age Harappan Civilization. *Sci. Rep.* 6, 26555. doi:10.1038/srep26555

Schumm, S. A. (2007). *River Variability and Complexity*. Cambridge: Cambridge University Press.

Sengupta, T., Deshpande Mukherjee, A., Bhushan, R., Ram, F., Bera, M. K., Raj, H., et al. (2020). Did the Harappan Settlement of Dholavira (India) Collapse during the Onset of Meghalayan Stage Drought? *J. Quat. Sci* 35, 382–395. doi:10.1002/jqs.3178

Seppä, H., Bjune, A. E., Telford, R. J., Birks, H. J. B., and Veski, S. (2009). Last Nine-Thousand Years of Temperature Variability in Northern Europe. *Clim. Past* 5, 523–535. doi:10.5194/cp-5-523-2009

Sha, L., Mahata, S., Duan, P., Luz, B., Zhang, P., Baker, J., et al. (2020). A Novel Application of Triple Oxygen Isotope Ratios of Speleothems. *Geochimica et Cosmochimica Acta* 270, 360–378. doi:10.1016/j.gca.2019.12.003

Sharma, C. P., Chahal, P., Kumar, A., Singhal, S., Sundriyal, Y., Ziegler, A. D., et al. (2021). Late Pleistocene–Holocene Flood History, Flood-Sediment Provenance and Human Imprints from the Upper Indus River Catchment, Ladakh Himalaya. *GSA Bull.* doi:10.1130/B35976.1

Shewale, M. P., and Kumar, S. (2005). *Climatological Features of Drought Incidences in India*. Pune, India: India Meteorological Department Pune.

Singh, D., Horton, D. E., Tsiang, M., Haugen, M., Ashfaq, M., Mei, R., et al. (2014). Severe Precipitation in Northern India in June 2013: Causes, Historical Context, and Changes in Probability. *Bull. Amer. Meteorol. Soc.* 95 (9), S58–S61.

Singh, G., Wasson, R. J., and Agrawal, D. P. (1990). Vegetational and Seasonal Climatic Changes since the Last Full Glacial in the Thar Desert, Northwestern India. *Rev. Palaeobotany Palynology* 64, 351–358. doi:10.1016/0034-6667(90)90151-8

Singh, I. B., Sharma, S., Sharma, M., Srivastava, P., and Rajagopalan, G. (1999). Evidence of Human Occupation and Climate of 30 Ka in the Alluviam of Southern Ganga Plain. *Curr. Sci.* 76 (7), 1022–1026.

Singh, P. (2002). "The Neolithic Cultures of Northern and Eastern India,". *Indian Archaeology in Retrospect: Prehistory*. Editors S. Settar and R. Korisettar (New Delhi: Indian Council of Historical Research and Manohar Publishers), Vol. 1, 127–150.

Singhvi, A. K., and Kar, A. (1992). *Thar Desert in Rajasthan*. Bangalore: Geological Society of India.

Sinha, A., Kathayat, G., Cheng, H., Breitenbach, S. F. M., Berkelhammer, M., Mudelsee, M., et al. (2015). Trends and Oscillations in the Indian Summer Monsoon Rainfall over the Last Two Millennia. *Nat. Commun.* 6, 6309. doi:10.1038/ncomms7309

Sinha, A., Stott, L., Berkelhammer, M., Cheng, H., Edwards, R. L., Buckley, B., et al. (2011). A Global Context for Megadroughts in Monsoon Asia during the Past Millennium. *Quat. Sci. Rev.* 30, 47–62. doi:10.1016/j.quascirev.2010.10.005

Sirocko, F., Sarnthein, M., Erlenkeuser, H., Lange, H., Arnold, M., and Duplessy, J. C. (1993). Century-scale Events in Monsoonal Climate over the Past 24,000 Years. *Nature* 364 (6435), 322–324. doi:10.1038/364322a0

Sridhar, A., Laskar, A., Prasad, V., Sharma, A., Tripathi, J. K., Balaji, D., et al. (2015). Late Holocene Flooding History of a Tropical River in Western India in Response to Southwest Monsoon Fluctuations: A Multi Proxy Study from Lower Narmada valley. *Quat. Int.* 371, 181–190. doi:10.1016/j.quaint.2014.10.052

Stanley, J.-D., Krom, M. D., Cliff, R. A., and Woodward, J. C. (2003). Short Contribution: Nile Flow Failure at the End of the Old Kingdom, Egypt: Strontium Isotopic and Petrologic Evidence. *Geoarchaeology* 18 (3), 395–402. doi:10.1002/gea.10065

Staubwasser, M., Sirocko, F., and Grootes, P. M. (2003). Climate Change at the 4.2 Ka BP Termination of the Indus valley Civilization and Holocene South Asian Monsoon Variability. *Geophys. Res. Lett.* 30 (8), 016822. doi:10.1029/2002gl016822

Staubwasser, M., Sirocko, F., Grootes, P. M., and Erlenkeuser, H. (2002). South Asian Monsoon Climate Change and Radiocarbon in the Arabian Sea during Early and Middle Holocene. *Paleoceanography* 17 (4), 1063. doi:10.1029/2000pa000608

Staubwasser, M., and Weiss, H. (2006). Holocene Climate and Cultural Evolution in Late Prehistoric-Early Historic West Asia. *Quat. Res.* 66, 372–387. doi:10.1016/j.yqres.2006.09.001

Thiagarajan, N., Subhas, A. V., Southon, J. R., Eiler, J. M., and Adkins, J. F. (2014). Abrupt Pre-bølling-allerød Warming and Circulation Changes in the Deep Ocean. *Nature* 511 (7507), 75–78. doi:10.1038/nature13472

Thomas, E. R., Wolff, E. W., Mulvaney, R., Steffensen, J. P., Johnsen, S. J., Arrowsmith, K., et al. (2007). The 8.2ka Event from Greenland Ice Cores. *Quat. Sci. Rev.* 26 (1-2), 70–81. doi:10.1016/j.quascirev.2006.07.017

Tiwari, M., Nagoji, S. S., and Ganeshram, R. S. (2015). Multi-centennial Scale SST and Indian Summer Monsoon Precipitation Variability since the Mid-holocene and its Nonlinear Response to Solar Activity. *The Holocene* 25 (9), 1415–1424. doi:10.1177/0959683615585840

Tripati, A. K., Sahany, S., Pittman, D., Eagle, R. A., Neelin, J. D., Mitchell, J. L., et al. (2014). Modern and Glacial Tropical Snowlines Controlled by Sea Surface Temperature and Atmospheric Mixing. *Nat. Geosci* 7, 205–209. doi:10.1038/ngeo2082

van der Plicht, J., Akkermans, P. M. M. G., Nieuwenhuyse, O., Kaneda, A., and Russell, A. (2011). Tell Sabi Abyad, Syria: Radiocarbon Chronology, Cultural Change, and the 8.2 Ka Event. *Radiocarbon* 53 (2), 229–243. doi:10.1017/s0033822200056514

von Rad, U., Schaaf, M., Michels, K. H., Schulz, H., Berger, W. H., and Sirocko, F. (1999). A 5000-yr Record of Climate Change in Varved Sediments from the Oxygen Minimum Zone off Pakistan, Northeastern Arabian Sea. *Quat. Res.* 51, 39–53. doi:10.1006/qres.1998.2016

Walker, M., Gibbard, P., Head, M. J., Berkelhammer, M., Björck, S., Cheng, H., et al. (2019). Formal Subdivision of the Holocene Series/epoch: A Summary. *J. Geol. Soc. India* 93 (2), 135–141. doi:10.1007/s12594-019-1141-9

Walker, M., Head, M. J., Berkelhammer, M., Björck, S., Cheng, H., Cwynar, L., et al. (2018). Formal Ratification of the Subdivision of the Holocene Series/Epoch (Quaternary System/Period): Two New Global Boundary Stratotype Sections and Points (GSSPs) and Three New Stages/subseries. *Episodes* 41 (4), 213–223. doi:10.18814/epiiugs/2018/018016

Wang, Y., Cheng, H., Edwards, R. L., He, Y., Kong, X., An, Z., et al. (2005). The Holocene Asian Monsoon: Links to Solar Changes and North Atlantic Climate. *Science* 308 (5723), 854–857. doi:10.1126/science.1106296

Webster, P. J., Magaña, V. O., Palmer, T. N., Shukla, J., Tomas, R. A., Yanai, M., et al. (1998). Monsoons: Processes, Predictability, and the Prospects for Prediction. *J. Geophys. Res. Oceans* 103. doi:10.1029/97jc02719

Weiss, H., Courty, M.-A., Wetterstrom, W., Guichard, F., Senior, L., Meadow, R., et al. (1993). The Genesis and Collapse of Third Millennium North Mesopotamian Civilization. *Science* 261, 995–1004. doi:10.1126/science.261.5124.995

Weiss, H. (2016). Global Megadrought, Societal Collapse and Resilience at 4.2-3.9 Ka BP across the Mediterranean and West Asia. *PAGES Mag.* 24, 62–63. doi:10.22498/pages.24.2.62

Weiss, H., Manning, S. W., Ristvet, L., Marl, L., Besonen, M., Mccarthy, A., et al. (2012). "Tell Leilan Akkadian Imperialization, Collapse, and Short-Lived Reoccupation Defined by High-Resolution Radiocarbon Dating," in *Seven Generations since the Fall of Akkad*. Editor H. Weiss (Wiesbaden: Harrassowitz Verlag, 163–192.

Weninger, B., Alram-Stern, E., Bauer, E., Clare, L., Danzeglocke, U., Jöris, O., et al. (2006). Climate Forcing Due to the 8200 Cal Yr BP Event Observed at Early Neolithic Sites in the Eastern Mediterranean. *Quat. Res.* 66, 401–420. doi:10.1016/j.yqres.2006.06.009

Wicks, K., and Mithen, S. (2014). The Impact of the Abrupt 8.2 Ka Cold Event on the Mesolithic Population of Western Scotland: a Bayesian Chronological Analysis Using 'activity Events' as a Population Proxy. *J. Archaeological Sci.* 45, 240–269. doi:10.1016/j.jas.2014.02.003

Witzel, M. (1987). in *India and the Ancient World. History, Trade and Culture before A.D. 650. Orientalia Lovaniensia Analecta Leuven*. Editors P. H. L. Eggermont Jubilee Volume and G. Pollet, 25, 173–213 .

Wolff, E. W., Chappellaz, J., Blunier, T., Rasmussen, S. O., and Svensson, A. (2010). Millennial-scale Variability during the Last Glacial: The Ice Core Record. *Quat. Sci. Rev.* 29, 2828–2838. doi:10.1016/j.quascirev.2009.10.013

Wright, R. P., Bryson, R. A., and Schuldenrein, J. (2008). Water Supply and History: Harappa and the Beas Regional Survey. *Antiquity* 82, 37–48. doi:10.1017/s0003598x00096423

Wright, R. P. (2009). *The Ancient Indus: Urbanism Economy, and Society*. Cambridge University Press.

Yadav, R. R. (2009). Tree Ring Imprints of Long-Term Changes in Climate in Western Himalaya, India. *J. Biosci.* 34, 699–707. doi:10.1007/s12038-009-0058-7

Yadav, R. R. (2013). Tree Ring-Based Seven-century Drought Records for the Western Himalaya, India. *J. Geophys. Res. Atmos.* 118, 4318–4325. doi:10.1002/jgrd.50265

Yadava, M. G., and Ramesh, R. (2005). Monsoon Reconstruction from Radiocarbon Dated Tropical Indian Speleothems. *The Holocene* 15 (1), 48–59. doi:10.1191/0959683605h1783rp

Yadava, M. G., Ramesh, R., and Pant, G. B. (2004). Past Monsoon Rainfall Variations in Peninsular India Recorded in a 331-Year-Old Speleothem. *The Holocene* 14 (4), 517–524. doi:10.1191/0959683604hl728rp

Yadava, M. G., Sarswat, K. S., Singh, I. B., and Ramesh, R. (2007). Evidences of Early Human Occupation in the limestone Cave of Bastar, Chhattisgarh. *Curr. Sci.* 92 (6), 820.

Zanchetta, G., Regattieri, E., Isola, I., Drysdale, R. N., Bini, M., Baneschi, I., et al. (2016). The So-Called "4.2 Event" in the central Mediterranean and its Climatic Teleconnections. *Alpine Mediterr. Quat.* 29, 5–17.

Zanchetta, G., van Welden, A., Baneschi, I., Drysdale, R., Sadori, L., Roberts, N., et al. (2016). Multiproxy Record for the Last 4500 Years from Lake Shkodra (Albania/Montenegro). *J. Quat. Sci.* 27, 780–789. doi:10.1002/jqs.2563

Conflict of Interest: The authors declare that the research was conducted in the absence of any commercial or financial relationships that could be construed as a potential conflict of interest.

frontiers
in Earth Science

ORIGINAL RESEARCH
published: 07 December 2021
doi: 10.3389/feart.2021.712443

Reconstructing 1200 years of Hydroclimate Variability in the Southern Margins of the Arabian Desert: Insights From a Paleo-Lake in Southern Yemen

Shah Parth[1]*, *James Russell*[2] and *Nicolas Waldmann*[1]

[1]*Dr. Moses Strauss Department of Marine Geosciences, Charney School of Marine Sciences, University of Haifa, Haifa, Israel,* [2]*Department of Earth, Environmental and Planetary Sciences, Brown University, Providence, RI, United States*

Edited by:
Davide Tiranti,
Agenzia Regionale per la Protezione Ambientale (ARPA), Italy

Reviewed by:
Priyeshu Srivastava,
University of São Paulo, Brazil
Steven L. Forman,
Baylor University, United States

***Correspondence:**
Shah Parth
pds.shah121@gmail.com

Specialty section:
This article was submitted to Quaternary Science, Geomorphology and Paleoenvironment, a section of the journal Frontiers in Earth Science

Received: *20 May 2021*
Accepted: *19 November 2021*
Published: *07 December 2021*

Citation:
Parth S, Russell J and Waldmann N (2021) Reconstructing 1200 years of Hydroclimate Variability in the Southern Margins of the Arabian Desert: Insights From a Paleo-Lake in Southern Yemen. Front. Earth Sci. 9:712443. doi: 10.3389/feart.2021.712443

The climate of the Arabian Desert is not well documented during the past two millennia due to the scarcity of continuous and well-dated terrestrial archives in the region. Reliable interpretation from the climatic records from this region are pivotal for identifying periodicities of inter-annual to multi-decadal variability and trends driven by shifts in position of the Intertropical Convergence Zone (ITCZ) and the strength of the monsoons. A high-resolution multiproxy approach is presented for a ~3.3 m composite core, GBW, from a karst lake located in Ghayl ba Wazir, southern Yemen. Sedimentary proxies, including particle size distribution, coupled with magnetic susceptibility (MS) and geochemistry (XRF), provide a comprehensive picture of sediment depositional changes that may be linked to climate and environmental variability over the southern Arabian Desert. The chronology of the GBW core is provided by five radiocarbon (^{14}C) dates from terrestrial macrofossils (wood and twigs) extracted from sediment samples and indicates the core extends to ~900 CE. Our data indicates generally wetter conditions from 930 to 1400 CE corresponding to the "Medieval climate anomaly (MCA)" followed by arid phases during 1,410–1700 CE coinciding with the "Little Ice Age (LIA)". Evidence for a drier LIA include high authigenic calcium precipitation [Ca/(Al + Fe + Ti)], decreased TOC/TIC values, and gypsum precipitation, whereas the wetter MCA is characterized by higher detrital element ratios (Ti/Al, K/Al, Rb/Sr), and increased TOC/TIC and deposition of finer sediments (EM1). Furthermore, end-member mixing analyses (EMMA) derived from the grain-size distribution (EM2 and EM3) corroborates the deposition of coarser silt sediment through wind erosion and production of carbonate sand during the LIA concurrently with low lake levels under generally dry conditions. Aridity during the LIA is consistent with evidence and theory for weakened boreal summer monsoons during intervals of northern hemisphere cooling.

Keywords: lake sediment, paleoclimate, late holocene, Indian Summer Monsoon, XRF, Yemen, medieval climate anomaly, little ice age

INTRODUCTION

Large sub-tropical desert belts on Earth are formed due to a drastic decline in the distribution of rainfall that results from changes in atmospheric circulation (Edgell, 2006; Warner, 2009). Continuous terrestrial records located near desert margins (e.g., lacustrine, fluvial, cave and aeolian) have provided valuable insights into past climate and hydrological changes, which were often linked to fluctuations in the strength and latitudinal penetration of the summer monsoons (Singhvi and Kar, 2004; Sinha et al., 2006; Lespez et al., 2011; Wassenburg et al., 2016, among others). Lacustrine sediments, in particular, have provided valuable paleoenvironmental records from these regions (Abbott et al., 1997; Davies, 2006; Andersson et al., 2011) as they combine continuity with very high resolution. However, such records are only partially preserved or totally missing in the mid-and low-latitude desert belts.

Lakes situated near major global atmospheric circulation systems are likely to be highly susceptible to subtle changes in climate over time. The Arabian Peninsula is one of these locations as its northern areas are impacted by the Northern Westerlies Wind belt, while the southern margins are influenced by the Indian Summer Monsoon (ISM) circulation, with the latter linked to latitudinal changes in the Inter-Tropical Convergence Zone (ITCZ) position (Staubwasser et al., 2002; Gupta et al., 2003). Mechanisms influencing the current precipitation in the SW margins of the Arabian Peninsula are linked to shifts in the Red Sea Trough (RST), which is a low-pressure semi-permanent active zone over the Red Sea that generates local convective rainfall (Farquharson et al., 1996; Al-ameri et al., 2014). However, the precipitation pattern in the region is also modulated by the ISM, which brings moisture towards the southern Arabian Peninsula associated with northwards migrations of the ITCZ (Rodwell and Hoskins, 1996; Enzel et al., 2015). Holocene climate reconstruction from Yemen shows significant changes in the hydrological balance, probably as a response to the magnitude of monsoonal precipitation over time (Davies, 2006; Lézine et al., 2010; Berger et al., 2012). However, the existing lacustrine records are of relatively low temporal resolution. Other records, such as isotope data from speleothems, have proved to be valuable archives of climate change at high resolution, although with less continuity (Shakun et al., 2007; Fleitmann et al., 2011; Van Rampelbergh et al., 2013).

Hemispheric to global reconstructions have shown that warmth during the last two millennium reached a peak during the Medieval Climate Anomaly (MCA; from ~950 to ~1350 CE; Gayo et al., 2012), followed by increased cooling conditions during the Little Ice Age (LIA; ~1,500 to ~1800 CE; Matthews and Briffa, 2005; Miller et al., 2012), and anthropogenic post-industrial warming (Levitus et al., 2001). In fact, these two climate intervals (MCA and LIA) are defined in terms of temperature changes in the northern hemisphere; however, the temperature shifts in sub-tropical and tropical regions probably triggered changes in the moisture balance, which in turn gauged the amount and intensity of precipitation (Trenberth et al., 2003). The causes for the MCA and LIA have been widely discussed and linked to natural mechanisms, including solar and volcanic forcing as well as anthropogenic processes such as land cover decrease (Shindell et al., 2001; Ruddiman, 2013; among others). However, disagreement continues on the exact timing of both MCA and LIA intervals, which appear desynchronized worldwide (Crowley and Lowery, 2000; Broecker, 2001; Neukom et al., 2019), with many studies pointing to profound differences in temperature and precipitation gradients (e.g., Cronin et al., 2010; Jomelli et al., 2016). For example, while tropical East Africa experienced arid conditions during the MCA due to weak East African monsoons (Tierney et al., 2011), drier conditions associated with a positive phase of the North Atlantic Oscillation (NAO) characterizes the southern Levant during the same interval (Toker et al., 2012; Kushnir and Stein, 2019). Thus, there is a need to increase information density from climate archives around the globe to produce a reliable dataset for understanding the mechanisms and modalities of these two climate systems (MCA and LIA). The current study aims to enhance our understanding of the impact of these two climate phases by exploring sub-tropical hydrologic changes recorded in Gayal el Bazal, a lacustrine sedimentary sequence from southern Yemen, and it's the relation with tropical monsoonal circulation.

STUDY AREA

Gayal el Bazal is located in the town of Ghayl Ba Wazir, at 85 m above mean sea level, in the southern part of the Hadhramwat province, between the base of the Jabal Hasusah mountain cliffs and the Arabian Sea (**Figure 1A**). The geology of the region includes the Ghabar Group, which consists of metamorphic to anchi-metamorphic units, namely sandstone, greywacke, conglomerate, rhyolite, and quartzite rocks (As-Saruri and Wiefel, 2012). The region is characterized by several karstic sinkholes developed as a result of the dissolution of gypsum and limestone units from the Cretaceous Rus Formation (Hehmeyer et al., 2002). Lake Gayal el Bazal has occupied one of these sinkholes until very recently when it was reduced to small residual pools (**Figure 1D**), likely resulting from human groundwater withdrawal and agriculture. Currently, the small lake area (0.1 km^2, **Figure 1C**) is utilized by local communities for agriculture, mainly tobacco and palm plantations. The hydrological balance of the Gayal el Bazal is primarily controlled by summer precipitation (with an estimated mean of ~56 mm/yr) that falls over the main feeding Wadi Huwairah watershed (**Figure 1B**) and by an unknown amount of groundwater infiltration from the local aquifers. This limited precipitation amount promotes conditions of extreme pluvial events, with flash floods leaving a dramatic effect on local social and economic sustainability (Llasat et al., 2010). As for the water output balance, evaporation accounts for the sole estimated water output with unknown rates.

The climate of the studied area is characterized by extremely hot and dry conditions, with a monthly average ranges from 40°C to 43°C during summer and 28°C–31°C during winter (Bakhlah and Hassan, 2012). A hyper-arid desert dominates the east and north of our site (Almazroui, 2012), while the south part is slightly more temperate due to the Arabian Sea proximity (Hadden, 2012). Some minimal moisture appears to pass

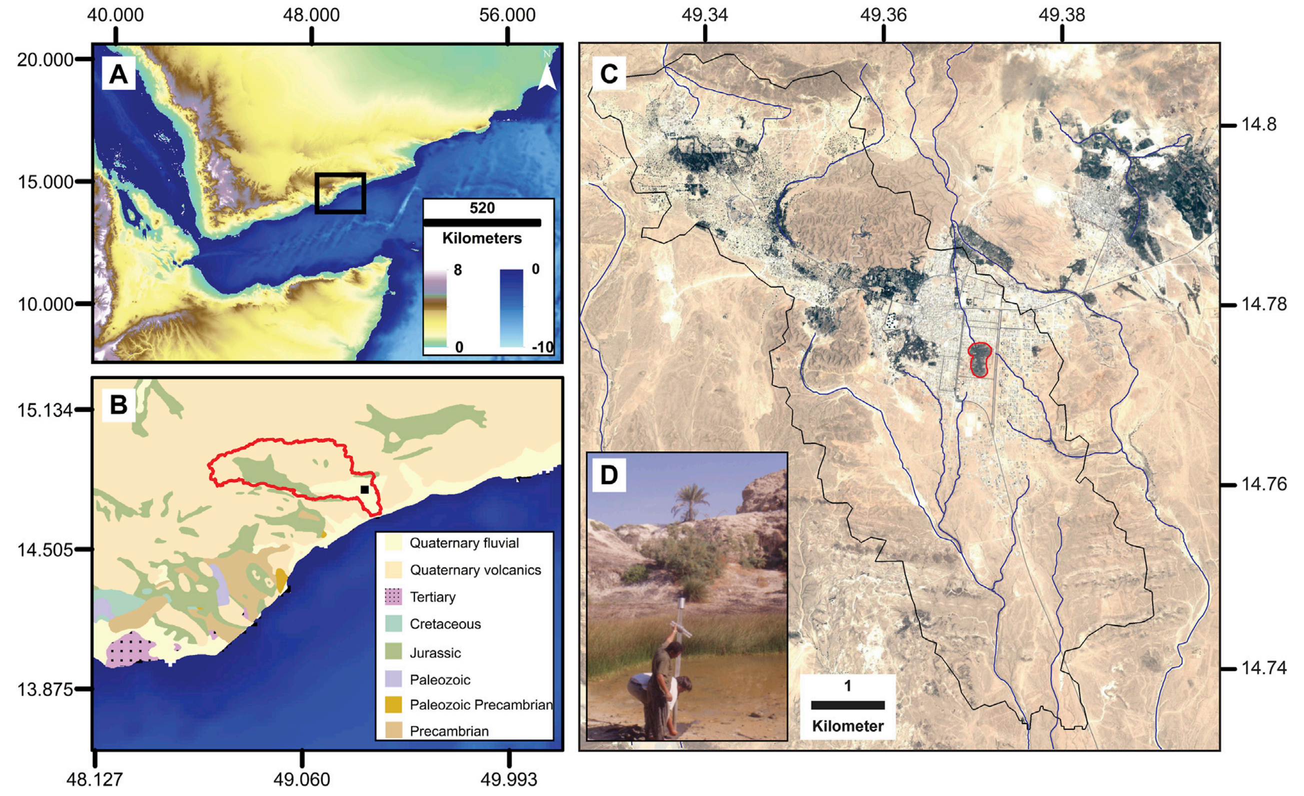

FIGURE 1 | (A) A SRTM 30 m elevation map of the SW part of the Arabian Peninsula with the studied area in Southern Yemen highlighted in a black square. **(B)** Geological map of the studied area marked in (a), highlighting the Wadi Huwairah watershed (red polygon) and the location of Gayal el Bazal (black square) (modified after Pollastro et al., 1999). The black square stands for the Gayal el Bazal area. **(C)** Detailed map of the Gayal el Bazal area. Black polygon marks the Gayal el Bazal Lake watershed with the riverine network system. The lake location is marked by a red polygon (Google Earth image, 2004). **(D)** Field photograph showing lake setting and core collection using Livingstone piston corer.

across the Hadhramaut Mountains to the north (that reach ~1,300 m) as a consequence of local orographic uplift and to reach the Arabian Desert, although the rates of this humidity are mostly unknown (Fleitmann et al., 2007). Most of the seasonal precipitation (~60%) over the region of Gayal el Bazal occurs during the spring months of March-April-May (MAM) through RST (**Figure 2B**; Baseer et al., 2019). During the summer season June-July-August (JJA), the moisture (~30%) is contributed by the ISM (**Figure 2C**; Fleitmann and Matter, 2009), and limited moisture is provided in the form of the winter season as a result of increasing outbreaks of North Westerly (NW) circulation (**Figure 2D**; Hasanean and Almazroui, 2015).

MATERIALS AND METHODS

Sample Collection

Three sites were cored in the Gayal el Bazal paleo-lake system aiming to retrieve a spatial coverage of the different sedimentary facies. The cores named Yemen-GBW01-2A (IGSN: CDR0000GK), Yemen-GBW01-2B (IGSN: CDR0000GL), Yemen-GBW01-3B (IGSN: CDR0000GM) were retrieved during a field campaign in December 2001 using a Livingstone piston corer, and cores measured 271, 95, and 108 cm (respectively) and were transported to the LacCore repository facility in Minnesota (United States) for curation and preservation.

Lab Measurements

Once in the lab, the cores were submitted to a set of non-destructive measurements, including magnetic susceptibility using a Bartington loop mounted to a Geotek multi-sensor core logger at a 5 mm (2.5 mm up and down) resolution and the data smoothed over 50 data points. Following this step, the cores were cut lengthwise into two halves (working and archive). While the archive halves were used for lithological description, imaging, and measurement of the elemental content using an ITRAX µX-Ray Fluorescence (XRF) core scanner, the working halves were used for destructive measurements (physical sampling). XRF measurements were done at a 0.5 cm resolution with the Cr and Mo tubes for identifying lighter and heavier elements, respectively (Croudace et al., 2006). The scanner generates element-related X-ray fluorescence peaks, and intensity is expressed in counts per second (cps), reflecting each given elemental concentrations (Löwemark et al., 2011; Rothwell, 2015; Chawchai et al., 2016). A semi-

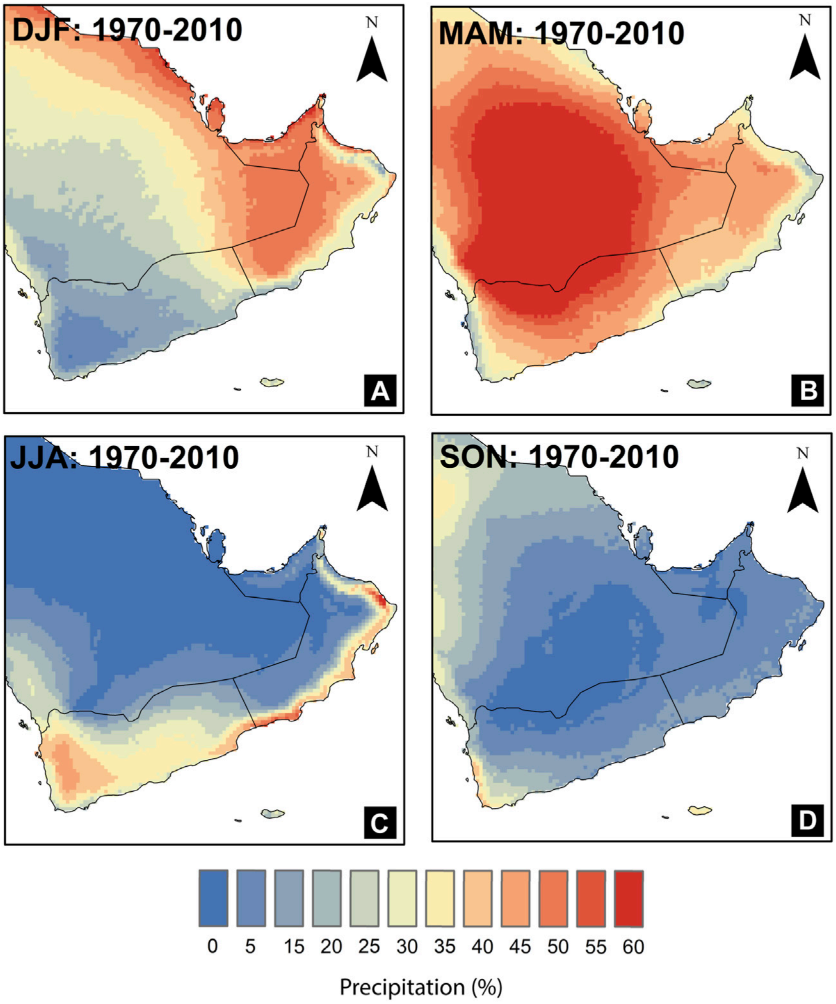

FIGURE 2 | The proportion of rainfall (1970–2010) by seasons: **(A)** winter (Dec-Feb), **(B)** spring (Mar-May), **(C)** summer (Jun-Aug), and **(D)** fall (Sept-Nov) (Source: WorldClim 2021).

quantitative analysis of the elements can be performed by normalizing element counts with total counts or Al to make a better comparison within intervals. Considering the parameters used during the XRF measurements, Al counts were reliable and were selected for normalization.

X-ray diffraction (XRD) measurements were carried out using a Rigaku Miniflex X-ray Diffractometer for the mineralogical study of the sediments. The mineral identification was carried out using PDXL 2 software, which uses a profile- and peak-based search approach based on detailed peak information. The quantitative analysis using reference intensity ratio determined the relative abundance of individual minerals.

Further destructive measurements include total inorganic and total organic carbon (TIC and TOC, respectively) at a ~3 cm resolution using a Skalar Primacs Series Total carbon analyzer. The samples were freeze-dried, weighed, and homogenized before the measurement. TIC was determined by acidification in the IC compartment at low temperature (100°C), which releases CO_2 to measure the abundance of inorganic carbon in the sediments. For TOC, dried sediments were treated with 1N HCl in order to remove carbonates, followed by heating the sample in the TC compartment at 700°C in the presence of pure Oxygen resulting in CO_2 releasing and generation of the abundance of organic carbon in the sediments.

Granulometric analysis was conducted using a Beckman Coulter LS 13 320 mw laser diffraction particle size analyzer on the same sampling resolution (~3 cm; n = 139). The sediments were pretreated with 10 ml H_2O_2 (30%) for organic matter removal and followed by acidifying using 1N HCl for removal of carbonate from the sediments (Murray, 2002; Vaasma, 2008). The solution containing digested sediments was washed with distilled water several times to remove the extra oxidizing reagents. The solution was homogenized with an ultrasonic bath prior to measurement. The grain size distribution was calculated for 100 grain size classes (particles sizes between 0.04 and 2000 μm), and the analytical error was less than 1%.

The chronology was established using AMS radiocarbon (^{14}C) dating carried out at Poznań Radiocarbon Laboratory, Poland, on

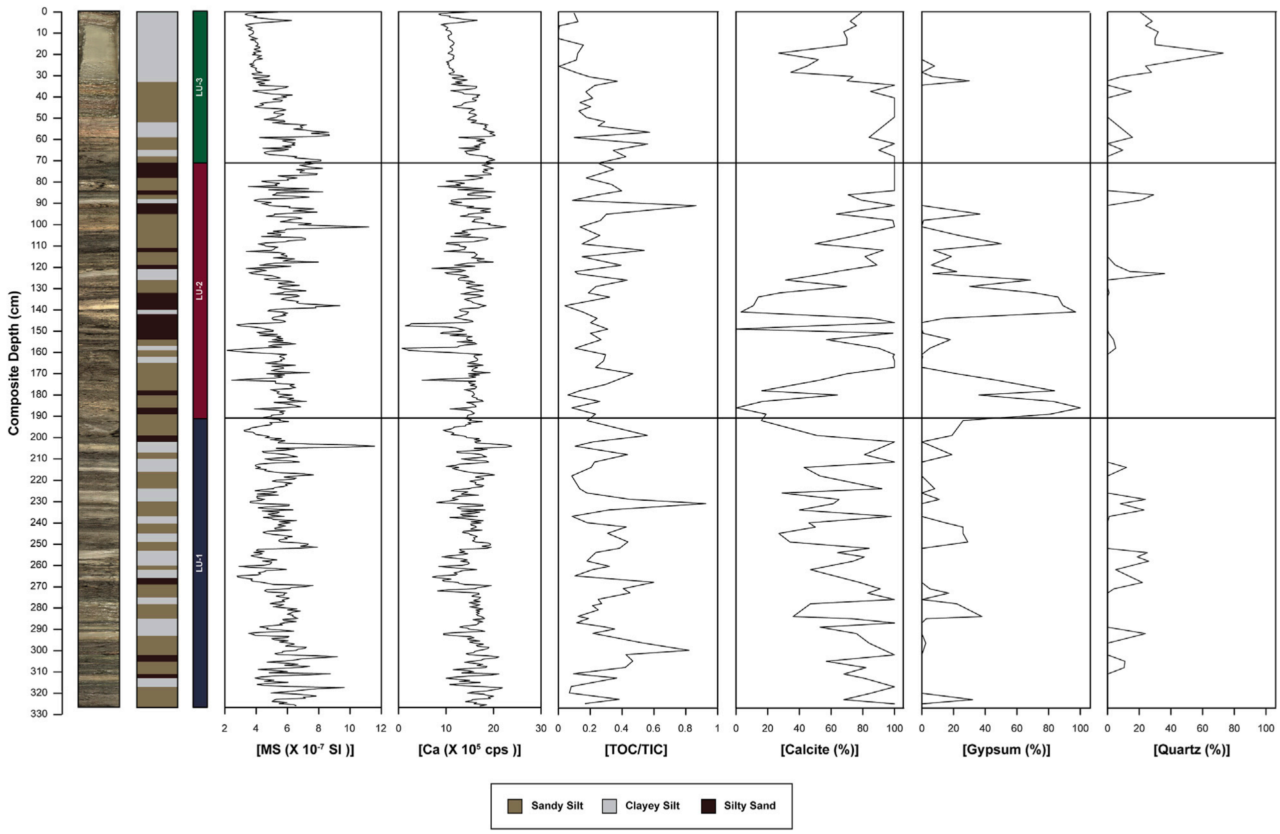

FIGURE 3 | The lithology of Gayal el Bazal sediment core showing the magnetic susceptibility (MS), the XRF (Ca counts), the XRD data (calcite, gypsum and quartz abundance), and TOC/TIC values.

wood and plant remains. Samples were selected from 5 different layers representing the whole composite core and weighed between ~5—15 mg for sufficient precision of ^{14}C dating. The raw AMS radiocarbon dates were calibrated using the OxCal program (Bronk Ramsey, 2009) with the most recent IntCal20 calibration curve (Reimer et al., 2020).

Statistical Approaches

For XRF data interpretation, a statistical approach was applied to understand possible grouping and disentangle complex signals out of the dataset. Further statistical analyses of the data [such as calculation of the principal component analysis (PCA)] were carried out using princomp function in R-Studio software (Mardia et al., 1979; Venables and Ripley, 2002). PCA is an important tool used for reducing the multivariate data into fewer dimensions and can help aid the interpretation of multiple elements. PCA transforms an original set of N-variables into a new set of N-principal components, which are orthogonal to each other (Xue et al., 2011). Each component is weighted in light of a linear combination of the original variables.

End-member mixing analysis (EMMA) was applied on the grain size parameters to understand the sediment mixtures in a series of sedimentary components (end members) reflecting the transport mechanisms and sediment sources (Dietze et al., 2012, 2013; Mishra et al., 2019). End member mixing analysis is a statistical tool that can disentangle the modes of transport of the sediments from polymodal particle size distribution (Weltje, 1997). The number of modes of transportation was selected based on a best-fit model for grain size distribution, representing the relation between the number of end members and the coefficient of determination (r^2). After optimizing all the parameters (n, q, l), the statistical analysis was performed using EMMA function based on *EMMA*geo-package, in R-language (Dietze et al., 2012).

RESULTS

Stratigraphy and Lithology

A composite core record was generated based on correlation of the different cores sequences and through a detailed identification of the same lithology units and layers in all sections. The composite core GBW reaches 3.26 m in length, and three different lithological units are established (LU-1 to LU-3) and distinguished by distinct sedimentary facies (**Figure 3**).

- *Unit LU-1* (326–191 cm) is characterized by clayey silt and sandy silt beds separated by minor erosional contacts. The

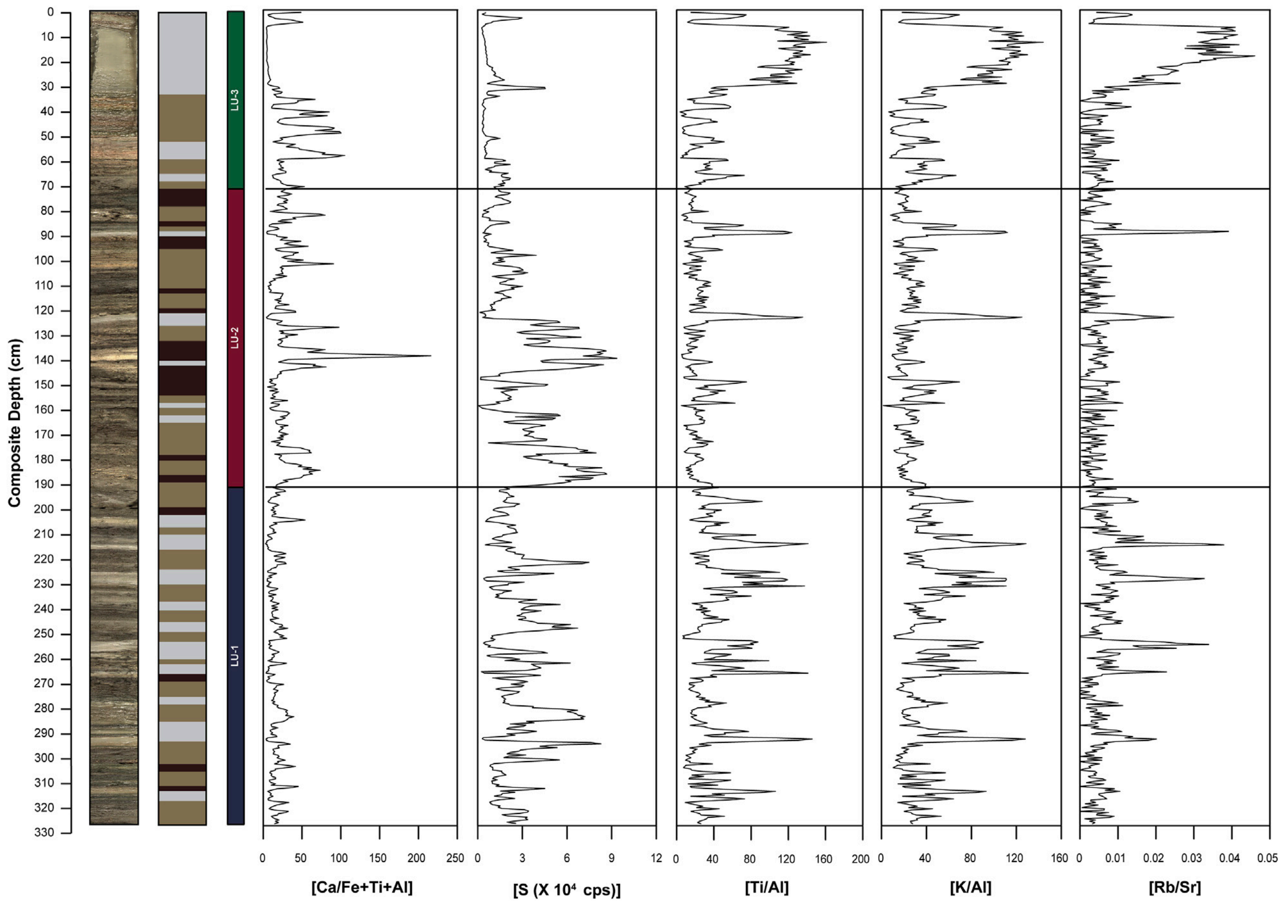

FIGURE 4 | Major XRF data presented in the paper and compared with a high-resolution core image of GBW. The elemental variability of Ca/(Al + Fe + Ti), S counts, Ti/Al, K/Al, and Rb/Sr is shown (see text for more details).

mineralogical composition is dominated by calcite which is the most abundant mineral (range 16–100%), followed by gypsum (0–38%) and quartz (0–26%). There are increases in quartz minerals at 217–208 cm, 267–250 cm, and 295–286 cm intervals; **Figure 3**. The MS values in LU-1 range from 2.78 to 11.57 × 10^{-7} SI and average ~5.46 × 10^{-7} SI. MS decreases at 326–265 cm and 251–224 cm and increases from 205 to 200 cm, where the highest values are observed for this unit (**Figure 3**). The Ca abundance displays a similar pattern or curve with MS values for those intervals (r = 0.93; **Figure 3**). TOC/TIC content in the LU-1 unit varies between 0.07 and 0.92, with higher values of TOC/TIC in specific layers (217–208 cm, 237–222 cm, 267–250 cm, and 295–286 cm) (**Figure 3**).

- U*nit LU-2* (191–71 cm) is marked by silty sand and sandy silt and the appearance of gypsum. The sediments in the unit mainly contain calcite (0.4–100%) and gypsum (0–100%) abundance minerals with a trace amount of quartz (0–36%). The MS values range from 2.5 to 11.2 × 10^{-7}SI with an average of 5.7 × 10^{-7}SI, and higher values are for intervals from 102 to 99 cm, 136–139 cm. The higher value of MS is also marked by higher values of Ca counts, coarser grain size (silty sand layers), and increased gypsum abundance (**Figure 3**). TOC/TIC values range from 0.04 to 0.86 and average 0.25 in the LU-2 unit. Lower TOC/TIC are observed for intervals 98–93 cm, 146–126 cm, and 191–174 cm (**Figure 3**). The LU-2 unit is also marked by deposition of clayey silt sediments at 90.5–87.5 cm and 125–121 cm (**Figure 3**).
- *Unit LU-3* (71–1 cm) consists of clayey silts and sandy silts with abundant quartz compared to the rest of the sequence. Specifically, the interval 29–1 cm is marked by a clayey silt bed with increased quartz mineral for that interval (**Figure 3**). The MS values fluctuate from 3.3 to 11.2 × 10^{-7} SI and average ~5.34 × 10^{-7} SI. Lower values of MS are observed from interval 29–1 cm (**Figure 3**). TOC/TIC content in this unit varies between 0.23 and 0.57 and showing lower values of TOC/TIC are observed from 63 to 50 cm (**Figure 3**).

Geochemistry and Statistical Analysis

XRF analyses document considerable variations in the counts for major elements like Al, Si, S, Cl, K, Ca, Ti, Mn, Fe, Sr and minor elements like Rb and Zr, which we interpret to reflect

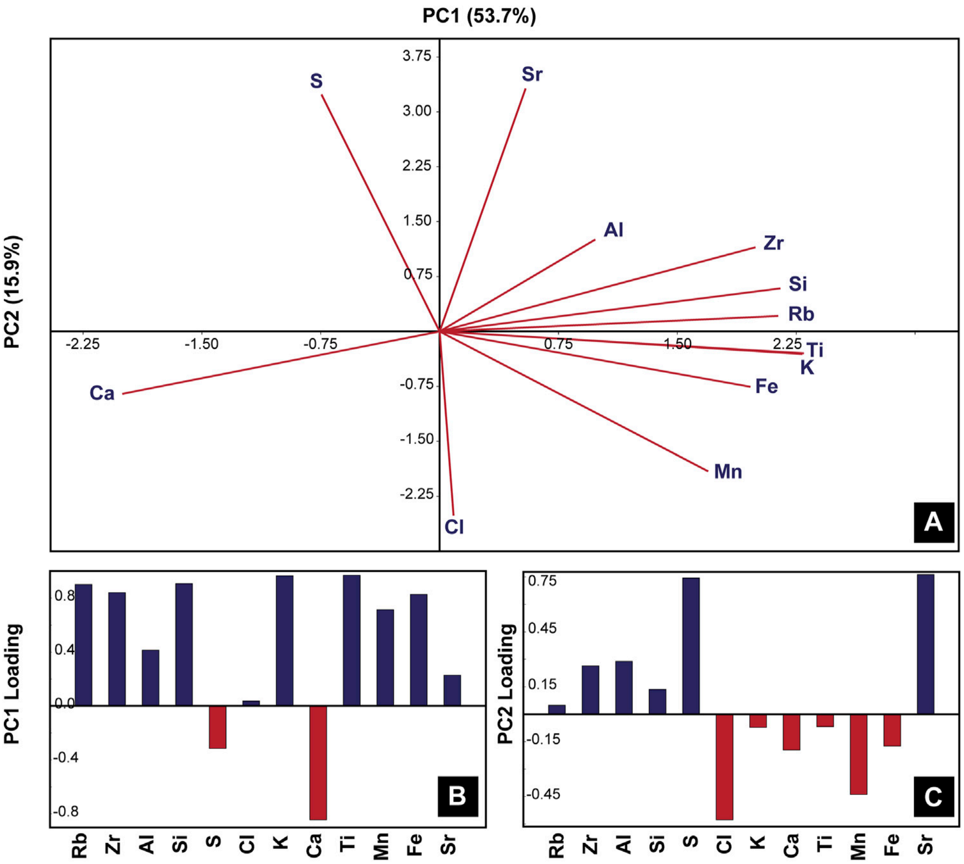

FIGURE 5 | Statistical analyses of the XRF data. **(A)** Principal Component Analysis (PCA) and biplot between PC1 and PC2 showing the geochemical parameters of composite core GBW. **(B)** Loadings of principal components (PC1) derived from elemental data. **(C)** Loadings of principal components (PC2) derived from elemental data.

relative abundance changes. Element abundance and ratios like Ca/(Al + Fe + Ti), S counts, Ti/Al, K/Al, and Rb/Sr show significant variability through the whole GBW composite core (**Figure 4**). The element ratios like Ti/Al, K/Al, and Rb/Sr exhibits similar stratigraphic patterns. Unit LU-1 records the higher values of Ti/Al, K/Al, and Rb/Sr from 217 to 208 cm, 237–222 cm, 267–250 cm, and 295–286 cm (**Figure 4**). Unit LU-2 also shows sharp spikes in Ti/Al, K/Al, and Rb/Sr from 90.5 to 87.5 cm and 125–121 cm (**Figure 4**). However, Ca/(Al + Fe + Ti) sharply increases at 98–93 cm, 146–126 cm, and 191–174 cm and higher values of S counts from 126 to 146 and 162–191 (**Figure 4**). In Unit LU-3, Ti/Al, K/Al, and Rb/Sr increases from 35 to 1 cm. Additionally, Ca/(Al + Fe + Ti) shows increase trend interval between 59–34 cm (**Figure 4**).

The principal component (PC) analysis reveals two components explaining ~69% variability in the dataset (**Figure 5A**). PC1 receives positive loading from Ti, K, Fe, Si, Rb, Al, and Zr and negative loading from Ca (**Figure 5B**). The PC2 has positive loading from S and Sr but negative loading from Cl (**Figure 5C**). The biplot of PC1 and PC2 shows elements like Ti, K, Fe, and Rb are oppositely associated with Ca, Sr, and S (**Figure 5A**).

Grain Size Distribution and Statistical Approach

The clastic grain size distribution of the GBW composite core is largely characterized by silt with minor variations of sand and clayey silt fractions. The mean grain size of the core ranges from 3.1 to 7.1 ϕ and the coarsest grain size fraction is found at 152–144 cm and finest fraction at 260 to 253 cm (**Figure 6**). The overlay of all grain size data from all samples revealed a polymodal distribution, and hence end-member analysis has been applied. The EMMA of grain size distribution in GBW core yielded an optimal model with five end members and explained 65% variability of the total dataset. End member 1 (EM1) represents the finest particle fraction in the core with the dominant modal grain size of 7.1 and is in the range of clayey silt. For EM2, the dominant modal grain size is 4.8 and lies in the range of medium to coarser silt. Furthermore, EM3 (mode = 3.2 ϕ), EM4 (mode = 1.4 ϕ) and EM5 (mode = 0.65 ϕ) are in the range of fine, medium and coarse sand, respectively. Unit LU-1 is marked by the increased relative abundance of EM1 from 216 to 209 cm and 269–265 cm and a higher abundance of EM2 between 278–276 cm and 305–296 cm (**Figure 6**). Unit LU-2 represents higher contribution from EM3, EM4 and EM5 for

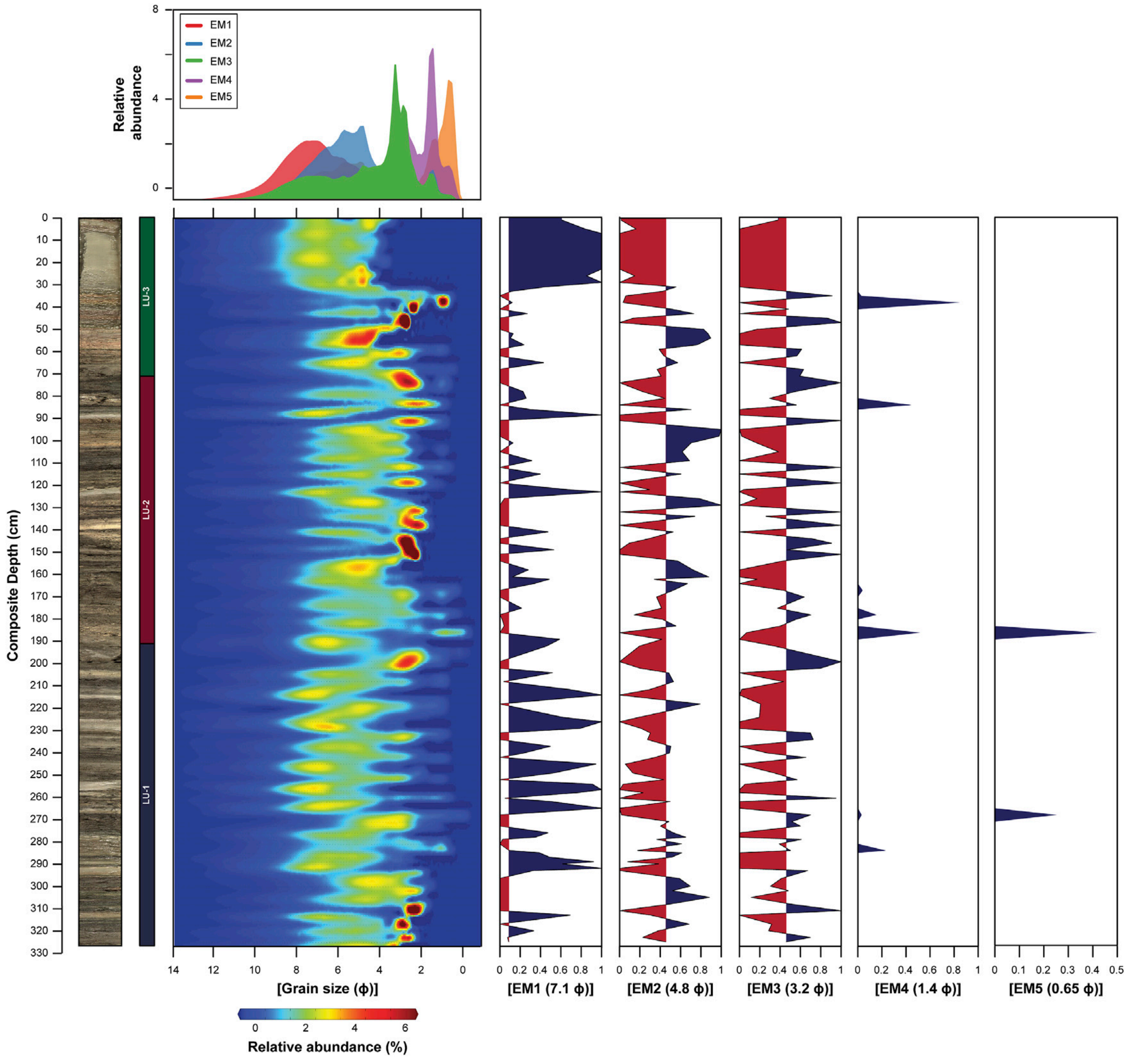

FIGURE 6 | Overlay of the grain size distribution of all samples and particle distribution through down-core sediments and five end members with their relative abundance plotted against the composite depth.

intervals ~86–84 cm, 175–167 cm, 180–178 cm, 189–186 cm and significant contribution from EM2 for 109–95 cm, ~118–115 cm, ~129–126 cm, and 161–158 cm (**Figure 6**). Unit LU-3 has pronounced contribution from EM1 from 29 to 1 cm and EM2 from 57 to 50 cm. For EM3, EM4, and EM5, representing coarser particle size fractions are higher for 41–35 cm in the unit (**Figure 6**).

Chronology

The age model for GBW is based on five accelerator mass spectrometry (AMS) radiocarbon dates on terrestrial fragments (wood, twig, and plant remain) picked from intervals 62, 112, 157, 242, and 325 cm depth of the GBW composite core. The radiocarbon dates can also be affected by the reservoir effect, which can skew results such that older radiocarbon ages can appear than the equivalent age of the sample (Philippsen, 2013). However, in the GBW composite core, radiocarbon ages are based on the most reliable material, including terrestrial macrofossils (short-lived twigs remains) for younger sediments in the lake (Marshall et al., 2007). Calibration of obtained ^{14}C dates was done with the IntCal20 calibration curve (**Table 1**; Reimer et al., 2020), and the age-depth model was carried out using a Poisson process model deposition (P_Sequence; Ramsey, 2008) (**Figure 7**).

DISCUSSION

Variability of Allochthonous vs Autochthonous Depositional Patterns in GBW

The elemental analysis documents a series of processes occurring in the lake environment, including changes in the origin and

TABLE 1 | Radiocarbon ages for the GBW core based on OxCal calibration (Reimer et al., 2020).

Composite Depth (cm)	*AMS ^{14}C (BP)*	*Calibrated ^{14}C (CE)*	*Error*	*Lab no*
62.5	200 ± 30	1768	30	Poz-127874
112.5	370 ± 30	1,565	30	Poz-120224
157.5	400 ± 30	1,481	30	Poz-127875
242.5	675 ± 30	1,326	30	Poz-120852
325.5	1,140 ± 30	914	30	Poz-120852

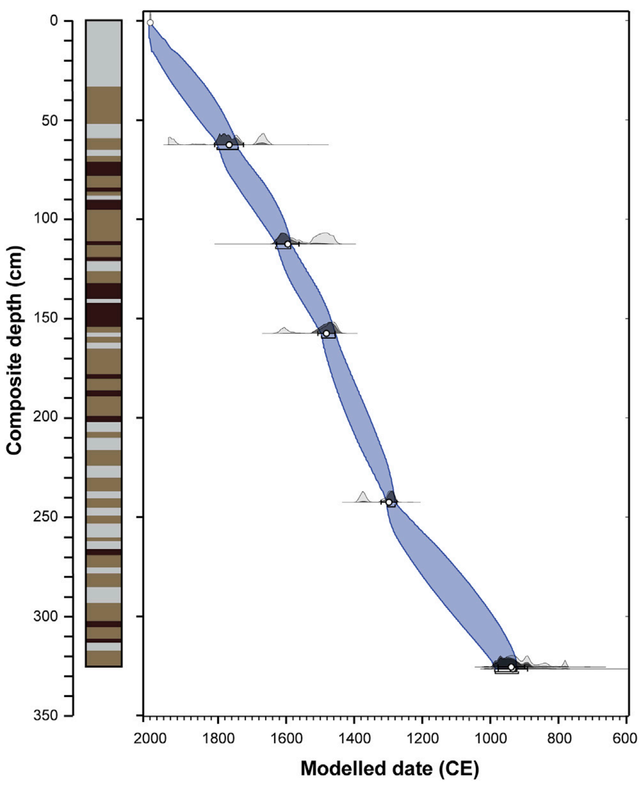

FIGURE 7 | Age-depth model for the GBW core with grey lines indicating confidence limits and blue curve showing age-depth interpolation.

provenance of particles (e.g., allochthonous vs autochthonous), oxidation/reduction conditions in the lake bottom, water velocities and depth variabilities through time (Engstrom and Wright, 1984; Zolitschka et al., 2002; Boyle, 2005; Weltje and Tjallingii, 2008; Löwemark et al., 2011). These can in turn, reflect changes in climatic and limnological conditions. We interpret that the inorganic geochemical compositions of the GBW core are primarily controlled by both allogenic processes (fluvial (wadi) discharge and aeolian input) coupled with authigenic processes (i.e. precipitation of evaporite minerals).

The statistical analyses of the elemental record (PC1) carried out on the XRF data show that Ti, K, Si, Rb, and Zr follow the same behavior, with elements like Mn and Fe partially following the same positive axis (**Figures 5A,B**). Previous studies carried out on similar settings points that Ti and K are geochemically stable lithogenic elements, which are hosted by resistant minerals and are conservative in most geochemical environments, and thus reflect detrital input into the lake (Boës et al., 2011). Changes in the concentration of Ti and K can be related to either stronger catchment runoff, which reflects wetter conditions, or enhanced aeolian deposition, hence a low precipitation regime (Hou et al., 2017). In the studied core, we observe a direct association of Ti and K with the clayey silt or finer fraction (EM1) of the sediment (r = ~0.78, **Figure 8**) and hence these elements probably represent detrital origin. Many studies done in lakes dominated by the siliciclastic type of sedimentation have shown that Fe and Mn can originate from detrital input and catchment runoff, though they can often be related to redox conditions in the sediment/water interface (Davison, 1993). Therefore, interpretation of their temporal behavior in the depositional system should carefully be considered in light of variability occurring in the other measured elements. In GBW, PC1 data reveals that Fe is aligned with detrital elements (Ti, K); hence we estimate that it also represents an allogenic provenance (**Figures 5A,B**). Although many studies use Si to estimate diatom blooms (Schettler et al., 2006), which may occur during episodes of increase in nutrient input from aeolian transport or volcanoclastic materials (Peinerud, 2000) however, our statistical analysis shows a close association of Si with Ti and K, which is carried by the silicate fraction and may indicate a terrigenous source for Si (**Figures 5A,B**).

Rb appears to be associated with fine-grained siliciclastic rocks (Kylander et al., 2011). In our core, this element shows a positive correlation with Al and K (**Figures 5A,B**); hence can be used to measure the amount of siliciclastic material depositing in the basin. The Rb/Sr ratio is often associated with the chemical weathering of catchment rock and can be interpreted as the changes in fluxes of dissolved materials within from catchment (Miriyala et al., 2017). This behavior suggests positive loading on PC1 indicates detrital influx into the lake system. Ca is on the negative axis of PC1, and hence we estimate that it shows a non-detrital origin; therefore, it indicates authigenic processes occurring in the lake (**Figures 5A,B**) (Zhao et al., 2010). We, accordingly, suggest that the elemental ratios of Ti/Al, K/Al, and Rb/Sr (or PC1 score) are well suited for estimating changes in the terrestrial sediment supply through time and can hence be used to reconstruct past fluvial discharge (Neugebauer et al., 2016).

PC2 is defined by positive loading of Sr and S and negative loading of Cl (**Figure 5C**); hence this principal component appears to indicate *in-situ* precipitation of carbonates. Moreover, Ca indicates authigenic origin due to its negative loading with PC1 (**Figure 5B**) and has no major correlation with S and Sr (**Figure 5C**). However, there is a possibility of allogenic sources of Ca to the lake basin cannot be omitted, and could consist of both fluvial and aeolian origins. Detailed XRD

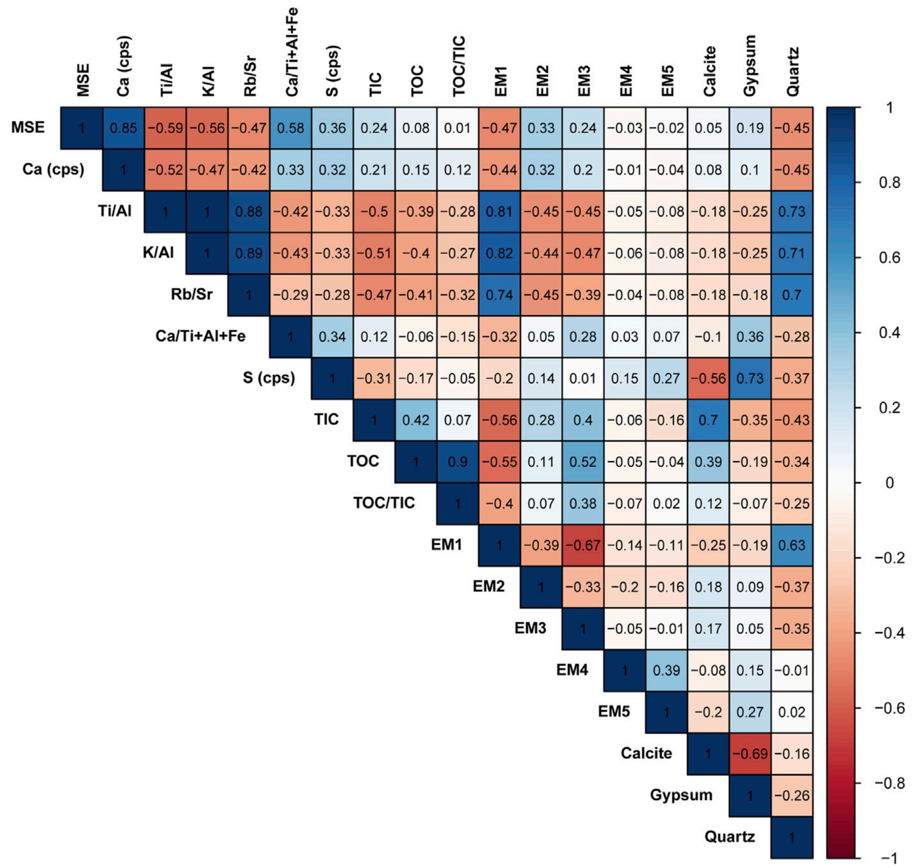

	MSE	Ca (cps)	Ti/Al	K/Al	Rb/Sr	Ca/Ti+Al+Fe	S (cps)	TIC	TOC	TOC/TIC	EM1	EM2	EM3	EM4	EM5	Calcite	Gypsum	Quartz
MSE	1	0.85	−0.59	−0.56	−0.47	0.58	0.36	0.24	0.08	0.01	−0.47	0.33	0.24	−0.03	−0.02	0.05	0.19	−0.45
Ca (cps)		1	−0.52	−0.47	−0.42	0.33	0.32	0.21	0.15	0.12	−0.44	0.32	0.2	−0.01	−0.04	0.08	0.1	−0.45
Ti/Al			1	1	0.88	−0.42	−0.33	−0.5	−0.39	−0.28	0.81	−0.45	−0.45	−0.05	−0.08	−0.18	−0.25	0.73
K/Al				1	0.89	−0.43	−0.33	−0.51	−0.4	−0.27	0.82	−0.44	−0.47	−0.06	−0.08	−0.18	−0.25	0.71
Rb/Sr					1	−0.29	−0.28	−0.47	−0.41	−0.32	0.74	−0.45	−0.39	−0.04	−0.08	−0.18	−0.18	0.7
Ca/Ti+Al+Fe						1	0.34	0.12	−0.06	−0.15	−0.32	0.05	0.28	0.03	0.07	−0.1	0.36	−0.28
S (cps)							1	−0.31	−0.17	−0.05	−0.2	0.14	0.01	0.15	0.27	−0.56	0.73	−0.37
TIC								1	0.42	0.07	−0.56	0.28	0.4	−0.06	−0.16	0.7	−0.35	−0.43
TOC									1	0.9	−0.55	0.11	0.52	−0.05	−0.04	0.39	−0.19	−0.34
TOC/TIC										1	−0.4	0.07	0.38	−0.07	0.02	0.12	−0.07	−0.25
EM1											1	−0.39	−0.67	−0.14	−0.11	−0.25	−0.19	0.63
EM2												1	−0.33	−0.2	−0.16	0.18	0.09	−0.37
EM3													1	−0.05	−0.01	0.17	0.05	−0.35
EM4														1	0.39	−0.08	0.15	−0.01
EM5															1	−0.2	0.27	0.02
Calcite																1	−0.69	−0.16
Gypsum																	1	−0.26
Quartz																		1

FIGURE 8 | A Pearson correlation matrix of elemental abundance and ratios, mineral abundance, different end members of grain size, MS, and TOC/TIC data of the GBW composite core.

measurements reveal that the GBW core contains calcite and gypsum, with the occasional appearance of quartz. The studies also show that calcite might constitute a major percentage of dust particles in the Arabian desert (Al-Dousari and Al-Awadhi, 2012; Al-Dousari et al., 2013). In general, Ca represents an arid environment; hence, to estimate the authigenic deposition of Ca, the ratio between Ca/(Al + Fe + Ti) might represent a reliable proxy of precipitation changes in the region (Mueller et al., 2009). Higher values of this ratio can imply an increase in lake water salinity coupled with lower runoff from the catchment, which might point to dry conditions. S counts show a good correlation with gypsum abundance (r = 0.73, **Figure 8**), and their down-core shifts in the sediment can be associated with lower lake levels or shallow water depths, indicating dry climatic conditions in the region.

Correlation of Magnetic Susceptibility, Total Inorganic Carbon/Total Organic Carbon With Elemental Proxies

The magnetic susceptibility (MS) properties of sediments are influenced by the presence of Fe-bearing ferromagnetic minerals and serve as a proxy to disentangle the abundance of paramagnetic and diamagnetic minerals, such as carbonates, quartz, and clays (Bareille et al., 1994; Schnurrenberger et al., 2003). Previous studies have shown that MS can be a reliable indicator of both external processes (e.g., weathering magnitude and volcanism) and internal chemical cycling in the lacustrine environment, particularly the oxidation state in the sediment-water interface that can influence magnetite dissolution or formation (Rawat et al., 2021). In GBW, MS values are relatively low (averaging ~5.6 × 10^{-7} SI) compared to carbonate rich lakes (Wünnemann et al., 2010; Pleskot et al., 2018), which can be associated to an increase in the presence of diamagnetic minerals or due to presence of negative magnetic susceptibility values of rocks in the catchment area (e.g. sandstone, greywacke, conglomerate, quartzite and carbonates). The MS values in the GBW sediments are mainly controlled by the minerals of Ca in the sediment as a high correlation is observed between Ca counts and MS values (r = 0.82, **Figure 3** and **Figure 8**). Our GBW core is highly enriched in calcite (a typical diamagnetic mineral) with frequent intercalations of gypsum (least diamagnetic mineral), and we find that the layers enriched by gypsum have relatively higher values of MS compared with those enriched by calcite (Ivakhnenko et al., 2015). Furthermore, studies have shown that sediment consisting of higher carbonate or organic matter can dilute the concentration of magnetic minerals, also leading to low MS values

(Hounslow and Maher, 1999). In several previous studies, MS values have been shown to increase with decreasing grain-size fraction (Thompson and Morton, 1979; Dessai et al., 2009). However, in GBW high values of MS are not necessarily associated with changes in the grain size distribution. The MS values are also lower for higher detrital influx events where quartz is found due to its diamagnetic properties, however it doesn't show any significant variation throughout the GBW core.

The Total Carbon (TC) budget of a lake is primarily controlled by chemical and biochemical processes associated with the balance between the water input and the evaporation of lake water (Håkanson and Jansson, 1983). TIC is primarily controlled clastic sediment input or precipitation/evaporation processes, depending on whether carbonate minerals are allogenic or authigenic. In turn, TIC can serve as a proxy for temperature and precipitation changes (Yanhong et al., 2007). We estimate that TIC values increases during drier conditions due to the increased carbonaceous dust influx as it correlates quite well with calcite mineral abundance (r = 0.7). Hence for those intervals, lower values of TOC/TIC reflect intervals with sandy silt units. TOC indicates the productivity of the lake, oxic state of the bottom waters and can also be used to track changes in the organic deposition conditions through the sedimentary sequence (Chen et al., 2001; Xu et al., 2007). The organic matter in the lake can be derived from the allochthonous input through catchment runoff or wadi influx and from autochthonous sources. However, in general, low productive lakes get the significant contribution of organic matter from the allochthonous terrestrial sources (Dean and Gorham, 1998). Hence, the primary source of TOC for the paleo-lake Gayal el Bazal is the terrigenous sediment supply during the relatively wetter condition in the region. The TIC and TOC data thus are complex to interpret due to uncertainty in the sources of these materials to the sediment through time. Nevertheless, the TOC/TIC data used in conjunction with other proxies (e.g., Ti/Al, K/Al, and Rb/Sr or PC1 score) provide information about different sedimentary processes, such as fluvial vs. aeolian input to the lake, and thus reflect rainfall changes. We further suggest that the high preservation conditions of the organic matter result from relatively fast burial processes, which in turn might indicate deposition during intense floods.

Deposition and Transport Mechanism of Sediments

The depositional patterns of lake sediment are controlled by sediment transport mechanisms such as fluvial inflows, aeolian transport, and turbid inflows (Solohub and Klovan, 1970; Sly, 1994; Lou et al., 2000; Stuut et al., 2002). These different transport mechanisms and depositional conditions can yield high variability in grain size distribution and grain morphology (e.g., sphericity and roundness; Håkanson and Jansson, 1983; McLaren and Bowles, 1985; Sun et al., 2002; Last, 2005; Vandenberghe, 2013). Processes like these can create complex distributions in the particle size variation; thus, disentangling the sources is a must. To un-mix the modes of deposition into the lake system, end-member mixing analysis (EMMA) is applied to provide meaningful end members associated with various depositional processes. This approach, applied on the GBW core, resulted in five particle populations of modes attributed to different transport mechanisms. EM1 is the finest grain size fraction (7.1 ϕ), which a large majority falls under the clayey silt class and reflects the fluvial or *wadi* influx into the lake. Previous studies have shown that during pluvial events in arid environments, clayey silt is deposited in the basin, mostly due to surface runoff (Lézine et al., 1998, 2007). Furthermore, heavy elements (e.g., Ti, K, and Rb) and PC1 score are closely associated with EM1 variation, which are introduced to the basin also through surface runoff (r = ~0.8; **Figure 8**). Hence, finer fraction EM1 along with other proxies (detrital elements and PC1) are interpreted as increased precipitation in the region. EM2 consists of medium to coarse silt (4.8 ϕ) and reveals the aeolian mode of transport of sediments into the basin. It is consistent with available records showing that the southern Arabian Peninsula is highly influenced by aeolian processes (Khalaf and Al-Hashash, 1983; Al-Dousari et al., 2013). The greater abundance of EM2 reflects coarser aeolian dust advected from proximal sources, as it is larger in size than the dust particles from distal source (Crouvi et al., 2008). EM3 is situated around a fine sand fraction (3.1 ϕ) which would have formed due to the lowering of lake level or shallow near the shore. Hence, this end member, along with increased authigenic Ca precipitation (Ca/(Al + Fe + Ti)) in the lake, represents dry episodes with shallow water conditions, characterized by higher hydraulic energy conditions and deposition of coarser sediments in the lake. The greater abundance of EM3 is attributed to lower lake stands that probably resulted from periods of increased aridity and decreased water supply from the wadi catchment. EM4 (mode = 1.4 ϕ) and EM5 (mode = 0.65 ϕ) represent the coarsest sediment fraction and indicate extreme erosional events. Those intervals with a high abundance of EM4 and EM5 are followed by a higher abundance of EM1 (clayey silt). Hence we suggest that these two end members are indicative of coarser erosional material from the catchment.

Unraveling the Medieval Climate Anomaly and Little Ice Age in Yemen

The sedimentary record from the GBW core reveals the past 1,200 years' climatic changes in the southern Arabian Peninsula and is divided into three stages based on the down-core variation (**Figure 9**).

Unit LU-1 (~920–~1400 CE)

Unit LU-1 is dominated by detrital influx to the lake, as is marked by a higher PC1 score and an increase in TOC/TIC interpreted as resulting from augmentation in catchment runoff during pluvial episodes (**Figure 9**). The intervals from 930–1000 CE, 1,060–1110 CE, 1,140–1200 CE, 1,220–1280 CE, and ~1,330–1400 CE are sustained periods of wetness as represented by increased catchment erosion and augmentation of the clayey silt fraction (EM1 score) (**Figure 9**). These periods coincide with the Medieval Climate Anomaly (MCA; ~900–1350 CE; Gayo et al., 2012), which is an interval characterized by a shift in atmospheric circulation in the northern hemisphere that has left signals in sedimentary archives around the globe (Graham et al., 2011;

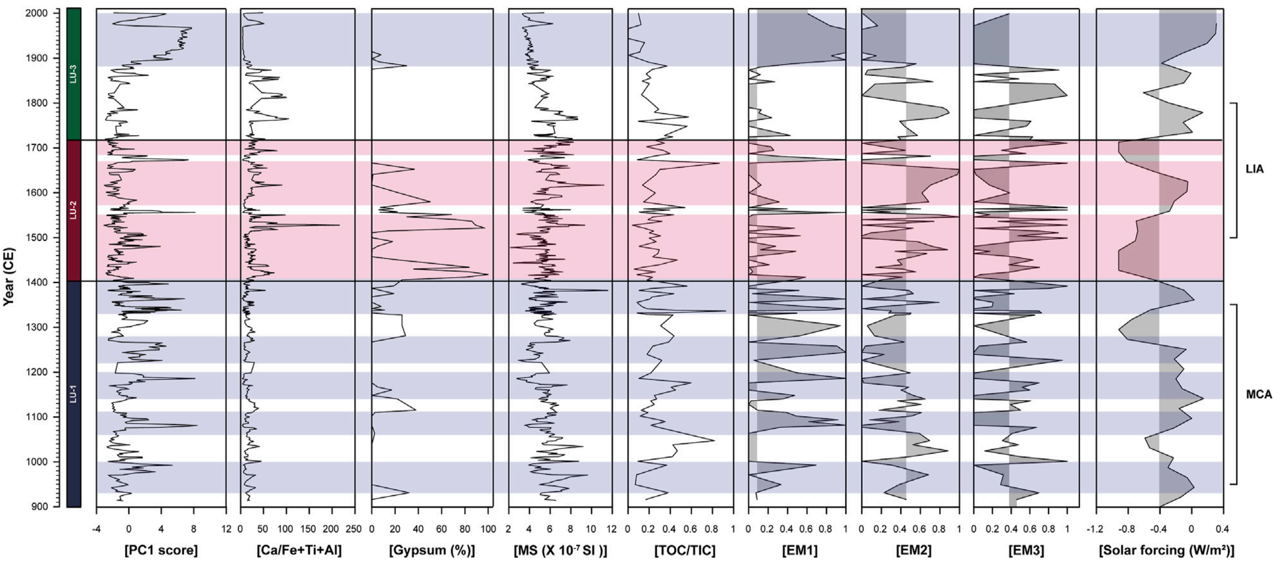

FIGURE 9 | Multiproxy data obtained from Gayal el Bazal from 900 CE to 2000 CE showing three units (marked by blue and red stripes) indicating wet and dry intervals, respectively (Steinhilber et al., 2012).

Lüning et al., 2018). The synchroneity and extent of the climate pattern during this period are debated (Mann et al., 2009), yet it is widely recognized as a relatively warming interval in the northern hemisphere. However, it appears that the MCA interval in our record does not uniformly represent wet conditions but shows the inception of a major wet interval probably associated with increase warmth and humid conditions. Enhanced precipitation in the region during the MCA is consistent with regional records (Gupta et al., 2003; Fleitmann et al., 2004). The possible causes of the MCA are debatable as different forcing mechanisms, such as solar, volcanic, greenhouse gases, and land cover/use changes, occurred individually, and their combination all likely influenced this climatic shift. The simulation provided by Community Earth System Model-Last Millennium Ensemble (CESM-LME) captures globally warmer conditions during the MCA due to weaker volcanic forcing relative to radiative forcing that characterized the Little Ice Age (LIA; ~1,500–1800 CE, Otto-Bliesner et al., 2016). Fluctuations in the regional climate during the MCA can also be attributed to changes in the intensity of solar irradiance and thus inducing enhanced wet conditions in the region, which led to an increase in the input of allogenic materials into the lake (**Figure 9**). We estimate that this anomaly could have been triggered by the northward migration of the ITCZ linked to increased solar forcing (Broccoli et al., 2006; Kuhnert and Mulitza, 2011), which led to an increase in humidity in the southern margins of the Arabian Peninsula during the MCA.

Unit LU-2 (~1,400–1720 CE)

The LU-2 unit is defined by increased Ca/(Al + Fe + Ti), gypsum abundance, and higher EM2 abundance, which we believe represent an increase in the evaporite formation and aeolian influx to the lake basin. During 1,410–1450 CE, 1,500–1580 CE, and 1,640–1690 CE, higher values of Ca/(Al + Fe + Ti) and increased abundance of gypsum indicate periods of decline in lake level, which exemplify for dry climatic conditions in the region (**Figure 9**). In fact, the EM2 abundance from 1,430 to 1670 CE significantly increases due to drier conditions. These dry episodes appear to prevail during the LIA when coarser silt sediments were brought into the lake and were consequently winnowed under lower lake levels. Aridity during the LIA is consistent with regional evidence (Felis et al., 2018) and follows proposed theories for weakened boreal summer monsoons during an interval of northern hemisphere cooling (Feng and Hu, 2008; **Figure 9**).

Conversely to the MCA interval, with a southward migration of the ITCZ during the inception of the LIA, an increase in the interhemispheric temperature contrast and enhanced high-latitude ice cover resulted in arid climatic conditions on the southern margins of the Arabian Peninsula (Schneider et al., 2014). Hence precipitation changes in Yemen during both the MCA and LIA anomalies were possibly driven by changes in the mean position of ITCZ. However, we infer that the LIA was not extremely dry, as we do not see evidence for compete desiccation of the lake and formation of soils.

Unit LU-3 (~1720–2000 CE)

This unit consists of post-LIA sediments and is defined by higher detrital input to the lake post-1900 CE. These intervals are defined by higher values of PC1 score and finer sediment (EM1 score) fraction but lower values of TOC/TIC (**Figure 9**). The unit is also marked by a higher aeolian influx due to an increase in the abundance of EM2 (**Figure 9**). However, uncertainty in our age-depth model is high for this section, as it is difficult to accurately constrain the timing of initial influx of detrital material to the lake. However, it occurred after the LIA and is marked by the inception of wetter conditions. Several

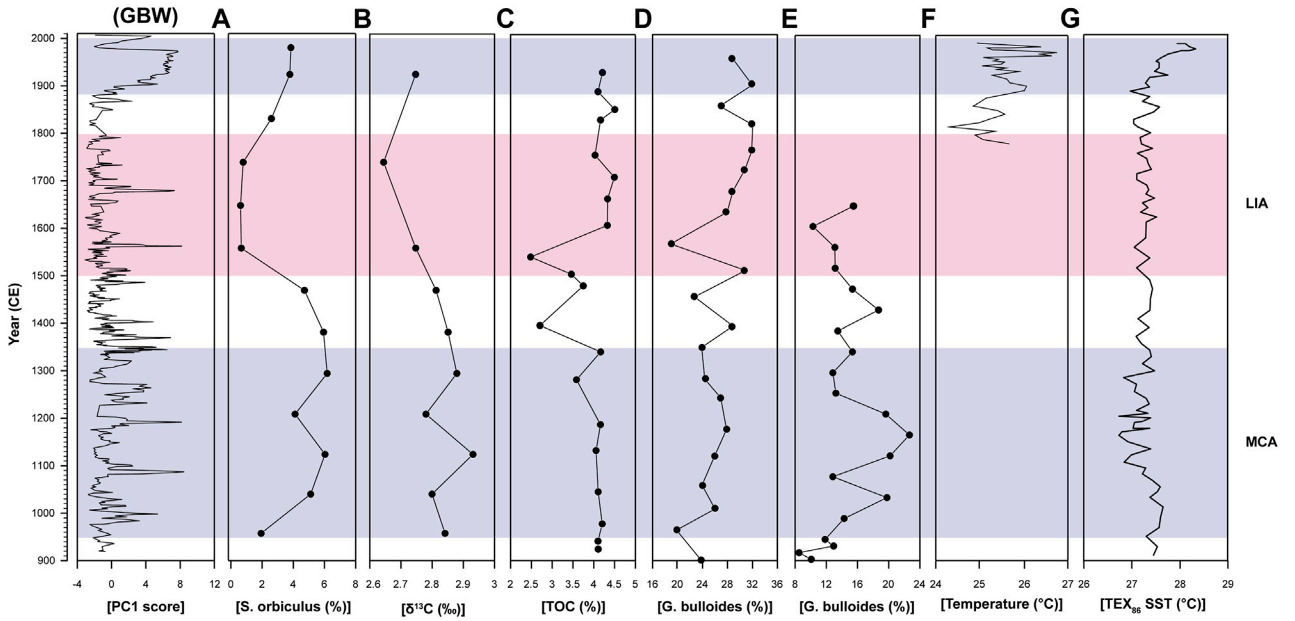

FIGURE 10 | Comparison of the GBW record with other regional paleoclimatic data. **(A)** δ^{13}C and **(B)** TOC, both from Shuaiba Lagoon (Saudi Arabia; Abu-Zied and Bantan, 2015), **(C)** TOC values from Naro Moru Tarn (Mount Kenya; Fastook et al., 1999), **(D)** G. Bulloides from core RC2735 (Anderson et al., 2010) and **(E)** G. Bulloides from core ODP Hole 723A (Gupta et al., 2003), both from the Arabian Sea (Oman margin). **(F)** TEX86 temperature reconstruction from Lake Turkana (Berke et al., 2012). **(G)** δD_{wax} data for the past millennium from a Gulf of Aden core (Tierney et al., 2015).

studies have reported warm and wet conditions following the LIA (Kotlia et al., 2012; Lüning et al., 2019), and our GBW record follows a similar trend. We suggest that this pattern is promoted by an active Red Sea Trough system that enhances precipitation over the southern Arabian Peninsula (Almazroui, 2012; Baseer et al., 2019).

Climate Variability in the Region

Based on the multiproxy approach of this study, high rainfall intervals were identified during ~930–1400 CE, with lower magnitudes occurring during ~1,410–1700 CE (**Figure 9**). A similar precipitation trend is witnessed in other well-dated sites from NW Arabia and eastern Africa, suggesting warm and humid conditions during the MCA followed by a cold and dry condition during the LIA (Lüning et al., 2017). A late Holocene study from Shuaiba Lagoon, Saudi Arabia, reveals high paleo-tidal elevation as shown by enrichment in δ^{13}C and δD of *Sorites orbiculus* indicating wet climatic condition during 1,000–1550 CE followed by aridity from 1,550 to 1850 CE due to MCA and LIA influence in the region (**Figure 10A**; Abu-Zied and Bantan, 2015). Furthermore, marine records retrieved on the Arabian Sea also report increased monsoonal activity 750–1150 CE and a weaker monsoon during 1,350–1550 CE (**Figures 10D,E**), which correlate well with two large temperature excursions during the late Holocene (Anderson et al., 2010). Additional records from Mount Kenya (**Figure 10C**) and Lake Turkana (**Figure 10F**) report cooler on average temperatures during the LIA but no indication of the MCA (Fastook et al., 1999; Berke et al., 2012). In contrast, a study based on sea surface temperature (SST) reconstruction from the Gulf of Aden using GDGTs shows no major indication for substantial temperature change during the MCA and LIA (**Figure 10G**; Tierney et al., 2015). This pattern can potentially be arguable due to major cold upwelling in the Arabian Sea that results from stronger Indian Summer Monsoons (SW winds) that brings colder, nutrient-rich waters from the Indian Ocean. The relationship between cold upwelling conditions during higher solar irradiance was already established by a previous study from the Oman margin (**Figure 10E**; Gupta et al., 2005), showing strong SW monsoons during the MCA (equivalent to a solar maxima interval) and weaker strengths during the LIA (solar minima). Hence, both climatic anomalies are well documented in many segments of East Africa, Saudi Arabia, and the Arabian Sea which most likely are triggered by changes in solar and volcanic forcing and ocean cycles.

CONCLUSION

This study integrated magnetic susceptibility, geochemical, and TOC/TIC analyses, coupled with end-member mixing analysis derived from particle size measurements carried out on a ~3.3 m long core retrieved from Gayal el Bazal (southern Yemen) utilized to understand the late Holocene climatic fluctuations in the region. The current study shows that sediment accumulating in the lake comprises of allochthonous material (derived during pluvial events through surface runoff), precipitation of authigenic evaporite minerals (formed following changes in water composition and inflow strength during dry intervals), and aeolian activity (indicated by an increase in EM2 and calcite minerals). The multiproxy investigation displays enhanced precipitation during the MCA, marked by an increase in detrital elements, higher TOC/TIC content, and dominance of EM1 (clayey silt fraction), which represent higher surface runoff in the lake watershed. Additionally, the higher contribution of EM2 (coarser silt fraction) appears to indicate aeolian input, coupled with increased gypsum production during the LIA, which indicate drier conditions. Our results show that the evolution of the Gayal el Bazal Lake has been mainly controlled by climatic factors (Solar and volcanic forcing), as the MCA and LIA are well imprinted in the sedimentary record. We further suggest that the Gayal el Bazal sedimentary archive has reliably responded to centennial-scale latitudinal variability of the ITCZ and associated with ISM. Comparison with other marine and terrestrial records from the Arabian Peninsula and Eastern Africa shows a similar climate pattern during the LIA and MCA intervals. We conclude that this work documents, for the first time, a continuous lacustrine record from southern Yemen that reliably responds to climate variability associated with the MCA and the LIA. Our work also proposes that the region's hydroclimate balance is sensitive to changes in solar activity, and thus if an extended solar minimum prevails in the future, it could affect the region, causing increased drought.

DATA AVAILABILITY STATEMENT

The original contributions presented in the study are included in the article/Supplementary Material, further inquiries can be directed to the corresponding author.

AUTHOR CONTRIBUTIONS

SP, JR, and NW designed the study. JR collected the samples, SP performed the measurements and carried out analysis on the samples, drafted the manuscript, and designed figures. NW and JR supervised the project made a substantial contribution to the concept or design of the article. All authors provided critical feedback and helped shape the research, analysis, and manuscript.

FUNDING

This research was supported by grants from PBC Fellowship program for International PhD students offered by the Council for Higher Education of Israel to SP.

ACKNOWLEDGMENTS

We are thankful to LacCore (National Lacustrine Core Facility), Department of Earth Sciences, University of Minnesota, for providing the sediments for the project. The authors acknowledge assistance with fieldwork from Douglas Schnurrenberger, who led fieldwork, and Prof. Juris Zarins. The American Institute for Yemeni Studies is thanked for their assistance with field logistics and project permitting. The authors warmly thanks Nimer Taha for assistance with grain size, XRD, and TOC/TIC measurements. This project was partially funded by Israel Science Foundation grant number 3413/21.

REFERENCES

Abbott, M. B., Seltzer, G. O., Kelts, K. R., and Southon, J. (1997). Holocene Paleohydrology of the Tropical Andes from lake Records. *Quat. Res.* 47 (1), 70–80. doi:10.1006/qres.1996.1874

Abu-Zied, R. H., and Bantan, R. A. (2015). Palaeoenvironment, Palaeoclimate and Sea-Level Changes in the Shuaiba Lagoon during the Late Holocene (Last 3.6 Ka), Eastern Red Sea Coast, Saudi Arabia. *The Holocene* 25 (8), 1301–1312. doi:10.1177/0959683615584204

Al-ameri, A., Schneider, M., Abu Lohom, N., and Sprenger, C. (2014). The Hydrogen (δD) and Oxygen (δ18 O) Isotopic Composition of Yemen's Rainwater. *Arab. J. Sci. Eng.* 39 (1), 423–436. doi:10.1007/s13369-013-0869-6

Al-Dousari, A. M., Al-Awadhi, J., and Ahmed, M. (2013). Dust Fallout Characteristics within Global Dust Storm Major Trajectories. *Arab J. Geosci.* 6 (10), 3877–3884. doi:10.1007/s12517-012-0644-0

Al-Dousari, A. M., and Al-Awadhi, J. (2012). Dust Fallout in Northern Kuwait, Major Sources and Characteristics. *Kuwait J. Sci.* 39 (2A), 171–187.

Almazroui, M. (2012). Dynamical Downscaling of Rainfall and Temperature over the Arabian Peninsula Using RegCM4. *Clim. Res.* 52, 49–62. doi:10.3354/cr01073

Anderson, D. M., Baulcomb, C. K., Duvivier, A. K., and Gupta, A. K. (2010). Indian Summer Monsoon during the Last Two Millennia. *J. Quat. Sci.* 25 (6), 911–917. doi:10.1002/jqs.1369

Andersson, R. A., Kuhry, P., Meyers, P., Zebühr, Y., Crill, P., and Mörth, M. (2011). Impacts of Paleohydrological Changes on N-Alkane Biomarker Compositions of a Holocene Peat Sequence in the Eastern European Russian Arctic. *Org. Geochem.* 42 (9), 1065–1075. doi:10.1016/j.orggeochem.2011.06.020

As-Saruri, M. A., and Wiefel, H. (2012). The Lithostratigraphic Subdivision of the Proterozoic Basement Rocks of the Mudiyah-Mukalla Area, Yemen. *Arab. J. Geosci.* 5 (5), 1127–1150. doi:10.1007/s12517-011-0295-6

Bakhlah, M. S., and Hassan, A. S. (2012). The Effect of Roof Colour on Indoor House Temperature in Case of Hadhramout, Yemen. *Am. Trans. Eng. Appl. Sci.* 1 (4), 2229–1652.

Bareille, G., Grousset, F. E., Labracherie, M., Labeyrie, L. D., and Petit, J.-R. (1994). Origin of Detrital Fluxes in the Southeast Indian Ocean during the Last Climatic Cycles. *Paleoceanography* 9 (6), 799–819. doi:10.1029/94pa01946

Baseer, M. N., Awad, A. M., and Almazroui, M. (2019). Climatology of the spring Red Sea Trough. *Int. J. Climatol.* 39 (11), 4218–4233. doi:10.1002/joc.6069

Berger, J.-F., Bravard, J.-P., Purdue, L., Benoist, A., Mouton, M., and Braemer, F. (2012). Rivers of the Hadramawt Watershed (Yemen) during the Holocene: Clues of Late Functioning. *Quat. Int.* 266, 142–161. doi:10.1016/j.quaint.2011.10.037

Berke, M. A., Johnson, T. C., Werne, J. P., Schouten, S., and Sinninghe Damsté, J. S. (2012). A Mid-holocene thermal Maximum at the End of the African Humid Period. *Earth Planet. Sci. Lett.* 351-352, 95–104. doi:10.1016/j.epsl.2012.07.008

Boës, X., Rydberg, J., Martinez-Cortizas, A., Bindler, R., and Renberg, I. (2011). Evaluation of Conservative Lithogenic Elements (Ti, Zr, Al, and Rb) to Study Anthropogenic Element Enrichments in lake Sediments. *J. Paleolimnol.* 46 (1), 75–87.

Boyle, J. F. (2005). "Inorganic Geochemical Methods in Palaeolimnology," in *Tracking Environmental Change Using Lake Sediments* (Springer Netherlands), 83–141.

Broccoli, A. J., Dahl, K. A., and Stouffer, R. J. (2006). Response of the ITCZ to Northern Hemisphere Cooling. *Geophys. Res. Lett.* 33 (1), L01702. doi:10.1029/2005gl024546

Broecker, W. S. (2001). Was the Medieval Warm Period Global. *Science* 291 (5508), 1497–1499. doi:10.1126/science.291.5508.1497

Bronk Ramsey, C. (2009). Bayesian Analysis of Radiocarbon Dates. *Radiocarbon* 51 (1), 337–360. doi:10.1017/s0033822200033865

Chawchai, S., Kylander, M. E., Chabangborn, A., Löwemark, L., and Wohlfarth, B. (2016). Testing Commonly Used X-ray Fluorescence Core Scanning-Based

Proxies for Organic-Rich lake Sediments and Peat. *Boreas* 45 (1), 180–189. doi:10.1111/bor.12145

Chen, F., Zhu, Y., Li, J., Shi, Q., Jin, L., and Wünemann, B. (2001). Abrupt Holocene Changes of the Asian Monsoon at Millennial- and Centennial-Scales: Evidence from lake Sediment Document in Minqin Basin, NW China. *Chin.Sci.Bull.* 46 (23), 1942–1947. doi:10.1007/bf02901902

Cronin, T. M., Hayo, K., Thunell, R. C., Dwyer, G. S., Saenger, C., and Willard, D. A. (2010). The Medieval Climate Anomaly and Little Ice Age in Chesapeake Bay and the North Atlantic Ocean. *Palaeogeogr. Palaeoclimatol. Palaeoecol.* 297 (2), 299–310. doi:10.1016/j.palaeo.2010.08.009

Croudace, I. W., Rindby, A., and Rothwell, R. G. (2006). ITRAX: Description and Evaluation of a New Multi-Function X-ray Core Scanner. *Geol. Soc. Lond. Spec. Publications* 267 (1), 51–63. doi:10.1144/gsl.sp.2006.267.01.04

Crouvi, O., Amit, R., Enzel, Y., Porat, N., and Sandler, A. (2008). Sand Dunes as a Major Proximal Dust Source for Late Pleistocene Loess in the Negev Desert, Israel. *Quat. Res.* 70 (2), 275–282. doi:10.1016/j.yqres.2008.04.011

Crowley, T. J., and Lowery, T. S. (2000). How Warm Was the Medieval Warm Period? *AMBIO: A J. Hum. Environ.* 29 (1), 51–54. doi:10.1579/0044-7447-29.1.51

Davies, C. P. (2006). Holocene Paleoclimates of Southern Arabia from Lacustrine Deposits of the Dhamar highlands, Yemen. *Quat. Res.* 66 (3), 454–464. doi:10.1016/j.yqres.2006.05.007

Davison, W. (1993). Iron and Manganese in Lakes. *Earth-Science Rev.* 34 (2), 119–163. doi:10.1016/0012-8252(93)90029-7

Dean, W. E., and Gorham, E. (1998). Magnitude and Significance of Carbon Burial in Lakes, Reservoirs, and Peatlands. *Geol* 26 (6), 535–538. doi:10.1130/0091-7613(1998)026<0535:masocb>2.3.co;2

Dessai, D. V. G., Nayak, G. N., and Basavaiah, N. (2009). Grain Size, Geochemistry, Magnetic Susceptibility: Proxies in Identifying Sources and Factors Controlling Distribution of Metals in a Tropical Estuary, India. *Estuarine, Coastal Shelf Sci.* 85 (2), 307–318. doi:10.1016/j.ecss.2009.08.020

Dietze, E., Hartmann, K., Diekmann, B., IJmker, J., Lehmkuhl, F., Opitz, S., et al. (2012). An End-Member Algorithm for Deciphering Modern Detrital Processes from lake Sediments of Lake Donggi Cona, NE Tibetan Plateau, China. *Sediment. Geology.* 243-244, 169–180. doi:10.1016/j.sedgeo.2011.09.014

Dietze, E., Wünnemann, B., Hartmann, K., Diekmann, B., Jin, H., Stauch, G., et al. (2013). Early to Mid-holocene lake High-Stand Sediments at Lake Donggi Cona, Northeastern Tibetan Plateau, China. *Quat. Res.* 79 (3), 325–336. doi:10.1016/j.yqres.2012.12.008

Edgell, H. (2006). *Arabian Deserts: Nature, Origin and Evolution*. Springer Science & Business Media.

Engstrom, D. R., and Wright, H. E., Jr (1984). “Chemical Stratigraphy of lake Sediments as a Record of Environmental Change,” in *Lake Sediments and Environmental History: Studies in Palaeolimnology and Palaeoecology in Honour of Winifred Tutin*. Editors E. Y. Haworth and J. W. G. Lund (Leicester: Leicester University Press), 11.

Enzel, Y., Kushnir, Y., and Quade, J. (2015). The Middle Holocene Climatic Records from Arabia: Reassessing Lacustrine Environments, Shift of ITCZ in Arabian Sea, and Impacts of the Southwest Indian and African Monsoons. *Glob. Planet. Change* 129, 69–91. doi:10.1016/j.gloplacha.2015.03.004

Farquharson, F. A. K., Plinston, D. T., and Sutcliffe, J. V. (1996). Rainfall and Runoff in Yemen. *Hydrological Sci. J.* 41 (5), 797–811. doi:10.1080/02626669609491546

Fastook, J. L., Holmgren, K., Matthews, J. A., Odada, E., Karlén, W., Malmström, M., et al. (1999). Glacier Fluctuations on Mount Kenya since ~ 6000 Cal. Years BP: Implications for Holocene Climatic Change in Africa. *Stockholm* 28, 409–418.

Felis, T., Ionita, M., Rimbu, N., Lohmann, G., and Kölling, M. (2018). Mild and Arid Climate in the Eastern Sahara-Arabian Desert during the Late Little Ice Age. *Geophys. Res. Lett.* 45 (14), 7112–7119. doi:10.1029/2018gl078617

Feng, S., and Hu, Q. (2008). How the North Atlantic Multidecadal Oscillation May Have Influenced the Indian Summer Monsoon during the Past Two Millennia. *Geophys. Res. Lett.* 35 (1), L01707. doi:10.1029/2007gl032484

Fleitmann, D., Burns, S. J., Mangini, A., Mudelsee, M., Kramers, J., Villa, I., et al. (2007). Holocene ITCZ and Indian Monsoon Dynamics Recorded in Stalagmites from Oman and Yemen (Socotra). *Quat. Sci. Rev.* 26 (1-2), 170–188. doi:10.1016/j.quascirev.2006.04.012

Fleitmann, D., Burns, S. J., Neff, U., Mudelsee, M., Mangini, A., and Matter, A. (2004). Palaeoclimatic Interpretation of High-Resolution Oxygen Isotope Profiles Derived from Annually Laminated Speleothems from Southern Oman. *Quat. Sci. Rev.* 23 (7-8), 935–945. doi:10.1016/j.quascirev.2003.06.019

Fleitmann, D., Burns, S. J., Pekala, M., Mangini, A., Al-Subbary, A., Al-Aowah, M., et al. (2011). Holocene and Pleistocene Pluvial Periods in Yemen, Southern Arabia. *Quat. Sci. Rev.* 30 (7-8), 783–787. doi:10.1016/j.quascirev.2011.01.004

Fleitmann, D., and Matter, A. (2009). The Speleothem Record of Climate Variability in Southern Arabia. *Comptes Rendus Geosci.* 341 (8-9), 633–642. doi:10.1016/j.crte.2009.01.006

Gayo, E. M., Latorre, C., Santoro, C. M., Maldonado, A., and De Pol-Holz, R. (2012). Hydroclimate Variability in the Low-Elevation Atacama Desert over the Last 2500 Yr. *Clim. Past* 8 (1), 287–306. doi:10.5194/cp-8-287-2012

Graham, N. E., Ammann, C. M., Fleitmann, D., Cobb, K. M., and Luterbacher, J. (2011). Support for Global Climate Reorganization during the "Medieval Climate Anomaly. *Clim. Dyn.* 37 (5), 1217–1245. doi:10.1007/s00382-010-0914-z

Gupta, A. K., Anderson, D. M., and Overpeck, J. T. (2003). Abrupt Changes in the Asian Southwest Monsoon during the Holocene and Their Links to the North Atlantic Ocean. *Nature* 421 (6921), 354–357. doi:10.1038/nature01340

Gupta, A. K., Das, M., and Anderson, D. M. (2005). Solar Influence on the Indian Summer Monsoon during the Holocene. *Geophys. Res. Lett.* 32 (17), 1–4. doi:10.1029/2005gl022685

Hadden, R. L. (2012). *The Geology of Yemen: An Annotated Bibliography of Yemen’s Geology, Geography and Earth Science*. Fort Belvoir, VA: Corps of Engineers Alexandria.

Håkanson, L., and Jansson, M. (1983). *Principles of lake Sedimentology*, 109. New Jersey: Blackburn Press, 24–31.

Hasanean, H., and Almazroui, M. (2015). Rainfall: Features and Variations over Saudi Arabia, a Review. *Climate* 3 (3), 578–626. doi:10.3390/cli3030578

Hehmeyer, I., Keall, E. J., and Rahimi, D. A. N. (2002). Ghayl Bā Wazīr: Applied Qanāt Technology in the Fissured Karst Landscape of Southern Yemen. *Proc. Semin. Arab. Stud.*, 32 83–97.

Hou, J., Tian, Q., Liang, J., Wang, M., and He, Y. (2017). Climatic Implications of Hydrologic Changes in Two lake Catchments on the central Tibetan Plateau since the Last Glacial. *J. Paleolimnol.* 58 (2), 257–273. doi:10.1007/s10933-017-9976-9

Hounslow, M. W., and Maher, B. A. (1999). Source of the Climate Signal Recorded by Magnetic Susceptibility Variations in Indian Ocean Sediments. *J. Geophys. Res.* 104 (B3), 5047–5061. doi:10.1029/1998jb900085

Ivakhnenko, O. P., Abirov, R., and Logvinenko, A. (2015). New Method for Characterisation of Petroleum Reservoir Fluidmineral Deposits Using Magnetic Analysis. *Energ. Proced.* 76, 454–462. doi:10.1016/j.egypro.2015.07.877

Jomelli, V., Lane, T., Favier, V., Masson-Delmotte, V., Swingedouw, D., Rinterknecht, V., et al. (2016). Paradoxical Cold Conditions during the Medieval Climate Anomaly in the Western Arctic. *Sci. Rep.* 6 (1), 32984–32989. doi:10.1038/srep32984

Khalaf, F., and Al-Hashash, M. (1983). Aeolian Sedimentation in the north-western Part of the Arabian Gulf. *J. Arid Environments* 6, 319–332. doi:10.1016/s0140-1963(18)31411-3

Kotlia, B. S., Ahmad, S. M., Zhao, J.-X., Raza, W., Collerson, K. D., Joshi, L. M., et al. (2012). Climatic Fluctuations during the LIA and post-LIA in the Kumaun Lesser Himalaya, India: Evidence from a 400 Y Old Stalagmite Record. *Quat. Int.* 263, 129–138. doi:10.1016/j.quaint.2012.01.025

Kuhnert, H., and Mulitza, S. (2011). Multi-decadal Variability and Late Medieval Cooling of Near-coastal Sea Surface Temperatures in the Eastern Tropical North Atlantic. *Paleoceanography* 26 (4), PA4224. doi:10.1029/2011pa002130

Kushnir, Y., and Stein, M. (2019). Medieval Climate in the Eastern Mediterranean: Instability and Evidence of Solar Forcing. *Atmosphere* 10 (1), 29. doi:10.3390/atmos10010029

Kylander, M. E., Ampel, L., Wohlfarth, B., and Veres, D. (2011). High-resolution X-ray Fluorescence Core Scanning Analysis of Les Echets (France) Sedimentary Sequence: New Insights from Chemical Proxies. *J. Quat. Sci.* 26 (1), 109–117. doi:10.1002/jqs.1438

Last, W. M. (2005). “Textural Analysis of Lake Sediments,” in *Tracking Environmental Change Using Lake Sediments* (Springer), 41–81.

Lespez, L., Le Drezen, Y., Garnier, A., Rasse, M., Eichhorn, B., Ozainne, S., et al. (2011). High-resolution Fluvial Records of Holocene Environmental Changes in the Sahel: The Yamé River at Ounjougou (Mali, West Africa). *Quat. Sci. Rev.* 30 (5-6), 737–756. doi:10.1016/j.quascirev.2010.12.021

Levitus, S., Antonov, J. I., Wang, J., Delworth, T. L., Dixon, K. W., and Broccoli, A. J. (2001). Anthropogenic Warming of Earth's Climate System. *Science* 292 (5515), 267–270. doi:10.1126/science.1058154

Lézine, A. M., Robert, C., Cleuziou, S., Inizan, M. L., Braemer, F., Saliège, J. F., et al. (2010). Climate Change and Human Occupation in the Southern Arabian Lowlands during the Last Deglaciation and the Holocene. *Glob. Planet. Change* 72 (4), 412–428. doi:10.1016/j.gloplacha.2010.01.016

Lézine, A. M., Saliège, J. F., Robert, C., Wertz, F., and Inizan, M. L. (1998). Holocene Lakes from Ramlat As-Sab'atayn (Yemen) Illustrate the Impact of Monsoon Activity in Southern Arabia. *Quat. Res.* 50 (3), 290–299. doi:10.1006/qres.1998.1996

Lézine, A. M., Tiercelin, J. J., Robert, C., Saliège, J. F., Cleuziou, S., Inizan, M. L., et al. (2007). Centennial to Millennial-Scale Variability of the Indian Monsoon during the Early Holocene from a Sediment, Pollen and Isotope Record from the Desert of Yemen. *Palaeogeogr. Palaeoclimatol. Palaeoecol.* 243 (3-4), 235–249. doi:10.1016/j.palaeo.2006.05.019

Llasat, M. C., Llasat-Botija, M., Prat, M. A., Porcú, F., Price, C., Mugnai, A., et al. (2010). High-impact Floods and Flash Floods in Mediterranean Countries: The FLASH Preliminary Database. *Adv. Geosci.* 23, 47–55. doi:10.5194/adgeo-23-47-2010

Lou, J., Schwab, D. J., Beletsky, D., and Hawley, N. (2000). A Model of Sediment Resuspension and Transport Dynamics in Southern Lake Michigan. *J. Geophys. Res.* 105 (C3), 6591–6610. doi:10.1029/1999jc900325

Löwemark, L., Chen, H. F., Yang, T. N., Kylander, M., Yu, E. F., Hsu, Y. W., et al. (2011). Normalizing XRF-Scanner Data: A Cautionary Note on the Interpretation of High-Resolution Records from Organic-Rich Lakes. *J. Asian Earth Sci.* 40 (6), 1250–1256. doi:10.1016/j.jseaes.2010.06.002

Lüning, S., Gałka, M., Danladi, I. B., Adagunodo, T. A., and Vahrenholt, F. (2018). Hydroclimate in Africa during the Medieval Climate Anomaly. *Palaeogeogr. Palaeoclimatol. Palaeoecol.* 495, 309–322. doi:10.1016/j.palaeo.2018.01.025

Lüning, S., Gałka, M., and Vahrenholt, F. (2017). Warming and Cooling: The Medieval Climate Anomaly in Africa and Arabia. *Paleoceanography* 32 (11), 1219–1235. doi:10.1002/2017pa003237

Lüning, S., Schulte, L., Garcés-Pastor, S., Danladi, I. B., and Gałka, M. (2019). The Medieval Climate Anomaly in the Mediterranean Region. *Paleoceanogr. Paleoclimatology* 34 (10), 1625–1649. doi:10.1029/2019pa003734

Mann, M. E., Zhang, Z., Rutherford, S., Bradley, R. S., Hughes, M. K., Shindell, D., et al. (2009). Global Signatures and Dynamical Origins of the Little Ice Age and Medieval Climate Anomaly. *Science* 326 (5957), 1256–1260. doi:10.1126/science.1177303

Mardia, K. V., Kent, J. T., and Bibby, J. M. (1979). *Multivariate Analysis*, 15. London: Academic Press Inc. (London) Ltd, 518.

Marshall, W. A., Gehrels, W. R., Garnett, M. H., Freeman, S. P. H. T., Maden, C., and Xu, S. (2007). The Use of 'bomb Spike' Calibration and High-Precision AMS 14C Analyses to Date Salt-Marsh Sediments Deposited during the Past Three Centuries. *Quat. Res.* 68 (3), 325–337. doi:10.1016/j.yqres.2007.07.005

Matthews, J. A., and Briffa, K. R. (2005). The 'little Ice Age': Re-evaluation of an Evolving Concept. *Geografiska Annaler: Ser. A, Phys. Geogr.* 87 (1), 17–36. doi:10.1111/j.0435-3676.2005.00242.x

McLaren, P., and Bowles, D. (1985). The Effects of Sediment Transport on Grain-Size Distributions. *J. Sediment. Petrol.* 55 (4), 457–470. doi:10.1306/212f86fc-2b24-11d7-8648000102c1865d

Miller, G. H., Geirsdóttir, Á., Zhong, Y., Larsen, D. J., Otto-Bliesner, B. L., Holland, M. M., et al. (2012). Abrupt Onset of the Little Ice Age Triggered by Volcanism and Sustained by Sea-ice/ocean Feedbacks. *Geophys. Res. Lett.* 39 (2), L06605. doi:10.1029/2011gl050168

Miriyala, P., Sukumaran, N. P., Nath, B. N., Ramamurty, P. B., Sijinkumar, A. V., Vijayagopal, B., et al. (2017). Increased Chemical Weathering during the Deglacial to Mid-holocene Summer Monsoon Intensification. *Sci. Rep.* 7 (1), 44310–44311. doi:10.1038/srep44310

Mishra, P. K., Parth, S., Ankit, Y., Kumar, S., Ambili, V., Kumar, V. V., et al. (2019). Geochemical and Sedimentological Characteristics of Surface Sediments from Ashtamudi Estuary, Southern India: Implications for Provenance and Modern Sedimentary Dynamics. *Environ. Earth Sci.* 78 (14), 1–11. doi:10.1007/s12665-019-8376-z

Mueller, A. D., Islebe, G. A., Hillesheim, M. B., Grzesik, D. A., Anselmetti, F. S., Ariztegui, D., et al. (2009). Climate Drying and Associated forest Decline in the Lowlands of Northern Guatemala during the Late Holocene. *Quat. Res.* 71 (2), 133–141. doi:10.1016/j.yqres.2008.10.002

Murray, M. R. (2002). Is Laser Particle Size Determination Possible for Carbonate-Rich lake Sediments. *J. Paleolimnol.* 27 (2), 173–183. doi:10.1023/a:1014281412035

Neugebauer, I., Schwab, M. J., Waldmann, N. D., Tjallingii, R., Frank, U., Hadzhiivanova, E., et al. (2016). Hydroclimatic Variability in the Levant during the Early Last Glacial (~ 117-75 Ka) Derived from Micro-facies Analyses of Deep Dead Sea Sediments. *Clim. Past* 12 (1), 75–90. doi:10.5194/cp-12-75-2016

Neukom, R., Steiger, N., Gómez-Navarro, J. J., Wang, J., and Werner, J. P. (2019). No Evidence for Globally Coherent Warm and Cold Periods over the Preindustrial Common Era. *Nature* 571 (7766), 550–554. doi:10.1038/s41586-019-1401-2

Otto-Bliesner, B. L., Brady, E. C., Fasullo, J., Jahn, A., Landrum, L., Stevenson, S., et al. (2016). Climate Variability and Change since 850 CE: An Ensemble Approach with the Community Earth System Model. *Bull. Am. Meteorol. Soc.* 97 (5), 735–754. doi:10.1175/bams-d-14-00233.1

Peinerud, E. K. (2000). Interpretation of Si Concentrations in lake Sediments: Three Case Studies. *Environ. Geology.* 40 (1-2), 64–72. doi:10.1007/pl00013330

Philippsen, B. (2013). The Freshwater Reservoir Effect in Radiocarbon Dating. *Heritage Sci.* 1 (1), 1–19. doi:10.1186/2050-7445-1-24

Pleskot, K., Tjallingii, R., Makohonienko, M., Nowaczyk, N., and Szczuciński, W. (2018). Holocene Paleohydrological Reconstruction of Lake Strzeszyńskie (Western Poland) and its Implications for the central European Climatic Transition Zone. *J. Paleolimnol* 59 (4), 443–459. doi:10.1007/s10933-017-9999-2

Pollastro, R. M., Karshbaum, A. S., and Viger, R. J. (1999). *Open-File Report 97-470B Maps Showing Geology, Oil and Gas fields and Geologic Provinces of the Arabian Peninsula*. Reston, VA: US Geological Survey.

Ramsey, C. B. (2008). Deposition Models for Chronological Records. *Quat. Sci. Rev.* 27 (1-2), 42–60. doi:10.1016/j.quascirev.2007.01.019

Rawat, V., Rawat, S., Srivastava, P., Negi, P. S., Prakasam, M., and Kotlia, B. S. (2021). Middle Holocene Indian Summer Monsoon Variability and its Impact on Cultural Changes in the Indian Subcontinent. *Quat. Sci. Rev.* 255, 106825. doi:10.1016/j.quascirev.2021.106825

Reimer, P. J., Austin, W. E. N., Bard, E., Bayliss, A., Blackwell, P. G., Bronk Ramsey, C., et al. (2020). The IntCal20 Northern Hemisphere Radiocarbon Age Calibration Curve (0-55 Cal kBP). *Radiocarbon* 62 (4), 725–757. doi:10.1017/rdc.2020.41

Rodwell, M. J., and Hoskins, B. J. (1996). Monsoons and the Dynamics of Deserts. *Q.J R. Met. Soc.* 122, 1385–1404. doi:10.1002/qj.49712253408

Rothwell, R. G. (2015). "Twenty Years of XRF Core Scanning Marine Sediments: What Do Geochemical Proxies Tell Us," in *Micro-XRF Studies Of Sediment Cores* (Dordrecht: Springer), 25–102.

Ruddiman, W. F. (2013). The Anthropocene. *Annu. Rev. Earth Planet. Sci.* 41, 45–68. doi:10.1146/annurev-earth-050212-123944

Schettler, G., Liu, Q., Mingram, J., Negendank, J. F. W., and Negendank, F. W. (2006). Palaeovariations in the East-Asian Monsoon Regime Geochemically Recorded in Varved Sediments of Lake Sihailongwan (Northeast China, Jilin Province). Part 1: Hydrological Conditions and Dust Flux. *J. Paleolimnol* 35 (2), 239–270. doi:10.1007/s10933-005-0096-6

Schneider, T., Bischoff, T., and Haug, G. H. (2014). Migrations and Dynamics of the Intertropical Convergence Zone. *Nature* 513 (7516), 45–53. doi:10.1038/nature13636

Schnurrenberger, D., Russell, J., and Kelts, K. (2003). Classification of Lacustrine Sediments Based on Sedimentary Components. *J. Paleolimnol.* 29 (2), 141–154. doi:10.1023/a:1023270324800

Shakun, J. D., Burns, S. J., Fleitmann, D., Kramers, J., Matter, A., and Al-Subary, A. (2007). A High-Resolution, Absolute-Dated Deglacial Speleothem Record of Indian Ocean Climate from Socotra Island, Yemen. *Earth Planet. Sci. Lett.* 259 (3-4), 442–456. doi:10.1016/j.epsl.2007.05.004

Shindell, D. T., Schmidt, G. A., Mann, M. E., Rind, D., and Waple, A. (2001). Solar Forcing of Regional Climate Change during the Maunder Minimum. *Science* 294 (5549), 2149–2152. doi:10.1126/science.1064363

Singhvi, A. K., and Kar, A. (2004). The Aeolian Sedimentation Record of the Thar Desert. *J. Earth Syst. Sci.* 113 (3), 371–401. doi:10.1007/bf02716733

Sinha, R., Smykatz-Kloss, W., Stüben, D., Harrison, S. P., Berner, Z., and Kramar, U. (2006). Late Quaternary Palaeoclimatic Reconstruction from the Lacustrine Sediments of the Sambhar Playa Core, Thar Desert Margin, India. *Palaeogeogr. Palaeoclimatol. Palaeoecol.* 233 (3-4), 252–270. doi:10.1016/j.palaeo.2005.09.012

Sly, P. G. (1994).*Sedimentary Processes in Lakes* in *Lakes* (Springer), 65–89.

Solohub, J. T., and Klovan, J. E. (1970). Evaluation of Grain-Size Parameters in Lacustrine Environments. *J. Sediment. Res.* 40 (1), 81–101. doi:10.1306/74d71efb-2b21-11d7-8648000102c1865d

Staubwasser, M., Sirocko, F., Grootes, P. M., and Erlenkeuser, H. (2002). South Asian Monsoon Climate Change and Radiocarbon in the Arabian Sea during Early and Middle Holocene. *Paleoceanography* 17 (4), 15–12. doi:10.1029/2000pa000608

Steinhilber, F., Abreu, J. A., Beer, J., Brunner, I., Christl, M., Fischer, H., et al. (2012). 9,400 Years of Cosmic Radiation and Solar Activity from Ice Cores and Tree Rings. *Proc. Natl. Acad. Sci.* 109 (16), 5967–5971. doi:10.1073/pnas.1118965109

Stuut, J. B. W., Prins, M. A., Schneider, R. R., Weltje, G. J., Fred Jansen, J. H., and Postma, G. (2002). A 300-kyr Record of Aridity and Wind Strength in Southwestern Africa: Inferences from Grain-Size Distributions of Sediments on Walvis Ridge, SE Atlantic. *Mar. Geol.* 180 (1-4), 221–233. doi:10.1016/s0025-3227(01)00215-8

Sun, D., Bloemendal, J., Rea, D. K., Vandenberghe, J., Jiang, F., An, Z., et al. (2002). Grain-size Distribution Function of Polymodal Sediments in Hydraulic and Aeolian Environments, and Numerical Partitioning of the Sedimentary Components. *Sediment. Geol.* 152 (3-4), 263–277. doi:10.1016/s0037-0738(02)00082-9

Thompson, R., and Morton, D. J. (1979). Magnetic Susceptibility and Particle-Size Distribution in Recent Sediments of the Loch Lomond Drainage basin, Scotland. *J. Sediment. Res.* 49 (3), 801–811. doi:10.1306/212f7851-2b24-11d7-8648000102c1865d

Tierney, J. E., Ummenhofer, C. C., and Demenocal, P. B. (2015). Past and Future Rainfall in the Horn of Africa. *Sci. Adv.* 1 (9), e1500682. doi:10.1126/sciadv.1500682

Tierney, J. E., Russell, J. M., Damsté, J. S. S., Huang, Y., and Verschuren, D. (2011). Late Quaternary Behavior of the East African Monsoon and the Importance of the Congo Air Boundary. *Quat. Sci. Rev.* 30 (7-8), 798–807. doi:10.1016/j.quascirev.2011.01.017

Toker, E., Sivan, D., Stern, E., Shirman, B., Tsimplis, M., and Spada, G. (2012). Evidence for Centennial Scale Sea Level Variability during the Medieval Climate Optimum (Crusader Period) in Israel, Eastern Mediterranean. *Earth Planet. Sci. Lett.* 315-316, 51–61. doi:10.1016/j.epsl.2011.07.019

Trenberth, K. E., Dai, A., Rasmussen, R. M., and Parsons, D. B. (2003). The Changing Character of Precipitation. *Bull. Am. Meteorol. Soc.* 84 (9), 1205–1218. doi:10.1175/bams-84-9-1205

Vaasma, T. (2008). Grain-size Analysis of Lacustrine Sediments: a Comparison of Pre-treatment Methods. *Estonian J. Ecol.* 57 (4), 231–243. doi:10.3176/eco.2008.4.01

Van Rampelbergh, M., Fleitmann, D., Verheyden, S., Cheng, H., Edwards, L., De Geest, P., et al. (2013). Mid- to Late Holocene Indian Ocean Monsoon Variability Recorded in Four Speleothems from Socotra Island, Yemen. *Quat. Sci. Rev.* 65, 129–142. doi:10.1016/j.quascirev.2013.01.016

Vandenberghe, J. (2013). Grain Size of fine-grained Windblown Sediment: A Powerful Proxy for Process Identification. *Earth-Science Rev.* 121, 18–30. doi:10.1016/j.earscirev.2013.03.001

Venables, W. N., and Ripley, B. D. (2002). *Exploratory Multivariate Analysis*. New York, NY): Springer, 301–330. doi:10.1007/978-0-387-21706-2_11

Warner, T. (2009). *Desert Meteorology*. Cambridge: Cambridge University Press.

Wassenburg, J. A., Dietrich, S., Fietzke, J., Fohlmeister, J., Jochum, K. P., Scholz, D., et al. (2016). Reorganization of the North Atlantic Oscillation during Early Holocene Deglaciation. *Nat. Geosci* 9 (8), 602–605. doi:10.1038/ngeo2767

Weltje, G. J. (1997). End-member Modeling of Compositional Data: Numerical-Statistical Algorithms for Solving the Explicit Mixing Problem. *Math. Geol.* 29 (4), 503–549. doi:10.1007/bf02775085

Weltje, G. J., and Tjallingii, R. (2008). Calibration of XRF Core Scanners for Quantitative Geochemical Logging of Sediment Cores: Theory and Application. *Earth Planet. Sci. Lett.* 274 (3-4), 423–438. doi:10.1016/j.epsl.2008.07.054

WorldClim (2021). Available at: https://worldclim.org/(Accessed March 17, 2021).

Wünnemann, B., Demske, D., Tarasov, P., Kotlia, B. S., Reinhardt, C., Bloemendal, J., et al. (2010). Hydrological Evolution during the Last 15 Kyr in the Tso Kar lake basin (Ladakh, India), Derived from Geomorphological, Sedimentological and Palynological Records. *Quat. Sci. Rev.* 29 (9-10), 1138–1155. doi:10.1016/j.quascirev.2010.02.017

Xu, H., Hou, Z. H., Ai, L., and Tan, L. C. (2007). Precipitation at Lake Qinghai, NE Qinghai–Tibet Plateau, and its Relation to Asian Summer Monsoons on Decadal/interdecadal Scales during the Past 500 Years. *Palaeogeogr. Palaeoclimatol. Palaeoecol.* 254 (3-4), 541–549. doi:10.1016/j.palaeo.2007.07.007

Xue, J., Lee, C., Wakeham, S. G., and Armstrong, R. A. (2011). Using Principal Components Analysis (PCA) with Cluster Analysis to Study the Organic Geochemistry of Sinking Particles in the Ocean. *Org. Geochem.* 42 (4), 356–367. doi:10.1016/j.orggeochem.2011.01.012

Yanhong, Y., Andreas, L., Bernd, W., Li, S., and Wang, S. (2007). Holocene Climate Change in the Central Tibetan Plateau Inferred by Lacustrine Sediment Geochemical Records. *Sci. China Ser. D: Earth Sci.* 50 (10), 1548–1555. doi:10.1007/s11430-007-0113-x

Zhao, C., Yu, Z., Zhao, Y., Ito, E., Kodama, K. P., and Chen, F. (2010). Holocene millennial-scale climate variations documented by multiple lake-level proxies in sediment cores from Hurleg Lake, Northwest China. *J Paleolimnol* 44 (4), 995–1008. doi:10.1007/s10933-010-9469-6

Zolitschka, B., Mingram, J., Van Der Gaast, S., Jansen, J. F., and Naumann, R. (2002). *Sediment Logging Technique in Tracking Environmental Change Using lake Sediments*. Dordrecht: Springer, 137–153.

Conflict of Interest: The authors declare that the research was conducted in the absence of any commercial or financial relationships that could be construed as a potential conflict of interest.

frontiers
in Earth Science

ORIGINAL RESEARCH
published: 14 December 2021
doi: 10.3389/feart.2021.789291

Mid-Late Holocene Sub-Millennial Scale Inverse Trends of South Asian Summer and Winter Monsoons in Sri Lanka

Kasun Gayantha[1], Patrick Roberts[2], Joyanto Routh[3], Oshan Wedage[2,4], Florian Ott[2,5], Peter Frenzel[6], Rohana Chandrajith[7] and Gerd Gleixner[1]*

[1]Department of Biogeochemical Processes, Max Planck Institute for Biogeochemistry, Jena, Germany, [2]Department of Archaeology, Max Planck Institute for the Science of Human History, Jena, Germany, [3]Department of Thematic Studies-Environmental Change, Linköping University, Linköping, Sweden, [4]Department of History and Archaeology, University of Sri Jayewardenepura, Gangodawila, Sri Lanka, [5]GFZ—German Research Centre for Geosciences, Section 5.2 Climate Dynamics and Landscape Evolution, Potsdam, Germany, [6]Institute of Earth Sciences, Friedrich Schiller University, Jena, Germany, [7]Department of Geology, Faculty of Science, University of Peradeniya, Peradeniya, Sri Lanka

Edited by:
Davide Tiranti,
Agenzia Regionale per la Protezione Ambientale (ARPA), Italy

Reviewed by:
Jianbao Liu,
Institute of Tibetan Plateau Research (CAS), China
Amzad Hussain Laskar,
Physical Research Laboratory, India

***Correspondence:**
Gerd Gleixner
gerd.gleixner@bgc-jena.mpg.de

Specialty section:
This article was submitted to Quaternary Science, Geomorphology and Paleoenvironment,
a section of the journal
Frontiers in Earth Science

Received: *04 October 2021*
Accepted: *25 November 2021*
Published: *14 December 2021*

Citation:
Gayantha K, Roberts P, Routh J, Wedage O, Ott F, Frenzel P, Chandrajith R and Gleixner G (2021) Mid-Late Holocene Sub-Millennial Scale Inverse Trends of South Asian Summer and Winter Monsoons in Sri Lanka.
Front. Earth Sci. 9:789291.
doi: 10.3389/feart.2021.789291

The South Asian Monsoon (SAM) brings precipitation crucial for agriculture across the densely populated region of South Asia. Identifying the key long-term drivers of the SAM is essential to improve the predictability of future monsoonal trends in the context of current global climate scenarios and increasingly frequent drought and flooding events in this part of the world. Here, we reconstruct ~6000 years of climatic and environmental history of the South Asian summer monsoon-fed Bolgoda South Lake and the Horton Plains, and the winter monsoon-fed Panama lagoon, in Sri Lanka to better understand monsoonal operation over this island and its connection to broader climate systems. Multiple proxies (diagnostic biomarkers, hydrogen and carbon isotopes of individual *n*-alkane, grain size, and Zr/Rb elemental ratio) indicate a sub-millennial scale decreasing trend of summer monsoon rainfall in the wet zone of Sri Lanka alongside an increasing trend of winter monsoon rainfall in the dry zone during the last ~6000 years. We also observed multi-centennial scale arid events in the Bolgoda South Lake and Horton Plains records at ~3,500 and ~1,000 cal years BP. Inverse monsoonal behavior during the mid- and late Holocene seems to be led by the southward migration of the mean latitudinal position of ITCZ, induced by varying solar energy distribution between the Northern and Southern hemispheres due to Earth's processional cycle. Our observations are broadly supported by existing paleoclimatic records from the Indian sub-continent, but abrupt arid phases are asynchronous in the regional records. In addition, these short-term arid conditions do not show systematic correlations with the different modes of climate variables known to have teleconnections with the Indian Ocean monsoon.

Keywords: paleoclimate, Indian Ocean Monsoon, ITCZ, South Asia, biomarker, compound specific isotopes analysis, XRF, microfauna

INTRODUCTION

The South Asian Monsoon (SAM) is a major component of the Asian monsoon system that plays a critical role in global climate and the socio-economic conditions of the nearly one quarter of the world's human population that lives in in South Asia (Gupta et al., 2020). The SAM brings rainfall to the Indian subcontinent and even a slight shift in intensity and duration of the SAM can cause extreme events such as droughts, floods, and mudslides that are occurring increasingly frequently and impacting many regions (Mirza, 2011). The seasonal migration of the equatorial low-pressure trough commonly called Inter Tropical Convergence Zone (ITCZ), determines the timing, intensity, and direction of tropical monsoon winds and the accompanying rainfall (An et al., 2015; Mohtadi et al., 2016). This migration is thought to be mainly controlled by the annual solar cycle causing variations in the solar induced cross-equatorial pressure gradient. However, alterations to monsoonal operation in the past had the potential to impact environments and societies across South Asia, as predicted scenarios for change suggest it will in the future.

The SAM consists of two primary rainfall seasons. In the boreal summer, the ITCZ migrates northward and brings summer monsoon rainfall (Southwest monsoon; SWM) to the Indian sub-continent, including Sri Lanka (**Figure 1**). Based on the wind and moisture distribution, the SWM can be further divided into the Arabian Sea Branch (ASB) and the Bay of Bengal Branch (BBB), and the latter brings precipitation to Sri Lanka and most of north-eastern India (Dixit and Tandon, 2016). In the boreal winter, the ITCZ retreats southward and reaches its southern-most position around January. This retreat results in a reversal of wind direction and provides the winter monsoon rainfall (Northeast monsoon; NEM) to the southern tip of India and the northern and eastern parts of Sri Lanka (**Figure 1**; Banerji et al., 2020; Gupta et al., 2020). Modern instrumental records and paleoclimate records suggest teleconnections between the SAM and different modes of climate variables, mainly, El Niño Southern Oscillation (ENSO), North Atlantic Oscillation

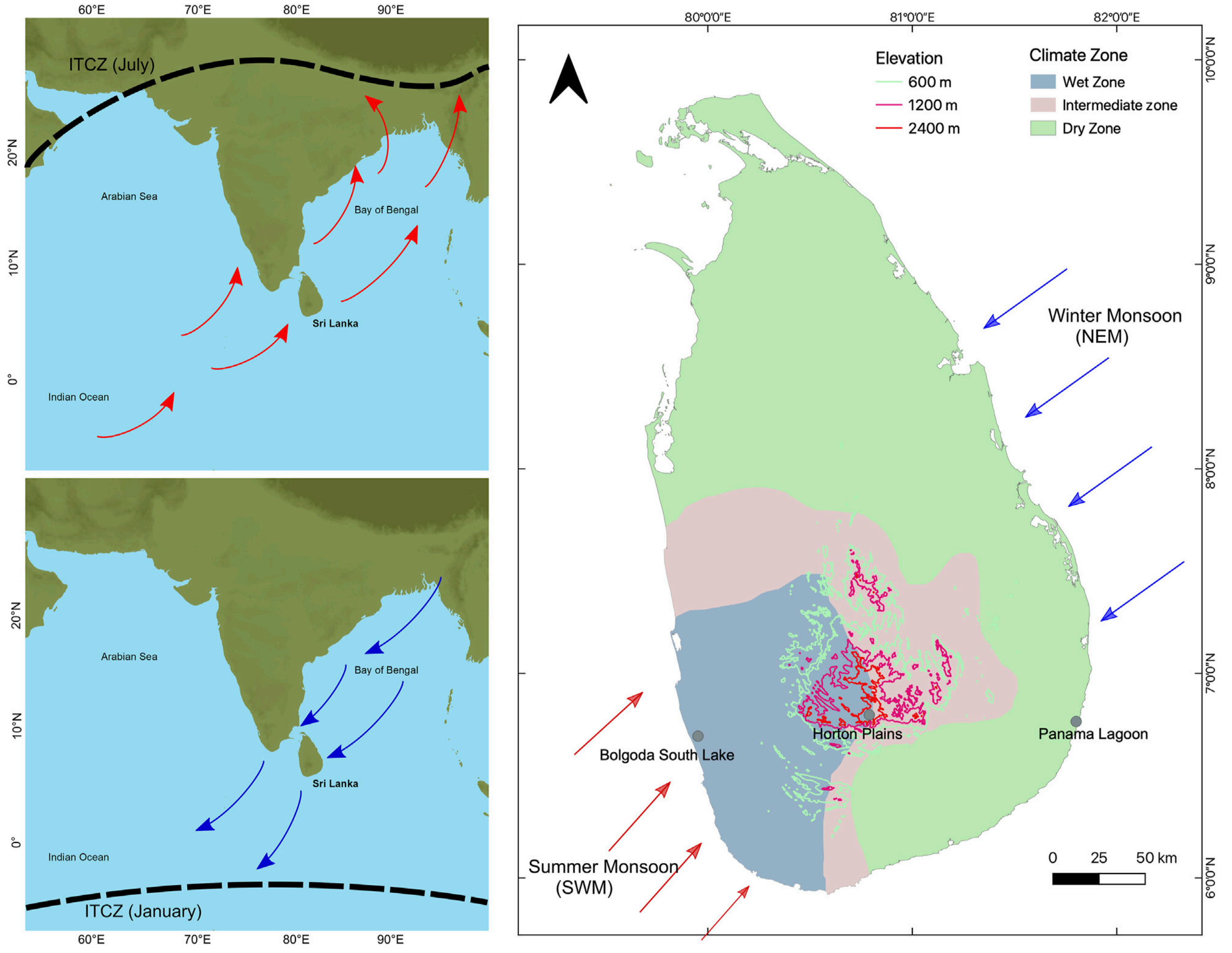

FIGURE 1 | Seasonal migration of ITCZ and occurrence of summer and winter monsoon over the Indian sub-continent **(Left)**. Influence of summer (SWM) and winter (NEM) monsoons in Sri Lanka and climate zones (wet, dry, and intermediate) defined by the rainfall variability due to the rain shadow effect **(right)**.

(NAO) and Indian Ocean Dipole (IOD) (Banerji et al., 2020; Gupta et al., 2020). However, large variations in this general pattern are known, especially for regions more distant to the equator, which makes it difficult to identify key patterns and driving forces of change (Achyuthan et al., 2016; Misra et al., 2019).

Looking at SAM operation in the past, a gradual weakening of the summer monsoon is observed in records outside the Indian sub-continent since the mid Holocene, which is attributed to a southward migration of the mean latitudinal position of ITCZ (Haug, 2001; Fleitmann et al., 2007). This migration is likely caused by the Earth's precession cycle distributing solar insolation differently to the northern and southern hemisphere. However, so far, additional support for this hypothesis over the Indian sub-continent is needed as the ISM records are very heterogeneous and asynchronous (Banerji et al., 2020; Gupta et al., 2020). Furthermore, although some records from the South Indian peninsular are significantly influenced by the Indian Winter Monsoon (IWM), (e.g., Veena et al., 2014; Rajmanickam et al., 2017; Sandeep et al., 2017), data from sites that mainly report IWM variability (e.g., Ranasinghe et al., 2013a; Böll et al., 2014; Misra et al., 2019) are scarce. Due to the large spatial (latitudinal) difference between the available summer and winter monsoon records, it is not easy to compare and understand the relationship between these two major components of the SAM system and their key driving forces.

As an island located close to the equator and in a central position within the seasonal ITCZ migration path, Sri Lanka is influenced by both summer (Southwest monsoon; SWM) and winter (Northeast monsoon; NEM) monsoon rainfall. Therefore, migration of the mean latitudinal position of ITCZ can inversely influence the seasonal lengths of SWM and NEM of Sri Lanka. The central highlands act as an orographic barrier, facilitating the tracking of these seasonal rainfall patterns (SWM and NEM) separately with a very low spatial distribution. These unique geographical and geomorphological settings of the island enable comparative reconstruction of South Asian summer and winter monsoon variability by filling the above knowledge gaps about the operation of Indian Ocean Monsoon. However, there is a relative dearth of long-term climate archives such as natural lakes, peat bogs, and speleothems in Sri Lanka. Hence, researchers have turned to available brackish water coastal lakes and lagoons (e.g., Ranasinghe et al., 2013b; Ratnayake et al., 2017; Gayantha et al., 2020) to reconstruct the past climate. Isolated peat deposits in the Horton Plains in Central Highlands have also been used to infer broad changes in rainfall patterns during the Holocene (Premathilake and Risberg, 2003; Premathilake, 2012). However, the coastal water bodies consist of signals from both terrestrial and marine environments that demand more specific and sensitive environmental proxies for identifying the different organic matter sources and ongoing biogeochemical processes. Moreover, these records have yet to reach their full potential in chronological resolution and use multi-proxy data to infer paleoclimate changes.

To understand the relationship between South Asian summer and winter monsoon variability and orbitally-induced mean position migration of ITCZ, we reconstruct climatic and environmental changes, focusing specifically on rainfall variability at three different sites in Sri Lanka—Bolgoda South Lake, Horton Plains, and Panama Lagoon—that also cover the major climate and altitudinal zones of the island (**Figure 1**). Our multi-proxy data enable comparison of the operation of the ISM and IWM over the last 6,000 years of the Holocene and, through comparison with available regional records, provide insights into climate forcings that drive the operation of the SAM. Historical records available for the last ~2500 years in Sri Lanka indicate the ancient kingdoms moved towards the southwest of the island (i.e., dry zone to wet zone) with increased human settlement of the wet zone over time (De Silva, 1981). Here we also try to understand the influence of long-term monsoon variability on past human settlement patterns in Sri Lanka. The resulting relatively well-established chronology for ISM and IWM variability in Sri Lanka not only provides insights into changing environments of relevance to past human societies in this part of the world, but also provides a framework for predicting future changes in the SAM in South Asia under different scenarios of global climate change.

STUDY AREA

Climate, Topography, and Vegetation of Sri Lanka

Sri Lanka has a tropical monsoonal climate with seasonally varying monsoon systems (Malmgren et al., 2003). The two principal monsoon rainfall seasons are separated by two short inter-monsoon periods that are associated with changing wind direction as part of the annual/seasonal ITCZ migration (**Figure 1**). The summer monsoon (Southwest Monsoon/*Yala*; SWM) is active in Sri Lanka between May and September and brings >2500 mm of annual rainfall to the southwestern portion of the island. The central highlands of Sri Lanka, which reach a maximum height of ~2,500 m a.s.l., act as an orographic barrier to these moisture-laden winds, creating a rain shadow effect to the leeward east and northeast and the prevalence of dry conditions outside of Sri Lanka's southwest during this season. The winter monsoon (Northeast Monsoon/*Maha*; NEM) brings rainfall between December and February to the northern and eastern portions of Sri Lanka from the Bay of Bengal. By the time the winter monsoon reaches Sri Lanka, having travelled over the Indian sub-continent, these winds bring less moisture than the summer monsoon winds. Nevertheless, the winter monsoon contributes to the majority of the annual rainfall of ~1750 mm for the northern and eastern portions of the island. The inter-monsoon rainfall occurs when the ITCZ moves over Sri Lanka bringing thunderstorm-type convectional rain and tropical depressions/cyclones (Malmgren et al., 2003; Hapuarachchi and Jayawardena, 2015; also see **Supplementary Figure S1**).

These climate conditions (amount of rainfall) lead to the division of Sri Lanka into three main climate "zones" (sub regions)—the wet, dry, and intermediate zones (**Figure 1**). The central part of the island is mountainous and consists of complex topographical features such as ridges, peaks, plateaus, basins, valleys, and escarpments. The rest of the island is generally flat except for some small hills in the lowlands (**Figure 1**). As noted above, these topographical features can strongly influence the different climate elements in Sri Lanka. The three climatic "zones" and topographical features shape the vegetation cover in Sri Lanka. Tropical rainforests and wet zone grasslands characterize the lowland wet zone (below ca. 900 m). The highland wet zone (above ca. 900 m) consists of tropical montane rainforest and montane grasslands (Patana). The lowland dry zone is characterized by seasonal rainforests (mixed-evergreen forests/dry monsoon forests) and dry zone upland and lowland savannas (Talawa and Damana; Perera, 1975; Erdelen, 1988). In addition, significant amounts of mangrove vegetation can also be found along the coastal water bodies, i.e., lagoons and estuaries, in Sri Lanka (Ranawana, 2017).

The Study Sites

The study areas in this investigation were selected to cover the different climatic, topographic, and vegetation zones in Sri Lanka and reconstruct past trends in both the southwest and northeast monsoons (see **Figure 1**).

Bolgoda South Lake

Bolgoda South Lake (BGSL) is a part of the Bolgoda Lake system located in the coastal lowland wet zone of western Sri Lanka (6° 40′ 57" – 6° 41′ 42″N; 79° 56′ 20″—79° 57′ 54″E) (see **Supplementary Figure S2**). The South Lake is located around 2.8 km from the coast, and it has a surface area of ~2 km^2 with an average depth of ~2 m. Between the lake and the sea, hills, and ridges (height up to 20 m) spread along N-S direction forming a morphological barrier that protect BGSL from direct marine influence. It naturally discharges its water into the Indian Ocean via Bolgoda North Lake. BGSL is fed by a small stream from the eastern side, and the lake also directly connects to the Indian Ocean via a narrow artificial stream (recently made) from the western side of the lake. The lake is currently identified as a slightly brackish water body. The BGSL and its catchment receive an annual rainfall of about 2,550 mm from the southwest (summer) monsoon between May and September. Floating and submerged aquatic plants are common in the lake, with a few mangrove swamps/marshes observed along its southern margin (Ranwella, 1995).

Panama Lagoon

Panama Lagoon (PN) is a shallow estuarine lagoon (highly brackish water lagoon) located on the southeastern coast of the dry zone (6° 45′52″- 6° 46′29″N; 81°48′ 20″—81°49′31″E). It has a surface area of ~0.73 km^2 and an average depth of 1.48 m. A tributary brings freshwater into the lagoon from the upland region to the west. The salinity of the lagoon varies between 4.5 and 26.6 ppt with monthly variations (Ellepola and Ranawana, 2015). (see **Supplementary Figure S2**). Panama lagoon is mainly influenced by northeastern (winter) monsoon rainfall between November and January which brings 90% of rainfall into this region with an annual average of 800 mm (Chandrajith et al., 2014). The catchment area of PN is covered by tropical dry evergreen forests (dry monsoon forests). Mangrove vegetation occurs as fringes around a significant part of the lagoon (Ellepola and Ranawana, 2015).

Horton Plains

The Horton Plains (HP) is a national park and a UNESCO World Heritage site located at the eastern extremity of the Central Highlands of Sri Lanka (6° 47– 6° 50′N, 80° 46′– 80° 51′E). The national park covers 31.6 km^2 and is located at an altitude between 2100–2300 m a.s.l. The HP is a gently undulating highland plateau with diverse landscapes, including mires, plains, forested hilltops, grassy slopes, precipices, brooks, and waterfalls (Premathilake and Risberg, 2003). Tributaries of three of the major river systems of Sri Lanka (Mahaweli, Kelani, and Walawe) start in the Horton Plains, forming an essential component of the hydrological regime of the island. The HP is one of the few areas of the island strongly influenced by both southwest monsoon (SWM/summer monsoon) and northeast monsoon (NEM/winter monsoon) rains. Nonetheless, SWM rainfall has the dominant impact on climate and vegetation in HP today. Although the mean annual rainfall in the wet zone is about 2540 mm, for the HP it can exceed 5000 mm. Due to its higher elevation and precipitation, the HP has a markedly colder and wetter climate than the rest of the island, with an unpredictable mountainous microclimate (Chandrajith et al., 2014). The mean annual temperature is 15°C, and January and February are, on average, the driest months of the year. The vegetation in HP mainly consists of Upper Montane Rain Forests (also referred to as Cloud Forests) and Wet Patana grasslands. In addition, a narrow ecotonal belt consisting of shrubs and herbs can be identified (DWC, 2007). (see **Supplementary Figure S2**).

MATERIALS AND METHODS

Sampling/Sediment Core Collection

70 and 100 cm long sediment cores were taken from Bolgoda South Lake and Panama Lagoon, respectively, using a UWITEC free-fall gravity corer. A 150 cm long peat core was taken from the Horton Plains peat bog using a Russian peat corer. Water quality parameters (i.e., temperature, pH, conductivity, and dissolved oxygen) were measured *in situ* during the sampling campaign in Sri Lanka. δD and δO values of collected water samples from the sites were measured later at the Stable Isotope Laboratory, MPI-BGC, Jena using a High-Temperature Conversion—Isotope Ratio Mass Spectrometer (HTC-IRMS).

The sediment cores retrieved from Bolgoda South Lake (BGSL) and Panama lagoon (PN) were split into two identical longitudinal sections. One section was archived at the German Research Centre for Geosciences (GFZ), Potsdam, Germany, after visually recording the lithological characteristics. The remaining split section was used for XRF core scanning in German Research Centre for Geosciences (GFZ), Potsdam, Germany followed by sub-sampling into 1-cm intervals for geochemical analyses (see below). Only half cores were retrieved with the Russian peat corer, so no archived sections are available for the Horton Plains (HP) core. The HP cores were also sliced into 1-cm intervals for geochemical analyses (XRF core scanning was not viable for this core). The sub-samples were freeze-dried and stored in zip-lock bags in the laboratory at room temperature before pre-treatment and analysis.

^{14}C Dating and Construction of Age-Depth Models

Mollusk shells and bulk organic carbon were extracted from sediment samples and analyzed for ^{14}C ages to establish the chronology and produce age-depth models for different sites. Considering the diverse organic matter/carbon sources of Panama lagoon, we selected only mollusk shells for ^{14}C dating the PN core. In the BGSL core, shells or plant macrofossils were unavailable for ^{14}C dating. In BGSL, terrestrial OM sources are dominant (see below), and there is a minimal direct influence from the ocean. Hence, bulk sediment (bulk organic carbon) was selected for ^{14}C dating. Ten mollusk shells were selected from the PN core, and 12 bulk sediment samples were selected from the BGSL core for ^{14}C dating. In the HP core, 15 peat/organic-rich bulk sediment samples were used for ^{14}C dating after sieving the freeze-dried material with a 1-mm sieve to remove rootlets that could be observed primarily in the top ~50 cm of the core (also see the **Supplementary Tables S1, S2, and S3**).

^{14}C dating was carried out using an Accelerated Mass Spectrometer MICADAS (Ionplus, Dietikon, Switzerland) at the ^{14}C Laboratory, Max Planck Institute for Biogeochemistry, Jena, Germany (see details about sample preparation in Steinhof et al., 2017). Age-depth models were developed using the R-software package BACON (rbacon) (Blaauw and Christen, 2011). BACON uses Bayesian statistics to reconstruct age-depth models by dividing a core into many vertical sections (of default thickness = 5 cm), and through millions of Markov Chain Monte Carlo (MCMC) iterations estimates the accumulation rate (in years/cm) for each of these sections. Using the starting dates for the first section, the accumulation rates for each section are compiled together to form the age-depth model (Blaauw and Christen, 2011).

Due to its direct connection to the sea and high marine influence the ^{14}C dates of shells in the PN core were calibrated using the Marine20 curve (Reimer et al., 2020) and the post-bomb curve NH Zone 3 was applied for negative ^{14}C ages (Hua et al., 2013). In addition, ^{14}C ages in shells were corrected for the local marine reservoir age ($\Delta R = 133 \pm 65$) based on data from the online Marine Reservoir Database at Queen's University, Belfast, United Kingdom. Bulk organic carbon ^{14}C dates in the BGSL and HP core were calibrated using the IntCal20 curve (Reimer et al., 2020).

Grain Size Analysis

Grain size analysis was performed on 10 sediment samples from BGSL and 11 samples from PN. 4–6 g of freeze-dried sediment from each layer were used, and the analysis was carried out according to Kilmer and Alexander (1949). First, 0.05% sodium hexametaphosphate was added to the sample to separate the grains. Then, sediment grains greater than 63 μm (sand fraction) were separated by wet sieving using a 63 μm mesh. The sieved extracts, consisting of particles <63 μm (i.e., silt and clay), were homogenized using a Sonic Vibra-Cell VC 750 with an ultrasonic stirrer. The samples were analyzed for grain size using a Sedigraph Micromeritics III Particle Size Analyzer at Linköping University, Sweden. The results were expressed as weight percentages of sand, silt, and clay.

X-Ray Fluorescence Core Scanning

XRF core scanning was conducted only for the BGSL and PN sediment cores as high organic matter and water content in peat, such as that from HP, creates high analytical uncertainties. XRF core scanning was conducted with the ITRAX μ-XRF core scanner at GFZ, Potsdam Germany at 5-mm resolution. Elemental intensities (c.p.s.) of Al, Si, S, Cl, K, Ca, Ti, V, Mn, Fe, Ni, Cu, Rb, Sr, Zr, and relative variations in the coherent and incoherent radiation, were obtained non-destructively. We used the μ-XRF core scanner with a Chromium X-ray source operated at 30kV and 55 mA for 10 S to generate energy-dispersive XRF radiation. The elemental intensities were non-linearly correlated to the elemental concentrations because the direct conversion of the intensity of a single element to its concentration is problematic. This uncertainty in measurement is due to many factors such as matrix effects and varying physical properties of sediments in the core (e.g., water content and grain-size distribution, irregularities of the split core surface, and spatial variations in the thickness of an adhesive pore-water film which forms directly below the protective foil covering the core surface) (Weltje and Tjallingii, 2008). Hence, the results are presented as log ratios of two elemental intensities that are linearly correlated with the log ratios of two elemental concentrations to eliminate the analytical problems with the measurements. (Weltje and Tjallingii, 2008; Martin-Puertas et al., 2017).

Total Organic Carbon Analysis

22 samples from BGSL, 19 samples from PN, and 70 samples from HP were selected for total organic carbon analysis. Around 5—10 mg of freeze-dried sediment was weighed into tin capsules and inorganic carbon was removed by the gradual addition of totally 120 µl H_2SO_3 (Bisutti et al., 2004). All tin capsules were introduced into an Elemental Analyzer (NA 1110, CE Instruments) and combusted with pure O_2 at 1020°C. Each sample was measured in duplicate at stable isotope laboratory, Max Planck Institute for Biogeochemistry, Jena, Germany (see details about analytical methods in Brooks et al., 2003). An in-house standard (acetanilide) was measured with the samples for quality control. Relative standard deviation (CV) of the acetanilide standard was 2.9%.

Biomarker Extraction and Analysis

The sediment subsamples were freeze-dried and homogenized before geochemical analysis (lipid extractions). In addition, mollusk shells were removed from the sediment by sieving with a 2-mm sieve or through manual extraction using tweezers, where necessary. 5–15 g of freeze-dried sediment were used for extraction, depending on the TOC contents of samples. Higher amounts of samples were used for lipid extraction in the PN core due to relatively low TOC content in the sediments. Nineteen samples from the PN core, 26 samples from the BGSL core, and 21 samples from the HP core were selected for lipid extraction considering the sediment accumulation rates throughout the cores. Lipid extraction was done using dichloromethane (CH_2Cl_2) and methanol (CH_3OH) (9:1 v/v mixture) on a Büchi Speedextractor (E-916, Büchi Labortechnik AG, Switzerland). The total lipid extracts (TLE) were then concentrated on a Büchi Syncore under reduced pressure.

The TLE was then separated into four fractions: F1 (alkane/non-polar hydrocarbon); F2 (aromatic hydrocarbon and ketone); F3 (alcohol and sterol); and F4 (fatty acids and other polar lipids) using the Solid Phase Extraction (SPE) technique on silica gel (0.040–0.063 mm mesh; Merck, Darmstadt, Germany) according to the modified method from Rach et al. (2014). The F1 fraction containing alkanes was eluted with 12 ml of hexane and subsequently de-sulphurised by elution through activated copper powder (with 1 M HCl) in a glass pipet column. The F2 fraction containing aromatic hydrocarbons and ketones was eluted on the same column using 12 ml of hexane: dichloromethane (DCM) (1:1, v/v) mixture. Subsequently, the alcohols and sterols (F3 fraction) were eluted with 12 ml of DCM: acetone (9:1, v/v) mixture, and finally, fatty acids and other polar compounds (F4 fraction) were eluted with 12 ml of DCM: methanol (1:1, v/v) mixture. The F3 fraction was derivatized with bis(trimethylsilyl) trifluoroacetamide (BSTFA) and pyridine, and heated at 75°C for 2 h. All extracts were then dried under a gentle stream of nitrogen before being re-dissolved in an equal volume (1 ml or 1.5 ml) of the solvent/solvent mixture.

An aliquot of the extracts (180 µl of F1, F2, and F3 fractions) was spiked with androstane (20 µl) as an internal standard for quantification. The samples were analyzed on an Agilent 6890N gas chromatograph (GC) interfaced with a 5973 MSD quadruple mass spectrometer (MS) with a DB-5 (5% phenyl methyl siloxane) fused silica capillary column (30 m length, 0.25 mm inner diameter, 0.25 µm film thickness) at Linköping University, Sweden. The samples were injected in splitless mode (1 µl inlet pressure of 10 psi with a flow rate 54.3 ml/min), and the injector temperature was maintained at 300°C. A constant flow (1.3 ml/min) of He was used as the carrier gas. The GC oven was initially maintained at 35°C for 1 min. The temperature was increased first to 130°C at 20°C/min and then to 320°C at 6°C/min where it was maintained isothermally for 15 min. The MS was operated at 70 eV under full scan mode (m/z 40—600), and the ion source and MS quadrupole temperatures were maintained at 230°C and 150°C, respectively. Compounds in the samples were identified based on their retention times relative to an external *n*-alkane standard mixture (*n*-C_{15} to *n*-C_{33}) and fragmentation patterns in the NIST MS Library (Version 2.0) and Lipid library (2011). Quantification of the biomarkers was done relative to the peak area of androstane (internal standard).

Compound Specific Isotope Analysis of *n*-Alkanes

The volume of the *n*-alkane fraction was reduced to 50 µl to increase the concentration by drying under a gentle stream of nitrogen before compound specific isotope analysis, due to relatively low concentrations of the compounds in samples. Stable hydrogen and carbon isotope (δD and $\delta^{13}C$) analysis of individual *n*-alkanes (*n*-C_{15} to *n*-C_{33}) was performed using a coupled gas chromatograph isotope ratio mass spectrometer (GC-IRMS system) equipped with a 7890A gas chromatograph (Agilent Technologies, Palo Alto, United States) linked *via* GC Isolink and ConFlo IV interface to a Delta V Plus Isotope Ratio Mass Spectrometer (Thermo Fisher Scientific, Bremen Germany) at the Max Planck Institute for Biogeochemistry, Jena, Germany. The GC was equipped with a DB1-MS column (60 m length, 0.25 mm inner diameter, 0.25 mm film thickness) for hydrogen isotope measurements and DB-1 MS column (30 m length, 0.25 mm inner diameter, 0.25 mm film thickness) for carbon isotope measurements. The sample was injected in splitless mode at 280°C and 2 µl of the extract was injected. The He carrier gas flow was maintained at 1.3 ml/min. The GC oven was maintained for 1 min at 110°C, before the temperature was increased to 320°C, at 5°C/min and held isothermally for 9 min.

Each sample was measured in triplicate with a standardized mixture of *n*-alkanes (C_{15} to C_{33} *n*-alkane standard mixture) of known isotopic composition measured after every sample (3 GC injections). Only peaks with an amplitude >150 mV were used for evaluation. The carbon and hydrogen isotopic values were converted to the Vienna Pee Dee Belemnite (V-PDB) and Vienna Standard Mean Ocean Water (V-SMOW) scales, respectively, using the values of the above-mentioned *n*-alkane standard mixture (offset correction). In addition, drift corrections were applied, determined by the standards run after every sample (Werner and Brand, 2001). In addition, the H_3^+ factor was determined daily (5.50 ± 0.5; $n = 25$); it remained constant over the measurement period indicating a stable condition in the ion source.

Statistical Analysis

A hierarchal cluster analysis according to Ward's method was performed for *n*-C_{15} to *n*-C_{33} in each site. A Principal Component Analysis (PCA) was also performed for *n*-alkane distributions at each location to identify the correlation between different *n*-alkanes within the zones identified by cluster analysis. Only *n*-alkanes with a relative abundance >5% in any sample were shown in the PCA biplots of each site to avoid visual overloading of variables. The statistical analyses were performed using the R statistical software package (R Core Team, 2020) and R package "factoextra" for visualization (Kassambara and Mundt, 2020).

RESULTS

Stratigraphy and Chronology

The Bolgoda South Lake sediments mainly consisted of light and dark greyish color sandy-silty clay. Shells were rare in this core except for a single horn gastropod (~3 cm long) between 39 and 41 cm depths (identified as a gastropod belonging to the family Potamididae) and some tiny mollusk shell fragments in a brownish sand layer deposited between 5.5 and 2 cm depth. This sand layer deposited between 5.5—2 cm showed characteristics of a high energy depositional event that is most likely linked to the 2004 tsunami, which is known to have significantly impacted the region (Wijetunge, 2006). Shell fragments with modern ^{14}C ages (see **Supplementary Table S2**) and the uneven or inclined lower stratigraphical boundary of this sand layer further support this interpretation (Jackson,

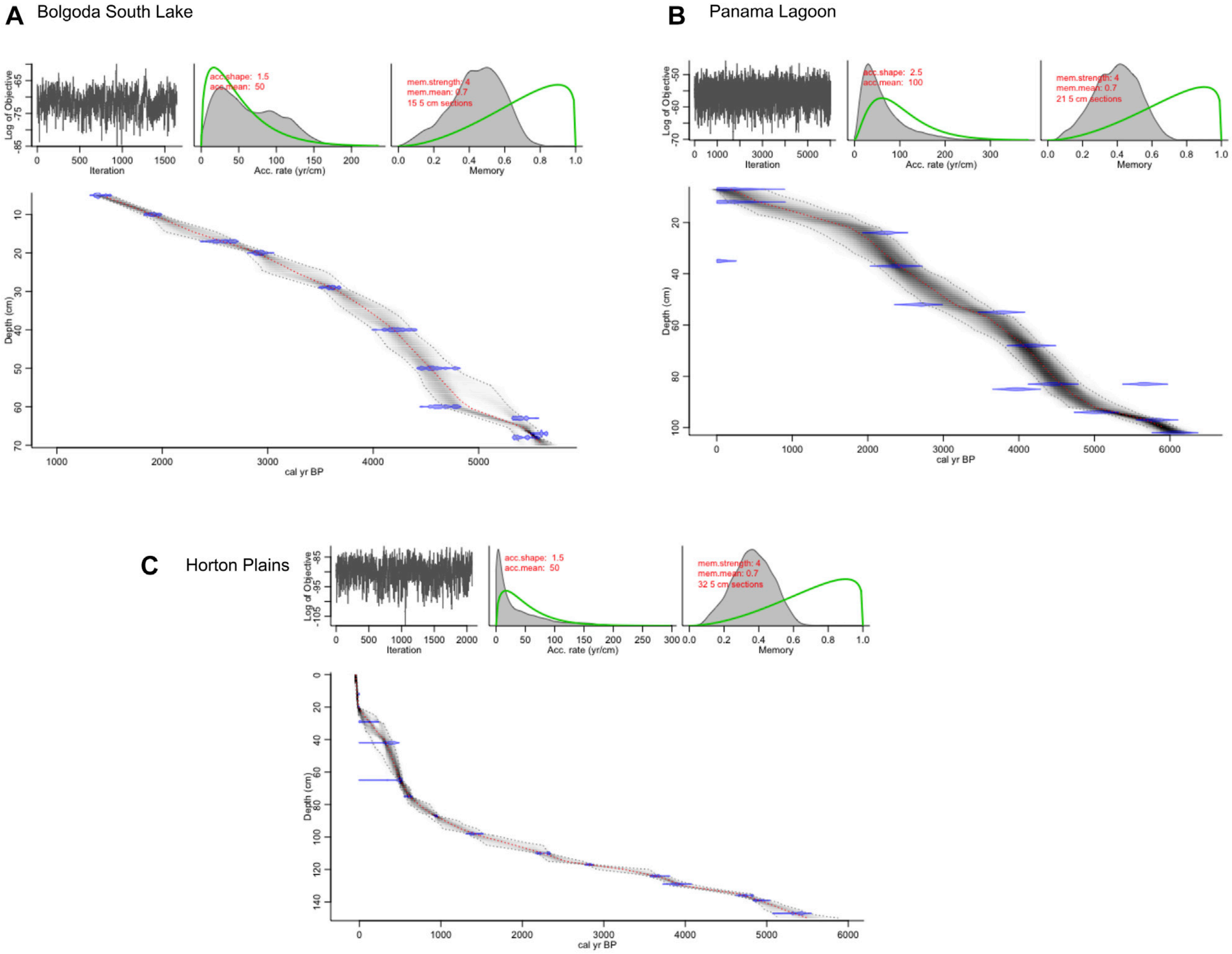

FIGURE 2 | BACON age-depth models for **(A)** Bolgoda South Lake (bulk organic carbon), **(B)** Panama Lagoon (mollusc shells) and **(C)** Horton Plains (bulk organic carbon); Upper panels represent Markov Chain Monte Carlo (MCMC) iterations **(left panel)**, the prior and posterior distributions for the accumulation rate **(middle panel)**, and memory **(right panel)**. Bottom panel indicate the calibrated ^{14}C dates (transparent blue) and the age-depth model (darker greys indicate more likely calendar ages and grey stippled lines infer 95% confidence intervals).

2008; Goff et al., 2012). The uppermost 2 cm layer was characterized by dark grey clayey sediments without shells (see **Supplementary Figure S3**). For the BGSL core, ages ranged between 5620 cal yr BP and 1410 cal yr BP (model median ages) according to the BACON age-depth model constructed based on ^{14}C ages in bulk sediments (**Figure 2A**). The age-depth model truncated at ca.1410 cal yr BP just below the sand layer (tsunami deposit) at 5 cm depth. This suggests that there is a depositional hiatus present at 5 cm depth that is possibly due to erosion of the top sediment layers during the tsunami. The ^{14}C age of the top 1 cm layer (present surface layer) at BGSL indicated that an (old carbon) reservoir age of 599 ± 19 ^{14}C years exists for the lake that was subsequently used for reservoir correction for all ^{14}C dates, assuming the reservoir age is constant throughout the studied period. The marshlands or mangrove swamps located adjacent to the south of the lake likely cause this old carbon reservoir effect (Last and Smol, 2002) (see **Supplementary Figure S2**).

The Panama Lagoon sediment core consisted of a greyish sandy-silty clay containing many shells throughout the core. From 90 to 37 cm depth, the core was characterized by many intact and semi-intact mollusk shells, including gastropods and bivalves, with horn gastropods being the most abundant. These gastropods were identified as *Cerethedia cingulate,* a species found today in brackish water mudflats and mangrove habitats. From ca. 10 to 5 cm depth, a light-colored sand layer was present with some shell fragments and an uneven lower boundary which was similar to that found near the top of the Bolgoda South Lake core. This deposit was likewise linked to the 2004 tsunami in the Indian Ocean with an uneven lower boundary and negative ^{14}C ages of mollusk shell fragments (modern ages). However, no significant erosion can be identified due to the tsunami waves, unlike at BGSL. The uppermost ca. 5 cm layer was characterized by a dark brown layer rich in partially decomposed organic detritus (see **Supplementary Figure S3**). The age model of Panama

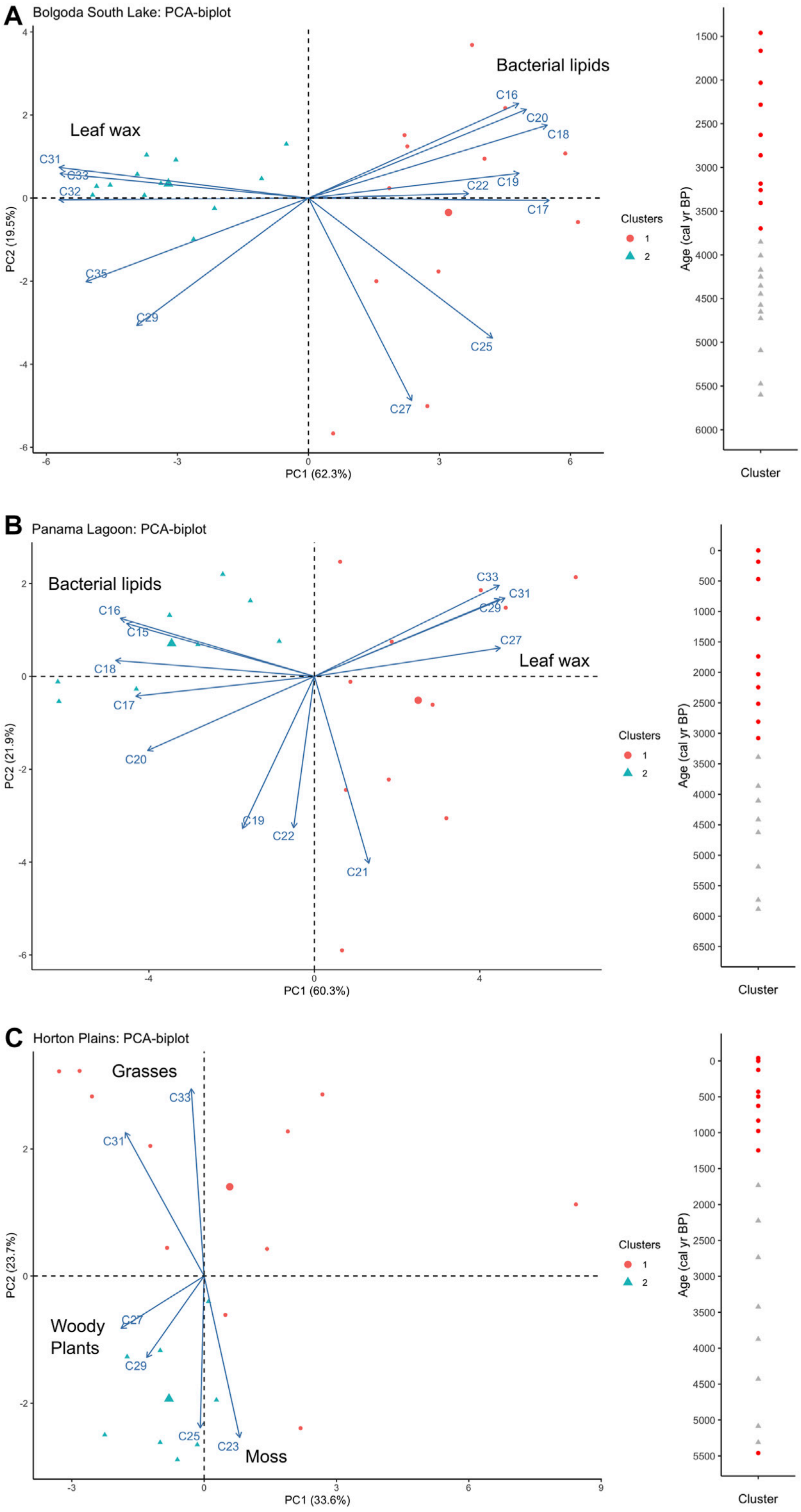

FIGURE 3 | n-Alkane distribution in PCA biplots **(left)** and hierarchal cluster plot **(right)** for **(A)** Bolgoda South Lake, **(B)** Panama Lagoon, and **(C)** Horton Plains.

lagoon (PN) constructed based on ^{14}C ages of mollusk shells (**Figure 2B**) showed a chronology extending from 5920 cal yr BP to the present (model median ages). The age model truncated at 7 cm, just below the sand layer that was identified as a deposit left behind by the 2004 tsunami. Unconsolidated sediments above this layer (the upper 5 cm) were considered as recently deposited sediments. In Panama lagoon, the regional marine reservoir age of the shells (133 ± 65 yr BP) was applied for the reservoir correction of ^{14}C shell dates.

The Horton Plains peat core consisted of dark brown non-laminated peat deposits. The coring was stopped at 150 cm depth because it was difficult to penetrate an identified sandy layer. Between ca. 50 cm and the core top, the peat deposit included partially decomposed or undecomposed rootlets (see **Supplementary Figure S3**). The retrieved HP core revealed a depositional history spanning from 5500 cal yr BP (model median age) to the present based on the bulk ^{14}C dates in the peat sequence (**Figure 2C**). However, rapid accumulation rates can be observed at HP, from ca.75 cm to the top of the core (between ca. 600 cal yr BP—present) with significant age uncertainties during this period.

Biomarker Variation

n-Alkanes

In sediment cores retrieved from the three sites along a transect, we identified and measured the concentrations of *n*-alkanes between *n*-C_{15} and *n*-C_{35} chain-length (see also **Supplementary Figure S4**). Each sediment core was divided into two zones (clusters) by hierarchical cluster analyses, based on the relative distribution of *n*-alkanes that is taken to indicate different OM sources for the cores. Dominant *n*-alkanes in these clusters were identified using PCA biplots for each core (**Figure 3**).

In BGSL, PC1 accounted for 62.3% variance and was characterized by high positive loadings of short-chain *n*-alkanes from C_{16} to C_{22} (predominantly even chain *n*-alkanes) and high negative loadings of long-chain *n*-alkanes from C_{31} to C_{35} (odd chain *n*-alkanes predominant). Short-chain even carbon number *n*-alkanes such as C_{16}, C_{18}, and C_{20} commonly occur in inter-tidal hypersaline environments such as lagoons and estuaries. They generally occur in autochthonous bacterial (secondary) lipids as a product of decaying algal mats or marine algae in saline environments (e.g., Nishimura and Baker, 1986; Elias et al., 1997; Ekpo et al., 2005; Aloulou et al., 2010; Aghadadashi et al., 2017). The abundance of these *n*-alkanes can thus be used as a proxy to trace marine influence (e.g., sea water intrusion or marine transgression) in coastal water bodies. Long-chain odd carbon number predominant *n*-alkanes such as C_{27} C_{29}, C_{31}, C_{33}, and C_{35}, are mainly derived from the leaf waxes of terrestrial higher plants (Meyers, 2003; Eglinton and Eglinton, 2008). Cluster 1 in BGSL showed positive scores with PC1, whereas cluster 2 showed negative scores (**Figure 3A**). This trend implies that cluster 1 in BGSL is characterized by mainly *n*-C_{16}, C_{18}, and C_{20} alkanes (bacterial lipids) whereas cluster 2 mainly consisted of *n*-C_{31}, C_{33}, and C_{35} alkanes (leaf wax).

In PN, an inverse pattern of *n*-alkane distributions can be identified based on hierarchical cluster analyses and PCA. PC1 in PN core accounted for 60.3% of variance characterized by high negative loadings of short-chain *n*-alkanes from C_{15} to C_{20} (predominantly even *n*-alkanes) and high positive loadings of long-chain *n*-alkanes from C_{27} to C_{33} (predominantly odd *n*-alkanes). Cluster 1 in PN showed positive scores with PC1, whereas cluster 2 indicated negative scores (**Figure 3B**). This trend implied that cluster 1 in PN was characterized mainly by *n*-C_{27}, C_{29}, C_{31}, and C_{33} alkanes (leaf wax), whereas cluster 2 consisted of *n*-C_{16}, C_{18}, and C_{20} alkanes (bacterial lipids). PC1 scores changed rapidly from negative to positive scores in the BGSL core at ~ 3750 cal yr BP while in the PN core, this occurred relatively smoothly at ~ 3200 cal yr BP (**Figures 4A,B**).

A different pattern of *n*-alkane distributions was identified in the HP peat core based on multivariate statistical analysis. According to the PCA biplot of HP, PC1 and PC2 accounted for 33.6 and 23.7% of the total variance, respectively (**Figure 3C**). The loadings of the dominant *n*-alkanes correlated with the PC2 axis rather than the PC1 axis in the PCA biplot. Longer chain *n*-alkanes (namely C_{31} and C_{33}) derived from grass (Eglinton and Eglinton, 2008) correlated positively with PC2, whereas mid-chain *n*-alkanes C_{23} and C_{25} originated from mosses (like *Sphagnum*) (Naafs et al., 2019) correlated negatively with PC2. The present-day environment and abundance of *Sphagnum* growing near to the HP coring location further supports this interpretation.

In addition, *n*-C_{27} and C_{29}, derived mainly from woody plants (Meyers, 2003), showed a moderate negative correlation with PC2. Therefore, PC2 scores at HP appear to generally represent variation between grass (*n*-C_{31} and C_{33} alkane) and moss (*n*-C_{23}, C_{25} alkane). The majority of cluster 1 depths showed positive scores with PC2, whereas cluster 2 depths showed negative scores with PC2 (**Figure 3C**). At HP, PC2 scores were negative with a general core upward trend towards positive scores between ~5500 and 1700 cal yr BP. From ~1700 cal yr BP to present PC2 scores were primarily positive albeit with significant fluctuations.

Sterols

The BGSL and PN cores included mangrove-derived triterpenols, primarily taraxerol (e.g., Ranjan et al., 2015; Gayantha et al., 2020). Due to the different total organic carbon (TOC) ranges at BGSL and PN, taraxerol contents were expressed as TOC normalized values to compare the two sites. According to the results, the high average value of taraxerol was observed in the PN core relative to BGSL. In BGSL, taraxerol varied from 717—2578 ng/g dw (dry weight) TOC without any clear trends through the core (**Figure 4A**). In the PN core, taraxerol varied from 626—4801 ng/g dw TOC with a clear increasing core upward trend until the tsunami layer (**Figure 4B**). In the HP core several sterols and stanols were identified, namely cholesterol, cholestanol, campesterol, campestanol, stigmasterol, sitosterol, and sitostanol. The 5α-sterol to Δ^5stanol (C_{28}, C_{29}) ratio in HP, which is suggested as a proxy for peat humification (Routh et al., 2014; Naafs et al., 2019), showed a general core upward decreasing trend (**Figure 4C**).

Compound Specific Carbon and Hydrogen Isotope Variation in *n*-Alkanes

Among the three sites, core average *n*-alkane δD values of long-chain *n*-alkanes (*n*-C_{33}, C_{31}, and C_{29}) in HP showed the lowest values followed by PN. BGSL showed high (most enriched)

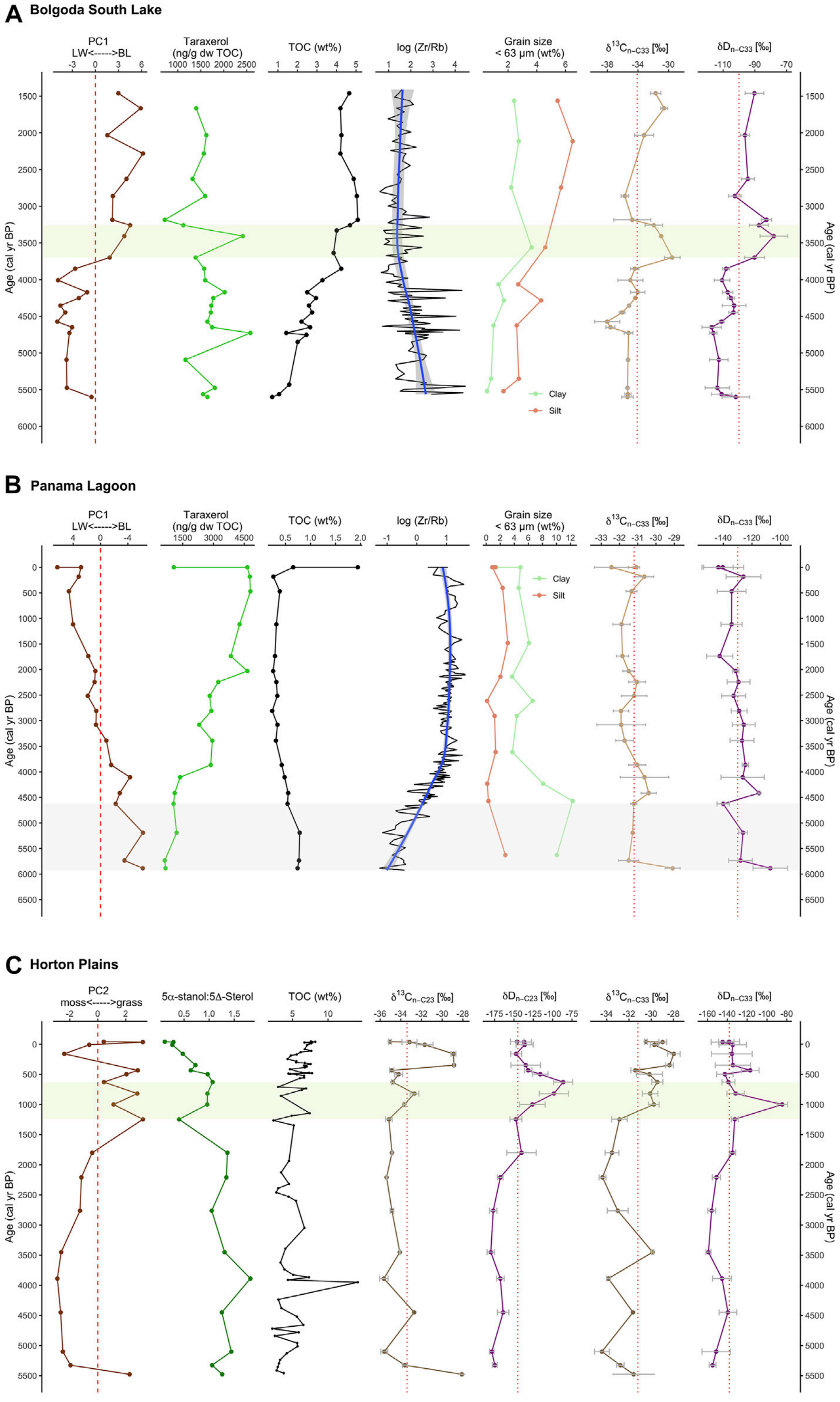

FIGURE 4 | Trends of Leaf wax (LW) and bacterial lipid (BL) derived n-alkane (PC1), taraxerol, total organic carbon (TOC), Zr/Rb element ratio, grain size (<63 μm) and carbon and hydrogen isotopes of leaf wax derived n-alkane (n-C_{33}) in **(A)** Bolgoda South Lake and **(B)** Panama Lagoon; Trends of moss and grass derived n-alkane (PC2), Stanol: Sterol ratio, TOC, carbon and hydrogen isotopes of moss derived (n-C_{23}) and grass derived (n-C_{33}) alkane in **(C)** Horton Plains.

TABLE 1 | Average, minimum and maximum $\delta^{13}C$ and δ D values of dominant n-alkanes in each core.

***n*-alkane**		**Panama Lagoon**			**South Bolgoda Lake**			***n*-alkane**		**Horton Plains**		
$\delta^{13}C$		Average ‰	Min ‰	Max ‰	Average ‰	Min ‰	Max ‰	$\delta^{13}C$		Average ‰	Min ‰	Max ‰
	C33	−31.2	−32.4	−29.1	−34.1	−38.0	−29.5		C33	−31.2	−34.4	−28.0
	C31	−32.3	−34.3	−29.3	−33.8	−37.4	−30.0		C31	−34.0	−35.9	−31.9
	C29	−29.7	−31.4	−27.3	−31.3	−34.7	−28.0		C29	−31.7	−33.4	−27.7
	C16	−29.8	−31.3	−28.2	−28.1	−30.4	−23.0		C25	−34.1	−36.5	−29.5
	C18	−29.5	−32.5	−25.7	−17.4	−22.6	−12.4		C23	−33.4	−35.6	−28.1
δD	C33	−130	−144	−107	−100	−117	−78	δD	C33	−138	−159	−85
	C31	−133	−152	−99	−133	−140	−106		C31	144	−166	−111
	C29	−221	−239	−206	−197	−217	−177		C29	−237	−253	−209
	C16	−75	−92	−57	−40	−75	−5		C25	−249	−275	−208
	C18	−92	−116	−49	−73	−109	−47		C23	−145	−180	−86

average δD values in long-chain *n*-alkanes (**Table. 1**). Generally, winter monsoon rainfall is more negative in D and ^{18}O in contrast to summer monsoon rainfall in Sri Lanka and India (Srivastava et al., 2014; Edirisinghe et al., 2017). The primary source of moisture for winter monsoon (or NEM) is the Bay of Bengal where several large rivers discharge their water from the Indian sub-continent. Therefore, the isotope values of water (δD and $\delta^{18}O$) in Bay of Bengal are relatively negative (Singh et al., 2010; Achyuthan et al., 2013) in contrast to the western (open) Indian Ocean, which is the moisture source for summer monsoon (or SWM) rainfall. This seasonal effect (summer and winter monsoon precipitation due to changing the wind direction) is clearly reflected in the sediment leaf wax *n*-alkane (C_{29} and C_{33}) δD average values in the BGSL and PN cores (**Table. 1**). In addition, the lowest average leaf wax δD values in HP, relative to both BGSL and PN, reflect the altitude effect on precipitation in the central highlands.

Comparison of the average $\delta^{13}C$ values of long-chain *n*-alkanes at the three sites indicated no significant differences between the core average values. However, at PN, slightly higher average values were found than at BGSL and HP (**Table. 1**). Short-chain *n*-alkanes (*n*-C_{16} and C_{18}) were only present in the coastal sites (BGSL and PN). These sites indicated relatively higher average $\delta^{13}C$ values in BGSL relative to PN, particularly for *n*-C_{18} alkanes. Average δD values were also relatively high in BGSL short-chain *n*-alkanes, particularly for *n*-C_{16} alkanes (**Table 1**). Mid-chain *n*-C_{23} and C_{25} alkane $\delta^{13}C$ values in HP showed slightly lower values than long-chain *n*-alkanes in the same core (**Table. 1**).

Long-chain *n*-alkane carbon and hydrogen isotopic variations showed a generally inverse relationship between the BGSL and PN cores. In the BGSL core, δD and $\delta^{13}C$ values for *n*-C_{33} alkanes showed a general core upward increasing trend in their values. Particularly, high $\delta D_{n\text{-}C33}$ values were observed at ca. 3400 cal yr BP (26 cm depth), deviating from the general trend (**Figure 4A**). In contrast to the overall core upward increasing trend at BGSL, δD and $\delta^{13}C$ values of *n*-C_{33} showed a general core upward decreasing trend in PN (**Figure 4B**). In contrast to BGSL and PN, trends for δD *n*-alkane (i.e., *n*-C_{23} and C_{33}) values in the HP core varied somewhat differently from their corresponding $\delta^{13}C$ *n*-alkane values (**Figure 4C**). Noticeably higher $\delta D_{n\text{-}C33}$ and $\delta D_{n\text{-}C23}$ values occurred at ~1000 cal yr BP and ~630 cal yr BP, respectively. In addition, peak values of $\delta^{13}C_{n\text{-}C23}$ and $\delta^{13}C_{n\text{-}C33}$ can be observed between 350—160 cal yr BP.

Regarding the δD values of the HP *n*-alkanes, a core upward increasing trend for *n*-C_{23} was observed with maximum values at ~ 630 cal yr BP followed by a gradual decline. $\delta D_{n\text{-}C33}$ also showed a core upward increasing trend, reaching its peak value ~1000 cal yr BP (**Figure 4C**). The δD peak thus appeared slightly earlier in long-chain *n*-alkanes than in mid-chain *n*-alkanes. $\delta^{13}C$ of *n*-C_{23} alkanes showed relatively low (below average) and stable values between ~5480—440 cal yr BP followed by a sharp peak between 350 and 160 cal yr BP and then a rapidly decreasing trend towards the top of the core. However, $\delta^{13}C_{n\text{-}C33}$ showed relatively low values (below −30‰) between ~5330 and 1250 cal yr BP and shifted to relatively higher values (above -30‰) towards the present (**Figure 4C**).

Total Organic Carbon

The highest average total organic carbon (TOC wt%) values were observed in the HP peat deposit, followed by the BGSL and PN cores, respectively. In the HP peat deposit, TOC values varied between 2.13—14.20% with an average of 5.49%. The BGSL core had an average TOC value of 3.11%, varying between 0.71 and 5.09%. In both the BGSL and HP sites the TOC showed a core upward increasing trend (**Figures 4A,C**). TOC content was relatively low in the PN core with an average of 0.52 wt%. Except for the relatively high value (1.94%) in the organic-rich surface layer at the top of the core, TOC content was <1% and showed a gentle core upward increasing trend (**Figure 4B**).

Grain Size Distribution and Zr/Rb Log-Ratio

Grain size and elemental composition data are only available for Bolgoda South Lake and Panama lagoon core. Both the BGSL and PN cores showed very high contributions from sand (>63 μm) that represented 94 and 93% of the mean values, respectively. However, for the finer fraction (<63 μm, i.e., silt and clay), silt dominated at BGSL, whereas clay dominated in the PN core. In the BGSL core, both silt and clay fractions showed core upward increasing trends that are distinct for silt (**Figure 4A**). In contrast, at PN, the clay fraction was relatively high and extended from

~6000 to 4700 cal yr BP. After that, the clay fraction decreased and showed a stable or slightly decreasing trend until the present. It is, by contrast, difficult to see a clear trend in silt (**Figure 4B**).

The Zr/Rb ratio of sediment supports the low-resolution grain size data in our records (see discussion). The log ratio of Zr/Rb XRF element intensities showed an overall decreasing trend in BGSL with the lowest values around 3800 cal yr BP. By contrast, in PN, the Zr/Rb log-ratio showed an overall increasing trend with the highest values occurring around 3600 cal yr BP.

DISCUSSION

Behavior of Monsoon Rainfall and Environmental Impacts in Sri Lanka

Along the transect from the west to the east coast, running through the central highlands of Sri Lanka, the three sampled sites indicate clear paleoenvironmental changes related to monsoon variability since the mid-Holocene. Here, we discuss the multi-proxy data in the Bolgoda South Lake, Panama Lagoon, and Horton Plains to understand the long-term variability of the Indian Ocean monsoon rainfall and its related environmental changes in Sri Lanka during the last ~6000 cal yr BP.

Bolgoda South Lake

This summer monsoon (or SWM) fed coastal brackish water lake demonstrated a depositional history spanning from ~5600 to 1400 cal yr BP. Terrestrial plants (leaf wax *n*-alkanes) dominate between ~5600 and 3850 cal yr BP in BGSL (cluster 2), whereas bacterial lipids are predominant between 3850 and 1400 cal yr BP (cluster 1) (**Figure 3A**). As indicated by BGSL PC1 scores, a rapid shift of the dominant OM source, from terrestrial plants to marine bacterial lipids, can be observed ~3800 cal yr BP (**Figure 4A**). Thus, the marine influence (sea water intrusion) appears to have increased in the BGSL catchment from 3850 to 1400 cal yr BP, likely as a product of decreasing freshwater input into the αlake. Taraxerol is a reliable proxy for the presence of mangrove vegetation surrounding coastal water bodies (Ranjan et al., 2015; Gayantha et al., 2020). However, in BGSL, taraxerol does not show a clear trend throughout the core, with minimal variation from its core average value. This trend indicates that the mangrove vegetation in the vicinity of the site may have been stable over time (**Figure 4A**). Furthermore, we infer that salinity changes due to varying marine influence were not significant enough to cause notable changes in the mangrove vegetation around this lake.

Grain size variation primarily reflects energy-driven processes in the lake catchment. High rates of precipitation trigger enhanced erosion and stream discharge that brings coarse particles (sand and coarse silt) to the lake bottom. Conversely, weak precipitation or dry climatic conditions lead to the accumulation of more fine clay particles in sedimentary sequences (Peng et al., 2005; Gayantha et al., 2017). In BGSL, increasing trends of clay and silt content (representing a low energy environment) towards the top of the core reflects the weakening of inland precipitation over time (**Figure 4A**). This low-resolution grain size distribution trend is further supported by high-resolution Zr/Rb ratios, which are widely utilized as a proxy for grain size variation (Kylander et al., 2011; Davies et al., 2015). Zirconium is typically associated with the coarse fraction in sediments (medium to coarse silt), whereas Rb is enriched in the fine clay fraction. Therefore, higher values of Zr/Rb indicate coarse sediment and lower values demonstrate finer sediment grains (Kylander et al., 2011). The Zr/Rb ratio in the BGSL core shows an overall core upward decreasing trend, indicating that the finer fraction is increasing in BGSL. The lowest values can be observed ~3750 cal yr BP indicating minimum freshwater discharge and erosion in the catchment. This observation might be connected to a decline in catchment precipitation and/or arid conditions (**Figure 4A**). TOC is mainly associated with the clay fraction in sediments. Therefore, the observed core upward increasing trend of TOC can also be explained by the increasing clay fraction in lake sediments (**Figure 4A**).

Changes in stable hydrogen and oxygen isotopes (δD and δ^{18}O) in meteoric water are recorded in archives such as continental ice cores (Thompson et al., 1985) and speleothems (Liu et al., 2015; Liu et al., 2020). However, these types of archives are very limited to specific geographical regions, and therefore, measuring the hydrogen isotope ratios (δD values) in biomarkers such as sediment leaf wax *n*-alkane is a promising method that has been developed recently (Sachse et al., 2012). δD in sedimentary OM can provide palaeohydrological information, i.e. amount, trajectory and source of precipitation (Holtvoeth et al., 2019). Hydrogen isotopes of plant water and plant tissues will, however, be significantly modified due to processes impacting transpiration (i.e., aridity) prior to biosynthesis. Therefore, δD in terrestrial plant lipids reflect a combined signal of precipitation and evapotranspiration (Sessions et al., 1999; Sachse et al., 2012). δ^{13}C variability of leaf wax *n*-alkanes can reflect the water stress of higher plants when there is no major shift in vegetation (C_3 vs C_4) and atmospheric CO_2 during the period of concern (Diefendorf and Freimuth, 2017). Both δD and δ^{13}C values of leaf wax-derived *n*-C_{33} alkanes show an overall core upward increasing trend at BGSL, indicating a weakening of rainfall in the catchment and increasing aridity from ~5600 to 1450 cal yr BP (**Figure 4A**). Relatively higher δD and δ^{13}C values deviated from the general trend between 3700 and 3200 cal yr BP, suggesting the prevalence of drought-like conditions due to a weakening of the summer monsoon (**Figure 4A**). A shift of $\delta D_{n\text{-}C33}$ to lower values ~3800 cal yr BP indicates the rapid decrease of summer monsoon at this time, coinciding with the rapid shift of OM sources in the sediments (i.e., from leaf wax to bacterial lipids) and the lowest Zr/Rb values (**Figure 4A**). Overall, the proxy results suggest a decreasing trend of summer (or SWM) monsoon in the area from 5600 to 1400 cal yr BP with apparent failure of rain ~3700 cal yr BP and droughts between 3700 and 3200 cal yr BP.

Panama Lagoon

Panama Lagoon is predominantly influenced by winter monsoon (or NEM) rainfall, and the obtained core revealed a depositional history from ~5900 cal yr BP to the present. All the proxy records showed inverse trends/variations in Panama lagoon compared to Bolgoda South Lake, except the taraxerol contents. Bacterial lipids are dominant between 5900 and 3400 cal yr BP (cluster 2), and leaf wax biomarkers are predominant between 3400 and the present (cluster 1) (**Figure 3B**). In addition, PC1 scores in PN gradually increase (negative to positive scores) with time, indicating a gradual decrease of marine influence at the site, in stark contrast to BGSL. This is likely due to increasing freshwater input into the lagoon with time. The taraxerol content showed a gradually increasing trend with time, indicating increasing mangrove vegetation at the site. This suggests that, with additional stream water input, the lagoon water reached optimal salinity levels that enabled mangrove vegetation to flourish around the lagoon. This changeover suggests that Panama lagoon turned from a high salinity to a low salinity brackish water body due to enhanced freshwater input. This changing marine influence is also confirmed by the data from microfauna analysis (see **Supplementary Figures S5, S6**).

Notably, high clay content can be observed between ~5900 and 4500 cal yr BP, and this is also confirmed by low (negative) Zr/Rb log-ratios during this period. After that, clay content/fine particles showed no significant variation until the present. The higher clay content between ~5900 and 4500 cal yr BP suggests a low energy environment, probably due to the weakening of stream discharge. This can occur as a result of significant declines in rainfall and/or a sea level high stand that further diminished the input of stream water into the lagoon. TOC values also show a slight decreasing trend until the organic detritus-rich topmost layer, that may relate to the decreasing clay content in the PN core over time.

In contrast to BGSL, δD and $\delta^{13}C$ of leaf wax-derived n-C_{33} alkanes in Panama lagoon show an overall decreasing trend, indicating a gradual increase in the amount of winter monsoon precipitation and decreasing aridity in the area from ~5900 cal yr BP to present. At ~ 4600 cal yr BP, relatively low values of $\delta D_{n\text{-}C33}$ can be observed deviating from the general trend, suggesting high rainfall around this time. The coarse sediment fraction also increased at PN over this period, further supporting this interpretation. However, the rainfall is not notably low between 5900—4600 cal yr BP according to leaf wax hydrogen isotopes values. Therefore, it is probably a period with a high sea level stand that diminished the energy of freshwater discharge into the lagoon, resulting in high clay content in the sediment. Previous studies related to past sea level changes in Sri Lanka have also suggested sea level transgression between 7000 and 4900 cal yr BP, but the sea level generally stabilized after this period (Weerakkody, 1992; Ranasinghe et al., 2013a).

The core average $\delta^{13}C_{n\text{-}C33}$ value of PN is slightly higher than for BGSL (about 3‰) but varies within a narrow range (**Table. 1**). This is probably due to the relatively high abundance of C_4 plants in the dry zone in contrast to the wet zone. However, the values still indicate that the area was dominated by C_3 vegetation without a large shift in vegetation types (C_3-C_4 transition) (Diefendorf and Freimuth, 2017; Holtvoeth et al., 2019).

Horton Plains

Today, the Horton Plains area in the Central Highlands is influenced by both SWM (summer) and NEM (winter) rainfall but with a dominant impact from SWM. Therefore, the HP peat deposit is expected to preserve mixed signals of both types of precipitation. This high-altitude peat deposit reveals a depositional history of ~5500 cal yr BP with a rapid accumulation rate in the top ~70 cm of the core. Moss and woody plants dominate between 5400 and 1800 cal yr BP (cluster 2), whereas grasses dominate from ~1800 cal yr BP to the present (cluster 1) (**Figure 3C**). PC2 scores indicate that the change of moss and woody plant-dominant peat to grass-dominant peat occurs around 1700 cal yr BP (**Figure 4C**).

The presence of C_{28} and C_{29} sterols, such as campesterol, stigmasterol and β-sitosterol, can provide additional insights into input from higher plants and mosses (Ronkainen et al., 2014). 5α-stanols are the saturated counterparts of Δ^5-sterols produced by anaerobic microbial hydrogenation (Routh et al., 2014). Hence, the Σ 5α-stanol: Σ Δ^5-sterol ratio can be used to trace the degree of microbial hydrogenation or humification in peat (Routh et al., 2014; Naafs et al., 2019). The Σ 5α-stanol: Σ Δ^5-sterol ratios in HP are very low (below 0.5) in the acrotelm (top-most ~20 cm) that yielded modern ages (negative ^{14}C values). In the anaerobic cattotelm (below ~20 cm), the Σ 5α-stanol: Σ Δ^5-sterol ratio showed a downcore increasing trend, indicating that microbial hydrogenation increases down the core (**Figure 4C**). TOC content also decreases downcore, further supporting the observation of post-diagenetic changes after deposition (**Figure 4C**). Transformation of plant derived Δ^5-sterols to their correspondent 5α-stanols preferentially occurs under anoxic conditions (Naafs et al., 2019). Therefore, low values of Σ 5α-stanol: Σ Δ^5-sterol ratio suggest oxic conditions in the peat, probably due to a lowering of the water table during dry periods. From ~5500 to 1800 cal yr BP, the Σ 5α-stanol: Σ Δ^5-sterol ratio varies in a narrow range but shows very low values at ~1200 cal yr BP, indicating more oxic conditions (low water table) related to the onset of a dry period.

In HP, both terrestrial plants and moss provide information on paleo-hydrological changes in the area in slightly different ways during the last ~5500 cal yr BP. Grass (n-C_{33}) records the H isotopic ratios of acrotelm water originating from precipitation and is little affected by evaporation, whereas moss (n-C_{23}) records water inside its cells and between its leaves which is strongly affected by local evaporation (Nichols et al., 2010). However, the influence of summer and winter monsoon in the area, with distinct isotopic signatures, and their fluctuations in amount, makes the interpretations complicated.

Overall, a core upward increasing trend of moss-derived $\delta D_{n\text{-}C23}$ and grass-derived $\delta D_{n\text{-}C33}$ values from ~5500 cal yr BP to present indicates overall decreasing trends of precipitation in the area. Both grass and moss hydrogen isotopic variations show very similar behavior from ~5500 to ~ 1250 cal yr BP indicating low evaporation. However, from ~ 1250 cal yr BP to present they show somewhat different behavior and there is an asynchrony between their peak values. This is probably due to the relatively increased contribution of winter monsoonal precipitation (with a concomitant failure of summer monsoon) during this period as well as the different ways in which grasses and mosses record local hydrological conditions. Since, the moss provides more of an evaporation signal rather than source water signal (Nichols

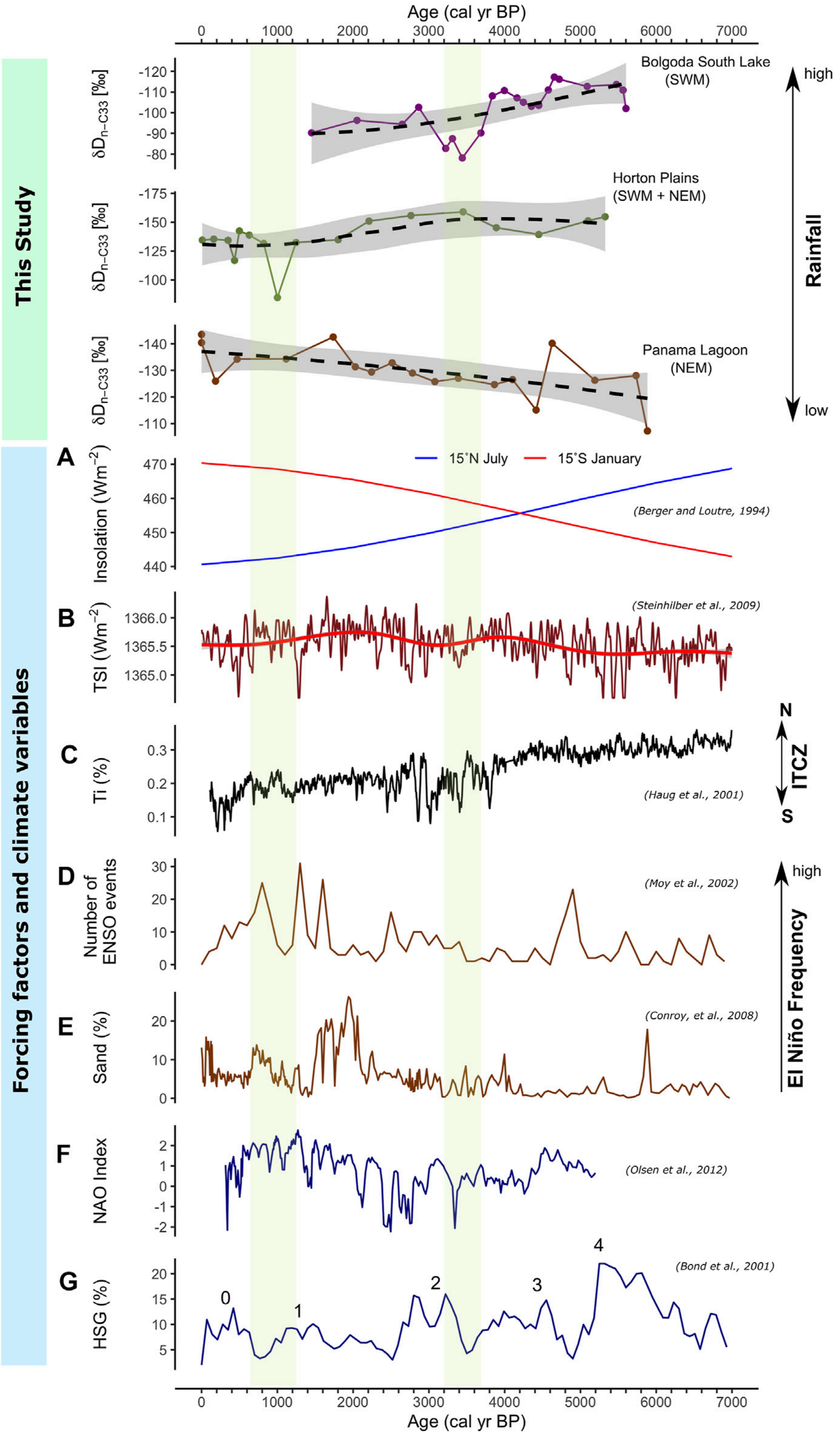

FIGURE 5 | Comparison of reconstructed monsoonal variations in Sri Lanka with different forcing and modes of climate variables during the last 7000 years. Two green bars represent the arid phases identified in our study. **(A)** Solar insolation (Berger and Loutre, 1994), **(B)** Total Solar Irradiance (TSI) (Steinhilber et al., 2009), **(C)** Ti content in Cariaco Basin sediments (Haug, 2001), **(D)** Number of ENSO events per 100 yrs (Moy et al., 2002), **(E)** Percentage of sand in El Junco Lake, Galápagos (Conroy et al., 2008), **(F)** Reconstructed North Atlantic Oscillation Index (Olsen et al., 2012), **(G)** Hematite-Stained Grains (HSG) percentage in North Atlantic deep-sea sediment and Bond events (Bond et al., 2001).

et al., 2010), we can assume that the peak in aridity should be around 600 cal yr BP based on the values obtained.

The *n*-alkane isotope trends ($\delta D_{n\text{-}C33}$, $\delta D_{n\text{-}C23}$ and $\delta^{13}C_{n\text{-}C33}$), and relatively low Σ 5α-stanol: $\Sigma \Delta^5$-sterol ratios, indicate a failure of rainfall starting at ~1250 and the onset of a relatively dry climate period between 1000 and 600 cal yr BP at HP. This is further supported by shifting dominant OM sources in the HP peat core, from moss and woody plants to grasses, which occurred around the same time according to the PC2 score variations.

However, we cannot identify the arid phase recorded in Bolgoda South Lake in Horton Plains despite both sites are dominantly influenced by SWM. This could be due to the HP is also significantly influenced by NEM in addition to SWM (see **Supplementary Figure S1**), which brings relatively isotopically depleted moisture contrast to SWM, that can mask the arid phase caused by the failure of SWM in HP.

South Asian Monsoon During the Middle and Late Holocene

Organic geochemical proxies, especially leaf wax hydrogen (and carbon) isotopes, lithogenic metal element ratios (Zr/Rb), and grain size distributions in Bolgoda South Lake indicate an overall decreasing trend of SAM (Southwest monsoon) in Sri Lanka between ~5600 and 1400 cal yr BP. In contrast, the same proxies in the Panama lagoon indicate an overall increasing trend of South Asian Winter monsoon rainfall (Northeast monsoon) during ~5900 cal yr BP to the present. Proxy records from the Horton Plains show more similar variations to the Bolgoda South Lake records, indicating an overall decreasing trend of summer monsoon rainfall (**Figure 5**). Despite the fact that Bolgoda South Lake is missing records from ~1400 cal yr BP to present, our previous study from North Bolgoda Lake (Gayantha et al., 2017; Gayantha et al., 2020) is able to confirm a weakening trend of summer monsoon rainfall in the area during this time (between 1400 cal yr BP—present). Therefore, we can reasonably assume that the weakening trend of summer monsoon rainfall identified in Bolgoda South Lake continues until the present.

The results from Bolgoda South Lake, Panama lagoon and the Horton Plains indicate a sub-millennial scale inverse relationship between South Asian summer and winter monsoon rainfall in Sri Lanka from the mid- Holocene onwards. This inverse relationship between summer and winter monsoon trends generally correlates with the Earth's precession (orbital forcing)-controlled inverse distribution of solar insolation between the Northern and Southern hemispheres during the middle and late Holocene (**Figure 5**; Berger and Loutre, 1994). These changes in solar energy distribution primarily induced the southward migration of the mean latitudinal position of the ITCZ according to established records in different parts of the globe (**Figure 5**; Fleitmann et al., 2003; Haug, 2001; Schneider et al., 2014). These show that the northernmost (in boreal summer) and southernmost (in boreal winter) positions of the ITCZ, moved southward from the middle Holocene. Being an island located in the path of the seasonal migration path of ITCZ, this phenomenon would have influenced the long-term (sub-millennial scale) inverse variation of the seasonal lengths, and thus the amounts of summer and winter monsoon rainfall, in Sri Lanka. However, our interpretations on this inverse trend between summer and winter monsoon precipitations are specifically for the SAM and not address the East Asian Monsoon. In addition to the broad patterns of the different monsoonal rains, we also observed multi-centennial scale failure in the summer monsoon between ~3700—3200 cal yr BP, leading to aridity in the lowland wet zone of Sri Lanka (**Figures 4**, **5**). Severe and prolonged droughts have been identified across various portions of Asia between approximately 4500 and 3500 cal yr BP leading to supposed social "collapse" at certain sites such as Harappa and Mohenjo-Daro (Staubwasser and Weiss, 2006; Sinha et al., 2011; Kathayat et al., 2017).

In addition to insolation and ITCZ-related processes, other possible mechanisms affecting the observed rainfall variations have also been suggested. An increased ENSO frequency during the Late Holocene, in contrast to the mid-Holocene (Moy et al., 2002; Conroy et al., 2008), may have significantly influenced the weakening of summer monsoon rainfall during the Holocene (**Figure 5**). Generally, El Niño conditions in the Pacific Ocean cause the failure of Indian summer monsoon rainfall and results in drought conditions in South Asia including Sri Lanka (Rasmusson and Carpenter, 1983; Kumar et al., 2006; Zubair et al., 2007; Sinha et al., 2011). In contrast, a positive correlation has been identified between El Niño and NEM in Southern India (Yadav, 2012). However, only the second inter monsoon (SIM) rainfall (October—November) in Sri Lanka show a positive correlation with El Niño conditions in Sri Lanka (Kane, 1998; Malmgren et al., 2003; Hapuarachchi and Jayawardena, 2015). Therefore, increasing El Niño frequency during the Late Holocene (**Figure 5**) could have diminished the summer monsoon rainfall in Sri Lanka. In addition, increasing the El Niño frequency can further drag the ITCZ southward, as observed during the LIA, that again causes a weakening of the Indian summer monsoon rainfall (Brown and Johnson, 2005; Banerji et al., 2019). However, according to the reconstructed ENSO records (Moy et al., 2002; Conroy et al., 2008), there is a more abrupt increase in the frequency of El Niño from middle to late Holocene rather than gradual variation. In addition, during the last ~1000 yrs BP, it shows a decreasing trend (**Figure 5D**). Therefore, it is obvious that increasing El Niño frequency could only have a partial influence on the observed inverse rainfall trends between the South Asian summer and winter monsoon. However, rapid increase of El Niño frequency between ~600 and 1200 cal yr BP (Moy et al., 2002) possibly have led the arid phase recorded in Horton plains around ~1000 cal yr BP (**Figure 4©**).

The peak of the arid phase identified in this study, ~3500 cal yr BP, coincides with a sharp negative excursion of the NAO index (**Figure 5**; Olsen et al., 2012) and shows a partial overlap with Bond event number 2 (**Figure 5**; Bond et al., 2001). Similarly, the onset of dry conditions at Horton Plains around 1000 cal yr BP also partially correlates with Bond event 1 (**Figure 5**; Bond et al., 2001; Steinhilber et al., 2009). A negative NAO results in cold

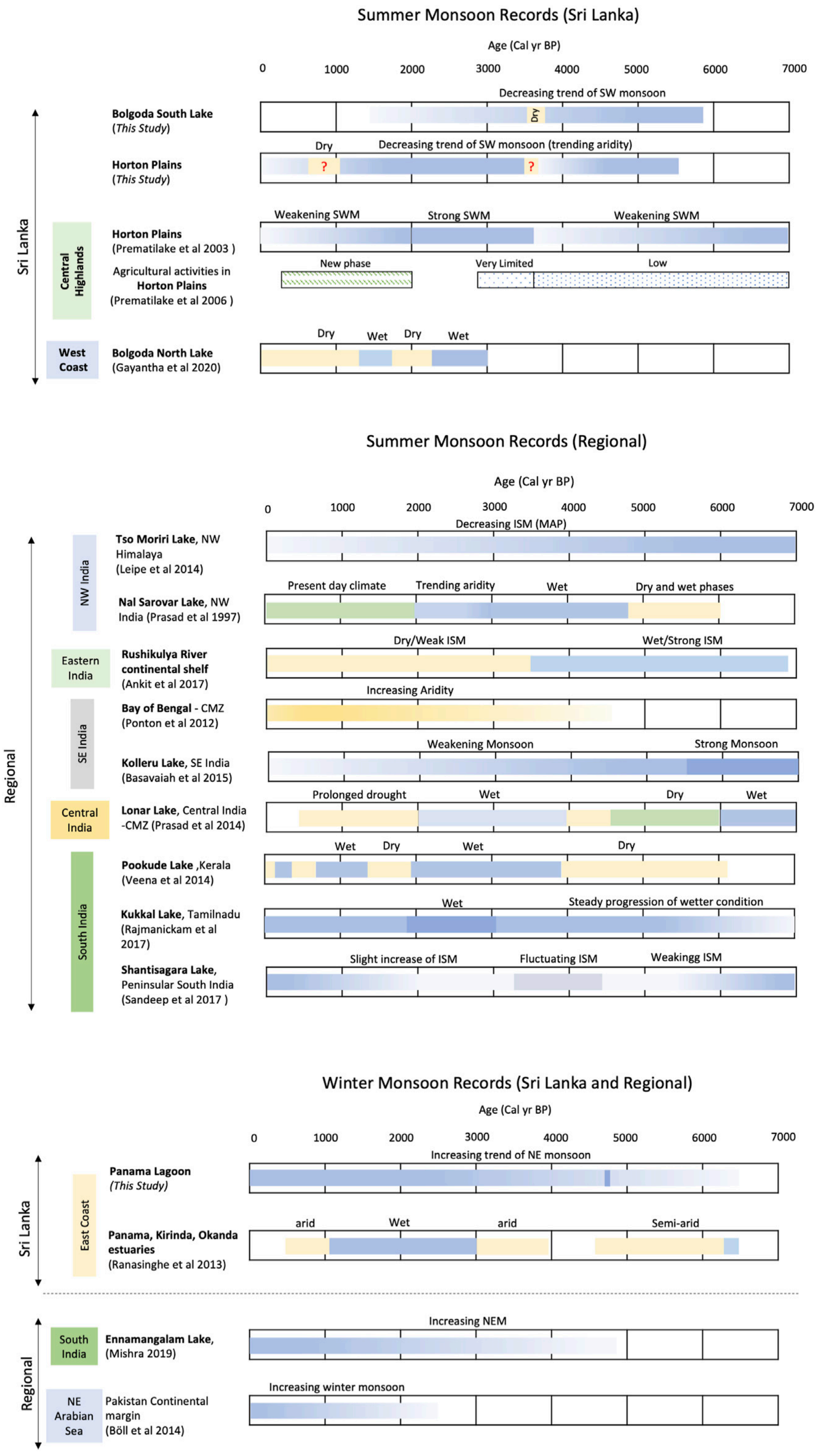

FIGURE 6 | Comparison with selected paleoclimate records in the region. Both summer and winter monsoonal records are presented.

winters in northern Europe, causing expanding ice sheets and increased snow cover over Eurasia. Similarly, Bond events represent North Atlantic ice rafting events (~1500 years cycle) related to cold periods in the Northern subpolar regions. These events are generally synchronous with periods of low solar activity during the Holocene (Bond et al., 2001; Banerji et al., 2020). These conditions also lead to failures in the development of a low-pressure trough in the northern and central parts of India, reducing South Asian summer monsoon rainfall over the Indian sub-continent (Bamzai and Shukla, 1999; Gupta et al., 2020). However, only Bond events 1 and 2 show at least partial correlation with the arid phases identified in our records. Whereas the rest of the Bond events or negative NAO conditions do not appear to lead to clear arid phases in our records. Therefore, it is unclear how exactly these arid events are induced by the interaction of different global climate variables and more high-resolution records are needed to answer this question.

Mid-Late Holocene Human-Environment Interactions in Sri Lanka

Many paleoclimate records available in Sri Lanka and India imply a general weakening trend of Indian summer monsoon during the middle and late Holocene (Prasad et al., 1997; Premathilake and Risberg, 2003; Ponton et al., 2012; Leipe et al., 2014; Prasad et al., 2014; Basavaiah et al., 2015; Ankit et al., 2017; Gayantha et al., 2017; Ratnayake et al., 2017; Gayantha et al., 2020, see **Figure 6**). The notable exception to this trend can be observed in the records from the South Indian peninsular region, which imply a progressive or stepwise increase in rainfall and/fluctuation in intensity in some cases (Veena et al., 2014; Rajmanickam et al., 2017; Sandeep et al., 2017, see **Figure 6**). However, these regions receive a significant amount of rainfall from the NEM (winter monsoon; between 17 and 49%) in addition to SWM (summer monsoon) rainfall (Sreekala et al., 2012). Indeed, the proxies used to reconstruct monsoon variability in these previous studies cannot distinguish between the source of monsoon rainfall (SWM or NEM). Regional records for winter monsoon rainfall variation are extremely limited. Some only cover the Late Holocene, while others show no clear trends. Nevertheless, in general, the available records show an overall increasing winter monsoon rainfall towards the present (Ranasinghe et al., 2013b; Böll et al., 2014; Mishra et al., 2019; see **Figure 6**). Our evidence from Sri Lanka allows us to contribute to existing work by isolating the impacts of the SWM and NEM in different sedimentary archives, supporting a decline in SWM precipitation and increase in NEM precipitation over the past 6,000 years in South Asia (**Figure 6**).

Prehistoric farming populations seem to have emerged in the lowland dry zone of Sri Lanka around 2900 cal yr BP (Deraniyagala, 1992; Myrdal-Runebjer, 1996). Dense rainforest in the wet zone and mountainous regions, by contrast, seem to have only seen limited agricultural activities at this time (Roberts et al., 2015). Flat terrain, savannah-type forests, and more stable NE monsoon rainfall may have attracted prehistoric and early historical agricultural societies to the lowlands of the dry zones. Notably, the extensive urban kingdoms of Anuradhapura and Polonnaruwa, associated with rice agriculture as well as the tending of orchards, emerged between ~2,500 and 800 cal yr BP with sophisticated hydraulic technology in the lowland dry zone (Jayasena et al., 2011; Bebermeier et al., 2017; Abeywardana et al., 2019). Around 900–800 cal yr BP, however, these kingdoms appear to have begun to shift towards the southwest and central highland areas (towards the wet zone through the intermediate zones), with invasions and failure in the hydraulic systems both postulated as potential drivers (Deraniyagala, 1992; Gilliland et al., 2013). Unfortunately, our NEM records are not of sufficient resolution to clearly understand the influence of rainfall on the abandonment of ancient kingdoms in the dry zone during this period (see Lucero et al., 2015), necessitating further work. That said, we can see that SWM rainfall in Sri Lanka has been decreasing continuously until the present in the lowland wet zone (similar to the highland wet zone) due to the key influence of orbital forcing factors. This weakening of SWM rainfall might have led to a decline in rainforest density (shrinking of the rainforest areas) in the wet zone of Sri Lanka, turning the southwestern areas of Sri Lanka into landscapes more suitable for rice agriculture at a time when cities were relocating from the northeastern portions of the island (Lucero et al., 2015).

CONCLUSION

The inverse relationship between South Asian summer and winter monsoons in Sri Lanka supports the hypothesis that the Earth's precession controlled the southward migration of the mean latitudinal position of the ITCZ during the last ~6000 cal yr BP, changing the distribution of interhemispheric solar insolation. The southward migration of the northernmost and southernmost positions of the ITCZ during this period increased the seasonal length of the winter monsoon in Sri Lanka while decreasing the seasonal length of the summer monsoon, resulting in an inverse relationship between summer and winter monsoon. The more abrupt weakening phases of rainfall is more pronounced in the summer monsoonal records, suggesting that the summer monsoon is more sensitive to other factors/teleconnections relative to the winter monsoon. However, systematic correlation between different climate variables (eg; NAO, Bond events and ENSO) and these arid events cannot always be identified in our records, suggesting these teleconnections are more complex and strongly influenced by regional factors. Nevertheless, the identified overall weakening trend of Southwest monsoon variability could have perhaps played an important role in social, economic, and political change witnessed across Sri Lanka between 2,500 and 9.00 years ago. Further well-dated high-resolution records are necessary to confirm and understand human-environment interactions in this part of the tropics during the Late Holocene, as well as the primary drivers of abrupt aridity events seen in the available records.

DATA AVAILABILITY STATEMENT

The original contributions presented in the study are included in the article/**Supplementary Material**, further inquiries can be directed to the corresponding author

AUTHOR CONTRIBUTIONS

GG designed the research idea. KG, GG, PR, OW, FO, RC, and JR participated field work. PF conducted microfauna analysis. JR conducted grain size analysis. KG conducted biomarker and CSIA analysis. KG wrote the manuscript. All authors contributed for reviewing the manuscript.

FUNDING

KG acknowledge Max Planck Society and International Max Planck Research School for Global Biogeochemical Cycles (IMPRS-gBGC) for funding this research project.

ACKNOWLEDGMENTS

We are grateful to Achim Brauer, GFZ, Potsdam for his consent and support to use the laboratory facilities. We thank Steffen Ruehlow, Maria Foerster, Sussane Karlsson and Oliver Rach for technical support and guidance in the laboratories. We also thank Axel Steinhof for ^{14}C measurements and Jana Ilgner for participating field work. Markus Lange helped with statistical analysis. Rik Tjallingii helped with XRF measurements. We are grateful to Sri Lanka Navy for supporting the fieldwork. We also thank Department of Wildlife Conservation, Irrigation Department, Department of Coastal Conservation, and Geological Survey and Mines Bureau of Sri Lanka for granting permission to conduct field work in the sites.

SUPPLEMENTARY MATERIAL

The Supplementary Material for this article can be found online at: https://www.frontiersin.org/articles/10.3389/feart.2021.789291/full#supplementary-material

Supplementary Figure S1 | Monthly average rainfall and temperature variations in three cities of Sri Lanka. **(A)** Sri Jayawardenepura-Colombo (Western province; lowland-wet zone), **(B)** Nuwara Eliya (Central province; central highlands-wet zone), **(C)** Arugambay (Eastern province; lowland-dry zone); NEM = Northeast monsoon, FIM = First Inter-monsoon, SWM = Southwest Monsoon, SIM = Second Inter-monsoon (data source: https://en.climate-data.org/).

Supplementary Figure S2 | Selected sites for the study; **(A)** Bolgoda South Lake; **(B)** Panama Lagoon; **(C)** Horton Plains.

Supplementary Figure S3 | Lithology and stratigraphy of the retrieved sediment/peat cores in the three sites.

Supplementary Figure S4 | Relative distribution of n-alkane (n-C_{15}–C_{33}) in the three sites.

Supplementary Figure S5 | Semiquantitative distribution of microfossils (Foraminifera, Ostracoda) and other taxa in Panama Lagoon sediment core. For additional information see **Supplementary Figure S6**.

Supplementary Figure S6 | Environmental Information (marine influence and water depth) derived from microfossil distribution in Panama Lagoon. The Foraminifer Abnormality Index (FAI) indicates the percentage of malformed foraminifer tests caused by environmental stress like non-marine salinity or pollution. PC1 and PC2 are sample scores on the two first axes of a PCA based on microfossil distributions. For detailed distributions see **Supplementary Figure S5**.

Supplementary Table S1 | ^{14}C dates of Bolgoda South Lake.

Supplementary Table S2 | ^{14}C dates of Panama Lagoon.

Supplementary Table S3 | ^{14}C dates of Horton Plains.

REFERENCES

Abeywardana, N., Pitawala, H. M. T. G. A., Schütt, B., and Bebermeier, W. (2019). Evolution of the Dry Zone Water Harvesting and Management Systems in Sri Lanka during the Anuradhapura Kingdom; a Study Based on Ancient Chronicles and Lithic Inscriptions. *Water Hist.* 11, 75–103. doi:10.1007/s12685-019-00230-7

Achyuthan, H., Deshpande, R. D., Rao, M. S., Kumar, B., Nallathambi, T., Shashi Kumar, K., et al. (2013). Stable Isotopes and Salinity in the Surface Waters of the Bay of Bengal: Implications for Water Dynamics and Palaeoclimate. *Mar. Chem.* 149, 51–62. doi:10.1016/j.marchem.2012.12.006

Achyuthan, H., Farooqui, A., Gopal, V., Phartiyal, B., and Lone, A. (2016). "Late Quaternary to Holocene Southwest Monsoon Reconstruction: A Review Based on Lake and Wetland Systems (Studies Carried Out during 2011-2016)". *Proc. Indian Natl. Sci. Acad.* 82, 847–868. doi:10.16943/ptinsa/2016/48489

Aghadadashi, V., Mehdinia, A., and Molaei, S. (2017). Origin, Toxicological and Narcotic Potential of Sedimentary PAHs and Remarkable Even/odd N-Alkane Predominance in Bushehr Peninsula, the Persian Gulf. *Mar. Pollut. Bull.* 114, 494–504. doi:10.1016/j.marpolbul.2016.10.013

Aloulou, F., Kallel, M., Dammak, M., Elleuch, B., and Saliot, A. (2010). Even-numbered N-Alkanes/n-Alkenes Predominance in Surface Sediments of Gabes Gulf in Tunisia. *Environ. Earth Sci.* 61, 1–10. doi:10.1007/s12665-009-0315-y

Ankit, Y., Kumar, P., Anoop, A., Mishra, P. K., and Varghese, S. (2017). Mid-late Holocene Climate Variability in the Indian Monsoon: Evidence from continental Shelf Sediments Adjacent to Rushikulya River, Eastern India. *Quat. Int.* 443, 155–163. doi:10.1016/j.quaint.2016.12.023

Bamzai, A. S., and Shukla, J. (19991999). Relation between Eurasian Snow Cover, Snow Depth, and the Indian Summer Monsoon: An Observational Study. *J. Clim.*, 2. doi:10.1175/1520-044210.1175/1520-0442(1999)012<3117:rbescs>2.0.co;2

Banerji, U. S., Arulbalaji, P., and Padmalal, D. (2020). Holocene Climate Variability and Indian Summer Monsoon: An Overview. *The Holocene* 30, 744–773. doi:10.1177/0959683619895577

Banerji, U. S., Bhushan, R., and Jull, A. J. T. (2019). Signatures of Global Climatic Events and Forcing Factors for the Last Two Millennia from the Active Mudflats of Rohisa, Southern Saurashtra, Gujarat, Western India. *Quat. Int.* 507, 172–187. doi:10.1016/j.quaint.2019.02.015

Basavaiah, N., Mahesh Babu, J. L. V., Gawali, P. B., Naga Kumar, K. C. V., Demudu, G., Prizomwala, S. P., et al. (2015). Late Quaternary Environmental and Sea Level Changes from Kolleru Lake, SE India: Inferences from mineral Magnetic, Geochemical and Textural Analyses. *Quat. Int.* 371, 197–208. doi:10.1016/j.quaint.2014.12.018

Bebermeier, W., Meister, J., Withanachchi, C., Middelhaufe, I., and Schütt, B. (2017). Tank cascade Systems as a Sustainable Measure of Watershed Management in South Asia. *Water* 9, 231–316. doi:10.3390/w9030231

Berger, A., and Loutre, M. F. (1994). Precession, Eccentricity, Obliquity, Insolation and Paleoclimates" in *Long-Term Climatic Variations*. Springer, 107–151. doi:10.1007/978-3-642-79066-9_5

Bisutti, I., Hilke, I., and Raessler, M. (2004). Determination of Total Organic Carbon - an Overview of Current Methods. *Trac Trends Anal. Chem.* 23, 716–726. doi:10.1016/j.trac.2004.09.003

Blaauw, M., and Christen, J. A. (2011). Flexible Paleoclimate Age-Depth Models Using an Autoregressive Gamma Process. *Bayesian Anal.* 6, 457–474. doi:10.1214/11-BA61810.1214/ba/1339616472

Böll, A., Lückge, A., Munz, P., Forke, S., Schulz, H., Ramaswamy, V., et al. (2014). Late Holocene Primary Productivity and Sea Surface Temperature Variations in the Northeastern Arabian Sea: Implications for winter Monsoon Variability. *Paleoceanography* 29, 778–794. doi:10.1002/2013PA002579

Bond, G., Kromer, B., Beer, J., Muscheler, R., Evans, M. N., Showers, W., et al. (2001). Persistent Solar Influence on north atlantic Climate during the Holocene. *Science* 294, 2130–2136. doi:10.1126/science.1065680

Brooks, P. D., Geilmann, H., Werner, R. A., and Brand, W. A. (2003). Improved Precision of coupled?13C and?15N Measurements from Single Samples Using an Elemental Analyzer/isotope Ratio Mass Spectrometer Combination with a post-column Six-Port Valve and Selective CO2 Trapping; Improved Halide Robustness of the Combustion Reactor Using CeO2. *Rapid Commun. Mass. Spectrom.* 17, 1924–1926. doi:10.1002/rcm.1134

Brown, E. T., and Johnson, T. C. (2005). Coherence between Tropical East African and South American Records of the Little Ice Age. *Geochem. Geophys. Geosyst.* 6, a–n. doi:10.1029/2005GC000959

Chandrajith, R., Chaturangani, D., Abeykoon, S., Barth, J. A. C., van Geldern, R., Edirisinghe, E. A. N. V., et al. (2014). Quantification of Groundwater-Seawater Interaction in a Coastal sandy Aquifer System: A Study from Panama, Sri Lanka. *Environ. Earth Sci.* 72, 867–877. doi:10.1007/s12665-013-3010-y

Conroy, J. L., Overpeck, J. T., Cole, J. E., Shanahan, T. M., and Steinitz-Kannan, M. (2008). Holocene Changes in Eastern Tropical Pacific Climate Inferred from a Galápagos lake Sediment Record. *Quat. Sci. Rev.* 27, 1166–1180. doi:10.1016/j.quascirev.2008.02.015

Davies, S. J., Lamb, H. F., and Roberts, S. J. (2015). "Micro-XRF Core Scanning in Palaeolimnology: Recent Developments," in *Micro-XRF Studies of Sediment Cores* (Springer), 189–226. doi:10.1007/978-94-017-9849-5_7

De Silva, K. M. (1981). *A History of Sri Lanka*. Oakland, CA: Univ of California Press.

Deraniyagala, S. U. (1992). *The Prehistory of Sri Lanka; an Ecological Perspective*. Sri Lanka: Department of Archaeological Survey.

Diefendorf, A. F., and Freimuth, E. J. (2017). Extracting the Most from Terrestrial Plant-Derived N-Alkyl Lipids and Their Carbon Isotopes from the Sedimentary Record: A Review. *Org. Geochem.* 103, 1–21. doi:10.1016/j.orggeochem.2016.10.016

Dixit, Y., and Tandon, S. K. (2016). Hydroclimatic Variability on the Indian Subcontinent in the Past Millennium: Review and Assessment. *Earth-Sci. Rev.* 161, 1–15. doi:10.1016/j.earscirev.2016.08.001

DWC (2007). "Biodiversity Baseline Survey: Horton Plains National Park. Consultancy Services Report prepared by Green, M.J.B.," in *ARD Inc in Association With Infotech IDEAS and GREENTECH Consultants*. Editors S. M. D. A. U. De Alwis, P. N. Dayawansa, R. How, B. M. P. Singhakumara, D. Weerakoon, and M. R. Wijesinghe (Colombo, Sri Lanka: Sri Lanka Protected Areas Management and Wildlife Conservation Project (PAM&WCP/CONSULT/02/BDBS), Department of Wildlife Conservation, Ministry of Environment and Natural Resources), 40.

Edirisinghe, E. A. N. V., Pitawala, H. M. T. G. A., Dharmagunawardhane, H. A., and Wijayawardane, R. L. (2017). Spatial and Temporal Variation in the Stable Isotope Composition (δ18O and δ2H) of Rain across the Tropical Island of Sri Lanka. *Isotopes Environ. Health Stud.* 53, 628–645. doi:10.1080/10256016.2017.1304936

Eglinton, T. I., and Eglinton, G. (2008). Molecular Proxies for Paleoclimatology. *Earth Planet. Sci. Lett.* 275, 1–16. doi:10.1016/j.epsl.2008.07.012

Ekpo, B. O., Oyo-Ita, O. E., and Wehner, H. (2005). Even-n-alkane/alkene Predominances in Surface Sediments from the Calabar River, SE Niger Delta, Nigeria. *Naturwissenschaften* 92, 341–346. doi:10.1007/s00114-005-0639-8

Elias, V. O., Simoneit, B. R. T., and Cardoso, J. N. (1997). Even N-Alkane Predominances on the Amazon Shelf and a Northeast Pacific Hydrothermal System. *Naturwissenschaften* 84, 415–420. doi:10.1007/s001140050421

Ellepola, G., and Ranawana, K. B. (2015). Panama Lagoon : A Unique Mangrove Ecosystem in the East Coast of Sri Lanka. *Wetl. Sri Lanka* 2, 10–19.

Erdelen, W. (1988). Forest Ecosystems and Nature Conservation in Sri Lanka. *Biol. Conservation* 43, 115–135. doi:10.1016/0006-3207(88)90086-9

Fleitmann, D., Burns, S. J., Mangini, A., Mudelsee, M., Kramers, J., Villa, I., et al. (2007). Holocene ITCZ and Indian Monsoon Dynamics Recorded in Stalagmites from Oman and Yemen (Socotra). *Quat. Sci. Rev.* 26, 170–188. doi:10.1016/j.quascirev.2006.04.012

Fleitmann, D., Burns, S. J., Mudelsee, M., Neff, U., Kramers, J., Mangini, A., et al. (2003). Holocene Forcing of the Indian Monsoon Recorded in a Stalagmite from Southern Oman. *Science* 300, 1737–1739. doi:10.1126/science.1083130

Gayantha, K., Routh, J., Anupama, K., Lazar, J., Prasad, S., Chandrajith, R., et al. (2020). Reconstruction of the Late Holocene Climate and Environmental History from North Bolgoda Lake, Sri Lanka, Using Lipid Biomarkers and Pollen Records. *J. Quat. Sci* 35, 514–525. doi:10.1002/jqs.3196

Gayantha, K., Routh, J., and Chandrajith, R. (2017). A Multi-Proxy Reconstruction of the Late Holocene Climate Evolution in Lake Bolgoda, Sri Lanka. *Palaeogeogr. Palaeoclimatol. Palaeoecol.* 473, 16–25. doi:10.1016/j.palaeo.2017.01.049

Gilliland, K., Simpson, I. A., Adderley, W. P., Burbidge, C. I., Cresswell, A. J., Sanderson, D. C. W., et al. (2013). The Dry Tank: Development and Disuse of Water Management Infrastructure in the Anuradhapura Hinterland, Sri Lanka. *J. Archaeological Sci.* 40, 1012–1028. doi:10.1016/J.JAS.2012.09.034

Goff, J., Chagué-Goff, C., Nichol, S., Jaffe, B., and Dominey-Howes, D. (2012). Progress in Palaeotsunami Research. *Sediment. Geology.* 243-244, 70–88. doi:10.1016/j.sedgeo.2011.11.002

Gupta, A. K., Prakasam, M., Dutt, S., Clift, P. D., and Yadav, R. R. (2020). "Evolution and Development of the Indian Monsoon," in *Geodynamics of the Indian Plate* (Springer), 499–535. doi:10.1007/978-3-030-15989-4_14

Hapuarachchi, H. A. S. U., and Jayawardena, I. M. S. P. (2015). Modulation of Seasonal Rainfall in Sri Lanka by ENSO Extremes. *December Sri Lanka J. Meteorol.* 1, 3–11.

Haug, G. H., Hughen, K. A., Sigman, D. M., Peterson, L. C., and Röhl, U. (2001). Southward Migration of the Intertropical Convergence Zone through the Holocene. *Science* 293, 1304–1308. doi:10.1126/science.1059725

Holtvoeth, J., Whiteside, J. H., Engels, S., Freitas, F. S., Grice, K., Greenwood, P., et al. (2019). The Paleolimnologist's Guide to Compound-specific Stable Isotope Analysis - an Introduction to Principles and Applications of CSIA for Quaternary lake Sediments. *Quat. Sci. Rev.* 207, 101–133. doi:10.1016/j.quascirev.2019.01.001

Hua, Q., Barbetti, M., and Rakowski, A. Z. (2013). Atmospheric Radiocarbon for the Period 1950-2010. *Radiocarbon* 55, 2059–2072. doi:10.2458/azu_js_rc.v55i2.16177

Jackson, K. L. (2008). *Paleotsunami History Recorded in Holocene Coastal Lagoon Sediments , Southeastern Sri LankaPaper 171Open Access Theses*.

Jayasena, H. A. H., Chandrajith, R., and Gangadhara, K. R. (2011). Water Management in Ancient Tank Cascade Systems (TCS) in Sri Lanka : Evidence for Systematic Tank Distribution. *J. Geol. Soc. Sri Lanka Prof. C. B. Dissanayake Felicitation* 14, 27–33.

Kane, R. P. (1998). ENSO Relationship to the Rainfall of Sri Lanka. *Int. J. Climatol* 18., 859–871. doi:10.1002/(SICI)1097-0088(19980630)18:8<859:AID-JOC264>3.0.CO;2-W10.1002/(sici)1097-0088(19980630)18:8<859:aid-joc264>3.0.co;2-w

Kassambara, A., and Mundt, F. (2020). *Factoextra: Extract and Visualize the Results of Multivariate Data Analyses*. R package version 1.0.7 https://CRAN.R-project.org/package=factoextra.

Kathayat, G., Cheng, H., Sinha, A., Yi, L., Li, X., Zhang, H., et al. (2017). The Indian Monsoon Variability and Civilization Changes in the Indian Subcontinent. *Sci. Adv.* 3, 1–9. doi:10.1126/sciadv.1701296

Kilmer, V. J., and Alexander, L. T. (1949). Methods of Making Mechanical Analyses of Soils. *Soil Sci.* 68, 15–24. doi:10.1097/00010694-194907000-00003

Kumar, K. K., Rajagopalan, B., Hoerling, M., Bates, G., and Cane, M. (2006). Unraveling the Mystery of Indian Monsoon Failure during El Niño. *Science* 314, 115–119. doi:10.1126/science.1131152

Kylander, M. E., Ampel, L., Wohlfarth, B., and Veres, D. (2011). High-resolution X-ray Fluorescence Core Scanning Analysis of Les Echets (France) Sedimentary Sequence: New Insights from Chemical Proxies. *J. Quat. Sci.* 26, 109–117. doi:10.1002/jqs.1438

Last, W. M., and Smol, J. P. (2002). *Tracking Environmental Change Using lake Sediments: Volume 1: basin Analysis, Coring, and Chronological Techniques*. Springer Science & Business Media.

Leipe, C., Demske, D., and Tarasov, P. E. (2014). A Holocene Pollen Record from the Northwestern Himalayan lake Tso Moriri: Implications for Palaeoclimatic and Archaeological Research. *Quat. Int.* 348, 93–112. doi:10.1016/j.quaint.2013.05.005

Liu, J., Chen, J., Zhang, X., Li, Y., Rao, Z., and Chen, F. (2015). Holocene East Asian Summer Monsoon Records in Northern China and Their Inconsistency with Chinese Stalagmite δ18O Records. *Earth-Science Rev.* 148, 194–208. doi:10.1016/j.earscirev.2015.06.004

Liu, X., Liu, J., Chen, S., Chen, J., Zhang, X., Yan, J., et al. (2020). New Insights on Chinese Cave δ18O Records and Their Paleoclimatic Significance. *Earth-Science Rev.* 207, 103216. doi:10.1016/j.earscirev.2020.103216

Lucero, L. J., Fletcher, R., and Coningham, R. (2015). From 'collapse' to Urban Diaspora: the Transformation of Low-Density, Dispersed Agrarian Urbanism. *Antiquity* 89, 1139–1154. doi:10.15184/aqy.2015.51

Malmgren, B. A., Hulugalla, R., Hayashi, Y., and Mikami, T. (2003). Precipitation Trends in Sri Lanka since the 1870s and Relationships to El Niño-Southern Oscillation. *Int. J. Climatol.* 23, 1235–1252. doi:10.1002/joc.921

Martin-Puertas, C., Tjallingii, R., Bloemsma, M., and Brauer, A. (2017). Varved Sediment Responses to Early Holocene Climate and Environmental Changes in Lake Meerfelder Maar (Germany) Obtained from Multivariate Analyses of Micro X-ray Fluorescence Core Scanning Data. *J. Quat. Sci.* 32, 427–436. doi:10.1002/jqs.2935

Meyers, P. A. (2003). Applications of Organic Geochemistry to Paleolimnological Reconstructions: a Summary of Examples from the Laurentian Great Lakes. *Org. Geochem.* 34, 261–289. doi:10.1016/S0146-6380(02)00168-7

Mirza, M. M. Q. (2011). Climate Change, Flooding in South Asia and Implications. *Reg. Environ. Change* 11, 95–107. doi:10.1007/s10113-010-0184-7

Mishra, P. K., Ankit, Y., Gautam, P. K., and Anoop, A. (2019). Inverse Relationship between South-West and north-east Monsoon during the Late Holocene: Geochemical and Sedimentological Record from Ennamangalam Lake, Southern India. *Catena* 182, 104117. doi:10.1016/j.catena.2019.104117

Misra, P., Tandon, S. K., and Sinha, R. (2019). Holocene Climate Records from lake Sediments in India: Assessment of Coherence across Climate Zones. *Earth-Science Rev.* 190, 370–397. doi:10.1016/j.earscirev.2018.12.017

Mohtadi, M., Prange, M., and Steinke, S. (2016). Palaeoclimatic Insights into Forcing and Response of Monsoon Rainfall. *Nature* 533, 191–199. doi:10.1038/nature17450

Moy, C. M., Seltzer, G. O., Rodbell, D. T., Anderson, D. M., Moy, A. D., Seltzer, G. O., et al. (2002). Variability of El Niño/Southern Oscillation Activity at Millennial Timescales during the Holocene Epoch. *Nature* 420, 162–165. doi:10.1038/nature01194

Myrdal-Runebjer, E. (1996). Rice and Millet: An Archaeological Case Study of a Sri Lankan Transbasin Reservoir System. *Gotarc Ser. B. Gothenbg. Archaeol. These.*

Naafs, B. D. A., Inglis, G. N., Blewett, J., McClymont, E. L., Lauretano, V., Xie, S., et al. (2019). The Potential of Biomarker Proxies to Trace Climate, Vegetation, and Biogeochemical Processes in Peat: A Review. *Glob. Planet. Change* 179, 57–79. doi:10.1016/j.gloplacha.2019.05.006

Nichols, J., Booth, R. K., Jackson, S. T., Pendall, E. G., and Huang, Y. (2010). Differential Hydrogen Isotopic Ratios of Sphagnum and Vascular Plant Biomarkers in Ombrotrophic Peatlands as a Quantitative Proxy for Precipitation-Evaporation Balance. *Geochimica et Cosmochimica Acta* 74, 1407–1416. doi:10.1016/j.gca.2009.11.012

Nishimura, M., and Baker, E. W. (1986). Possible Origin of with a Remarkable Even-To-Odd Predominance in Recent marine Sediments. *Geochimica et Cosmochimica Acta* 50, 299–305. doi:10.1016/0016-7037(86)90178-X

Olsen, J., Anderson, N. J., and Knudsen, M. F. (2012). Variability of the North Atlantic Oscillation over the Past 5,200 Years. *Nat. Geosci* 5, 808–812. doi:10.1038/ngeo1589

Peng, Y., Xiao, J., Nakamura, T., Liu, B., and Inouchi, Y. (2005). Holocene East Asian Monsoonal Precipitation Pattern Revealed by Grain-Size Distribution of Core Sediments of Daihai Lake in Inner Mongolia of north-central China. *Earth Planet. Sci. Lett.* 233, 467–479. doi:10.1016/j.epsl.2005.02.022

Perera, N. P. (1975). A Physiognomic Vegetation Map of Sri Lanka (Ceylon). *J. Biogeogr.* 2, 185–203. doi:10.2307/3037990

Ponton, C., Giosan, L., Eglinton, T. I., Fuller, D. Q., Johnson, J. E., Kumar, P., et al. (2012). Holocene Aridification of India. *Geophys. Res. Lett.* 39, a–n. doi:10.1029/2011GL050722

Prasad, S., Anoop, A., Riedel, N., Sarkar, S., Menzel, P., Basavaiah, N., et al. (2014). Prolonged Monsoon Droughts and Links to Indo-Pacific Warm Pool: A Holocene Record from Lonar Lake, central India. *Earth Planet. Sci. Lett.* 391, 171–182. doi:10.1016/j.epsl.2014.01.043

Prasad, S., Kusumgar, S., and Gupta, S. K. (1997). A Mid to Late Holocene Record of Palaeoclimatic Changes from Nal Sarovar: a Palaeodesert Margin lake in Western India. *J. Quat. Sci.* 12, 153–159. doi:10.1002/(SICI)1099-1417(199703/04)12:2<153:AID-JQS300>3.0.CO;2-X

Premathilake, R. (2012). Human Used Upper Montane Ecosystem in the Horton Plains, central Sri Lanka - a Link to Lateglacial and Early Holocene Climate and Environmental Changes. *Quat. Sci. Rev.* 50, 23–42. doi:10.1016/j.quascirev.2012.07.002

Premathilake, R., and Risberg, J. (2003). Late Quaternary Climate History of the Horton Plains, central Sri Lanka. *Quat. Sci. Rev.* 22, 1525–1541. doi:10.1016/S0277-3791(03)00128-8

R Core Team (2020). *R: A Language and Environment for Statistical Computing*. Vienna, Austria: R Foundation for Statistical Computing. https://www.r-project.org/https://www.r-project.org/.

Rach, O., Brauer, A., Wilkes, H., and Sachse, D. (2014). Delayed Hydrological Response to Greenland Cooling at the Onset of the Younger Dryas in Western Europe. *Nat. Geosci* 7, 109–112. doi:10.1038/ngeo2053

Rajmanickam, V., Achyuthan, H., Eastoe, C., and Farooqui, A. (2017). Early-Holocene to Present Palaeoenvironmental Shifts and Short Climate Events from the Tropical Wetland and lake Sediments, Kukkal Lake, Southern India: Geochemistry and Palynology. *The Holocene* 27, 404–417. doi:10.1177/0959683616660162

Ranasinghe, P. N., Ortiz, J. D., Moore, A. L., McAdoo, B., Wells, N., Siriwardana, C. H. E. R., et al. (2013a). Mid-Late Holocene Coastal Environmental Changes in southeastern Sri Lanka: New Evidence for Sea Level Variations in Southern Bay of Bengal. *Quat. Int.* 298, 20–36. doi:10.1016/j.quaint.2013.02.030

Ranasinghe, P., Ortiz, J., Smith, A., Griffith, E., Siriwardana, C., De Silva, S., et al. (2013b). Mid- to Late-Holocene Indian winter Monsoon Variability from a Terrestrial Record in Eastern and southeastern Coastal Environments of Sri Lanka. *The Holocene* 23, 945–960. doi:10.1177/0959683612475141

Ranawana, K. B. (2017). Mangroves of Sri Lanka. *Publ. Seacology-sudeesa Mangrove Mus.* 1, 25–28.

Ranjan, R. K., Routh, J., Val Klump, J., and Ramanathan, A. (2015). Sediment Biomarker Profiles Trace Organic Matter Input in the Pichavaram Mangrove Complex, southeastern India. *Mar. Chem.* 171, 44–57. doi:10.1016/j.marchem.2015.02.001

Ranwella, S. P. (1995). *A Checklist of Vertebrates of Bolgoda South Lake Area*. Dehiwala, Sri Lanka: Young Zoologists' Association.

Rasmusson, E. M., and Carpenter, T. H. (1983). The Relationship between Eastern Equatorial Pacific Sea Surface Temperatures and Rainfall over India and Sri Lanka. *Mon. Wea. Rev.* 111, 517–528. doi:10.1175/1520-0493(1983)111<0517

Ratnayake, A. S., Sampei, Y., Ratnayake, N. P., and Roser, B. P. (2017). Middle to Late Holocene Environmental Changes in the Depositional System of the Tropical Brackish Bolgoda Lake, Coastal Southwest Sri Lanka. *Palaeogeogr. Palaeoclimatol. Palaeoecol.* 465, 122–137. doi:10.1016/j.palaeo.2016.10.024

Reimer, P. J., Austin, W. E. N., Bard, E., Bayliss, A., Blackwell, P. G., Bronk Ramsey, C., et al. (2020). The IntCal20 Northern Hemisphere Radiocarbon Age Calibration Curve (0-55 Cal kBP). *Radiocarbon* 62, 725–757. doi:10.1017/RDC.2020.41

Roberts, P., Perera, N., Wedage, O., Deraniyagala, S., Perera, J., Eregama, S., et al. (2015). Direct Evidence for Human Reliance on Rainforest Resources in Late Pleistocene Sri Lanka. *Science (80-).* 347, 1246–1249. doi:10.1126/science.aaa1230

Ronkainen, T., McClymont, E. L., Tuittila, E.-S., and Väliranta, M. (2014). Plant Macrofossil and Biomarker Evidence of Fen-Bog Transition and Associated Changes in Vegetation in Two Finnish Peatlands. *The Holocene* 24, 828–841. doi:10.1177/0959683614530442

Routh, J., Hugelius, G., Kuhry, P., Filley, T., Tillman, P. K., Becher, M., et al. (2014). Multi-proxy Study of Soil Organic Matter Dynamics in Permafrost Peat Deposits Reveal Vulnerability to Climate Change in the European Russian Arctic. *Chem. Geology.* 368, 104–117. doi:10.1016/j.chemgeo.2013.12.022

Sachse, D., Billault, I., Bowen, G. J., Chikaraishi, Y., Dawson, T. E., Feakins, S. J., et al. (2012). Molecular Paleohydrology: Interpreting the Hydrogen-Isotopic

Composition of Lipid Biomarkers from Photosynthesizing Organisms. *Annu. Rev. Earth Planet. Sci.* 40, 221–249. doi:10.1146/annurev-earth-042711-105535

Sandeep, K., Shankar, R., Warrier, A. K., Yadava, M. G., Ramesh, R., Jani, R. A., et al. (2017). A Multi-Proxy lake Sediment Record of Indian Summer Monsoon Variability during the Holocene in Southern India. *Palaeogeogr. Palaeoclimatol. Palaeoecol.* 476, 1–14. doi:10.1016/j.palaeo.2017.03.021

Schneider, T., Bischoff, T., and Haug, G. H. (2014). Migrations and Dynamics of the Intertropical Convergence Zone. *Nature* 513, 45–53. doi:10.1038/nature13636

Sessions, A. L., Burgoyne, T. W., Schimmelmann, A., and Hayes, J. M. (1999). Fractionation of Hydrogen Isotopes in Lipid Biosynthesis. *Org. Geochem.* 30, 1193–1200. doi:10.1016/s0146-6380(99)00094-7

Singh, A., Jani, R. A., and Ramesh, R. (2010). Spatiotemporal Variations of the δ18O-salinity Relation in the Northern Indian Ocean. *Deep Sea Res. Oceanographic Res. Pap.* 57, 1422–1431. doi:10.1016/j.dsr.2010.08.002

Sinha, A., Stott, L., Berkelhammer, M., Cheng, H., Edwards, R. L., Buckley, B., et al. (2011). A Global Context for Megadroughts in Monsoon Asia during the Past Millennium. *Quat. Sci. Rev.* 30, 47–62. doi:10.1016/j.quascirev.2010.10.005

Sreekala, P. P., Rao, S. V. B., and Rajeevan, M. (2012). Northeast Monsoon Rainfall Variability over South Peninsular India and its Teleconnections. *Theor. Appl. Climatol.* 108, 73–83. doi:10.1007/s00704-011-0513-x

Srivastava, R., Ramesh, R., and Rao, T. N. (2014). Stable Isotopic Differences between Summer and winter Monsoon rains over Southern India. *J. Atmos. Chem.* 71, 321–331. doi:10.1007/s10874-015-9297-1

Staubwasser, M., and Weiss, H. (2006). Holocene Climate and Cultural Evolution in Late Prehistoric-Early Historic West Asia. *Quat. Res.* 66, 372–387. doi:10.1016/j.yqres.2006.09.001

Steinhilber, F., Beer, J., and Fröhlich, C. (2009). Total Solar Irradiance during the Holocene. *Geophys. Res. Lett.* 36, L19704. doi:10.1029/2009GL040142

Steinhof, A., Altenburg, M., and Machts, H. (2017). Sample Preparation at the Jena 14C Laboratory. *Radiocarbon* 59, 815–830. doi:10.1017/RDC.2017.50

Thompson, L. G., Mosley-Thompson, E., Bolzan, J. F., and Koci, B. R. (1985). A 1500-year Record of Tropical Precipitation in Ice Cores from the Quelccaya Ice Cap, Peru. *Science* 229, 971–973. doi:10.1126/science.229.4717.971

Veena, M. P., Achyuthan, H., Eastoe, C., and Farooqui, A. (2014). A Multi-Proxy Reconstruction of Monsoon Variability in the Late Holocene, South India. *Quat. Int.* 325, 63–73. doi:10.1016/j.quaint.2013.10.026

Weerakkody, U. (1992). The Holocene Coasts of Sri Lanka. *Geographical J.* 158, 300–306. doi:10.2307/3060299

Weltje, G. J., and Tjallingii, R. (2008). Calibration of XRF Core Scanners for Quantitative Geochemical Logging of Sediment Cores: Theory and Application. *Earth Planet. Sci. Lett.* 274, 423–438. doi:10.1016/j.epsl.2008.07.054

Werner, R. A., and Brand, W. A. (2001). Referencing Strategies and Techniques in Stable Isotope Ratio Analysis. *Rapid Commun. Mass. Spectrom.* 15, 501–519. doi:10.1002/rcm.258

Wijetunge, J. J. (2006). Tsunami on 26 December 2004: Spatial Distribution of Tsunami Height and the Extent of Inundation in Sri Lanka. *Sci. Tsunami Hazards* 24, 225–239.

Yadav, R. K. (2012). Why Is ENSO Influencing Indian Northeast Monsoon in the Recent Decades? *Int. J. Climatol.* 32, 2163–2180. doi:10.1002/joc.2430

Zhisheng, A., Guoxiong, W., Jianping, L., Youbin, S., Yimin, L., Weijian, Z., et al. (2015). Global Monsoon Dynamics and Climate Change. *Annu. Rev. Earth Planet. Sci.* 43, 29–77. doi:10.1146/annurev-earth-060313-054623

Zubair, L., Siriwardhana, M., Chandimala, J., and Yahiya, Z. (2007). Predictability of Sri Lankan Rainfall Based on ENSO. *Int. J. Climatol.* 28, 91–101. doi:10.1002/joc.1514

Conflict of Interest: The authors declare that the research was conducted in the absence of any commercial or financial relationships that could be construed as a potential conflict of interest.

Advantages of publishing in Frontiers

OPEN ACCESS
Articles are free to read
for greatest visibility
and readership

FAST PUBLICATION
Around 90 days
from submission
to decision

HIGH QUALITY PEER-REVIEW
Rigorous, collaborative,
and constructive
peer-review

TRANSPARENT PEER-REVIEW
Editors and reviewers
acknowledged by name
on published articles

Frontiers
Avenue du Tribunal-Fédéral 34
1005 Lausanne | Switzerland

Visit us: www.frontiersin.org
Contact us: frontiersin.org/about/contact

REPRODUCIBILITY OF RESEARCH
Support open data
and methods to enhance
research reproducibility

DIGITAL PUBLISHING
Articles designed
for optimal readership
across devices

FOLLOW US
@frontiersin

IMPACT METRICS
Advanced article metrics
track visibility across
digital media

EXTENSIVE PROMOTION
Marketing
and promotion
of impactful research

LOOP RESEARCH NETWORK
Our network
increases your
article's readership